Transactions of the ASME

Journal of Applied Mechanics

Published Quarterly by The American Society of Mechanical Engineers

VOLUME 47 • NUMBER 3 • SEPTEMBER 1980

Journal of Applied Mechanics (ISSN 0021-8936) is edited and published quarterly at the offices of The American Society of Mechanical Engineers, United Engineering Center, 345 E. 47th St., New York, N. Y. 10017. ASME-TWX No. 710-581-5267, New York. Second Class postage paid at New York, N. Y., and at additional mailing offices.

CHANGES OF ADDRESS must be received at Society headquarters seven weeks before they are to be effective. Please send old label and new address.

PRICES: To members, $25.00, annually; to nonmembers, $50.00. Single copies, $15.00 each. Add $1.50 for postage to countries outside the United States and Canada.

STATEMENT from By-Laws. The Society shall not be responsible for statements or opinions advanced in papers or . . . printed in its publications (B13, Par. 4).

INDEXED by the Engineering Index, Inc.

(Contents continued on Page 696)

CONTENTS (CONTINUED)

DESIGN DATA AND METHODS

BRIEF NOTES

DISCUSSIONS

BOOK REVIEWS

(Contents continued on Inside Back Cover)

CONTENTS (CONTINUED)

ERRATUM

L.-S. Yao
Assistant Professor,
Department of Mechanical and Industrial Engineering,
University of Illinois at Urbana-Champaign,
Urbana, Ill. 61801
Assoc. Mem. ASME

I. Catton
Professor.
Mem. ASME

J. M. McDonough
Research Engineer.
Student Mem. ASME

Department of Chemical, Nuclear, and Thermal Engineering,
University of California,
Los Angeles, Calif. 90024

Asymmetric Boundary Layer on a Nonisothermally Heated Cone

The development of a three-dimensional boundary layer along a heated cone is analyzed. The surface of the cone is heated under the condition of constant wall heat flux. The perturbation solution is obtained for the flow close to the leading edge where the buoyancy force can be treated as a higher-order effect. A finite-difference solution is obtained for the flow far downstream from the leading edge where buoyancy is one of the cominant forces. The numerical results clearly describe the boundary-layer development along heated cones of different cone angles as well as the heat transfer rate. Boundary-layer stability is briefly discussed in terms of the boundary-layer shape factor.

Introduction

Axisymmetric forced-convection laminar boundary layers exist for both external flows (over a swimming body) and internal flows (pipe flow), and are important for various engineering applications. Extensive studies have been conducted also due to their fundamental importance in laminar flow theory [1]; in particular, heating seems to be an effective way to stabilize the water boundary layer and to delay the growth of Tollmien-Schlichting instability waves [2].

The effects of buoyancy-induced secondary flow, which destroys the axisymmetry of the laminar boundary layer over an axisymmetric body (or in a circular pipe), has rarely been studied due to the complex three-dimensional flow. Some perturbation solutions have been obtained for both external flow (longitudinal cylinders or cones) [3, 4] and internal flow (pipe flow) [1]. Although the perturbation solutions are valid only in a narrow region close to the leading edge of an axisymmetric body (or the entrance of a pipe), the results indicate that the classical heat-transfer correlation and the flow velocity distributions, which do not consider the asymmetric secondary-flow effect, can be in error.

The buoyancy effect on the development of the boundary layer predicted by the perturbation method is always symmetric or antisymmetric with respect to $\phi = 90°$ [5]. This kind of simple three-dimensional flow exists only in the narrow region close to the leading edge of an axisymmetric body (or the entrance of pipe). A solution valid downstream of this region, where the secondary flow cannot be treated as a higher-order effect, is needed for practical applications.

A recent finite-difference solution of cylinder flow reveals that the three-dimensional boundary layer develops downstream in a way quite different than predicted by the perturbation solution. In this paper the three-dimensional boundary layer along a cone, whose surface is heated under the condition of constant wall heat flux, is considered. A perturbation analysis is performed to determine the relevant coordinate scales as well as the magnitude of the velocity scales. A finite-difference method is then used to solve the three-dimensional boundary-layer flow. The physical model considered is a semi-infinite cone which is aligned with its axis parallel to a uniform free stream and normal to the direction of gravity. This closely models the front part of an axisymmetric body with a sharp nose tip (see Fig. 1). The free stream is assumed to have a velocity u_∞ and temperature T_∞. Since the change in the fluid density is usually small compared with the fluid density, the Boussinesq approximation is adopted to simplify the analysis.

The perturbation solution indicates that the buoyancy-effect amplifies downstream for cones whose half angle, α, is less than 70°; for the cone whose angle is larger than 70°, the buoyancy effect on the development of the axial velocity decreases downstream. This suggests that the perturbation solution is valid uniformly for the flow over cones of $\alpha > 70°$. In this paper, we concentrate on the boundary-layer flow which experiences an increasing bouyancy effect downstream. Two cone angles, $\alpha = 10°$ and 30°, are selected to demonstrate the difference of the flow development due to the interaction of the axial pressure gradient and the buoyancy forces.

The numerical results show that the perturbation solution is valid only when $\bar{x} < 0.1\, l/\epsilon^{2/3-5n}$ for a cone angle is smaller than 70°. The

Contributed by the Applied Mechanics Division for publication in the JOURNAL OF APPLIED MECHANICS.

Discussion on this paper should be addressed to the Editorial Department, ASME, United Engineering Center, 345 East 47th Street, New York, N. Y. 10017, and will be accepted until December 1, 1980. Readers who need more time to prepare a discussion should request an extension from the Editorial Department. Manuscript received by ASME Applied Mechanics Division, July, 1979; final revision, March, 1980.

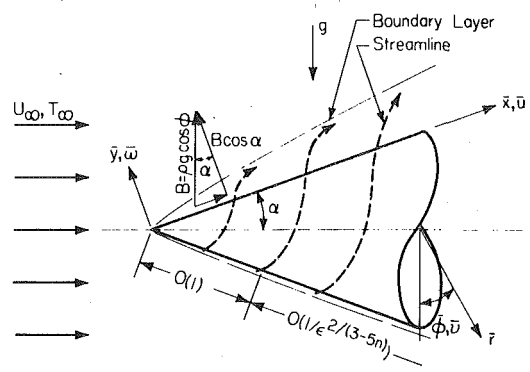

Fig. 1 Physical model and coordinates

physical meanings of l, ϵ, and n are explained in equations (2) and (3). The development of the boundary layer is influenced by two components of the buoyancy force. One is parallel to the cone surface along the axial direction. This force acts as a favorable body force along the upper half of the cone and as an unfavorable body force along the lower part. Since its magnitude is proportional to $\sin\alpha$ it is important for the flow past a cone of moderate cone angle, say $\alpha = 30°$. The other component of the buoyancy force is perpendicular to the free stream. This force drives the secondary flow and is important for small-angle cone flow, say $\alpha = 10°$. Due to the competition of these two components of the buoyancy force, the boundary-layer development along a heated cone is quite different for cones of different angles. Moreover, the heat transfer characteristics of the three-dimensional boundary layer differ considerably from those of a two-dimensional forced-convection boundary layer.

Analysis

The flow past a heated cone can be described by the Boussinesq approximation of the Navier-Stokes equations. In the coordinates shown in Fig. 1, the governing equations are as follows:

$$\frac{1}{\bar{r}}\left[\frac{\partial(\bar{r}\bar{u})}{\partial\bar{x}}+\frac{\partial(\bar{r}\bar{w})}{\partial\bar{y}}+\frac{\partial\bar{v}}{\partial\phi}\right]=0 \tag{1a}$$

$$\bar{u}\frac{\partial\bar{u}}{\partial\bar{x}}+\bar{w}\frac{\partial\bar{u}}{\partial\bar{y}}+\frac{\bar{v}}{\bar{r}}\frac{\partial\bar{u}}{\partial\phi}-\frac{\bar{v}^2}{\bar{r}}\sin\alpha=\frac{-1}{\rho_\infty}\frac{\partial\bar{P}}{\partial\bar{x}} -(g\beta\Delta T)\cos\phi\sin\alpha+\frac{\nu}{\bar{r}}\left\{\frac{\partial}{\partial\bar{y}}\left[\bar{r}\left(\frac{\partial\bar{u}}{\partial\bar{y}}-\frac{\partial\bar{w}}{\partial\bar{x}}\right)\right] +\frac{\partial}{\partial\phi}\left[\frac{1}{\bar{r}}\frac{\partial\bar{u}}{\partial\phi}-\frac{1}{\bar{r}}\frac{\partial(\bar{r}\bar{v})}{\partial\bar{x}}\right]\right\} \tag{1b}$$

$$\bar{u}\frac{\partial\bar{v}}{\partial\bar{x}}+\bar{w}\frac{\partial\bar{v}}{\partial\bar{y}}+\frac{\bar{v}}{\bar{r}}\frac{\partial\bar{v}}{\partial\phi} +\frac{(\bar{u}\sin\alpha+\bar{w}\cos\alpha)\,\bar{v}}{\bar{r}}=\frac{-1}{\bar{r}\,\rho_\infty}\frac{\partial\bar{P}}{\partial\phi} +(g\beta\Delta T)\sin\phi+\nu\left\{\frac{\partial}{\partial\bar{y}}\left[\frac{1}{\bar{r}}\frac{\partial(\bar{r}\bar{v})}{\partial\bar{y}}-\frac{1}{\bar{r}}\frac{\partial\bar{w}}{\partial\phi}\right]+\frac{\partial}{\partial\bar{x}} \times\left[\frac{1}{\bar{r}}\frac{\partial(\bar{r}\bar{v})}{\partial\bar{x}}-\frac{1}{\bar{r}}\frac{\partial\bar{u}}{\partial\phi}\right]\right\} \tag{1c}$$

$$\bar{u}\frac{\partial\bar{w}}{\partial\bar{x}}+\bar{w}\frac{\partial\bar{w}}{\partial\bar{y}}+\frac{\bar{v}}{\bar{r}}\frac{\partial\bar{w}}{\partial\phi}-\frac{\bar{v}^2}{r}\cos\phi=\frac{-1}{\rho_\infty}\frac{\partial\bar{P}}{\partial\bar{y}}-(g\beta\Delta T)\cos\phi\cos\alpha +\frac{\nu}{\bar{r}}\left[\frac{\partial}{\partial\phi}\frac{1}{\bar{r}}\left[\frac{\partial\bar{w}}{\partial\phi}-\frac{\partial(\bar{r}\bar{v})}{\partial\bar{y}}\right]+\frac{\partial}{\partial\bar{x}}\left[\bar{r}\left(\frac{\partial\bar{w}}{\partial\bar{x}}-\frac{\partial\bar{u}}{\partial\bar{y}}\right)\right]\right\} \tag{1d}$$

$$\bar{u}\frac{\partial T}{\partial\bar{x}}+\bar{w}\frac{\partial T}{\partial\bar{y}}+\frac{\bar{v}}{\bar{r}}\frac{\partial T}{\partial\phi}=\kappa\left[\frac{\partial^2T}{\partial\bar{x}^2}+\frac{\partial^2T}{\partial\bar{y}^2}+\frac{1}{\bar{r}^2}\frac{\partial^2T}{\partial\phi^2}\right] \tag{1e}$$

Inviscid flow past a heated cone behaves identically to that past an unheated cone since no heat is transferred outside the thermal boundary layer. The fluid temperature outside the thermal boundary is uniform and equals the free-stream temperature. The flow is axisymmetric with respect to the cone axis, see Fig. 1. The solution of the inviscid flow (see [6]) along the cone surface, which is required to evaluate the pressure gradient of the boundary-layer equations, is

$$\bar{u}=u_\infty\,\bar{x}^n, \tag{2}$$

where u_∞ is the undisturbed free-stream velocity; and n, (the value of which can be found from [6]) is related to the cone angle.

Upstream Solution. Equations (1) are simplified for the boundary layer by introducing the following dimensionless variables:

$$\begin{aligned}
x_1 &= \bar{x}/l, \quad y_1=\bar{y}(\mathrm{Re}^{1/2})/l,\\
r &= \bar{r}/l = x_1\sin\alpha + y_1/\mathrm{Re}^{1/2}\cos\alpha && \text{(coordinates)}\\
u_1 &= \bar{u}/u_\infty, \quad v_1=\bar{v}/u_\infty, && \text{(velocities}\\
w_1 &= w(\mathrm{Re}^{1/2})/u_\infty\\
\theta_1 &= k(\mathrm{Re}^{1/2})/lq_w)(T-T_\infty) && \text{(temperature)}\\
\mathrm{Re} &= (u_\infty l)/\nu && \text{(Reynolds No.)}\\
\mathrm{Gr} &= (\beta g l^4\, q_w)/(k\nu^2) && \text{(Grashof No.)}\\
P_1 &= \bar{p}/\rho_\infty\, u_\infty{}^2 && \text{(pressure)}\\
\mathrm{Pr} &= \nu_\infty/\alpha; && \text{(Prandtl No.)}\\
\kappa &= k/\rho_\infty\, c_p; && \text{(thermal diffusivity)}\\
\epsilon &= \mathrm{Gr}/\mathrm{Re}^{5/2}
\end{aligned} \tag{3}$$

The wall heat flux, q_w, is assumed constant in this work. l is taken to be the distance from the cone apex to the location where the inviscid velocity along the cone surface reaches u_∞. The normal coordinate, y, is scaled to reflect that the thickness of the boundary layer is proportional to $1/\mathrm{Re}^{1/2}$.

In terms of the dimensionless variables defined in equations (3), equations (1) become

$$\frac{1}{x_1}\frac{\partial(x_1u_1)}{\partial x_1}+\frac{\partial w_1}{\partial y_1}+\frac{1}{x_1\sin\alpha}\frac{\partial v_1}{\partial\phi}=0 \tag{4a}$$

$$u_1\frac{\partial u_1}{\partial x_1}+w_1\frac{\partial u_1}{\partial y_1}+\frac{v_1}{x_1\sin\alpha}\frac{\partial u_1}{\partial\phi}-\frac{v_1{}^2}{x_1}= -\frac{\partial P_1}{\partial x_1}-\epsilon\theta_1\cos\phi\sin\alpha+\frac{\partial^2u_1}{\partial y_1{}^2} \tag{4b}$$

$$u_1\frac{\partial v_1}{\partial x_1}+w_1\frac{\partial v_1}{\partial y_1}+\frac{v_1}{x_1\sin\alpha}\frac{\partial v_1}{\partial\phi}+\frac{u_1v_1}{x_1} =\frac{-1}{x_1\sin\alpha}\frac{\partial P_1}{\partial\phi}+\epsilon\theta_1\sin\phi+\frac{\partial^2v_1}{\partial y_1{}^2} \tag{4c}$$

$$\frac{\partial P_1}{\partial y_1}=0(1/\mathrm{Re}^{1/2}) \tag{4d}$$

$$u_1\frac{\partial\theta_1}{\partial x_1}+w_1\frac{\partial\theta_1}{\partial y_1}+\frac{v_1}{x_1\sin\alpha}\frac{\partial\theta_1}{\partial\phi}=\frac{1}{\mathrm{Pr}}\frac{\partial^2\theta_1}{\partial y_1{}^2} \tag{4e}$$

after neglecting smaller-order terms.

Equation (4d) states that the variation of the pressure across the thin boundary layer is a higher-order effect. Therefore, the pressure gradients in equations (4b) and (4c) can be evaluated from equation (2). They are

$$\frac{\partial P_1}{\partial x_1}=-nx_1{}^{2n-1} \quad \text{and} \quad \frac{\partial P_1}{\partial\phi}=0 \tag{5}$$

ϵ represents the ratio of the buoyancy force to the viscous force inside the boundary layer. Its value depends on the fluid properties, the flow speed, and the heat transfer rate; it is usually quite small for the practical problems in which we are interested. In this paper, we will restrict attention to the case where ϵ is small. From equations (4b) and (4c), one can conclude that the buoyancy, the driving force to cause the asymmetric flow, can be treated as a perturbation quantity if ϵ is small. The advantage of this is quite obvious. The zeroth-order

solution of equations (4), without considering the buoyancy effect, is simply the axisymmetric cone flow for forced convection; and a similarity solution exists for such a flow. Since the perturbation equations of higher orders are linear, their solutions should be expressible in terms of a similarity variable. This is true for the problem studied here.

The velocities and temperature can be expressed in terms of the stream functions and the temperature functions as

$$u_1 = x_1^n \left[f_0' + \epsilon x_1^{[(3-5n)/2]} \frac{\cos\phi}{\sin\alpha} F_1' + \ldots \right] \tag{6a}$$

$$v_1 = \epsilon x_1^{[(3-3n)/2]} F_2' \sin\phi + \ldots \tag{6b}$$

$$w_1 = \sqrt{\frac{2}{n+3}}\, x_1^{[(n-1)/2]} \left[\left(\frac{1-n}{2}\eta f_0' - \frac{n+3}{2} f_0 \right) + \epsilon x_1^{[(3-5n)/2]} \left\{ \frac{1-n}{2}\eta F_1' + (2n-3) F_1 - F_2 \right\} \frac{\cos\phi}{\sin\alpha} + \ldots \right] \tag{6c}$$

$$\theta_1 = \sqrt{\frac{2}{n+3}}\, x_1^{[(1-n)/2]} \left[\bar{\theta}_0 + \epsilon x_1^{[(3-5n)/2]} G \frac{\cos\phi}{\sin\alpha} + \ldots \right] \tag{6d}$$

where the functions f_0, F_1, F_2, $\bar{\theta}_0$, and G depend on η only; and $\eta = y_1 \sqrt{[(n+3)/2]}\, x_1^{n-1}$ is the similarity variable. The ordinary differential equations which govern the functions f_0, F_1, F_2, $\bar{\theta}_0$, and G can be obtained by substituting equations (5) and (6) into equations (4), and then separating the terms of equal order in ϵ. They are

$$f_0''' + f_0 f_0'' + [2n/(n+3)]\,(1 - f_0'^2) = 0 \tag{7a}$$

$$\theta_0'' + \mathrm{Pr}[f_0 \bar{\theta}_0' + [(n-1)/(n+3)]\, f_0' \bar{\theta}_0] = 0, \tag{7b}$$

and

$$F_1''' + f_0 F_1'' - \frac{(4-2n)}{n+3} f_0' F_1' + \frac{6-4n}{n+3} f_0'' F_1 + f_0'' F_2 = -\sqrt{\frac{n+3}{2}} \sin^2\alpha\, \bar{r}_0, \tag{8a}$$

$$F_2''' + f_0 F_2'' - \frac{6-4n}{n+3} f_0' F_2' = \sqrt{\frac{n+3}{2}} \bar{\theta}_0, \tag{8b}$$

$$1/\mathrm{Pr}\, G'' + f_0 G' + \frac{6n-4}{n+3} f_0' G = \frac{1-n}{2} F_1' \bar{\theta}_0 - (3-2n) F_1 \bar{\theta}_0' - F_2 \bar{\theta}_0' \tag{8c}$$

The associated boundary conditions are

$$f_0(0) = f_0'(0) = F_1(0) = F_1'(0) = F_2(0) = F_2'(0) = 0 \quad \text{(no-slip condition);} \tag{9a}$$

$$\bar{\theta}_0'(0) = -1, \quad G(0) = 0 \quad \text{(constant wall heat flux);} \tag{9b}$$

$$f_0'(\infty) \to 1, \quad F_1'(\infty) = F_2'(\infty) = \bar{\theta}_0(\infty) = G(\infty) \to 0 \quad \text{(match with the inviscid solution).} \tag{9c}$$

The term f_0 in equation (7a) simply describes the flow past an unheated cone, as given by Mangler. $\bar{\theta}_0$ in equation (7b), is the forced-convection temperature distribution with the constant wall heat flux condition. F_1, from equation (8a) represents the change of the axial boundary layer due to the buoyancy force as well as to the secondary flow, F_2 from equation (8b). G, from equation (8c), represents the temperature redistribution due to the free convection. The values of the functions f_0, F_1, F_2, $\bar{\theta}_0$, and G can be obtained in a straightforward manner by numerically integrating equations (7) and (8) with the boundary conditions given by equations (9). However, equations (6) reveal that the perturbation solution is valid only when $\epsilon x_1^{[(3-5n)/2]} < 1$. In other words, the originally small asymmetric flow grows downstream and cannot be treated as a perturbed quantity when $x_1 > \epsilon^{[2/(5n-3)]}$ with $n < 0.6$. The restriction of $n < 0.6$ corresponds to cones whose half angle is approximately smaller than 70°. For $n > 0.6$ (cone whose half angle is larger than 70°) the flow far away from the apex will eventually approach the axisymmetric flow since the influence of the buoyancy force is overwhelmed by the favorable pressure gradient along the cone surface.

In this paper, we consider only small-angle cones, i.e., $n < 0.6$. Here, the buoyancy force becomes one of the dominant forces when x is not small. Also, the perturbation solution (6) can be applied only in the region close to the cone apex. In the following, we will construct a solution which is not only valid for small $\bar{x}$ (approximately $0(l)$) but which can also be applied farther downstream. Therefore, we do not present the upstream solutions (6) in this paper.

Downstream Solutions. The downstream dimensionless variables can readily be found from equations (6). They are

$$x_2 = \frac{\bar{x}}{l\epsilon^{[-2/(3-5n)]}}, \quad y_2 = \frac{\bar{y}(\mathrm{Re})^{1/2}}{l\epsilon^{[(n-1)/(3-5n)]}}; \quad \text{(coordinates);} \tag{10a}$$

$$u_2 = \frac{\bar{u}}{u_\infty \epsilon^{[(-2n)/(3-5n)]}}, \quad v_2 = \frac{\bar{v}}{u_\infty \epsilon^{[(-2n)/(3-5n)]}}, \quad w_2 = \frac{\bar{w}(\mathrm{Re})^{1/2}}{u_\infty \epsilon^{[(n-1)/(3-5n)]}}; \quad \text{(velocities);} \tag{10b}$$

$$P_2 = \frac{\bar{P}}{\rho_\infty u_\infty{}^2 \epsilon^{[(-4n)/(3-5n)]}}; \quad \text{(pressure);} \tag{10c}$$

$$\theta_2 = \frac{k(\mathrm{Re})^{1/2}}{l q_w \epsilon^{[(n-1)/(3-5n)]}} (T - T_\infty); \quad \text{(temperature)} \tag{10d}$$

From now on, all the variables are defined in the downstream coordinates.

In terms of the dimensionless variables in equations (10), equations (1), after neglecting the smaller-order terms, become

$$\frac{1}{x_2}\frac{\partial(x_2 u_2)}{\partial x_2} + \frac{\partial w_2}{\partial y_2} + \frac{1}{x_2 \sin\alpha}\frac{\partial v_2}{\partial\phi} = 0 \tag{11a}$$

$$u_2 \frac{\partial u_2}{\partial x_2} + w_2 \frac{\partial u_2}{\partial y_2} + \frac{v_2}{x_2 \sin\alpha}\frac{\partial u_2}{\partial\phi} - \frac{v_2^2}{x_2} = n x_2^{2n-1} - \theta_2 \cos\phi \sin\alpha + \frac{\partial^2 u_2}{\partial y_2{}^2} \tag{11b}$$

$$u_2 \frac{\partial v_2}{\partial x_2} + w_2 \frac{\partial v_2}{\partial y_2} + \frac{v_2}{x_1 \sin\alpha}\frac{\partial v_2}{\partial\phi} + \frac{u_2 v_2}{x_2} = \theta_2 \sin\phi + \frac{\partial^2 v_2}{\partial y_2{}^2}, \tag{11c}$$

$$u_2 \frac{\partial\theta_2}{\partial x_2} + w_2 \frac{\partial\theta_2}{\partial y_2} + \frac{y_2}{x_2 \sin\alpha}\frac{\partial\theta_2}{\partial\phi} = \frac{1}{\mathrm{Pr}}\frac{\partial^2\theta_2}{\partial y_2{}^2} \tag{11d}$$

The only difference between equations (4) and (11) is that the buoyancy forces in equations (11) are 0(1). This indicates that the buoyancy forces are as important as the other forces; and the interaction of the axial boundary layer flow and the secondary flow becomes a dominant effect.

The upstream solutions (6) can be rewritten in the downstream coordinates. They are

$$u_2 = x^n \left[f_0' + x^{[(3-5n)/2]} F_1' \frac{\cos\phi}{\sin\alpha} + \ldots \right] \tag{12a}$$

$$v_2 = x^{[(3-3n)/2]} F_2' \sin\phi + \ldots \tag{12b}$$

$$w_2 = \sqrt{\frac{2}{n+3}}\, x^{[(n-1)/2]} \left[\left(\frac{1-n}{2}\eta f_0' - \frac{n+3}{2} f_0 \right) + x_2^{[(3-5n)/2]} \times \left\{ \frac{1-n}{2}\eta F_1' + (2n-3) F_1 - F_2 \right\} \frac{\cos\phi}{\sin\alpha} + \ldots \right] \tag{12c}$$

$$\theta_2 = \sqrt{\frac{2}{n+3}}\, x^{[(1-n)/2]} \left[\bar{\theta}_0 = x^{[(3-5n)/2]} G \frac{\cos\theta}{\sin\alpha} + \ldots \right] \tag{12d}$$

where

$$\eta = y_2 \sqrt{\frac{n+3}{2} x_2^{n-1}} = y_1 \sqrt{\frac{n+3}{2} x_1^{n-1}} \tag{12e}$$

Comparison of equations (4) and (11) shows that the solution of equations (4) is included in the solution of equations (11). Equations (12) provide another check to insure that the solution of equations (11) is uniformly valid from the cone apex to the downstream region as long as the transverse curvature can be neglected.

Numerical Computation

Equations (11) represent a three-dimensional boundary layer influenced by buoyancy forces. The sixth term of equation (11*b*) is the component of the buoyancy force which is parallel to the cone surface. This force behaves as a favorable body force along the upper half of the cone, and as an unfavorable body force along the lower half of the cone. It can stabilize the flow along the upper half of the cone and destabilize the flow along the lower half. The magnitude of this force is proportional to $\sin\alpha$. For a small-angle cone, its effect is weak; however, for a large-angle cone, it has a significant effect on the development of the boundary layer, and can trigger boundary-layer separation at a sufficient distance downstream from the cone apex.

Another component of the buoyancy force, the fifth term of equation (11*c*), is along the circumferential direction and is the driving force for secondary flows. This force seems to have a stronger influence on the development of the boundary layer for cones of small-angle.

An analytical solution of equations (11) is unlikely to be found; and a finite-difference method is used here. Parabolic coordinates are probably most convenient for solving equations (11) numerically (see Smith and Clutter, [7] Dwyer, [8]). Also, from equations (12), one can see the x_2-dependence of the boundary-layer development. Another transformation will be introduced in order to reduce the variation of the boundary-layer growth downstream and to reduce the possibility of numerical instability caused by the fast developing boundary layer.

The velocities are transformed as follows:

$$u_3 = x_2^{-n} u_2$$

$$v_3 = x_2^{-n} v_2$$

$$w_3 = \sqrt{[(n+3)/2]}\, x_2^{[(1-n)/2]}\, w_2, \tag{13}$$

Then, equations (11) in the parabolic coordinates (x_2, η, ϕ) become

$$x_2\frac{\partial u_3}{\partial x_2} + (1+n)\,u_3 + \frac{n-1}{2}\,\eta\frac{\partial u_3}{\partial \eta} + \frac{\partial w_3}{\partial \eta} + \frac{1}{\sin\alpha}\frac{\partial v_3}{\partial \phi} = 0 \tag{14a}$$

$$x_2 u_3\frac{\partial u_3}{\partial x_2} + (nu_3{}^2 - v_3{}^2) + \left(w_3 + \frac{n-1}{2}\,\eta u_3\right) \times \frac{\partial u_3}{\partial \eta} + \frac{v_3}{\sin\alpha}\frac{\partial u_3}{\partial \phi} = n - x_2{}^{1-2n} \times \theta\cos\phi\sin\alpha + \frac{n+3}{2}\frac{\partial^2 u_3}{\partial \eta^2} \tag{14b}$$

$$x_2 u_3\frac{\partial v_3}{\partial x_2} + (1+n)\,u_3 v_3 + \left(w_3 + \frac{n-1}{2}\,\eta u_3\right) \times \frac{\partial v_3}{\partial \eta} + \frac{v_3}{\sin\alpha}\frac{\partial v_3}{\partial \phi} = x_2{}^{1-2n}\,\theta\sin\phi + \frac{n+3}{2}\frac{\partial^2 v_3}{\partial \eta^2} \tag{14c}$$

$$x_2 u_3\frac{\partial \theta}{\partial x_2} + \left(w_3 + \frac{n-1}{2}\,\eta u_3\right)\frac{\partial \theta}{\partial \eta} + \frac{v_3}{\sin\alpha}\frac{\partial \theta}{\partial \phi} = \frac{1}{\mathrm{Pr}}\frac{n+3}{2}\frac{\partial^2 \theta}{\partial \eta^2} \tag{14d}$$

Boundary Conditions. The local boundary conditions that are required to solve equations (14) are

$$\text{At } \eta = 0, \quad u_3 = v_3 = w_3 \quad \text{(no-slip condition)}; \tag{15a}$$

$$\frac{\partial \theta}{\partial \eta} = -1 \quad \text{(constant wall heat flux)}; \tag{15b}$$

$$\text{As } \eta \to \infty, \quad u_3 \to 1, \quad v \text{ and } \theta \to 0 \quad \text{(matching with the free stream)} \tag{15c}$$

Along the symmetry line, $\phi = 0°$, the conditions are

$$v_3 = 0, \quad \frac{\partial u_3}{\partial \phi} = \frac{\partial w_3}{\partial \phi} = \frac{\partial \theta}{\partial \phi} = 0 \tag{16}$$

Values of the dependent variables are required along $\phi = 0°$ to start the numerical computation at each x_2-station. The equations that govern the flow along the symmetry line can be obtained by taking the limit of equations (14) according to equation (16); this gives

$$x_2\frac{\partial u_3}{\partial x_2} + (1+n)\,u_3 + \frac{n-1}{2}\,\eta\frac{\partial u_3}{\partial \eta} + \frac{\partial w_3}{\partial \eta} + \frac{1}{\sin\alpha}\frac{\partial v_3}{\partial \phi} = 0 \tag{17a}$$

$$x_2 u_3\frac{\partial u_3}{\partial x_2} + (nu_3{}^2 - v_3{}^2) + \left(w_3 + \frac{n-1}{2}\,\eta u_3\right)\frac{\partial u_3}{\partial \eta} = n - x_2{}^{1-2n}\,\theta\sin\alpha + \frac{n+3}{2}\frac{\partial^2 u_3}{\partial \eta^2} \tag{17b}$$

$$x_2 u_3\frac{\partial}{\partial x_2}\left(\frac{\partial v_3}{\partial \phi}\right) + \frac{1}{\sin\alpha}\left(\frac{\partial v_3}{\partial \phi}\right)^2 + \left(w_3 + \frac{n-1}{2}\,\eta u_3\right) \times \frac{\partial}{\partial \eta}\left(\frac{\partial v_3}{\partial \phi}\right) + (1+n)u_3\left(\frac{\partial v_3}{\partial \phi}\right) = x^{1-2n}\theta + \frac{n+3}{2}\frac{\partial^2}{\partial \eta^2}\left(\frac{\partial v_3}{\partial \phi}\right) \tag{17c}$$

$$x_2 u_3\frac{\partial \theta}{\partial x_2} + \left(w_3 + \frac{n-1}{2}\,\eta u_3\right)\frac{\partial \theta}{\partial \eta} = \frac{n+3}{2\mathrm{Pr}}\frac{\partial^2 \theta}{\partial \eta^2} \tag{17d}$$

Equations (16) hold at $\phi = 0$, and can be solved with the conditions given by equations (15) first at any particular x_2-station. Then this solution can be used as the initial condition to start the computation of equations (14) in the azimuthal direction.

The upstream conditions, equations (12), can be applied at a small x_2 (say, $x_2 < 0.1$) as the initial conditions of equations (14). But since the upstream solutions, equations (12), are included in the downstream solution of equations (14), it is more convenient to start computation at the cone apex ($x_2 - 0$). The velocity profiles and the temperature distribution at $x_2 - 0$ can be obtained by solving the limiting forms of equation (14) as $x_2 \to 0$. They are

$$(1+n)\,u_3 + \frac{n-1}{2}\,\eta\frac{\partial u_3}{\partial \eta} + \frac{\partial w_3}{\partial \eta} + \frac{1}{\sin\alpha}\frac{\partial v_3}{\partial \phi} = 0 \tag{18a}$$

$$(nu_3{}^2 - v_3{}^2) + \frac{v_3}{\sin\alpha}\frac{\partial u_3}{\partial \phi} + \left(w_3 + \frac{n-1}{2}\,\eta u_3\right)\frac{\partial u_3}{\partial \eta} = n + \frac{n+3}{2}\frac{\partial^2 u_3}{\partial \eta^2} \tag{18b}$$

$$(1+n)\,u_3 v_3 + \frac{v_3}{\sin\alpha}\frac{\partial v_3}{\partial \phi} + \left(w_3 + \frac{n-1}{2}\,\eta u_3\right)\frac{\partial v_3}{\partial \eta} = \frac{n+3}{2}\frac{\partial^2 v_3}{\partial \eta^2} \tag{18c}$$

$$\frac{v_3}{\sin\alpha}\frac{\partial \theta}{\partial \phi} + \left(w_3 + \frac{n-1}{2}\,\eta u_3\right)\frac{\partial \theta}{\partial \eta} = \frac{n+3}{2\mathrm{Pr}}\frac{\partial^2 \theta}{\partial \eta^2} \tag{18d}$$

The value of v_3 which satisfies equations (15) and (18*c*) is zero. This indicates that the flow at the cone apex is axisymmetric. In fact, the solution of equations (18) is simply a forced-convection cone flow with the uniform wall heat flux which is represented by the functions of f_0 and $\bar{\theta}$ in equations (12). In other words, f_0 describes the boundary layer along an unheated cone. Equations (14), (16), and (17) are discretized by the following difference approximation. First-order derivatives in the x_2 and ϕ-directions are approximated by forward differences; and in the η-direction both first and second-order derivatives are replaced by central differences. The scheme is fully implicit; and Picard iteration is used to solve the resulting nonlinear algebraic equations.

The numerical experiments show that the convergence to two to three significant digits can be achieved by taking $\Delta\eta = 0.05$, $\Delta\phi = \pi/16$, and $\Delta x_2 = 0.1$, for $z_2 \geq 0.2$. However, near the cone apex, a finer x_2-grid is required. For $x_2 \leq 0.2$, $\Delta x_2 = 0.005$ is used; for $x_2 \geq 0.2$, Δx_2 is gradually increased to 0.1. The details of the numerical technique can be found in Yao, et al. (8).

Results and Discussion

Buoyancy forces influence boundary-layer development along a heated cone, and this influence is cumulative. Near the cone apex there is little effect on the boundary layer due to buoyancy; and the flow is nearly axisymmetric. But further downstream buoyancy effects begin to accumulate, and the flow becomes asymmetric.

The upstream solution, equations (6), indicates that asymmetry of the axial velocity develops downstream proportional to $x_2{}^{(3-5n)/2}$, and the secondary velocity increases as $x_2{}^{[3/2(1-n)]}$. This shows that

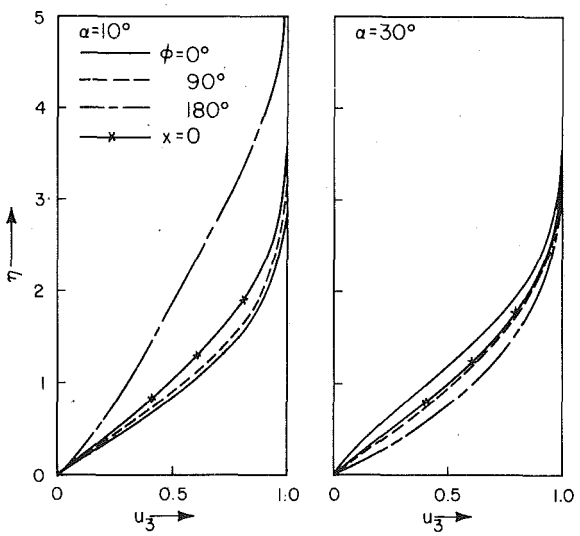

Fig. 2 Axial velocity, u_3 at $x = 1.0$, Pr = 1

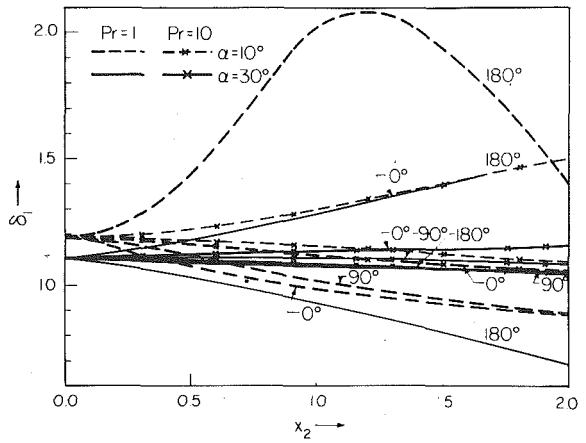

Fig. 3 Displacement thickness

the buoyancy effect on the axial velocity increases downstream when n is smaller than 0.6.

A comparison of the first two terms of equation (6a) shows that the initial small buoyancy forces become a dominant effect at $x \simeq l/\epsilon^{[2/(3-5n)]}$ when $n < 0.6$. This suggests that the upstream solution is only valid for small x_2 when $n < 0.6$.

The buoyancy forces affect the boundary-layer development in two ways. First is the effect of the component of the buoyancy force parallel to the cone surface. This force directly affects the development of the axial boundary layer and seems important for a large-angle cone since its magnitude depends on sin α. $\alpha = 30°$ is selected to demonstrate its effect.

The component of the buoyancy force normal to the free stream drives the secondary boundary-layer flow. The axial boundary layer develops asymmetrically to accommodate the development of the secondary boundary layer, i.e., in order to satisfy mass conservation. This effect seems important for a small-angle cone. $\alpha = 10°$ is chosen to illuminate the details of this case.

The axial velocity profile at $x_2 = 0$ for $\alpha = 10°$ is plotted in Fig. 2. Since the flow is buoyancy free at the cone apex, the axial velocity is axisymmetric. Downstream from the cone apex, e.g., $x_2 = 1$ (see Fig. 2), the asymmetry of the axial velocity has developed. The data show that for Pr = 1, the downstream velocity profile becomes fuller around most of the cone, except in a small region close to the top, where the profile actually is less full. This results from the secondary flow sucking the fluid, and driving it circumferentially toward the top. The boundary layer is thinned on the bottom of the cone ($\phi = 0°$); and this causes a fuller axial velocity profile. The fluid is then accumulated on the top of the cone, causing thickening of the boundary layer, and a less full axial velocity profile. The flow development for Pr = 10 is similar to that for Pr = 1, but smaller in magnitude for any prescribed x-distance. Therefore, the results of Pr = 10 are now shown in Fig. 2.

The displacement thickness for a three-dimensional boundary layer is not easy to be defined. For a cone flow, the maximum azimuthal velocity is about 20 percent of the maximum axial velocity. The displacement thickness, $\bar{\delta}_1$, is approximately evaluated by ignoring the azimuthal velocity and is estimated as

$$\bar{\delta}_1 = l \times \epsilon^{n-1/3-5n} \times \mathrm{Re}^{-0.5} \times x_2{}^{1-n/2} \times \delta, \qquad (19a)$$

where

$$\delta_1 = \int_0^\infty (1 - U_3)\, d\eta \qquad (19b)$$

The values of δ_1 are given in Fig. 3 for Pr = 1, and 10. For an unheated cone flow, δ_1 is constant and its value depends on the cone angle. For the flow past a heated cone, δ_1 varies along the cone surface due to the contribution of the buoyancy forces. The variation of δ_1 provides an information of the thickness distribution of the three-dimensional boundary layer. Fig. 3 clearly indicates that the boundary layer is thickened on the top of the cone and thinned over the remainder of the cone surface. For Pr = 10, the boundary layer develops at a slower rate that for Pr = 1. The influence of the buoyancy forces still exists, but it takes a greater distance to reveal itself. The surprising result for Pr = 1 is that the boundary layer reaches it thickest point at $x = 1.18$; then its thickness starts to decrease downstream. This may be due to the thinning of the boundary layer over the rest of the cone, which pulls the boundary layer on the top of the cone thin as the fluid flows further downstream. Also, this may be partially due to the favorable axial pressure gradient. No flow separation is found for $\alpha = 10°$. The computation is stopped at $x_2 = 2$ which is too short a distance to observe a similar development for Pr = 10.

For a large-angle cone, say $\alpha = 30°$, the boundary layer develops in a quite different way. The axial velocity profiles, shown in Fig. 2, become fuller around most of the cone than at the $x_2 = 0$, except along the bottom of the cone, where they are less full. This indicates that the component of the axial buoyancy force parallel to the cone surface, functions as a favorable body force along the upper half of the cone and as an unfavorable body force along the lower part of the cone. For a large-angle cone, the buoyancy force along the axial direction has a stronger influence on the development of the axial boundary layer than does the the developing secondary boundary-layer flow. Therefore, the axial velocities develop in an opposite way for a large-angle cone from that for a small-angle cone. As would be expected, the displacement thickness of the boundary-layer for $\alpha = 30°$ also develops in a way opposite that for $\alpha = 10°$. The boundary layer is thinned along the upper surface of the cone and is thickened along the lower surface of the cone.

The numerical scheme fails to converge at $x_2 = 1.67$ on the bottom of the cone ($\phi = 0°$). The reason for this failure is not known with certainty, but may simply indicate that there is no solution (or possibly many solutions) to the governing equations from this point on. Five iterations, or fewer are required at most stations in order to obtain a converged solution; however, at $x_2 = 1.67$ and $\phi = 0°$, convergence is not achieved, even for 50 iterations. Although the unconverged results behave smoothly and seem to indicate a reverse flow, we do not believe they represent the physical solution. Since the boundary layer does grow thick along $\phi = 0°$ when the buoyancy force acts unfavorably on the boundary layer, the failure of the numerical solution may indicate flow separation. But it is well known that the boundary-layer equations cannot describe separated flow; hence, the

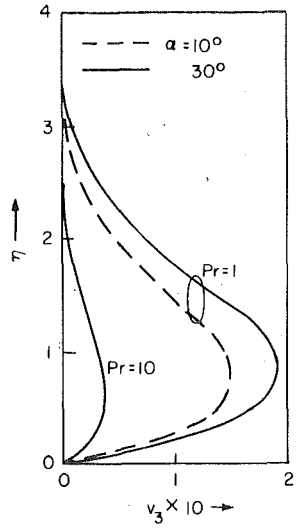

Fig. 4 Azimuthal velocity, v_3, at $x_2 = 1$ and $\phi = 90°$

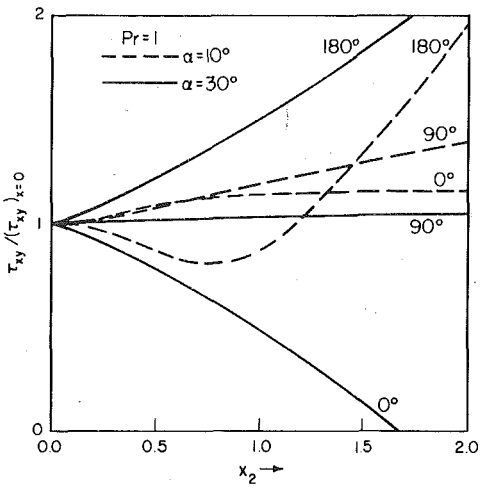

Fig. 5 Axial shear stress distribution

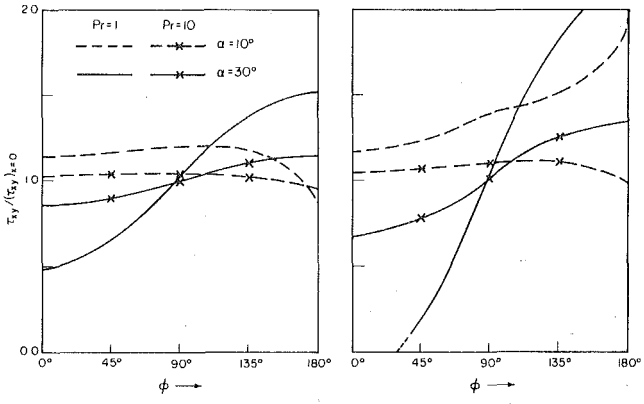

Fig. 6(*a*) Fig. 6(*b*)

Fig. 6(*a*) Shear stress ratio at $x_2 = 1$; (*b*) shear stress ratio at $x_2 = 2$

numerical results become meaningless at the point of separation, and beyond.

Equation (12*b*) shows that the circumferential velocity varies with $\sin\phi$. v_2 equals zero at $\phi = 0°$, reaches its maximum value at $\phi = 90°$, and then decreases to zero at $\phi = 180°$. In the region close to the cone apex, v_2 is symmetric with respect to $\phi = 90°$. Further downstream, the maximum v_2 does not occur at $\phi = 90°$. This explains why the boundary layer is thinned over most of the cone surface. Typical v profiles are given in Fig. 4. The magnitude of v_3 is larger for a large-angle cone than for a small-angle cone. Also, its magnitude varies inversely with the Prandtl number. For Pr = 10, the difference in v between the $\phi = 10°$ and 30° cases is too small to be shown on the scale of Fig. 4.

The axial shear stress, τ_{xy}, normalized by its value at $x_2 = 0$, is given in Fig. 5 for Pr = 1. The distribution of the shear stress for Pr = 10 is similar to that for Pr = 1, but smaller in magnitude as would be expected from the earlier discussion. Therefore, it is not shown in Fig. 5.

For $\alpha = 10°$, the axial shear stress increases along the bottom of the cone and decreases along the top of the cone. According to the upstream solution (6), the variation of τ_{xy} along the ϕ-direction is proportional to $\cos\phi$, and is antisymmetric with respect to $\phi = 90°$. Numerical results indicate that the antisymmetry of τ_{xy} with respect to $\phi = 90°$ holds only for small x_2. Instead, the value of τ_{xy} along $\phi = 0°$ becomes larger than that along $\phi = 90°$ at $x_2 = 0.52$. A careful comparison of τ_{xy} along $\phi = 0°$, 90°, and 180° indicates that the antisymmetry of τ_{xy} with respect to $\phi = 90°$ starts to deviate fairly close to the cone apex. This implies that the upstream solution can, at most, be applied for $x_2 < 0.1$.

The axial shear stress along $\alpha = 180°$ drops for $x_2 \leq 1.18$ and then starts to increase at a fast rate. This is due to the thinning boundary layer downstream of $x^2 = 1.18$.

The behavior of the axial shear stress for $\alpha = 30°$ is much simpler than that for $\alpha = 10°$. The shear stress increases downstream along $\phi = 180°$ due to the favorable buoyancy force. The upstream solution predicts that τ_{xy} along $\phi = 90°$ is not affected by the buoyancy force. The numerical solution, however, shows its value increases slightly downstream. τ_{xy} decreases drastically downstream along $\phi = 0°$ due to the unfavorable buoyancy force; its value reaches zero at $x = 1.67$. This suggests that the local boundary layer may separate from the wall at this point, as conjectured in the foregoing.

The circumferential variation of τ_{xy} is shown in Fig. 6 for $x_2 = 1$ and 2. For $\alpha = 30°$, the minimum τ_{xy} always occurs along the bottom of the cone. Its value monotonically increases and reaches its maximum at the top of the cone. For $\alpha = 10°$, the maximum τ_{xy} does not necessarily occur at a fixed ϕ. For Pr = 1, at $x_2 = 1$, the maximum τ_{xy} is at $\phi \sim 100°$; at $x_2 = 2$, the maximum τ_{xy} occurs at $\phi = 180°$. Evidently, the changing patterns of the axial shear stress distribution are due to the competition of the requirement of mass conservation due to the developing secondary boundary layer, the axial component of the buoyancy force, and the axial pressure gradient.

If the flow does separate along the bottom of the cone with $\alpha = 30°$ and Pr = 1, the shear stress shown at $x_2 = 2$ in Fig. 6 may be used to determine the size of the separated flow region. However, the separation of the boundary layer hinted at by the numerical results reveals need for further study.

Typical temperature distributions at $x_2 = 1$ for cone angles $\alpha = 10°$ and 30° are shown in Fig. 7. For $\alpha = 10°$, the hottest point occurs along the cone top; the coldest point is along the cone bottom. For $\alpha = 30°$, the temperature distribution is the other way around. The circumferential changes in temperature at $x_2 = 1$ for Pr = 1 are too small to be shown on the scale of Fig. 7. But an asymmetric temperature distribution does develop downstream, and can be clearly shown as in Fig. 8. It is interesting to note that the degree of asymmetry of the wall temperature for $\alpha = 30°$ is smaller than that of $\alpha = 10°$. Another interesting result is that the temperature along the bottom of the 30° cone develops smoothly. No drastic rising of the temperature at $x_2 = 1.67$ which one may expect because of the flow separation. We do not know how to explain this phenomenon; however, we guess that a circulating flow may be developed in the neighborhood of $x_2 = 1.67$ due to the three-dimensional flow separation. The circulating flow

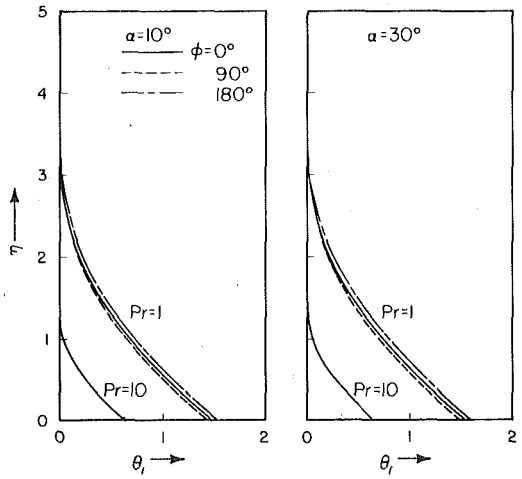

Fig. 7 Temperature distribution at $x_2 = 1$

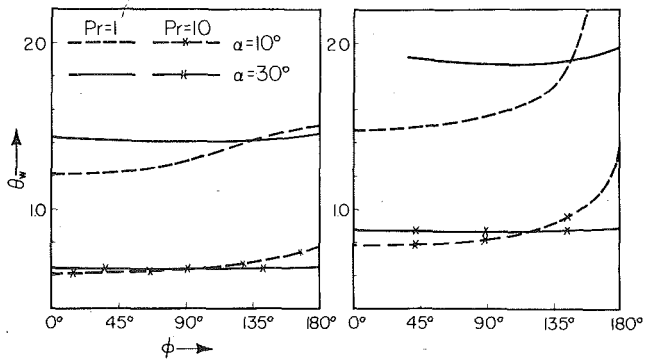

Fig. 9(*a*) Fig. 9(*b*)

Fig. 9(*a*) Surface temperature at $x_2 = 1$; (*b*) surface temperature at $x_2 = 2$

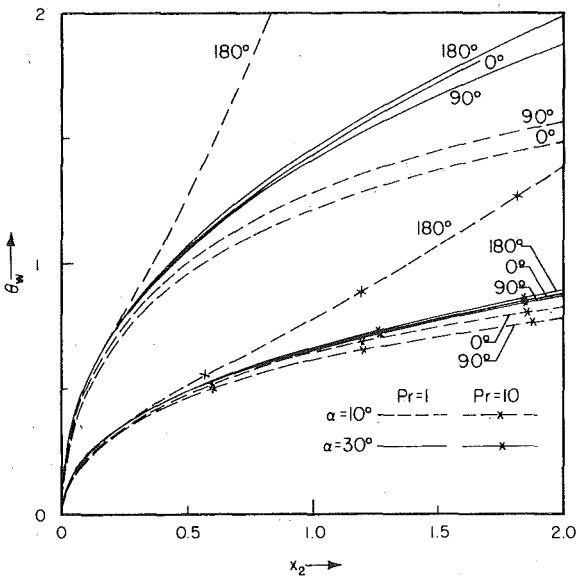

Fig. 8 Surface temperature

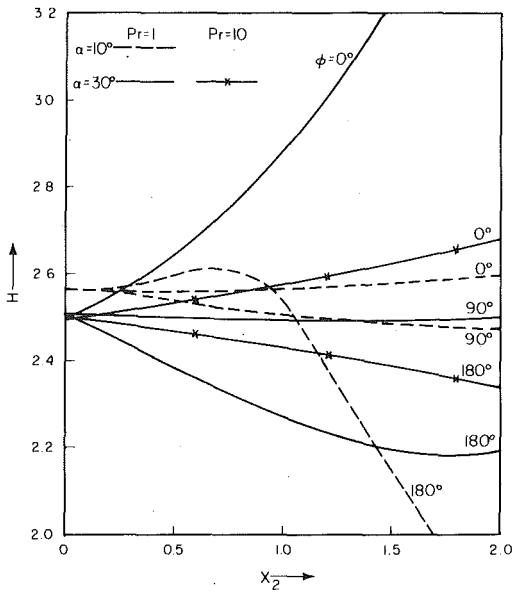

Fig. 10 Shape factor

acts as a good agency to transfer heat between the cone surface and the free stream. It should be noted that the solution broke down at $x_2 = 1.67$.

The circumferential variation of the wall temperature is given in Fig. 9 for $x_2 = 1$ and $x_2 = 2$, respectively. For $\alpha = 10°$, the temperature is fairly constant for $\phi \leq 90°$, but monotonically increases over the upper surface of the cone. The circumferential temperature variation for $\alpha = 30°$ is relatively small compared with that for $\alpha = 10°$. At $x_2 = 2$ for Pr = 1 and $\alpha = 30°$, the wall temperature does show a rising tendency around from $\phi = 40°$ to $\phi = 0°$. Since the numerical solution is not valid between $\phi = 0°$ and 40°, no definite conclusion can be made at the present time.

The axial velocity profile is substantially distorted by free convection, and, as a result, the buoyancy forces will have a strong effect on the boundary-layer stability. The detail structure of the boundary-layer transition is beyond the scope of this paper; instead, the shape factor, H, the ratio of the displacement thickness to the momentum thickness, is plotted in Figs. 10 and 11 to show the relative importance of the buoyancy forces on the boundary-layer transition.

The momentum thickness is approximately estimated as

$$\bar{\delta}_2 = l \times \epsilon^{n-1/3-5n} \times \mathrm{Re}^{-0.5} \times x_2{}^{1-n/2} \times \delta_2, \qquad (20a)$$

where

$$\delta_2 = \int_0^\eta U_3(1 - U_3)\, d\eta \qquad (20b)$$

The axial variation of H is given in Fig. 10. For $\alpha = 10°$ and Pr = 1, H decreases along the bottom of the cone and then gradually increases. At $x_2 = 0.9$, the value of H becomes larger than its value at $x_2 = 0$. In other words, the buoyancy forces stabilize the boundary layer along the bottom of the cone up to $x_2 = 0.9$. Downstream from $x_2 = 0.9$, the buoyancy forces destabilize the boundary layer. Along the top of the cone, the layer is less stable up to $x_2 \simeq 0.67$, then the buoyancy forces stabilize the boundary layer further downstream. Along $\phi = 90°$, the buoyancy forces always stabilize the boundary layer. For Pr = 10, the variations of H are smaller to those of Pr = 1 for $x_2 < 0.4$; therefore, they are not shown in Fig. 10.

For $\alpha = 30°$, the buoyancy forces always stabilize the boundary layer along the top of the cone and destabilize it along the bottom. The value of H is monotonically decreasing from the bottom of the cone

to the top. For $\alpha = 10°$, the minimum H does not always occur at either the top or the bottom of the cone. For Pr = 1, the most stable flow is at $\phi = 130°$; for Pr = 10, the minimum H occurs about $\phi = 90°$.

We can conclude from Fig. 11 that a flow transition study without considering buoyancy effects can be quite misleading. Further, the circumferential variation of H depends on the cone angle as well as the heating rate. This creates further doubts about the reliability of predictions of flow transition on a heated axisymmetric body based on two-dimensional flow geometry.

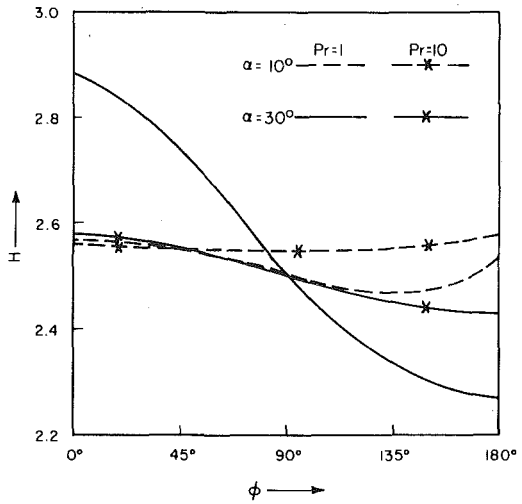

Fig. 11 Shape factor at $x_2 = 1$

References

1 Yao, L. S., *Journal of Fluid Mechanics,* Vol. 88, Part 3, 1978, pp. 465–483.

2 Aroesty, J., and Berger, S. A., "Controlling the Separation of Laminar Boundary Layers in Water: Heating and Suction," The RAND Corp., R-1989-ARPA, 1975.

3 Yao, L. S., and Catton, I., ASME *Journal of Heat Transfer,* Vol. 99, 1977, pp. 122–124.

4 Yao, L. S., and Catton, I., "Free-Forced Convection From a Heated Cone," *Proceedings, 6th International Heat Transfer Conference,* Toronto, Canada, MC-3, 7–11 Aug. 1978, pp. 13–18.

5 Yao, L. S., "Variable Viscosity Effect on the Laminar Water Boundary Layer on Heated Cones," ASME JOURNAL OF APPLIED MECHANICS, Vol. 45, pt. 3, 1978, pp. 481–486.

6 Mangler, W., "Special Exact Solution," Section 1.2 of *Boundary Layers,* ed., Tollmien W.; see also, *Laminar Boundary Layers,* ed. Rosenhead, L., 1948.

7 Smith, A. M. O., and Clutter, D. W., *AIAA Journal,* Vol. 1, No. 9, 1963, pp. 2062–2071.

8 Dwyer, H. A., *AIAA Journal,* Vol. 6, No. 7, 1968, pp. 1336–1342.

9 Yao, L. S., Catton, I., and McDonough, J. M., "Buoyancy-Driven Asymmetric Water Boundary Layer Along a Heated Cylinder," *Journal of Fluid Mechanics,* Vol. 98, Part 2, 1980, pp. 417–433.

W. E. Scott

Department of Engineering Science
and Mechanics,
University of Tennessee and
The Ballistic Research Laboratories,
Knoxville, Tenn. 37916

The Null Dynamical Effect, and Some Frequency Spectra, of Resonant Inertial Pressure Waves in a Rapidly Rotating, Right Circular, Sectored Cylinder

It is shown that inertial waves in the form of standing asymmetrical pressure waves can exist in an incompressible liquid in a rotating sectored cylinder in a rigid body (e.g., a top or a missile) executing a small amplitude gyroscopic motion about its center of mass. Some of the frequency spectra of these waves are presented along with the result that sectoring the cylinder into any number of equal sectors results in eliminating the destabilizing effect of these waves (i.e., the amplitude growth of the motion of the rigid container) when there is a "Stewartson" resonance between the frequency of one of the inertial modes and the frequency of the nutational component of the motion of the container. Experimental results are in reasonable agreement with the theory.

1 Introduction

There are a number of excellent analyses of the problem of fluid motion in a closed, rapidly rotating container undergoing a forced motion (see Greenspan [1] and his very extensive bibliography). In most of these, however, the problem considered is: Given the forced motion of the container, find the motion of the fluid. The extension of these problems wherein one, having found the motion of the fluid, then attempts to determine the effect of that motion on the motion of the container, does not seem to have such an extensive bibliography. In fact, when the problem is further specialized to that of determining the response of the container to the resonant inertial oscillations (Greenspan [1], Kelvin [2], and Bjerkness [3]) generated in the fluid by the container motion, this author is aware only of the work by Greenhill [4], Hough [5], and Stewartson [6]. Each of the latter considers the oscillating fluid dynamic torque exerted on a rapidly spinning, gyrating container, the motion of which induced the oscillations of the contained incompressive fluid. They show that, if the frequency of the inertial oscillations is equal, or nearly so, to the frequency of the nutational component of the gyroscopic motion of the container, the amplitude of motion of the container may grow. None of the authors attempts a physical explanation of this particular amplitude growth phenomenon; it is now, however, reasonably clear that it is due to the fact that an inertial oscillation in the container cavity can have associated with it an asymmetrical pressure distribution. When a state of resonance exists between the frequency of the nutational component of the gyroscopic motion of the container and the frequency of the inertial oscillation, the asymmetrical pressure distribution in the liquid has wavelike properties and moves around inside the container cavity, "keeping step" with the appropriate phase of the nutational motion of the container. This effectively enables any destabilizing effect of this pressure distribution to persist, thereby effecting an amplitude growth of the motion of the container. Fig. 1 is an attempt to illustrate this for standing inertial pressure waves in a gyrating cylindrical container. This figures shows several instantaneous angular positions of a top or missile spinning with angular speed Ω and performing the first half of a (greatly exaggerated in amplitude) purely nutational motion (the processional component of the motion is assumed to be zero since we are ignoring the effect of external torques) with frequency $\Omega/8$ about its center of mass. Shown is the liquid filled cylinder (inside the top or missile) in which the pressure distribution, at the walls of the cylinder, is taken to be $A \cos\theta \cos(\Omega t/8) \sin\{(2j+1)\pi z/2c\} + \rho\Omega^2 a^2/2$, and is sketched in with arrows at the top and bottom planes of the cylinder. An arrow falling outside the cylinder represents a pressure in excess of $\rho\Omega^2 a^2/2$, and vice versa. We have assumed that the frequency of the relevant inertial mode is also $\Omega/8$, and that the time interval between successive

Contributed by the Applied Mechanics Division for publication in the JOURNAL OF APPLIED MECHANICS.

Discussion on this paper should be addressed to the Editorial Department, ASME, United Engineering Center, 345 East 47th Street, New York, N. Y. 10017, and will be accepted until December 1, 1980. Readers who need more time to prepare a discussion should request an extension from the Editorial Department. Manuscript received by ASME Applied Mechanics Division, February, 1979; final revision, July, 1979.

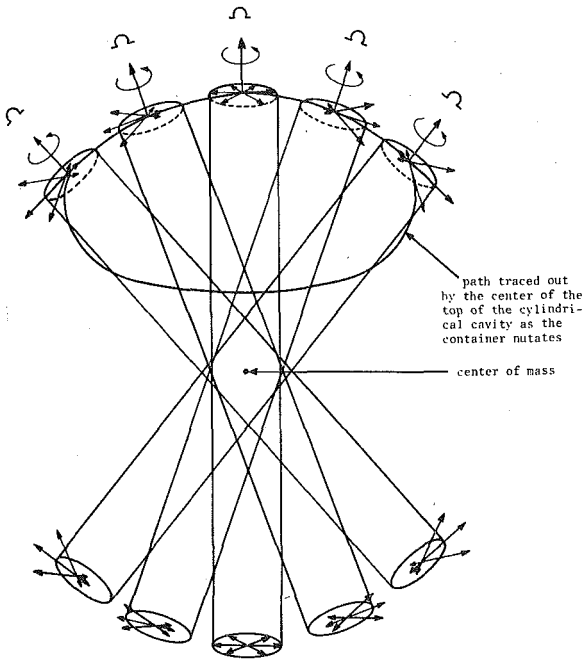

Fig. 1 Inertial pressure wave distribution (at the top and bottom of the vertical wall) for a liquid filled cylinder executing a coning motion about its center of mass

angular positions of the container is the period of the angular speed Ω. Observe that the pressure distribution at the top of the cylinder is equal and opposite to that at the bottom, and that the observed tendency of the resultant "couple" to overturn the cylinder persists throughout the nutation cycle (except when the pressure becomes merely $\rho\Omega^2a^2/2$, where the tips of the arrows fall on the circle) *only* because of resonance, i.e., the assumed equality of the frequency of the inertial mode and the nutational frequency of the container. It is the persistence, throughout most of the nutation cycle, of this overturning effect that physically explains the destabilizing effect of the resonant inertial oscillations.

One method of correcting or preventing this amplitude growth (or dynamic instability) depicted in Fig. 1 would seem to be to effect a decoupling or a detuning of the oscillations of the liquid and its container. The obvious way to do this would be to alter the frequency of the resonant inertial mode of the spinning liquid. If the amount of the liquid and the cavity size are fixed, an internal alteration of the cavity geometry would seem to be an effective way to alter any of the inertial mode frequencies. One such alteration would be the compartmentation of the cavity by radial barriers, separated by an angle β and extending the length of the cavity, resulting in a cylindrical cavity having a cut pie shaped end view cross section (Fig. 2). Scott [7] showed that time-dependent, asymmetrical pressure waves like those in Fig. 1 can exist in such a configuration. In addition to markedly expanding the table in [7], here it is shown that the dynamical effect of these waves on the motion of the container is markedly different from the situation for the cavity with no barriers, i.e., the Stewartson problem.

2 Analysis

The Fluid Dynamical Equations and the Boundary Conditions. The intent of the analysis is to make a comparison with the results of the problem studied by Stewartson [6]. Hence, we follow, somewhat closely, his analysis. So, assume that the container of Fig. 2, and the XYZ-axes shown there, are initially rotating uniformly about the Z-axis with angular speed Ω. Let the liquid in the container have the same angular velocity. Then, the absolute velocity of the liquid at some point $\mathbf{R}$ is

$$\mathbf{v} = \Omega \times \mathbf{R} \tag{1}$$

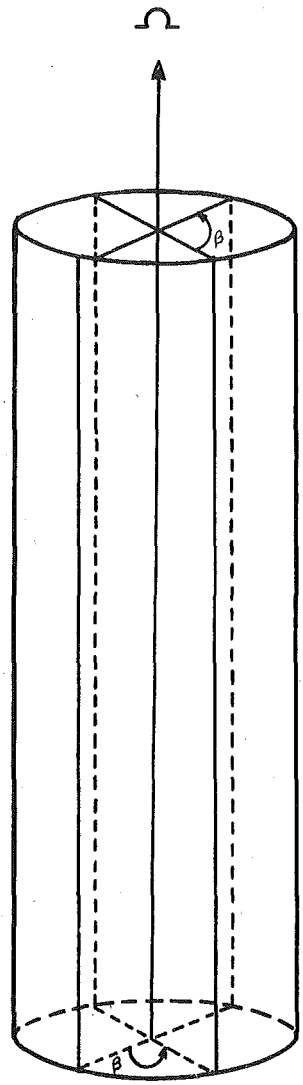

Fig. 2 A barriered cavity, with angle β between the barriers

Now, imagine the container is perturbed so that it has angular velocity components ω_X, ω_Y, and 0 about the XYZ-axes. Then, that point in the liquid formerly having the absolute velocity (1) now has the absolute velocity

$$\mathbf{u} = \mathbf{q} + \mathbf{v} = \mathbf{q} + \Omega \times \mathbf{R} \tag{2}$$

where $\mathbf{q}$, the fluid velocity perturbation generated by the angular velocity perturbation (ω_X, ω_Y, 0), is the velocity with respect to the rotating XYZ-axes. We have, then, for the Euler equation in the rotating XYZ frame:

$$(\partial/\partial t)(\mathbf{q} + \Omega \times \mathbf{R}) + \Omega \times (\mathbf{q} + \Omega \times \mathbf{R}) + \mathbf{q} \cdot \nabla(\mathbf{q} + \Omega \times \mathbf{R}) = -\nabla P \tag{3}$$

If we take Ω as constant and use the fact that $\mathbf{q}\cdot\nabla(\Omega \times \mathbf{R}) = \Omega \times \mathbf{q}$ and $\Omega \times (\Omega \times \mathbf{R}) = -\nabla\Omega^2r^2/2$, where r is the cylindrical radial coordinate, then (3) can be written:

$$\partial\mathbf{q}/\partial t + 2\Omega \times \mathbf{q} + \mathbf{q} \cdot \nabla\mathbf{q} = -\nabla(P - \rho\Omega^2r^2/2)/\rho \equiv -\nabla p' \tag{4}$$

In this equation, we have neglected the gravitational body force because either the missile is assumed to be freely falling, or else, for the top, we have assumed $\Omega^2a^2 \gg gc$, where c is the half height of the cylinder.

Consistent with our assumption that $\mathbf{q}$ is a perturbation, we neglect the $\mathbf{q}\cdot\nabla\mathbf{q}$ term in (4), giving us a linear equation. Following Greenspan [1], we can eliminate $\mathbf{q}$ from this linear equation, getting:

$$\partial^2\nabla^2 p'/\partial t^2 + (2\Omega)^2\partial^2 p'/\partial z^2 = 0, \tag{5}$$

a "wavy" equation for the pressure.

To arrive at the eigenfrequencies and boundary conditions for this equation, we let $p' = pe^{i\lambda t}$, $\mathbf{q} = \mathbf{Q}e^{i\lambda t}$, $\omega_X' = \omega_X e^{i\lambda t}$, and $\omega_Y' = \omega_Y e^{i\lambda t}$. (5) is now

$$\nabla^2 p + (2\Omega/i\lambda)^2\partial^2 p/\partial z^2 = 0 \tag{6}$$

and (4) becomes

$$i\lambda\mathbf{Q} + 2\boldsymbol{\Omega} \times \mathbf{Q} = -\nabla p \tag{7}$$

Equations (6) and (7) are, in our notation, Greenspan's [1] equations 2.7.3 and 2.7.1. Solving equation (7) for $\mathbf{Q}$, one gets

$$\mathbf{Q} = \{(2\Omega/i\lambda)\mathbf{k} \times \nabla p - \nabla p - (2\Omega/i\lambda)\mathbf{k}(2\Omega/i\lambda)\mathbf{k} \cdot \nabla p\}/[i\lambda\{1 + (2\Omega/i\lambda)^2\}] \tag{8}$$

which, in our notation, is Greenspan's 2.7.2.

The boundary conditions for (6) now follow from the fact that $\mathbf{Q}$ in (8) is the velocity amplitude of the liquid with respect to the rotating XYZ-axes of Fig. 3. Hence, if $\mathbf{R}_b$ is a position vector (of some point on the boundary of the container) in the rotating XYZ-frame, the, since $(\omega_X\mathbf{I} + \omega_Y\mathbf{J}) \times \mathbf{R}_b$ would then be the velocity of that point with respect to these same axes, it follows that the inviscid boundary condition is

$$\mathbf{Q} \cdot \mathbf{n} = (\omega_X\mathbf{I} + \omega_Y\mathbf{J}) \times \mathbf{R}_b \cdot \mathbf{n} \tag{9}$$

$\mathbf{n}$ is the unit outward normal to the container surface. Hence, from (8) and (9), the boundary conditions for equation(6) are

$$[\partial p/\partial z]_{z=\pm c} = -i\lambda r(\omega_X \sin\theta - \omega_Y \cos\theta) \tag{10}$$

$$[\partial p/\partial r + (2\Omega/i\lambda r)\partial p/\partial\theta]_{r=a} = -i\lambda z[1 + (2\Omega/i\lambda)^2](\omega_Y \cos\theta - \omega_X \sin\theta) \tag{11}$$

$$[(2\Omega/i\lambda)\partial p/\partial r - \partial p/r\partial\theta]_{\theta=0,\beta,2\beta,3\beta,\cdots} = -i\lambda z[1 + (2\Omega/i\lambda)^2](\omega_X \cos\theta + \omega_Y \sin\theta) \tag{12}$$

where β is the angle between successive barriers.

We can markedly simplify this set of boundary conditions by making (11) and (12) homogeneous. Hence, let $p = \Phi + i\lambda zr(\omega_X \sin\theta - \omega_Y \cos\theta) - 2zr\Omega(\omega_X \cos\theta + \omega_Y \sin\theta)$. This yields, for (10)–(12), and (6):

$$[\partial\Phi/\partial z]_{z=\pm c} = -2i\lambda r(\omega_X \sin\theta - \omega_Y \cos\theta) + 2\Omega r(\omega_X \cos\theta + \omega_Y \sin\theta) \tag{13}$$

$$[\partial\Phi/\partial r + (2\Omega/i\lambda r)\partial\Phi/\partial\theta]_{r=a} = 0 \tag{14}$$

$$[(2\Omega/i\lambda)\partial\Phi/\partial r - \partial\Phi/r\partial\theta]_{\theta=0,\beta,2\beta,3\beta,\cdots} = 0 \tag{15}$$

$$\nabla^2\Phi + (2\Omega/i\lambda)^2\partial^2\Phi/\partial z^2 = 0 \tag{16}$$

Equation (16) and boundary conditions (13)–(15) now appear to be a rather straightforward Sturm-Liouville-type boundary-value problem, amenable to the usual separation of variable process. We now show, however, that such is not the case.

The Nonexistence of Separation of Variable Solutions of the Governing Equations. We now demonstrate that equation (6) has no separation of variables solutions that define an inertial wave and which also satisfy boundary conditions (14) and (15). We show this by setting $\Phi = f(r)g(\theta)h(z)$. Then, from (14) we have

$$f'(a)g(\theta) - (2\Omega i/\lambda a)f(a)g'(\theta) = 0 \tag{17}$$

hence

$$g(\theta) = Ce^{-i\lambda a\theta f'(a)/2\Omega f(a)} \tag{18}$$

From (15), at $\theta = \beta$, we have

$$(2\Omega i/\lambda)g(\beta)f'(r) + f(r)g'(\beta)/r = 0 \tag{19}$$

Hence, using (18), we have

$$f'(r) - a(\lambda/2\Omega)^2 f'(a)f(r)/rf(a) = 0 \tag{20}$$

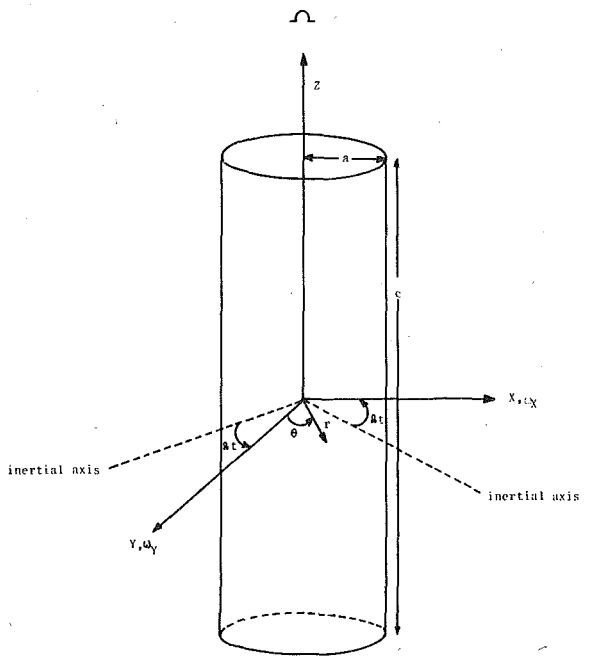

Fig. 3 The rotating coordinate system

At $r = a$, this yields

$$f'(a) - a(\lambda/2\Omega)^2 f'(a)f(a)/af(a) = 0 \tag{21}$$

Hence, $\lambda = 2\Omega$. However, Greenspan [1] shows that, for containers of finite volume, inertial wave frequencies are upper bounded by 2Ω. Hence, inertial wave solutions of the form $f(r)g(\theta)h(z)$ don't exist, i.e., such a representation is incompatible with the foregoing boundary conditions. The physical reason for this can be extracted from an observation made by Taylor [8]: the structure of any wave in a rotating fluid is a function of whether the wave is prograde or retrograde (Coriolis coupling of the radial and circumferential particle velocity components effects this circumstance). Hence, this different structure (of a prograde and a retrograde wave) precludes their addition in an attempt to get zero circumferential particle velocity all along a radial barrier, as boundary condition (15) stipulates; but this is exactly what one does in attempting to satisfy this boundary condition. Proudman [9] very painfully discovered this in his long and unsuccessful effort to solve the similar boundary-value problem of determining the tidal wave frequencies in a rotating, semicircular sea. It is interesting to note Proudman's observation that for a nonrotating sea, the problem is almost trivial.

Attempts to obviate the aforementioned mathematical difficulty associated with the physical processes at the radial barriers in this three-dimensional problem via the use of integral transform techniques (Laplace, Hankel, Fourier, and Mellin), conformal mapping, stream function expansion techniques, Greens functions, similarity solutions, Galerkin methods, or Wiener-Hopf techniques all fail for one or more reasons to generate functions that satisfy all of the boundary conditions. Even the Rayleigh-Ritz technique is of no avail for the author can't even conjure up a function that satisfies all of the boundary conditions. Hence, the author was forced to "rescue from the archives" the Null function method of Goldsbrough [10]. This is a technique Goldsbrough devised to solve a similar boundary-value problem (with similar difficulties with the boundary conditions) for waves in a sea (on the rotating earth) bounded by meridians of longitude and parallels of latitude. Basically, Goldsbrough's Null function method is somewhat akin to that of Galerkin, for it constructs a solution of the governing partial differential equation. However, Goldsbrough's approach uses the orthogonal functions generated by solving another problem, namely that of determining the tidal wave frequencies in a sea on the rotating earth bounded by parallels of latitide only. His final solution is in terms of a "Fourier series" of these

orthogonal functions, and the heart of the method is the procedure for effecting the requisite form of the nonseparation of variable Fourier representation. For all of the gory details, one can consult the original work; briefly, however, the following is the gist of the Goldsbrough Null function technique as applied to this problem. Consider the expression

$$\Phi = J_\alpha(r\gamma/a)(A\cos\alpha\theta + B\sin\alpha\theta)\cosh(kz/a)\sqrt{[1-(2\Omega/\lambda)^2]}$$

which is a solution for the Stewartson problem, and where α, γ, and k are separation constants, and where A and B are constants. We extract from this expression cos $\alpha\theta$ and sin $\alpha\theta$ and expand them in Fourier series in the interval $0 < \theta < \beta$. We then subtract these expressions from the functions they represent, and then multiply each term by the appropriate expansion of unity (i.e., $1 = \Sigma_j A_j J_\alpha(r\gamma_j/a)$) in a Fourier-Bessel series based on the orthogonality of the J_α's. One then appends an appropriate expression for the z-dependence. Finally, noting the effect of each operator in equation (16) on each function that appears in the foregoing construction (which is the Null function since it is identically zero in $0 < \theta < \beta$), one modifies this function so that it is no longer identically zero (and hence is no longer the Null function) but does become the Null function when substituted into (16). Hence, this modified function is the solution, and the process of generating it generates an infinity of constants that can be adjusted to make this function satisfy the difficult boundary condition (15).

This author will be the first to agree that this is a "brute force" technique, and that there ought to be a better method of attack. The author was unable to find one. Even the very elegant modal analysis of Greenspan [1] becomes cumbersome when one is finally forced to write out, explicitly, the functional form of the modes. And if these forms are separable, one is ultimately forced to the same tedious and involved algebra as in the Goldsbrough approach. The author presents the Goldsbrough approach for the additional reason that it seems to have been overlooked in the literature, and because it can effect the solution of difficult boundary-value problems in other areas.

Before carrying out the analysis, we find it appropriate to remark that there is some independent evidence for the validity of this technique. For example, the problem of determining the tidal wave frequencies of water in a rotating, square basin has boundary condition difficulties similar to this problem. Taylor [8], leaning heavily on its two-dimensionality, solved the problem. Jeffreys [11], from his analysis of tidal wave frequencies in an elliptical basin, argues that several of Taylor's conclusions are incorrect. Goldsbrough [12], using his Null function technique, confirms Heffrey's criticisms. Grace [13], Corkan and Doodson [14], and Rao [15], all working with stream function expansions, confirm Goldsbrough. One great advantage of the Goldsbrough approach is that it is not limited to two dimensions as is the stream function expansion approach.

The Goldsbrough Solution and the Frequency Equation. We follow the aforementioned recipe and begin construction of G, the Goldsbrough Null function for the region $0 < \theta < \beta$, by expanding the trigonometric functions that appear in the Stewartson problem in a Fourier series in that interval and then subtracting the series from the function, thus

$$\begin{aligned}G \equiv \cos(2m\pi\theta/\beta) - (4/\pi)\sum_{k=1}^{\infty}(2k-1)\sin\{(2k-1)\pi\theta/\beta\}/[(2k\\ -1)^2-(2m)^2] + \sin(2m\pi\theta/\beta) - [-(4/\pi)]\sum_{k=1}^{\infty}2m\cos\{(2k\\ -1)\pi\theta/\beta\}/[(2k-1)^2-(2m)^2] + \cos\{(2m-1)\pi\theta/\beta\}\\ -(4/\pi)\sum_{k=1}^{\infty}2k\sin(2k\pi\theta/\beta)/[(2k)^2-(2m-1)^2]\\ +\sin\{(2m-1)\pi\theta/\beta\} - [-(4/\pi)]\sum_{k=1}^{\infty}(2m-1)\\ \times\cos(2k\pi\theta/\beta)/[(2k)^2-(2m-1)^2] \quad (22)\end{aligned}$$

This expression, in which m is an integer, is identically zero in the interval $0 < \theta < \beta$ because the Σ terms are the Fourier expansions of the non-Σ terms in that interval. The angle between the barriers, β, is such that $n\beta = 2\pi$, where n is the number of barriers.

Following Goldsbrough, we now judiciously modify expression (22) so that it is nonzero, involves the orthogonal Bessel functions appearing in the Stewartson solution, and is a solution of equation (16). To effect this, it is convenient to take advantage of the fact that boundary condition (14) is independent of whether or not there are barriers. So, in terms of

$$J_\alpha(\gamma r/a)[A\cos\alpha\theta + B\sin\alpha\theta]\cosh(kz/a)\sqrt{[1-(2\Omega/\lambda)^2]},$$

a representative solution for the Stewartson nonbarriered cavity, boundary condition (14) is

$$\begin{aligned}\{(d/dr)J_\alpha(\gamma r/a)[A\cos\alpha\theta + B\sin\alpha\theta]\\ +(2\Omega/i\lambda r)J_\alpha(r\gamma/a)[-A\sin\alpha\theta + B\cos\alpha\theta]\}_{r=a} = 0 \quad (14a)\end{aligned}$$

Equating to zero the coefficients of cos $\alpha\theta$ and sin $\alpha\theta$, and then insisting that A and B be nonzero, one gets

$$\{[dJ_\alpha(r\gamma/a)/dr]^2 - [(2\Omega\alpha/r\lambda)J_\alpha(r\gamma/a)]^2\}_{r=a} = 0 \quad (23)$$

where $\alpha = 2m\pi/\beta$, $(2m-1)/\pi/\beta$, $2k\pi/\beta$, or $(2k-1)/\pi/\beta$, $J_\alpha(\gamma r/a)$ is the first kind Bessel function of order α, and γ is a separation constant. We now use the fact that the orthogonality of the Bessel functions implied by this relationship allows one to write

$$1 = \sum_{\nu=1}^{\infty} A_\nu J_\alpha(r\gamma_\nu{}^\alpha/a) \quad (24)$$

where $\gamma_\nu{}^\alpha$ is the νth zero of equation (23), and where

$$A_\nu{}^\alpha = \int_0^a rJ_\alpha(r\gamma_\nu{}^\alpha/a)dr \Big/ \int_0^a rJ_\alpha(r\gamma_\nu{}^\alpha/a)dr \quad (25)$$

Hence, we write (22) as

$$\begin{aligned}G \equiv 1\cdot\cos(2m\pi\theta/\beta) - 1\cdot(4/\pi)\sum_{k=1}^{\infty}(2k-1)\sin\{(2k\\ -1)\pi\theta/\beta\}/[(2k-1)^2-(2m)^2] + 1\cdot\sin(2m\pi\theta/\beta) - 1\cdot(-4/\pi)\\ \times\sum_{k=1}^{\infty}2m\cos\{(2k-1)\pi\theta/\beta\}/[(2k-1)^2-(2m)^2]\\ +1\cdot\cos\{(2m-1)\pi\theta/\beta\} - 1\cdot(4/\pi)\sum_{k=1}^{\infty}2k\sin(2k\pi\theta/\beta)/[(2k)^2\\ -(2m-1)^2] + 1\cdot\sin\{(2m-1)\pi\theta/\beta\} - 1\cdot(-4/\pi)\sum_{k=1}^{\infty}(2m-1)\\ \times\cos(2k\pi\theta/\beta)/[(2k)^2-(2m-1)^2] \quad (22a)\end{aligned}$$

and then replace unity, i.e., 1, in this expression by the appropriate form of equation (24). We then use the fact that

$$\begin{aligned}[\nabla^2 - (2\Omega/\lambda)^2\partial^2/\partial z^2]\cos\alpha\theta J_\alpha(r\gamma_\nu{}^\alpha/a)\cosh[\epsilon z/a\sqrt{\{1-(2\Omega/\lambda)^2\}}\\ = \{\epsilon^2/a^2 - (\gamma_\nu{}^\alpha/a)^2\}\cos\alpha\theta J_\alpha(r\gamma_\nu{}^\alpha/a)\\ \times\cosh[\epsilon z/a\sqrt{\{1-(2\Omega/\lambda)^2\}}] \quad (26)\end{aligned}$$

where the term being operated on by $\{\nabla^2 - (2\Omega/\lambda)^2\partial^2/\partial z^2\}$ is, formally, similar to a separable solution of the nonbarriered problem, but where ϵ, which is not equal to $\gamma_\nu{}^\alpha$, as it is for the Stewartson problem, is an yet undetermined separation constant for the separated ordinary differential equations in z and r. We can thus write the following modification of equation (22a) (which we will label Φ rather than G because it will then no longer be identically zero in $0 < \theta < \beta$, i.e., it will no longer be the Null function):

$$\begin{aligned}\Phi = \{A\cosh(\epsilon z/a\sqrt{}) + B\sinh(\epsilon z/a\sqrt{})\}\\ \times\left[\sum_{\nu=1}^{\infty}\sum_{m=0}^{\infty}\left\{A^M J_M(A_M\cos M\theta + B_M\sin M\theta)/(\epsilon,\gamma,M)\right.\right.\\ \left.\left.-(4/\pi)\sum_{k=1}^{\infty}A_\nu{}^{k'}J_{k'}[A_M(k'\pi/\beta)\sin k'\theta\right.\right. \quad (27)\end{aligned}$$

$$- B_M 2m \cos k'\theta]/(\epsilon, \gamma, k')(k'^2\beta/\pi^2 - 4m^2)\Big\}$$

$$+ \sum_{\nu=1}^{\infty} \sum_{m=1}^{\infty} \Big\{A^{m'} J_{m'}[A_{m'} \cos m'\theta + B_{m'} \sin m'\theta]/(\epsilon, \gamma, m')$$

$$- (4/\pi) \sum_{k=1}^{\infty} A^K J_K [A_{m'} 2k \sin K\theta - B_{m'}(m'\beta/\pi)$$

$$\times \cos K\theta]/(\epsilon, \gamma, K)(4k^2 - m'^2\beta^2/\pi^2)\Big]\Big\} \quad (27)$$

(*Cont.*)

In this equation, for the sake of brevity, we have set $\sqrt{[1 - (2\Omega/\lambda)^2]} \equiv \sqrt{}$, $M \equiv 2m\pi/\beta$, $(\epsilon/a)^2 - (\gamma_\nu{}^\alpha/a)^2 \equiv (\epsilon, \gamma, \alpha)$, $k' \equiv (2k-1)\pi/\beta$, $m' \equiv (2m-1)\pi/\beta$, $K \equiv 2k\pi/\beta$, and $J_\alpha(r\gamma_\nu{}^\alpha/a) \equiv J_\alpha$.

Expression (27) is a solution of equation (6); for, not only when substituted into (6) does it yield the Null function G (and hence zero), but also (*a*) by construction it satisfies boundary condition (14), (*b*) there are sufficient constants to assure satisfaction of the other two boundary conditions, and (*c*) all of the functions, of which the A_α's and B_α's are coefficients, are convergent throughout the sector and are finite on $r = a$, $z = \pm c$, and $\theta = 0, \beta$. On the other hand, as Greenspan [1] makes clear, there may be a practical problem with the rapidity of convergence of the series expression for the solution owing to the inhomogeneous boundary condition (13) and the fact that the mere presence of the inertial waves implies discontinuities in the flow field. We shall return to this matter in Section 3. Finally, with respect to expression (27), note that p', the solution of equation (5), will consist of terms of the form $h_1(r)h_2(\theta)h_3(z)e^{i\lambda t}$, a form indicating that the pressure waves are stationary rather than progressive. It is obvious, however, that the solution is not the simple separation of variable form $T(t)U(r)V(\theta)W(z)$; rather it is an infinite sum of separable solutions, none of which alone satisfies the boundary conditions. What we have, in essence, is a "Fourier series" of separable solutions.

The substitution of expression (27) into boundary condition (13) gives immediately $A = 0$, a result allowing one to absorb B into the A_α's and B_α's. Then expanding the cosines and sines on the right-hand side of equation (13) into Fourier series in the interval 0 to β and expanding r in a Bessel function series

$$\left(r = \sum_{\nu=1}^{\infty} C_\nu{}^\alpha J_\alpha[r\gamma_\nu{}^\alpha/a],\right.$$

where

$$C_\nu{}^\alpha = \int_0^a r^2 J_\alpha(r\gamma_\nu{}^\alpha/a)dr \Big/ \left. \int_0^a r J_\alpha{}^2(r\gamma_\nu{}^\alpha/a)dr\right)$$

and then equating the series on both sides of the equation term by term, one can determine the A_α's and the B_α's. The denominator of each of these constants contains the term $\cosh\{\epsilon c/a\sqrt{[1 - 4/(\lambda/\Omega)^2]}\}$, where ϵ is the as yet undetermined separation constant. Since these A_α's and B_α's determine the amplitude of the pressure fluctuations, it follows that these amplitudes become infinite when $c/a\sqrt{\{1 - 4/(\lambda/\Omega)^2\}} = (2j+1)\pi i/2$, $j = 0, 1, 2, \ldots$. This expression would determine the resonant frequency λ in terms of the geometry of the cavity if we knew ϵ, the aforementioned separation constant. As we shall show, however, the frequency equation we are about to derive will also involve ϵ and λ; hence, we can use this relation to eliminate the unknown separation constant ϵ, leaving the frequency equation in terms of λ alone.

We now consider boundary condition (15). The frequency equation, which will result from this relation because it will give us finally an equation involving only λ as the unknown, can be gotten most expeditiously if we use the two identities and the expansion involving Bessel functions that follow:

$$(d/dr)J_\alpha(r\gamma_\nu{}^\alpha/a) = (\gamma_\nu{}^\alpha/2a)[J_{\alpha-1}(r\gamma_\nu{}^\alpha/a) - J_{\alpha+1}(r\gamma_\nu{}^\alpha/a)] \quad (28)$$

$$J_\alpha(r\gamma_\nu{}^\alpha/a) = (r/2\alpha)[J_{\alpha+1}(r\gamma_\nu{}^\alpha/a) + J_{\alpha-1}(r\gamma_\nu{}^\alpha/a)] \quad (29)$$

$$J_\alpha(r\gamma_\nu{}^\alpha/a) = \sum_{p=0}^{\infty} (2p+\alpha)\Gamma(p+\alpha)_2 F_1(-p, \alpha+p, a+1, [\gamma_\nu{}^\alpha]^2)J_{\alpha+2p}(r/a)/\{p!\Gamma(\alpha+1)\}$$

$$\equiv \sum_{p=0}^{\infty} H_{p,\alpha} J_{\alpha+2p}(r/a) \quad (30)$$

Equation (30) is the Neuman expansion (Erdelyi [16]) of $J_\alpha(r\gamma_\nu{}^\alpha/a)$, and ${}_2F_1(\ \ )$ is the hypergeometric function.

Upon using (27)–(30) in equation (15), one gets n identical sets of two equations, one for $\theta = \beta$, say, and one for $\theta = 2\beta$. Hence, one need consider only any two. Following Goldsbrough, one finds that adding and subtracting the two equations give two equations much simpler to work with. And in our case, since the goal is the frequency equation which will result from setting a certain determinate equal to zero, we can omit consideration of the equation resulting from addition because the sum has as a multiplier the term

$$A_\nu{}^0 = \int_0^a [rJ_0(r\gamma_\nu{}^0/a)dr/E = -(a/\gamma_\nu{}^0)^2 J_0'(\gamma_\nu{}^0)/E,$$

where

$$E = \int_0^a rJ_0{}^2(r\gamma_\nu{}^0/a)dr.$$

From boundary condition (23), the numerator of the right-hand side of this equation is zero. Hence, adding the two equations ultimately leads to a determinant that is identically zero and thus yields no information. So, considering only the result from subtracting the two equations, one gets

$$\sum_{\nu=1}^{\infty} \sum_{m=1}^{\infty} \sum_{p=0}^{\infty} \Big\{(8\Omega/i\sigma\pi) \sum_{k=1}^{\infty} A_\nu{}^{k'} H_{p,k'} 2mB_M[J_{k'+p_-'} - J_{k'+p_+'}]/[(k'\beta/\pi)^2 - (2m)^2](\epsilon, \gamma, k') + (2\Omega/i\sigma)$$

$$\times A_\nu{}^{m'} H_{p,m'} A_{m'}[J_{m'+p_-'} - J_{m'+p_+'}]/(\epsilon, \gamma, m') + (4/\pi) \sum_{k=1}^{\infty} A_\nu{}^{k'}(2k - 1)k' A_M H_{p,k'}[J_{k'+p_+'} + J_{k'+p_-'}]/(k'+2p)[(k'\beta/\pi)^2 - (2m)^2](\epsilon, \gamma, k') + A_\nu{}^{m'} m' B_{m'} H_{p,m'}[J_{m'+p_+'} + J_{m'+p_-'}]/(m'+2p)(\epsilon, \gamma, m')\Big\} = 0, \quad (31)$$

where now $J \equiv J(r/a)$, $p_-' \equiv 2p - 1$, $p_+' \equiv 2p + 1$.

Interpreting both "sides" of equation (31) to be expansions in Bessel functions of odd order, we can then set the two "series" equal term by term. In other words, we successively equate to zero the coefficients of $J_{e-1}, J_{e+1}, J_{e+3}, \ldots J_{3e-1}, J_{3e+1}, J_{3e+3}, \ldots J_{5e-1}, J_{5e+1}, J_{5e+3}, \ldots J_{7e-1}, J_{7e+1}, \ldots$, etc., where $e \equiv \pi/\beta$. This process gives us an infinite set of equations involving the A_α's and the B_α's. The condition that these constants be nonvanishing is that the determinant formed from their coefficients must vanish. Hence

$$\begin{vmatrix} D_{e-1,1}D_{e-1,2}D_{e-1,3}D_{e-1,4}D_{e-1,5} & \cdots \\ D_{e+1,1}D_{e+1,2}D_{e+1,3}D_{e+1,4}D_{e+1,5} & \cdots \\ \cdots & \cdots \\ D_{3e-1,1}D_{3e-1,2}D_{3e-1,3}D_{3e-1,4}D_{3e-1,5} & \cdots \\ D_{3e+1,1}D_{3e+1,2}D_{3e+1,3}D_{3e+1,4}D_{3e+1,5} & \cdots \\ \cdots & \cdots \\ D_{5e-1,1}D_{5e-1,2}D_{5e-1,3}D_{5e-1,4}D_{5e-1,5} & \cdots \\ D_{5e+1,1}D_{5e+1,2}D_{5e+1,3}D_{5e+1,4}D_{5e+1,5} & \cdots \\ \cdots & \cdots \end{vmatrix} = 0 \quad (32)$$

where, for example, $D_{e-1,1} = (2\Omega/i\lambda) \sum_{\nu=1}^{\infty} A_\nu{}^{\pi/\beta} H_{0,\pi/\beta})/(\epsilon, \gamma, \pi/\beta)$, $D_{3e-1,1} = 0$, $D_{3e+1,4} = (4/\pi) \sum_\nu{}^{\infty} A^{3\pi/\beta}(4\Omega/i\lambda)[H_{0,3\pi/\beta}]/5(\epsilon, \gamma, 3\pi/\beta)$, etc.

Equation (32) contains the unknowns ϵ and λ. However, from the equation $\epsilon c/a\sqrt{\{1 - (2\Omega/\lambda)^2\}} = (2j+1)\pi i/2$, we can solve for ϵ in terms of λ. Making this substitution in (32), we have an equation involving only the resonant frequency λ. Hence, it is the frequency equation. However, with λ, the frequency, as the unknown, the equation is formidable (the $A_\nu{}^\alpha$'s are functions of λ, for instance). Hence, we

Table 1 Dimensionless inertial wave frequencies versus various cavity fineness ratios for several different angles between the barriers

λ/Ω	$\lambda/\Omega + 1$	$c/[a(2j+1)]_S$	$C_{\pi/4}'$	$C_{\pi/3}'$	$C_{2\pi/5}'$	$C_{\pi/2}'$	C_{π}'	$C_{2\pi}'$
−1.00	0.00	0.995	0.0420	0.0973	0.1746	0.3081	0.3621	0.3674
−0.96	0.04	1.042	0.0443	0.1020	0.1845	0.3263	0.3806	0.3890
−0.92	0.08	1.091	0.0467	0.1069	0.1948	0.3439	0.4003	0.4124
−0.88	0.12	1.144	0.0493	0.1121	0.2058	0.3624	0.4213	0.4377
−0.84	0.16	1.201	0.0522	0.1175	0.2179	0.3829	0.4439	0.4654
−0.80	0.20	1.262	0.0552	0.1231	0.2311	0.4051	0.4682	0.4958
−0.76	0.24	1.382	0.0586	0.1291	0.2453	0.4293	0.4945	0.5295
−0.72	0.28	1.399	0.0623	0.1353	0.2612	0.4559	0.5235	0.5669
−0.68	0.32	1.478	0.0663	0.1418	0.2789	0.4854	0.5551	0.6088
−0.64	0.36	1.565	0.0709	0.1485	0.2984	0.5184	0.5902	0.6561
−0.60	0.40	1.662	0.0749	0.1519	0.3095	0.5513	0.6261	0.7093

follow both Goldsbrough [10] and Stewartson [6] and we fix λ at some reasonable value and we then let the frequency equation determine $c/a(2j+1)$, the cavity fineness ratio, which one can extract much more easily. The determinant was programmed on the HP9830 and was solved by considering successively a 2×2 determinant, then a 3×3, then a 4×4, etc., until there was no change in the fourth significant figure. In this manner we constructed Table 1 for values of $\beta = \pi/4$, $\pi/3$ $2\pi/5$, $\pi/2$, π, 2π. The slowness of convergence alluded to earlier did not seem to manifest itself here, for in no case was more than a 4×4 determinant needed, nor more than nine (9) terms needed in any summation. This agrees with some comments by Goldsbrough [10]. Perhaps the situation is saved by our interest being the eigenvalues and not an actual evaluation of the velocity or the pressure. In addition, since it is nonhomogeneity in the boundary conditions that induces the slowness of convergence, it is relevant to note that the transformation that follows equation (12) made two of the boundary conditions homogeneous, leaving the inhomogeneity in the boundary condition that was easy to satisfy.

In Table 1, λ/Ω is the dimensionless frequency one would measure in the rotating frame, and $\lambda/\Omega + 1$ is the dimensionless frequency one would measure in an inertial frame. $[c/a(2j+1)]_S$ is the Stewartson [6] fineness ratio value for a nonbarriered cavity. The negative sign for λ/Ω means that one in the rotating frame is rotating faster than the stationary wave appears to precess progradely. Finally, in Table 1, $C_\beta' \equiv c/[a(2j+1)]_\beta$, e.g., $C_{\pi/4}' \equiv c/[a(2j+1)]$ for $\beta = \pi/4$.

The salient feature about barriered cavities that Table 1 illustrates is that sectoring a cylinder increases the inertial mode frequencies as measured in an inertial frame. Relative to the experiments about to be described, a pertinent way of stating this is that, given a cavity of fixed radius but variable height, increasing the number of barriers necessitates making the cavity shorter if one wishes to maintain the same inertial mode frequency, i.e., sectoring a cylinder necessitates making it more dumpy if one doesn't wish to change the inertial mode frequency.

3 The Null Dynamical Effect of the Resonant Inertial Oscillations: Experimental Verification

The determination of the torque on the container due to the asymmetrical pressure fluctuations associated with the inertial oscillations in the sectors involves products of integrals over r, θ, and z. The θ integral has the form

$$\sum_{n=1}^{2\pi/\beta} \int_{(n-1)\beta}^{n\beta} g(\theta) d\theta,$$

where $g(\theta)$, the integrand, can be $\cos\theta \cos(2m\pi\theta/\beta)$, or $\cos\theta \sin(2m\pi\theta/\beta)$, or $\sin\theta \cos[(2m-1)\pi\theta/\beta]$, etc. Recalling the restriction that $2\pi/\beta$ must be an integer, one can show easily that these integrals sum to zero! This means, of course, that there is no net torque on the cavity due to the oscillations; and since this is the torque that produces the unstable container motion when the cavity is not sectored (Stewartson [6]), one concludes that due to this cancellation effect, the insertion of radial barriers in a cylindrical container can ameliorate the destabilizing effect of the inertial oscillations no matter what is the state of resonance. The physical reason for this is that the pressure

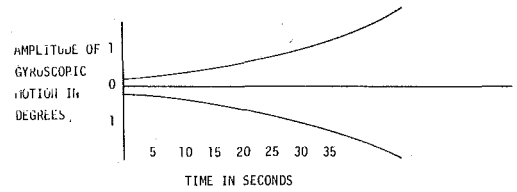

Fig. 4 Amplitude of gyroscopic motion (in degrees) versus time (in seconds) for a 100 percent liquid-filled, nonbarriered, resonant cavity; $[c/a(2j+1)]_S = 1.05$, $\Omega = 4000$ rpm, $\tau_0 = 0.048$

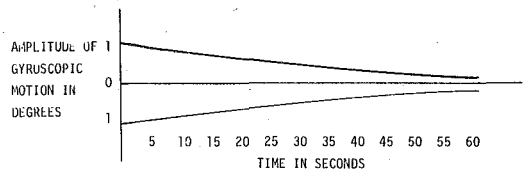

Fig. 5 Amplitude of gyroscopic motion (in degrees) versus time (in seconds) for a 100 percent liquid-filled, 90° sectored cylinder; $[c/a(2j+1)]_{90°} = 1.05$, $\Omega = 4000$ rpm, $\tau_0 = 0.40$

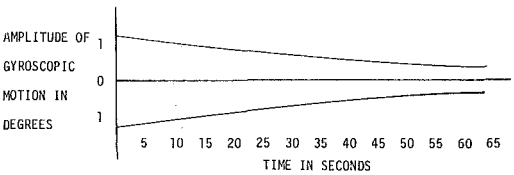

Fig. 6 Amplitude of gyroscopic motion (in degrees) versus time (in seconds) for an empty cylinder, $\Omega = 4000$ rpm, nutational frequency = 0.48

distribution due to the inertial oscillations in any given sector is a function of the geometry of that particular sector and not its angular orientation within the cavity, i.e., in so far as the inertial oscillations in a sector are concerned, the liquid does not know where it is. As experimental proof of the foregoing conclusion, we show in Fig. 4 the amplitude growth rate for a gyroscope containing a 100 percent water-filled cylinder having a $c/a(2j+1)$ value, i.e., a fineness ratio, of 1.05. (for details of the apparatus and the experiments, see Scott [17]). From Stewartson's tables [6] we find, for that fineness ratio, a dimensionless inertial wave frequency, τ_0 ($\equiv 1 + \lambda/\Omega$), of value 0.048. Adjusting the gyroscope to have that value for its nutational frequency, we have resonance and we observe the amplitude of the gyroscopic motion to grow as in Fig. 4. Inserting 90° barriers in the same cavity, thereby altering the inertial wave frequency to a value numerically far from any value in Stewartson's tables (and hence removing the system from resonance) and additionally (as shown previously) simultaneously reducing to zero the net torque due to the inertial oscillations, we observe in Fig. 5 the amplitude of motion of the gyroscope to decay (as it should according to the theory) with nearly the same decay rate as when empty (Fig. 6).

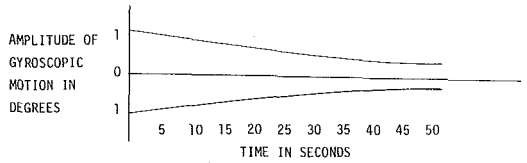

Fig. 7 Amplitude of gyroscopic motion (in degrees) versus time (in seconds) for a 100 percent liquid-filled resonant sectored cavity, with four 90° sectors; Ω = 4000 rpm, $[c/a(2j+1)]_{90°} = 0.3298$, $\tau_0 = 0.048$

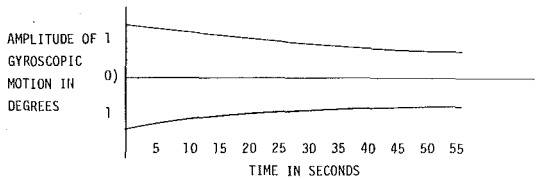

Fig. 8 Amplitude of gyroscopic motion (in degrees) versus time (in seconds) for a liquid-filled resonant cavity with only one 90° sector; Ω = 4000 rpm, $[c/a(2j+1)]_{90°} = 0.3298$, $\tau_0 = 0.048$

We next consider a resonant sectored cavity. According to Table 1, a value of $c/a(2j+1)$ of 0.3298 for a cavity with $\beta = 90°$ gives a τ_0 value (i.e., a $\lambda/\Omega + 1$ value) for the liquid of 0.048. As just mentioned, adjusting the nutational motion of the gyroscope to have a nutational frequency of that value, we have resonance. However, the zero net torque (as the theory indicates) should result in a gyroscope damping at nearly the same rate as in Fig. 5 (where there was no resonance). That Fig. 7 seems experimentally to confirm this conclusion is comforting, even though the author is well aware that the figure may simply mean that the resonant frequency has been miscalculated.

4 Concluding Remarks

An objection to the experimental results can be raised by pointing out that, unlike the case for the unsectored cylinder where the resonance can be inferred from the visual observations of the amplitude growth (Scott [17]), no such observations can be made here because of the cancelling effect of the several sectors. Ideally, then, one should use the pressure measurement technique of Aldridge and Toomre [18] to determine the inertial modes. However, not only did we not have immediate access to such an apparatus, but also since the gyroscope had been very effective even in determining the small frequency shifts due to the effect of viscosity on the inertial modes (Karpov, [19]), we chose to use it to consider the effect of a single sector. So, consider again the previous case, but with a single 90° sector rather than four, and with the remainder of the cavity being filled with lucite having the same density as the liquid (a one centistoke viscosity silicone oil). Again adjusting the gyroscope to have a nutation frequency of 0.048, we have resonance. However, in the final expression for the torque on a single sector, terms like $\rho\pi a^2(2c)$, the mass of the liquid, appear as multiplicative factors, thereby governing the magnitude of the torque. If this mass is too small, then even the amplification at exact resonance may not be large enough to overcome the natural amplitude decay rate of the gyroscope. Accordingly, it appears that the mass of the liquid in this single sector, one fourth that of the preceding experiment, was too small to effect an amplitude growth of the gyroscope (see Fig. 8). The use of a larger cavity or a heavier liquid was then in order. Unfortunately, we had only one gyroscope, which did not allow the use of a larger cylinder (Scott [17]). Also, the use of mercury, which would have been the ideal liquid to solve the small mass problem, was disallowed by safety personnel at the Ballistic Research Laboratories.

In spite of the small mass, we should, nevertheless, expect a decrease in the natural damping rate of the gyroscope. Figs. 8 and 9 give some evidence of this, evidence that is admittedly perhaps not very convincing because the difference in slopes in Fig. 9 is not too far removed from noise level. We remark, however, that the reproducibility of the experiments does tend to remove some of the inconclusiveness. In addition, Karpov [19] showed that dissipation effects that may cloud the issue in these experiments are almost negligible for the low viscosity liquids used (water and silicone oil). Finally, in response to any concern that imperfect density matching of the lucite and liquid might affect the decay rate, we remark the Murphy and Nicolaides [20] showed that such an asymmetry would change the gyroscopic motion to a tricyclic one. We observed no evidence of such an effect in these experiments.

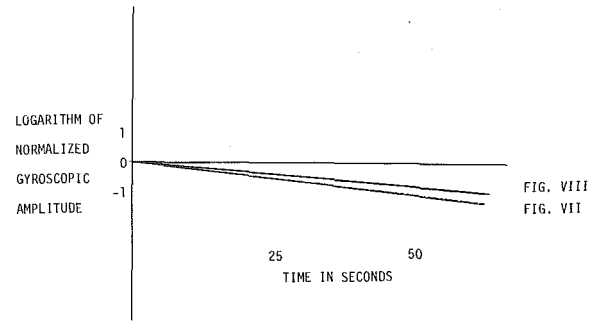

Fig. 9 Logarithm of the normalized gyroscopic amplitudes in Figs. 7 and 8 versus time in seconds

References

1 Greenspan, H. P., *The Theory of Rotating Fluids,* Cambridge University Press, London, 1968, pp. 51–54, 68–78, 81–85, 305–320.

2 Kelvin, Lord, "Vibrations of a Columnar Vortex," *Philosophical Magazine,* Vol. 10, 1880, p. 155.

3 Bjerkness, V., et al., *Physikalische Hydrodynamik,* Springer, Berlin, 1933.

4 Greenhill, A. G., "Vibrations of an Ellipsoid Containing Fluid," *Proceedings of the Cambridge Philosophical Society,* Vol. 4, 1883, p. 4.

5 Hough, S. S., "The Oscillations of a Rotating Ellipsoidal Shell Containing Fluid," *Philosophical Transactions of the Royal Society,* Series A, Vol. 186, 1896, p. 469.

6 Stewartson, K., "On the Stability of a Spinning Top Containing Fluid," *Journal of Fluid Mechanics,* Vol. 5, 1959, pp. 577–592.

7 Scott, W. E., "The Frequency of Inertial Waves in a Rotating, Sectored Cylinder," ASME JOURNAL OF APPLIED MECHANICS, Vol. 43, 1976, pp. 571–574.

8 Taylor, G. I., "Tidal Oscillations in Gulfs and Rectangular Basins," *Proceedings of the London Mathematical Society,* Vol. 20, 1922, p. 148.

9 Proudman, J., "On Some Cases of Tidal Motion on Rotating Sheets of Water," *Proceedings of the London Mathematical Society,* Vol. 2, 1913, p. 12.

10 Goldsbrough, G. R., "Tidal Oscillations on Rotating Globes," *Proceedings of the Royal Society,* Series A, Vol. 117, 1928, p. 692.

11 Jeffreys, H., "The Free Oscillations of Water in an Elliptical Lake," *Proceedings of the London Mathematical Society,* Vol. 23, 1925, p. 455.

12 Goldsbrough, G. R., "Tidal Oscillations in Rectangular Basins," *Proceedings of the Royal Society,* Series A, Vol. 132, 1931, pp. 689–701.

13 Grace, S. F., "Tidal Oscillations on Rectangular Seas," *Monthly Notices of the Royal Astronomical Society,* Vol. 11, 1931, p. 8.

14 Corkan, R. H., and Doodson, A. T., "Free Tidal Oscillations in a Rotating Square Sea," *Proceedings of the Royal Society,* Series A, Vol. 215, 1952, p. 147.

15 Rao, D. B., "Free Gravitational Oscillations in Rotating Rectangular Basins," *Journal of Fluid Mechanics,* Vol. 25, 1966, p. 523.

16 Erdelyi, A., *Higher Transcendental Functions,* McGraw-Hill, New York, Vol. 2, 1953, p. 64, equation 19.6.

17 Scott, W. E., "Amplitude Dependent Behavior of a Liquid Filled Gyroscope," *Journal of Fluid Mechanics,* Vol. 60, 1973, Part 4, p. 751.

18 Aldridge, K., and Toomre, A., "Inertial Oscillations of a Rotating Fluid Sphere," *Journal of Fluid Mechanics,* Vol. 37, 1969, Part 2, p. 307.

19 Karpov, B. G., "Liquid Filled Gyroscope: The Effect of Reynolds Number on Resonance," United States Army Ballistic Research Laboratories Report Number 1302, 1965.

20 Murphy, C. H., and Nicolaides, J. D., "A Generalized Ballistic Force System," United States Army Ballistic Research Laboratories Report Number 933, 1955, Aberdeen Proving Ground.

J. Sanders
Graduate Student,
Department of Aerospace Engineering
and Mechanics,
University of Minnesota,
Minneapolis, Minn. 55455

V. O'Brien
Principal Staff Physicist,
Applied Physics Laboratory,
Johns Hopkins University,
Laurel, Md. 20810

D. D. Joseph
Professor,
Department of Aerospace Engineering
and Mechanics,
University of Minnesota,
Minneapolis, Minn. 55455

Stokes Flow in a Driven Sector by Two Different Methods

A biorthogonal series expansion and a numerical finite-difference approximation are applied to the problem of steady Stokes flow in a driven sector of 10° total angle, providing mutual support of the theoretical techniques. For this problem the method of biorthogonal series is faster, cheaper, and more accurate.

Introduction

In this paper we model the Stokes flow in a long driven sector, using finite differences and a biorthogonal series expansion to compare the results. The problem is chosen from a modified Couette flow including a sector cavity [1]. Our aim is to examine closely the results of the approximate finite difference solution and to advertise the biorthogonal series for solving biharmonic boundary-value problems in domains where separation of variables is possible (a very common problem in fluid mechanics and elasticity). The analytic method is elucidated in [2, 3]. New aspects concerning the computation are developed here.

Mathematical Formulation

The slow motion of a Newtonian liquid, neglecting gravity (Stokes flow) for two-dimensional flow is described by

$$\nabla^4 \Psi = 0 \tag{1}$$

where Ψ is the stream function and ∇^2 is the Laplacian operator. Using polar coordinates (r, φ, z),

$$\nabla^2 = \frac{1}{r}\frac{\partial}{\partial r}\left(r\frac{\partial}{\partial r}\right) + \frac{1}{r^2}\frac{\partial^2}{\partial \varphi^2}$$

and the velocity $\mathbf{v} = \text{rot}\,(\Psi \mathbf{e}_z)$. In our model there shall be viscous nonslip at the solid walls $\varphi = \pm\beta$ and $r = r_0$. At the outer radius $r = r_1 = 1$ we prescribe the vorticity $\Omega = 1 - \sin^3(\pi\varphi/2\beta)$, where $\Omega = -\nabla^2\Psi$, and no flow through the surface shall be possible (Fig. 1). For our comparison we chose $r_0 = 0.05$ and $2\beta = 10°$.

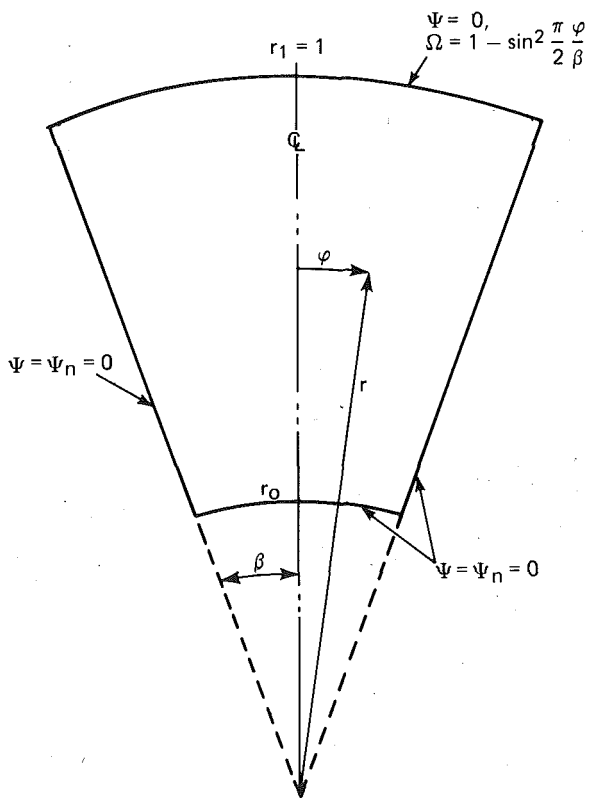

Fig. 1 The biharmonic sector problem

The Series Solution

The theory of biorthogonal series for biharmonic functions as described in [2, 3] allows us to write the solution of (1) in the form

Contributed by the Applied Mechanics Division for publication in the JOURNAL OF APPLIED MECHANICS.

Discussion on this paper should be addressed to the Editorial Department, ASME, United Engineering Center, 345 East 47th Street, New York, N. Y. 10017, and will be accepted until December 1, 1980. Readers who need more time to prepare a discussion should request an extension from the Editorial Department. Manuscript received by ASME Applied Mechanics Division, May, 1979; final revision, October, 1979.

Table 1 The first five eigenvalues (note that $\lambda_{-n} = \bar{\lambda}_n$ where overbar denotes complex conjugate)

n	λ_n
1	$25.14114414 + 12.86408537i$
2	$62.38088865 + 17.74998684i$
3	$98.82482881 + 20.31681729i$
4	$135.06392018 + 22.08005326i$
5	$171.21595479 + 23.42596613i$

$$\Psi = \sum_{-\infty}^{\infty} \left(C_n r^{\lambda_n} + D_n r^{-\lambda_n+2} \right) \frac{\phi_1^{(n)}(\varphi)}{\lambda_n(\lambda_n - 2)} \tag{2}$$

where $\phi_1^{(n)}(\varphi) = \cos(\lambda_n - 2)\beta \cos\lambda_n\varphi - \cos\lambda_n\beta \cos(\lambda_n - 2)\varphi$, the λ_n are roots of $\sin[2\beta(\lambda_n - 1)] + (\lambda_n - 1)\sin 2\beta = 0$ (see Table 1) and $C_0 = D_0 = 0$. The boundary conditions at $\varphi = \pm\beta$ are already satisfied, so that the constants C_n and D_n will have to match the conditions at the inner and outer radius.

We introduce the biorthogonal sequence $\boldsymbol{\phi}^{(n)}, \boldsymbol{\psi}^{(n)}$, where

$$\boldsymbol{\phi}^{(n)} = \left(\phi_1^{(n)}, \phi_2^{(n)} \right) \text{ with } \phi_2^{(n)} \equiv \phi_1^{(n)''}(\varphi)/\lambda_n(\lambda_n - 2),$$

corresponding adjoint $\boldsymbol{\psi}^{(n)}$ with

$$\psi_1^{(n)} \equiv \frac{(\lambda_n - 2)}{\lambda_n} \cos(\lambda_n - 2)\beta \cos\lambda_n\varphi - \frac{\lambda_n}{\lambda_n - 2} \cdot \cos\lambda_n\beta \cos(\lambda_n - 2)\varphi; \; \psi_2^{(n)} \equiv \phi_1^{(n)}$$

such that

$$\langle \boldsymbol{\psi}^{(n)T} A \boldsymbol{\phi}^{(m)} \rangle \equiv \int_{-\beta}^{\beta} \boldsymbol{\psi}^{(n)T} A \boldsymbol{\phi}^{(m)} \, d\varphi = 0 \quad \text{for} \quad (\lambda_n - 1)^2 \neq (\lambda_m - 1)^2$$

$$= F_n \quad \text{for} \quad (\lambda_n - 1)^2 = (\lambda_m - 1)^2 \tag{3}$$

and the biorthogonality matrix

$$A = \begin{pmatrix} 0 & -1 \\ 1 & 2 \end{pmatrix}.$$

The "Fourier" coefficients C_n and D_n are determined by the biorthogonality condition

$$\left\langle \boldsymbol{\psi}^{(n)T} A \begin{pmatrix} \Psi_{rr} + \frac{1}{r}\Psi_r \\ \Psi_{\varphi\varphi} \end{pmatrix} \right\rangle \Bigg|_{r=r_1} = -\left\langle \boldsymbol{\psi}^{(n)T} A \begin{pmatrix} 1 - \sin^2\left(\frac{\pi\varphi}{2\beta}\right) \\ 0 \end{pmatrix} \right\rangle \tag{4a}$$

and

$$\left\langle \boldsymbol{\psi}^{(n)T} A \begin{pmatrix} \Psi_r \\ \Psi_{\varphi\varphi} \end{pmatrix} \right\rangle \Bigg|_{r=r_0} = 0. \tag{4b}$$

Further details of the theory can be found in [2]. We solve the linear system (4) by truncation, i.e., replace the "∞" sign in (2) by a finite number. At this point it is interesting to look at equations (4) in detail,

$$(C_n + D_n)F_n + \sum_{m=-\infty}^{\infty} \left(\frac{2}{\lambda_m - 2} C_m - \frac{2}{\lambda_m} D_m \right) \langle \phi_1^{(n)} \phi_1^{(m)} \rangle = -\left\langle \boldsymbol{\psi}^{(n)T} A \begin{pmatrix} 1 - \sin^2\frac{\pi\varphi}{2\beta} \\ 0 \end{pmatrix} \right\rangle \tag{5a}$$

where

$$F_n = 4\left(\frac{\beta \cos^2\lambda_n\beta}{\lambda_n} - \frac{\beta \cos^2(\lambda_n - 2)\beta}{(\lambda_n - 2)} - \frac{1}{\lambda_n(\lambda_n - 2)} \sin 2\beta \cos\lambda_n\beta \cos(\lambda_n - 2)\beta \right),$$

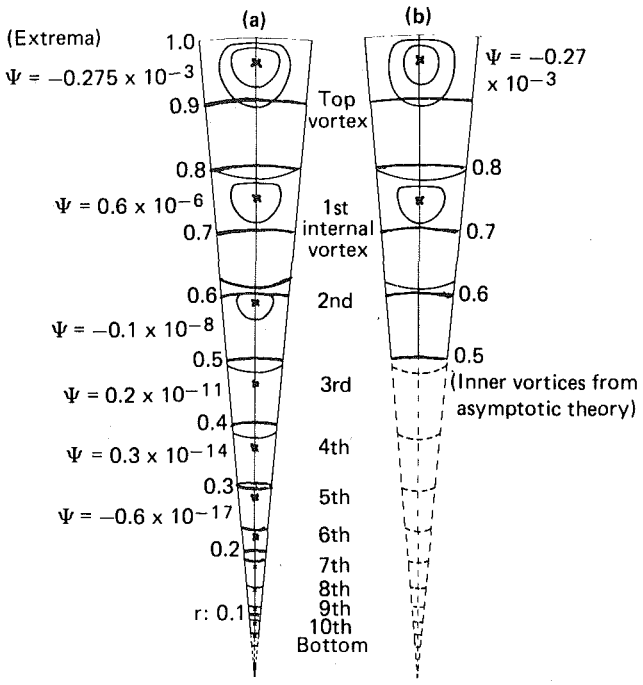

Fig. 2 Sector solutions (streamlines); extrema at vortex centers, X; (a) biorthogonal series solution; (b) approximate solution

Table 2 Coefficients in the biorthogonal series (scientific notation: the second number is the power of ten)

	Real	Imaginary
C_1	(0.208369 + 01,	−0.219573 + 00)
C_2	(−0.266598 + 00,	0.440204 + 00)
C_3	(−0.851842 − 01,	0.559270 − 01)
C_4	(−0.332293 − 01,	0.152098 − 01)
C_5	(−0.162217 − 01,	0.596175 − 02)
D_1	(−0.201026 − 62,	0.686494 − 62)
D_2	(0.760589 − 112,	0.229382 − 111)
D_3	(0.459605 − 159,	0.613469 − 159)
D_4	(−0.258214 − 206,	0.221233 − 206)
D_5	(0.697736 − 254,	0.252238 − 254)

and

$$\sum_{m=-\infty}^{\infty} r_0^{\lambda_m} C_m \left(2\langle \phi_1^{(n)} \phi_2^{(m)} \rangle + \frac{\langle \phi_1^{(n)} \phi_1^{(m)} \rangle}{r_0(\lambda_m - 2)} - \langle \psi_1^{(n)} \phi_2^{(m)} \rangle \right) + r_0^{-\lambda_m} D_m \left(2r_0^2 \langle \phi_1^{(n)} \phi_2^{(m)} \rangle - \frac{r_0}{\lambda_m} \langle \phi_1^{(n)} \phi_1^{(m)} \rangle - r_0^2 \langle \psi_1^{(m)} \phi_1^{(m)} \rangle \right) = 0. \tag{5b}$$

For the chosen β, the real parts of the eigenvalues λ_n are very large (Table 1), so that for $r_0 = 0.05$ the coefficients in (5b) suggest that the C_m are large compared with the D_m. Therefore (5a) or (4a) can be solved for the C_m, neglecting the D_m, which then can be easily found from (5b) or (4b) (or find $\tilde{D}_m = r_0^{-\lambda_m} D_m$). Thus the system (4) or (5) is split into two systems that can be solved consecutively. This reflects the fact that the boundary condition at r_0 does not have any significant influence on the flow, except very close to r_0 where the $D_n r^{-\lambda_n+2}$ term in (2) is dominating (even when the D_n are small). Note that the $D_n = 0$ for $r_0 = 0$.

Result. Sufficient accuracy of the truncated series can be obtained for five terms in the series. The coefficients C_n and D_n converge rapidly as n increases; see Table 2. The residual error in the boundary

Table 3 Boundary values at the inner and outer radius; a_1, b_1, c_1, and d_1 are the indicated values at the boundary; they are compared to: a_2 the prescribed vorticity at $r = 1$, $b_2 = c_2$ the zero stream function values and d_2 the zero gradient value at $r = 0.05$

φ	a_1 $\Omega(r = 1)$	a_2 $1 - \sin^2 \varphi\pi/10°$	b_1 $\Psi(r = 1)$	b_2 $\Psi(r = 1)$	c_1 $\Psi(r = 0.05)$	c_2 $\Psi(r = 0.05)$	d_1 $\partial\Psi/\partial r$ $(r = 0.05)$	d_2 $\partial\Psi/\partial r$ $(r = 0.05)$
0°	0.9990	1	$-0.659 \cdot 10^{-7}$	0	$0.141 \cdot 10^{-39}$	0	$0.231 \cdot 10^{-35}$	0
1°	0.9056	0.9045	$0.552 \cdot 10^{-7}$	0	$-0.149 \cdot 10^{-39}$	0	$-0.220 \cdot 10^{-35}$	0
2°	0.6530	0.6545	$0.204 \cdot 10^{-7}$	0	$0.156 \cdot 10^{-39}$	0	$0.182 \cdot 10^{-35}$	0
3°	0.3481	0.3455	$-0.452 \cdot 10^{-7}$	0	$-0.115 \cdot 10^{-39}$	0	$-0.103 \cdot 10^{-35}$	0
4°	0.0910	0.0955	$0.129 \cdot 10^{-6}$	0	$-0.337 \cdot 10^{-40}$	0	$-0.757 \cdot 10^{-36}$	0
5°	−0.0052	0	0	0	0	0	$0.407 \cdot 10^{-46}$	0

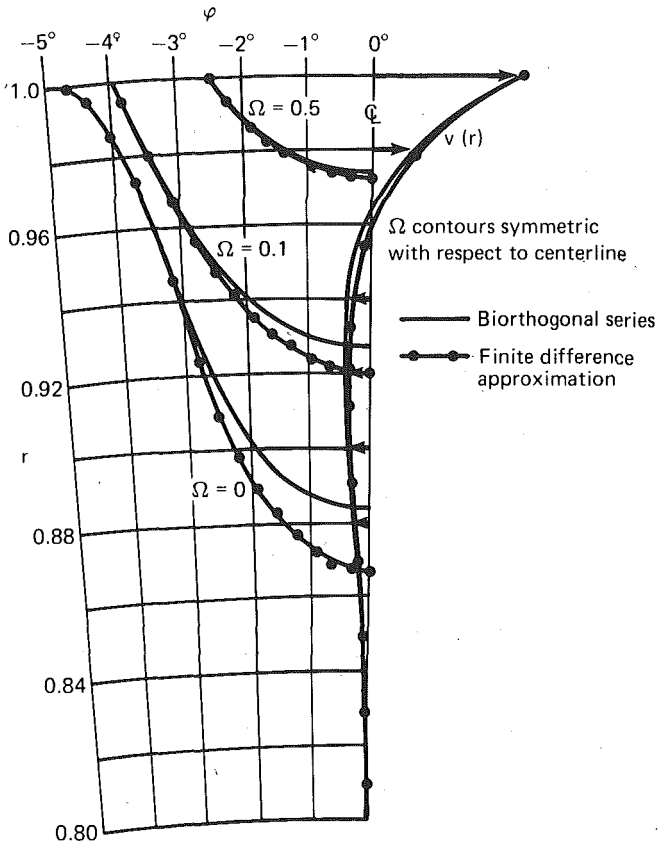

Fig. 3 Comparisons of the velocity and vorticity in the outer region; —— biorthogonal series; - - -0- - - approximate solution

conditions is insignificant; see Table 3. The Ψ boundary conditions are satisfied exactly on the sidewalls, $\beta = \pm 5°$. The stream function Ψ (Fig. 2(a)) and vorticity (Fig. 3) show details of the solution.

The Numerical Solution

Now the same problem is solved numerically using finite differences. A successive over-relaxation method is used, alternating between Ψ and Ω with a fixed relaxation factor for each as described in [4]. The relaxation factors were not optimized. In order to work in a rectangular plane a new radial coordinate $\eta = \ln r$ is introduced. Compromising between the desired accuracy and the cost of the computations, we use meshes of $h_\eta = 0.023404$ and $h_\varphi = 0.005454$.

Result. The stream function Ψ (Fig. 2(b)) and the vorticity Ω are calculated until their residual values are less than 10^{-9} and 10^{-6}, respectively. Asymptotic theory,[1] utilizing the first eigenvalue (after Moffatt [5] with Burggraf correction [6]), is used to fill in the inner part of the sector where Ω residuals exceed the functional values. Results are shown in Fig. 2(b) and Fig. 3.

Comparison

The profiles of the center-line velocity are compared in Fig. 3. The velocity at the center of the outside arc is 0.0201 for the approximate numerical solution and 0.0196 in the analytical result.

It is obvious that the result of the biorthogonal series solution is more accurate and because of the easy, straightforward computation its use should be preferred for similar problems. The computation of the numerical solution was carried out on an IBM 360/91 requiring about 66 sec of computing time compared to only fractions of a second for the series (on a Cyber 74). However, this test has shown that the numerical results may be good enough for many applications (within the two top vortices, where the liquid flows fastest, the streamline error lies within the mesh length) and the method can be applied to more general, nonseparable domains. The truncation error can be reduced by a finer mesh computation.

References

1 O'Brien, V., "Steady Circular Shear Flow Over a Sector Cavity," (submitted elsewhere).

2 Liu, C. H., and Joseph, D. D., "Stokes Flow in Wedge-Shaped Trenches," *Journal of Fluid Mechanics*, Vol. 80, Part 3, 1977, pp. 443–463.

3 Joseph, D. D., "A New Separation of Variables Theory for Problems of Stokes Flow and Elasticity," (Sept. 1977), to appear.

4 Erhlich, L. W., "Solving the Biharmonic Equation as Coupled Finite-Difference Equations," *SIAM Journal of Num. Anal.*, Vol. 8, 1971, pp. 278–287.

5 Moffatt, H. K., "Viscous and Resistive Eddies Near a Sharp Corner," *Journal of Fluid Mechanics*, Vol. 18, Part 1, 1964, pp. 1–18.

6 Burggraf, O. R., "Analytical and Numerical Studies of the Structure of Steady Separated Flows," *Journal of Fluid Mechanics*, Vol. 24, Part 1, 1966, pp. 113–151.

[1] Neglecting the boundary condition at r_0 which cannot be satisfied.

A. Mir-Mohamad-Sadegh
Postdoctoral Scholar.
Assoc. Mem. ASME

K. R. Rajagopal
Lecturer.

Department of Applied Mechanics and Engineering Sciences,
The University of Michigan,
Ann Arbor, Mich. 48109

The Flow of a Non-Newtonian Fluid Past Projections and Depressions

The plane flow of a homogenous incompressible second-order fluid past projections or depressions of arbitrary shape is considered. A numerical technique based on a boundary integral equation is developed and the problem of the flow past a rectangular slot of depth d and width W is solved.

1 Introduction

A numerical scheme based on boundary integral equations is developed to determine the flow characteristics of a homogenous incompressible fluid of second grade past a projection or a depression of arbitrary shape. Restricting attention to a rectangular slot of finite depth, the streamlines, due to the flow of a second-grade fluid past such a slot, are determined. While the problem of the flow a Navier-Stokes fluid past a circular projection or depression has been obtained by Schubert [1], the technique used depends on conformal transformations which cannot be used when arbitrary shapes are involved, unlike the technique developed herein. It is also pointed out that the technique could be gainfully employed in determining the "hole pressure error" due to the flow of such a non-Newtonian fluid past a hole of finite depth. After a few preliminary remarks regarding the equations governing the flow of the fluid under consideration, in Section 2, we develop the boundary integral equation corresponding to the partial differential equations governing the motion of the fluid in Section 3. The details of the computations in terms of certain characteristic parameters is outlined in Section 4. The results and certain extensions of the technique are discussed in Sections 5 and 6, respectively.

2 Preliminaries

The Cauchy stress $\mathbf{T}$ in a homogenous incompressible fluid of second grade[1] is given by

$$\mathbf{T} = -p\mathbf{1} + \mu\mathbf{A}_1 + \alpha_1\mathbf{A}_2 + \alpha_2\mathbf{A}_1^2, \tag{1}$$

where μ is the coefficient of viscosity, α_1 and α_2 the normal stress moduli, $-p\mathbf{1}$ the constitutively indeterminate spherical stress due to the constraint of incompressibility, and $\mathbf{A}_1$ and $\mathbf{A}_2$ the first two Rivlin-Ericksen tensors defined through

$$\mathbf{A}_1 = \text{grad } \mathbf{v} + (\text{grad } \mathbf{v})^T, \tag{2a}$$

and

$$\mathbf{A}_2 = \dot{\mathbf{A}}_1 + \mathbf{A}_1(\text{grad } \mathbf{v}) + (\text{grad } \mathbf{v})^T\mathbf{A}_1. \tag{2b}$$

In equation (2b) the dot denotes material time differentiation.

We are interested in obtaining the stream function due to the flow of a second-grade fluid between two infinitely parallel plates D apart, the bottom plate having either a depression or a projection of arbitrary shape (see Fig. 1). The flow is due to both the top plate shearing with a velocity V in the x-coordinate direction and pressure gradients along the x-direction.

By virtue of Tanner's theorem [7] and the uniqueness[2] of plane creeping flows of second-grade fluids, as far as the velocity field is concerned, it is sufficient that we obtain the solution for the velocity corresponding to the flow of a Navier-Stokes fluid across the slot. The balance of linear momentum in the case of a Navier-Stokes fluid in plane motion, in a Cartesian coordinate system, reduces to

$$\nabla^4\psi = 0 \quad \text{in} \quad \Omega,$$

where

$$\nabla^4 \equiv \frac{\partial^4}{\partial x^4} + 2\frac{\partial^4}{\partial x^2\partial y^2} + \frac{\partial^4}{\partial y^4} \tag{3}$$

is the usual biharmonic operator, and ψ is the stream function defined through

$$u(x, y) = \pm\frac{\partial\psi}{\partial x},$$

[1] The constitutive relation (1) has been employed both in the sense of a second-order approximation to a general simple fluid [2, 3] as well as an exact model in its own right [4]. Suffice it is to say that our results do not depend on either point of view, our results being applicable in either case. We refer the reader to [4–6] for details regarding the differing points of view.

Contributed by the Applied Mechanics Division for presentation at the Winter Annual Meeting, Chicago, Ill., November 16–21, 1980, of THE AMERICAN SOCIETY OF MECHANICAL ENGINEERS.

Discussion on this paper should be addressed to the Editorial Department, ASME, United Engineering Center, 345 East 47th Street, New York, N. Y. 10017, and will be accepted until December 1, 1980. Readers who need more time to prepare a discussion should request an extension from the Editorial Department. Manuscript received by ASME Applied Mechanics Division, October, 1979. Paper No. 80-WA/APM-8.

[2] The uniqueness theorem for plane creeping flows of a fluid modeled by equation (1) has been established by Fosdick and Rajagopal [5] for the exact model and Huilgol [8] for the model in the sense of second-order approximations.

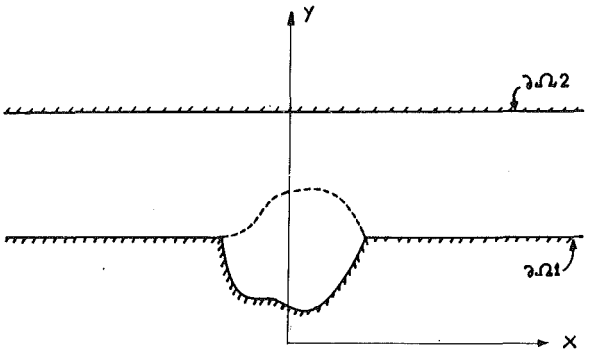

Fig. 1 Flow domain with arbitrary projection or depression

$$v(x, y) = \mp \frac{\partial \psi}{\partial y},$$

where u and v are the velocities in the x and y-directions, respectively. For the problem in question, the appropriate boundary conditions are (see Fig. 1)

$$\psi(x, y) = \begin{cases} 0 & \text{on} \quad \partial\Omega_1 \\ \text{Constant } (C) & \text{on} \quad \partial\Omega_2 \end{cases} \tag{4}$$

$$\frac{\partial \psi}{\partial n}(x, y) = \begin{cases} 0 & \text{on} \quad \partial\Omega_1 \\ V & \text{on} \quad \partial\Omega_2 \end{cases}$$

$$\psi(x, y) \to f(y) \quad \text{as} \quad x \to \pm\infty,$$

where n is the coordinate direction along the unit outward normal $\mathbf{n}$ to the boundary of Ω.

In the next section we obtain the boundary integral equation corresponding to the equations (3) and (4).

3 The Boundary Integral Equation

Consider the problem

$$\nabla^4 \psi = 0 \quad \text{in} \quad \Omega \tag{5}$$

with the boundary conditions

$$\psi(x, y) = f(x, y) \quad \text{on} \quad \partial\Omega,$$

and

$$\frac{\partial \psi}{\partial n}(x, y) = g(x, y) \quad \text{on} \quad \partial\Omega, \tag{6}$$

where $\partial\Omega$ is the boundary of Ω. The solution ψ for the problem represented by equations (5) and (6) is uniquely determined in Ω, [9], and has the following form:

$$\psi = r^2\phi + \theta, \tag{7}$$

where ϕ and θ are harmonic functions and $r^2 = x^2 + y^2$. On embedding Ω in an infinite domain, and assuming a layer of fictitious source points on $\partial\Omega$, the harmonic functions ϕ and θ can then be expressed as [10]

$$\phi(\mathbf{x}) = \int_\Omega T(\xi) G(\mathbf{x}, \xi) ds(\xi), \tag{8}$$

and

$$\theta(\mathbf{x}) = \int_{\partial\Omega} Q(\xi) G(\mathbf{x}, \xi) ds(\xi), \tag{9}$$

where $\mathbf{x}$ and ξ denote points in Ω and $\partial\Omega$, respectively. $G(\mathbf{x}, \xi)$ is the Green's function (influence function) and $T(\xi)$ and $Q(\xi)$ are the source points associated with ϕ and θ, respectively. Substitution of equations (8) and (9) into equation (7) leads to

$$\psi(\mathbf{x}) = r^2(\mathbf{x}) \int_{\partial\Omega} T(\xi) G(\mathbf{x}, \xi) ds(\xi) + \int_{\partial\Omega} Q(\xi) G(\mathbf{x}, \xi) ds(\xi). \tag{10}$$

As $\mathbf{x}$ approaches a point $\mathbf{x}'$ belonging to the boundary, we obtain from the boundary conditions (6) that

$$f(\mathbf{x}') = r^2(\mathbf{x}') \int_{\partial\Omega} T(\xi) G(\mathbf{x}', \xi) ds(\xi) + \int_{\partial\Omega} Q(\xi) G(\mathbf{x}', \xi) ds(\xi), \tag{11}$$

and

$$g(\mathbf{x}') = r^2(\mathbf{x}') \int_{\partial\Omega} T(\xi) \frac{\partial G}{\partial n_{\mathbf{x}'}}(\mathbf{x}', \xi) ds(\xi) + \frac{\partial r^2(\mathbf{x}')}{\partial n_{\mathbf{x}'}} \int_{\partial\Omega} T(\xi) G(\mathbf{x}', \xi) ds(\xi) + \int_{\partial\Omega} Q(\xi) \frac{\partial}{\partial n_{\mathbf{x}'}} G(\mathbf{x}', \xi) ds(\xi), \tag{12}$$

where $\partial/\partial n_{\mathbf{x}'}$ denotes partial differentiation in the direction of the unit outward normal at the point $\mathbf{x}'$. $T(\xi)$ and $Q(\xi)$ can now be obtained from the coupled boundary integral equations (11) and (12).

For the two-dimensional problem under question

$$G(\mathbf{x}, \xi) = \frac{1}{2\pi} \ln r(\mathbf{x}, \xi). \tag{13}$$

In order to solve the boundary integral equation (11) and (12), we shall discretize the boundary into N intervals $\Delta S_j (j = 1, \ldots N)$, and assume that the fictitious source points $T(\xi)$ and $Q(\xi)$ are constant over each of these intervals. The boundary integral equations then reduce to

$$f(\mathbf{x}') = \frac{r^2(\mathbf{x}')}{2\pi} \sum_{j=1}^{N} T(\xi) \int_{\Delta S_j} \ln r(\mathbf{x}', \xi) ds_j + \frac{1}{2\pi} \sum_{j=1}^{N} Q(\xi) \int_{\Delta S_j} \ln r(\mathbf{x}', \xi) ds_j, \tag{14}$$

and

$$g(\mathbf{x}') = \frac{r^2(\mathbf{x}')}{2\pi} \sum_{j=1}^{N} T(\xi) \int_{\Delta S_j} \frac{\partial}{\partial n_{\mathbf{x}'}} \ln r(\mathbf{x}', \xi) ds_j + \frac{\partial r^2(\mathbf{x}')}{\partial n_{\mathbf{x}'}} \cdot \frac{1}{2\pi} \sum_{j=1}^{N} T(\xi) \int_{\Delta S_j} \ln r(\mathbf{x}, \xi) ds_j + \frac{1}{2\pi} \sum_{j=1}^{N} Q(\xi) \int_{\Delta S_j} \frac{\partial}{\partial n_{\mathbf{x}'}} \ln r(\mathbf{x}', \xi) ds_j. \tag{15}$$

When ξ approaches $\mathbf{x}'$, the integrals involving both $\ln r(\mathbf{x}', \xi)$ and $(\partial/\partial n_{\mathbf{x}'}) \ln r(\mathbf{x}', \xi)$ become singular and it can be easily verified that

$$\int_{\Delta S} \ln r(\mathbf{x}', \xi) ds(\xi) = \Delta S \left(\ln \left| \frac{\Delta S}{2} \right| - 1 \right), \tag{16}$$

and

$$\int_{\Delta S} \frac{\partial}{\partial n_{\mathbf{x}'}} \ln r(\mathbf{x}', \xi) ds(\xi) = \pi, \tag{17}$$

where ΔS is an interval containing the point $\mathbf{x}'$. Thus equations (14) and (15) reduce to

$$f_i = \frac{r_i^2}{2\pi} \left[\Delta S_i \left(\ln \left| \frac{\Delta S_i}{2} \right| - 1 \right) T_i + \sum_{\substack{j=1 \\ j \neq i}}^{N} \ln r_{ij} T_j \Delta S_j \right] + \frac{1}{2\pi} \left[\Delta S_i \left(\ln \left| \frac{\Delta S_i}{2} \right| - 1 \right) Q_i + \sum_{\substack{j=1 \\ j \neq i}}^{N} \ln r_{ij} Q_j \Delta S_j \right] \tag{18}$$

and

$$g_i = \frac{r_i^2}{2\pi} \left[\pi T_i + \sum_{\substack{j=1 \\ j \neq i}}^{N} \frac{\partial}{\partial n_i} \ln r_{ij} T_j \Delta S_j \right] \tag{19}$$

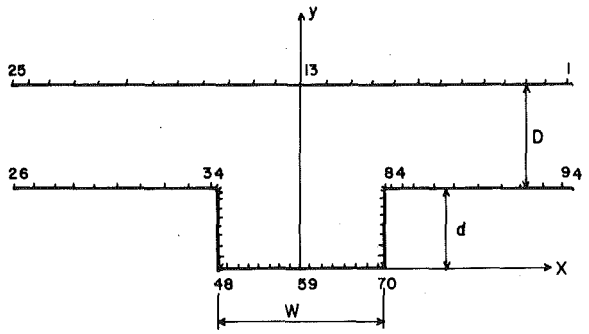

Fig. 2 Mesh arrangement in a rectangular slot of depth d and width W

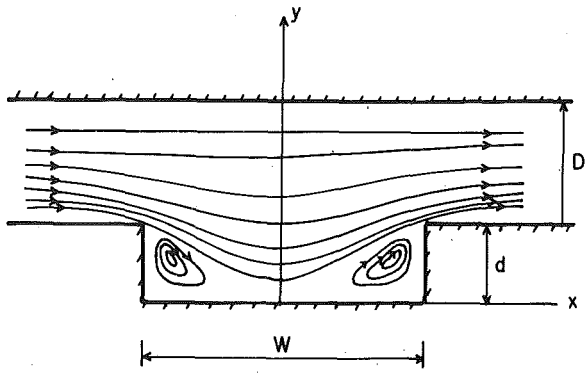

Fig. 3 Streamline pattern for $z = 1$ and $P = 0.5$

$$+\frac{\partial r_i^2}{\partial n_i}\left[\Delta S_i\left(\ln\left|\frac{\Delta S_i}{2}\right|-1\right)T_i+\sum_{\substack{j=1\\ j\neq i}}^{N}\ln r_{ij}T_j\Delta S_j\right]$$

$$+\frac{1}{2\pi}\left[\pi Q_i+\sum_{\substack{j=1\\ j\neq i}}^{N}\frac{\partial}{\partial n_i}\ln r_{ij}Q_j\Delta S_j\right], \quad (19)$$

(*Cont.*)

where the suffixes i and j denote the value of the functions at the points $\mathbf{x}'$ and $\boldsymbol{\xi}$, belonging to the N discretized intervals, respectively. Finally, equations (18) and (19) can be expressed in the form

$$\frac{1}{2\pi}\begin{bmatrix}A & B\\ C & D\end{bmatrix}\begin{bmatrix}T\\ Q\end{bmatrix}=\begin{bmatrix}f\\ g\end{bmatrix}, \quad (20)$$

where

$$A = r_i^2\left(\ln\left|\frac{\Delta S_i}{2}\right|-1\right)+\sum_{\substack{j=1\\ j\neq i}}^{N} r_i^2\ln r_{ij}, \quad (21)$$

$$B = \left(\ln\left|\frac{\Delta S_i}{2}\right|-1\right)+\sum_{\substack{j=1\\ j\neq i}}^{N}\ln r_{ij}, \quad (22)$$

$$C = r_i^2\pi+\frac{\partial r_i^2}{\partial n}\left(\ln\left|\frac{\Delta S_i}{2}\right|-1\right)\Delta S_i + \sum_{\substack{j=1\\ j\neq i}}^{N}\left[r_i^2\frac{\partial}{\partial n}\ln r_{ij}+\frac{\partial r^2}{\partial n}\ln r_{ij}\right]\Delta S_j, \quad (23)$$

$$D = \pi+\sum_{\substack{j=1\\ j\neq i}}^{N}\frac{\partial}{\partial n}r_{ij}\Delta S_i, \quad (24)$$

$$\overline{T}_k = \int_{\Delta S_k} T_k ds_k, \quad (25)$$

$$\overline{Q}_k = \int_{\Delta S_k} Q_k ds_k, \quad (26)$$

and

$$\overline{g}_k = \int_{\Delta S_k} g_k ds_k. \quad (27)$$

The system of equations represented by (20) can be solved for $\overline{T}$ and $\overline{Q}$ and once $\overline{T}$ and $\overline{Q}$ are determined, we can determine the stream function ψ from

$$\psi(\mathbf{x}) = \frac{r^2(\mathbf{x})}{2\pi}\sum_{j=1}^{N}\ln r(\mathbf{x},j)T_j+\frac{1}{2\pi}\sum_{j=1}^{N}\ln r(\mathbf{x},j)Q_j. \quad (28)$$

In the next section we shall provide an example which is of significance in rheology.

4 Computation

We shall plot the streamlines due to the flow of a second-grade fluid past a rectangular slot of finite width and depth as shown in Fig. 2. We subdivide the boundary into 92 meshes (see Fig. 2) and define nondimensional quantities

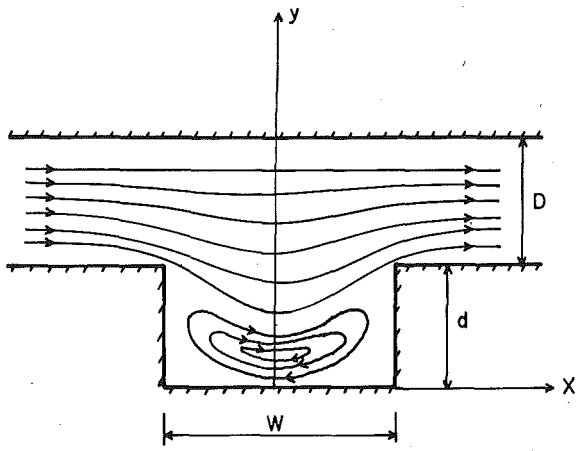

Fig. 4 Streamline pattern for $z = 1$ and $P = 1$

$$z = \frac{C}{VD}, \quad P = d/w$$

where C and V are the boundary conditions in equation (4), and d is the depth of the slot and w the width of the slot. A computer program has been written to calculate $\overline{T}$ and $\overline{Q}$ from equation (20). With the help of $\overline{T}$ and $\overline{Q}$ so determined, the streamlines are plotted employing equation (28).

5 Results and Discussion

First, we computed the streamlines due to the flow corresponding to $z = 0$ and $P = 0$, which is the flow between two infinitely flat plates. We find that our results are in very good agreement with the classical couette flow solution. We find that depending on the nondimensional numbers z and P there exists two distinct streamline patterns, namely, Figs. 3 and 4. Fig. 3 corresponds to $z = 1$ and $P = 0.5$ wherein there are two distinct groups of eddies. In fig. 4 which corresponds to $z = 1$ and $P = 1$, we find that these distinct eddies have coalesced.

To plot the streamlines due to the flow past a projection or depression of arbitrary shapes poses little problem. The same computer program can be employed with a different set of field points to solve the appropriate problem.

Finally, we wish to add that the boundary integral technique has the advantage of being accurate in addition to permitting a more efficient use of the computer in comparison to other numerical techniques.

6 Determination of Pressure Error

The hole pressure error, due to the flow of a second-grade fluid past a slot of finite depth, can be expressed in terms of the values of ψ_{xx},

ψ_{xy}, and ψ_{yy} at the points 0 and C (see Fig. 2), where ψ_{xx} denotes $\partial^2/\partial x^2$, etc. An expression for these partial derivatives can be obtained in a manner similar to that in which equation (28) was obtained, and hence the hole pressure error can be computed. A slight modification of the computer program can be made to determine the variation of the hole pressure error, with the nondimensional quantity d/w, for a fixed D/W.

References

1 Schubert, A. R., "Flow of an Incompressible Fluid Past Projections and Depressions," *AIAA Journal,* Vol. 5, 1967, pp. 373–375.

2 Coleman, B. D., and Noll, W., "An Approximation Theorem for Functionals With Applications in Continuum Mechanics," *Arch. Ratl. Mech. Anal.,* Vol. 6, 1960, pp. 355–370.

3 Langlois, W. E., "Steady Flow of a Slightly Viscoelastic Fluid Between Rotating Spheres," *Quart. Appl. Math.,* Vol. 21, 1963, pp. 61–71.

4 Dunn, J. E., and Fosdick, R. L., "Thermodynamics, Stability and Boundedness of Fluids of Complexity 2 and Fluids of Second Grade," *Arch. Ratl. Mech. Anal.,* Vol. 56, 1974, pp. 191–252.

5 Fosdick, R. L., and Rajagopal, K. R., "Uniqueness and Drag for Fluids of Second Grade in Steady Motion," *International Journal of Nonlinear Mechanics,* Vol. 13, pp. 131–137.

6 Fosdick, R. L., and Rajagopal, K. R., "Anomalous Features in the Model of Second-Order Fluids," *Arch. Ratl. Mech. Anal.,* Vol. 70, 1979, pp. 145–152.

7 Tanner, R. I., "Plane Creeping Flows of Incompressible Second-Order Fluids," *Physics of Fluids,* Vol. 9, 1966, pp. 1246–1247.

8 Huilgol, R. R., "On Uniqueness and Nonuniqueness in the Plane Creeping Flows of Second-Order Fluids," *SIAM Journal of Applied Mathematics,* Vol. 24, 1973, pp. 226–233.

9 Hadamard, J., "Mémoire sur le Probléme d'analyse Relatif a l'équilibre des Plaques Élastiques Encastrées," *Mém Prés. div Sav. Acd. Sci.,* France, Vol. 33, 1908, pp. 1–216.

10 Rajagopal, K. R., and Mir-Mohamad-Sadegh, A., "A Boundary Integral Approach for Determining the Pressure Error," *Rheologica Acta,* Vol. 19, 1980, pp. 12–18.

J. L. Gupta

Professor,
Department of Mathematics,
Birla Engineering College,
Vallabb Vidyanagar 388 120,
Gujarat, India

Fluid Motion Past a Porous Circular Cylinder With Initial Pressure Gradient

The problem of two-dimensional flow, past a porous circular cylinder, with initial pressure gradient is solved using the method of matched asymptotic expansions. It is found that the drag force experienced by the cylinder is increased due to initial gradient although it remains smaller than the drag force experienced by an identical impervious body.

Introduction

The limits and nature of the validity of Darcy law has been a subject of every day interest to the industry for many years. It is well known that as the Reynolds number, characteristic of the flow through porous media, becomes large, Darcy law loses its predictive accuracy in the laminar regime itself [1] and ultimately becomes void. Similarly for very slow speeds, the flow description deviates from the "Darcy flow regime." This clearly shows that Darcy law is valid only over a limited range of Reynolds number.

In particular, for very slow velocities, it has been found experimentally that the fluid moves more slowly than is predicted by Darcy law. Consequently, a limiting velocity may exist under which the Darcy law ceases to be valid. This phenomenon was first observed by Schmidt (see [2]). Lower limit of validity of Darcy law is induced by the increasing effects of molecular forces. The region where the molecular forces influence the seepage is called the region of microseepage. The idea of limit gradient, also called initial gradient, at which the fluid motion occurs, was set forth empirically by Puzyrevskaya [3]. The existence of the pressure gradient shows that in certain conditions, account must also be taken of the rheological aspect of motion [4]. In dense clays and heavy loams, in which the water is of a molecularly bound nature, seepage starts only when the pressure gradient exceeds a certain value.

The existence of initial gradient in clayey and other fine grained soils has been attributed to the predominance of surface forces over gravity forces existing in fine grained soil and generally these surface forces are strong enough to counteract a certain portion of applied pressure gradient [5]. It is therefore natural to expect that the lower the porosity and smaller the grain size, the higher will be the surface forces resulting in an increase in initial pressure gradient.

Consequences of the existence of initial gradient are of potential interest in several disciplines such as ground water movement and drainage in clayey soils, soil water movement to plant roots, etc. In drainage problems, nonrecognition of the role of initial gradient will result in inefficient layout of drains [6]. Valsangkar and Subramanya [7] and Arumagam [8] recently investigated the effect of initial gradient on various physical problems of interest in the field of drainage and irrigation.

The mathematical formulation and application to some simple problems of the phenomenon of motion with initial gradient was first given by Gheorghitza [9] which was later generalized by himself [10] to include the nonlinear effects caused due to microinhomogeneity of the macroscopically homogeneous porous medium because of the varied effects of the rheological properties of the medium. Later Gheorghitza [11] himself solved the problem of motion of a sphere, with initial gradient in Stokes flow.

Here, we propose to solve the two-dimensional problem of flow past a circular porous cylinder with initial gradient, by the method of matched asymptotic expansions as have been done by Kaplun [12] for an impervious cylinder and by Shi and Braden [13] for the flow past a permeable cylinder.

Mathematical Formulation

Consider the flow of an incompressible viscous fluid past a circular porous cylinder of radius a and permeability k'. Let the free-stream velocity be $U\hat{i}$ with origin of the coordinates at the center of the cylinder (see Fig. 1). We assume $\mathbf{q}'$ to be the filtration velocity and K^* to be the initial gradient which is the critical value of the pressure gradient $\nabla P'$, P' being the pressure in porous medium. Flow through the porous medium starts when $|\nabla P'|$ exceeds K^*, otherwise the porous body behaves as an impervious one, and the analysis of flow past an impervious body holds for this case [12].

Contributed by the Applied Mechanics Division for publication in the JOURNAL OF APPLIED MECHANICS.

Discussion on this paper should be addressed to the Editorial Department, ASME, United Engineering Center, 345 East 47th Street, New York, N. Y. 10017, and will be accepted until December 1, 1980. Readers who need more time to prepare a discussion should request an extension from the Editorial Department. Manuscript received by ASME Applied Mechanics Division, August, 1977; final revision, December, 1979.

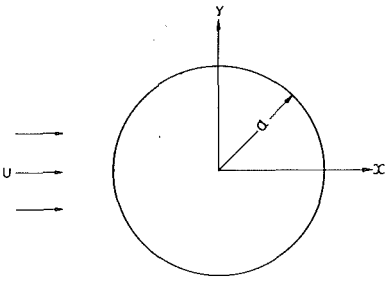

Fig. 1 Configuration of the problem

Introducing the following dimensionless quantities

$$p = \frac{a(p' - p_\infty)}{\mu U}, \quad \mathbf{q} = \frac{\mathbf{q}'}{U}, \quad r = \frac{r'}{a}, \quad k = \frac{k'}{a^2}$$

$$P = \frac{a(P' - P_\infty)}{\mu U}, \quad \mathbf{Q} = \frac{\mathbf{Q}'}{U}, \quad K = \frac{a^2 K^*}{\mu U}, \tag{1}$$

the equations governing the flow outside the cylinder take the form

$$\mathrm{Re}\,(\mathbf{q}\cdot\nabla)\mathbf{q} + \nabla p = \nabla^2\mathbf{q} \tag{2}$$

$$\nabla\cdot\mathbf{q} = 0 \tag{3}$$

while the flow in the porous matrix is governed by

$$\mathbf{Q} = \begin{cases} 0 & \text{for } |\nabla P| \leq K \\ -k\left[\nabla P - K\dfrac{\nabla P}{|\nabla P|}\right] & \text{for } |\nabla P| > K \end{cases} \tag{4}$$

$$\nabla\cdot\mathbf{Q} = 0 \tag{5}$$

where the Reynolds number $\mathrm{Re} = aU\rho/\mu$, ρ being the density and μ being the dynamic viscosity of the fluid.

The concerned boundary conditions are

$$p(1, \theta) = P(1, \theta) \tag{6}$$

$$q_r(1, \theta) = Q_r(1, \theta) \tag{7}$$

$$q_\theta(1, \theta) = 0 \tag{8}$$

$$\mathbf{q}(r, \theta) = \hat{i} \text{ as } r \to \infty \tag{9}$$

where the subscripts r and θ denote the radial and transverse components, respectively.

Solution

It is clear from the physical aspect of the problem that the Reynolds number $\mathrm{Re} < 1$. The set of equations (2)–(5) with the conditions (6)–(9) can be solved by introducing three simultaneous asymptotic expansions—an interior expansion which is valid in the porous matrix, the inner expansion which holds good near the cylinder, and an outer expansion which describes the flow phenomenon far away from the surface of the cylinder. We now give the construction of these expansions and the corresponding equations which hold in the respective regions.

Inner Expansion. We take the inner expansion of the form

$$\mathbf{q} = \epsilon\mathbf{q}_0 + \epsilon^2\mathbf{q}_1 + \ldots. \tag{10}$$

$$p = \epsilon p_0 + \epsilon^2 p_1 + \ldots. \tag{11}$$

where ϵ is some function of Re, the exact form of which will be determined by matching.

The governing equations for the foregoing expansions are well-known Stokes equations

$$\nabla^2\mathbf{q}_n = \nabla p_n; \quad n = 0, 1, 2, \ldots. \tag{12}$$

$$\nabla\cdot\mathbf{q}_n = 0 \tag{13}$$

Interior Expansion. In view of (10) and (11) and the boundary conditions (6) and (7), the interior expansion should be of the form

$$\mathbf{Q} = \epsilon\mathbf{Q}_0 + \epsilon^2\mathbf{Q}_1 + \ldots. \tag{14}$$

$$P = \epsilon P_0 + \epsilon^2 P_1 + \ldots. \tag{15}$$

Further the equations (4), (14), and (15) suggest the form of the perturbation expansion of K as

$$K = \epsilon K_0 + \epsilon^2 K_1 + \ldots. \tag{16}$$

In view of the similarity of phenomena and nature of the solution to be expected in our present problem with respect to the motion of a permeable cylinder with zero initial gradient [13], we observe that a linear function of x satsifies the equation for P which is obtained from (4) and (5) as

$$\nabla^2 P = \frac{K}{|\nabla P|}\left[\nabla^2 P - \frac{\nabla P\cdot\nabla(|\nabla P|^2)}{2|\nabla P|^2}\right] \tag{17}$$

The governing equations for the various order interior expansions can be obtained from (4) and (14)–(16).

Outer Expansion. In the Oseen region, the inertial and visous terms become comparable to each other, hence we introduce the outer variables as [13]

$$\tilde{x} = \mathrm{Re}\, x, \quad \tilde{y} = \mathrm{Re}\, y \tag{18}$$

and

$$\tilde{\mathbf{q}} = \mathbf{q} \quad \text{and} \quad \tilde{p} = \frac{1}{\mathrm{Re}}p \tag{19}$$

The equations governing the flow field in the outer region are

$$(\tilde{\mathbf{q}}\cdot\tilde{\nabla})\tilde{\mathbf{q}} + \tilde{\nabla}\tilde{p} = \tilde{\nabla}^2\tilde{\mathbf{q}} \tag{20}$$

$$\tilde{\nabla}\cdot\tilde{\mathbf{q}} = 0 \tag{21}$$

Outer expansions are of the form

$$\tilde{\mathbf{q}} = \hat{i} + \epsilon\tilde{\mathbf{q}}_1 + \ldots.. \tag{22}$$

$$\tilde{p} = \epsilon\tilde{p}_1 + \ldots. \tag{23}$$

The governing equations for the outer expansions would, then be given by

$$\left(\tilde{\nabla}^2 - \frac{\partial}{\partial\tilde{x}}\right)\tilde{\mathbf{q}}_n = \tilde{\nabla}\tilde{p}_n + \sum_{i=1}^{n-1}(\tilde{\mathbf{q}}_i\cdot\tilde{\nabla})\tilde{\mathbf{q}}_{n-1}$$

$$n = 1, 2, 3, \ldots \tag{24}$$

$$\tilde{\nabla}\cdot\tilde{\mathbf{q}}_n = 0 \tag{25}$$

It is required that the outer solution, besides satisfying the boundary condition at infinity, matches asymptotically with the inner solution in some overlapping domain.

Zeroth-Order Inner and Interior Solutions. In view of the matching condition of $\mathbf{q}_0$ with the outer limit $\hat{i}$, the zeroth-order inner and interior solutions satisfying the boundary conditions are obtained as

$$p_0 = -\frac{2x}{r^2} \tag{26}$$

$$\mathbf{q}_0 = \hat{i}\left[\log r + \frac{1 + 2k - kK_0}{2}\right] - \frac{x}{r}\nabla r - \frac{1 + 2k - kK_0}{2}\nabla\left(\frac{x}{r^2}\right) \tag{27}$$

$$P_0 = -2x \tag{28}$$

$$\mathbf{Q}_0 = \begin{cases} 0 & \text{for } 2 \leq K_0 \\ k(2 - K_0)\hat{i} & \text{for } 2 > K_0 \end{cases} \tag{29}$$

with

$$\lim_{\mathrm{Re}\to 0}(-\epsilon\log\mathrm{Re}) = 1 \tag{30}$$

The form of (30), without loss of generality, may be written as

$$-\epsilon \log \mathrm{Re} = 1 + b_1\epsilon + b_2\epsilon^2 + \ldots \tag{31}$$

where $b_n'^s$ will be found later.

First-order Outer Solution. We obtain the appropriate first-order outer solutions which match completely up to an order ϵ with the inner solutions as

$$\tilde{p}_1 = -\frac{2\tilde{x}}{\tilde{r}^2} \tag{32}$$

$$\tilde{\mathbf{q}}_1 = -2\hat{i}e^{\tilde{x}/2}K_0(\tilde{r}/2) + 2\tilde{\nabla}[e^{\tilde{x}/2}K_0(\tilde{r}/2) + \log \tilde{r}] \tag{33}$$

where $K_0(\tilde{r}/2)$ is the modified Bessel function of the second kind and zero order and the value of b_1 in the expression (31) is obtained as

$$b_1 = \gamma - \log 4 - \frac{1 + 2k - K_0 k}{2} \tag{34}$$

where γ is the Euler's constant.

First-Order Inner and Interior Expansions. The first-order inner and interior expansion which satisfy the appropriate boundary and matching conditions up to an order ϵ^2, obtained are

$$p_1 = P_1 = 0 \tag{35}$$

and

$$\mathbf{q}_1 = -\frac{K_1 k}{2}\left[\hat{i} - \nabla\frac{x}{r^2}\right] \tag{36}$$

$$\mathbf{Q}_1 = \begin{cases} 0 & \text{for} \quad 0 \leqslant K_1 \\ -kK_1\hat{i} & \text{for} \quad 0 > K_1 \end{cases} \tag{37}$$

with

$$b_2 = \frac{K_1 k}{2} \quad \text{and} \quad b_n = 0 \quad \text{for} \quad n \geqslant 3 \tag{38}$$

Now, the form of ϵ is completely known from (31), (34), and (38) and may be written as

$$\epsilon = 2[1 + (1 - 2K_1 k\epsilon_c{}^2)^{1/2}]^{-1} \times \epsilon_c \tag{39}$$

where

$$\epsilon_c = \frac{1}{\log \dfrac{4\mu \exp[(1 - K_0/2)k]}{Ua} + \dfrac{1}{2} - \gamma} \tag{40}$$

Second-Order Outer Solution. The second-order outer solution $\tilde{\mathbf{q}}_2$ can be obtained by solving the equations

$$\left(\tilde{\nabla}^2 - \frac{\partial}{\partial\tilde{x}}\right)\tilde{\mathbf{q}}_2 = \tilde{\nabla}\tilde{p}_2 + (\tilde{\mathbf{q}}_1\cdot\tilde{\nabla})\tilde{\mathbf{q}}_1 \tag{41}$$

$$\tilde{\nabla}\cdot\tilde{\mathbf{q}}_2 = 0 \tag{42}$$

with the boundary condition that it vanishes at infinity. Now, since, there are no unbounded terms in the second-order inner solution to be matched, it is required that $\tilde{\mathbf{q}}_2$ must be continuous at the origin. It implies, in turn, that $\tilde{\mathbf{q}}_2$ should only be the particular solution $\tilde{\mathbf{q}}_{2_p}$ of (41) and (42).

Now, since the body, in the Oseen limit is transcendentally small, only $\tilde{\mathbf{q}}_2$ ($\tilde{r} \to 0, \theta$) matters for matching purposes.

Following Kaplun [12] we have

$$\tilde{\mathbf{q}}_2(\tilde{r} \to 0, \theta) = -0.87\hat{i} \tag{43}$$

Third-Order Inner and Interior Solutions. The third-order inner and interior solutions which satisfy corresponding boundary and matching conditions are obtained as

$$P_2 = 1.74\frac{x}{r^2}, \quad P_2 = 1.74\,x$$

$$\mathbf{q}_2 = 0.87\left[\hat{i}\left(\log r + \frac{1 + 2K}{2}\right) - \frac{x}{r}\nabla r - \frac{1 + 2k}{2}\nabla\left(\frac{x}{r^2}\right)\right] \tag{44}$$

$$-\frac{kK_2}{2}[\hat{i} - \nabla(x/r^2)] \tag{45}$$

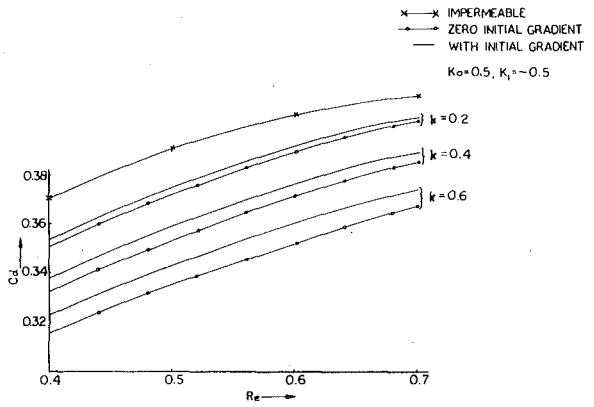

Fig. 2 Drag coefficient C_d versus Reynolds number Re

$$\mathbf{Q}_2 = \begin{cases} 0 & \text{for} \quad -1.74 \leqslant K_2 \\ -k\hat{i}(1.74 + K_2) & \text{for} \quad -1.74 > K_2 \end{cases} \tag{46}$$

Drag. The drag force experienced by the cylinder, obtained by using the momentum integral is

$$D_i = \iint_S [-pni + \tau_{ij}n_j - q_i q_j n_j]ds \tag{47}$$

Coefficient of drag C_d is obtained as

$$C_d = \frac{D_x}{4\pi\mu U} = [\epsilon - 0.87\epsilon^3 + o(\epsilon^3)] \tag{48}$$

where

$$\epsilon = 2[1 + (1 - 2K_1 k\epsilon_c{}^2)^{1/2}]^{-1} \times \epsilon_c \tag{49}$$

and

$$\epsilon_c = \frac{1}{\log \dfrac{4}{\mathrm{R}_e}\cdot\exp\left[k\left(1 - \dfrac{K_0}{2}\right)\right] + \dfrac{1}{2} - \gamma} \tag{50}$$

We find here that similar drag formula as (48) holds in the problems of flow past (*i*) an impervious cylinder, and (*ii*) a permeable cylinder with zero initial pressure gradient, the difference is in the expressions of the perturbation parameter in the three cases. If ϵ_p and ϵ_i are the perturbation parameters in the cases of permeable and impervious cylinders, respectively, it may be seen that

$$\epsilon_p < \epsilon < \epsilon_i \tag{51}$$

The obvious implication of (51) is that the drag force is increased due to the effect of initial gradient, although it still remains smaller than the drag force experienced by the identical impervious body. This result may also be observed from the graphical representation in Fig. 2 where variation of C_d with R_e is shown. It may also be observed from Fig. 2 that for the same initial pressure gradient, the rate of increase in the drag force, due to it, increases with increasing permeability. The graph also shows that the increase in permeability results in the decrease in C_d.

If the initial gradient K is taken zero in the present analysis, we recover the results due to Shi and Braden [13]. The results due to Kaplun [12] and Proudman and Pearson [14] for the flow past an impervious cylinder may be obtained by taking $k = 0$ in the present results.

References

1 Tek, M. R., "Development of a Generalized Reynolds Equation," *Journal of Petroleum Technology*, Vol. 9, No. 6, 1957, pp. 45–47.

2 Declaux, E., "Recherches sur les lois des Mouvements les liquides dans les Espaces Capillaires," *Annales des Chimie Physique*, Vol. 25, No. 4, 1872, pp. 442–451.

3 Puzyrevskaya, T. N., "Prosatchivanije Vody Tcherez Pestchanye Grunty," *Izvestiya N.I.I.G.*, Leningrad, 1931.

4 Merkel, W., "Rheology of Water in Sand and Gravel," *Symposia Darcy Dijon de l'Association Internationale d' Hydrologie,* Vol. 2, Publication No. 41, Louvain, 1956, pp. 207.

5 Miller, R. J., and Low, P. F., "Threshold Gradient for Water Flow in Clay Systems," *Soil Science Society of America,* Vol. 27, No. 6, 1963, pp. 605–609.

6 Basak, P., "Flow Through Soil With Initial Gradient," *Indian Journal of Meteorology, Hydrology and Geophysics,* Vol. 28, No. 1, 1977, pp. 103–106.

7 Valsanglear, A. J., and Subramanya, K., "Drainage in Soils With Initial Gradient," *American Society of Civil Engineers Transactions, Journal of Irrigation and Drainage Division,* Vol. 98, No. 2, 1972, pp. 309–316.

8 Arumagam A., "Partially Penetrating Well in a Semi-Infinite Media With Initial Gradient," *Indian Geotechnique Journal,* Vol. 1, 1975, pp. 44–50.

9 Gheorghitza, St.I., "Motion With Initial Gradient," *Quarterly Journal of Mechanics and Applied Mathematics,* Vol. 12, No. 3, 1959, pp. 280–286.

10 Gheorghitza, St.I., "On the Slow Motion in Porous Media," *Revue de Mathematiques Pures et Appliquees,* Vol. 6, No. 1, 1961, pp. 133–140.

11 Gheorghitza, St.I, "Two Generalizations of the Stokes Formula for a Porous Sphere," *Zeitschrift für Angewandte Mathematik und Mechanik,* Vol. 46, No. 2, 1966, pp. 135–139.

12 Kaplun, S., "Low Reynolds Number Flow Past a Circular Cylinder," *Journal of Mathematics and Mechanics,* Vol. 6, No. 5, 1957, pp. 595–603.

13 Shi, Y. Y., and Braden, R. E., Jr., "Effect of Permeability on the Slow Motion of a Cylinder," *Developments in Theoretical and Applied Mechanics,* ed., Shaw, W. A., Vol. 3, Pergamon Press, 1966, pp. 761–775.

14 Proudman, I., and Pearson, J. R. A., "Expansions at Small Reynolds Numbers for the Flow Past a Sphere and a Circular Cylinder," *Journal of Fluid Mechanics,* Vol. 2, 1957, pp. 237–263.

J. T. Jenkins[1]

Visiting Summer Faculty,
Sandia Laboratories,
Albuquerque, New Mex. 87115
Mem. ASME

Static Equilibrium of a Fluid-Saturated Porous Solid

The equilibrium equations for a fluid-saturated, porous elastic solid are obtained by a variational method. The total energy of the body is assumed to be the sum of that of the fluid and that of the solid, and the free energy of the solid is taken to be sensitive to its porosity.

Introduction

We develop the equilibrium theory for a fluid-saturated porous solid using a principle of virtual work introduced in a similar context by Kenyon [1]. The free energy of the system is supposed to be the sum of that of the solid and that of the fluid. Here, each of these energies is taken to be independent of the presence of the other constituent and the free energy of the solid is assumed to depend upon the volume fraction of the solid as well as upon its deformation. In this event the balance laws and boundary conditions are simple in form and have easy physical interpretations. In particular, the pressure in the pore fluid is seen to be the "external" generalized force associated with changes in the solid volume fraction. Such a generalized force appears in the theory for granular materials proposed by Goodman and Cowin [2] and in a corresponding theory for porous solids put forth by Nunziato and Cowin [3]. With this form of the free energy it is possible to relate these balance laws to those of the appropriate specializations of the more general and somewhat more complicated theories of Drumheller and Bedford [4] and Nunziato and Walsh [5] and to recover, in a somewhat different guise, several results obtained by Biot [6] in his specialization of a more general variational principle to fluid saturated porous solids. The common feature of all of the theories already mentioned is that the apparent density of each constituent may be changed in two ways: by changing its volume fraction; or by changing its true density. In this respect these theories differ from the perhaps more familiar mixture theories reviewed, for example, by Bowen [7].

Equilibrium

The total density ρ of the fluid-saturated porous solid is the sum of the apparent solid density ρ_1 and the apparent fluid density ρ_2. The apparent density of the fluid may be expressed in terms of the solid volume fraction ν and the true density γ of the pore fluid as

$$\rho_2 = (1 - \nu)\gamma. \tag{1}$$

There is, of course, a similar decomposition for the apparent density of the solid.

The volume density of free energy W is supposed to be given as the sum of contributions from the solid and the fluid,

$$W = \rho_1\psi_1 + \rho_2\psi_2, \tag{2}$$

where, for the solid,

$$\psi_1 = \psi_1(\nu, F_{iA}), \tag{3}$$

with $F_{iA} \equiv x_{i,A}$—the deformation gradients associated with the mapping $x_i = x_i(X_A)$ from a reference configuration; and, for the fluid,

$$\psi_2 = \psi_2(\gamma). \tag{4}$$

The energies are assumed to be unchanged in rigid motions of the material. The energy summation apparently ignores any energy of interaction between the solid and fluid. However, for the fluid-saturated porous solids, this additional energy is likely to be that associated with wetting the interior of the solid and, as Biot [6] points out, it may be considered to be part of the energy of the solid. In mixture theories formulated to describe molecular diffusion such a summed energy is known to be realistic only for mixtures of perfect gases [7].

In any event, the principle of virtual work based on this energy has the form [1],

$$\delta\int_V W dV = \int_V \delta W dV + \int_S (\rho_1\psi_1\delta x_i + \rho_2\psi_2\delta y_i)dS_i$$
$$= \int_S (T_i\delta x_i - Pn_i\delta y_i)\, dS + \int_V (\rho_1 f_i\delta x_i + \rho_2 b_i\delta y_i)dV, \tag{5}$$

where the integrations are to be carried out over a volume V fixed in space bounded by the surface S, and y_i is the position of a fluid element. The virtual displacements δx_i and δy_i are calculated following fixed material points of the solid and fluid, respectively. Associated with δx_i are the surface traction T_i and the body force f_i; corresponding to δy_i are the pressure P and the body force b_i. The first

[1] Presently, Associate Professor, Department of Theoretical and Applied Mechanics, Cornell University, Ithaca, N.Y. 14853.

Contributed by the Applied Mechanics Division for publication in the JOURNAL OF APPLIED MECHANICS.

Discussion on this paper should be addressed to the Editorial Department, ASME, United Engineering Center, 345 East 47th Street, New York, N. Y. 10017, and will be accepted until December 1, 1980. Readers who need more time to prepare a discussion should request an extension from the Editorial Department. Manuscript received by ASME Applied Mechanics Division, November, 1979; final revision, January, 1980.

equality follows from the variational form of the transport theorem [8].

The variations of F_{iA}, ν, and γ are taken to be those induced at a fixed spatial point by the virtual displacements. In this case

$$\delta F_{iA} = \delta x_{i,k} F_{kA} - F_{iA,k}\delta x_k. \tag{6}$$

Fluid mass conservation requires that the virtual displacement δy_i and the variations of γ and ν be related by

$$\delta[\gamma(1-\nu)] + [\gamma(1-\nu)\delta y_i]_{,i} = 0. \tag{7}$$

Solid mass conservation is satisfied by regarding ρ_1 as given in terms of the determinant J of F_{iA} by

$$\rho_1 = \rho_0 J^{-1}, \tag{8}$$

where ρ_0 is the, supposedly constant, apparent density of the solid in its reference configuration.

Upon carrying out the variation in (5), respecting (6) and employing (7) to eliminate $\delta\gamma$ in favor of $\delta\nu$ and δy_i, then integrating by parts, and collecting coefficients of like terms, we obtain

$$\begin{aligned}\int_V \Bigg\{ &\left[\left(\frac{\partial W}{\partial F_{iA}} F_{kA}\right)_{,k} + \frac{\partial W}{\partial F_{kA}} F_{kA,i} + \rho_1 f_i\right]\delta x_i \\ &- \gamma\left[\left(\frac{\partial W}{\partial \gamma}\right)_{,i} + (1-\nu)^{-1}\frac{\partial W}{\partial \gamma}\nu_{,i} - \rho_2 b_i\right]\delta y_i \\ &- \left[(1-\nu)^{-1}\gamma\frac{\partial W}{\partial \gamma} + \frac{\partial W}{\partial \nu}\right]\delta\nu\Bigg\} dV \\ &- \int_S \Bigg[\left(\frac{\partial W}{\partial F_{iA}} F_{kA} n_k + \rho_1\psi_1 n_i - T_i\right)\delta x_i \\ &- \left(\gamma\frac{\partial W}{\partial \gamma} - \rho_2\psi_2 + P\right) n_i \delta y_i\Bigg] dS = 0 \end{aligned} \tag{9}$$

Using the assumed additivity (2) of W and introducing the definitions

$$t_{ik} \equiv \rho_1 \frac{\partial \psi_1}{\partial F_{iA}} F_{kA}, \quad \pi \equiv \gamma^2 \frac{d\psi_2}{d\gamma} \tag{10}$$

and

$$\mu \equiv \psi_2 + \gamma^{-1}\pi, \quad p \equiv (1-\nu)\pi, \quad g \equiv -\rho_1 \frac{\partial \psi_1}{\partial \nu}, \tag{11}$$

we may write the local balance laws resulting from the variational principle as

$$t_{ik,k} - p_{,i} + \rho_2\mu_{,i} + \rho_1 f_i = 0, \tag{12}$$

$$\mu_{,i} - b_i = 0, \tag{13}$$

and

$$g - \pi = 0, \tag{14}$$

in V, and the boundary conditions as

$$T_i = t_{ik} n_k, \tag{15}$$

and

$$P = p, \tag{16}$$

on S.

The familiar definitions (10) and the form of the boundary conditions (15) and (16) lead to the identification of t_{ik} as the apparent stress in the solid, π as the pore pressure in the fluid, and p as the apparent pore pressure. The assumed invariance of ψ_1 in rigid motions insures that the stress is symmetric.

The balance laws (12) and (13) are the same as those obtained by Kenyon [1]. The balance of force for the solid (12) contains explicit contributions arising from the pore pressure. These are written here in terms of the apparent pore pressure p and the function μ. As discussed by Biot [6] and Kenyon [1], μ is analogous to the chemical potential of a diffusing fluid in a classical mixture theory for molecular diffusion. Note that the force balance for the pore fluid (13) requires that an external force compatible with equilibrium must be the gradient of a potential function ϕ,

$$b_i = -\phi_{,i}. \tag{17}$$

In this event (13) integrates to

$$\mu + \phi = c, \tag{18}$$

where c is a constant. With the definition $(11)_1$, it's possible to show, as does Biot [6], that (18) is the static form of an energy integral for inviscid compressible fluids (Lamb [9, Chapter II]):

$$\int \gamma^{-1} d\pi + \phi = c; \tag{19}$$

and this provides the more familiar identification of μ as the pressure function of classical hydrodynamics.

The final condition (14) resulting from the variation provides a relation between the pore pressure of the fluid, the deformation of the matrix, and the solid volume fraction. Kenyon [1] did not obtain this balance law because he did not allow the free energy of the matrix to depend upon its volume fraction. He did, however, later adopt a somewhat similar relation when dealing with an incompressible matrix and incompressible pore fluid [10].

Using (14) it is also possible to obtain an explicit interpretation of a generalized force that appears in theories for porous solids [3] and their fluid counterparts, granular materials [2]. In these theories only the free energy of the matrix is taken into account and a balance law for "equilibriated force" serves to determine the solid volume fraction and contains an external generalized force. If here we had felt that it were necessary to suppose that the free energy of the porous solid depended upon the spatial gradients of the solid volume fraction, the static version of the balance of equilibriated force would have been obtained in place of (14) with the important difference that, because the free energy of the pore fluid had been included in the variation, the negative of the pore pressure π would stand in place of the volume density of external generalized force. The analogous result for granular materials is obtained from the theory for the porous solid by requiring that the free energy depend on F_{iA} only through J. The identification of the volume density of external generalized force with the negative of the pore pressure had been anticipated by Jenkins [11]; who, however, did not distinguish between the pore pressure and that fraction of it communicated to the matrix.

In order to relate the stress relations and balance laws to those in Kenyon's [10] theory for incompressible constituents, it is necessary to adopt a more symmetric notation and to write the free energy of the solid as a function of F_{iA} and the true solid density γ_1

$$\psi_1(F_{iA}, \nu) = \psi_1(F_{iA}, \rho_0\gamma_1^{-1}J^{-1}) \equiv \bar{\psi}_1(F_{iA}, \gamma_1). \tag{20}$$

The latter is the form of this free energy favored by Drumheller and Bedford [4]. In terms of it, $(10)_1$ becomes, through an application of the chain rule,

$$t_{ik} = \tau_{ik} - \nu\pi_1\delta_{ik}, \tag{21}$$

where

$$\tau_{ik} \equiv \rho_1 \frac{\partial \bar{\psi}_1}{\partial F_{iA}} F_{kA} \quad \text{and} \quad \pi_1 \equiv \gamma_1^2 \frac{\partial \bar{\psi}_1}{\partial \gamma_1}; \tag{22}$$

while the balance law (14) takes the form

$$\gamma_1^2 \frac{\partial \bar{\psi}_1}{\partial \gamma_1} - \gamma_2^2 \frac{\partial \bar{\psi}_2}{\partial \gamma_2} = 0, \tag{23}$$

or

$$\pi_1 - \pi_2 = 0. \tag{24}$$

Thus, in equilibrium, the true pore pressure of the fluid is balanced by a true "matrix pressure" in the solid. As a consequence of (24), the total stress may be written as

$$t_{ik} - p\delta_{ik} = \tau_{ik} - \pi_2\delta_{ik}. \tag{25}$$

Then, if the total surface traction $T_i - Pn_i$ is supposed to be a contact

traction τ_i less the pressure π of that pore fluid exterior to the solid,

$$T_i - Pn_i = \tau_i - \pi n_i, \tag{26}$$

it is natural to follow Kenyon [10] in supposing that the pressure in the pore fluid is continuous over the boundary of the solid and in inferring from the boundary condition on the total stress that τ_{ik} is the apparent contact stress in the solid.

The forms of the stress relations and balance equations appropriate to incompressible materials may be obtained from the principle of virtual work by introducing Lagrange multipliers. For example, when the pore fluid is incompressible, π_2 is the multiplier associated with this constraint and, as such, is determined up to a constant by (18). Then (12) and (14) serve to determine x_i and γ_1 (or ν). When both the pore fluid and the material of the matrix are incompressible, π_2 and π_1 are, respectively, the multipliers associated with these constraints. In this case, π_2 is determined as before; then π_1 is fixed by (14).

The general thermodynamical theories for chemical reacting mixtures of solids and fluids that have been proposed by Drumheller and Bedford [4] and Nunziato and Walsh [5] can be specialized to apply to a single fluid saturated porous solid. When this is done it is relatively easy to recover from them the equilibrium theory previously outlined provided that in the equilibrium specialization of these general theories the form of the free energy given by (2)–(4) is used. The advantage in relating the three equilibrium theories is that in some applications it may be easier to generate a nonequilibrium theory for the fluid saturated porous solid by adding the appropriate inertial, thermal, and dissipative terms to the equilibrium theory obtained here rather than simplifying either of the general theories. This, for example, is the approach adopted by Biot [6].

Acknowledgment

This work was sponsored by the U.S. Department of Energy under Contract Number DE-AC04-76-DP00789 to Sandia Laboratories—a U.S. Department of Energy facility. During the course of this research I benefitted from discussions with D. S. Drumheller, D. E. Kenyon, and J. W. Nunziato.

References

1 Kenyon, D. E., "Thermostatics of Solid-Fluid Mixtures," *Arch. Rat'l. Mech. Anal.*, Vol. 6, 1976, pp. 117–129.

2 Goodman, M. A., and Cowin, S. C., "A Continuum Theory for Granular Materials," *Arch. Rat'l. Mech. Anal.*, Vol. 44, 1972, pp. 249–266.

3 Nunziato, J. W., and Cowin, S. C., "A Nonlinear Theory of Elastic Materials With Voids," *Arch. Rat'l. Mech. Anal.*, Vol. 72, 1979, pp. 175–201.

4 Drumheller, D. S., and Bedford, A., "A Thermomechanical Theory for Reacting Immiscible Mixtures," *Arch. Rat'l. Mech. Anal.*, in press.

5 Nunziato, J. W., and Walsh, E. K., "On Ideal Multiphase Mixtures With Chemical Reaction and Diffusion," *Arch. Rat'l. Mech. Anal.*, in press.

6 Biot, M. A., "Theory of Finite Deformations of Porous Solids," *Indiana U. Math. J.*, Vol. 21, 1972, pp. 597–620.

7 Bowen, R. M., "Theory of Mixtures," *Continuum Physics: Volume III, Mixtures and EM Field Theories*, Eringen, A.C., ed., Academic Press, New York, 1976.

8 Truesdell, C., and Toupin, R. A., "The Classical Field Theories," *Handbuch der Physik III/1*, Flügge, S., ed., Springer Verlag, Berlin, 1960.

9 Lamb, H. *Hydrodynamics*, Cambridge University Press: Cambridge, 1932.

10 Kenyon, D. E., "The Theory of an Incompressible Solid-Fluid Mixture," *Arch. Rat'l. Mech. Anal.*, Vol. 62, 1976, pp. 131–147.

11 Jenkins, J. T., "Static Equilibrium of Granular Materials," ASME JOURNAL OF APPLIED MECHANICS, Vol. 42, 1975, pp. 603–606.

W. H. Yang

The University of Michigan,
Ann Arbor, Mich. 48109
Mem. ASME

Pipe Flow of Plastic Materials

Plastic materials behave as both solids and fluids. When forced to move in a pipe, they flow as a solid plug with a slipping boundary. Depending on the cross-sectional shape of the pipe, the slipping boundary may not coincide with the inner boundary of the pipe. When such is the situation, there exist dead regions in the flow. This is undesirable when the material is time degradable as those encountered in the food processing and chemical industry. Two formulations of nonlinear programming problems governing the pipe flow are presented. They correspond, respectively, to the lower bound and upper bound theorems of plasticity. An efficient method is developed for the nonlinear programming problem formulated from the upper bound theorem. Application of the method to two examples are demonstrated.

Introduction

It is a widely acceptable theory that for a class of materials, there exist a yield function $f(\sigma)$ of the stress tensor. For the stress states in the set

$$E = \{\sigma: f(\sigma) < f(\sigma^*)\} \tag{1}$$

the material behaves as a solid, where σ^* denotes the states of all yield stresses. Under these yield stresses which satisfy

$$f(\sigma^*) = \text{constant} \tag{2}$$

the material flows as a fluid. This class of materials is called perfectly plastic [1]. The yield functions are theoretically convex.

This simple switching type of nonlinear behavior has made the mathematical formulations for such problems difficult to solve. Only limited number of problems with relatively simple domains are solved often by a special technique to each of the problems. Two general theorems [2] are available to bound the exact solutions. A lower bound solution which satisfies the equilibrium equation and stress boundary conditions

$$\nabla \cdot \sigma = \mathbf{b} \text{ in } \mathbf{D} \text{ and } \mathbf{n} \cdot \sigma = \mathbf{t} \text{ on } \partial\mathbf{D} \tag{3}$$

where $\mathbf{b}$ and $\mathbf{t}$ are known vectors and the yield criterion

$$f(\sigma) \leq \text{constant} \tag{4}$$

bounds the exact solution from below. An upper bound solution which assumes a physically reasonable kinematics of flow and satisfies integral equilibrium bounds the exact solution from above.

It is conceivable that the exact solution can be approached by a minimization procedure applied to all possible upper bound solutions or a maximization to lower bound solutions. These ideas lead to formulations of mathematical programming problems. Although some problems of this type are solvable in principle, the large size of the finite dimensional space of numerical approximation and computational inefficiency have kept most solutions from easy reach.

Both maximization and minimization formulations on the pipe flow problems are presented. A possible method for the lower bound formulation and its computational inefficiency are discussed. The upper bound formulation leads to minimization of a nonlinear functional with simple bounds on the variables as constraints. An efficient method for this formulation which applies to general pipe cross sections is developed and applied to two examples.

The Problem

Pipe flows of highly viscous materials like cream and grease and granular materials like sand and coal powder behave similarly that they flow under a critical pressure gradient below which static equilibrium is maintained without flow of material. The perfect plastic model [1] can best approximate this behavior. In this section, two formulations for such flow problems are presented.

By a semi-inverse assumption similar to the Saint-Venant's on the torsion problem [3], we assume the nontrivial stress components in a steady-state pipe flow in z-direction to be

$$\sigma_{xx} = \sigma_{yy} = \sigma_{zz} = -Cz$$
$$\sigma_{zx} = \sigma_{zx}(x, y), \quad \sigma_{zy} = \sigma_{zy}(x, y) \tag{5}$$

where C is a positive constant having the meaning of hydrostatic pressure differential per unit pipe length. The nontrivial equilibrium equation is

$$\frac{\partial \sigma_{zx}}{\partial x} + \frac{\partial \sigma_{zy}}{\partial y} = C \tag{6}$$

The yield criterion (von Mises or Tresca) reduces to

$$\sigma_{zx}^2 + \sigma_{zy}^2 \leq \sigma_0^2 \tag{7}$$

where σ_0 is the yield stress in shear.

Any solution that satisfies (6) and (7) is a lower bound solution. The maximization of lower bound solutions leads to the following nonlinear programming problem:

Contributed by the Applied Mechanics Division for publication in the JOURNAL OF APPLIED MECHANICS.

Discussion on this paper should be addressed to the Editorial Department, ASME, United Engineering Center, 345 East 47th Street, New York, N. Y. 10017, and will be accepted until December 1, 1980. Readers who need more time to prepare a discussion should request an extension from the Editorial Department. Manuscript received by ASME Applied Mechanics Division, May, 1979; final revision, August, 1979.

$$\text{Maximize} \quad C$$

$$\text{Subject to} \quad \frac{\partial \sigma_{zx}}{\partial x} + \frac{\partial \sigma_{zy}}{\sigma y} = C \tag{9}$$

$$\sigma_{zx}^2 + \sigma_{zy}^2 \leq \sigma_0^2$$

Since the constraint set is convex, the problem has a unique solution. Presence of quadratic constraints in (9) makes the problem difficult to solve. An attempt [4] is made to linearize the quadratic constraints by a set of piecewise linear inequalities and using the finite elements to discretize the differential equation in (9). The resulting linear programming problem can be solved but rather inefficiently.

Two dual formulations [4, 5] can be solved more efficiently but the mathematical language used in [4, 5] may not be understood by engineers who actually need to solve these problems with complex domains.

An intuitive approach is adopted for the presentation of the upper bound formulation which is the dual of (9). Let the cross-section of the pipe interior be the domain Ω bounded by a closed curve Γ. If the plug flow involves material contained in a subdomain $\Omega' \subset \Omega$ where Ω' is bounded by Γ' with outward normal n, the stress acting on the lateral plug surface is $\sigma_{nz} = \sigma_0$. The z equilibrium on the plug of unit length is

$$\oint_{\Gamma'} \sigma_0 ds = \iint_{\Omega'} C dA \tag{10}$$

where C is the same as that in (9). For any reasonably assumed Γ', C computed from (10) is an upper bound to the exact value which is the solution to the nonlinear programming problem

$$\text{Minimize} \quad p = \oint_{\Gamma'} ds \Big/ \iint_{\Omega'} dA$$
$$\text{Subject to} \quad \Omega' \subseteq \Omega \tag{11}$$

where $p = C/\sigma_0$. This is the inverse of the standard isoperimetric problem [6, 7].

$$\text{Maximize} \quad \iint_{\Omega'} dA \Big/ \oint_{\Gamma'} ds$$
$$\text{Subject to} \quad \Omega' \subseteq \Omega \tag{12}$$

for which exact solutions exist for a few simple domains.

An efficient numerical method for the solutions of problem (11) with a general domain is given in the next section.

The Method

For a general cross section Ω, we assume there exist an origin $O \in \Omega$ such that the polar description $R = R(\theta)$ of Γ is a single-valued function. Let the slip domain Ω' be bounded by $r = r(\theta)$ then

$$r(\theta) \leq R(\theta) \tag{13}$$

The nonlinear programming problem (11) takes the form

$$\text{Minimize} \quad p = \oint \sqrt{r'^2 + r^2}\, d\theta / \oint \tfrac{1}{2} r^2 d\theta$$
$$\text{Subject to} \quad r \leq R \tag{14}$$

which is a one-dimensional problem for optimal function $r(\theta)$.

A finite-element scheme may be used to discretize the integrals in (14). We prefer the more familiar Simpson's rule [8] with the 2π angle measure devided into $2N$ equal intervals. The finite dimensional space approximation of (14) has the form

$$\text{Minimize} \quad p = f(\mathbf{r})$$
$$\text{Subject to} \quad 0 \leq r_i \leq R_i, \quad i = 1, 2, \ldots, 2N \tag{15}$$

where $\mathbf{r}$ and $\mathbf{R}$ are vector representations of $r(\theta)$ and $R(\theta)$.

Let $g_i = \partial f/\partial r_i$ and set

$$g_i = 0 \quad \text{if} \quad \partial f/\partial r_i < 0 \quad \text{and} \quad r_i = R_i \quad i = 1, 2, ., 1, 2, ., 2N \tag{16}$$

The gradient vector so constructed is a projected gradient along active constraint boundaries.

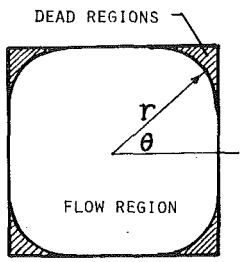

θ (°)	$r_{COMP.}$	r_{EXACT}
0.0	1.000	1.000
4.5	1.003	1.003
9.0	1.012	1.012
13.5	1.028	1.023
18.0	1.051	1.051
22.5	1.082	1.082
27.0	1.121	1.121
31.5	1.156	1.153
36.0	1.182	1.176
40.5	1.197	1.190
45.0	1.203	1.197

Fig. 1 Comparison of computer and exact solutions

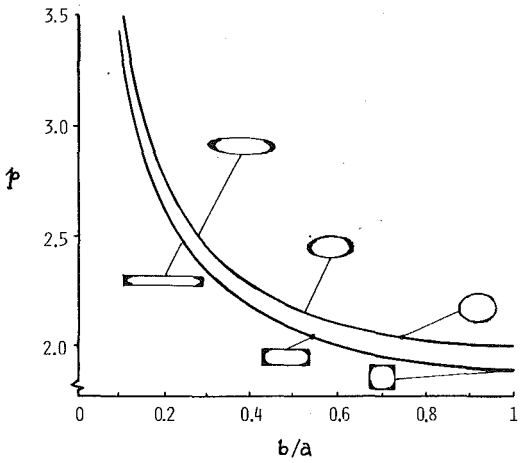

Fig. 2 Pressure per length required for plastic flow

We may start from an initial solution say $\mathbf{r}^{(0)} = \mathbf{R}$ and improve the solution by the updating

$$\mathbf{r}^{(k+1)} = \mathbf{r}^{(k)} - \alpha \mathbf{g}^{(k)} \quad k = 0, 1, 2, \ldots \tag{17}$$

where α is the descent parameter obtained by a linear search [9]. Quadratic minimization is used along the direction of $-\mathbf{g}$ in the example problems to determine α at each step.

The updated $\mathbf{r}$ must satisfy $\mathbf{0} \leq \mathbf{r} \leq \mathbf{R}$. This projected gradient algorithm converges rather rapidly as demonstrated in the following examples. The efficiency of the algorithm may be improved further, but it is adequate for all practical purposes.

The method should apply to a wide variety of pipe cross sections of practical interest. It tolerates certain nonconvex domains provided the condition of single-valued $R(\theta)$ is satisfied.

Examples

Applications of the method to a family of rectangular and a family of elliptic pipes are presented here with the square and circular ones as special cases.

1 **Rectangular Pipes.** Consider first the flow in a 2×2 square pipe for which the exact solution, $p_{\min} = 1 + \sqrt{\pi}/2$, is known [5]. By symmetry, only one-eighth of the domain ($0 \leq \theta \leq \pi/4$) needs be considered for the computer solution. For $N = 20$, ($\Delta\theta = \pi/160$), the computed and the exact solutions are presented in Fig. 1 both numerically and graphically. The graphic display cannot show the error of $\mathbf{r}_{comp}$ in the 4th digit. Such accuracy is achieved with 74 iterations at a mere 2.03 sec CPU time.

A family of rectangular domains ($2a \times 2b$) with the same area as that of 2×2 square is considered. We have therefore the relation $ab = 1$. For various b/a ratios, the required pressure per unit length is shown in Fig. 2. For $b/a \leq 0.530159$ four dead regions merge into two.

2 Elliptic Pipes. In this family, a special case is the circular domain of radius 1. There is no dead region and $p = 2$ is the minimum solution to (14).

The family of ellipses with major and minor semiaxes a and b ($ab = 1$) has the same area. For $b/a \geq 0.733576$, there is no dead region in the flow. The dead regions for other elliptic domains are shown in Fig. 2 along the pressure curve.

The extensive parametric computations in the examples has set back a mere 10 dollars from an estimated computing budget of 150 dollars.

Final Remarks

An intuitive approach often produces excellent mathematical formulation to a physical problem. The method presented is simple and efficient for the plastic flow in pipes of an arbitrary cross section.

If the problem of the square pipe is solved by an incremental elastoplastic computer code, four plastic zones will first be developed at the midpoints of the edges. The zones will then spread and have finite area. They will finally join together and reduce to a closed curve with zero area. Complicated local loading and unloading must be examined at each increment during computation. Approaching the flow solution, the matrix equation involved in the incremental method becomes increasingly ill-conditioned [10] and therefore more difficult to solve. The mathematical programming approach avoids these difficulties and directly seeks the flow solution. It is more suitable for this problem.

The field of plasticity experiences slow development especially in the solution methods area. The type of nonlinearities in plasticity lend the problems to numerical approaches. The incremental method has produced a large number of solutions. The mathematical programming approach deserves more attention and study.

References

1 Prager, W., and Hodge, P. G., *Theory of Perfectly Plastic Solids,* Wiley, 1951.

2 Kachanov, L. M., *Fundamentals of the Theory of Plasticity,* Mir Publishers, Moscow, 1974.

3 Timoshenko, S., and Goodier, J. N., *Theory of Elasticity,* 2nd ed., McGraw-Hill, New York, 1951.

4 Watson, L., and Yang, W. H., "Some Numerical Methods for Limit Analysis in Continuum Mechanics," *Comp. Meth. Appl. Mech. Eng.,* Vol. 15, 1978, pp. 353–364.

5 Strang, G., A Minimax Problem in Plasticity Theory," *Springer Lecture Notes on Functional Analysis Methods in Numerical Analysis,* Amer. Math. Soc., 1977.

6 Garvin, A. D., "A Note on Demar's 'A Simple Approach to Isoperimetric Problems in the Plane,' " and an epilogue, *Math. Magazine,* Vol. 48, 1975, pp. 219–221.

7 Lin, T. P., Maximum Area Under Constraint," *Math. Magazine,* Vol. 50, 1977, pp. 32–34.

8 Conte, S. D., and deBoor, C., *Elementary Numerical Analysis, An Algorithmic Approach,* 2nd ed., McGraw-Hill, New York, 1972.

9 Luenberger, D. G., *Introduction to Linear and Nonlinear Programming,* Addison-Wesley, 1973.

10 Forsythe, G., and Moler, C., *Computer Solution of Linear Algebraic Systems,* Prentice-Hall, Englewood Cliffs, N. J., 1967.

A. I. Beltzer

Head of Department,
Holon Center for Technological Education,
52 Golomb Street,
P.O. Box 305,
Holon, Israel

Random Response of a Rigid Sphere Embedded in a Viscoelastic Medium and Related Problems

Random and harmonic responses are considered for a rigid movable sphere embedded in a viscoelastic medium. The solution takes into account the filtering effect of the viscoelastic medium on the traveling random waves. The sphere can be also randomly located with respect to a plane at which the spectral density of incident stochastic waves is prescribed. For a Maxwellian medium with small losses the exact stationary response is derived. The results regarding the nonstationary response of the sphere embedded in a Kelvin-Voight medium are obtained numerically. It is shown that the results obtained are applicable to the prediction of mechanical properties of composite materials, as well as to those of buried structures, when these objects are excited by incompletely known or random disturbances.

1 Introduction

Scattering of waves by an obstacle embedded in an infinite deformable solid has been intensively studied for the past 20-odd years following the work by Ying and Truell [1]. The continuing interest is due to the importance of this phenomenon to the mechanics of materials and structures and to seismic engineering. An extensive bibliography on this subject is given by Scott [2]. Accordingly, we do not provide here a complete list of references. The monograph by Pao and Mow [3] and the review papers by Achenbach [4] and Datta [5] cover the majority of the existing results. Recent works by Pao [6], Waterman [7], Lewis, Kraft, and Hom [8], Gaunaurd and Überall [9], and Mei [10] provide an extension of the basic approaches and techniques.

All these works deal with deterministic incident waves which are supposed to be fully and exactly known. In distinction to such a formulation the information available on natural or artificially created disturbances usually involves uncertainty to a greater or lesser degree. Moreover, in some problems the disturbance acting upon the obstacle is essentially random. Appropriate examples may be found in the works of Beran [11], Lin [12], Bolotin [13], and Newmark and Rosenblueth [14].

It is obvious that to be more practical the analysis of scattering phenomena should be combined with an account of random factors inherent in actual physical situations and, in particular, with an account of the random nature of the propagated disturbances. Beltzer [15] has considered the random response of a rigid sphere embedded in a purely elastic medium.[1] This study has been primarily devoted to a mathematical treatment of the problem.

It should be noted that a rigid insert in a deformable solid is an interesting example of a coupled system and, in addition to its engineering applications, is important from a theoretical viewpoint. Indeed, it is a generalization of the well-known simple models which consist of masses, springs, and dashpots. One of the important differences is the presence of radiation damping in the general case considered here.

The present paper uses essentially results given by Pao and Mow [16] and by Mow [17] on rigid inclusion motion in a perfectly elastic medium excited by a harmonic wave. The work deals with the following as yet untreated problems:

1 The harmonic response of a rigid sphere embedded in a viscoelastic and, hence, sound absorbing medium.

2 A description of the propagation process of random viscoelastic waves and the prediction of their action on a randomly located spherical insert, including the transient and steady cases.

3 Some applications of the results to the mechanics of composite materials and to the protection of buried structures when these objects are excited by incompletely known or random disturbances.

2 Harmonic Response of a Rigid Sphere Embedded in a Viscoelastic Medium

We deal with an infinite isotropic viscoelastic medium with mass

Contributed by the Applied Mechanics Division for publication in the JOURNAL OF APPLIED MECHANICS.

Discussion on this paper should be addressed to the Editorial Department, ASME, United Engineering Center, 345 East 47th Street, New York, N.Y. 10017, and will be accepted until December 1, 1980. Readers who need more time to prepare a discussion should request an extension from the Editorial Department. Manuscript received by ASME Applied Mechanics Division, July, 1979; final revision, January, 1980.

[1] See also, a recent paper by A. Beltzer, B. Robinson, and N. Rudy "The Effect of Random Compressional Waves on a Rigid Sphere Embedded in an Elastic Medium," *Journal of Sound and Vibration* Vol. 66, No. 4, 1979, pp. 513–519.

density ρ and with complex dilatational and shear compliances D_* and S_*, respectively. The medium contains a rigid movable sphere of density ρ_0 and radius a. The sphere is located at the origin of the coordinate system and is excited by plane harmonic P-waves traveling in the positive z-direction.

Since the boundary conditions at the sphere surface, which match the displacements of the medium with those of an insertion do not depend explicitly on time, the response of the sphere can be obtained directly from the solution for an elastic medium by means of the well-known correspondence principle [18]. The same conclusion can also be reached by reproducing the derivation presented by Pao and Mow [16] and by Mow [17] for the perfectly elastic case, making one change only: the two real wave numbers should be replaced by their complex generalizations.

Making the indicated changes the displacement W of the sphere is found to be

$$W = \phi_0 i k_D H(\omega) e^{-i\omega t} \tag{1}$$

where $\phi_0 i k_D$ is the amplitude of the incident wave, $W_{(i)}$, and $H(\omega)$, the admittance function is as follows:

$$H(\omega) = 3me^{-in}(-\chi^2 n^2 - 3i\chi n + 3)/\{\chi^2 n^4 + i[\chi^2(2+m) + \chi(1+2m)]n^3 - [\chi^3(2+m) + 9m\chi + 2m + 1]n^2 - i9(\chi+1)mn + 9m\} \tag{2}$$

with $X = k_S/k_D'$ $n = ak_D$ and $m = \rho/\rho_0$.

The complex wave numbers k_D and k_S appearing in (2) are expressed in terms of the compliances D_* and S_* by

$$k_D = \omega(\rho|D_*|)^{1/2} e^{i\phi_D/2}; \quad k_S = \omega(\rho|S_*|)^{1/2} e^{i\phi_S/2} \tag{3}$$

where

$$D_* = D_1 - iD_2 = |D_*|e^{-i\phi_D}; \quad S_* = S_1 - iS_2 = |S_*|e^{-i\phi_S} \tag{4}$$

Substitution of the expressions (3) into equation (2) makes it possible to determine $H(\omega)$ and hence $|H(\omega)|^2$ which governs the steady-state response. This function is plotted in Fig. 1 according to equations (2) and (3) and the appropriate equations of Maxwell and Kelvin-Voight models [18]. Thus the energy losses which take place in the surrounding medium lead to a decrease in the resonance amplitude in comparison with the perfectly elastic medium. However the details of the response depend upon the viscoelastic model.

3 The Effect of Random Viscoelastic Waves on Spherical Discontinuity

We proceed now to the analysis of the response to a disturbance which is taken to be a superposition of traveling P-waves with random amplitudes and phases. In distinction to purely elastic waves, where the stochastic process describing such a disturbance is easily constructed [15], the case of viscoelastic random waves involves some peculiarities due to their dispersion and attenuation.

The approach similar to that of control theory [19] can be adopted to describe the interaction between random disturbances and a discontinuity located in a viscoelastic medium. We shall suppose without loss of generality that the disturbance has zero mean.

To make clearer the physical situation, it can be assumed that the viscoelastic waves emanate from the plane $z = -z_0 (z_0 \geq 0)$ which vibrates with random complex amplitudes $B(\omega)$ (Fig. 2). This leads to the description of the incident waves, $W_{(i)}$, in the form of the two stochastic integrals

$$W_{(i)}(t,z) = \int_{-\infty}^{\infty} e^{-i\omega t} e^{ik_D(\omega)\bar{z}} dB(\omega) = \int_{-\infty}^{\infty} e^{-i\omega t} dA(\omega, z) \tag{5}$$

where $\bar{z} = z + z_0$, $k_D(\omega) = k_D{}^0(\omega) + ik_D{}^1(\omega)$ is the complex dilatational wave number and $B(\omega)$ and $A(\omega, z)$ are complex random processes with uncorrelated increments. This expression shows that $B(\omega)$ and $A(\omega, z)$ and the associated spectral densities $S_B(\omega)$ and $S_A(\omega, z)$ are related by

$$A(\omega, z) = \int_{-\infty}^{\omega} e^{ik_D(\epsilon)\bar{z}} dB(\epsilon) \quad (-\infty < \omega < \infty) \tag{6}$$

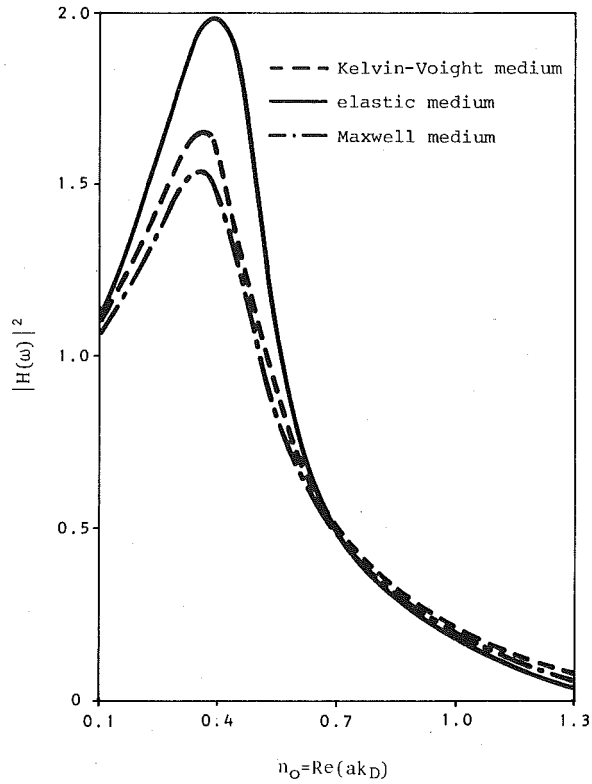

Fig. 1 Transmittance function versus real part of wave number, $\nu = 0.3$; $m = 0.2$. Maxwell medium: Im $(ak_S) = 7.10^{-2}$; Im $(ak_D) = 5.10^{-2}$. Kelvin-Voight medium: Im $(ak_S) = 10^{-1} \cdot n_0^2$; Im $(ak_D) = 8.10^{-2} n_0^2$.

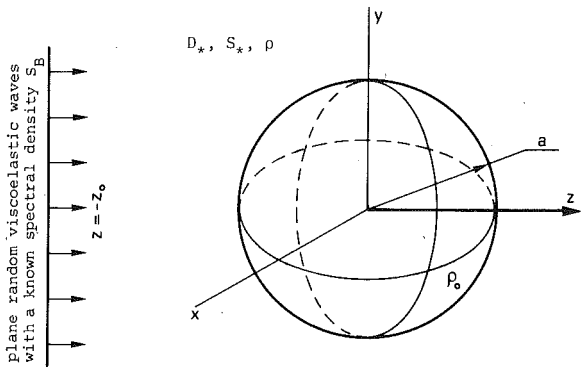

Fig. 2 Geometry of problem

and

$$S_A(\omega, z)/S_B(\omega) = |e^{ik_D(\omega)\bar{z}}|^2 = e^{-2k_D{}^1(\omega)\bar{z}} \tag{7}$$

The relationships (6) and (7) reflect the filtering behavior of the viscoelastic medium. As is seen from (7) only the imaginary part of the wave number affects the spectral density of a process when the stationary process is considered.

Let us now suppose that the discontinuity occurs at $z = 0$ with admittance function $H(\omega)$. Taking into account the time-invariance of the system it can be found that the response W of the discontinuity and its nth derivative $W^{(n)}$ have the following variance functions when z_0 is held constant:

$$\text{Var}\,[W^{(n)}] = \int_{-\infty}^{\infty} \omega^{2n} |H(\omega)|^2 S_A(\omega, 0) d\omega = \int_{-\infty}^{\infty} \omega^{2n} |H(\omega)|^2 e^{-2k_D{}^1(\omega)z_0} \tag{8}$$

$$\times S_B(\omega)d\omega (n = 0, 1, 2, \ldots) \quad (8)$$

(*Cont.*)

When the distance z_0 of a plane with a known spectral density $S_B(\omega)$ is also a random variable, the additional averaging must be done by means of a probability function for z_0. This yields

$$\langle \mathrm{Var}\,[W^{(n)}]\rangle_{z_0} = \int_{-\infty}^{\infty} \omega^{2n}|H(\omega)|^2\langle e^{-2k_D{}^1(\omega)z_0}\rangle_{z_0} S_B(\omega)d\omega \quad (9)$$

where $\langle\rangle_{z_0}$ designates the averaging with respect to z_0.

By adopting the theory of nonstationary stochastic process we now extend the results expressed by equations (7) and (9) to the transient case. It can be assumed for this purpose that the nonstationary random vibrations with a known spectral density $S_B(\omega_1, \omega_2)$ take place at $z = -z_0$. Then the spectral density at the plane z is

$$S_A(\omega_1, \omega_2, z) = e^{ik_D(\omega_1)\bar{z}}e^{-ik_D{}^*(\omega_2)\bar{z}}S_B(\omega_1, \omega_2) \quad (10)$$

Here the asterisk designates the complex conjugate.

The nonstationary variance for the displacement of the insert is

$$\langle \mathrm{Var}\,[W(t)]\rangle_{z_0} = \lim_{\epsilon\to 0} \int_{-\infty}^{\infty}\int \langle\Gamma(\omega_1)\rangle_{z_0}\langle\Gamma^*(\omega_2)\rangle_{z_0}$$

$$\times S_B(\omega_1, \omega_2)\exp[-it(\omega_1 - \omega_2) - i\epsilon\omega_2]d\omega_1, d\omega_2 \quad (11)$$

where

$$\langle\Gamma(\omega)\rangle_{z_0} = H(\omega)\langle e^{ik_D(\omega)z_0}\rangle_{z_0} \quad (12)$$

Thus, if $S_B(\omega)$ and the probability function for z_0 are known, the problem is one of evaluating the integrals (9) or (11). Straightforward application of the residue method in its routine form to evaluate these integrals leads to computations which are tedious at best. Moreover, depending upon the types of roots the result is expressed by different analytical formulas. Therefore, in general, a numerical approach is preferable. However, it is clear that the derivation of an analytical solution is very desirable from a variety of viewpoints. In the following section, we deal with this problem.

4 Stationary Response of a Sphere to Narrow-Band Random Process

Let us consider a rigid sphere with a center at $z = 0$, which is excited by random P-waves of a displacement traveling in a Maxwellian medium (Fig. 2). We assume that ϕ_D and ϕ_s in equations (3) and (4) are small, which is a usual restriction in the dynamics of viscoelastic composites [20]. The stochastic generalization of an harmonic wave is a so-called narrow-band process [13]. We suppose that such a process takes place at $z = -z_0$. This means that

$$S_B(\omega) = bK_0[(\omega_-{}^2 + b^2)^{-1} + (\omega_+{}^2 + b^2)^{-1}]/2\pi$$

and

$$S_A(\omega, z) = e^{-2k_D{}^1\bar{z}}S_B(\omega) \quad (13)$$

where K_0 is the variance of the process, $\omega_\mp = \omega\mp\theta$, θ is the predominant frequency and b describes the "sharpness" of the peak at $\omega = \theta$. It should be noted that the relationship $\theta \gg \mu/\eta_{S,D}$ must be valid to insure that ϕ_D and ϕ_S are small.

Under this assumption, an exact and relatively compact solution can be obtained. It can be shown from (2), (9) and (13) that the following representation is true:

$$|H(\omega, z_0)|^2 S_A(\omega, z) = e^{-2k_D{}^1(a+z_0)}9m^2bK_0\tau^2 g_6(n_0)/h_6(n_0)h_6(-n_0)\pi \quad (14)$$

where

$$n_0 = \mathrm{Re}\,(ak_D);\ \tau = a/c;\ c^2 = (\lambda + 2\mu)/\rho;\ g_6(n_0) = \sum_{k=0}^{5} d_k n_0{}^{10-2k};\ h_6(n_0) = \sum_{k=0}^{6} c_k n_0{}^{6-k};\ k_D{}^1 = 0.5\,[(\lambda + 2\mu)\rho]^{1/2}/\eta_D.$$

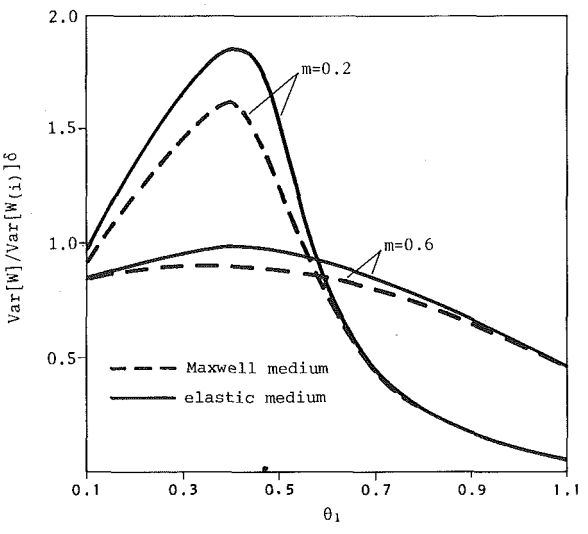

Fig. 3 Influence of viscosity on variance of inclusion displacement; Im (ak_D) = 5.10^{-2}; Im (ak_S) = 7.10^{-2}; ν = 0.3; b_{11} = 10^{-4}

The coefficients d_k and c_k and other required relationships are given in the Appendix. It can also be shown that all the roots of $h_6(n_0)$ are located in the upper half plane which makes it possible to use the integral formula due to Phillips [21]. This formula is also given in [22 N. 3.112, p. 218].

By means of this formula the variances of the insert displacement, the velocity and acceleration are found (using equation (9)) to be

$$\langle \mathrm{Var}\,[W]\rangle_{z_0} = VM_{60}/(a_0\Delta_6);\quad \langle \mathrm{Var}\,[W^{(1)}]\rangle_{z_0} = VM_{61}/(a_0\Delta_6\tau^2) \quad (15)$$

$$\langle \mathrm{Var}\,[W^{(2)}]\rangle_{z_0} = VM_{62}/(a_0\Delta_6\tau^4) \quad (16)$$

where

$$V = -9m^2K_0b\tau\delta;\quad \delta = \langle e^{-2k_D{}^1(a+z_0)}\rangle_{z_0}.$$

The Δ_6 and M_{6i} are the determinants of the 6×6 matrixs

$$\Delta_6 = \left|\begin{matrix} c_1 c_3 c_5 0 0 0 \\ \Delta \end{matrix}\right|;\quad M_{60} = \left|\begin{matrix} d_0 d_1 d_2 d_3 d_4 d_5 \\ \Delta \end{matrix}\right| \quad (17)$$

$$M_{61} = \left|\begin{matrix} d_1 d_2 d_3 d_4 d_5 d_0 \\ \Delta \end{matrix}\right|;\quad M_{62} = \left|\begin{matrix} d_2 d_3 d_4 d_5 d_0 d_1 \\ \Delta \end{matrix}\right|$$

where Δ is 5×6 matrix

$$\Delta = \begin{pmatrix} c_0 & c_2 & c_4 & c_6 & 0 & 0 \\ 0 & c_1 & c_3 & c_5 & 0 & 0 \\ 0 & c_0 & c_2 & c_4 & c_6 & 0 \\ 0 & 0 & c_1 & c_3 & c_5 & 0 \\ 0 & 0 & c_0 & c_2 & c_4 & c_6 \end{pmatrix}$$

The results obtained make it possible to estimate the influence of anyone of the parameters of the system on the variance of the inclusion displacement, velocity, and acceleration.

Fig. 3, computed from equation (15) exhibits the dependence of Var $[W]$ upon the predominant dimensionless frequency $\theta_1 = \theta\tau$ for some values of the density ratio, m. It follows from the comparison between Figs. 3 and 1 that Var $[W]$ is increased when θ_1 approaches the natural dimensionless frequency. Fig. 3 also shows the influence of energy losses which take place in the surrounding medium.

Fig. 4 shows the dependence of Var $[F]$ upon θ_1 where F is the force acting on the inclusion. It is computed by means of the equation Var $[F] = (4\pi a^3\rho_0/3)^2 \times$ Var $[W^{(2)}]$ and equation (16). As the figure and equation (16) show, the force is very sensitive to changes in at least the following parameters: half-transit time τ, density ratio m, radius a, and frequency θ_1.

It should be noted that as has been shown by Moon and Mow [23],

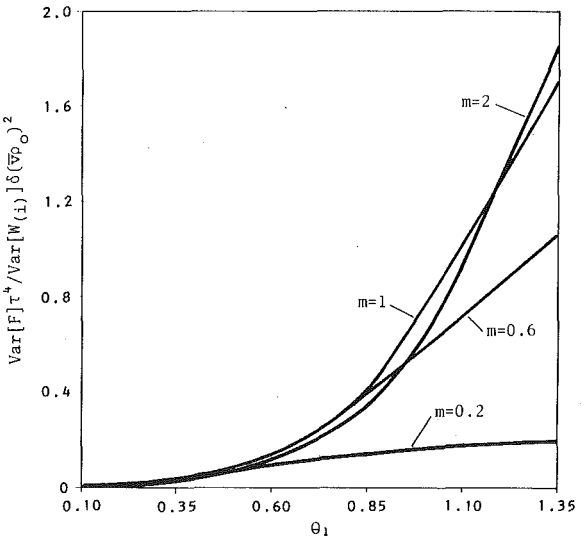

Fig. 4 Variance of force versus dimensionless forcing frequency θ_1 for various m; $\bar{v}$ = sphere volume; $\nu = 0.3$; $b_{11} = 10^{-4}$; Im (ak_S) = 7.10^{-3}; Im (ak_D) = 5.10^{-3}

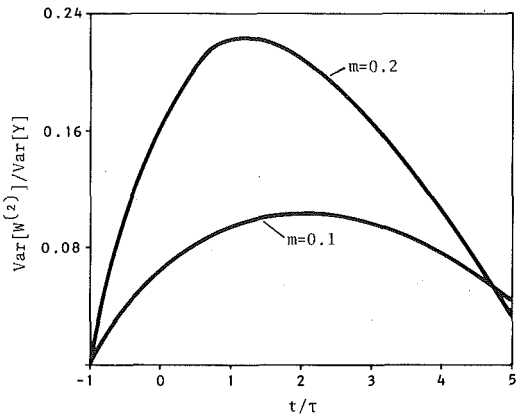

Fig. 5 Transient variance of sphere acceleration under shot-noise disturbance; $z_0 = 0$; $\nu = 0.3$; $N_1 = 10^3$; $N_2 = 10^6$; Im (ak_S) = $10^{-1} \cdot n_0^2$; Im (ak_D) = $8 \cdot 10^{-2} n_0^2$

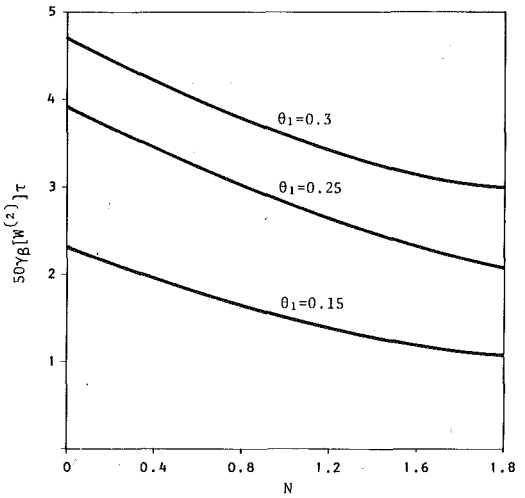

Fig. 6 Number of level crossings versus parameter N for various θ_1; m = 2; $b_{11} = 10^{-4}$; Im (ak_D) = 5.10^{-3}

and by Beltzer [24], the dynamic properties of a composite material containing dispersed rigid spheres can be predicted on the basis of the dynamics of a single particle if the mixture is dilute. Therefore, the high sensitivity of the force to deviations of the parameters takes place also for this case. This explains the significant dispersion of mechanical properties observed for composite materials.

Compact closed solution, such as the in the foregoing, can only rarely be found for problems of this type. In the general case a numerical approach is required.

5 Nonstationary Response and Some Applications of the Theory

The application of the results obtained to the analysis of the mechanical properties of the composite material was briefly noted in Section 4. We shall deal here, in greater detail, with applications to the protection of buried structures subject to incompletely known or random excitation.

Usually, the effect of a random ground shock on a structure is analyzed by means of a discrete model and the spatial shape and, hence, the scattering phenomena are not taken into account [25, 26]. The approach presented in Section 3 makes it possible to account for the propagation process of random viscoelastic waves from a randomly located source and the subsequent response of the structure including the transient and steady cases.

Let us consider the rigid sphere containing light equipment whose influence on the sphere motion can be neglected. The last restriction is usual for the practice of the analysis of ground shock action. It is important to predict the sphere acceleration since this function is the forcing term in the governing equations for the light equipment [25, 26].

The disturbance appearing during an earthquake can be described as a random wave of acceleration. As was shown by Mow [17], if the excitation is a wave of acceleration, and the acceleration of the sphere is considered as the response, then the same equation (2) yields the admittance function. Therefore, this time equation (11) yields the transient variance of the sphere acceleration and equation (9) governs the steady case.

One of the models of the ground shock disturbances is a shot noise, $F(t)$

$$F(t) = \sum_{K=1}^{N(t)} Y_k \delta(t - t_k) \tag{18}$$

where Y_k are identically distributed independent random variables and t_k are random times that obey the Poisson distribution with an expected nonstationary arrival rate $\lambda(t)$ [12, 26]. If this process takes place at $z = -z_0$ then

$$S_B(\omega_1, \omega_2) = (2\pi)^{-1} \mathrm{Var}\,[Y]\Lambda(\omega_1 - \omega_2) \tag{19}$$

where $\Lambda(\omega)$ is the Fourier transform of $\lambda(t)$.

For this case equation (11) yields the transient variance of the sphere acceleration if $S_B(\omega_1, \omega_2)$ is given by equation (19) and $H(\omega)$—by equation (2).

The results obtained by means of the numerical integration are given in Fig. 5 for the case $\lambda(t/\tau) = N_1 e^{-N_2 t^2/\tau^2}$ (N_1, N_2 – constants). It was assumed that the surrounding medium behaves as the model of Kelvin-Voight [18]. It should be noted that the motion of the insert begins at $t/\tau = -1$ when the wave has arrived at the incident side of the inclusion.

In the case of a stationary excitation the suitable functional for estimating the reliability of protection is the number of crossings of the critical level β per unit time of the function $W^{(2)}$. The expectation of this value, $\gamma_\beta[W^{(2)}]$, is determined by the Rice formula [27]. In the particular case considered in Section 4, and under the condition that the process is Gaussian, this formula yields

$$\gamma_\beta[W^{(2)}]\tau = (M_{61}/M_6)^{1/2} \exp(-N/2I)/\pi \tag{20}$$

where

$$N = \beta^2/\mathrm{Var}\,[W_{(i)}^{(2)}] \tag{21}$$

$$I = 9m^2 b\tau M_6/(a_0\Delta_6) \tag{22}$$

Thus the influence of the various parameters on the number of level crossings can be determined. Fig. 6, computed from (20), shows the influence of the parameter N, defined by (21), on the dependence $\gamma_\beta[W^{(2)}] = f(\theta_1)$.

The results obtained here also provide the estimation of the force on a sphere and therefore they are applicable to the dynamics of composite materials. In view of a single-valued dependence between the inclusion motion and the stresses at $r = a$ [3, 28] the functionals (8), (11), and (20) can be used to predict the fatique strength [12, 13] of the composite material.

6 Conclusion

Harmonic and random responses of a rigid movable sphere embedded in a viscoelastic medium have been studied theoretically. It was shown that the presence of energy losses in the surrounding medium affect the inclusion motion. This influence depends upon the viscoelastic model.

Expressions (7), (9), and (11) show that the interaction between viscoelastic waves and the discontinuity is different from that of random purely elastic waves, considered in [15]. It is of interest that only the imaginary part of the wave number affects the propagation of a stationary random disturbance. Since the viscoelastic waves are filtered during their propagation, the distance between an insert and a plane, at which the excitation had a prescribed spectral density, plays an essential role.

It can be concluded that the analysis of the scattering of random viscoelastic waves by an obstacle makes it possible to account more fully for actual physical situations and to extend the range of applications of the theory.

Acknowledgment

I wish to thank Prof. N. Rudy for his helpful comments; I also gratefully acknowledge the assistance of Mr. Ishai Abiri in performing the calculations, and of Mrs. Michele Katzir in typing the manuscript.

References

1 Ying, C. F., and Truell, R., "Scattering of a Plane Longitudinal Wave by a Spherical Obstacle in an Isotropically Elastic Solid," *Journal of Applied Physics,* Vol. 27, 1956, pp. 1086–1097.

2 Scott R. A., "Linear Elastic Wave Propagation, An Annoted Bibliography, Part 2," *The Shock and Vibration Digest,* Vol. 10, N. 3, 1978, pp. 11–39.

3 Pao, Y-H., and Mow, C. C., *Diffraction of Elastic Waves and Dynamic Stress Concentrations,* Grane, Russak, New York, 1972.

4 Achenbach, J. D., "The Dynamic Effects in Brittle Fracture," *Mechanics Today,* Nemat-Nasser, S., ed., Vol. 1, Pergamon Press, 1974.

5 Datta, S. K., "Scattering of Elastic Waves," *Mechanics Today,* Nemat-Nasser, S., ed., Vol. 4, Pergamon Press, 1978.

6 Pao, Y-H., "Betti's Identity and Transition Matrix for Elastic Waves," *Journal of the Acoustical Society of America,* Vol. 64, 1978, pp. 302–310.

7 Waterman, P. C., "Matrix Theory of Elastic Waves Scattering," *Journal of the Acoustical Society of America,* Vol. 60, 1976, pp. 567–580.

8 Lewis, T. S., Kraft, D. W., and Hom, N., "Scattering of Elastic Waves by a Cylindrical Cavity in a Solid," *Journal of Applied Physics,* Vol. 47, N. 5, 1976, pp. 1795–1798.

9 Gaunaurd, G. C., and Uberall, H., "Theory of Resonant Scattering From Spherical Cavities," *Journal of the Acoustical Society of America,* Vol. 63, N. 6, 1978, pp. 1699–1712.

10 Mei, C. C., "Extensions of Some Identities in Elastodynamic With Rigid Inclusions," *Journal of the Acoustical Society of America,* Vol. 64, (5), 1978, pp. 1514–1522.

11 Beran, M., *Statistical Continium Theories,* Wiley (Interscience), New York, 1968.

12 Lin, Y. K., *Probabilistic Theory of Structural Dynamics,* McGraw-Hill, New York, 1967.

13 Bolotin, V. V., *Statistical Methods in Structural Mechanics,* Holden-Day, Inc., San Francisco, 1968.

14 Newmark, N. M., and Rosenblueth, E., *Fundamentals of Earthquake Engineering,* Prentice-Hall, Inc., Englewood Cliffs, N.J., 1971.

15 Beltzer, A., "Response of a Rigid Sphere Embedded in an Elastic Medium to Random Disturbances," ASME JOURNAL OF APPLIED MECHANICS, Vol. 46, Dec. 1979, pp. 951–952.

16 Pao, Y. H., and Mow, C. C., "Scattering of Plane Compressional Waves by a Spherical Obstacle, *Journal of Applied Physics,* Vol. 34, 1963, pp. 493–499.

17 Mow, C. C., "Transient Response of a Rigid Spherical Inclusion in an Elastic Medium," ASME JOURNAL OF APPLIED MECHANICS, Vol. 32, 1965, pp. 637–642.

18 Bland, D. R., *The Theory of Linear Viscoelasticity,* Oxford, 1960.

19 Rozanov, V. A., *Random Processes,* Nauka, Moscow, 1971 (in Russian: *Cluchainue Protsesa*).

20 Schapery, R. A., "Viscoelastic Behavior and Analysis of Composite Materials," *Composite Materials,* eds., Brontman, L. J., and Krock, R. M., Vol. 2, *Mechanics of Composite Materials,* ed., Sendeckyi, G. P., Academic Press, 1974, pp. 86–105.

21 James, H. M., Nicols, N. B., and Phillips, R. S., *Theory of Servomechanisms,* McGraw-Hill, New York, 1947.

22 Gradsteyn, I. S., and Ryzhik, I. M., *Table of Integrals, Series and Products,* Academic Press, New York, 1965.

23 Moon, F. C., and Mow, C. C., "Wave Propagation in a Composite Material Containing Dispersed Rigid Spherical Inclusions," RAND Report RM-6139-PR, 1970.

24 Beltzer, A., "A Dynamic Model for Elastic Waves Propagation in a Material Containing Rigid Spheres," *Journal of the Acoustical Society of America* (accepted).

25 Singh, M. P., and Wen, Y-K., "Nonstationary Seismic Response of Light Equipment," *Journal of ASCE, Engineering Mechanics Division,* Dec. 1977, pp. 1035–1048.

26 Iwan, W. D., ed., *Applied Mechanics in Earthquake Engineering,* AMD, Vol. 8, ASME, New York, 1974.

27 Rice, S. O., "Mathematical Analysis of Random Noise," *Selected Papers on Noise and Stochastic Processes,* Wax. N., ed., Dover Publications, New York, 1954.

28 Datta, S. K., and Sangster, J. D., "Response of a Rigid Spheriodal Inclusion to an Incident Plane Compressional Elastic Wave," *SIAM Journal of Applied Mathematics,* Vol. 26, No. 2, Mar. 1974, pp. 350–369.

APPENDIX

1 $|H(\omega)|^2 = 9m^2 e^{-2n_1 g_4}(n_0)/h_4(n_0)h_4(-n_0)$

where

$$g_4(n_0) = \sum_{k=0}^{3} b_k n_0^{6-2k}; \quad h_4(n_0) = \sum_{k=0}^{4} a_k n_0^{4-k}; \quad b_0 = 0;$$

$$b_1 = \chi_0^4; \quad b_2 = \chi_0^2(2\bar{\delta}^2 - 6\gamma + 3);$$
$$b_3 = \delta^4 - 6\gamma\delta^2 + 15\bar{\delta}^2 - 18\gamma + 9;$$
$$a_0 = \chi_0^2; \quad a_1 = i(p_1 + 4n_1 p_0); \quad a_2 = p_2 + 3p_1 n_1;$$
$$a_3 = i(p_3 + 2n_1 p_2);$$
$$a_4 = p_4 - n_1 p_3$$

with

$$n_0 = \text{Re}\,(n) = \text{Re}\,(ak_D); \quad n_1 = \text{Im}\,(n); \quad \gamma = \text{Im}\,(ak_S);$$
$$q = \text{Im}\,(\chi)\omega; \quad \chi_0 = \text{Re}\,(\chi); \quad \bar{\delta} = \chi_0\epsilon; \quad \epsilon = q\tau;$$
$$p_1 = \chi_0^2(2 + m - 2\epsilon) + \chi_0(1 + 2m);$$
$$p_2 = \chi_0^2(-2 - m - \epsilon^2 + 4\epsilon + 2m\epsilon);$$
$$p_3 = \chi_0^2(-2\epsilon^2 - m\epsilon^2 + 4\epsilon + 2m\epsilon) + 9\chi_0(-m + m\epsilon) - 9m;$$
$$p_4 = \chi_0^2\epsilon^2(2 + m) - \chi_0 9m\epsilon + 9m;$$

2 $|H(\omega)|^2 \cdot S_A(\omega) = e^{-2k_D 1(a+z_0)} 9m^2 K_0 \tau^2 e^{-2n_1} g_6(n_0)/\pi h_6 \cdot(n_0)h_6(-n_0)$ where

$$g_6(n_0) = \sum_{k=0}^{5} d_k n_0^{10-2k}; \quad h_6(n_0) = \sum_{k=0}^{6} c_k n_0^{6-k}; \quad d_0 = d_1 = 0;$$

$$d_2 = b_1; \quad d_3 = b_2 + b_1 p; \quad d_4 = b_3 + b_2 p; \quad d_5 = b_3 p; \quad c_0 = a_0;$$
$$c_1 = i(-a_1 - 2b_{11}a_0);$$
$$c_2 = a_2 - a_0 p - 2b_{11}a_1; \quad c_3 = i(-a_3 + a_1 p - 2b_{11}a_2);$$
$$c_4 = a_4 - pa_2 - 2b_{11}a_3; \quad c_5 = i(a_3 p - 2b_{11}a_4); \quad c_6 = -a_4 p$$

where

$$p = \theta_1^2 + b_{11}^2; \quad \theta_1 = \theta\tau; \quad b_{11} = b\tau.$$

The compliances (equation (4)) are:

$$D_1 = (\lambda + 2\mu)^{-1}; \quad D_2 = (\eta_D\omega)^{-1};$$
$$S_1 = \mu^{-1}; \quad S_2 = (\eta_S\omega)^{-1}$$

R. Muki
Professor. Mem. ASME

S. B. Dong
Professor. Mem. ASME

Mechanics and Structures Department,
University of California,
Los Angeles, Calif. 90024

Elastostatic Far-Field Behavior in a Layered Half Space Under Surface Pressure[1]

Elastostatic problem of a half space with a layer of possibly distinct mechanical properties under arbitrary normal tractions on the surface is reconsidered to establish far-field asymptotic expansions of the displacements. This work was motivated by application of such far field solutions to problems of the layered half space by Global-Local Finite-Element Method (GLFEM). When the traction is a unit concentrated force, the asymptotic expansion is found to coincide, up to the second term of its inverse power series expansion with respect to the distance from the point at interface below the point of load application, with that of the classical Boussinesq solution with a suitably chosen coordinate system. This agreement between the two solutions is also observed for normal tractions on a bounded surface region. Comparative numerical results are given to demonstrate the modeling capabilities of the far-field asymptotic expansions in a GLFEM example. It's effectiveness is shown in terms of greater accuracy and computational efficiency over the conventional finite-element method.

1 Introduction

This paper is concerned with far-field asymptotic expansions of displacements in an elastic half space with an elastic layer of possibly distinct mechanical properties. The analysis presupposes perfect bond between the semi-infinite medium and the layer, while the loading is confined to normal tractions applied to a bounded portion of an otherwise free surface of the layer. The terms in the ensuing asymptotic series are ordered according to R^{-n} $(n = 1, 2, \ldots)$, where R is the distance from the point at interface below the centroid of load region, and explicitly relate the far-field behavior to the load distribution, the mechanical properties of both media, and the thickness of the layer. These asymptotic expansions illustrate Saint-Venant's principle by providing quantitative measures of decay in this particular instance.[2] The results are used in an application of the *Global-Local Finite-Element Method* (GLFEM) to elastostatic problems involving a layered, elastic half space.

Because of their relevance to pavement design,[3] geotechnical engineering, as well as many other applications, layered half-space problems have received repeated attention. Bufler's paper [3] contains a comprehensive review of elastostatic analyses of multilayered media. We shall rely on Bufler's summary of the literature and cite here only specific papers that bear directly on our present objectives. Of particular importance is Burmister's [4] exact solution to the problem of a layer perfectly bonded to a half space and subjected to a particular axisymmetric surface-pressure distribution. With the aid of this fundamental result, solutions corresponding to other normal loadings may be obtained by means of the Hankel transform. Reference should also be made to [5], where far-field asymptotic expansions of the displacements in a homogeneous, isotropic half space were systematically cataloged and their use in connection with GLFEM was examined. The present paper is thus an extension of [5].

GLFEM refers to a numerical analysis technique which employs both contemporary finite element and classical Rayleigh-Ritz displacement approximations [6–8]. This method enjoys the advantage of more accurate modeling with substantially fewer degrees of freedom as compared to the conventional finite-element method (FEM). For brevity, we will refer to the Rayleigh-Ritz displacement approximations as *global functions*. The primary role of global functions is to capture the behavior in the regions where conventional finite-element modeling becomes kinematically inadequate or computationally cumbersome. Finite-element modeling limitations arise in a host of problems involving local singularities or unbounded regions. Known analytical results containing the essence of the relevant local or far-field behavior can be incorporated into a finite-element analysis as global functions. It is evidently desirable to have such results available in as simple a mathematical form as possible. For this reason, asymptotic expansions, in which the leading terms portray the dominant behavior, are particularly appealing. Our recent experience with

[1] This research was supported by Electric Power Research Institute, Palo Alto, Calif.

[2] See Gurtin [1] for a review of the Saint-Venant principle for homogeneous isotropic elastic bodies.

[3] See Yang [2].

Contributed by the Applied Mechanics Division for presentation at the Winter Annual Meeting, Chicago, Ill., November 16–21, 1980, of THE AMERICAN SOCIETY OF MECHANICAL ENGINEERS.

Discussion on this paper should be addressed to the Editorial Department, ASME, United Engineering Center, 345 East 47th Street, New York, N. Y. 10017, and will be accepted until December 1, 1980. Readers who need more time to prepare a discussion should request an extension from the Editorial Department. Manuscript received by ASME Applied Mechanics Division, September, 1979. Paper No. 80-WA/APM-7.

GLFEM analysis of half-space problems [5] demonstrated a marked improvement in computational efficiency for achieving a desired accuracy over conventional finite-element methods.

Our first task here is to deduce a solution for a unit concentrated normal force on the surface of a layered half space from Burmister's solution by means of the Hankel transform. We will refer to this solution as the *generalized Boussinesq solution.* Asymptotic expansions of the displacements are then extracted from this integral representation using the method described in [9]. These details are covered in Section 2. It will become apparent that the first two terms in the expansions are quire simple in form and readily admit useful physical interpretation. Higher-order terms are obtainable, but only with the expense of increasingly elaborate algebra and without a commensurate gain in significance and usefulness. In Section 3, we focus on the asymptotic behavior of the layered half space under arbitrary normal surface tractions confined to a bounded region. For this case, the asymptotic expansions are constructed by superposition of the asymptotic results associated with the generalized Boussinesq solution. Again, the first two terms are quite simple and permit a convenient physical interpretation. Section 4 is devoted to a GLFEM numerical example in which the previously established far-field asymptotic behavior is utilized. From this, one can draw some interesting conclusions which provide guidance in the GLFEM modeling of soil-structure interaction.

2 The Generalized Boussinesq Problem

Consider a layer of thickness h perfectly bonded to a semi-infinite medium. Let μ', ν' and μ, ν denote the shear modulus and Poisson's ratio of the layer and the half space, respectively.[4] Establish a rectangular Cartesian coordinate system (x_1, x_2, x_3) with its origin at the interface of the two media. Let Λ' and Λ denote the domains occupied by the layer[5] $(-\infty < x_\alpha < \infty, -h < x_3 < 0)$ and the half space $(-\infty < x_\alpha < \infty, 0 < x_3 < \infty)$. Let u_i and σ_{ij} represent the Cartesian components of displacement and stress. We will have occasion to use circular cylindrical coordinates (r, θ, z) having the same origin and the z-axis coincident with the x_3-axis. The cylindrical components of displacement and stress are identified by subscripts (r, θ, z).

The problem for the layered half space subjected to an arbitrary axisymmetric surface pressure, $p(r)$, can be stated as follows. The fundamental equations within the classical theory of elasticity for both the layer and the half space are to be accompanied by the boundary conditions

$$\left.\begin{aligned} \sigma_{zz}(r, -h) &= \begin{cases} -p(r) & (0 \le r < a) \\ 0 & (a < r < \infty), \end{cases} \\ \sigma_{rz}(r, -h) &= 0 \qquad (0 \le r < \infty), \end{aligned}\right\} \tag{1}$$

the interface conditions

$$\left.\begin{aligned} u_r(r, 0+) &= u_r(r, 0-), \quad u_z(r, 0+) = u_z(r, 0-), \\ \sigma_{zz}(r, 0+) &= \sigma_{zz}(r, 0-), \quad \sigma_{zr}(r, 0+) = \sigma_{zr}(r, 0-) \\ &\qquad (0 \le r < \infty), \end{aligned}\right\} \tag{2}$$

and the regularity requirement that all displacements and stresses vanish as $R \to \infty$ where

$$R = (x_i x_i)^{1/2}. \tag{3}$$

Integral representations for the displacements due to $p(r)$ can be constructed by using the Hankel transform[6] and recognizing that Burmister's exact solution [4] in the kernal in that formula:

$$\left.\begin{aligned} u_r(r, z) &= \frac{1}{2\mu'} \int_0^\infty \hat{p}(\xi)\{[A'(\xi) + (1 + \xi z)C'(\xi)]\mathbf{e}^{\xi(z-h)} \\ &\quad + [B'(\xi) - (1 - \xi z)D'(\xi)]\mathbf{e}^{-\xi(z+h)}\}J_1(\xi r)d\xi, \\ u_z(r, z) &= \frac{1}{2\mu'} \int_0^\infty \hat{p}(\xi)\{[-A'(\xi) + (2 - 4\nu' - \xi z)C'(\xi)]\mathbf{e}^{\xi(z-h)} \\ &\quad + [B'(\xi) + (2 - 4\nu' + \xi z)D'(\xi)]\mathbf{e}^{-\xi(z+h)}\}J_0(\xi r)d\xi \\ &\qquad\qquad \text{in} \quad \Lambda', \end{aligned}\right\} \tag{4}$$

$$\left.\begin{aligned} u_r(r, z) &= \frac{1}{2\mu} \int_0^\infty \hat{p}(\xi)[B(\xi)\mathbf{e}^{-\xi(z+h)} \\ &\quad - (1 - \xi z)D(\xi)\mathbf{e}^{-\xi(z+h)}]J_1(\xi r)d\xi, \\ u_z(r, z) &= \frac{1}{2\mu} \int_0^\infty \hat{p}(\xi)[B(\xi)\mathbf{e}^{-\xi(z+h)} \\ &\quad + (2 - 4\nu + \xi z)D(\xi)\mathbf{e}^{-\xi(z+h)}]J_0(\xi r)d\xi \quad \text{in} \quad \Lambda. \end{aligned}\right\} \tag{5}$$

Here

$$\hat{p}(\xi) = 2\pi \int_0^a r p(r) J_0(\xi r) dr, \tag{6}$$

and

$$\left.\begin{aligned} A'(\xi) &= \frac{1}{2\Delta(\xi)}[\kappa(1 - 4\nu')(1 + 2\xi h) - \lambda \\ &\qquad + \kappa\lambda(4\nu' - 2\xi h)\mathbf{e}^{-2\xi h}], \\ B'(\xi) &= \frac{1}{2\Delta(\xi)}[(4\nu' + 2\xi h) - \lambda\mathbf{e}^{-2\xi h} \\ &\qquad + \kappa(1 - 4\nu')(1 - 2\xi h)\mathbf{e}^{-2\xi h}], \\ C'(\xi) &= \frac{1}{\Delta(\xi)}[\kappa(1 + 2\xi h) - \kappa\lambda\mathbf{e}^{-2\xi h}], \\ D'(\xi) &= \frac{1}{\Delta(\xi)}[1 - \kappa(1 - 2\xi h)\mathbf{e}^{-2\xi h}], \\ B(\xi) &= \frac{2(1 - \nu')}{\omega - 1} C'(\xi) - \frac{1}{2}(1 - 4\nu)(1 - \lambda)D'(\xi), \\ D(\xi) &= (1 - \lambda)D'(\xi) \end{aligned}\right\} \tag{7}$$

with

$$\left.\begin{aligned} \Delta(\xi) &= 2\pi[1 - (\lambda + \kappa + 4\kappa\xi^2 h^2)\mathbf{e}^{-2\xi h} + \kappa\lambda\mathbf{e}^{-4\xi h}], \\ \omega &= \frac{\mu'}{\mu}, \quad \kappa = \frac{\omega - 1}{\omega + 3 - 4\nu'} \\ \lambda &= 1 - \frac{4(1 - \nu')}{1 + (3 - 4\nu')\omega}. \end{aligned}\right\} \tag{8}$$

For the case of a unit concentrated compressive force applied at $r = 0$ on the surface, its pressure distribution is given by

$$p(r) = \frac{\delta(r)}{2\pi r}, \tag{9}$$

where $\delta(r)$ is the Dirac delta function. The Hankel transform of $p(r)$ is

$$\hat{p}(\xi) = 1. \tag{10}$$

As noted earlier, we refer to the displacements (4) and (5) with $\hat{p} = 1$ and the associated stresses as the generalized Boussinesq solution. We shall identify the components of this solution by means of a superscript "o".

For the particular case in which the elastic properties of the layer and the half space are the same, the generalized Boussinesq solution reduces to Boussinesq's solution. This reduction, however, leads to an elastostatic field that differs from its classical representation by a translation in x_3 direction because of the adopted coordinated system. Thus, for $\mu = \mu'$ and $\nu = \nu'$,

$$\overset{o}{u}_i(x_1, x_2, x_3) = \overset{*}{u}_i(x_1, x_2, x_3 + h) \quad \text{in} \quad \Lambda \quad \text{and} \quad \Lambda', \tag{11}$$

[4] Throughout this paper, quantities associated with the layer are distinguished by a prime from those pertaining to the half space.

[5] Greek and Roman subscripts have ranges (1, 2) and (1, 2, 3), respectively. The usual summation and differentiation conventions for indicial notation are employed. δ_{ij} denotes the Kronecker delta.

[6] See, for instance, Sneddon [10, p. 52].

where $\overset{*}{u}_i$ are displacements of the classical Boussinesq solution:

$$\overset{*}{u}_i(x_1, x_2, x_3) = \frac{1}{4\pi\mu}\left[\frac{x_i x_3}{R^3} - (1-2\nu)\frac{x_i(1-\delta_{i3})}{R(R+x_3)} + \frac{2(1-\nu)}{R}\delta_{i3}\right] \quad (-\infty < x_\alpha < \infty, \quad 0 < x_3 < \infty). \quad (12)^7$$

For future reference we record here the inverse power series of the displaced Boussinesq solution with respect to the distance from the origin:

$$\left.\begin{aligned}\overset{*}{u}_i(x_1, x_2, x_3 + h) &= \overset{*}{u}_i(x_1, x_2, 0) + \sum_{n=2}^{\infty} \overset{*}{f}_i^{(n)}(x_1, x_2, x_3)\frac{h^{n-1}}{r^n} \quad \text{in} \quad \Lambda' \\ \overset{*}{u}_i(x_1, x_2, x_3 + h) &= \overset{*}{u}_i(x_1, x_2, x_3) + \sum_{n=2}^{\infty} \overset{*}{F}_i^{(n)}(x_1, x_2, x_3)\frac{h^{n-1}}{R^n} \quad \text{in} \quad \Lambda,\end{aligned}\right\} \quad (13)$$

where, for every fixed n,

$$\left.\begin{aligned}\overset{*}{f}_i^{(n)}(x_1, x_2, x_3) &= O(1) \quad \text{as} \quad r \to \infty, \\ \overset{*}{F}_i^{(n)}(x_1, x_2, x_3) &= O(1) \quad \text{as} \quad R \to \infty.\end{aligned}\right\} \quad (14)$$

In particular, we have

$$\left.\begin{aligned}\overset{*}{f}_\alpha^{(2)} &= \left(1 + \frac{x_3}{h}\right)\overset{*}{F}_\alpha^{(2)}(x_1, x_2, 0), \quad \overset{*}{f}_3^{(2)} = 0, \\ \overset{*}{f}_\alpha^{(3)} &= 0, \quad \overset{*}{f}_3^{(3)} = \frac{\nu}{4\pi\mu}\left(1 + \frac{x_3}{h}\right)^2, \\ \overset{*}{F}_\alpha^{(2)} &= \frac{1}{4\pi\mu}\frac{x_\alpha}{R}\left[2(1-\nu) - \frac{3x_3^2}{R^2}\right],\end{aligned}\right\} \quad (15)$$

$$\left.\begin{aligned}\overset{*}{F}_3^{(2)} &= \frac{1}{4\pi\mu}\frac{x_3}{R}\left[2\nu - \frac{3x_3^2}{R^2}\right], \\ \overset{*}{F}_\alpha^{(3)} &= -\frac{3}{8\pi\mu}\frac{x_\alpha x_3}{R^2}\left[2(2-\nu) - \frac{5x_3^2}{R^2}\right], \\ \overset{*}{F}_3^{(3)} &= \frac{1}{4\pi\mu}\left[\nu - \frac{3}{2}(3+2\nu)\frac{x_3^2}{R^2} + \frac{15}{2}\frac{x_3^4}{R^4}\right].\end{aligned}\right\} \quad (16)$$

It can be shown that the two series in (13) converge for any positive r and R in the appropriate domains. At the same time, these series are asymptotic as $r \to \infty$ or as $R \to \infty$.

Our next objective is to extract the far-field behavior from the integral representations (4) and (5) with $\hat{p} = 1$. For this task the asymptotic formulas in [9] for integrals of the Lipshitz-Hankel type are needed, which we summarize as follows.

Let $\phi(\xi, z)$, for z on $[-h, 0]$, and $\Phi(\xi)$ be both N-times continuously differentiable with respect to ξ on $[0, \infty)$ and meet certain additional requirements stated in [9]. Then,

$$\int_0^\infty \phi(\xi, z) J_m(r\xi)d\xi = \frac{\sqrt{\pi}}{2^m}\sum_{n=0}^{N-1}\frac{1}{r^{n+1}} \times \frac{\Gamma(m+n+1)}{n!\Gamma((m-n+1)/2)\Gamma((m+n+2)/2)}\frac{\partial^n \phi}{\partial \xi^n}\bigg|_{\xi=0} + o(r^{-N}) \quad \text{as} \quad r \to \infty, \quad z \in [-h, 0], \quad (17)$$

$$\int_0^\infty \Phi(\xi)\mathbf{e}^{-\xi z} J_m(r\xi)d\xi = \sum_{n=0}^{N-1}\frac{1}{R^{n+1}}\frac{1}{n!}\int_0^\infty \eta^n \mathbf{e}^{-\eta\cos\psi} J_m(\eta\sin\psi)d\eta\frac{d^n\Phi}{d\xi^n}\bigg|_{\xi=0} + o(R^{-N}) \quad \text{as } R \to \infty, \quad z \in [0, \infty), \quad (18)$$

where $\cos\psi = z/R$ and $\sin\psi = r/R$. The integrals on the right in (18) are representable in terms of hypergeometric functions[8] which, for certain combinations of m and n, assume algebraic forms.

We list here the Cartesian displacement components of the far-field asymptotic expansion of the generalized Boussinesq solution.

$$\mathring{u}_i(x_1, x_2, x_3) = \overset{*}{u}_i(x_1, x_2, 0) + \mathring{f}_i^{(2)}(x_1, x_2, x_3)\frac{h}{r^2} + \mathring{f}_i^{(3)}(x_1, x_2, x_3)\frac{h^2}{r^3} + O(r^{-4}) \quad \text{as} \quad r \to \infty \quad \text{in} \quad \Lambda', \quad (19)$$

$$\mathring{u}_i(x_1, x_2, x_3) = \overset{*}{u}_i(x_1, x_2, x_3) + \mathring{F}_i^{(2)}(x_1, x_2, x_3)\frac{h}{R^2} + \mathring{F}_i^{(3)}(x_1, x_2, x_3)\frac{h^2}{R^3} + O(R^{-4}) \quad \text{as} \quad R \to \infty \quad \text{in} \quad \Lambda, \quad (20)$$

where

$$\left.\begin{aligned}\mathring{f}_i^{(2)} &= \left(1 + \gamma\frac{x_3}{h}\right)\overset{*}{F}_i^{(2)}(x_1, x_2, 0), \\ \mathring{f}_\alpha^{(3)} &= 0, \\ \mathring{f}_3^{(3)} &= \frac{1}{4\pi\mu}\left[c_0^{(3)} + c_1^{(3)}\frac{x_3}{h} + c_2^{(3)}\left(\frac{x_3}{h}\right)^2\right],\end{aligned}\right\} \quad (21)$$

$$\left.\begin{aligned}\mathring{F}_i^{(2)} &= (1+\gamma)\overset{*}{F}_i^{(2)}(x_1, x_2, x_3), \\ \mathring{F}_\alpha^{(3)} &= \frac{1}{2\mu}\frac{x_\alpha x_3}{R^2}\left[B_0^{(3)} + B_2^{(3)}\left(\frac{x_3}{R}\right)^2\right], \\ \mathring{F}_3^{(3)} &= \frac{1}{2\mu}\left[C_0^{(3)} + C_2^{(3)}\left(\frac{x_3}{R}\right)^2 + C_4^{(3)}\left(\frac{x_3}{R}\right)^4\right],\end{aligned}\right\} \quad (22)$$

$$\gamma = \frac{1}{1-\nu'}\left[(1-2\nu)\frac{\mu'}{\mu} - (1-2\nu')\right], \quad (23)$$

in which $\overset{*}{F}_i^{(2)}$ is given in (16), while $c_k^{(3)}$, $B_k^{(3)}$, $C_k^{(3)}$ are constants dependent upon ν, ν', μ'/μ. Because of the algebra involved, it is not convenient to seek explicit expressions for the constants $c_k^{(3)}$, $B_k^{(3)}$, $C_k^{(3)}$. However, they can be determined numerically without difficulty for specific values of ν, ν', and μ'/μ by use of (17) and (18).

On comparing the far-field expansion of the displaced Boussinesq solution (13) with that of the generalized Boussinesq solution (19) and (20), we observe the asymptotic relations

$$\mathring{u}_i(x_1, x_2, x_3) = \overset{*}{u}_i(x_1, x_2, x_3 + \mathbf{h}) + O(R^{-3}) \quad \text{as} \quad R \to \infty \quad \text{in} \quad \Lambda \quad \text{and} \quad \Lambda', \quad (24)^9$$

where

$$\mathbf{h} = (1+\gamma)h. \quad (25)$$

At this point we introduce scaled coordinates and scaled distance as

$$\tilde{x}_i = \frac{x_i}{1+\gamma}, \quad \tilde{R} = (\tilde{x}_i\tilde{x}_i)^{1/2} = \frac{R}{1+\gamma}. \quad (26)$$

Then it follows from (12), (24)–(26) that

$$\mathring{u}_i(x_1, x_2, x_3) = \frac{1}{1+\gamma}\overset{*}{u}_i(\tilde{x}_1, \tilde{x}_2, \tilde{x}_3 + h) + O(\tilde{R}^{-3}) \quad \text{as} \quad \tilde{R} \to \infty \text{ in} \quad \Lambda \quad \text{and} \quad \Lambda'. \quad (27)$$

As shown in (24), the generalized Boussinesq solution associated with the layer of thickness, h, has the same far-field behavior up to $O(R^{-2})$ with that for the displaced Boussinesq solution corresponding to a half space with the free surface at $x_3 = -\mathbf{h}$. Thus, within the current order estimate, the far-field displacements in the layered half space coincide with those for a homogeneous half space even though the far-field expansions refer to a point on the interface for the former

[7] See, for example, Love [11, p. 191], or Sokolnikoff [12, p. 339].

[8] See Watson [13, p. 384].

[9] The order statement $O(R^{-3})$ is equivalent to $O(r^{-3})$ in Λ'.

and to an interior point of the depth **h** from the free surface for the latter.

If we wish to have the translation for the displaced Boussinesq solution equal to the thickness of the layer, the elastic properties of the layer distinct from those for the half space emerge as a scaling factor, $1/(1+\gamma)$, both in coordinates and in magnitude as demonstrated in (27). The relation (27) will be employed in the numerical example to draw some information.

It should be mentioned that the formal differentiation of (24) is permissible and yields the same results which follow from the integral representations for the derivatives of $\mathring{u}_i$. This statement holds true also for the asymptotic relations (19) and (20).

3 Far-Field Displacement Due to an Arbitrary Pressure Over a Bounded Region

Let a pressure p act over a bounded region Π on the otherwise traction-free surface of the layered half space. Suppose also that the origin of the coordinate system coincides with the perpendicular projection of the centroid of Π at the plane $x_3 = 0$. Denote by P, P_α, and $P_{\alpha\beta}$ the total force, the first moment, and the second moment of p, respectively, i.e.,

$$P = \int_\pi p(x_1, x_2)dA, \quad P_\alpha = \int_\pi x_\alpha p(x_1, x_2)dA,$$

$$P_{\alpha\beta} = \int_\pi x_\alpha x_\beta p(x_1, x_2)dA. \tag{28}$$

By appealing to superposition, the displacements in the layered half space can be written as

$$u_i(x_1, x_2, x_3) = \int_\pi p(\xi_1, \xi_2)\mathring{u}_i(x_1 - \xi_1, x_2 - \xi_2, x_3)d\xi_1 d\xi_2 \quad \text{in } \Lambda' \text{ and } \Lambda, \tag{29}$$

where the kernel has the Taylor series representation

$$\mathring{u}_i(x_1 - \xi_1, x_2 - \xi_2, x_3) = \mathring{u}_i(x_1, x_2, x_3) - \xi_\alpha \mathring{u}_{i,\alpha}(x_1, x_2, x_3) + \frac{1}{2!}\xi_\alpha\xi_\beta \mathring{u}_{i,\alpha\beta}(x_1, x_2, x_3) - Q_i(x_1, x_2, x_3; \xi_1, \xi_2, \xi_3), \tag{30}$$

with

$$Q_i = \frac{1}{3!}\xi_\alpha\xi_\beta\xi_\gamma \mathring{u}_{i,\alpha\beta\gamma}(x_1 - \epsilon\xi_1, x_2 - \epsilon\xi_2, x_3), \tag{31}$$

for some ϵ on $(0, 1)$. We note here that the consecutive terms on the right-hand side of (30) are of $O(R^{-1})$, $O(R^{-2})$, $O(R^{-3})$, and $O(R^{-4})$ as $R \to \infty$, as is apparent from (24) and its differentiability.

Substitution of $\mathring{u}_i$ from (30) into (29) and utilization of (28) yield the asymptotic expansions of the displacements as $R \to \infty$ up to $O(R^{-3})$:

$$u_i(x_1, x_2, x_3) = P\mathring{u}_i(x_1, x_2, x_3) - P_\alpha \mathring{u}_{i,\alpha}(x_1, x_2, x_3) + \frac{P_{\alpha\beta}}{2!}\mathring{u}_{i,\alpha\beta}(x_1, x_2, x_3) + O(R^{-4}). \tag{32}$$

In anticipation of the GLFEM application, we recast (32) with the aid of (19), (20), and (24) into forms which are compact and can be directly employed as the required global functions. One such form is

$$u_i(x_1, x_2, x_3) = u_i^{\mathrm{II}}(x_1, x_2, x_3) + O(R^{-3}), \tag{33}$$

with

$$u_i^{\mathrm{II}}(x_1, x_2, x_3) = P\overset{*}{u}_i(x_1, x_2, x_3 + \mathbf{h}) - P_\alpha \overset{*}{u}_{i,\alpha}(x_1, x_2, x_3 + \mathbf{h}) \quad \text{in } \Lambda \text{ and } \Lambda' \tag{34}$$

Another form is

$$u_i(x_1, x_2, x_3) = u_i^{\mathrm{III}}(x_1, x_2, x_3) + O(R^{-4}) \tag{35}$$

with

$$\left.\begin{aligned} u_i^{\mathrm{III}}(x_1, x_2, x_3) &= P\overset{*}{u}_i(x_1, x_2, 0) + P\left(1 + \gamma + \frac{x_3}{h}\right)\overset{*}{F}_i^{(2)}(x_1, x_2, 0)\frac{h}{r^2} - P_\alpha \overset{*}{u}_{i,\alpha}(x_1, x_2, 0) + P\tilde{f}_i^{(3)}(x_1, x_2, x_3)\frac{h^2}{r^3} \\ &\quad - P_\alpha\left(1 + \gamma + \frac{x_3}{h}\frac{\partial}{\partial x_\alpha}\right)\left[\overset{*}{F}_i^{(2)}(x_1, x_2, 0)\frac{h}{r^2}\right] + \frac{1}{2!}P_{\alpha\beta}\overset{*}{u}_{i,\alpha\beta}(x_1, x_2, 0) \quad \text{in } \Lambda', \\ u_i^{\mathrm{III}}(x_1, x_2, x_3) &= P\overset{*}{u}_i(x_1, x_2, x_3) + P(1 + \gamma)\overset{*}{F}_i^{(2)}(x_1, x_2, x_3) \times \frac{h}{R^2} - P_\alpha \overset{*}{u}_{i,\alpha}(x_1, x_2, x_3) + P\tilde{F}_i^{(3)}(x_1, x_2, x_3)\frac{h^2}{R^3} \\ &\quad - P_\alpha(1 + \gamma)\frac{\partial}{\partial x_\alpha}\left[\overset{*}{F}_i^{(2)}(x_1 x_2, x_3)\frac{h}{R^2}\right] + \frac{1}{2!}P_{\alpha\beta}\overset{*}{u}_{i,\alpha\beta}(x_1, x_2, x_3) \quad \text{in } \Lambda. \end{aligned}\right\} \tag{36}$$

It follows from (33) and (35) that use of u_i^{II} and u_i^{III} as global functions approximates the far-field behavior up to $O(R^{-2})$ and $O(R^{-3})$, respectively. Note that although u_i^{II} is inherently less accurate that u_i^{III}, it is far more appealing because of its simplicity. Only a single expression is needed in u_i^{II} to describe the behavior in both domains Λ and Λ', whereas in u_i^{III}, there is a separate formula for each domain. Moreover, numerical evaluations of some constants in u_i^{III} are necessary before it can be used.

4 Numerical Example and Discussion

In our numerical example we consider a layered half space on which a uniform pressure of unit total force acts over a circular region with unit radius. For this loading the Hankel transform (6) of the pressure and the loading parameters (28) take the forms:

$$\hat{p}(\xi) = \frac{2}{\xi}J_1(\xi), \tag{37}$$

$$P = 1, \quad P_\alpha = 0, \quad P_{\alpha\beta} = \frac{1}{4}\delta_{\alpha\beta}. \tag{38}$$

Further, let the thickness of the layer be unity. For mechanical properties, we take $\nu = \nu' = 0.3$ and treat the shear-moduli ratio μ'/μ as a parameter to be varied. However, the bulk of the numerical results will be restricted to $\mu'/\mu = 2$ and $\mu'/\mu = 10$.

For comparison purposes the exact displacements along two lines from the center of the load region Π are evaluated: (a) along the axis of symmetry ($x_\alpha = 0, -1 < x_3 < \infty$) and (b) along a line on the surface ($0 < x_1 < \infty, x_2 = 0, x_3 = -1$). The integral representations for the exact solution appropriate for the uniform pressure are given by (4), (5), and (37). These results are shown by solid lines in Figs. 1 and 2 for $\mu'/\mu = 2$ and $\mu'/\mu = 10$.

We next examine the accuracy of the asymptotic displacements u_i^{II} and u_i^{III} by comparing them with the exact solution. Note from (34) and (38) that

$$u_i^{\mathrm{II}} = \overset{*}{u}_i(x_1, x_2, x_3 + \mathbf{h}) \tag{39}$$

This asymptotic result, for the lines (a) and (b), is plotted on Figs. 1 and 2 as dashed lines. In contrast, u_i^{III} given by (36) and (38) involves certain coefficients appearing in (21) and (22), which are found numerically. Along the lines (a) and (b) the asymptotic displacements u_i^{III} assume the following forms:

$$\left.\begin{aligned} (a) \qquad & \mu u_\alpha^{\mathrm{III}} = 0, \quad \mu u_3^{\mathrm{III}} = \frac{c_1}{z} - \frac{c_2}{z^2} + \frac{c_3}{z^3}, \\ \text{where} \qquad & z = x_3 \quad (1 \le z < \infty). \end{aligned}\right\} \tag{40}$$

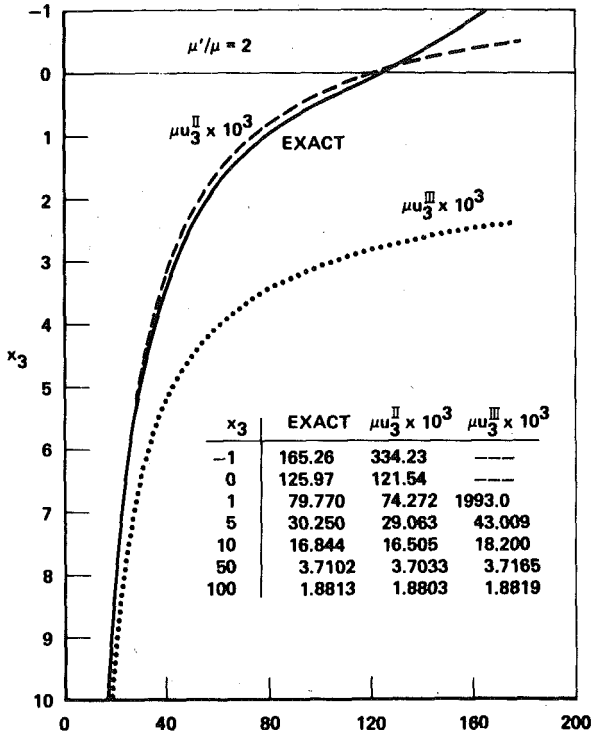

x_3	EXACT	$\mu u_3^{II} \times 10^3$	$\mu u_3^{III} \times 10^3$
−1	165.26	334.23	---
0	125.97	121.54	---
1	79.770	74.272	1993.0
5	30.250	29.063	43.009
10	16.844	16.505	18.200
50	3.7102	3.7033	3.7165
100	1.8813	1.8803	1.8819

Fig. 1(*a*) Displacement μu_3 along x_3-axis: $\mu'/\mu = 2$

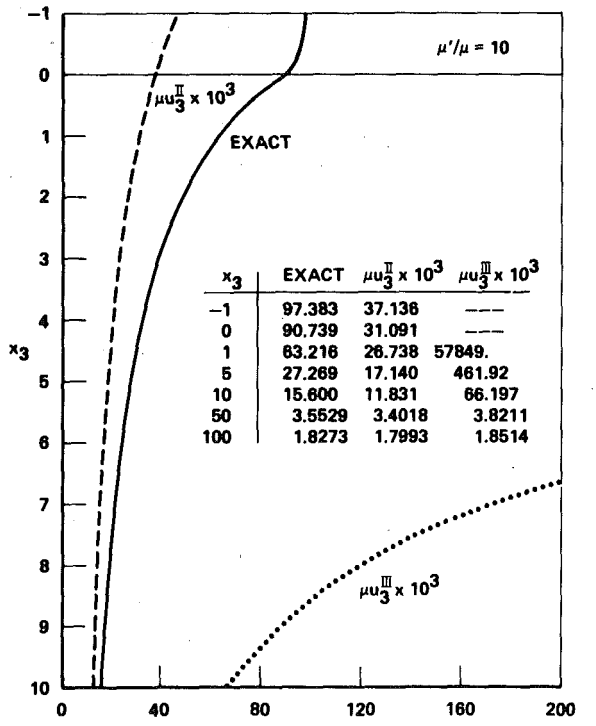

x_3	EXACT	$\mu u_3^{II} \times 10^3$	$\mu u_3^{III} \times 10^3$
−1	97.383	37.136	---
0	90.739	31.091	---
1	63.216	26.738	57849.
5	27.269	17.140	461.92
10	15.600	11.831	66.197
50	3.5529	3.4018	3.8211
100	1.8273	1.7993	1.8514

Fig. 1(*b*) Displacement μu_3 along x_3-axis: $\mu'/\mu = 10$

$$(b) \qquad \mu u_1^{III} = -\frac{c_4}{r} + \frac{c_5}{r^2}, \quad \mu u_2^{III} = 0, \quad \mu u_3^{III} = \frac{c_6}{r} - \frac{c_7}{r^3}, \qquad (41)$$

where

$$r = x_1 \quad (1 \le r < \infty).$$

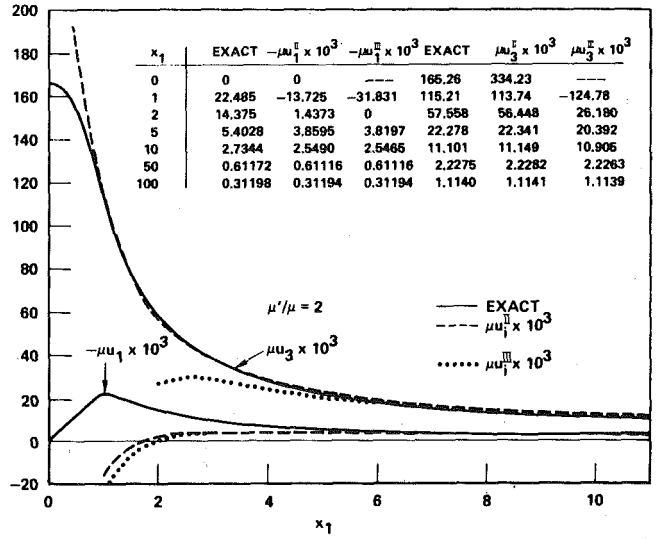

x_1	EXACT	$-\mu u_1^{II} \times 10^3$	$-\mu u_1^{III} \times 10^3$	EXACT	$\mu u_3^{II} \times 10^3$	$\mu u_3^{III} \times 10^3$
0	0	0	---	165.26	334.23	---
1	22.485	−13.725	−31.831	118.21	113.74	−124.78
2	14.375	1.4373	0	57.558	56.448	26.180
5	5.4028	3.8595	3.8197	22.278	22.341	20.392
10	2.7344	2.5490	2.5465	11.101	11.149	10.905
50	0.61172	0.61116	0.61116	2.2275	2.2282	2.2263
100	0.31198	0.31194	0.31194	1.1140	1.1141	1.1139

Fig. 2(*a*) Displacements on the surface: $\mu'/\mu = 2$

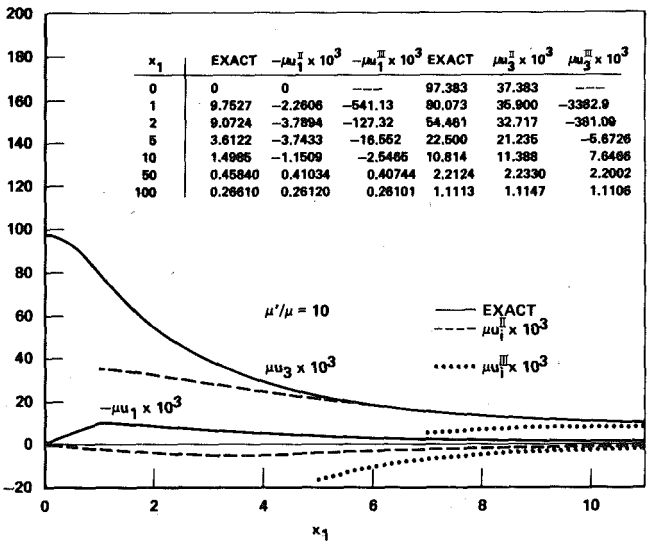

x_1	EXACT	$-\mu u_1^{II} \times 10^3$	$-\mu u_1^{III} \times 10^3$	EXACT	$\mu u_3^{II} \times 10^3$	$\mu u_3^{III} \times 10^3$
0	0	0	---	97.383	37.383	---
1	9.7527	−2.2606	−541.13	80.073	35.900	−3382.9
2	9.0724	−3.7894	−127.32	54.461	32.717	−381.09
5	3.6122	−3.7433	−16.552	22.500	21.235	−5.6726
10	1.4985	−1.1509	−2.5465	10.814	11.388	7.6486
50	0.45840	0.41034	0.40744	2.2124	2.2330	2.2002
100	0.26610	0.26120	0.26101	1.1113	1.1147	1.1106

Fig. 2(*b*) Displacements on the surface: $\mu'/\mu = 10$

with the constants c_n for $\mu'/\mu = 2$ and $\mu'/\mu = 10$ listed in Table 1. Note that the leading terms in (40) and (41) are those of Boussinesq's solution, and thus the constants c_1, c_4, and c_6 are independent of the stiffness ratio. This asymptotic result is superimposed on Figs. 1 and 2 as dotted lines. In addition, numerical vlues of u_i^{II} and u_i^{III} at discrete locations are given in the inlaid tables to reveal their quantitative differences. As anticipated, both asymptotic solutions gain accuracy with the distance from the center of II. The accuracy is slightly more favorable for u_i^{III} when R is large. However, departures from their exact values are greater for u_i^{III} than for u_i^{II} as this distance becomes small. This fact, coupled with the greater algebraic effort needed to obtain u_i^{III}, makes u_i^{II} much more attractive as a global function. Therefore, we will not consider u_i^{III} in our GLFEM example. It is also seen that these asymptotic displacements are sensitive to the shear-moduli ratio with the accuracy diminishing as μ'/μ increases.

In the GLFEM numerical example with u_i^{II} as the global function, a sequence of finite-element mesh sizes was considered. The master finite-element grid is shown in Fig. 3. This mesh sequence is obtained by successively removing elements that lie beyond a certain set of mesh radii. The displacements exterior to a mesh will be represented by $\alpha_{II} u_i^{II}$ with α_{II} as the global coefficient. If a global function is exact

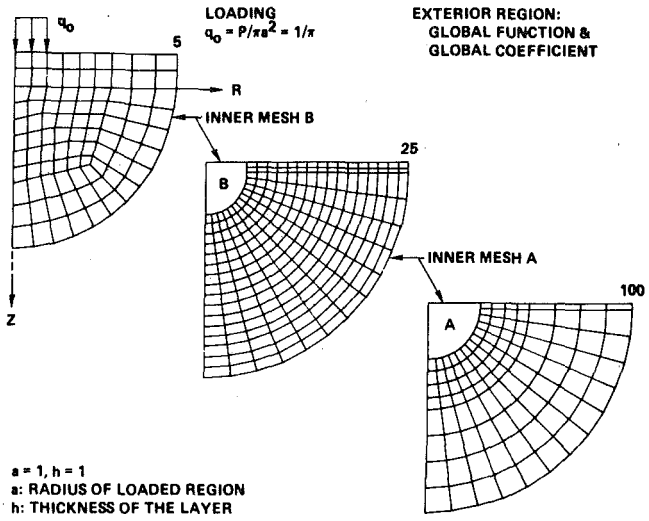

MASTER FINITE ELEMENT GRID OF LAYERED HALF SPACE

Fig. 3 Master finite-element grid of layered half space

Table 1 Coefficient c_n for μu_i^{III}

μ'/μ	2	10
c_1	0.190986	0.190986
c_2	0.300121	1.17320
c_3	2.10211	58.8307
c_4	0.0318310	0.0318310
c_5	0.0636620	0.572958
c_6	0.111409	0.111409
c_7	0.236193	3.49430

for the given loading, then the global coefficient should emerge from the GLFEM analysis as unity. Even though u_i^{II} is merely asymptotic as $R \to \infty$, global coefficients close to unity are indications of proper modeling of the far field. In Table 2 are shown the global coefficients obtained for various mesh radii for stiffness ratio 1, 2, 5, and 10. The values of the global coefficients for $\mu'/\mu = 1$ are quoted from [5] and as are all the other results for this stiffness ratio. Also given in Table 2 are the degrees of freedom from the mesh sizes. Table 3 gives the displacement μu_3 for $\mu'/\mu = 2, 10$ along the x_3-axis from both GLFEM and conventional FEM based on several meshes. In FEM, zero displacement conditions were imposed along the boundary of the mesh.

The accuracy inherent in GLFEM vis-a-vis conventional FEM may be seen in Figs. 4 and 5, where results for the depression at the center of the load region by the two methods are shown. In these figures, the relative error (the difference between the GLFEM or FEM result and its associated exact value divided by the exact value and expressed as a percentage) is plotted. The dependence of the mesh radius and the stiffness ratio on the results are clearly seen. Also included in these figures are GLFEM results based on the classical Boussinesq solution. The flat portions of the GLFEM curves in Figs. 4 and 5 indicate that

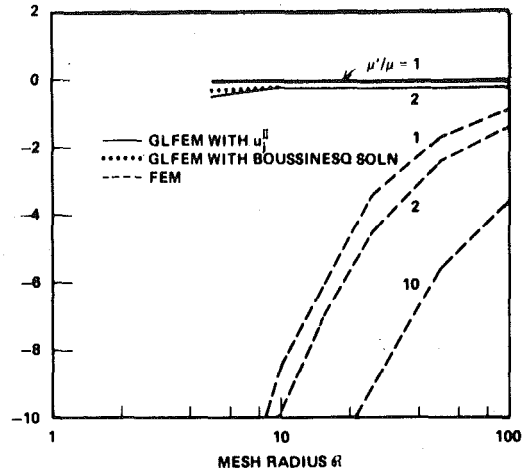

Fig. 4 Dependence of relative error of μu_3 at (0, 0, −1) upon mesh radius: $\mu'/\mu = 1, 2$

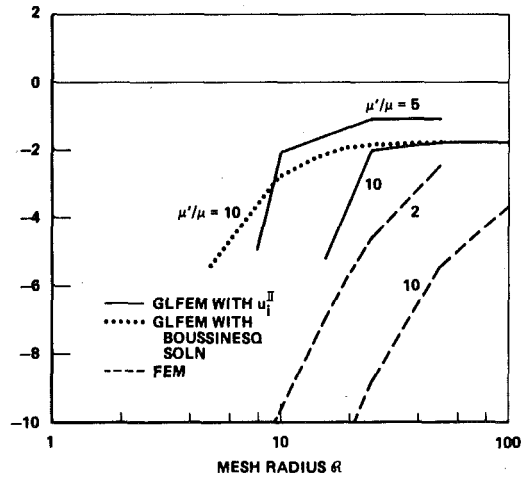

Fig. 5 Dependence of relative error of μu_3 at (0, 0, −1) upon mesh radius: $\mu'/\mu = 5, 10$

Table 2 Global coefficient

R	DOF \ μ'/μ	1	2	5	10
5	175 + 1	0.98949	1.00420	0.74876	0.54058
10	291 + 1	0.99668	1.00812	0.98972	0.73361
25	639 + 1	0.99776	1.00072	1.01386	1.01263
50	749 + 1	0.99881	0.99956	1.00485	1.01620

R = mesh radius

DOF = FEM degrees of freedom + one global coefficient

the associated mesh sizes incorporates the far-field behavior as accurately as would be possible using the given global function and the interior finite-element discretization pattern. Thus the beginning of the flat portion can be interpreted as the minimum required mesh radius. Any further improvement with additional degrees of freedom in the model should be invested in the refinement of the interior mesh

Table 3(*a*) GLFEM and FEM values of μu_3 along x_3-axis: $\mu'/\mu = 2$

	EXACT	GLFEM with u_i^{II}				FEM		
R	-	5	10	25	50	25	50	100
x_3 \ DOF	-	176	292	640	750	639	749	857
-1	165.26	164.45	164.87	164.87	164.82	157.66	161.13	162.92
0	125.97	124.86	125.45	125.47	125.42	118.21	121.72	123.53
1	79.770	78.068	78.781	78.819	78.763	71.517	75.056	76.868
5	30.250	29.185	29.986	30.099	30.045	22.687	26.294	28.136
10	16.844	16.574	16.639	16.895	16.847	9.4479	13.060	14.924
25	7.2296	7.2178	7.2460	7.1928	7.2108	0	3.3945	5.2621
50	3.7102	3.7189	3.7334	3.7060	3.7017	-	0	1.7696
100	1.8813	1.8882	1.8956	1.8817	1.8795	-	-	0

$\mu\, u_3(0,0,x_3) \times 10^3$ $(\mu'/\mu = 2)$

Table 3(*b*) GFLEM and FEM values of μu_3 along x_3-axis: $\mu'/\mu = 10$

	EXACT	GLFEM with u_i^{II}				FEM		
R	-	5	10	25	50	25	50	100
x_3 \ DOF	-	176	292	640	750	639	749	857
-1	97.383	75.599	89.112	95.427	95.669	88.798	92.107	93.830
0	90.739	68.374	82.211	88.688	88.944	82.046	85.373	87.103
1	63.216	41.631	55.115	61.700	61.967	55.048	58.389	60.124
5	27.269	9.2654	19.997	26.695	27.012	20.044	23.410	25.164
10	15.600	6.3956	8.6793	15.193	15.578	8.6103	11.960	13.726
25	6.8241	3.3151	4.4989	6.2100	6.7562	0	3.1542	4.9128
50	3.5529	1.8389	2.4956	3.4447	3.4569	-	0	1.6675
100	1.8273	0.97268	1.3200	1.8221	1.8285	-	-	0

$\mu\, u_3(0,0,x_3) \times 10^3$ $(\mu'/\mu = 10)$

and not in its enlargement. The conventional FEM results are much less accurate in comparison and lack the asymptotic flat portion in the range of mesh radii considered. Displacements obtained at other locations exhibit the same general trend for accuracy in terms of mesh radius and stiffness ratio.

As apparent in these two figures, the GLFEM solution improves with increasing mesh radius $\mathcal{R}$ and deteriorates as the stiffness ratio increases. With a view toward combining these two effects, we note from (24), (27), and (39) that

$$u_i^{II}(x_1, x_2, x_3) = \frac{1}{1+\gamma}\, u_i^*(\tilde{x}_1, \tilde{x}_2, \tilde{x}_3 + h), \tag{42}$$

where $\tilde{x}_i$ are scaled coordinates defined by (26). Thus u_i^{II} for any layered half space has, in scaled coordinates, exactly the same mathematical expression as that for a homogeneous half space except a multiplier $1/(1+\gamma)$. We may, therefore, expect the same degree of accuracy for a layered half space ($\gamma \neq 0$) and a homogeneous half space ($\gamma = 0$) if the scaled mesh radius $\tilde{\mathcal{R}}$ is the same, i.e.,

$$\tilde{\mathcal{R}}_\gamma = \tilde{\mathcal{R}}_0 = \mathcal{R}_0 \quad \text{or} \quad \mathcal{R}_\gamma = (1+\gamma)\mathcal{R}_0. \tag{43}$$

When the results in Figs. 4 and 5 are replotted in Fig. 6 in terms of $\tilde{\mathcal{R}}$, the GLFEM curves for various stiffness ratios are brought closer together even though they remain far from coalescence to a single curve. The FEM curves are also brought closer. For a fixed scaled mesh radius $\tilde{\mathcal{R}}$, the accuracy of GLFEM results deteriorate as μ'/μ increase while those of FEM improve. The better quality of the latter for large μ'/μ ratios is due to the diminishing multiplier $1/(1+\gamma)$ in (42) and hence vanishing displacements, which are more in agreement with the prescribed boundary conditions in conventional FEM. On the other hand, the deterioration of the GLFEM results may be attributed to the coarse mesh configuration in the vicinity of load region and the

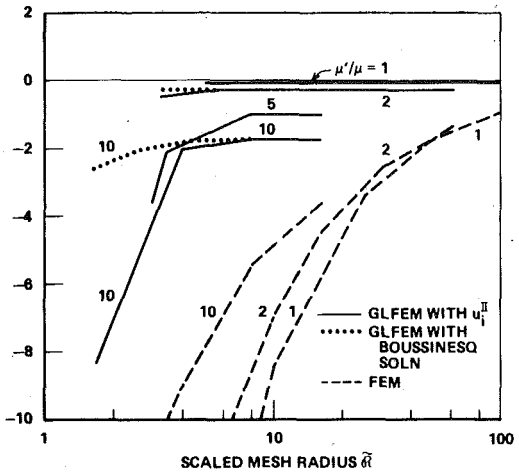

Fig. 6 Dependence of relative error of μu_3 at (0, 0, −1) upon scaled mesh radius

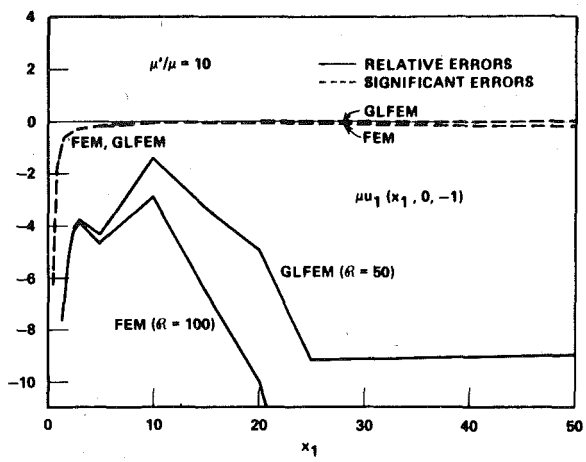

Fig. 8 Relative and significant errors of μu_1 at the surface: $\mu'/\mu = 10$

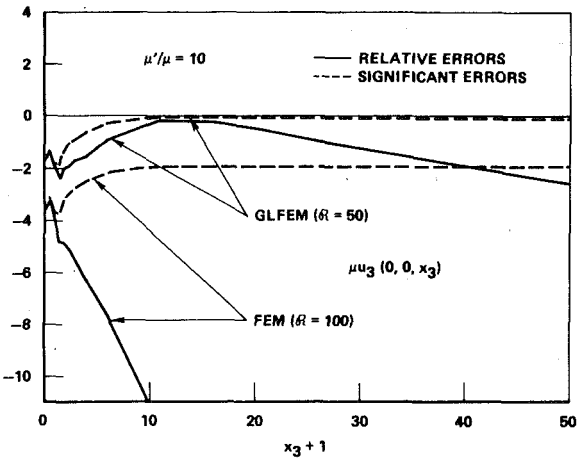

Fig. 7 Relative and significant errors of μu_3 along x_3-axis: $\mu'/\mu = 10$

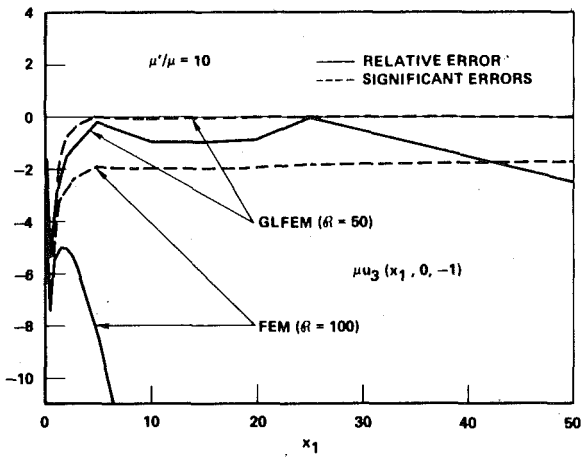

Fig. 9 Relative and significant errors of μu_3 at the surface: $\mu'/\mu = 10$

interface and to the high displacement gradients when μ'/μ is large.

The beginning of the asymptotic flat portions of the GLFEM curves for $1 \leq \mu'/\mu < 10$ occurred in the range $6 \leq \bar{\mathcal{R}} \leq 9$. Thus the finite-element mesh size $\mathcal{R}$ in a GLFEM application for a given μ'/μ ratio should be in the corresponding range $6(1+\gamma) \leq \mathcal{R} \leq 9(1+\gamma)$.

Finally, Figs. 7, 8, and 9 show, for $\mu'/\mu = 10$, errors of the GLFEM results for $\mathcal{R} = 50$ and those of the FEM results for $\mathcal{R} = 100$ along the two lines (a) and (b). In these figures the solid lines refer to the relative error as previously defined while the dashed lines refer to the significant error, i.e., the difference between the GLFEM or FEM results and their associated exact values divided by the largest displacement which, in this case, is $u_3(0, 0, -1)$. In fairness to conventional FEM, it is noted that even though the relative error increases with the distance from the center of Π, the corresponding significant error remains almost constant after a certain distance. Both relative and significant errors for the GLFEM results are much smaller than their FEM counterparts, except in the neighborhood of the load region, where errors are due to inadequate element discretization. Although the results for $\mu'/\mu = 2$ are not shown, they are similar in nature but are better than those for $\mu'/\mu = 10$.

5 Concluding Remarks

Far-field asymptotic expansion of displacements was established for a layered elastic half space under a concentrated normal force. This fundamental result designated as the generalized Boussinesq solution can be used to generate far-field asymptotic expansion for arbitrary normal loading by superposition. Far-field displacements for a uniform normal pressure confined to a circular surface region were established and their accuracy was compared with the exact solution. This expansion was applied as a global function in a GLFEM example to show its modeling capabilities. The benefits of GLFEM based on this asymptotic solution over conventional FEM solution were seen in the significant reduction in the number of degrees of freedom and the increased accuracy. With global functions derived from the generalized Boussinesq solution, soil-structure interaction problems involving a layered half space may be easily and economically explored.

Acknowledgment

The numerical evaluation of the exact solution was carried out by D. Goetschel and the numerical work of GLFEM by A. Tessler.

References

1 Gurtin, M., "The Linear Theory of Elasticity," *Encyclopedia of Physics*, Vol. VI a/2, pp. 1–295, Springer, 1972.

2 Yang, N. C., *Design of Functional Pavements*, McGraw-Hill, New York, 1972.

3 Bufler, H., "Theory of Elasticity of a Multilayered Medium," *Journal of Elasticity*, Vol. 2, 1971, pp. 125–143.

4 Burmister, D. M., "The General Theory of Stresses and Displacements in Layered System," *Journal of Applied Physics*, Vol. 16, 1945, pp. 89–94.

5 Muki, R., and Dong, S. B., "Some Remarks on the Use of Asymptotic Solutions in Global Local Finite-Element Analysis for an Elastic Half Space," *Recent Research on Mechanical Behavior of Solids*," University of Tokyo Press, 1979, pp. 55–78.

6 Mote, G. D., Jr., "Global-Local Finite Element," *International Journal for Numerical Methods in Engineering,* Vol. 3, 1971, pp. 565–574.
7 Bradford, L. G., et al., "Application of Global-Local Finite-Element Method to Fracture Mechanics," EPRI NP-239 Project 299-1, Electric Power Research Institute, Palo Alto, Calif. Sept. 1976.
8 Bradford, L. G., et al., "Glass—II Global-Local Finite-Element Analysis of Structural Systems," NP-1089, Project 299-1, Electric Power Research Institute, Palo Alto, Calif., June 1979.
9 Muki, R., "Uniform Asymptotic Expansions of Integrals of the Lipshitz Hankel Type," *SIAM Journal of Mathematical Analysis,* Vol. 3, 1972, pp. 285–290.
10 Sneddon, I. N., *Fourier Transforms,* McGraw-Hill, New York, 1951.
11 Love, A. E. H., *A Treatise on the Mathematical Theory of Elasticity,* 4th ed., Cambridge, 1972.
12 Sokolnikoff, I. S., *Mathematical Theory of Elasticity,* 2nd ed., McGraw-Hill, New York 1956.
13 Watson, G. N., *A Treatise on the Theory of Bessel Functions,* 2nd ed., Cambridge University Press, 1944.

K. Yamagishi
Research Engineer,
Bridgestone Tire Company,
Tokyo, Japan

J. T. Jenkins
Associate Professor,
Department of Theoretical
and Applied Mechanics,
Cornell University,
Ithaca, N. Y. 14853
Mem. ASME

The Circumferential Contact Problem for the Belted Radial Tire

Introduction

The equilibrium distribution of pressure along the circumference of a belted radial tire loaded at its hub and in contact with a rigid, flat, frictionless roadway is obtained here using simple beam theory. The hard rubber in which the steel or fabric belt is embedded is assumed to be an inextensible, initially circular ring, the side wall is supposed to be an elastic foundation, and the tread rubber is replaced by a second distribution of linear springs in order to account for tread compression.

In the past, bias ply and radial tires have often been modeled as a ring connected to a rigid hub by a distribution of springs representing the side wall. These springs transmit the load applied at the hub to the ring which is in contact with the roadway [1–4]. Using this model, Clark [5], for example, has discussed the contact problem of a rolling tire under load. The geometry of the contact region is determined kinematically and, in the static limit, the distribution of contact pressure is obtained in a balance between it and the transverse forces due to bending and the side wall springs. To obtain numerical results, the stiffness of these springs must be determined in an experiment. The load is then calculated by integrating the contact pressure over the contact region. However, as pointed out by Clark [6] in a review of such tire models, the transverse shear and bending moment are discontinuous at the edges of the contact region and a pressure distribution resembling that observed experimentally is obtained only if shear deformations are included.

Here, shear deformations are ignored, but the compressibility of the tread rubber is taken into account in a way proposed by Akasaka [7]. Following Rotta [8], the stiffness of the side wall spring is obtained in terms of the geometry of the side wall membrane and the inflation pressure. For the tire at rest, the linear differential equations governing the small deformations of the ring in the contact and free regions are derived, taking care to include the initial tension in the ring due to the inflation pressure. The solutions of these differential equations are easily obtained, and the arbitrary constants involved in the solutions are determined by using the symmetry of the problem and requiring continuity of displacement, moment, shear, and tension at the edges of the contact region. In the contact region there are two different types of exact solutions possible depending upon the relative magnitudes of the parameters that characterize the tire geometry, inflation pressure, bending stiffness, and side wall and tread spring moduli. The first solution is obtained for the relatively large diameter and highly inflated truck and bus tire, while the second solution applies to the smaller diameter and less highly inflated passenger car tire.

The geometrical and structural parameters are evaluated or estimated for a commercial steel belted radial truck and bus tire. The predicted distribution of contact pressure is compared with experiment.

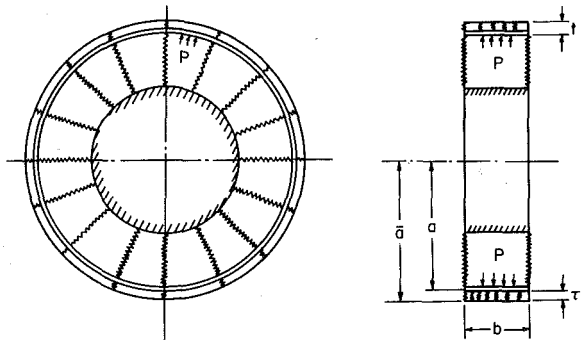

Fig. 1 The model tire

Equilibrium Equations

The model radial tire illustrated in Fig. 1 consists of a circular ring, representing the hard rubber of the tread region, connected to a

Contributed by the Applied Mechanics Division for publication in the JOURNAL OF APPLIED MECHANICS.
Discussion on this paper should be addressed to the Editorial Department, ASME, United Engineering Center, 345 East 47th Street, New York, N. Y. 10017, and will be accepted until December 1, 1980. Readers who need more time to prepare a discussion should request an extension from the Editorial Department. Manuscript received by ASME Applied Mechanics Division, March, 1979; final revision, November, 1979.

central rigid hub by a continuous distribution of identical linear springs that models the effect of the side wall membrane of the inflated tire. On the outside of the ring a similar distribution of springs, with a stiffness different from the first, represents the tire tread.

With the unit vectors **n** and **t**, respectively, normal and tangent to the deformed ring, the arc length s along the deformed ring, the circumferential tension T, the transverse shear V, the bending moment M, and the normal force density p, the local balance of force for the deformed ring is

$$\frac{d}{ds}(V\mathbf{n}) + \frac{d}{ds}(T\mathbf{t}) + p\mathbf{n} = 0. \tag{1}$$

Upon introducing the radius of curvature ρ of the deformed ring and the relations

$$\frac{d\mathbf{t}}{ds} = -\frac{1}{\rho}\mathbf{n}, \quad \frac{d\mathbf{n}}{ds} = \frac{1}{\rho}\mathbf{t}, \tag{2}$$

the tangential and normal components of the equilibrium equation (1) may be written as

$$\frac{dT}{ds} - \frac{V}{\rho} = 0, \tag{3}$$

and

$$\frac{dV}{ds} + \frac{T}{\rho} - p = 0, \tag{4}$$

respectively. The local balance of moment is

$$\frac{dM}{ds} - V = 0. \tag{5}$$

The ring is assumed to be inextensible; so

$$s = a\theta, \tag{6}$$

where a is the radius of the circular ring and θ is the angle from the vertical to a material point in the undeformed configuration. Because of the constraint, the tension T is determined by the equilibrium equations.

The ring is assumed to be a simple beam for which the relation between the bending moment and the change in curvature is

$$M = EI\left(\frac{1}{a} - \frac{1}{\rho}\right), \tag{7}$$

where E is the Young's modulus of the material of the beam, and I is the second moment of its cross-sectional area about the neutral axis.

The circumferential displacement $\overline{v}$, the normal displacement $\overline{w}$, and their derivatives are assumed to be so small that their products may be neglected. In this event

$$\frac{1}{\rho} = \frac{1}{a} - \frac{1}{a^2}(\overline{w}'' - \overline{v}'), \tag{8}$$

where a prime indicates a derivative with respect to θ. The inextensibility assumption, expressed in terms of $\overline{v}$ and $\overline{w}$, is, then,

$$\overline{v}' + \overline{w} = 0; \tag{9}$$

so, if $\overline{w}$ is known, $\overline{v}$ may be determined, up to an arbitrary constant, by an integration. From equations (7)–(9) the bending moment is given by

$$M = \frac{EI}{a^2}(\overline{w}'' + \overline{w}). \tag{10}$$

In the contact region the distributed load p is

$$p = bP - 2Q_0 - k_1\overline{w} - k_2\lambda, \tag{11}$$

where b is the width of the ring, P is the inflation pressure, Q_0 is the loading of the inflated side wall, k_1 is the stiffness of the side wall spring, k_2 is the stiffness of the tread spring, and λ is compression of the tread spring. The load Q_0 and the spring stiffness k_1 are determined in terms of the side wall geometry and the inflation pressure

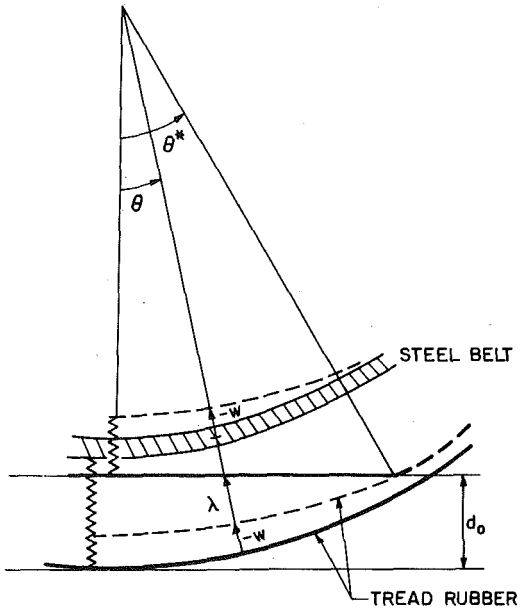

Fig. 2 The tread geometry and the contact angle

in the Appendix. From the geometry of the deformation given in Fig. 2, the tread spring compression is determined to be [7]

$$\lambda = \overline{w} + \frac{d_0}{\cos\theta} - \overline{a}\left(\frac{1}{\cos\theta} - 1\right), \tag{12}$$

where d_0 is the displacement of the point on the bottom of the tire, and $\overline{a}$ is the distance from the center of the tire to the bottom of the tread. To the accuracy of the approximations already introduced [7],

$$\lambda = \overline{w} + d_0 - \overline{a}(1 - \cos\theta). \tag{13}$$

In the free region the compression of the tread spring is zero, and the distributed load is given by equation (11) with the last term deleted.

The circumferential tension T is decomposed into two parts,

$$T = T_0 + \Delta T; \tag{14}$$

T_0 is the tension in the circular ring due to the inflation pressure P, and ΔT is the additional tension due to the deformation. For the inextensible circular ring subjected to the inflation pressure P, the equilibrium equations (3)–(5) and the constitutive equation (7) require that the moment and shear vanish, while

$$T_0 = abP - 2aQ_0. \tag{15}$$

The contact angle θ^*, at which contact between the tread and the the roadway is lost, is assumed to be known, and the differential equation governing $\overline{w}$ and ΔT are to be formulated and solved in the contact region and the free region subject to boundary conditions applied on the axis of symmetry and continuity conditions applied at θ^*.

The displacement d_0 of the bottom of the tire is determined by the condition that, at θ^*, the compression of the tread spring vanishes:

$$0 = \overline{w}(\theta^*) + d_0 - \overline{a}(1 - \cos\theta^*). \tag{16}$$

The contact pressure p_c is, then, given by

$$p_c = k_2\lambda = k_2[\overline{w} + d_0 - \overline{a}(1 - \cos\theta)], \tag{17}$$

and the total load W is obtained by integrating the contact pressure over the contact region,

$$W = 2b\int_0^{\theta^*} \overline{a}k_2[\overline{w} + d_0 - \overline{a}(1 - \cos\theta)]d\theta. \tag{18}$$

If equations (6), (10), (14), and (15) are used in the equilibrium equations (3)–(5), and terms of second order and higher in the deformation are disregarded, there results the three equations

$$(\Delta T)' - V = 0, \tag{19}$$

$$V' + \Delta T - \frac{T_0}{a}(\overline{w}'' + \overline{w}) + T_0 - pa = 0, \tag{20}$$

and

$$\frac{EI}{a^3}(\overline{w}''' + \overline{w}') - V = 0. \tag{21}$$

If ΔT is eliminated from equation (20) by a differentiation and a substitution, and equation (21) is used to express V in terms of the derivatives of $\overline{w}$, the single equation

$$\frac{EI}{a^4}(\overline{w}''' + \overline{w}')'' + \frac{EI}{a^4}(\overline{w}''' + \overline{w}') - \frac{T_0}{a^2}(\overline{w}'' + \overline{w})' - p' = 0 \tag{22}$$

is obtained for $\overline{w}$. Because p' is discontinuous at θ^*, this equation must be solved in each of the two regions; each solution must satisfy boundary conditions on the axis of symmetry, and the two solutions are joined by applying the appropriate continuity conditions at θ^*.

In the contact region, the displacement is normalized by a, and the nondimensional displacement is called w_c. Then, by equations (11) and (13), the form of equation (22) appropriate to the contact region is

$$w_c{}^{(5)} + (2 - \epsilon^{-4})w_c{}^{(3)} + (1 + \alpha_1\epsilon^{-4} + \alpha_2\epsilon^{-6})w_c{}^{(1)} = \alpha_3\epsilon^{-6}\sin\theta, \tag{23}$$

where

$$\epsilon^4 \equiv \frac{EI}{a^2T_0}, \quad \alpha_1 \equiv \frac{a^2k_1}{T_0} - 1, \quad \alpha_2 \equiv \frac{a^2k_2}{T_0}\epsilon^2, \quad \alpha_3 \equiv \alpha_2\frac{\overline{a}}{a}. \tag{24}$$

In the tire to be considered as an example, ϵ^4 is small, and α_1, α_2, and α_3 are order unity.

The particular solution of equation (23) is

$$w_{cp} = -\frac{\alpha_3}{(1 + \alpha_1{}^2)\epsilon^2 + \alpha_2}\cos\theta. \tag{25}$$

The characteristic equation of the homogeneous differential equation is

$$\sigma\{\sigma^4 - (2 - \epsilon^{-4})\sigma^2 + [1 + \alpha_1\epsilon^{-4} + \alpha_2\epsilon^{-6}] = 0. \tag{26}$$

The nature of the solutions of this characteristic equation depend upon whether $\delta \equiv 4[(1 + \alpha_1)\epsilon^2 + \alpha_2]\epsilon^2$ is less than, equal to, or greater than unity. For the truck and bus tire to be considered as an example, only the first of the three possibilities is or interest. The last possibility corresponds to the smaller, less highly inflated passenger car tire [10, 11].

When $\delta^2 < 1$, the roots are

$$\sigma = 0, \quad \sigma = \pm\gamma_1, \quad \sigma = \pm\gamma_2, \tag{27}$$

where γ_1 and γ_2 are given by

$$\sqrt{2}\,\gamma_1 = \sqrt{-2 + \epsilon^{-4}(1 + \sqrt{1 - \delta^2})}, \qquad \sqrt{2}\,\gamma_2 = \sqrt{-2 + \epsilon^{-4}(1 - \sqrt{1 - \delta^2})}, \tag{28}$$

and, for sufficiently small ϵ, both γ_1 and γ_2 are real.

In the free region the tread spring compression λ is zero, so by equation (11) the form of equation (22) governing the nondimensional displacement w_f in the free region is

$$w_f{}^{(5)} + (2 - \epsilon^{-4})w_f{}^{(3)} + (1 + \alpha_1\epsilon^{-4})w_f{}^{(1)} = 0. \tag{29}$$

The characteristic equation here is

$$\sigma[\sigma^4 - (\epsilon^{-4} - 2)\sigma^2 + (1 + \alpha_1\epsilon^{-4})] = 0. \tag{30}$$

Again there are three cases to consider, depending upon whether $\mu^2 \equiv 4(1 + \alpha_1)\epsilon^4$ is less than, equal to, or greater than unity. Only the first possibility is of practical interest.

When $\mu^2 < 1$, the roots are

$$\sigma = 0, \quad \sigma = \pm\gamma_3, \sigma = \pm\gamma_4, \tag{31}$$

where

$$\sqrt{2}\,\gamma_3 = \sqrt{-2 + \epsilon^{-4}(1 - \sqrt{1 - \mu^2})}, \qquad \sqrt{2}\,\gamma_4 = \sqrt{-2 + \epsilon^{-4}(1 + \sqrt{1 - \mu^2})}. \tag{32}$$

In each of the regions the solution involves the five arbitrary constants associated with the exponential solutions of the homogeneous differential equation. An integration of equation (9) gives the nondimensional circumferential displacement v in each region up to an arbitrary constant.

On the axis of symmetry the circumferential displacement and the transverse shear must vanish and the tangent must be horizontal. Hence, at $\theta = 0$,

$$v_c = w_c{}^{(1)} = w_c{}^{(3)} + w_c{}^{(1)} = 0; \tag{33}$$

while, at $\theta = \pi$,

$$v_f = w_f{}^{(1)} = w_f{}^{(3)} + w_f{}^{(1)} = 0. \tag{34}$$

At the edge of the contact region, the displacements, tangent, moment, shear, and tension must be continuous. Hence, at $\theta = \theta^*$,

$$w_c = w_f, \quad v_c = v_f, \quad w_c{}^{(1)} = w_f{}^{(1)}, \tag{35}$$

$$w_c{}^{(2)} + w_c = w_f{}^{(2)} + w_f, \quad w^{(3)} + w_c{}^{(1)} = w_f{}^{(3)} + w_f{}^{(1)}, \tag{36}$$

and, from equation (20),

$$\epsilon^4(w_c{}^{(4)} + w_c{}^{(2)}) - (w_c{}^{(2)} + w_c) + \alpha_3\epsilon^{-2}w_c = \epsilon^4(w_f{}^{(4)} + w_f{}^{(2)}) - (w_f{}^{(2)} + w_f) + \alpha_3\epsilon^{-2}w_f. \tag{37}$$

These 12 conditions determine the 12 arbitrary constants. The boundary conditions (33) at $\theta = 0$ are satisfied by retaining only those terms in the solution which are even about $\theta = 0$. Likewise, the boundary conditions (34) at $\theta = \pi$ are satisfied by retaining only those terms even about $\theta = \pi$. The remaining conditions (35) and (36) may be written more compactly as

$$v_c = v_f, \quad w_c = w_f, \quad w_c{}^{(l)} = w_f{}^{(l)} \tag{38}$$

where $l = 1, 2, 3$ and 4.

Given θ^*, the displacements w and v are determined at every point of the ring in the fashion just outlined. The displacement d_0 of the bottom of the tire is then given by equation (16), the distribution of contact pressure p_c over the contact region follows from equation (17), and the load W applied to the hub is obtained as a function of θ^* or, alternatively, as a function of d_0 through equation (18).

In the contact region, the solutions w_c and v_c of equation (23) and (9) which satisfy the boundary conditions (33) are, when $\delta^2 < 1$,

$$w_c = c_1 + c_2\cosh\gamma_1\theta + c_3\cosh\gamma_2\theta - \frac{\alpha_3}{(1 + \alpha_1)\epsilon^2 + \alpha_2}\cos\theta, \tag{39}$$

and

$$v_c = -c_1\theta - \frac{c_2}{\gamma_1}\sinh\gamma_1\theta - \frac{c_3}{\gamma_2}\sinh\gamma_2\theta + \frac{\alpha_3}{(1 + \alpha_1)\epsilon^2 + \alpha_2}\sin\theta. \tag{40}$$

For the passenger car tire, the homogeneous solution contains terms that oscillate [10, 11].

In the free region, the solutions w_f and v_f which satisfy the boundary conditions (34) are, when $\mu^2 < 1$,

$$w_f = c_4 + c_5\cosh[\gamma_3(\pi - \theta)] + c_6\cosh[\gamma_4(\pi - \theta)], \tag{41}$$

and

$$v_f = -c_4 + \frac{c_5}{\gamma_3}\sinh[\gamma_3(\pi - \theta)] + \frac{c_6}{\gamma_4}\sinh[\gamma_4(\pi - \theta)]. \tag{42}$$

The constants c_1 to c_6 are determined by the continuity conditions (35)–(37) applied at θ^*.

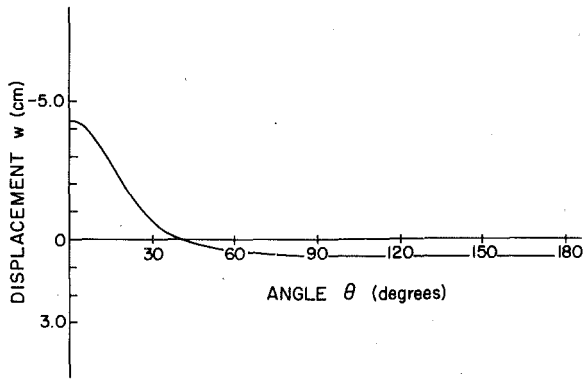

Fig. 3 The displacement of the inner breaker versus the circumferential angle as calculated

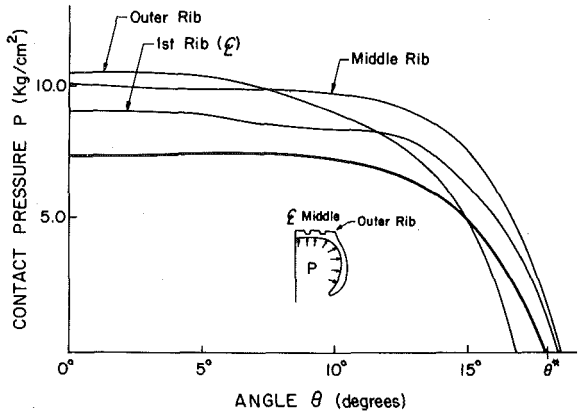

Fig. 4 The contact pressure versus the circumferential angle as determined experimentally at three stations across the tread and as calculated

Numerical Results

Numerical results are presented for the Bridgestone Radial Truck and Bus Tire 10.00–20. For this tire, the geometrical parameters identified in Fig. 1 are estimated to be

$$b = 14 \text{ cm}, \quad a = 50 \text{ cm}, \quad \tau = 2.2 \text{ cm},$$
$$t = 2.7 \text{ cm}, \quad \bar{a} = 52.7 \text{ cm}. \tag{43}$$

These quantities are determined from the tire in the following way: b is the width of the two center layers, or breakers, of the four layers that comprise the steel belt, a is the distance from the center of the hub to the innermost breaker, τ is the distance from the outermost breaker to the bottom of the tire, t is the distance from the innermost breaker to the bottom of the tire. The last four of these lengths are measured along the center line of the cross section.

The geometry of the side wall is idealized as a section of a circular cylinder shown in Fig. 5 of the Appendix. The angle ϕ_0 is taken to be the tangent angle of the radial cord in the inflated tire at the point on the cord at the edge of the center breakers. The chord of the circular arc of the side wall section is assumed to be the vertical distance from the point at which ϕ_0 is determined to the inner surface of the side wall. The radius r_0 of the circular arc is found from the length of the chord and the tangent angle. However, without performing a detailed analysis of the natural shape of the side wall, similar to those described by Böhm [4], it is not possible to determine ϕ_0 and r_0 exactly in the inflated tire from the geometry of the uninflated tire. Consequently, r_0 is here estimated from the uninflated cross section as 11 cm, and numerical results were obtained for several values of ϕ_0.

The cross section of the circular ring is assumed to be a rectangle of width b and thickness t. In calculating the bending stiffness of the ring the neutral axis of the rectangular cross section is supposed to be at the inner edge of the rectangle along the inner breaker of the relatively inextensible steel belt. The displacement $\bar{w}$ is that of this axis and the second moment I of the rectangular cross section is calculated with respect to it. The Young's modulus E of the ring is taken to be that of the rubber in the tread region; so $E = 50$ kg/cm^2 and $D = EI = 4590$ kg cm^2.

The stiffness k_2 of the tread spring is given in terms of E and the tread geometry by $k_2 = Eb/T = 318$ kg/cm^2. Note that it has been assumed that the tread resists both compression and bending.

The experiments on the truck and bus tire were performed at the relatively high inflation pressure $P = 7.0$ kg/cm^2; consequently, the numerical results presented here employ this value.

It is supposed that $\phi_0 = 75°$ and that the bending stiffness is D. Then, as detailed in the Appendix, $Q_0 = 1992$ kg, and $k_1 = 17.0$ kg/cm^2; so $T_0 = 2900$ kg, and $\epsilon^4 = 6.33 \times 10^{-4}$, $\alpha_1 = 13.66$, $\alpha_2 = 6.93$, $\alpha_3 = 7.30$. In this case, $\delta^2 = 0.735$ and $\mu^2 = 3.71 \times 10^{-2}$. Consequently, the displacements in the contact region are given by equations (39) and (40) in which, from equation (28), $\gamma_1 = 34.6$, $\gamma_2 = 19.6$, and $\alpha_3/[(1 + \alpha_1)\epsilon^2 + \alpha_2] = 1.000$; while the displacements in the free region are given by equations (41) and (42) in which, from equation (32), $\gamma_3 = 39.6$, $\gamma_4 = 3.7$.

For a given value of the contact angle, here taken to be $\theta^* = 18°$, the continuity conditions (38) result in a system of six linear algebraic equations for the six unknowns c_1 to c_6. Because of the presence in the relatively large values of γ_1 and γ_3, the matrix of the coefficients of c_1 to c_6 contains both extremely small and extremely large entries. Because it is difficult to calculate the inverse of such an ill-conditioned matrix by standard techniques, the problem is reformulated utilizing an approximation to the solutions (41) and (42) in the free region which avoids the numerical difficulties. In the free region these solutions are replaced by

$$w_f = \bar{c}_4 + \bar{c}_5 e^{-\gamma_3 \theta} + \bar{c}_6 e^{-\gamma_4 \theta}, \tag{44}$$

and

$$v_f = \bar{c}_4(\pi - \theta) + \frac{\bar{c}_5}{\gamma_3} e^{-\gamma_3 \theta} + \frac{\bar{c}_6}{\gamma_4} e^{-\gamma_4 \theta}. \tag{45}$$

The functions w_f and v_f satisfy exactly the differential equations (29) and (9), respectively; but only approximately satisfy the boundary conditions (34) at $\theta = \pi$.

In situations where the coefficient of the highest derivative in a differential equations is extremely small, it is anticipated that numerical difficulties will be encountered in determining the exact solution. In this problem, the fact that ϵ^4 is small indicates, for example, that the effects of bending are important only in the neighborhood of θ^*. In a sequel to this paper [9], singular perturbation solutions to equations (23) and (29) are obtained which illustrate the nature of the boundary layers about θ^* in which the effects of bending and shear are significant.

With (39), (40), (44), and (45) the continuity conditions (38) applied at $\theta^* = 18°$ determine the constants appearing in the solutions to be

$$c_1 = 4.52 \times 10^1, \quad c_2 = 1.89 \times 10^{-6}, \quad c_3 = 1.56 \times 10^{-3} \tag{46}$$

and

$$\bar{c}_4 = 6.69 \times 10^{-1}, \quad \bar{c}_5 = 2.45 \times 10^3, \quad \bar{c}_6 = -9.21. \tag{47}$$

With these values the solutions (44) and (45) give, at $\theta = \pi$,

$$v_f = 0, \quad w_f^{(1)} = 4.07 \times 10^{-3}(0.017°),$$
$$w_f^{(3)} + w_f^{(1)} = 4.065 \times 10^{-3}. \tag{48}$$

The last value is to be compared with the maximum value of the nondimensional shear, which is 750.4 at $\theta = \theta^*$. Thus the solutions (44) and (45) satisfy almost exactly the boundary conditions at $\theta = \pi$.

The displacement d_0 of the bottom of the tread, calculated using equation (16), is 4.6 cm. The deformation $\bar{w}$ of the inner breaker is sketched in Fig. 3. The distribution of the contact pressure is drawn in Fig. 4 superposed upon the experimental determinations of the pressure at various stations across the tread. The total load W sup-

ported by the tire, found through equation (18), is 2900 kg. In the experiment, d_0 = 4.6 cm and W = 3635 kg. Thus, while the contact pressure obtained from the mode is a smooth distribution with a shape similar to those of the experiments, the level of the contact pressure is somewhat low.

The distribution of pressure was found to be insensitive to increases of the side wall tangent angle ϕ_0. This was unexpected, because an increase in ϕ_0 reduces the shear Q_0 exerted upon the tread beam by the side wall, and this decrease in shear loading increases the tension T_0 in the ring. However an analysis of equation (56) of the Appendix shows that this increase in tension is compensated for by a reduction of the stiffness k_1 of the side wall spring.

It might be tempting to single out the linearization as the source of the disagreement between the analysis and the experiments, particularly since the change in nondimensional curvature in the contact region is close to unity on and near the axis of symmetry. However the nonlinear terms which have been neglected enter the governing equation multiplied by high powers of a small parameter; so their contribution to the equation is insignificant.

A more probable reason for the low level of the calculated contact pressure is that a distribution of normal loads due to meridional prestress and changes in the meridional curvature has been ignored in the model. A preliminary analysis [10] of the meridional section cut by the plane of symmetry that begins with the equilibrium equations for a cylindrical shell shows that the level of contact pressure is raised about 20 percent when this load is taken into account. This brings the calculated pressure distribution into good agreement with the experiments, and indicates that excellent results can be expected from a complete analysis of a cylindrical shell model.

However, before this analysis can be carried out, the circumferential problem must be solved as a true contact problem. That is, when the deflection d_0 of the bottom of the tread is specified, the contact angle θ^* should be determined in the course of solution. This problem is treated in the following paper [9].

Acknowledgment

The authors are indebted to F. C. Moon for several valuable suggestions. The first author's study and research were supported by the Bridgestone Tire Company.

References

1 Fiala, E., "Seitenkräfle am rollenden Luftreifen," *VDI-Zeitschrift,* Vol. 96, 1964, pp. 973–979.

2 Fiala, E., and Willumeit, H. P., "Radial Schwingungen von Gültel Radial Reifen," *Aubomobiltechnische Z.,* Vol. 68, 1966, pp. 33–38.

3 Frank, F., "Grundlagen zur Berechung der Seitenfuhrungsken-nenlinen von Reifen," *Kauchuck und Kunstoffe,* Vol. 18, 1965, pp. 513–533.

4 Bohm, F., "Mechanik des Gültelreifen," *Ing.-Archiv.* Vol. 35, 1966, pp. 82–101.

5 Clark, S. K., "The Rolling Tire Under Load," SAE Paper No. 650493, SAE Midyear Meeting, Chicago, Ill., May, 1965.

6 Clark, S. K., "The Contact Between Tire and Roadway," *Mechanics of Pneumatic Tires,* Clark, S. K., ed., NBS Monograph 122, Washington, D. C., 1971, pp. 445–499.

7 Akasaka, T., Kabe, K., and Sugimura, N., "Deformation and Chord Tension of a Compressed Bias Tire," *Ninetieth Anniversary Volume of Chuo University,* Chuo University, Tokyo, 1975, pp. 205–223 (in Japanese).

8 Rotta, J., "Zur Statik des Luftrelfen," *Ing.-Archiv.,* Vol. 17, 1949, pp. 129–141.

9 Yamagishi, K., and Jenkins, J. T., "Singular Perturbation Solutions of the Circumferential Contact Problem for the Belted Radial Truck and Bus Tire," ASME JOURNAL OF APPLIED MECHANICS, Vol. 47, 1980, pp. 519–524.

10 Yamagishi, K., "Contact Problems for the Radial Tire," PhD Dissertation, Cornell University, 1978.

11 Jenkins, J. T., "The Circumferential Contact Problem for the Belted Radial Passenger Car Tire," pending publication.

APPENDIX

Here Rotta's [8] model of the side wall is employed in order to determine the normal load on the ring due to the inflated side wall and the resistance of the inflated sidewall to deflections of the tread region.

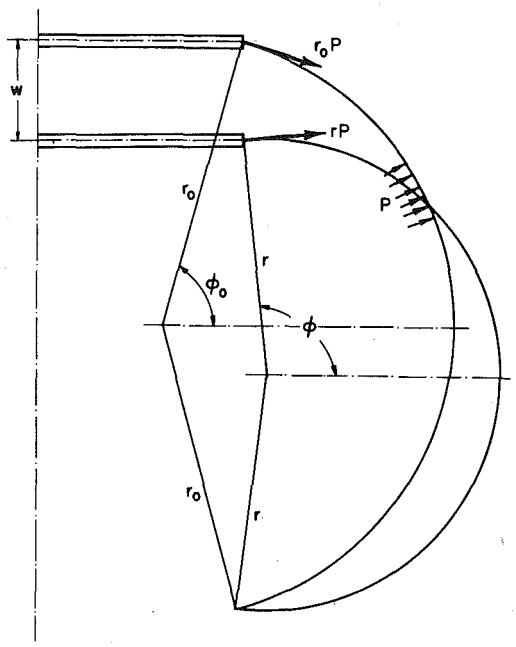

Fig. 5 The side wall geometry before and after deformation

The geometry of the side wall in the inflated tire and in the inflated tire with a displaced tread region is shown in Fig. 5. The subscript zero identifies quantities associated with the inflated, undeformed tire. For the purposes of these calculations the tread region is assumed to be rigid, and the side wall of the tire is assumed to be a cylindrical membrane reinforced by inextensible cords of length l running parallel to its circumference.

In the inflated, undeformed state the circumferential tension in the side wall is Pr_0. At the juncture of the side wall and the steel belt the side wall exerts upon the steel belt a horizontal force and a shear force $Q_0 = Pr_0 \cos \phi_0$ directed as shown in Fig. 5. After the deformation the vertical force $Q = Pr \cos \phi$. Their difference ΔQ,

$$\Delta Q = Pr \cos \phi - Pr_0 \cos \phi_0, \tag{49}$$

represents the resistance of the side wall to the displacement of the tread region. In order to determine the stiffness k_1 of the side wall spring it is first necessary to express ΔQ in terms of the displacement $\overline{w}$ of the steel belt.

The geometry of the deformed tire is related to that of the undeformed tire by the inextensibility of the cords

$$l = 2r_0\phi_0 = 2r\phi. \tag{50}$$

Before the deformation, $r_0 \sin \phi_0 = h_0/2$; while after the deformation,

$$r \sin \phi = \frac{h_0 + \overline{w}}{2} = r_0 \sin \phi_0 + \frac{\overline{w}}{2}. \tag{51}$$

Upon combining equations (50) and (51), ϕ is determined in terms of $\overline{w}$ by

$$\frac{\sin \phi}{\phi} = \frac{\sin \phi_0}{\phi_0} + \frac{\overline{w}}{2r_0\phi_0}. \tag{52}$$

Then r is obtained in terms of ϕ and $\overline{w}$ through (51).

The stiffness k_1 is twice the derivative of ΔQ with respect to $\overline{w}$ evaluated at $\phi = \phi_0$ and $w = 0$. With

$$r \cos \phi = \cot \phi \left(r_0 \sin \phi_0 + \frac{\overline{w}}{2} \right), \tag{53}$$

$$\frac{dr}{d\overline{w}} = \frac{\partial r}{\partial \phi}\frac{d\phi}{d\overline{w}} + \frac{\partial r}{\partial \overline{w}}, \tag{54}$$

and

$$\frac{d\phi}{d\bar{w}} = \frac{\phi^2}{2r_0\phi_0(\phi\cos\phi - \sin\phi)}; \tag{55}$$

$$k_1 \equiv 2\frac{d(\Delta Q)}{d\bar{w}}\bigg|_{\bar{w}=0} = P\frac{(\cos\phi_0 + \phi_0\sin\phi_0)}{(\sin\phi_0 - \phi_0\cos\phi_0)}. \tag{56}$$

This expression for the side wall stiffness is the same as that obtained by Rotta [8] by a different argument.

K. Yamagishi
Research Engineer,
Bridgestone Tire Company,
Tokyo, Japan.

J. T. Jenkins
Associate Professor,
Department of Theoretical and Applied Mechanics,
Cornell University,
Ithaca, N. Y. 14853
Mem. ASME

Singular Perturbation Solutions of the Circumferential Contact Problem for the Belted Radial Truck and Bus Tire

Introduction

Here, a singular perturbation technique is used to obtain asymptotic solutions to the differential equations, boundary conditions, and continuity conditions which govern the circumferential behavior of a model steel belted radial tire.

The formulation of the model is discussed in detail in a previous paper [1]. The belt is assumed to be inextensible and the tread region of the tire, consisting of the hard rubber in which the belt is embedded and the rubber of the tread, is idealized as a circular ring with a rectangular cross section which resists changes in curvature. The side wall of the tire is assumed to be an inflated membrane, with simple geometry and material properties, which, as a consequence of its inflation and subsequent deformation, exerts transverse forces upon the ring. The transverse force due to the inflation of the circular side wall modifies the initial tension in the circular ring due to the inflation pressures. That part of the transverse force due to the deformation of the side wall enters the model as a distribution of linear springs with a stiffness which may be calculated from the inflation pressure and the side wall geometry. The effect of the compression of the tread rubber is included by girdling the ring with an elastic foundation with a stiffness based upon the modulus of the tread rubber.

Because the tension in the ring is large compared to its bending stiffness, bending is important only in limited regions in the neighborhood of the point at which the model tire loses contact with the roadway. Mathematically, the large difference in the size of the tension and the bending stiffness renders the coefficient of the highest derivative of the governing differential equations extremely small. This small parameter is the source of the numerical difficulties which are encountered when attempting to obtain exact solutions [1]. One possible alternative to obtaining exact solutions is to consider approximate solutions which are series expansions in the small parameter. In situations in which the small parameter multiplies the highest derivative, an expansion of this type is not uniformly valid, but must be modified in regions where the highest derivative is important. These regions are the boundary layers. The expansions appropriate to each of the regions are joined, or matched, in their common region of validity. Such a singular perturbation analysis of the differential equations of the model radial tire is undertaken here for three reasons: first, because such an approach illuminates the physical phenomena by delineating the regions in which various physical effects are important; second, because the approximate solution which results is simple in form and easy to interpret; third, because such an analysis appears to provide the only means of obtaining solutions to contact problems for the cylindrical shell model of the tire. The problem considered here is similar to the "beam-string" discussed by Cole [2] and the nonuniform prestressed beam treated by Hutter and Pao [3]. An important difference is that the present problem is a contact problem; and, for a given vertical deflection of the tire bottom, the extent of tread in contact with the roadway is not known at the outset, but must be determined as part of the solution. Additional complications result from the initial curvature of the ring and the presence in the problem of a second small parameter, other than the ratio of the bending stiffness to the tension, which appears as a coefficient of high derivatives in the differential equation. In principle, these two small parameters may be varied independently, generating model tires of various sizes, side wall geometries, tread stiffnesses, and inflation pressures. However, in the problem at hand, it is convenient to relate the second of these small parameters to the first, converting the problem from one with two small parameters to a problem involving only one. In a tire of fixed geometry and tread displacement, as this parameter approaches zero the inflation pressure and the stiffness of the tread spring both increase without bound, but in a fixed ratio. In this "distinguished limit" corrections are obtained to previous analyses of simpler tire models, reviewed by Clark [4], which necessitate that a concentrated moment and a concentrated transverse shear be applied at the edge of the contact region.

Where the tire is in contact with the road, different solutions are found in each of three regions. In the boundary layer closest to the

Contributed by the Applied Mechanics Division for publication in the JOURNAL OF APPLIED MECHANICS.

Discussion on this paper should be addressed to the Editorial Department, ASME, United Engineering Center, 345 East 47th Street, New York, N. Y. 10017, and will be accepted until December 1, 1980. Readers who need more time to prepare a discussion should request an extension from the Editorial Department. Manuscript received by ASME Applied Mechanics Division, March, 1979; final revision, November, 1979.

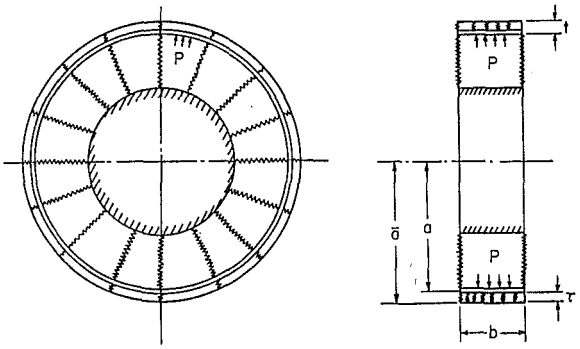

Fig. 1 The model of the steel belted radial tire

point at which contact is lost, bending and tension dominate. In an intermediate layer, the effects of tension and the tread spring are most important, while the deformation in the outer region, furthest from the contact point, is governed by the side wall and tread springs. In that part of the tire not in contact with the road, there are different solutions in each of two regions. In the boundary layer closest to the contact point, bending and tension again dominate, while the deformation in the outer region is governed by the side wall spring.

The Singular Perturbation Solutions

The differential equation governing the radial displacement $\bar{w}_c$ for the portion of the model steel belted radial tire shown in Fig. 1 which is at rest and in contact with a flat, smooth rigid roadway was determined in [1] to be

$$\bar{w}_c^{(5)} + \left(2 - \frac{a^2T_0}{EI}\right)\bar{w}_c^{(3)} + \left(1 + \frac{a^4}{EI}k_1 - \frac{a^2T_0}{EI}\right)\bar{w}_c^{(1)} + \frac{k_2a^4}{EI}\lambda^{(1)} = 0, \quad (1)$$

where the number in parenthesis indicates the number of derivatives with respect to the circumferential angle θ, a is the radius of the initially circular ring, T_0 is the initial tension in the ring, EI is the bending stiffness of the ring, k_1 is the stiffness of the side wall spring, k_2 is the stiffness of the tread spring and λ is the compression of the tread spring, given in equation (13) of [1] as

$$\lambda = \bar{w}_c + d_0 - \bar{a}(1 - \cos\theta), \quad (2)$$

where d_0 is the displacement of the bottom of the tire, and $\bar{a}$ is the distance from the center of the tire to the bottom of the tire.

In the noncontact, or free, region the differential equation governing the radial displacement $\bar{w}_f$ is

$$\bar{w}_f^{(5)} + \left(2 - \frac{a^2T_0}{EI}\right)\bar{w}_f^{(3)} + \left(1 + \frac{a^4}{EI}k_1 - \frac{a^2T_0}{EI}\right)\bar{w}_f^{(1)} = 0. \quad (3)$$

Because the ring is assumed to be inextensible, the circumferential displacement $\bar{v}$ is determined in each region by integrating the constraint equation

$$\bar{v}^{(1)} + \bar{w} = 0. \quad (4)$$

On the axis of symmetry, the circumferential displacement and the transverse shear must vanish, and the tangent must be horizontal. At $\theta = 0$, these conditions require

$$\bar{v}_c = \bar{w}_c^{(1)} = \bar{w}_c^{(3)} = 0, \quad (5)$$

so $\bar{v}_c$ is an odd function of θ and $\bar{w}_c$ is an even function of θ; while at $\theta = \pi$,

$$\bar{v}_f = \bar{w}_f^{(1)} = \bar{w}_f^{(3)} = 0, \quad (6)$$

thus $\bar{v}_f$ is an odd function of $\pi - \theta$ and $\bar{w}_f$ is an even function of $\pi - \theta$.

At the point, called the contact point, at which the tread loses contact with the road, θ is θ^*, and the displacements, tangent, transverse shear, bending, and circumferential tension must all be continuous. These conditions are equivalent to the requirements that, at $\theta = \theta^*$,

$$\bar{v}_c = \bar{v}_f, \quad \bar{w}_c = \bar{w}_f, \quad \bar{w}_c^{(l)} = \bar{w}_f^{(l)}, \quad (7)$$

where $l = 1, 2, 3$, and 4.

The differential equations (1) and (3) in the contact region and the free region may each be integrated once to give

$$\bar{w}_c^{(4)} + \left(2 - \frac{a^2T_0}{EI}\right)\bar{w}_c^{(2)} + \left(1 + \frac{a^4}{EI}k_1 + \frac{a^4}{EI}k_2 - \frac{a^2T_0}{EI}\right)\bar{w}_c = \frac{a^4k_2}{EI}(\bar{a} - d_0) - \frac{a^4k_2}{EI}\bar{a}\cos\theta + \frac{a^4\bar{c}}{EI}, \quad (8)$$

and

$$\bar{w}_f^{(4)} + \left(2 - \frac{a^2T_0}{EI}\right)\bar{w}_f^{(2)} + \left(1 + \frac{a^4}{EI}k_1 - \frac{a^2T_0}{EI}\right)\bar{w}_f = \frac{a^4\bar{c}}{EI}, \quad (9)$$

respectively. The constant of integration $\bar{c}$ is the same in both equations by virtue of the continuity conditions (7).

In each region the displacement $\bar{w}$ is nondimensionalized by a and the nondimensional displacement is denoted by w.

Estimates based on a real tire [1] indicate that the dimensionless ratio $\epsilon^4 \equiv EI/a^2T_0$ is extremely small; while the dimensionless ratios α_1, α_2, α_3, and α_4, defined by

$$\alpha_1 \equiv \frac{a^2k_1}{T_0} - 1, \quad \alpha_2 \equiv \frac{a^2k_2}{T_0}\epsilon^2, \quad \alpha_3 \equiv \alpha_2\frac{\bar{a}}{a}, \quad \alpha_4 \equiv \alpha_2\left(\frac{\bar{a} - d_0}{a}\right), \quad (10)$$

are all of order one. The asymptotic solutions to the differential equations which are obtained here are strictly valid only in the limit as ϵ goes to zero with α_1, α_2, α_3, and α_4 remaining fixed. Consequently, for a tire of given geometry with a definite tread displacement d_0, the process of passing to the limit corresponds, according to these definitions, to the consideration of a succession of such tires in which the bending stiffness EI decreases to zero, the initial tension T_0 or, equivalently, the inflation pressure P increases without bound, and the stiffness k_2 of the tread spring increases like $T_0^{3/2}$. Such a limit is called a distinguished limit, for in restricting attention to this limit a special case, involving the single small parameter ϵ, has been distinguished from the general case which involves the two small parameters ϵ and T_0/a^2k_2.

Expressed in terms of the dimensionless quantities, the differential equation (8) in the contact region becomes

$$\epsilon^6(w^{(4)} + 2w^{(2)} + w) - \epsilon^2(w^{(2)} - \alpha_1 w) + \alpha_2 w = \alpha_4 - \alpha_3\cos\theta + \epsilon^2 c \quad (11)$$

while the differential equation (9) in the free region becomes

$$\epsilon^4(w^{(4)} + 2w^{(2)} + w) - w^{(2)} + \alpha_1 w = c. \quad (12)$$

The methods used here to obtain asymptotic solutions to the differential equations (11) and (12) are discussed in detail in Cole's book [2].

To initiate the process, the constant c is expanded in a power series in ϵ,

$$c = A_0 + \epsilon A_1 + \epsilon^2 A_2 + \ldots, \quad (13)$$

where the coefficients of the powers of ϵ are constants.

In that portion of the contact region away from the contact point, the outer solution w_c^0 of the differential equation (11) is expressed as a power series in ϵ,

$$w_c^0 = w_0 + w_1\epsilon + w_2\epsilon^2 + \ldots, \quad (14)$$

where the coefficients of the powers of ϵ are functions of θ. Substitution of the two series (13) and (14) into the differential equation (11) yields, to third order,

$$\alpha_2 w_0 - \alpha_4 + \alpha_3 \cos\theta + \epsilon\alpha_2 w_1 + \epsilon^2(\alpha_2 w_2 - w_0^{(2)} + \alpha_1 w_0 - A_0) + \ldots = 0. \quad (15)$$

Consequently, the outer solution in the contact region is, to third order,

$$w_c{}^0 = \frac{\bar{a} - d}{a} - \frac{\bar{a}}{a}\cos\theta + \epsilon^2\left[\frac{\alpha_3}{{\alpha_2}^2}(1 + \alpha_1)\cos\theta - \frac{\alpha_1\alpha_4}{{\alpha_2}^2} + \frac{A_0}{\alpha_2}\right]. \quad (16)$$

Because $w_c{}^0$ is an even function of θ, it satisfies, to third order, the boundary conditions (5).

In a similar fashion, the outer solution $w_f{}^0$ in the free region which satisfies the differential equation (12) and the boundary conditions (6) is, to third order,

$$w_f{}^0 = \frac{A_0}{\alpha_1} + D_0\cosh\left[\sqrt{\alpha_1}(\pi - \theta)\right] + \epsilon\left\{\frac{A_1}{\alpha_1} + D_1\cosh\left[\sqrt{\alpha_1}(\pi - \theta)\right]\right\} + \epsilon^2\left\{\frac{A_2}{\alpha_1} + D_2\cosh\left[\sqrt{\alpha_1}(\pi - \theta)\right]\right\}, \quad (17)$$

where the coefficients of the hyperbolic cosines are constants.

In the part of the contact region close to the contact point the higher derivatives in the differential equation (11) are expected to become important. The way in which these terms increase in the neighborhood of the contact point may be determined by making a change in independent variable from θ to a "stretched" variable obtained by dividing the angle from the contact point by ϵ raised to some power. The power is to be chosen so that a balance between terms in the differential equation involving high derivatives dominates the remaining terms in the limit as ϵ goes to zero. Two such balances are found to be possible in equation (11). In one stretching, the first term in parentheses in equation (11) becomes negligible, and the balance is between the remaining terms which represent the effects of the initial tension and the tread spring. In the second stretching the terms in the parentheses balance one another, and the remaining terms become negligible in the limit. Here the dominant terms represent the effects of bending and the initial tension. Because the highest derivative in the differential equation is preserved in the second stretching, the solution to this equation can also satisfy the continuity conditions at the contact point. Consequently, there is the possibility of obtaining different solutions of the differential equation (11) in each of three parts of the contact region: the outer solution (16) in the region away from the contact point, an inner-inner solution in the boundary layer with the contact point as an end point, and an inner solution in the layer between the boundary layer and the outer region. This possibility will be realized if these solutions can be joined, or matched, in their common regions of validity.

A similar analysis in the free region shows that there is only one stretching which yields a balance, which dominates in the limit, between terms involving high derivatives. With this stretching the term in equation (12) multiplied by α_1 becomes negligible. Again the balance is between bending and initial tension, and the highest derivative is preserved. The free region, then, will contain a boundary layer, in which the inner solution applies, and an outer region, in which the outer solution (17) is valid, provided that these two solutions can be matched.

In the contact region, the differential equation governing the inner solution $w_c{}^i$ is obtained from equation (11) by the change of independent variable $\xi = (\theta^* - \theta)/\epsilon$. This equation is

$$-w^{(2)} + \alpha_2 w + \epsilon^2(w^{(4)} + \alpha_1 w) + 2\epsilon^4 w^{(2)} + \epsilon^6 w = \alpha_4 - \alpha_3\cos(\theta^* - \epsilon\xi) + \epsilon^2 c, \quad (18)$$

where the numbers in parentheses now indicate the number of derivatives with respect to ξ. With the expansions (13),

$$\theta^* = \theta_0{}^* + \theta_1{}^*\epsilon + \theta_2{}^*\epsilon^2 + \ldots, \quad (19)$$

in which the coefficients are constants to be determined,

$$\cos(\theta^* - \epsilon\xi) = \cos\theta_0{}^* - \epsilon(\theta_1{}^* - \xi)\sin\theta_0{}^* - \frac{1}{2}\epsilon^2[(\theta_1{}^* - \xi)^2\cos\theta_0{}^* + 2\theta_2{}^*\sin\theta_0{}^*], \quad (20)$$

and

$$w_c{}^i = w_0 + w_1\epsilon + w_2\epsilon^2 + w_3\epsilon^3 + \ldots, \quad (21)$$

in which the coefficients are functions of ξ, the differential equation (18) becomes, to fourth order,

$$\begin{aligned} &- w_0^{(2)} + \alpha_2 w_0 - \alpha_4 + \alpha_3\cos\theta_0{}^* \\ &\quad + \epsilon[-w_1^{(2)} + \alpha_2 w_1 - \alpha_3(\theta_1{}^* - \xi)\sin\theta_0{}^*] \\ &\quad + \epsilon^2\left\{-w_2^{(2)} + \alpha_2 w_2 + w_0^{(4)} + \alpha_1 w_0 - A_0 - \frac{\alpha_3}{2}[(\theta_1{}^* - \xi)^2\cos\theta_0{}^* + 2\theta_2{}^*\sin\theta_0{}^*]\right\} \\ &\quad + \epsilon^3\left\{-w_3^{(2)} + \alpha_2 w_3 + w_1^{(4)} + \alpha_1 w_1 - A_1 + \frac{\alpha_3}{6}[(\theta_1{}^* - \xi)^2\sin\theta_0{}^* - 6\theta_1{}^*\theta_2{}^*\cos\theta_0{}^* - 6\theta_3{}^*\sin\theta_0{}^*]\right\} = 0. \end{aligned} \quad (22)$$

The differential equations which result by separately equating the coefficients of the powers of ϵ to zero have the solutions

$$w_0 = B_0 e^{-\sqrt{\alpha_2}\xi} + \frac{\alpha_4}{\alpha_2} - \frac{\alpha_3}{\alpha_2}\cos\theta_0{}^*, \quad (23)$$

$$w_1 = B_1 e^{-\sqrt{\alpha_2}\xi} + \frac{\alpha_3}{\alpha_2}(\theta_1{}^* - \xi)\sin\theta_0{}^*, \quad (24)$$

$$w_2 = B_2 e^{-\sqrt{\alpha_2}\xi} + \frac{1}{2}\frac{\alpha_3}{\alpha_2}(\theta_1{}^* - \xi)^2\cos\theta_0{}^* - \frac{\alpha_1\alpha_4}{{\alpha_2}^2} + \frac{A_0}{\alpha_2} + \frac{\alpha_3}{\alpha_2}\theta_2{}^*\sin\theta_0{}^* + \frac{\alpha_3}{{\alpha_2}^2}(1 + \alpha_1)\cos\theta_0{}^*, \quad (25)$$

and

$$w_3 = B_3 e^{-\sqrt{\alpha_2}\xi} - \frac{\alpha_3}{\alpha_2}\sin\theta_0{}^*\left[\frac{1}{6}(\theta_1{}^* - \xi)^2 + \frac{\alpha_1}{\alpha_2}(\theta_1{}^* - \xi) - \theta_3{}^* + \frac{1}{3\alpha_2}\right] + \frac{\alpha_3}{\alpha_2}\theta_1{}^*\theta_2{}^*\cos\theta_0{}^* + \frac{A_1}{\alpha_2}, \quad (26)$$

where the exponential solutions with positive argument have been discarded because it is impossible to match them to the outer solution, and where the coefficients of the remaining exponentials are constants to be determined through the matching and the continuity conditions. Thus the inner solution in the contact region is determined up to fourth order.

The differential equation governing the inner-inner solution $w_c{}^{ii}$ in the contact region is obtained from equation (11) through the change of variable $\eta = (\theta^* - \theta)/\epsilon^2$ as

$$w^{(4)} - w^{(2)} + \epsilon^2\alpha_2 w + \epsilon^4(2w^{(2)} + \alpha_1 w) + \epsilon^8 w = \epsilon^2[\alpha_4 - \alpha_3\cos(\theta^* - \epsilon^2\eta)] + \epsilon^2 c, \quad (27)$$

where here the number in parentheses indicate the number of derivatives with respect to η. With the expansions (13), (19), (20) and

$$w_c{}^{ii} = w_0 + w_1\epsilon + w_2\epsilon^2 + w_3\epsilon^3 + w_4\epsilon^4 + \ldots, \quad (28)$$

in which the coefficients are functions of η, the differential equation (27) is, to fifth order,

$$\begin{aligned} &w_0^{(4)} - w_0^{(2)} + \epsilon(w_1^{(4)} - w_1^{(2)}) \\ &\quad + \epsilon^2(w_2^{(4)} - w_2^{(2)} + \alpha_2 w_0 - \alpha_4 + \alpha_3\cos\theta_0{}^*) \\ &\quad + \epsilon^3(w_3^{(4)} - w_3^{(2)} + \alpha_2 w_1 - \alpha_3\theta_1{}^*\sin\theta_0{}^*) \\ &\quad + \epsilon^4\left\{w_4^{(4)} - w_4^{(2)} + \alpha_2 w_2 + 2w_0^{(2)} + \alpha_2 w_0 - A_0 - \frac{\alpha_3}{2}[\theta_1{}^{*2}\cos\theta_0{}^* + 2(\theta^* - \eta)\sin\theta_0{}^*]\right\} = 0 \end{aligned} \quad (29)$$

The differential equations obtained by separately equating the coefficients to zero have the solutions

$$w_0 = C_1 + C_2\eta + C_3e^{-\eta}, \tag{30}$$

$$w_1 = C_4 + C_5\eta + C_6e^{-\eta}, \tag{31}$$

$$w_2 = C_7 + C_8\eta + C_9e^{-\eta} + \frac{1}{2}(\alpha_2C_1 - \alpha_4 + \alpha_3\cos\theta_0^*)\eta^2 + \frac{\alpha_2C_2}{6}\eta^3, \tag{32}$$

$$w_3 = C_{10} + C_{11}\eta + C_{12}e^{-\eta} + \frac{\alpha_2C_6}{2}\eta e^{-\eta} + \frac{\alpha_2C_4}{2}\eta^2 + \frac{\alpha_2C_5}{6}\eta^3 - \frac{1}{2}\alpha_3\theta_1^*\sin\theta_0^*\eta^2, \tag{33}$$

and

$$w_4 = \frac{A_0}{\alpha_2}C_{13} + C_{14}\eta + C_{15}e^{-\eta} + \frac{1}{2}\left(-\alpha_2C_7 - \alpha_2C_1 + \frac{\alpha_4}{2}\theta_1^*\cos\theta_0^* + \alpha_3\theta_2^*\sin\theta_0^*\right)\eta^2 - \frac{1}{6}(\alpha_2C_8 + \alpha_3\sin\theta_0^*)\eta^3 + \frac{\alpha_2}{24}(\alpha_2C_1 + \alpha_3\cos\theta_0^* - \alpha_3)\eta^4, \tag{34}$$

where the exponential solutions with positive argument have been discarded because it is impossible to match them to the inner solution. The arbitrary constants involved in the solutions are determined from the matchings and the continuity condition.

In the free region the inner solution $w_f{}^i$ is obtained to fourth order from the appropriate form of equation (12). Here the stretching is again $\eta = (\theta^* - \theta)/\epsilon^2$, leading from (12) to the differential equation

$$w^{(4)} - w^{(2)} + \epsilon^4(2w^{(2)} + \alpha_1 w) + \epsilon^8 w = \epsilon^4 c, \tag{35}$$

where the derivatives are with respect to η. The expansions (13) and

$$w_c{}^i = w_0 + w_1\epsilon + w_2\epsilon^2 + w_3\epsilon^3 + \ldots, \tag{36}$$

used in (35) result in the approximate differential equation

$$w_0^{(4)} - w_0^{(2)} + \epsilon(w_1^{(4)} - w_1^{(2)}) + \epsilon^2(w_2^{(4)} - w_2^{(2)}) + \epsilon^3(w_3^{(4)} - w_3^{(2)}) = 0 \tag{37}$$

to fourth order. Equating the coefficients to zero and solving the resulting differential equations, yields

$$w_0 = E_1 + E_2\eta + E_3e^{\eta}, \tag{38}$$

$$w_1 = E_4 + E_5\eta + E_0e^{\eta}, \tag{39}$$

$$w_2 = E_7 + E_8\eta + E_9e^{\eta}, \tag{40}$$

and

$$w_3 = E_{10} + E_{11}\eta + E_{12}e^{\eta}. \tag{41}$$

The exponentional solutions with negative argument cannot match with the outer solution.

The constants which appear in the expressions for the approximate solutions are determined by the continuity conditions (7) and by matching solutions in adjoining parts in each of the two regions. The constant coefficients in the expansion (19) for the contact angle are determined, for a given tread displacement d_0, from the contact condition which follows from equation (2) by requiring that $\lambda = 0$ at $\theta = \theta^*$. A solution is obtained to third order, for example, when the contants in the coefficients of the powers of ϵ up to and including the second in the expansions in each layer and in the outer regions have been determined.

In matching the inner solution to the inner-inner solution in the contact region the first four terms in the inner solution expansion are first expressed in terms of the inner-inner variable $\eta = \xi/\epsilon$. With η fixed, these terms are expanded in powers of ϵ and the first five terms, up to and including the fourth power of ϵ, are retained. The coefficients in this expansion are then separately equated to the coefficients of the first five terms of the inner-inner expansion. Such a four-five matching is found to be necessary in order to determine the solutions to third order. The conditions which result from this matching are $C_2 = 0$,

$$C_1 = B_0 + \frac{\alpha_4}{\alpha_2} - \frac{\alpha_3}{\alpha_2}\cos\theta_0^*. \tag{42}$$

$$C_4 = B_1 + \frac{\alpha_3}{\alpha_2}\theta_1^*\sin\theta_0^*, \tag{43}$$

$$C_5 = -B_0\sqrt{\alpha_2}, \tag{44}$$

$$C_7 = B_2 + \frac{\alpha_3}{2\alpha_2}\theta_1^*\cos\theta_0^* - \frac{\alpha_1\alpha_4}{{\alpha_2}^2} + \frac{\alpha_1\alpha_3}{{\alpha_2}^2}\cos\theta_0^* + \frac{\alpha_3}{\alpha_2}\theta_2^*\sin\theta_0^* + \frac{A_0}{\alpha_2} + \frac{\alpha_3}{{\alpha_2}^2}\cos\theta_0^*, \tag{45}$$

$$C_8 = -B_1\sqrt{\alpha_2} - \frac{\alpha_3}{\alpha_2}\sin\theta_0^*, \tag{46}$$

$$C_{10} = B_3 - \frac{1}{6}\frac{\alpha_3}{\alpha_2}\theta_1^{*2}\sin\theta_0^* - \frac{\alpha_1\alpha_3}{{\alpha_2}^2}\theta_1^*\sin\theta_0^* + \frac{\alpha_3}{\alpha_2}\theta_1^*\theta_2^*\cos\theta_0^* + \frac{\alpha_3}{\alpha_2}\theta_3^*\sin\theta_0 - \frac{1}{3}\frac{\alpha_3}{{\alpha_2}^2}\sin\theta_0^* + \frac{A_1}{\alpha_2}, \tag{47}$$

$$C_{11} = -B_0\frac{(\alpha_1 + \alpha_2{}^2)}{2\sqrt{\alpha_2}} - \frac{\alpha_3}{\alpha_2}\theta_1^*\cos\theta_0^* - B_2\sqrt{\alpha_2}, \tag{48}$$

and

$$C_{14} = -B_3\sqrt{\alpha_2} + \frac{1}{3}\frac{\alpha_3}{\alpha_2}\theta_1^*\sin\theta_0^* + \frac{\alpha_1\alpha_3}{{\alpha_2}^2}\sin\theta_0^*. \tag{49}$$

Any such matching procedure between the outer solution and the inner solution in the contact region is found to be identically satisfied to third order and, consequently, furnishes no new information.

In the free region a four-five matching of the outer solution and the inner solution yields $E_2 = E_5 = 0$,

$$E_1 = D_0\cosh[\sqrt{\alpha_1}(\pi - \theta_0^*)] + \frac{A_0}{\alpha_1}, \tag{50}$$

$$E_4 = -D_0\sqrt{\alpha_1}\theta_1^*\sinh[\sqrt{\alpha_1}(\pi - \theta_0^*)] + D_1\cosh[\sqrt{\alpha_1}(\pi - \theta_0^*)] + \frac{A_1}{\alpha_1}, \tag{51}$$

$$E_7 = \frac{1}{2}D_0\{\alpha_1\theta_1^{*2}\cosh[\sqrt{\alpha_1}(\pi - \theta_0^*)] - 2\sqrt{\alpha_1}\theta_2^*\sinh[\sqrt{\alpha_1}(\pi - \theta_0^*)]\} - D_1\sqrt{\alpha_1}\sinh[\sqrt{\alpha_1}(\pi - \theta_0^*)] + D_2\cosh[\sqrt{\alpha_1}(\pi - \theta_0^*] + \frac{A_2}{\alpha_1}, \tag{52}$$

$$E_8 = D_0\sqrt{\alpha_1}\sinh[\sqrt{\alpha_1}(\pi - \theta_0^*)], \tag{53}$$

$$E_{10} = D_3\cosh[\sqrt{\alpha_1}(\pi - \theta_0^*)] - D_2\sqrt{\alpha_1}\sinh[\sqrt{\alpha_1}(\pi - \theta_0^*)] + \frac{2A_3}{\alpha_1} + \frac{D_0}{6}\{-\alpha_1\sqrt{\alpha_1}\theta_1^{*3}\sinh[\sqrt{\alpha_1}(\pi - \theta_0^*)] + 6\alpha_1\theta_1^*\theta_2^*\cosh[\sqrt{\alpha_1}(\pi - \theta_0^*)] - 6\sqrt{\alpha_1}\theta_3^*\sinh[\sqrt{\alpha_1}(\pi - \theta_0^*)]\} + \frac{D_1}{2}\{\alpha_1\theta_1^{*2}\cosh[\alpha_1(\pi - \theta_0^*)] - 2\sqrt{\alpha_1}\theta_2^*\sinh[\sqrt{\alpha_1}(\pi - \theta_0^*)]\} \tag{54}$$

$$E_{11} = -D_0\alpha_1\theta_1^*\cosh[\sqrt{\alpha_1}(\pi - \theta_0^*)] + D_1\sinh[\sqrt{\alpha_1}(\pi - \theta_0^*)], \tag{55}$$

and

$$E_{14} = \frac{1}{4}D_0\alpha_1\sqrt{\alpha_1}\theta_1^{*2} - D_1\alpha_1\theta_1^*\cosh[\sqrt{\alpha_1}(\pi - \theta_0^*] + D_2\sqrt{\alpha_1}\sinh[\sqrt{\alpha_1}(\pi - \theta_0^*)]. \tag{56}$$

The second, third, fourth, and fifth of the continuity conditions (7), expressed in terms of η and derivatives with respect to η, are

$$w_c{}^{ii}(0) = w_f{}^{i}(0), \quad w_c{}^{ii'}(0) = w_f{}^{i'}(0), \tag{57}$$

and

$$w_c{}^{ii''}(0) = w_f{}^{i''}(0), \quad w_c{}^{ii'''}(0) = w_f{}^{i'''}(0). \tag{58}$$

These require that, at first order (ϵ^0), $C_3 = E_3 = 0$,

$$B_0 + \frac{\alpha_4}{\alpha_2} - \frac{\alpha_3}{\alpha_2}\cos\theta_0^* = D_0 \cosh\left[\sqrt{\alpha_1}(\pi - \theta_0^*)\right] + \frac{A_0}{\alpha_1}; \tag{59}$$

at second order (ϵ), $C_6 = E_6 = 0$,

$$B_1 + \frac{\alpha_3}{\alpha_2}\theta_1^* \sin\theta_0^* = -D_0\sqrt{\alpha_1}\theta_1^* \sinh\left[\sqrt{\alpha_1}(\pi - \theta_0^*)\right] + D_1 \cosh\left[\sqrt{\alpha_1}(\pi - \theta_0^*)\right] + \frac{A_1}{\alpha_1}; \tag{60}$$

at third order (ϵ^2).

$$B_2 + \frac{\alpha_3}{2\alpha_2}\theta_1^* \cos\theta_0^* - \frac{\alpha_1\alpha_4}{{\alpha_2}^2} + \frac{\alpha_1\alpha_3}{{\alpha_2}^2}\cos\theta_0^* + \frac{\alpha_3}{\alpha_2}\theta_2^* \sin\theta_0^* + \frac{A_0}{\alpha_2} + \frac{\alpha_3}{{\alpha_2}^2}\cos\theta_0^* = \frac{1}{2}D_0\{\alpha_1\theta_1^{*2}\cosh\left[\sqrt{\alpha_1}(\pi - \theta_0^*)\right] - 2\sqrt{\alpha_1}\theta_2^* \sinh\left[\sqrt{\alpha_1}(\pi - \theta_0^*)\right]\} - D_1\sqrt{\alpha_1}\sinh\left[\sqrt{\alpha_1}(\pi - \theta_0^*)\right] + D_2\cosh\left[\sqrt{\alpha_1}(\pi - \theta_0^*)\right] + \frac{A_2}{\alpha_1} + \alpha_2 B_0, \tag{61}$$

$$-\left(B_1\sqrt{\alpha_2} + \frac{\alpha_3}{\alpha_2}\sin\theta_0^*\right) = D_0\sqrt{\alpha_1}\sinh\left[\sqrt{\alpha_1}(\pi - \theta_0^*)\right], \tag{62}$$

$$C_9 = -E_9 = -\frac{1}{2}\alpha_2 B_0; \tag{63}$$

at fourth order (ϵ^3),

$$\left(B_0\frac{\alpha_1 + {\alpha_2}^2}{2\sqrt{\alpha_2}} + \frac{\alpha_3}{\alpha_2}\theta_1^* \cos\theta_0^* + B_2\sqrt{\alpha_2}\right) = +D_0\alpha_1\theta_1^* \cosh\left[\sqrt{\alpha_1}\,(\pi - \theta_0^*)\right] - D_1 \sinh\left[\sqrt{\alpha_1}\,(\pi - \theta_0^*)\right] + \alpha_2 B_0\sqrt{\alpha_2}\,, \tag{64}$$

and, at fifth order (ϵ^4),

$$-B_3\sqrt{\alpha_2} + \frac{1}{3}\frac{\alpha_3}{\alpha_2}\theta_1^* \sin\theta_0^* + \frac{\alpha_1\alpha_3}{{\alpha_2}^2}\sin\theta_0^* = \frac{1}{4}D_0\alpha_1\sqrt{\alpha_1}\theta_1^{*2} - D_1\alpha_1\theta_1^* \cosh\left[\sqrt{\alpha_1}(\pi - \theta_0^*)\right] + D_2\sqrt{\alpha_1}\sinh\left[\sqrt{\alpha_1}(\pi - \theta_0^*)\right]. \tag{65}$$

The last of the continuity conditions (7) has already been satisfied.

In order to apply the first of (7), the constraint condition (4) is integrated from 0 to π and the first of the boundary conditions (5) and (6) are employed; so that the continuity of v at $\theta = \theta^*$ requires that

$$\int_0^{\theta^*} w_c(\theta)d\theta = \int_{\theta^*}^{\pi} w_f(\theta)d\theta. \tag{66}$$

In order to use this condition to determine constants which appear in the expansion a composite solution is constructed for the contact region and for the free region. A composite solution is obtained in each region by adding together the solutions which are valid in each part and subtracting the terms which each pair of solutions has in common. These terms are those which have participated in the matching. The composite solution w_c in the contact region is, to third order,

$$w_c = \frac{\alpha_4}{\alpha_2} - \frac{\alpha_3}{\alpha_2}\cos\theta + B_0 e^{-\sqrt{\alpha_2}\xi} + \epsilon B_1 e^{-\sqrt{\alpha_2}\xi} + \epsilon^2\left[\frac{\alpha_3}{{\alpha_2}^2}(1 + \alpha_1)\cos\theta - \frac{\alpha_1\alpha_4}{{\alpha_2}^2} + \frac{A_0}{\alpha_2} + B_2 e^{-\sqrt{\alpha_2}\xi} - \frac{(\alpha_1 + {\alpha_2}^2)}{2\sqrt{\alpha_2}}B_0\xi e^{-\sqrt{\alpha_2}\xi} + C_9 e^{-\eta}\right]. \tag{67}$$

The composite solution w_f in the free region is, to third order,

$$w_f = D_0 \cosh\left[\sqrt{\alpha_1}(\pi - \theta)\right] + \frac{A_0}{\alpha_1} + \epsilon\left\{D_1 \cosh\left[\sqrt{\alpha_1}(\pi - \theta)\right] + \frac{A_1}{\alpha_1}\right\} + \epsilon^2\left\{D_2 \cosh\left[\sqrt{\alpha_1}(\pi - \theta)\right] + \frac{A_2}{\alpha_1} + E_9 e^{\eta}\right\}. \tag{68}$$

If the composite solutions are used in the continuity condition (66), after a long calculation there result the requirements that, at first order,

$$\frac{\alpha_4}{\alpha_2}\theta_0^* - \frac{\alpha_3}{\alpha_2}\sin\theta_0^* + \frac{D_0}{\sqrt{\alpha_1}}\sinh\left[\sqrt{\alpha_1}(\pi - \theta_0^*)\right] + \frac{A_0}{\alpha_1}(\pi - \theta_0^*) = 0, \tag{69}$$

at second order,

$$\frac{\alpha_4}{\alpha_2}\theta_1^* - \frac{\alpha_3}{\alpha_2}\theta_1^* \cos\theta_0^* + B_0 - D_0\theta_1^* \cosh\left[\sqrt{\alpha_1}(\pi - \theta_0^*)\right] - \frac{A_0}{\alpha_1}\theta_1^* + \frac{D_1}{\sqrt{\alpha_1}}\sinh\left[\sqrt{\alpha_1}(\pi - \theta_0^*)\right] + \frac{A_1}{\alpha_1}(\pi - \theta_0^*) = 0, \tag{70}$$

and, at third order,

$$\frac{\alpha_4}{\alpha_2}\theta_2^* + \theta_0^* \cos\theta_0^* - \frac{1}{2}\theta_1^{*2}\sin\theta_0^* + B_1 - \frac{A_0}{\alpha_1}\theta_2^* - D_1\theta_1^* \cosh\left[\sqrt{\alpha_1}(\pi - \theta_0^*)\right] - \frac{A_1}{\alpha_1}\theta_0^* + \frac{D_2}{\sqrt{\alpha_1}}\sinh\left[\sqrt{\alpha_1}(\pi - \theta_0^*)\right] + \frac{A_2}{\alpha_1}(\pi - \theta_0^*) = 0.$$

There remains the contact condition

$$a w_c{}^{ii}(0) + d_0 - \bar{\alpha}(1 - \cos\theta^*) = 0. \tag{71}$$

If this condition is expressed in terms of the expansions, it requires that, at first order, $B_0 = 0$, at second order, $B_1 = 0$, and, at third order,

$$\alpha_2{}^2 B_2 - \alpha_1\alpha_4 + \alpha_1\alpha_3\cos\theta_0^* + \alpha_2 A_0 + \alpha_3\cos\theta_0^* = 0. \tag{72}$$

and

$$B_3 - \frac{\alpha_1\alpha_3}{{\alpha_2}^2}\theta_1^* \sin\theta_0^* - \frac{1}{3}\frac{\alpha_3}{{\alpha_2}^2}\sin\theta_0^* + \frac{A_1}{\alpha_2} = 0. \tag{73}$$

In the contact region and the free region the constants appearing in the composite solutions (67) and (68) are determined, at first order by (59) with $B_0 = 0$, by using $B_1 = 0$ in (62), and by (69)

$$D_0 = -\frac{\alpha_3}{\alpha_2}\frac{\sin\theta_0^*}{\sqrt{\alpha_1}\sinh\left[\sqrt{\alpha_1}(\pi - \theta_0^*)\right]}, \tag{74}$$

$$A_0 = \frac{\alpha_1}{\alpha_2}\left\{\alpha_4 - \alpha_3\cos\theta_0^* + \frac{\alpha_3}{\sqrt{\alpha_1}}\sin\theta_0^* \coth\left[\sqrt{\alpha_1}(\pi - \theta_0^*)\right]\right\}, \tag{75}$$

where θ_0^* satisfies

$$\frac{\alpha_4}{\alpha_2}\theta_0^* - \frac{\alpha_3}{\alpha_2}\sin\theta_0^* - \frac{\alpha_3}{\alpha_2\alpha_1}\sin\theta_0^* + (\pi - \theta_0^*)$$
$$\times\left\{\frac{\alpha_4}{\alpha_2} - \frac{\alpha_3}{\alpha_2}\cos\theta_0^* + \frac{\alpha_3}{\alpha_2}\frac{\sin\theta_0^*}{\sqrt{\alpha_1}}\coth\left[\sqrt{\alpha_1}(\pi - \theta_0^*)\right]\right\} = 0 \quad (76)$$

At second-order use of $B_1 = 0$ and (74) in (60), and $B_0 = 0$ and (59) in (70) yields $A_1 = D_1 = 0$. Then (72) used in (64) gives

$$\sqrt{\alpha_2}[\alpha_3\cos\theta_0^* - D_0\alpha_1\alpha_2\cosh\left[\sqrt{\alpha_1}(\pi - \theta_0^*)\right]]\,\theta_1^*$$
$$= \alpha_2 A_0 + \alpha_3(1 + \alpha_1)\cos\theta_0^* - \alpha_1\alpha_4. \quad (77)$$

The constants which appear in the composite solutions at third order are determined by (61), (70), (65), and (73), which, because of their length, will not be repeated here. These four equations serve to determine the four constants A_2, D_2, B_2, and θ_2^*.

For small values of θ^* equation (76) for θ_0^* may be approximated up to an error involving $(\theta_0^*)^3$ by

$$\sqrt{\alpha_1}\left(1 - \frac{\pi}{2}\sqrt{\alpha_1}\right)(\theta_0^*)^2 + (1 - \pi\sqrt{\alpha_1})\,\theta_0^*$$
$$+ \alpha_1(1 - \alpha_3^{-1}\alpha_4)\pi = 0. \quad (78)$$

The quantity in the last parenthesis is the ratio of the bottom displacement d_0 to the radius $\bar{a}$ of the tire. In this approximation the contact angle depends upon this and upon α_1—essentially the strength of the side wall spring relative to the inflation pressure. This illustrates the importance of side wall design on the contact geometry.

Comparison With the Exact Solution

Numerical values of the parameters were determined for the Bridgestone Radial Truck and Bus Tire 10.00–20 in the way described in the preceding paper [1]. They are, for a bottom deflection d_0 of 4.6 cm.

$$\epsilon = 0.16, \quad \alpha_1 = 13.66, \quad \alpha_2 = 6.93, \quad \alpha_3 = 7.30, \quad \alpha_4 = 6.67. \quad (79)$$

Using these values equation (78) gives $\theta_0^* = 0.25$ (14.3°). To second order (77) and (78) yield

$$\theta^* \doteq \theta_0^* + \epsilon\theta_1^* = 17.96°. \quad (80)$$

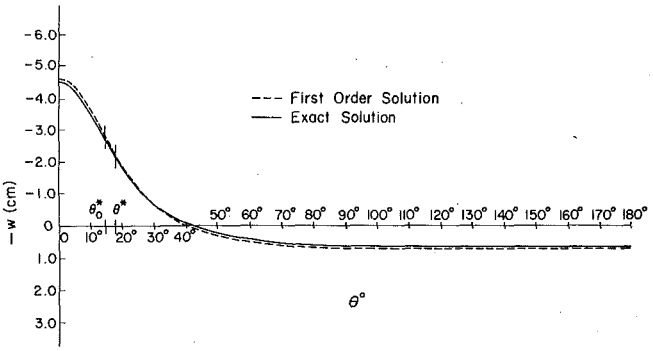

Fig. 2 The first-order solution for the radial displacement compared to the exact solution with the first-order contact angle θ_0^* and the exact contact angle θ^*

which compares quite favorably with the exact value of 18° [1].

With θ^*, the first-order terms in the composite solutions (67) and (68) were plotted against the exact solution in Fig. 2. Even at the lowest order of the approximation there is good agreement between the exact and approximate solutions.

Acknowledgments

The authors are indebted to J. D. Buckmaster, G. S. S. Ludford, and M. J. Normandia for helpful discussions on the asymptotic analysis. The first author's study and research were supported by the Bridgestone Tire Company.

References

1 Yamagishi, K., and Jenkins, J. T., "The Circumferential Contact Problem for the Belted Radial Tire," ASME JOURNAL OF APPLIED MECHANICS, Vol. 47, 1980, pp. 513–518.

2 Cole, J. D., *Perturbation Methods in Applied Mathematics*, Blaisdell, Waltham, Mass., 1968.

3 Hutter, H., and Pao, Y.-H., "Regular and Singular Perturbation Solutions for Bending and Torsion of Beams," *International Journal of Solids and Structures*, Vol. 7, 1971, pp. 1523–1537.

4 Yamagishi, K., "Contact Problems for the Radial Tire," PhD Dissertation, Cornell University, 1978.

L. M. Brock

Associate Professor,
Department of Engineering Mechanics,
University of Kentucky,
Lexington, Ky. 40506
Assoc. Mem. ASME

Exact Dynamic Surface Response for Sub and Through-Surface Slip

The motion of edge dislocations and slip on fault planes are important mechanisms involving sub and through-surface slip. Here exact solutions for largely arbitrary in-plane slip in a half plane along zones normal to the surface are derived and the general wavefront pattern described. For two examples of finite zones of uniform slip, the displacements on the free surface of the half plane are examined. In the case of the slip zone passing through the half-plane surface, separate and prominent systems of surface waves are seen to be generated at the surface-zone intersection point. Data illustrating this and other behavior is presented.

Introduction

Edge dislocation motion has been viewed as a mechanism for explaining effective strength [1] and plastic effects [2] in crystalline materials. Similarly, slip along faults in the earth's crust has been treated as a source of shallow-focus earthquakes [3]. In a continuum approach, both processes involve the extension of slip zones, i.e., surfaces over which material points initially adjacent across the surface undergo relative tangential motion.

Calculation of the dynamic displacement fields in materials due to slip zone motion is therefore an important problem, especially on the material surface. Indeed, surface responses may provide the only experimental data available for comparison with theoretical calculations. However, dynamic displacement calculations often use solutions for infinite media, and account for the material surface by imaging arguments or approximations [4–6]. Such approaches may be exact only for certain cases, such as two-dimensional antiplane strain [7] and may avoid the possibility that slip zones may reach the surface.

As a first step in a more exact approach, this article considers the two-dimensional problem of slip occurring over zones normal to the free surface of an isotropic, homogeneous, linearly elastic half plane. Slip occurs in the plane and the zones will be allowed to travel through the surface of the half plane. In this first step, the slip magnitude and zone location will be specified, thus making the mathematics more tractable. However, these properties will be largely arbitrary. Hopefully, some insight into more difficult problems involving prescribed slip zone stresses, for example, can be gained by studying the present solutions.

A general analysis leading to exact expressions for the displacements in the problem is outlined in the next few sections. The analysis is based on a recent treatment of wave propagation due to displacement discontinuities [8]. The general wavefront pattern is then discussed and two examples of slip zone motion with bearing on edge dislocation motion and fault slip are considered. In one example, the slip zone remains below the surface. In the other, the zone moves through the half-plane surface. Some numerical results for the surface displacements generated by each type are given and discussed.

Basic Problem

In terms of the Cartesian coordinates x, y consider the half plane $y > 0$, where c_a, c_b and $1/\tau$ are the dilatational and rotational wave speeds and shear modulus. For convenience the variable $s = c_a \times$(time) is introduced. For $s > 0$ the half plane is completely at rest. For $s > 0$, the tangential displacement discontinuity defined by $V(y,s)$ is induced along the positive y-axis where V is piecewise continuous and $|V|$ is finite for finite y, s and grows at less than exponential order as $|y| \to \infty$ or $s \to \infty$. Because of antisymmetry with respect to $x = 0$, attention can then be focused on the quarter-plane $x, y > 0$ by introducing the conditions

$$u = \tfrac{1}{2} V(y,s), \quad \sigma_x = 0 \tag{1}$$

for $s > 0$ as $x \to 0^+$, where u, v are the x, y-displacements. The stress-free half-plane surface requires that for $s > 0$ along $y = 0$,

$$\sigma_{xy},\ \sigma_y = 0 \tag{2a,b}$$

while the governing equations for $x, y, s > 0$ are

$$\tau m^2(\sigma_{x,x} + \sigma_{xy,y}) = \ddot{u}, \quad \tau m^2(\sigma_{xy,x} + \sigma_{y,y}) = \ddot{v} \tag{3a,b}$$

$$\tau m^2 \sigma_x = u_{,x} + (1 - 2m^2)v_{,y}, \quad \tau m^2 \sigma_y = v_{,y} + (1 - 2m^2)u_{,x} \tag{4a,b}$$

$$\tau \sigma_{xy} = u_{,y} + v_{,x}, \quad m = c_b/c_a \tag{5a,b}$$

Here $(\ )_{,z} \equiv \partial(\ )/\partial z$ and $(\dot{\cdot}) \equiv (\ )_{,s}$. The solutions should be bounded above almost everywhere in $x, y > 0$ for finite s while

$$s \le 0: \quad u,v = 0, \quad \dot{u},\dot{v} = 0 \tag{6}$$

Contributed by the Applied Mechanics Division for publication in the JOURNAL OF APPLIED MECHANICS.

Discussion on this paper should be addressed to the Editorial Department, ASME, United Engineering Center, 345 East 47th Street, New York, N. Y. 10017, and will be accepted until December 1, 1980. Readers who need more time to prepare a discussion should request an extension from the Editorial Department. Manuscript received by ASME Applied Mechanics Division, August, 1979; final revision, November, 1979.

Transform Solutions

The Laplace and Fourier sine and cosine transforms [9]

$$\hat{g} = \int_0^\infty g(s)e^{-ps}ds; \quad g^s, g^c = \int_0^\infty g(x)(\sin pqx, \cos pqx)dx \quad (7a\text{–}c)$$

over $s > 0$ and $x > 0$ are employed, where p is real and positive and large enough to insure convergence of (7a) while q is in general complex. Application of (7a,b) and (7a,c) to (2b), (3b), (4) and (2a), (3a), (5a), respectively, in light of (1) and (6) yields the transformed equations

$$m^2\hat{u}^c_{,yy} - p^2a^2\hat{u}^c + pq(1-m^2)\hat{v}^s_{,y} = \frac{m^2}{2}\frac{d\hat{V}(y)}{dy}, \quad a = (1+q^2)^{1/2} \quad (8)$$

$$\hat{v}^s_{,yy} - m^2p^2b^2\hat{v}^s + pq(m^2-1)\hat{u}^c_{,y} = -\frac{m^2}{2}pq\hat{V}(y), \quad b = (m^{-2}+q^2)^{1/2} \quad (9)$$

for $y > 0$ while for $y = 0$,

$$\hat{u}^c_{,y} + pq\hat{v}^s - \tfrac{1}{2}\hat{V}(y), \quad \hat{v}^s_{,y} - (1-2m^2)pq\hat{u}^c = 0 \quad (10)$$

For p real and positive a, b are defined in the plane cut along Re $(q) = 0$, $|\text{Im}\,(q)| > 1, 1/m$, respectively, so that Re (a), Re $(b) \geq 0$. Solutions to (8)–(10) which are bounded above in $y > 0$ are [8]

$$\hat{u}^c = A + B - \frac{q}{a}A_- + B_-, \quad \hat{v}^s = -\frac{a}{q}A - \frac{q}{b}B - A_+ + \frac{q}{b}B_+ \quad (11a,b)$$

$$Ae^{pay} = \frac{4b}{R_-}qTa_+(0) - \frac{R_+}{R_-}b_+(0), \quad A_\pm = a_+(y) \pm a_-(y) \quad (12)$$

$$Be^{pby} = \frac{4q^2}{R_-}Tb_+(0) - \frac{qR_+}{aR_-}a_+(0), \quad B_\pm = b_+(y) \pm b_-(y) \quad (13)$$

$$R_\pm = 4abq^2 \pm T^2, \quad T = b^2 + q^2 \quad (14)$$

$$2(a_+, a_-) = -m^2qa(\textstyle\int_y^\infty, \int_0^y)\,\hat{V}(z)e^{-pa|z-y|}dz \quad (15)$$

$$4(b_+, b_-) = -m^2T(\textstyle\int_y^\infty, \int_0^y)\,\hat{V}(z)e^{-pb|z-y|}dz \quad (16)$$

Here R_- is a form of the Rayleigh function which has simple zeroes at $q = \pm i/m_R$, $m_R = c_R/c_a$, where $c_R < c_b$ is the Rayleigh wave speed.

Transform Inversions for $x, y, s > 0$

The inverse Fourier sine and cosine transforms are [9]

$$g(x) = \frac{2}{\pi}\int_{iq_0}^{iq_0+\infty}(g^s \sin pqx, g^c \cos pqx)pdq \quad (17a,b)$$

where the real constant q_0 is chosen so that the integration path lies in the region of analyticity for g^s, g^c and convergence of (7b,c). For (11a,b) we can choose $q_0 = 0$. Upon performing the z-integrations in $a_\pm$, $b_\pm$ by parts and formally writing the operation (7a), it is readily shown that operating on (11b) with (17a) yields

$$2\pi\hat{v} = \int_0^\infty e^{-pt}\int_{-\infty}^\infty\left[\int_0^\infty\frac{\partial V}{\partial y}(z,t)(K_f + K_r)dz + V(0,t)K_0\right]e^{ipqx}dqdt + \int_0^\infty e^{-pt}V(y,t)\int_{-\infty}^\infty\frac{q}{b^2}e^{ipqx}dqdt \quad (18)$$

$$K_f = \text{sgn}\,(z-y)(K_ae^{-pa|y-z|} + K_be^{-pb|y-z|}) \quad (19)$$

$$K_r = (K_a^be^{-pbz} + K_a^ae^{-paz})e^{-pay} + (K_b^ae^{-paz} + K_b^be^{-pbz})e^{-pby} \quad (20)$$

$$K_0 = K_a^0e^{-pay} + K_b^0e^{-pby} \quad (21)$$

$$K_a = m^2q, K_a^0 = \frac{2qa}{m^2bR_-}, K_a^a = -\frac{R_+}{R_-}K_a, K_a^b = 2m^2q\frac{aT^2}{bR_-} \quad (22)$$

$$K_b = -m^2\frac{Tq}{2b^2}, K_b^0 = \frac{-Tq}{m^2b^2R_-}, K_b^b = \frac{R_+}{R_-}K_b, K_b^a = 4m^2\frac{Tq^3}{R_-} \quad (23)$$

The complex exponential and q-integration range $(-\infty, \infty)$ in (18) follow from (17a) and (11b) by recognizing that Im $(\hat{v}^s) = 0$, Im $(q) = 0$. The inverse of (18) can be obtained by following the Cagniard-deHoop [10] procedure. As outlined in [8], this scheme uses the Cauchy theorem to switch the q-integrations in (18) to Cagniard contours along which the resultant exponential factor for each term is recognized as the Laplace transform of the Dirac delta function. The result is that for $x, y, s > 0$

$$\pi v = \text{Im}\int_0^s\left[V(0,t)L_0 + \int_0^\infty\frac{\partial V}{\partial y}(z,t)(L_f + L_r)dz\right]dt + \frac{\pi}{2}V\left(y, s - \frac{x}{m}\right) \quad (24)$$

$$L_f = \text{sgn}\,(z-y)[K_a\dot{q}_aH(s-t-r_-) + K_b\dot{q}_bH(s-t-m^{-1}r_-)] \quad (25)$$

$$L_r = K_a^b\dot{q}_a^bH(s-t-n_a) + K_b^a\dot{q}_b^aH(s-t-n_b) + K_a^a\dot{q}_a^aH(s-t-r_+) + K_b^b\dot{q}_b^bH(s-t-\bar{r}_+) \quad (26)$$

$$L_0 = K_a^0\dot{q}_a^0H(s-t-r_+^0) + K_b^0\dot{q}_b^0H(s-t-\bar{r}_+^0) \quad (27)$$

where the K-functions now depend on similarly sub and superscripted q's. These quantities are, in turn, functions of $s - t$ representing Cagniard contours. In particular, where we replace $s - t$ by n for brevity,

$$ir_+^2q_b^b = (y+z)(m^{-2}r_+^2 - n^2)^{1/2} - nx, r_\pm = [x^2 + (y \pm z)^2]^{1/2} \quad (28)$$

$$r_+^2q_b^b = inx + (y+z)(n^2 - m^{-2}r_+^2)^{1/2} \quad (29)$$

for $\bar{r}_+ < n < m^{-1}r_+$ and $n > m^{-1}r_+$, respectively, where $\bar{r}_+ = m^{-1}r_+$ for $x < m(y+z)/(1-m^2)^{1/2}$ but otherwise $\bar{r}_+ = x + (y+z)(m^{-2}-1)^{1/2}$. Similarly, for $n > r_+$

$$r_+^2q_a^a = inx + (y+z)(n^2 - r_+^2)^{1/2} \quad (30)$$

The definitions for q_b and q_a follow from (29) and (30), respectively, by replacing $y + z$ with $|y - z|$. The definitions for q_a^0 and q_b^0 follow directly from (28)–(30) by setting $z = 0$. The contours q_a^b, q_b^a are defined as the q-solutions to, respectively, the equations

$$ay + bz - iqx = n > 0, \quad by + az - iqx = n > 0 \quad (31a,b)$$

where n_a and n_b in (26) are given by

$$n_a = m^{-1}r_1 + r_2, \quad n_b = m^{-1}r_2 + r_1 \quad (32)$$

$$r_1 = (x_0^2 + z^2)^{1/2}, \quad r_2 = [(x_0 - x)^2 + y^2]^{1/2} \quad (33)$$

and for n_b and n_a, respectively, x_0 must satisfy

$$mx_0r_2, \quad m^{-1}x_0r_2 = (x - x_0)r_1 \quad (34a,b)$$

Finally, in (25)–(27), $\bar{r}_+^0$ and r_+^0 follow from $\bar{r}_+$ and r_+ by setting $z = 0$ and $H(\ )$ is the Heaviside step function. Because Im $(L_f, L_r, L_0) = 0$ as $x \to 0$ (24) clearly satisfies the displacement boundary condition in (1). By a similar process, the inverse of (11a) for $x, y, s > 0$ is

$$\pi u = \text{Re}\int_0^s\left[V(0,t)L_0 + \int_0^\infty\frac{\partial V}{\partial y}(z,t)(L_f + L_r)dz\right]dt \quad (35)$$

where in (25)–(27) the K-functions are now defined by

$$K_a = m^2\frac{q^2}{a}, \quad K_a^0 = \frac{-2q^2}{m^2bR_-}, \quad K_a^a = \frac{R_+}{R_-}K_a, \quad K_a^b = -2m^2q^2\frac{T^2}{bR_-} \quad (36)$$

$$K_b = -m^2\frac{T}{2b}, \quad K_b^0 = \frac{T}{m^2bR_-}, \quad K_b^b = -\frac{R_+}{R_-}K_b, \quad K_b^b = -4m^2q^2\frac{bT}{R_-} \quad (37)$$

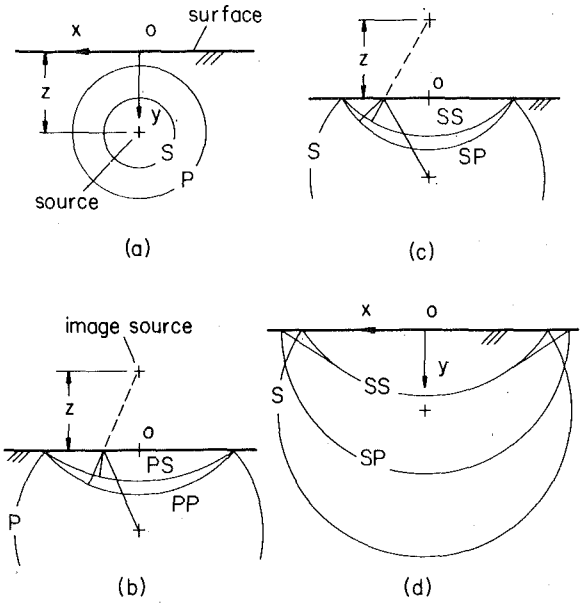

Fig. 1 Wavefront patterns in the half plane

When z/x, $y/x \to 0$ care must be taken in evaluating the integrals in (24) and (35) because the Cagniard contours collapse onto the positive Im (q)-axis. This necessitates deforming the contours about the Rayleigh pole due to R_- in the integrand denominators, which results in special contributions to the solution. In the surface displacement expressions presented later, these contributions will appear as Rayleigh surface waves.

General Wavefront Pattern

Some general information about the wavefront patterns in the half plane can be obtained by examining the Heaviside function arguments in (25)–(27). The L_f, L_r-terms in (24) and (35) represent the integral sums of the disturbances due to all displacement discontinuities occurring at a given $x = 0, y = z$ and instant $t > 0$. As indicated in Fig. 1(a), any one such discontinuity acts as a source which radiates dilatational and rotational rays. For $s > t$ these rays are of length $s - t$ and $m(s - t)$, respectively, thus defining the wavefronts shown in Fig. 1(a). The r_- defined in (28) is the distance from the source to any other point $x, y > 0$ in the half plane. The Heaviside functions in (25), therefore, show that the K_a and K_b-terms in (24) and (35) represent the dilatational and rotational disturbances received for $x, y, s > 0$ directly from the displacement discontinuity region. In seismology [11] these disturbances are called P and S-waves.

As seen in Fig. 1(b), a dilatational ray eventually reaches the half-plane surface and, in view of the stress-free surface conditions [12], is reflected as a dilatational and rotational ray. The dilatational ray leaves the surface at the same angle as the incident ray, so that the wavefront generated is the same as that which would arise from dilatational rays traveling from an image point $x = 0, y = -z$ in an unbounded material. The total distance traveled along the path from the source to the surface to a point $x, y > 0$ is the r_+ defined in (28). Clearly, then, the K_a^a-terms in (24) and (35) represent PP-waves, i.e., the dilatational surface reflection of P-waves. The rotational ray, however, does not leave the surface at the angle of incidence. It can be shown that (32) and (34b) give the elapsed time n_b/c_a between the generation of the source point dilatational ray and the receiving of the rotational reflection at $x, y > 0$. Therefore, the K_b^a-terms in (24) and (35) represent PS-waves, i.e., the rotational surface reflection of P-waves.

As seen in Fig. 1(c) by analogy with Fig. 1(b), the K_b^b and K_a^b-terms in (24) and (35) represent, respectively, SS and SP-waves, i.e., the rotational and dilatational surface reflections of S-waves. However, the SP and S/SS-wavefronts no longer intersect at the half-plane surface when the angle of the former becomes perpendicular to the surface there [13]. Subsequently, the wavefronts separate and the head waves shown in Fig. 1(d) are generated. It can be shown that the points $x, y > 0$ confined within the resulting wedgelike regions must satisfy the relations $m\bar{r}_+ < m(s - t) < r_+, x > m(y + z)/(1 - m^2)^{1/2}$, which are identical to those required when q_b^b is defined by (28). Thus the K_b^b-term occurring for this q_b^b in (24) and (35) represents the headwave contribution.

As indicated previously, the parameters and variables for the K_a^0 and K_b^0-terms follow from those for K_a^a and K_b^b, respectively, by setting $z = 0$. Therefore, the discussions for these terms need be modified only by placing the source point at $x, y = 0$. Then, the K_a^0 and K_b^0-terms represent, respectively, dilatational and rotational disturbances radiating from the origin $x, y = 0$, i.e., the corner of the quarter-plane of mathematical interest. The rotational disturbance may of course include head waves.

Returning to (24), the nonintegral term represents the propagation of the displacement induced by the displacement discontinuity along $x = 0$ normally into the quarter-plane $x > 0$ as a rotational wave. The argument of the term shows that an instantaneously induced discontinuity produces jumps at the wavefronts.

In summary, then, the b and a-subscripted terms in (24) and (35) represent, respectively, rotational and dilatational signals arriving at a location $x, y > 0$ due to the radiation of waves from points in the displacement discontinuity region. The L_f, or fundamental, terms represent signals received directly from the points while the L_r, or reflected, terms represent the signals received upon reflection by the half-plane surface. The L_0-terms represent signals received from a special point, the origin, $x, y = 0$. Finally, it should be noted that the aforementioned Rayleigh surface waves can be associated with the K_a^0, K_b^0-terms and P,S-wave reflections at $x, y = 0$. These wave contributions will be seen explicitly in the following two sections.

In light of these observations, (24) and (35) show that the reflected and fundamental terms depend on the spatial gradient of the displacement discontinuity and vanish when

$$V(y,s) = V(s) \tag{38}$$

Equation (38) also guarantees that the nonintegral term in (24) is a plane wave. Thus a spatially uniform relative displacement produces only plane waves perturbed by cylindrical, head and Rayleigh waves due to the "corner" at $x, y = 0$. On the other hand, (24) and (35) show that the origin terms depend on the displacement discontinuity at the half-plane surface. Thus, if $V(0, s) = 0$ for all $s > 0$, then the origin terms vanish. Finally, it is readily shown that the fundamental terms and the nonintegral terms represent the complete solutions for $y > 0$ to the present problems in the unbounded plane.

Half-Plane Surface Displacements

For $y = 0$, (24) reduces to

$$\pi v = \frac{\pi}{2G}(1 + d^2)\left(\frac{c}{d} - 1\right) V\left(0, s - \frac{x}{m_R}\right) H\left(s - \frac{x}{m_R}\right)$$
$$+ \int_0^\infty V(0,t) \frac{2\alpha Z T(iZ)}{m^4 x b(iZ)|R_-(iZ)|^2} H(s - t - x) H\left(\frac{x}{m} + t - s\right) dt$$
$$+ Im \int_0^s \int_0^\infty \frac{\partial V}{\partial y}(z,t)\,[L_a H(s - t - \rho_+)$$
$$+ L_b H(s - t - \bar{\rho}_+)]\,dz\,dt \tag{39}$$

$$L_a = -\frac{Tq}{R_-}\dot{q}, \quad L_b = -L_a, \quad \alpha = (Z^2 - 1)^{1/2}, \quad Z = \frac{s - t}{x} \tag{40}$$

$$G = \frac{c}{d}(1 + d^2) + \frac{d}{c}(1 + c^2) - 1 - d^2, \quad c = (1 - m_R^2)^{1/2},$$
$$d = \left(1 - \frac{m_R^2}{m^2}\right)^{1/2} \tag{41}$$

for $x, s > 0$. In (40) the L-functions depend on correspondingly subscripted q's which are themselves functions of s-t. With s-t replaced

by n for brevity, the q's are defined by (28)–(30), where now the superscripts are dropped and $y = 0$. Similarly, ρ_+ and $\bar{\rho}_+$ follow from r_+ and $\bar{r}_+$ by setting $y = 0$. The first term in (39) is the contribution obtained when, as $y \to 0$, the q_a^0, q_b^0-Cagniard contours are deformed around the pole at $q = i/m_R$. Analogously, for $x, s > 0, y = 0$ we find that (35) becomes

$$\pi u = \frac{\pi m_R^2}{4m^4 dG} V\left(0, s - \frac{x}{m_R}\right) H\left(s - \frac{x}{m_R}\right) - \int_0^\infty V(0,t) \frac{4\alpha Z^2}{m^4 x \beta |R_-(iZ)|^2} H(s - t - x) H\left(\frac{x}{m} + t - s\right) dt + \oint_0^\infty V(0,t) \frac{1}{m^4 x \beta |R_-(iZ)|^2} H\left(s - t - \frac{x}{m}\right) dt + \mathrm{Re} \int_0^s \int_0^\infty \frac{\partial V}{\partial y}(z,t)[L_a H(s - t - \rho_+) + L_b H(s - t - \bar{\rho}_+)] dz dt \quad (42)$$

where in this case

$$L_a = \frac{2bq^2}{R_-} \dot{q}, \quad L_b = \frac{-T^2}{2bR_-} \dot{q}, \quad \beta = (Z^2 - m^{-2})^{1/2} \quad (43)$$

In (42) the $\oint$-symbol denotes Principal Value integration when the zero of R_- at $Z = 1/m_R$ lies within the t-integration range. In (39) and (42) and L_a and L_b-terms represent the combined effects of, respectively, the *P,PP,PS* and *S,SS,SP*-waves. The remaining terms represent the dilatational, rotational, and Rayleigh waves generated by the L_0-terms. It will be seen that an important Rayleigh wave contribution also arises from the Principal Value integral in (42).

The next section considers the two example problems. Both examples are essentially superpositions of the following problem: At $s = 0$ a uniform displacement discontinuity of unit magnitude instantaneously appears in an undisturbed half plane along a semi-infinite region of the y-axis defined by $x = 0, y > h_0 > 0$. Subsequently, the region is defined by $x = 0, y > h(s)$ where $h(0) = h_0$ and $h(s)$ must be at least piecewise smooth. The displacement condition in (1) assumes the form

$$\tilde{v} = \tfrac{1}{2} H[y - h(s)] H(s) \quad (44)$$

where $\tilde{}$ denotes the solution to this particular problem. Then, for example, (39) becomes

$$\pi \tilde{v}(h) = \frac{\pi}{2G}(1 + d^2)\left(\frac{c}{d} - 1\right) H\left[-h\left(s - \frac{x}{m_R}\right)\right] H\left(s - \frac{x}{m_R}\right) + \int_0^\infty \frac{2\alpha Z T(iZ)}{m^4 x b(iZ) |R_-(iZ)|^2} H(-h) H(s - t - x) H\left(\frac{x}{m} + t - s\right) dt + \mathrm{Im} \int_0^s [L_a H(s - t - \rho_+) + L_b H(s - t - \bar{\rho}_+)] H(h) dt \quad (45)$$

where z is replaced by h and the t-dependence of h is understood unless specified otherwise. For convenience, the implicit dependence of $\tilde{v}$ on $h(s)$ is expressed.

Two Examples

Consider a slip zone of finite length and uniform tangential relative displacement v_0 which instantaneously appears at $s = 0$ within the half plane and moves along the y-axis. If the locations of the zone edges are $x = 0, y = h_\pm(s)$, where $h_+(s) > h_-(s)$ and $h_\pm(s)$ are at least piecewise smooth, then by superposition the resulting surface displacements u, v can be written as

$$u = v_0 \tilde{u}(h_-) - v_0 \tilde{u}(h_+), \quad v = v_0 \tilde{v}(h_-) - v_0 \tilde{v}(h_+) \quad (46a,b)$$

We consider two cases: In Case I the slip zone is of fixed length and moves into the half plane at a constant speed. Therefore

$$h_\pm(s) = h_0^\pm + ks, \quad h_0^+ = h_0^- + \Delta_0 \quad (47)$$

where k, Δ_0, h_0^- are positive real constants. In Case II, the same zone moves toward, and eventually through, the half-plane surface at a constant speed. Thus (47) can be adjusted by choosing $k < 0$. In Figs. 2 and 3 the surface displacements u, v are plotted versus s at the surface location $x = 1.0$ for both cases. Here $m = (1/3)^{1/2}$, $h_0^- = 1.0$, $\Delta_0 = 0.1$. In Case I, $k = 0.2$ while $k = -0.2$ in Case II. It is understood that values of $x, s, h_0^-, \Delta_0, u, v, v_0$ are all multiples of the same arbitrary length unit, while k is dimensionless.

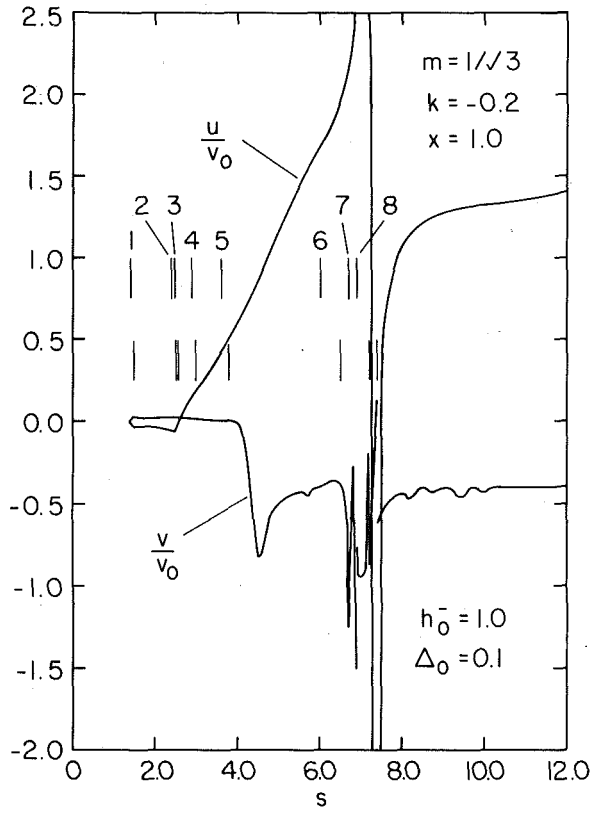

Fig. 2 Normal and tangential displacements at $x = 1.0$ on surface

Case II is plotted in Fig. 2, where the upper and lower sets of vertical dashes denote the first arrivals of waves associated with, respectively, the h_- and h_+-edges of the slip zone. As numbered from left to right, the dashes represent the

1. *P/PP/PS*-wavefront.
2. *SP*/head-wavefront (*SS/SP*-wavefront separation has occurred).
3. *S/SS*-wavefront.
4. Rayleigh wavefront due to *P*-wave reflection at $x, y = 0$.
5. Rayleigh wavefront due to *S*-wave reflection at $x, y = 0$.
6. Dilatational wavefront due to zone edge reaching $x, y = 0$.
7. Rotational wavefront due to zone edge reaching $x, y = 0$.
8. Rayleigh wavefront due to zone edge reaching $x, y = 0$.

Fig. 2 indicates that, in general, the tangential surface displacement u is of larger magnitude than the normal surface displacement v. It is noted that the wavefronts 6–8 signal prominent changes in u, v. In particular, finite discontinuities in v and infinite discontinuities in u occur at the Rayleigh wavefronts. The finite discontinuity follows from the first terms in (39) and (42). The infinite discontinuity can be extracted from the Principal Value integral in (42). It can be shown that for (47), $k < 0$,

$$\pi \tilde{u}(h) \sim \frac{-1}{4m^4 m_R^2 dG} \ln\left|s + \frac{h_0}{k} - \frac{x}{m_R}\right| \quad (48)$$

as $s \to (m_R^{-1} x - k^{-1} h_0^\pm)^+$. The wavefronts 1–3 have a smaller effect on u, v. The Rayleigh wavefronts 4, 5 are included in, respectively, the L_a, L_b-terms in (45) and its $\tilde{u}(h)$-counterpart. By following the work of [8, 14], these wave contributions near the wavefronts can be obtained for (47) as

$$\pi\tilde{u}_P^R(h) \sim -\frac{M(c)}{G'(c)}\,dx, \quad \pi\tilde{v}_P^R(h) \sim -\frac{N(c)}{2G'(d)}\,(1+d^2) \tag{49}$$

$$\pi\tilde{u}_S^R(h) \sim \frac{M(d)}{4G'(d)d}\,(1+d^2)^2 x, \quad \pi\tilde{v}_S^R(h) \sim \frac{N(d)}{2G'(d)}\,(1+d^2) \tag{50}$$

$$M(z) = m_R \ln\left\{\frac{x^2 + z^2h^2(s)}{[(m_Rs-x)^2 + z^2h_0^2]^{1/2}[(m_Rs+x)^2 + z^2h_0^2]^{1/2}}\right\} + kz\,\tan^{-1}\left[\frac{2m_Rzh_0s}{z^2h_0^2 + m_R^2s^2 - x^2}\right] \tag{51}$$

$$N(z) = m_R\,\tan^{-1}\left[\frac{2zh(s)x}{z^2h^2(s) - x^2}\right] - m_R\,\tan^{-1}\left[\frac{2zh_0x}{z^2h_0^2 + m_R^2s^2 - x^2}\right] + kz\,\ln\left[\frac{(m_Rs-x)^2 + z^2h_0^2}{(m_Rs+x)^2 + z^2h_0^2}\right] \tag{52}$$

$$m^2cdG'(z) = m_R(m_R^2 + k^2z^2)[c^2(1+m^2d^2) - cd(1+d^2)] \tag{53}$$

where the superscript R denotes the Rayleigh contribution, the subscripts denote the wave reflected at $x, y = 0$ while the $\pm$ notation on $h(s)$, h_0 is implied and $k = -0.2$. As indicated in Fig. 2, the Rayleigh contributions are finite at the wavefronts. It is also noted that they vanish at $x, y = 0$.

In Fig. 3, short-time plots of u, v for Case II are presented with complete plots for Case I. It is seen that, even prior to the slip zone arrival at the half-plane surface, the u,v-magnitudes for Case II are generally larger. The wavefronts 6–8 do not occur for Case I and are thus omitted in Fig. 3. However, another vertical dash pair, denoted by 9, does appear for Case I. In light of Fig. 1(c, d), the SP and SS-wavefronts generated by S-waves from the slip zone as it moves away from the surface will eventually always intersect at the surface location $x = 1.0$. The dashes identified by 9 indicate the arrivals of the first signals of this event from the two zone edges. These arrivals seem to have a noticeable effect on u, but an effect can also be detected for v. Fig. 3 shows that, as in Case II, the u-magnitudes are generally larger than those for v. However, the degree of difference, especially as s grows, appears to be much greater for Case I. Finally, the contributions near the Rayleigh wavefronts 4, 5 are again given by (49) and (50), where now $k = 0.2$.

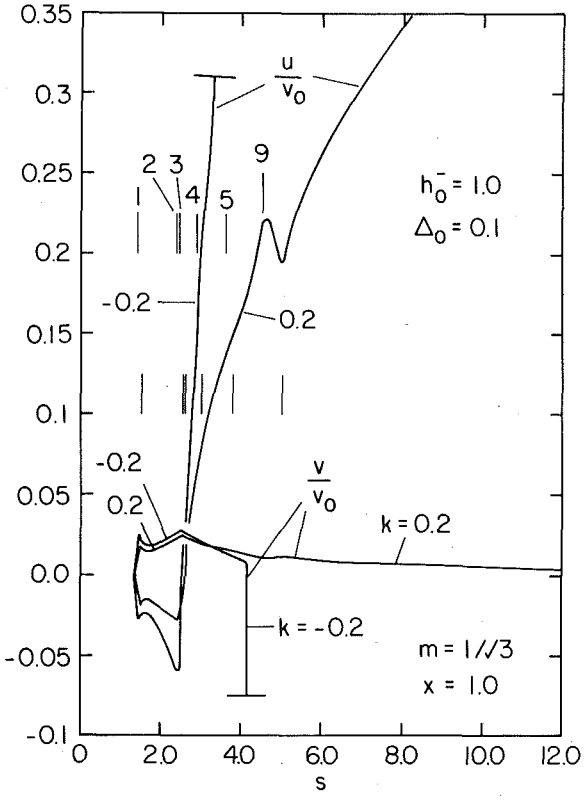

Fig. 3 Normal and tangential displacements at $x = 1.0$ on surface

Discussion

A general analysis for the two-dimensional dynamic problems of largely arbitrary tangential displacement discontinuities on planes normal to the surface of an elastic half plane has been outlined. Exact formulas for the in-plane displacements both within and on the surface were presented, and used to discuss some general wave propagation features of the solution. The results were specialized to examine the surface displacements for two types of instantaneously appearing uniform slip zones of fixed length. One type moved at a constant speed away from the half-plane surface. The second type moved at the same speed completely through the half-plane surface. The surface displacement behavior indicated that, not surprisingly, the displacement magnitudes are larger when the zone approaches the surface. In both cases, the tangential displacement magnitude is generally larger than the normal displacement magnitude. However, the degree of difference is greater when the zone moves away from the surface. More importantly, the behavior indicated that the passing of the slip zone through the surface generates separate and prominent wave disturbances. In particular, the Rayleigh wave disturbances cause both finite and infinite discontinuities in the surface displacements. Thus care is advised in using imaging arguments and approximations to study through-surface slip.

The analysis was motivated somewhat by the possibilities for studying edge dislocation motion and shallow focus earthquakes due to fault slip through surface displacement measurements. Thus the two examples could be classified as dislocation pairs of constant strength or as fault slip regions. However, these examples were meant to be representative of, and not necessarily identical to, actual models of such mechanisms.

It should be noted that the present general results can readily accommodate many features not mentioned or emphasized here, such as non-uniform or supersonic slip zone speeds, non-uniform slip over the zones, zones which move from equilibrium, zones which enter the half-plane, oscillating zones or multiple zones. Perhaps the generality of the analysis will allow insight into solutions, perhaps approximate, for specified stress problems. Moreover, the analysis can be used to study in more detail the contributions of the various waves mentioned here for different types of slip zones. In summary, then, it is hoped that the present results provide a useful starting point for the problem of studying physically important slip mechanisms through the associated dynamic surface disturbances.

Acknowledgment

This research was sponsored by NSF Grant ENG7811773 through the University of Kentucky Research Foundation. The suggestions of the reviewers are also appreciated.

References

1 Guy, A. G., *Elements of Physical Metallurgy*, 2nd ed., Addison-Wesley, Reading, Mass., 1959, pp. 107–118.

2 Mura, T., "Continuum Theory of Plasticity and Dislocations," *International Journal of Engineering Science*, Vol. 5, 1967, pp. 341–351.

3 Walsh, J., "Mechanisms of Strike Slip Faulting With Friction," *Journal of Geophysical Research*, Vol. 73, 1968, pp. 761–775.

4 Aki, K., "Seismic Displacements Near a Fault," *Journal of Geophysical Research*, Vol. 73, 1968, pp. 5359–5376.

5 Niazy, A., "Elastic Displacements Due to a Propagating Crack in an Infinite Medium," *Proceedings of an International Conference on Dynamic Crack Propagation*, Sih, G., ed. Noordhoff, Leyden, 1973, pp. 501–512.

6 Brock, L. M., "Surface Motions Due to Fault Slip in the Vertical Mode With Friction," *Bulletin of the Seismological Society of America*, Vol. 65, 1975, pp. 1653–1666.

7 Burridge, R., and Halliday, G. S., "Dynamic Shear Cracks With Friction as Models for Shallow Focus Earthquakes," *Geophysics Journal of the Royal Astronomical Society*, Vol. 25, 1971, pp. 261–283.

8 Brock, L. M., "Two Basic Wave Propagation Problems for the Non-uniform Motion of Displacement Discontinuities in a Half Plane," *International Journal of Engineering Science*, Vol. 17, 1979, pp. 1211–1223.

9 Sneddon, I. N., *The Use of Integral Transforms*, McGraw-Hill, New York, 1972, Chapters 2, 3.

10 deHoop, A. T., "A Modification of Cagniard's Method of Solving Seismic

Pulse Problems," *Applied Scientific Research,* Vol. 8, Series B, 1960, pp. 349–356.
11 Jeffreys, H., *The Earth,* 3rd ed. Cambridge University Press, 1952.
12 Lindsay, R. B., *Mechanical Radiation,* McGraw-Hill, New York, 1960, Chapter 2.
13 Achenbach, J. D., *Wave Propagation in Elastic Solids,* North-Holland, Amsterdam, 1973.
14 Chao, C. C., Bleich, H. H., and Sackman, J., "Surface Waves in an Elastic Half Space," ASME JOURNAL OF APPLIED MECHANICS, Vol. 28, 1961, pp. 300–301.

T. J. Delph[2]
G. Herrmann
Fellow ASME

Division of Applied Mechanics,
Stanford University,
Stanford, Calif. 94305

R. K. Kaul
State University of New York,
Buffalo, N.Y. 14214

Harmonic Wave Propagation in a Periodically Layered, Infinite Elastic Body: Plane Strain, Numerical Results[1]

Numerical results are presented for the dispersion spectrum for harmonic wave propagation in an unbounded, periodically layered elastic body in a state of plane strain. Both real and complex branches are considered. The spectrum is shown to be multiple-valued and quite intricate in detail. Some analytical properties of the Floquet surface are also discussed.

Introduction

The problem of harmonic waves in plane strain propagating through an unbounded, periodically layered elastic body has been analyzed recently by the present authors [1]. This problem is of interest due to its application to wave-propagation problems in layered composites and to the construction of acoustic filtering devices. In [1] we derived the dispersion equation for the layered elastic body and discussed some of the qualitative aspects of the dispersion spectrum, along with presenting a limited number of numerical results. In the present work we present a more detailed set of numerical results for this spectrum, evaluated over a limited range of wave numbers for a particular set of material parameters. Our purpose here is not only to illustrate the extraordinary complexity of the spectrum, but primarily to provide a set of benchmark data for use in the construction and validation of approximate theories for wave propagation in layered solids. The need for such data is apparent from the relatively large number of approximate theories which have appeared in recent years, the authors of these theories quite often comparing the predictions of their theories to the exact plane strain solution for an unbounded body. However, as we discussed in detail in [1], existing formulations of the unbounded body solution, such as in [2], may well be lacking in physical significance, and, in addition, the intricate coupling found to exist between real and complex branches has not been revealed so far. Hence it seems that a proper and detailed evaluation of this spectrum is in order.

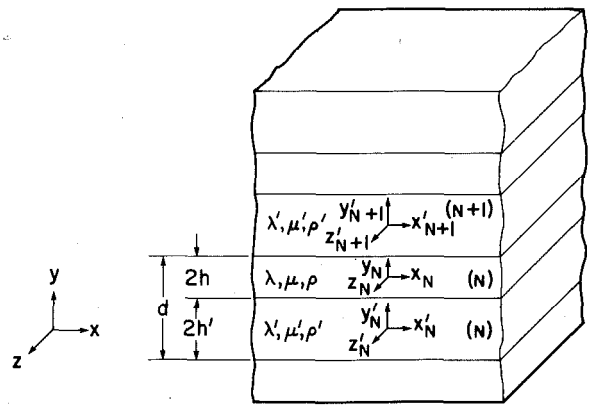

Fig. 1 Geometry of layered solid

To consider the problem in more detail, we assume the body to be as shown in Fig. 1, consisting of periodically alternating layers of homogeneous, isotropic elastic layers perfectly bonded to each other along their interfaces. Any two adjacent layers in the body comprise a unit cell, and this unit cell is completely invariant under a lattice translation along the positive and negative y-axes. For each unit cell, the layers have elastic constants $(\lambda; \mu)$, $(\lambda'; \mu')$, thicknesses $2h$; $2h'$, and densities ρ; ρ', respectively. The union of an infinite number of similar cells comprise the periodically layered, infinite, elastic body.

[1] This research was supported in part by ONR Contract N00014-76-C-0054 to Stanford University and by ONR Contract N00014-75-C-0302 to State University of New York.

[2] Now with Lehigh University, Bethlehem, Pa. 18015.

Contributed by the Applied Mechanics Division for presentation at the Winter Annual Meeting, Chicago, Ill., November 16–21, 1980, of THE AMERICAN SOCIETY OF MECHANICAL ENGINEERS.

Discussion on this paper should be addressed to the Editorial Department, ASME, United Engineering Center, 345 East 47th Street, New York, N. Y. 10017, and will be accepted until December 1, 1980. Readers who need more time to prepare a discussion should request an extension from the Editorial Department. Manuscript received by ASME Applied Mechanics Division, October, 1978; final revision, January, 1980. Paper No. 80-WA/APM-3.

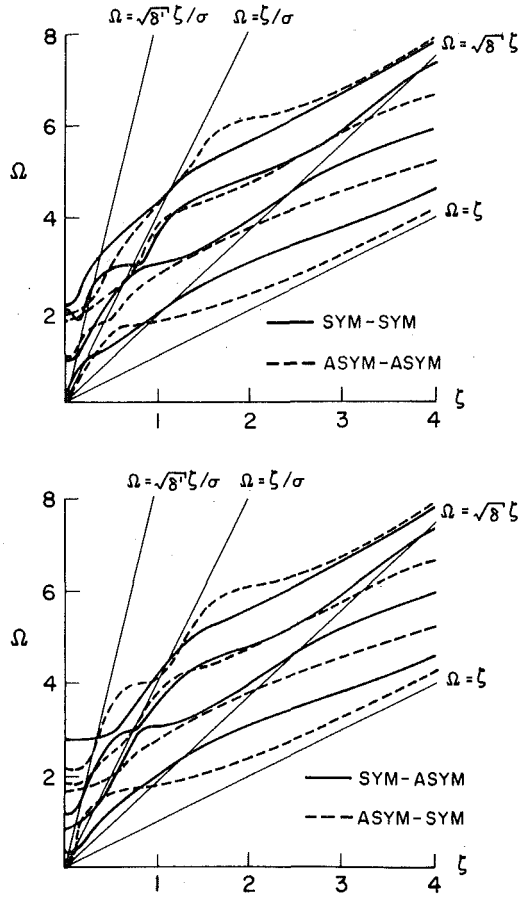

Fig. 2 Spectral lines corresponding to modes of opposite symmetry, at the ends of the Brillouin zones

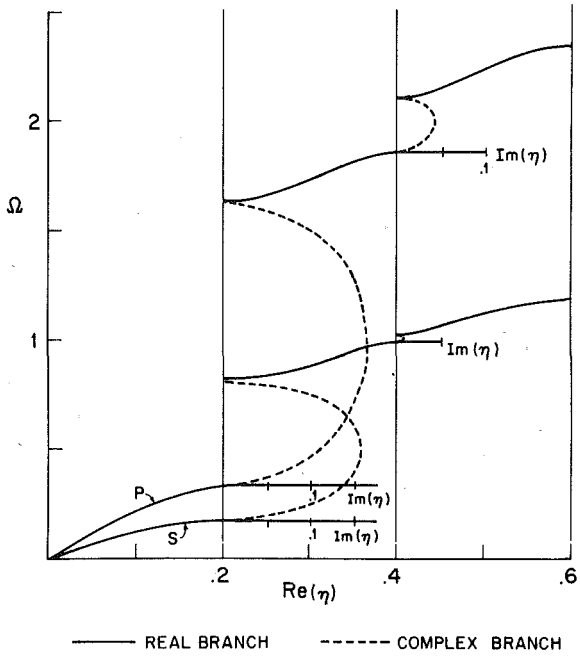

Fig. 3 *P* and *S* surfaces in the $\zeta = 0$ plane, with complex branches

Let u, v, and w be the Cartesian components of displacement in the x, y, and z-directions, respectively. For plane strain motion, we take $w \equiv 0$; $u, v \neq 0$. Then, as shown in detail in [1], application of the methods of classical elasticity and Floquet's theory of differential equations with periodic coefficients leads to the dispersion equation expressed in the form of an 8×8 complex-valued determinant ([1, equation (12)].

The dispersion equation relates two-nondimensional wave numbers $\eta \equiv (2hk_y)/\pi$ and $\zeta \equiv (2hk_x)/\pi$ to a nondimensional frequency $\Omega = (2h\omega)/(\pi\sqrt{\mu/\rho})$. Here k_y is the wave number of the Floquet wave measured in the y-direction, k_x the wave number in the x-direction, and ω the frequency in radians per unit of time. Thus the dispersion equation implicitly represents a multiple-valued surface in frequency-wave-number space, with frequency as a real parameter.

Since the dispersion equation is in general far too complex to be evaluated analytically, numerical computations are required. This paper presents the results of such an evaluation for a limited range of wave numbers over the first two Brillouin zones. Some earlier numerical results are given in [2]. The parameters used in this study are $\gamma = 0.02$, $\sigma^2 = 0.06$, $\epsilon = 4$, $\nu = 0.30$, and $\nu' = 0.35$. Here $\gamma = \mu/\mu'$, $\sigma^2 = (\mu\rho')/(\mu'\rho)$, $\epsilon = h'/h$, and ν and ν' are Poisson's ratio for the layers with unprimed and primed constants, respectively.

Real Branches

It was shown in [1] that the dispersion equation for plane strain motion factors along the ends of the Brillouin zones, were $\eta = n/(1 + \epsilon)$, $(n = 0, 1, 2 \ldots)$, into the product of two 4×4 determinants. These determinants were then shown to represent the dispersion equations for motion in which the u component of displacement is either symmetric or antisymmetric about the layer midplanes. For even values of n, the two factors correspond to motion in which the u displacement is either symmetric or antisymmetric about both layer midplanes in the unit cell ([1, equations (13)–(14)]. These cases will be referred to as symmetric-symmetric and antisymmetric-antisymmetric motion, respectively. For odd values of n, one factor represents motion in which the u displacement is symmetric in the layers with unprimed constants and antisymmetric in the layers with primed constants (symmetric-antisymmetric motion, [1, equation (16)]. The other factor represents the converse situation, antisymmetric-symmetric motion ([1, equation (17)]. The first four branches of each mode are shown in Fig. 2. As noted previously, these curves define the ends of the Brillouin zones on the dispersion surface.

Similarly in the $\zeta = 0$ plane, the dispersion equation may also be shown to factor into the product of two 4×4 determinants, one of which represents a longitudinal (P) wave propagating normal to the layering and the other a shear (S) wave propagating normal to the layering, [1]. The spectral lines for these two cases are shown in Fig. 3, along with the complex branches originating at the ends of the Brillouin zones. The surfaces which emanate from the longitudinal and shear wave spectral lines in the $\zeta = 0$ plane will henceforth be called the P and S surfaces, respectively. The S surface will generally be the lower of the two.

Fig. 4 shows the intersection of the S surface with planes of constant ζ over the first two Brillouin zones, plotted on an extended zone scheme. It is of interest to note that, while the derivative $\partial\Omega/\partial\eta$ was always positive on the extended zone scheme in the antiplane strain case [3], this is not so in general in the plane strain case. In fact, $\partial\Omega/\partial\eta$ may change sign within a Brillouin zone, as may be seen by comparing the curves for $\zeta = 0.10$ and $\zeta = 0.30$ in the first Brillouin zone. This change in sign occurs between $\zeta = 0.26$ and $\zeta = 0.27$ and is illustrated in Fig. 5. The derivative $\partial\Omega/\partial\eta$ becomes positive again around $\zeta = 0.82$ and remains positive thereafter. A similar behavior occurs in the second Brillouin zone, where $\partial\Omega/\partial\eta$ becomes negative around $\zeta = 0.48$ and remains so for increasing ζ.

It was noted previously that lines defining the ends of the Brillouin zones were given by the factored forms of the dispersion equation, i.e., symmetric-symmetric modes, etc. For conciseness, let SSl denote the spectral line for the first symmetric-symmetric mode, AS2 the second antisymmetric-symmetric mode, etc. This notation will be useful for labeling points on the ends of Brillouin zones. Then the S surface in the first Brillouin zone is found to be bounded in the $\eta = 0$ plane by

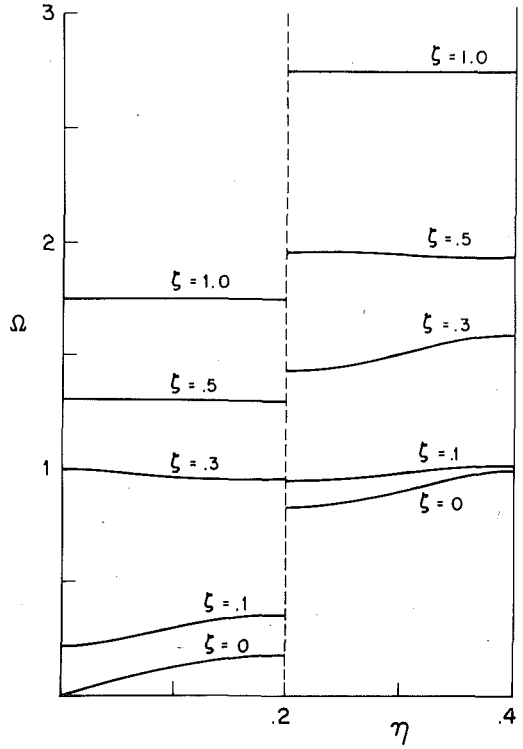

Fig. 4 Curves of constant ζ on the *S* surface

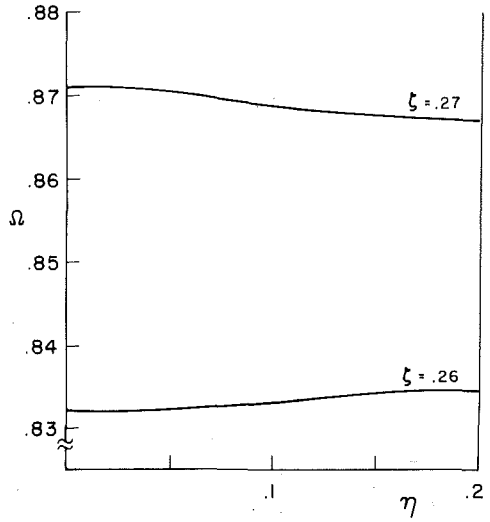

Fig. 5 Curves of constant ζ on the *S* surface for $\zeta = 0.26, 0.27$

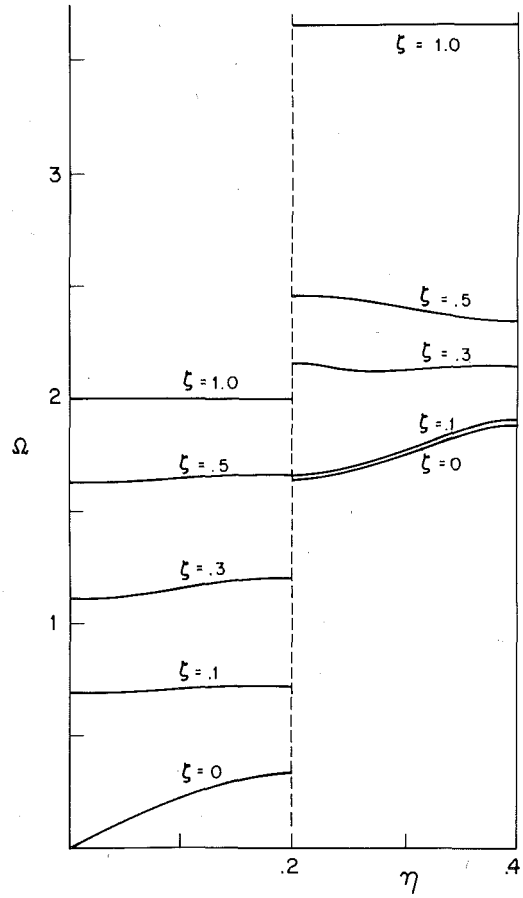

Fig. 6 Curves of constant ζ on the *P* surface

AA1 to $\zeta = 0.33$, by SS1 to $\zeta = 0.82$, and by AA1 thereafter. In the $\eta = 0.20$ plane, the bounding lines are AS1 to $\zeta = 0.04$, SA1 to $\zeta = 0.82$, and AS1 thereafter. The portion of the surface in the second Brillouin zone is bounded in the $\eta = 0.20$ plane by SA2 to $\zeta = 0.15$, by AS1 to $\zeta = 0.44$, by SA2 to $\zeta = 0.57$, and by AS2 thereafter. In the $\eta = 0.40$ plane, the surface is bounded by SS2 to $\zeta = 0.35$ and then by AA2 thereafter.

Fig. 6 shows the intersection of the *P* surface with planes of constant ζ over the first two Brillouin zones. An especially interesting feature is the existence of a local minimum in the curve for $\zeta = 0.30$ in the second Brillouin zone, at about $\eta = 0.30$. This minimum first appears at the left-hand end of the zone at $\zeta = 0.26$ and moves from left to right within the zone with increasing ζ until it reaches the right-hand end of the zone at $\zeta = 0.32$. From $\zeta = 0.32$ to $\zeta = 0.77$, $\partial\Omega/\partial\eta$ is negative over the entire second zone, but becomes positive again at $\zeta = 0.77$ and remains so for increasing ζ.

In the first Brillouin zone, the *P* surface is bounded in the $\eta = 0$ plane by SS1 to $\zeta = 0.33$, by AA1 to $\zeta = 0.82$ and by SS1 thereafter. In the $\eta = 0.20$ plane, the bounding lines are SA1 to $\zeta = 0.04$, AS1 to $\zeta = 0.15$, SA2 to $\zeta = 0.44$, AS1 to $\zeta = 0.82$, and SA1 thereafter. In the second Brillouin zone, the surface is bounded in the $\eta = 0.20$ plane by AS2 to $\zeta = 0.22$, by SA3 to $\zeta = 0.29$, by AS3 to $\zeta = 0.73$, by SA3 to $\zeta = 1.25$, by AS3 to $\zeta = 2.58$, by SA3 to $\zeta = 2.82$, and by AS3 thereafter. In the $\eta = 0.40$ plane, the surface is bounded by AA3 to $\zeta = 0.12$, by SS3 to $\zeta = 0.18$, by AA3 to $\zeta = 0.77$, by SS3 to $\zeta = 1.25$, by AA3 to $\zeta = 2.58$, by SS3 to $\zeta = 2.82$, and by AA3 thereafter.

Complex Branches

We will now focus our attention on the complex portion of the spectrum, considering first the branches for which η takes on complex values. As shown in [4], these branches originate from points on the real spectrum at the end of the Brillouin zones and from other points on branches where $\partial\Omega/[\partial \text{ Re } (\eta)] = 0$. Along branches originating from the end of the Brillouin zones, the real part of η in general remains constant while the imaginary part varies. Complex branches will also arise from points on other complex branches where $\partial\Omega/[\partial \text{ Im } (\eta)] = 0$. To avoid excessive detail, results are presented here only for the range $0 \leq \zeta \leq 0.35$ over the first two Brillouin zones.

We consider first the left-hand end of the first Brillouin zone, in the plane Re $(\eta) = 0$. As the spectral lines SS1 and AA1 move away from the origin (Fig. 2), simultaneously complex branches originate from these lines and run down to the $\Omega = 0$ plane. Fig. 7 illustrates these branches at $\zeta = 0.10$, where again the imaginary axis has been rotated 90° onto the real plane for clarity. This situation continues to between $\zeta = 0.25$ and $\zeta = 0.26$, where an interesting phenomenon occurs. Here the branches are observed to touch each other at a point

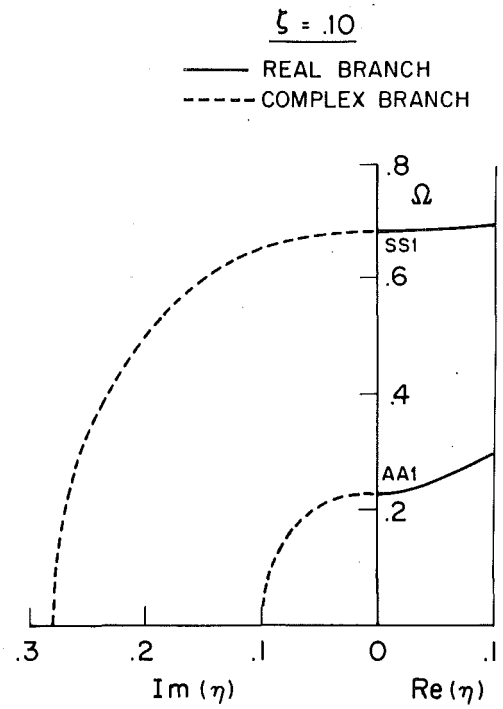

Fig. 7 Real and complex branches originating from the left-hand end of the first Brillouin zone ($\zeta = 0.10$)

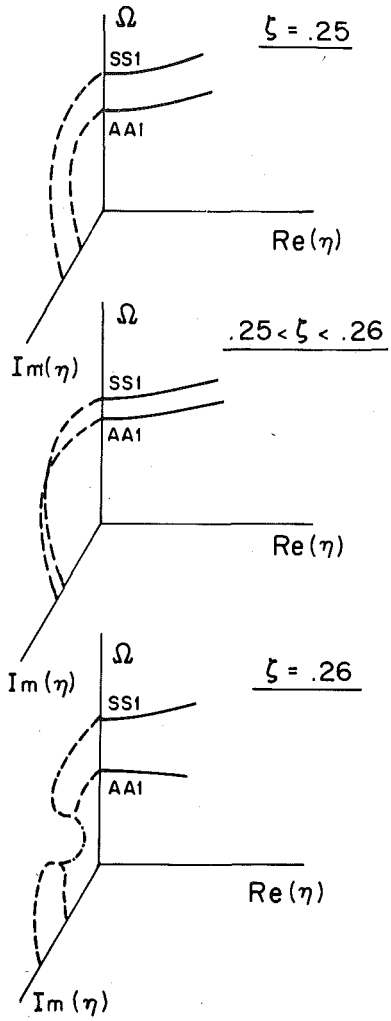

Fig. 8 Intersection, splitting, and rejoining of complex branches between $\zeta = 0.25$ and $\zeta = 0.26$

along the curves and then with increasing ζ, to split and rejoin into branches having different endpoints. This process is shown qualitatively in Fig. 8. Here, and henceforth, we denote real branches by solid lines, complex branches upon which the real part of the wave number remains constant by dashed lines, and complex branches upon which both the real and imaginary parts vary by dashed and dotted lines. The branches which originally ran from SS1 and AA1 to the $\Omega = 0$ plane are seen to split and rejoin into a single branch running from SS1 to AA1 and another which loops up from and back to the $\Omega = 0$ plane. For $\zeta = 0.26$, a short complex branch upon which both Re (η) and Im (η) vary connects a local minimum in the SS1-AA1 branch to a local maximum in the branch originating and ending in the $\Omega = 0$ plane. This is in accordance with the previously stated result that complex branches may also arise from portions of the spectrum where $\partial\Omega/[\partial \text{ Im } (\eta)] = 0$. The local minimum in the SS1-AA1 branch disappears around $\zeta = 0.27$, as shown in Fig. 9. The situation shown in Fig. 9 remains qualitatively unaltered through $\zeta = 0.35$.

Now consider the complex branches in the Re (η) = 0.20 plane. Here the situation is considerably more complicated. Fig. 10 shows the branches for $\zeta = 0$ (see also Fig. 3). Here the P and SV waves uncouple, leading to intersections between the complex branches. However, once ζ increases away from zero, the P and SV waves become coupled and the complex branches immediately split at their points of intersection and rejoin into different branches, accordilng to the process described earlier. Fig. 11 shows a qualitative sketch of the rejoined branches at $\zeta = 0.02$. The intersections of the P and S surfaces with the $\zeta = 0.02$ plane are labeled accordingly. The local maximum in the AS1-SA1 branch and the local minimum in the SA2-AS3 branch disappear between $\zeta = 0.10$ and $\zeta = 0.15$, and with them the complex branch connecting the two. Also, the AS1 and SA1 spectral lines intersect at $\zeta = 0.04$, so the relative position of these two is reversed.

At $\zeta = 0.15$, the SA2 and AS1 spectral lines intersect, and a variant of the splitting and rejoining process is observed. Fig. 12 shows the branches before the intersection, at $\zeta = 0.14$, and afterwards at $\zeta = 0.16$. The AS1-SA1 and AS3-SA2 branches are seen to merge and rejoin into an AS3-SA1 branch and an AS1-SA2 branch.

The situation shown in Fig. 12 for $\zeta = 0.16$ continues qualitatively unaltered with increasing ζ until a value of ζ between $\zeta = 0.25$ and ζ

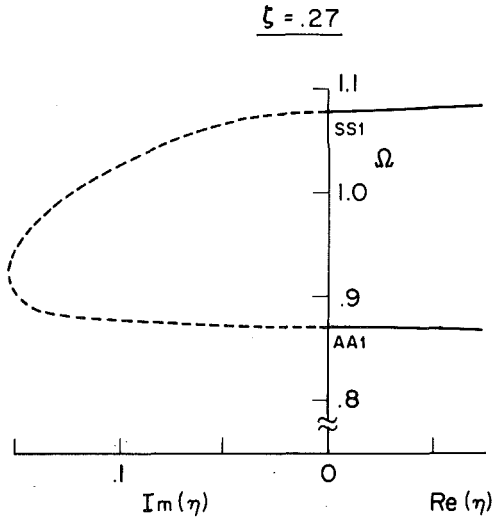

Fig. 9 Real and complex branches originating from the left-hand end of the first Brillouin zone ($\zeta = 0.27$)

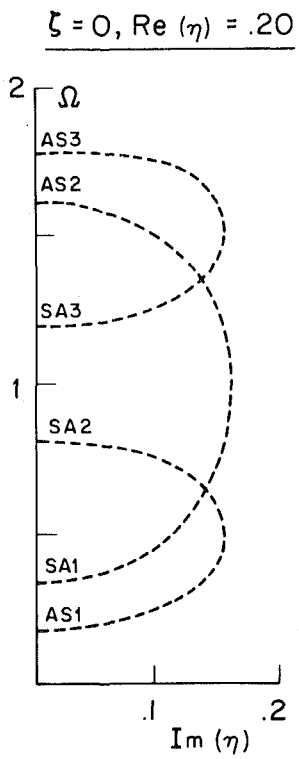

Fig. 10 Complex branches for Re (η) = 0.20, ζ = 0

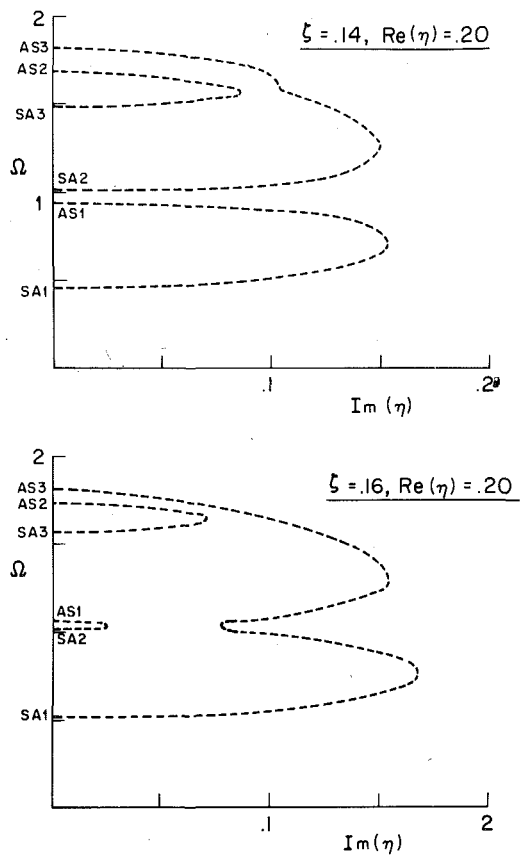

Fig. 12 Complex brances for Re (η) = 0.20, ζ = 0.14, 0.16

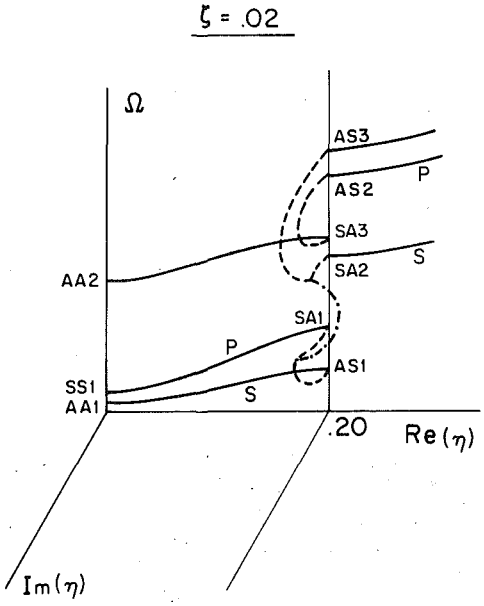

Fig. 11 Qualitative sketch of spectrum for ζ = 0.02

= 0.26. Here an intersection, splitting, and rejoining of the AS3-SA1 and the SA3-AS2 branches occurs, resulting in a local maximum in the newly formed AS2-SA1 branch. At the same point, a local minimum is observed to form in the real branch on the P surface in the second Brillouin zone, and is connected by a complex branch to the local maximum in the AS2-SA1 branch. This process is sketched qualitatively in Fig. 13.

As ζ increases, the local minimum in the real branch moves from left to right through the second Brillouin zone until it reaches the right-hand end at about ζ = 0.32. Now the derivative $\partial\Omega/[\partial \text{ Re } (\eta)]$ is completely negative on the P surface throughout the second Brillouin zone. A local minimum now forms in the complex branch originating from the right-hand end of the zone, and the complex branch which previously ran to the minimum in the real branch, now runs to this minimum. Fig. 14 illustrates qualitatively the situation for ζ = 0.29 and ζ = 0.34.

We will now briefly consider those branches of the spectrum for which ζ takes on complex values. These branches originate from the real spectrum in the Re (ζ) = 0 plane, and from other lines in the real spectrum along which $\partial\Omega/[\partial \text{ Re } (\zeta)] = 0$. In general, the real part of ζ remains constant along branches originating in the Re (ζ) = 0 plane, while the imaginary part varies. Complex branches may also be expected to originate from points on other complex branches where $\partial\Omega/[\partial \text{ Im } (\zeta)] = 0$.

Fig. 15 shows a qualitative sketch of the branches with complex ζ along the end of the first Brillouin zone in the plane Re (η) = 0.20 (see also Fig. 2). Here the dispersion spectrum uncouples into symmetric-antisymmetric and antisymmetric-symmetric motion. A particularly interesting feature is the existence of a complex branch running from a local minimum in the real AS3 branch down to a point in the Ω = 0 plane.

We have restricted ourselves in this section to a discussion of those portions of the complex spectrum where only one of the two wave numbers (either η or ζ) takes on complex values, while the other remains real. However, there exist portions of the spectrum upon which both wave numbers are complex-valued. These portions of the spectrum are shown to originate from points at which either $\partial\Omega/\partial[\text{Re } (\eta)] = \partial\Omega/\partial[\text{Re } (\zeta)] = 0$ or $\partial\Omega/\partial[\text{Im } (\eta)] = \partial\Omega/\partial[\text{Im } (\zeta)] = 0$. They describe in general a five-dimensional surface in frequency-wave-number space.

As an example, consider the point η = 0.20, ζ = 0 at the end of the first Brillouin zone. From this point there arises a surface upon which both Im (η) and Im (ζ) vary, and upon which Re (η) and Re (ζ) may

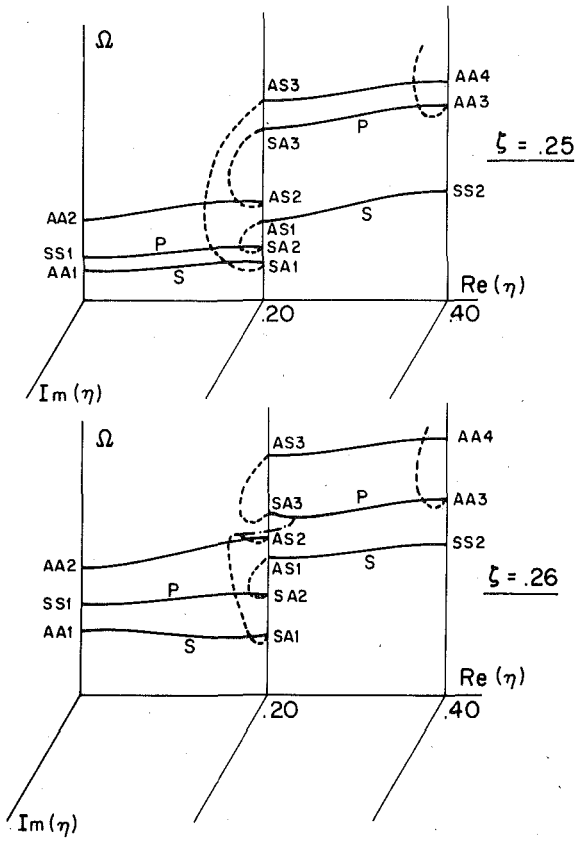

Fig. 13 Qualitative sketch of spectrum for $\zeta = 0.25, 0.26$

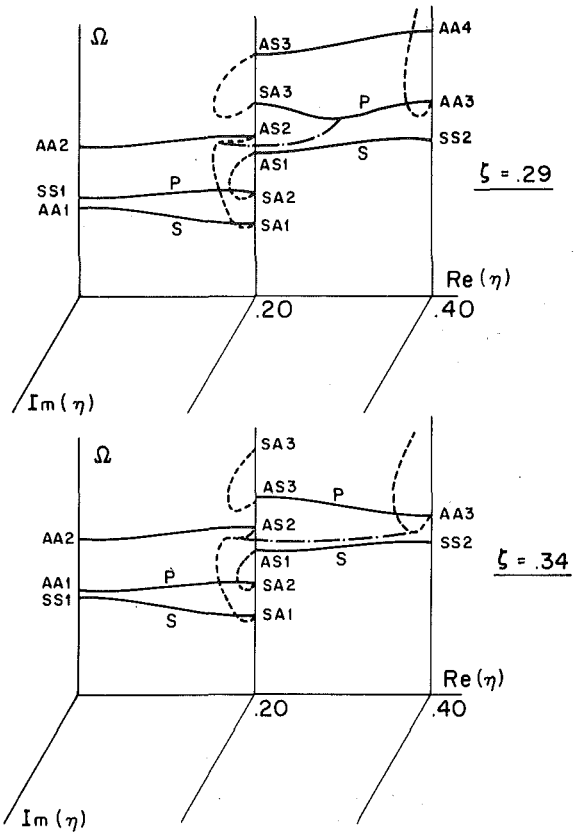

Fig. 14 Qualitative sketch of spectrum for $\zeta = 0.29, 0.34$

vary as well. Fig. 10 shows a section of this surface in the Im $(\zeta) = 0$ plane, while Fig. 15 shows a section in the Im $(\eta) = 0$ plane.

Discussion

It is evident from the numerical results presented in the last section that the dispersion spectrum for plane strain motion is quite complicated. This complexity makes the task for properly interpreting the spectrum a difficult one. By proper interpretation of the spectrum we mean the selection of those portions of the spectrum for which energy is propagated in the positive coordinate directions, and which can be reached from the zero frequency plane by a path along every point of which energy is propagated in the positive coordinate directions.

For real wave numbers, the selection of portions of the spectrum for which energy is propagated in the positive coordinate direction corresponds to the selection of portions of the spectrum for which the components of the group velocity $\partial\Omega/[\partial \text{ Re } (\zeta)]$ and $\partial\Omega/[\partial \text{ Re } (\eta)]$ are both positive. The interpretation of the antiplane strain spectrum [4] is thus straightforward, since both these derivatives are always positive (or zero) on the extended zone scheme.

In the plane strain spectrum, however, $\partial\Omega/[\partial \text{ Re } (\zeta)]$ and $\partial\Omega/[\partial \text{ Re } (\eta)]$ have been shown to change signs several times within a Brillouin zone, indicating the presence of saddle points and critical points of more complicated nature. The interpretation problem is further complicated by the fact that any portion of the dispersion surface may be reached by one of a number of different paths by traveling along different real and complex branches.

Perhaps the major difficulty which remains to be resolved before the plane strain spectrum can be successfully interpreted is the determination of the portion of the complex branches of the spectrum which correspond to energy propagation along the positive coordinate axes. The criterion for making this determination along real portions of the spectrum has already been stated. However, for complex portions of the spectrum, no corresponding criterion exists.

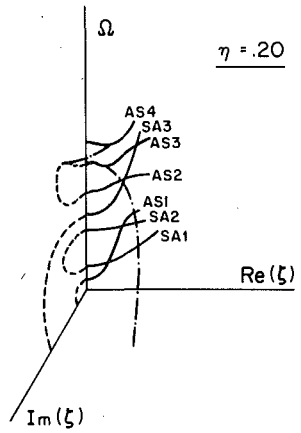

Fig. 15 Qualitative sketch of real and complex branches for $\eta = 0.20$

For these reasons, a proper interpretation of the plane strain spectrum cannot be given at this time, pending a more detailed analysis leading to a resolution of the difficulties mentioned. The interpretation must therefore be deferred to later studies which involve the application of Morse theory for the study of critical points.

In addition, there are a number of other problems connected with this subject, which have not yet had a satisfactory answer. It is well known that for the Floquet exponent $n\pi/d < k_y < (n+1)\pi/2$, $n = 0, 1, 2, \ldots$, the two linearly independent solutions for the potentials $\phi(x, y_N; t)$ and $\psi(x, y_N; t)$ are quasi-periodic or "almost-periodic" in the sense of Bohr. At the end points of the Brillouin zone, one of the solutions is periodic with period (half period) d when n is even (odd). For a second-order ordinary differential equation with periodic coefficients, such as equation (5) of [1], it can be shown that when k_y

$= n\pi/d$, the second independent solution is a sum of a periodic part and a linearly varying part, and as such it is aperiodic. These solutions and their explicit forms still remain to be determined in the case of plane strain problems. The ability to solve initial-boundary-value problems depends upon a detailed knowledge of the properties of these solutions.

It is also known [5] that there exists coincidence of frequencies for suitable values of parameters. It can be shown that if $F(\Omega, \xi_k) = 0$ ($k = 1,2$) is the dispersion equation, which is a function of one real and two complex variables, then the slope of the surface at the point of coincidence is given by

$$\frac{\partial \Omega}{\partial \xi_k} = \frac{1}{F_{\Omega\Omega}} \left[-F_{\Omega\xi_k} \pm \sqrt{F^2_{\Omega\xi_k} - F_{\Omega\Omega} F_{\xi_x \xi_x}} \right] \quad k = 1, 2,$$

and the second derivatives are not independent but satisfy the condition

$$(F_{\Omega\xi_1} F_{\Omega\xi_2} - F_{\Omega\Omega} F_{\xi_1\xi_2})^2 - (F^2_{\Omega\xi_1} - F_{\Omega\Omega} F_{\xi_1\xi_1})(F^2_{\Omega\xi_2} - F_{\Omega\Omega} F_{\xi_2\xi_2}) = 0.$$

At the point of coincidence, the two linearly independent solutions for the potentials ϕ and ψ are both periodic. However, the qualitative nature of the displacement field has not been examined so far. The problem of coexistence in the theory of ordinary differential equations with periodic coefficients has a long history and was only recently explained fully. An understanding of similar phenomenon in the present context requires further study.

References

1 Delph, T. J., Herrmann, G., and Kaul, R. K., "Harmonic Wave Propagation in a Periodically Layered, Infinite Elastic Body: Plane Strain, Analytical Results," ASME JOURNAL OF APPLIED MECHANICS, Vol. 46, 1979, pp. 113–119.

2 Sve, C., "Time Harmonic Waves Traveling Obliquely in a Periodically Laminated Medium," ASME JOURNAL OF APPLIED MECHANICS, Vol. 38, 1971, pp 447–482.

3 Delph, T. J., Herrmann, G., and Kaul, R. K., "Harmonic Wave Propagation in a Periodically Layered, Infinite Elastic Body: Antiplane Strain," ASME JOURNAL OF APPLIED MECHANICS, Vol. 45, 1978, pp. 343–349.

4 Onoe, M., McNiven, H. D., and Mindlin, R. D., "Dispersion of Axially Symmetric Waves in Elastic Rods," ASME JOURNAL OF APPLIED MECHANICS, Vol. 29, 1962, pp. 729–734.

5 Delph, T. J., Herrmann, G., and Kaul, R. K., "Coalescence of Frequencies and Conical Points in theDispersion Spectra of Elastic Bodies," *International Journal of Solids and Structures,* Vol. 13, 1977, pp 423–436.

R. Kant[1]
Graduate Research Assistant.

D. B. Bogy
Professor of Applied Mechanics.
Mem. ASME

Department of Mechanical Engineering,
University of California,
Berkeley, Calif. 94720

The Elastostatic Axisymmetric Problem of a Cracked Sphere

The problem of a cracked sphere is solved with the use of Boussinesq stress functions. Two coordinate systems—oblate spheroidal for representing the crack surface and spherical polars for the spherical surface—are used to satisfy boundary conditions. Integral representations and transformations of harmonic functions are used to relate stress functions in the two coordinate systems. This procedure leads to a system of algebraic equations which is solved, for axisymmetric tractions on both the surfaces. Graphical results are presented for one specific loading case.

1 Introduction

The motivation for solving the elasticity problem for a cracked sphere was the need of this solution in order to solve the problem of a cracked spherical inclusion in a dissimilar matrix. This cracked inclusion solution is presented in the companion paper in this issue of the JOURNAL OF APPLIED MECHANICS on Pages ?. It is often found in testing of metallic materials with brittle inclusions that the latter fracture at a relatively low load level, and this fracture event is the source of detectable elastic wave motion (see Bianchetti, Hamstad, and Mukherjee [1]). It is of interest to solve the cracked and uncracked inclusion problems in order to determine the amount of elastic energy released by the fracture event.

The two-dimensional analog of the cracked sphere problem has been solved by Erdogan and Gupta [2], but the techniques used there are not applicable to the spherical geometry. The cracked sphere solution is obtained here by the superposition of two other solutions: one is the solution for a penny-shaped crack in an infinite medium and the other is the solution for an uncracked sphere. The solution of the crack problem exists in the literature in several different forms, but none of these forms was found to be suitable for use in the superposition scheme for solving the cracked sphere problem. For this we need the solution for arbitrary axisymmetric normal and shearing tractions applied to the crack faces. Furthermore, this solution must have a mathematical representation that permits the evaluation of the normal and shearing tractions on the spherical surface of interest. Such a solution is derived in Section 2 for the crack in an infinite medium in terms of oblate spheroidal coordinates. Sack [3] has also solved the problem of a crack in an infinite medium using oblate spheroidal coordinates. However, the solution obtained in [3] contains incorrectly defined Legendre functions of the second kind. Also, Sack's transformation of harmonic functions from oblate spheroidal coordinates to spherical coordinates leads to functions that are not harmonic, therefore, they cannot be used as Boussinesq potentials. Furthermore, the problem considered in [3] is restricted to uniform pressure distribution on the crack faces. For our purposes we need nonuniform pressure and shear distributions on the crack faces.

The axisymmetric solution for the uncracked sphere is given by Sternberg, Eubanks, and Sadowsky [4] in terms of interior spherical harmonics. In order to use this solution in the superposition scheme for solving the cracked sphere problem it is necessary to evaluate the normal and shearing tractions on the crack face of interest. Transformations are obtained between spherical and oblate spheroidal coordinates which enable us to make the needed traction calculations. Superposition of these two solutions leads to the cracked sphere solution in series form.

One particular loading is considered and stress distributions are calculated on the equitorial plane outside the crack for various ratios of the crack and sphere radii. The stress-intensity factor is also computed, and its dependence on this ratio is also graphically illustrated.

2 Crack in an Infinite Medium

1 Coordinate Systems and Separable Solutions. The axisymmetric problem of a penny-shaped crack is solved here using Boussinesq stress functions referred to oblate spheroidal coordinates defined as follows:

$$\left.\begin{aligned} x &= a\sqrt{(1+\xi^2)(1-\eta^2)}\cos\phi \\ y &= a\sqrt{(1+\xi^2)(1-\eta^2)}\sin\phi \\ z &= a\xi\eta \end{aligned}\right\} \tag{1}$$

where $0 \le \xi < \infty$, $-1 \le \eta \le 1$.

The surfaces ξ = constant (positive) are oblate spheroids of thickness $2\xi a$ along the axis, and of equitorial radius $a\sqrt{\xi^2+1}$. The surfaces η = constant are hyperboloids of one sheet, asymptotic to the cone of angle $\cos^{-1}\eta$ with respect to the z-axis. The surface $\xi = 0$ is

[1] Now at Bell Laboratories, Whippany, N.J. 07981.

Contributed by the Applied Mechanics Division for publication in the JOURNAL OF APPLIED MECHANICS.

Discussion on this paper should be addressed to the Editorial Department, ASME, United Engineering Center, 345 East 47th Street, New York, N.Y. 10017, and will be accepted until December 1, 1980. Readers who need more time to prepare a discussion should request an extension from the Editorial Department. Manuscript received by ASME Applied Mechanics Division, September, 1979; final revision, January, 1980.

a disk of radius a in the x, y plane, with center at the origin. The degenerate surface $\eta = 1$ is the positive z-axis and likewise $\eta = -1$ is the negative z-axis; also the surface $\eta = 0$ is the x, y plane except for the part inside the disk of radius a, centered at origin.

The separable solutions $\Phi(\phi)H(\eta)X(\xi)$ of Laplace's equation in oblate spheroidal coordinates are determined by

$$\left.\begin{aligned} &\frac{d^2\Phi}{d\phi^2} + m^2\Phi = 0,\\ &\frac{d}{d\eta}\left[(1-\eta^2)\frac{dH}{d\eta}\right] + n(n+1)H = \frac{m^2H}{1-\eta^2},\\ &-\frac{d}{d\xi}\left[(1+\xi^2)\frac{dX}{d\xi}\right] + n(n+1)X = \frac{m^2X}{1+\xi^2}. \end{aligned}\right\} \tag{2}$$

The solutions are products of the following type:

$$\begin{Bmatrix}\sin m\phi\\ \cos m\phi\end{Bmatrix} \times \begin{Bmatrix}P_n^m(\eta)\\ Q_n^m(\eta)\end{Bmatrix} \times \begin{Bmatrix}P_n^m(i\xi)\\ Q_n^m(i\xi)\end{Bmatrix}, \tag{3}$$

where P_n^m and Q_n^m are the Legendre polynomials and Legendre functions of the second kind, respectively. Because of axial symmetry only the terms with $m = 0$ are considered. Regularity requirements at $\eta = \pm 1$ and $\xi \to \infty$ exclude the use of $P_n(i\xi)$ and $Q_n(\eta)$. Thus the required solutions for the exterior of an oblate spheroid are

$$\phi_n(\xi, \eta) = P_n(\eta)Q_n(i\xi). \tag{4}$$

Additional harmonic functions ψ_n are generated from these by observing that if ϕ_n is harmonic then so is grad $z \cdot$ grad ϕ_n. In oblate spheroidal coordinates such $\psi_n(\xi, \eta)$ are related to $\phi_n(\xi, \eta)$ by

$$\psi_n(\xi, \eta) = \frac{1}{a}\left[\eta\frac{\xi^2+1}{\xi^2+\eta^2}\frac{\partial\phi_n}{\partial\xi} + \xi\frac{1-\eta^2}{\xi^2+\eta^2}\frac{\partial\phi_n}{\partial\eta}\right]. \tag{5}$$

Substituting (4) and (5) into

$$2\mu\mathbf{u} = \nabla\phi \tag{6}$$

$$2\mu\mathbf{u} = \nabla(z\psi) - [4(1-\nu)\psi\mathbf{k}] \tag{7}$$

referred to oblate spheroidal coordinates (see [6]), we obtain the first Boussinesq solution (generated by ϕ_n) and the second Boussinesq solution (generated by ψ_n):

First Boussinesq Solution $[F_n]$

$$\left.\begin{aligned} 2\mu u_\eta^{(n)} &= \frac{1}{a}\sqrt{\frac{1-\eta^2}{\xi^2+\eta^2}}\frac{\partial\phi_n}{\partial\eta}\\ 2\mu u_\xi^{(n)} &= \frac{1}{a}\sqrt{\frac{\xi^2+1}{\xi^2+\eta^2}}\frac{\partial\phi_n}{\partial\xi} \end{aligned}\right\} \tag{8}$$

$$\left.\begin{aligned} \sigma_{\xi\xi}^{(n)} &= \frac{1}{a^2}\left[\left(\frac{\xi^2+1}{\xi^2+\eta^2}\right)\frac{\partial^2\phi_n}{\partial\xi^2} + \frac{\xi(\eta^2-1)}{(\xi^2+\eta^2)^2}\frac{\partial\phi_n}{\partial\xi} + \frac{\eta(1-\eta^2)}{(\xi^2+\eta^2)^2}\frac{\partial\phi_n}{\partial\eta}\right]\\ \sigma_{\xi\eta}^{(n)} &= \frac{1}{a^2}\frac{\sqrt{(\xi^2+1)(1-\eta^2)}}{(\xi^2+\eta^2)}\\ &\quad\times\left[\frac{\partial^2\phi_n}{\partial\xi\partial\eta} - \frac{\eta}{\xi^2+\eta^2}\frac{\partial\phi_n}{\partial\xi} - \frac{\xi}{\xi^2+\eta^2}\frac{\partial\phi_n}{\partial\eta}\right]\\ \sigma_{\eta\eta}^{(n)} &= \frac{1}{a^2(\xi^2+\eta^2)}\\ &\quad\times\left[(1-\eta^2)\frac{\partial^2\phi_n}{\partial\eta^2} - \frac{\eta(1+\xi^2)}{\xi^2+\eta^2}\frac{\partial\phi_n}{\partial\eta} + \frac{(1+\xi^2)\xi}{\xi^2+\eta^2}\frac{\partial\phi_n}{\partial\xi}\right]\\ \sigma_{\phi\phi}^{(n)} &= \frac{1}{a^2(\xi^2+\eta^2)}\left[\xi\frac{\partial\phi_n}{\partial\xi} - \eta\frac{\partial\phi_n}{\partial\eta}\right] \end{aligned}\right\} \tag{9}$$

Second Boussinesq Solution $[G_n]$

$$\left.\begin{aligned} 2\mu u_\eta^{(n)} &= \frac{1}{a}\sqrt{\frac{1-\eta^2}{\xi^2+\eta^2}}\left[a\xi\psi_n + a\xi\eta\frac{\partial\psi_n}{\partial\eta} - 4(1-\nu)a\xi\psi_n\right]\\ 2\mu u_\xi^{(n)} &= \frac{1}{a}\sqrt{\frac{1+\xi^2}{\xi^2+\eta^2}}\left[a\eta\psi_n + a\xi\eta\frac{\partial\psi_n}{\partial\xi} - 4(1-\nu)a\eta\psi_n\right] \end{aligned}\right\} \tag{10}$$

$$\left.\begin{aligned} \sigma_{\xi\xi}^{(n)} &= \frac{\xi\eta}{a}\left(\frac{\xi^2+1}{\xi^2+\eta^2}\right)\frac{\partial^2\psi_n}{\partial\xi^2}\\ &\quad+\left[\frac{\xi^2 n}{a}\frac{(\eta^2-1)}{(\xi^2+\eta^2)^2} - \frac{(1-2\nu)}{a}\eta\left(\frac{1+\xi^2}{\xi^2+\eta^2}\right)\right]\frac{\partial\psi_n}{\partial\xi}\\ &\quad+\left[\frac{1}{a}\frac{\xi(1-\eta^2)}{(\xi^2+\eta^2)}\left(\frac{\eta^2}{\xi^2+\eta^2} - 2\nu\right)\right]\frac{\partial\psi_n}{\partial\eta}\\ \sigma_{\xi\eta}^{(n)} &= \frac{1}{a}\frac{\sqrt{(\xi^2+1)(1-\eta^2)}}{(\xi^2+\eta^2)}\\ &\quad\times\left\{\xi\eta\frac{\partial^2\psi_n}{\partial\xi\partial\eta} - \eta\left[\frac{\xi^2}{\xi^2+\eta^2} + (1-2\nu)\right]\frac{\partial\psi_n}{\partial\eta}\right.\\ &\quad\left.-\xi\left[\frac{\eta^2}{\xi^2+\eta^2} + (1-2\nu)\right]\frac{\partial\psi_n}{\partial\xi}\right\}\\ \sigma_{\eta\eta}^{(n)} &= \frac{1}{a}\left(\frac{1-\eta^2}{\xi^2+\eta^2}\right)\xi\eta\frac{\partial^2\psi_n}{\partial\eta^2}\\ &\quad-\left\{\frac{\xi}{a(\xi^2+\eta^2)}\left[\frac{\eta^2(1+\xi^2)}{(\xi^2+\eta^2)} + 2(\nu-1)(1-\eta^2)\right]\right\}\frac{\partial\psi_n}{\partial\eta}\\ &\quad+\left[\frac{(1+\xi^2)\eta}{a(\xi^2+\eta^2)}\left(\frac{\xi^2}{\xi^2+\eta^2} - 2\nu\right)\right]\frac{\partial\psi_n}{\partial\xi}\\ \sigma_{\phi\phi}^{(n)} &= -\frac{1}{a(\xi^2+\eta^2)}\left[\eta\frac{\partial\psi_n}{\partial\xi} + \xi\frac{\partial\psi_n}{\partial\eta}\right]. \end{aligned}\right\} \tag{11}$$

The displacement component u_ϕ and the stress components $\sigma_{\xi\phi}$ and $\sigma_{\eta\phi}$ which vanish identically by virtue of assumed symmetry are omitted here.

2 The Axisymmetric Problem of an Arbitrarily Loaded Crack. Consider a penny-shaped crack of radius a in the x, y plane of an infinite medium and centered at the origin. Furthermore, assume that this crack is loaded with general axisymmetric surface tractions given by

$$\sigma_{\xi\xi}(0, \eta) = f(\eta), \quad \sigma_{\xi\eta}(0, \eta) = g(\eta). \tag{12}$$

In order to satisfy these boundary conditions at the crack face we need to evaluate from the first and second Boussinesq solutions the expressions for $\sigma_{\xi\xi}$ and $\sigma_{\xi\eta}$ at the crack face $\xi = 0$. Using (4) and (5) in (9) and (11), respectively, we find

$[F_n]$:

$$\left.\begin{aligned} &\sigma_{\xi\xi}^{(n)}(0, \eta)\\ &\quad= \frac{n(n+1)}{a^2\eta^3(2n+1)}[nP_{n+1}(\eta) + (n+1)P_{n-1}(\eta)]Q_n(i0)\\ &\sigma_{\xi\eta}^{(n)}(0, \eta)\\ &\quad= \frac{\sqrt{1-\eta^2}}{a^2\eta^3(2n+1)}[(n-1)P'_{n+1}(\eta) + (n+2)P'_{n-1}(\eta)]Q'_n(i0) \end{aligned}\right\} \tag{13}$$

$[G_n]$:

$$\left.\begin{aligned} &\sigma_{\xi\xi}^{(n)}(0, \eta)\\ &\quad= \frac{2(\nu-1)n(n+1)}{a^2\eta^3(2n+1)}[nP_{n+1}(\eta) + (n-1)P_{n-1}(\eta)]Q_n(i0)\\ &\sigma_{\xi\eta}^{(n)}(0, \eta) = \frac{(2\nu-1)\sqrt{1-\eta^2}}{a^2\eta^3(2n+1)}\\ &\quad[(n-1)P'_{n+1}(\eta) + (n+2)P'_{n-1}(\eta)]Q'_n(i0) \end{aligned}\right\} \tag{14}$$

The form of these expressions suggests that in order to satisfy the boundary conditions at the crack face $\xi = 0$ we should expand the following functions into Legendre-Fourier series:

$$\eta^3 f(\eta) = \sum_{n=0}^{\infty} f_n P_n(\eta), \quad \frac{\eta^3}{\sqrt{1-\eta^2}}g(\eta) = \sum_{n=1}^{\infty} g_n P'_n(\eta) \tag{15}$$

in which f_n, g_n are determined by

$$f_n = \frac{2n+1}{2}\int_{-1}^{1}\eta^3 f(\eta)P_n(\eta)d\eta \tag{16}$$

$$g_n = \frac{(2n+1)(n-1)!}{2(n+1)!}\int_{-1}^{1}\eta^3\sqrt{1-\eta^2}g(\eta)P_n'(\eta)d\eta \quad (Cont.) \tag{16}$$

We also observe from (13) and (14) and the definition of $P_n(\eta)$ that the stress quantities $\sigma_{\xi\xi}^{(n)}$ from both $[F_n]$ and $[G_n]$ are regular in the region exterior to the crack only for even n (except for $n = 0$) while the $\sigma_{\xi\eta}^{(n)}$ are regular in the same region for odd n. The other terms possess singularities at $\eta = 0$, which is the entire $z = 0$ plane except for a disk of radius a, and must therefore be omitted. In order to accomplish this it is useful to define solutions $[A_n]$, $[B_n]$ by

$$\left.\begin{aligned}[A_n] &= n(n-1)[F_n]\\ [B_n] &= n(n-1)[G_n]\end{aligned}\right\}, \tag{17}$$

which will omit the singular solution for $n = 0$ and will aid us in obtaining the coefficients of superposition by recursive computation. We now assume the solution in the form

$$[S] = \sum_{n=0}^{\infty} a_n[A_n] + b_n[B_n]. \tag{18}$$

The boundary conditions at $\xi = 0$ supply a system of equations for the coefficients of superposition a_n, b_n. Upon substitution of (13) and (14) into (17), with the use of (15), we obtain

$$\left.\begin{aligned}\sum_{n=0}^{\infty} f_nP_n &= \sum_{n=0}^{\infty}[a_n + 2(\nu-1)b_n]\\ &\quad\times\left\{\frac{n^2(n^2-1)}{a^2}[nP_{n+1} + (n+1)P_{n-1}]\frac{Q_n(i0)}{(2n+1)}\right\}\\ \sum_{n=1}^{\infty} g_nP_n' &= \sum_{n=1}^{\infty}[a_n + (2\nu-1)b_n]\\ &\quad\times\left\{\frac{n(n-1)}{a^2}[(n-1)P_{n+1}' + (n+2)P_{n-1}']\frac{Q_n'(i0)}{(2n+1)}\right\}.\end{aligned}\right\} \tag{19}$$

Equating coefficients of the same degree Legendre polynomials on both sides, we get

$$\left\{\begin{aligned} &f_n - \frac{(n-1)^3[(n-1)^2-1]Q_{n-1}(i0)}{a^2(2n-1)}a_{n-1}\\ &\qquad - \frac{2(\nu-1)n(n-1)^3(n-2)Q_{n-1}(i0)}{a^2(2n-1)}b_{n-1}\\ &g_n - \frac{(n-1)(n-2)^2Q_{n-1}'(i0)}{a^2(2n-1)}a_{n-1}\\ &\qquad - \frac{(2\nu-1)(n-1)(n-2)^2Q_{n-1}'(i0)}{a^2(2n-1)}b_{n-1}\end{aligned}\right\}$$

$$= \frac{1}{a^2(2n+3)}\begin{bmatrix}(n+1)^2[(n+1)^2-1](n+2)Q_{n+1}(i0) & n(n+1)^2(n+2)^2(2\nu-1)Q_{n+1}(i0)\\ n(n+1)(n+3)Q_{n+1}'(i0) & n(n+1)(n+3)(2\nu-1)Q_{n+1}'(i0)\end{bmatrix}\begin{Bmatrix}a_{n+1}\\ b_{n+1}\end{Bmatrix}$$

$$n = 1,2,\ldots \tag{20}$$

For the problems of practical interest the tractions on the two crack faces are equal in magnitude and opposite in sign. This means that $f(\eta)$ and $g(\eta)$ are even functions of η. It follows that the Legendre-Fourier expansion for $\eta^3 f(\eta)$ in (15) contains only odd degree Legendre polynomials while that for $(\eta^3/\sqrt{1-\eta^2})g(\eta)$ contains derivatives of only even degree polynomials. Thus $f_n = 0$ for even integers n while $g_n = 0$ for odd integers n. It further follows that a_{2n}, b_{2n} determined by (20) depend only on f_n while a_{2n+1}, b_{2n+1} depend only on g_n. These equations must be solved recursively. Nevertheless it is possible to write them in explicit form once the series has been truncated at a suitable integer $n = N$. It is useful to write the resulting system symbolically in matrix form as

$$\left.\begin{aligned}[A_{ij}^1]\{a_j\} + [A_{ij}^2]\{b_j\} &= \{f_i\}\\ [A_{ij}^3]\{a_j\} + [A_{ij}^4]\{b_j\} &= \{g_i\}\end{aligned}\right\}$$

$$i = 1,2,\ldots N. \tag{21}$$

Also we may represent the solution of these equations by

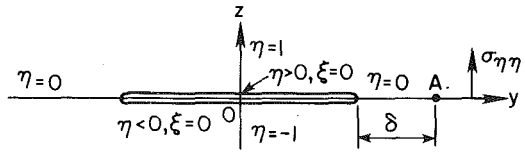

Fig. 1 The geometry of the crack

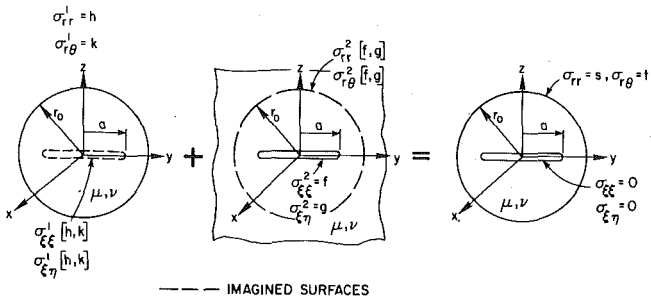

Fig. 2 The superposition of solutions S^1 and S^2

$$\left.\begin{aligned}\{a_i\} &= [\omega_{ij}^1]\{f_j\} + [\omega_{ij}^2]\{g_j\}\\ \{b_i\} &= [\omega_{ij}^3]\{f_j\} + [\omega_{ij}^4]\{g_j\}\end{aligned}\right\} i = 1,2,\ldots N \tag{22}$$

which formally completes the solution to the crack problem.

An alternate formulation of the crack problem rests on the known symmetry of the solutions and the fact that certain displacement components in the plane $\eta = 0$ must vanish. We can demonstrate that the solution just obtained satisfies these properties. In particular, consider the solution for the case $g(\eta) = 0$, that is, when the crack is opened by nonuniform pressure only. It can easily be shown by use of (4) and (5) in (8) and (10) that $u_\eta = 0$ at $\eta = 0$.

3 The Problem of a Cracked Sphere

The axisymmetric elastostatic problem of the cracked sphere is treated here by employing the axisymmetric solution for a sphere under tractions together with the solution given in the previous section for the tractions applied to the surface of a penny-shaped crack in an infinite medium. In order to superpose these two solutions we must make use of appropriate transformations, which allow us to pass from spherical polar to oblate spheroidal representations and vice-versa.

1 Statement of the Problem. We consider a homogeneous isotropic elastic sphere of radius r_0 which possesses a circular crack of radius a centered at the center of the sphere, oriented perpendicular to the symmetry axis and lying in the x, y plane. Assume the spherical surface is loaded with the general axisymmetric tractions

$$\left.\begin{aligned}\sigma_{rr}(r_0, p) = s(p) &= \sum_{n=0}^{\infty} s_nP_n(p)\\ \sigma_{r\theta}(r_0, p) = t(p) &= \overline{p}\sum_{n=1}^{\infty} t_nP_n'(p),\end{aligned}\right\} \tag{23}$$

where the coefficients of the Legendre-Fourier expansion s_n, t_n are determined as in (15). The surface of the crack is free of tractions, i.e. (see Fig. 1).

$$\sigma_{\xi\xi}(0, \eta) = \sigma_{\xi\eta}(0, \eta) = 0 \tag{24}$$

This problem is solved by superposing solutions as depicted in Fig. 2 and demanding that

$$\left.\begin{aligned}\sigma_{\xi\xi}^1[h, k] + f = 0,\ \sigma_{\xi\eta}^1[h, k] + g = 0 \quad &\text{at } \xi = 0,\\ h + \sigma_{rr}^2[f, g] = s,\ k + \sigma_{r\theta}^2[f, g] = t \quad &\text{at } r = r_0,\end{aligned}\right\} \tag{25}$$

Where superscript "1" denotes the uncracked sphere solution, for arbitrary *initially unknown* tractions represented by h, k and superscript "2" denotes the crack solution, given in the previous section

for arbitrary *initially unknown* tractions represented by f and g. These four unknown functions are determined by the four equations in (25), which result from the superposition

$$[S] = [S^1] + [S^2]. \tag{26}$$

2 Tractions on the Imagined Crack Face From the Uncracked Sphere Solution. Let the spherical surface be loaded with arbitrary axisymmetric tractions,

$$\left.\begin{aligned} \sigma^1_{rr}(r_0, p) &= h(p) = \sum_{n=0}^{\infty} h_n P_n(p) \\ \sigma^1_{r\theta}(r_0, p) &= k(p) = \bar{p} \sum_{n=1}^{\infty} k_n P'_n(p) \end{aligned}\right\} \tag{27}$$

Then the uncracked sphere solution as given by Sternberg, Eubanks, and Sadowsky [4], using solid spherical harmonics as Boussinesq potentials, has the form

$$[S^1] = \sum_{n=0}^{\infty} c_n[C_n] + d_n[D_n], \tag{28}$$

where $[C_n]$ are given by

$$2\mu u_r^{(n)} = nr^{n-1}P_n, \quad 2\mu u_\theta^{(n)} = -\bar{p}r^{n-1}P'_n \tag{29}$$

$$\left.\begin{aligned} \sigma_{rr}^{(n)} &= n(n-1)r^{n-2}P_n \\ \sigma_{\theta\theta}^{(n)} &= r^{n-2}[P'_{n-1} - n(n-1)P_n] \\ \sigma_{\phi\phi}^{(n)} &= r^{n-2}P'_{n-1} \\ \sigma_{r\theta}^{(n)} &= \bar{p}r^{n-2}(1-n)P'_n \end{aligned}\right\} \tag{30}$$

while the solutions $[D_n]$ are given by

$$\left.\begin{aligned} 2\mu u_r^{(n)} &= nr^n(n-3+4\nu)P_{n-1}, \\ 2\mu u_\theta^{(n)} &= -\bar{p}r^n(n+4-4\nu)P'_{n-1} \end{aligned}\right\} \tag{31}$$

$$\left.\begin{aligned} \sigma_{rr}^{(n)} &= nr^{n-1}[n(n-3) - 2\nu]P_{n-1} \\ \sigma_{\theta\theta}^{(n)} &= r^{n-1}\{(n+4-4\nu)P'_n - n[(n+1)^2 \\ &\qquad + (n+1) + 1 - 2\nu]P_{n-1}\} \\ \sigma_{\phi\phi}^{(n)} &= r^{n-1}[n(2n+1)(1-2\nu)P_{n-1} - (n+4-4\nu)P'_n] \\ \sigma_{r\theta}^{(n)} &= -\bar{p}r^{n-1}[(n+1)^2 - 2(n+1) - 1 + 2\nu]P'_{n-1}. \end{aligned}\right\} \tag{32}$$

In the equations (30) and (32) we observe that the solutions $[C_0]$, $[C_1]$, and $[D_0]$ correspond to vanishing stresses throughout the sphere, thus these solutions represent rigid displacement. Equilibrium requires that the tractions in (27) satisfy

$$h_1 - 2k_1 = 0 \tag{33}$$

and the coefficients c_n, d_n in (28) are determined in terms of h_n, k_n by

$$\left.\begin{aligned} c_n &= \\ &\frac{1}{r_0^{n-2}} \frac{[(n^2+2n-1+2\nu)h_n + (n+1)(n^2-n-2-2\nu)k_n]}{2(n-1)[n^2+n+1+(2n+1)\nu]} \\ &\qquad\qquad n = 2, 3 \ldots \\ d_{n+1} &= -\frac{h_n + nk_n}{2r_0^n[n^2+n+1+(2n+1)\nu]} \\ &\qquad\qquad n = 0, 1 \ldots \end{aligned}\right\} \tag{34}$$

The coefficients c_0, c_1, and d_0 are taken to be zero to eliminate arbitrary rigid displacements.

In order to find the tractions at the imagined crack surface in the uncracked sphere we must transform the solutions $[C_n]$ and $[D_n]$ into oblate spheroidal coordinates. This we do by first transforming the interior spherical harmonics $r^nP_n(p)$ into their oblate spheroidal forms (see [5, Appendix B] for the derivation of this transformation).

$$r^nP_n(p) = \frac{a^n}{i^n} \sum_{k=0}^{n} \theta_k^n P_k(\eta)P_k(i\xi) \tag{35}$$

where a is the crack radius, $i = \sqrt{-1}$, and

$$\theta_k^n = \int_{-1}^{1} \tau^n P_k(\tau)d\tau$$

The oblate spheroidal form of the solid spherical harmonics is then used in (6) and (7) referred to their oblate spheroidal form [6]. This computation yields the oblate spheroidal form of $[C_n]$ and $[D_n]$. Substitution of these transformed Boussinesq stress functions into (28) enables us to determine the tractions at the imagined crack faces $\xi = 0$.

$$\begin{aligned} \sigma^1_{\xi\xi}(0, \eta) = \frac{1}{\eta^3} \sum_{n=0}^{\infty} \Big\{ & c_n \sum_{q=0}^{n} [\epsilon_1(n, q)P_{q+1}(\eta) + \epsilon_2(n, q)P_{q-1}(\eta)] \\ & + d_n \sum_{q=0}^{n} [\delta_1(n, q)P_{q+2}(\eta) + \delta_2(n, q)P_q(\eta) \\ & + \delta_3(n, q)P_{q-2}(\eta)] \Big\} \\ \sigma^1_{\xi\eta}(0, \eta) = \frac{\sqrt{1-\eta^2}}{\eta^3} \sum_{n=0}^{\infty} \Big\{ & c_n \sum_{q=0}^{n} [\epsilon_3(n, q)P'_{q+1}(\eta) \\ & + \epsilon_4(n, q)P'_{q-1}(\eta)] \\ & + d_n \sum_{q=0}^{n} [\delta_4(n, q)P'_{q+2} + \delta_5(n, q)P'_q + \delta_6(n, q)P'_{q-2}] \Big\} \end{aligned} \tag{36}$$

where

$$\begin{aligned} &\epsilon_1(n, q) = \tau_1(n, q)q, \qquad \epsilon_3(n, q) = \tau_2(n, q)(q-1), \\ &\epsilon_2(n, q) = \tau_1(n, q)(q+1), \; \epsilon_4(n, q) = \tau_2(n, q)(q+1), \\ &\delta_1(n, q) = \tau_3(n, q)(q^2+3q+2) - (n-3+4\nu)\epsilon_1(n+1, q+1), \\ &\delta_2(n, q) = \frac{\tau_3(n, q)(4q^3+6q^2-1)}{(2q-1)} - (n-3+4\nu)\epsilon_2(n+1, q+1), \\ &\delta_3(n, q) = \frac{\tau_3(n, q)(2q^3-q^2+3q)}{(2q-1)} \\ &\delta_4(n, q) = \tau_4(n, q)(q^2+q) - (n-3+4\nu)\epsilon_3(n+1, q+1), \\ &\delta_5(n, q) = \tau_4(n, q)(2q^2-3) - (n-3+4\nu)\epsilon_4(n+1, q+1), \\ &\delta_6(n, q) = \frac{\tau_4(n, q)(2q^3+5q^2+3q)}{(2q-1)}, \\ &\tau_1(n, q) = \frac{q(q+1)a^{n-2}\theta_q^n P_q(i0)}{(2q+1)i^n}, \\ &\tau_2(n, q) = \frac{a^{n-2}\theta_q^n P'_q(i0)}{i^n(2q+1)}, \\ &\tau_3(n, q) = \frac{2(\nu-1)(2n+1)a^{n-1}\theta_q^n P'_q(i0)}{(2q+1)(2q+3)i^n}, \\ &\tau_4(n, q) = \frac{(2\nu-1)(2n+1)a^{n-1}\theta_q^n P_q(i0)}{(2q+3)(2q+1)i^n}. \end{aligned} \tag{37}$$

Equations (36) can be written symbolically in matrix form as

$$\begin{aligned} \sigma^1_{\xi\xi}(0, \eta) &= \{P_n(\eta)\}\{([\alpha^1_{ni}]\{c_i\} + [\beta^1_{ni}]\{d_i\})\}\frac{1}{\eta^3} \\ \sigma^1_{\xi\eta}(0, \eta) &= \frac{\sqrt{1-\eta^2}}{\eta^3}\{P'_n(\eta)\}\{([\gamma^1_{ni}]\{c_i\} + [\zeta^1_{ni}]\{d_i\})\} \end{aligned} \tag{38}$$

By the use of (34), we may substitute for c_i and d_i in terms of h_i, k_i, the coefficients of the unknown prescribed tractions on the spherical surface. But we find it more convenient to work with the coefficients of superposition c_i, d_i.

3 Tractions at the Imagined Spherical Surface From the Solution for a Crack in the Infinite Medium. The axisymmetric solution for a crack in an infinite medium was given in the previous section in a form that is useful for our purposes. For normal and shearing tractions on the crack face given by $f(\eta)$ and $g(\eta)$, respectively, with Legendre-Fourier expansions given by (15) the solution $[S^2]$ is given in the form

$$[S^2] = \sum_{n=0}^{\infty} a_n[A_n] + b_n[B_n] \tag{39}$$

with a_n, b_n determined in terms of f_n, g_n by equation (20).

In order to determine normal and shearing stresses at an imagined spherical surface, we must transform solutions $[A_n]$, $[B_n]$ used in (18) into spherical polar coordinates. This is accomplished with the aid of the following transformation for exterior oblate spheroidal harmonics (see [5, Appendix B] for the derivation of this expression)

$$P_n(\eta)Q_n(i\xi) = \frac{2^n(n!)^2}{i^{n+1}(2n+1)!}\sum_{m=0}^{\infty} M_m^n \left(\frac{a}{r}\right)^{2m+n+1} P_{2m+n}(p) \tag{40}$$

in which M_m^n are the coefficients of the series for the hypergeometric function

$$F\left[\frac{n+1}{2}, \frac{n+2}{2}; n+\frac{3}{2}, \left(\frac{iX}{a}\right)^2\right]$$

defined by

$$F[a, b; c, x] = 1 + \frac{ab}{c}x + \frac{ab}{c}\frac{(a+1)(b+1)}{(c+1)}\frac{x^2}{2!} + \ldots = 1 + M_1^{(a,b,c)}x + M_2^{(a,b,c)}x^2 + \ldots \tag{41}$$

and

$$X = z + i(x\cos u + y \sin u)$$

This spherical polar form (40) of the exterior oblate spheroidal harmonics is then used in (6) and (7) referred to their spherical polar form. This computation yields the spherical polar form of $[A_n]$, $[B_n]$. Substitution of these Boussinesq stress functions into (39) enables us to determine the tractions at the imagined spherical surface r = r_0.

$$\sigma_{rr}^2(r_0, p) = \sum_{n=0}^{\infty}\sum_{m=0}^{\infty}\{a_n f_1(m, n)P_{2m+n}(p) + b_n[f_2(m, n)P_{2m+n}(p) + f_3(m, n)P_{2m+n+2}(p)]\} \tag{42}$$

$$\sigma_{r\theta}^2(r_0, p) = \bar{p}\sum_{n=0}^{\infty}\sum_{m=0}^{\infty}\{a_n\bar{f}_1(m, n)P'_{2m+n}(p) + b_n[\bar{f}_2(m, n)P'_{2m+n}(p) + \bar{f}_3(m, n)P'_{2m+n+2}(p)]\}$$

where

$$f_1(m, n) = n(n-1)G(n)M_m^n(2m+n+1)(2m+n+2)\frac{a^{2m+n+1}}{r_0^{2m+n+3}},$$

$$f_2(m, n) = -\frac{(2m+n+1)(2m+n+5-4\nu)}{(4m+2n+3)}f_1(m, n),$$

$$f_3(m, n) = -\frac{[(2m+n+2)(2m+n+5)-2\nu]}{(4m+2n+3)}f_1(m, n),$$

$$\bar{f}_1(m, n) = n(n-1)G(n)M_m^n(2m+n+2)\frac{a^{2m+n+1}}{r_0^{2m+n+3}}, \tag{43}$$

$$\bar{f}_2(m, n) = -\frac{(2m+n+1)(2m+n+5-4\nu)}{(4m+n+3)}\bar{f}_1(m, n),$$

$$\bar{f}_3(m, n) = -\frac{[(2m+n+1)^2 + 2(2m+n+1) - 1 + 2\nu](2m+n+1)}{(4m+n+3)(2m+n+2)} \times \bar{f}_1(m, n)$$

$$G(n) = [2^n(n!)^2]/i^{n+1}(2n+1)!$$

Upon collecting coefficients of $P_n(p)$ and $P'_n(p)$ in (42) and arranging them in matrix form, we find

$$\sigma_{rr}^2(r_0, p) = \{P_n\}\{([\alpha_{ni}^2]\{a_i\} + [\beta_{ni}^2]\{b_i\})\}$$
$$\sigma_{r\theta}^2(r_0, p) = \bar{p}\{P'_n\}\{([\gamma_{ni}^2]\{a_i\} + [\zeta_{ni}^2]\{b_i\})\} \tag{44}$$

By use of (22) we may substitute for a_i, b_i in terms of f_n, g_n, the coefficients of the unknown prescribed tractions on the crack face, to obtain

$$\sigma_{rr}^2(r_0, p) = \{P_n\}\{([\alpha_{ni}^2][\omega_{ij}^1] + [\beta_{ni}^2][\omega_{ij}^3])\{f_j\} + ([\alpha_{ni}^2][\omega_{ij}^2] + [\beta_{ni}^2][\omega_{ij}^4])\{g_j\}\} \tag{45}$$

$$\sigma_{r\theta}^2(r_0, p) = \bar{p}\{P'_n\}\{([\gamma_{ni}^2][\omega_{ij}^1] + [\zeta_{ni}^2][\omega_{ij}^3])\{f_j\} + ([\gamma_{ni}^2][\omega_{ij}^2] + [\zeta_{ni}^2][\omega_{ij}^4])\{g_j\}\}$$

4 Superposition of the Two Solutions. The superposition given in (25) determines $f(\eta)$, $g(\eta)$, $h(p)$, $k(p)$ so that the prescribed boundary conditions at the crack face, and the spherical surface are satisfied. The conditions at the crack face given in the first and second of (25), with (38) and (12), (15) yield

$$\left.\begin{aligned}\{f_n\} &= -[\alpha_{ni}^1]\{c_i\} - [\beta_{ni}^1]\{d_i\}\\ \{g_n\} &= -[\gamma_{ni}^1]\{c_i\} - [\zeta_{ni}^1]\{d_i\}.\end{aligned}\right\} \tag{46}$$

The conditions at the surface given in the third and fourth of (25) with (22), (44), (45), and (46) yield

$$\begin{aligned}&\{([\alpha_{ij}^2][\omega_{jk}^1] + [\beta_{ij}^2][\omega_{jk}^3])[-\alpha_{kn}^1] + ([\alpha_{ij}^2][\omega_{jk}^2] + [\beta_{ij}^2][\omega_{jk}^4])[-\gamma_{kn}^1] + [I_{in}]\}\{c_i\}\\ &\quad + \{([\alpha_{ij}^2][\omega_{jk}^1] + [\beta_{ij}^2][\omega_{jk}^3])[-\beta_{kn}^1] + ([\alpha_{ij}^2][\omega_{jk}^2] + [\beta_{ij}^2][\omega_{jk}^4])[-\zeta_{kn}^1] + [J_{in}]\}\{d_i\} = \{s_n\}\\ &\{([\gamma_{ij}^2][\omega_{jk}^1] + [\zeta_{ij}^2][\omega_{jk}^3])[-\alpha_{kn}^1] + ([\gamma_{ij}^2][\omega_{jk}^2] + [\zeta_{ij}^2][\omega_{jk}^4])[-\gamma_{kn}^1] + [F_{in}]\}\{c_i\}\\ &\quad + \{([\gamma_{ij}^2][\omega_{jk}^1] + [\zeta_{ij}^2][\omega_{jk}^3])[-\beta_{kn}^1] + ([\gamma_{ij}^2][\omega_{jk}^2] + [\zeta_{ij}^2][\omega_{jk}^4])[-\zeta_{kn}^1] + [G_{in}]\}\{d_i\} = \{t_n\}\end{aligned} \tag{47}$$

where $[I]$, $[J]$, $[F]$, and $[G]$ are defined, from (27)–(31), as follows:

$$\sigma_{rr}^1(r_0, p) = \{P_n\}\{[I_{ni}]\{c_i\} + [J_{ni}]\{d_i\}\}$$
$$\sigma_{r\theta}^1(r_0, p) = \bar{p}\{P'_n\}\{[F_{ni}]\{c_i\} + [G_{ni}]\{d_i\}\} \tag{48}$$

These equations determine the coefficients c_i, d_i for given prescribed traction coefficients $\{s_n\}$ and $\{t_n\}$. The tractions prescribed on the spherical surface of solution S^1 are then determined by using (30) and (32) in (28). Likewise the functions $f(\eta)$, $g(\eta)$ which represent tractions on the crack face are obtained from (46) and (15).

The implied computations were carried out in [5] for several particular loadings on the cracked sphere. In each case the series were truncated with sufficient accuracy after 22 terms. Here we present results only for the case of

Radial Tensile Tractions Near the Poles. In this case the applied tractions were chosen as

$$\sigma_{rr}(r_0, p) = s(p) = \begin{cases}(1+\cos 5\theta)/2, & 0 \le \theta \le 36°\\ & 144° \le \theta \le 180°\\ 0, & \text{otherwise}\end{cases} \tag{49}$$

$$\sigma_{r\theta}(r_0, p) = t(p) = 0$$

While this loading is somewhat artificial and of little physical relevance it represents a crude approximation to the problem of concentrated loads at the poles and therefore allows comparison with the results of Rosenthal and Sternberg [8] in the limit of a small crack. Comparisons of this type are needed in order to test the suitability of the solution derived here for numerical computations in the case of more general loading. We also derive, in the context of this example, asymptotic results needed for calculating stress-concentration factors from our solution. The results are summarized in Figs. 3 and 4. In Fig. 3 the normal stress on the equitorial plane is shown for the four values

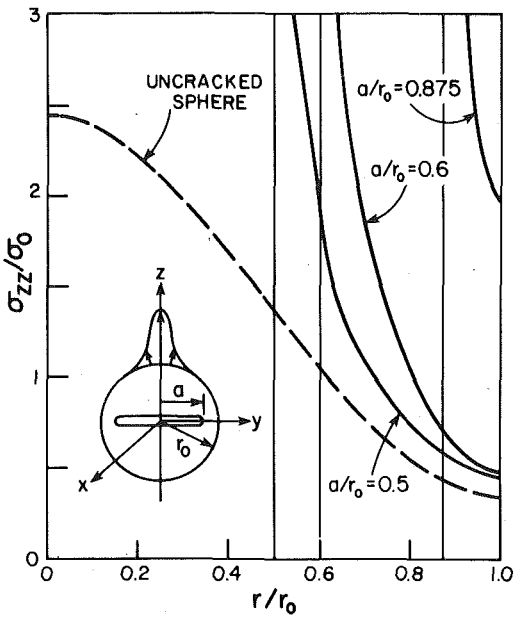

Fig. 3 Normal stresses on the equator plane for tensile tractions near the poles ($r_0 = 2$, $\nu = 0.25$, σ_0 = Total load/πr_0^2)

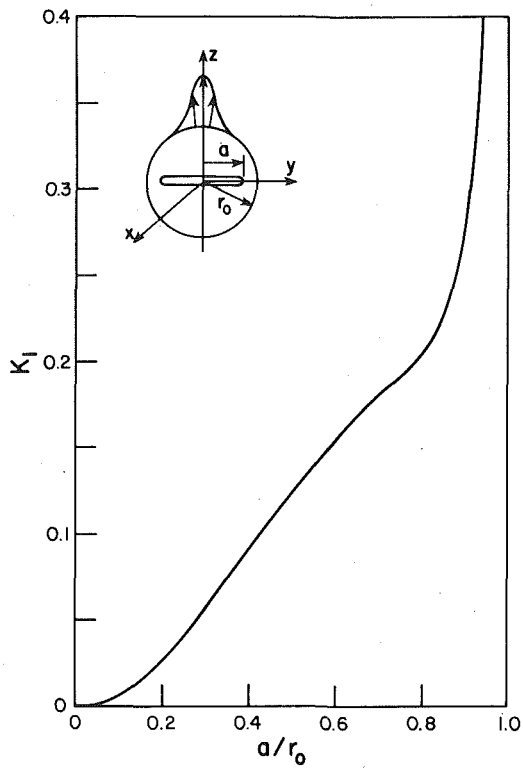

Fig. 4 Variation with a/r_0 of the increase in the stress-intensity factor for radial tensile tractions near the poles ($r_0 = 2$, $\nu = 0.25$)

of $a/r_0 = 0, 0.05, 0.6, 0.875$. For $a/r_0 = 0$, the sphere has no crack and the normal stress distribution varies only slightly from the results for concentrated radial loads applied at the poles given by Rosenthal and Sternberg [8]. For the other values of a/r_0 the normal stress vanishes on the crack face, is unbounded at the crack tip, and monotonically decreases with the radius outside the crack. As the crack radius approaches that of the sphere the tensile stress at $r = r_0$ becomes unbounded. This trend can be seen in Fig. 3.

The stress-intensity factor for the cracked sphere is calculated on the basis of the results derived for the crack in the infinite medium since in the superposition the solution S^1 is everywhere bounded and a singularity occurs only in S^2. Consider a point A on the plane $\eta = 0$ at a distance δ from the crack tip (Fig. 1). The value of the coordinate ξ at this point is

$$\xi \simeq \left(\frac{2\delta}{a}\right)^{1/2}, \tag{50}$$

and the stress-intensity factor is defined as

$$K_1 = \lim_{\delta \to 0} (2\delta)^{1/2} \sigma_{\eta\eta}(\xi, 0). \tag{51}$$

Using (9) and (11) in conjunction with (4), (5) and (15), we obtain from (18)

$$\sigma_{\eta\eta}(\xi, 0) = \sum_{n=0}^{\infty} \{a_n + 2((\nu - 1)b_n\} \frac{n(n-1)}{a^2} \times \left[\frac{1+\xi^2}{\xi^3} Q_n'(i\xi) - \frac{n(n+1)Q_n(i\xi)}{\xi^2}\right] P_n(0). \tag{52}$$

in which a_n, b_n are determined by (20). By use of the Legendre equation and recursion relation for $Q_n(i\xi)$ we obtain the following asymptotic expression, for all even n:

$$\frac{1+\xi^2}{\xi^3} Q_n'(i\xi) - \frac{n(n+1)Q_n(i\xi)}{\xi^2} = G(n) i\xi^{-2} + O(1) \quad \text{as} \quad \xi \to 0 \tag{53}$$

in which $G(n)$ is obtained from the recursion relations for $Q_n(i\xi)$. Therefore

$$\sigma_{\eta\eta}(\xi, 0) = \sum_{n=0}^{\infty} \{a_n + 2(\nu - 1)b_n\} \frac{n(n-1)}{a^2} \times [G(n) i\xi^{-1} + O(1)] P_n(0) \quad \text{as} \quad \xi \to 0 \tag{54}$$

In the particular case when the crack in the half space is opened by uniform pressure p_0 the series terminates at $n = 2$ and the quantity $G(2)$ equals $-3/2$, so that in this case

$$a_2 + 2(\nu - 1)b_2 = -p_0 a^2 / 3\pi. \tag{55}$$

Use of (55) in (54) in conjunction with (50) and (51) yields the stress-intensity factor for the case of a uniformly loaded crack in an infinite medium in agreement with known results. In the case of the sphere the stress-intensity factor is obtained from (54) and (51) with a_n, b_n, determined from the values of c_n and d_n obtained from (47) and their use in (46) and then (22). For the loading in (49) the stress-intensity factor K_1 is plotted as a function of a/r_0. As can be seen K_1 is monotonically increasing with a/r_0 and becomes unbounded as $a/r_0 \to 1$.

Other loading cases considered in [5] include a radial compressive ring load near the equator and the case of uniform radial tension on the spherical surface. In both of these cases the crack face is traction-free. The case of a pressurized crack with a traction-free spherical surface is also considered in [5]. This problem differs from the uniform radial tension case only by a uniform uniaxial stress state, but the computations used were entirely different. The agreement of the results gave added confidence in the numerical procedure and degree of accuracy. These results are omitted here for the sake of brevity. Readers interested in these solutions are referred to [5].

Acknowledgment

The authors wish to thank Dr. M. A. Hamstad for suggesting this problem and for his interest and helpful discussions. The support of Lawrence Livermore Laboratory is also gratefully acknowledged.

References

1 Bianchetti, R., Hamstad, M. A., and Mukherjee, A. K., "Origin of Burst-Type Acoustic Emission in Unflawed 7075-76 Aluminum," *Journal of Testing and Evaluation*, Vol. 4, No. 5, Sept. 1976, pp. 313–318.

2 Erdogan, F., and Gupta, G. D., "The Inclusion With a Crack Crossing the Boundary," *International Journal of Fracture Mechanics*, Vol. 11, No. 1, Feb. 1975.

3 Sack, R. A., "Extension of Griffith's Theory of Rupture to Three Dimensions," *Proceedings of the Physical Society,* Vol. 58, 1946.

4 Sternberg, E., Eubanks, R. A., and Sadowsky, M. A., "On the Axisymmetric Problem of Elasticity Theory for a Region Bounded by Two Concentric Spheres," *Proceedings of the First National Conference of Applied Mechanics,* 1951, pp. 209–215.

5 Kant, R., "The Elastostatic Axisymmetric Problem of Cracked Sphere Embedded in a Dissimilar Matrix," PhD Thesis, Mechanical Engineering Department, University of California, Berkeley, 1979.

6 Sadowsky, M. A., and Sternberg, E., "Stress Concentration Around a Triaxial Ellipsoidal Cavity," ASME JOURNAL OF APPLIED MECHANICS, Vol. 16, No. 2, 1949.

7 Morse, P. M., and Feshback, H., *Methods of Theoretical Physics,* Vols. 1 and 2, McGraw-Hill, New York, 1953.

8 Sternberg, and Rosenthal, F., "The Elastic Sphere Under Concentrated Loads," ASME JOURNAL OF APPLIED MECHANICS, Vol. 19, 1952, pp. 413–419.

R. Kant[1]
Graduate Research Assistant.

D. B. Bogy
Professor of Applied Mechanics.
Mem. ASME

Department of Mechanical Engineering,
University of California,
Berkeley, Calif. 94720

The Elastostatic Axisymmetric Problem of a Cracked Sphere Embedded in a Dissimilar Matrix

The axisymmetric elastostatic problem of a cracked sphere embedded in a dissimilar matrix is solved by using the solution for a spherical cavity in an infinite medium together with the axisymmetric solution for a cracked sphere given in the companion paper in this issue of the JOURNAL OF APPLIED MECHANICS, *Pages 538–544. Numerical results are presented for (a) interface stress for various composites (b) dependence of the stress-intensity factor on the material parameters and ratios of crack to sphere radii, (c) the difference in the elastic strain energy for a cracked and uncracked composite.*

1 Introduction

The aim of this investigation is to calculate the amount of energy released when a crack forms in a spherical inclusion when the dissimilar matrix is loaded in uniaxial tension at points remote from the inclusion. The fracture of such brittle inclusions has been observed by Bianchetti, et al. [1], and these fracture events release energy in the form of elastic wave motion that can be detected by electromechanical transducers attached to the specimen. The nondestructive testing technique known as "acoustic emission" is used to observe the motion. In order for this technique to be useful in the characterization as well as location of such "mini earthquakes" the procedure needs to be calibrated. Such a calibration process will be aided by an estimate of the energy released in an event that is subsequently detected.

The basic elasticity problem to be solved is that of the cracked spherical inclusion. In [2], the problem of a cracked sphere with arbitrary axisymmetric tractions on its surface was solved. This solution is used here in conjunction with the solution for the opposite tractions applied to a spherical cavity in an infinite medium to solve the composite problem of a cracked spherical inclusion. The geometry and coordinate systems employed are defined in [2], and this reference will be used here as if it were part of the present paper to avoid unnecessary repetition.

2 Cracked Sphere Embedded in a Dissimilar Matrix

1 Statement of the Problem. Consider the sphere, with elastic constants ν', μ', of radius r_0 containing a penny-shaped crack of radius a lying axisymmetrically in the x-y plane with the crack faces traction-free. Suppose this cracked sphere is embedded in a dissimilar matrix with elastic constants ν'', μ'', and assume a biaxial stress state exists at distances remote from the sphere. Then the regularity, interface, and boundary conditions are given by

$$\sigma''_{zz} \to T_1, \quad \sigma''_{xx} = \sigma''_{yy} \to T_2 \quad \text{as} \quad r \to \infty \tag{1}$$

$$\begin{aligned} \sigma'_{rr}(r_0,p) &= \sigma''_{rr}(r_0,p) \quad u'_r(r_0,p) = u''_r(r_0,p) \\ \sigma'_{r\theta}(r_0,p) &= \sigma''_{r\theta}(r_0,p) \quad u'_\theta(r_0,p) = u''_\theta(r_0,p) \end{aligned} \tag{2}$$

and

$$\sigma'_{\xi\xi}(0,\eta) = \sigma'_{\xi\eta}(0,\eta) = 0. \tag{3}$$

First assume that the interface stresses in (2) have the following Legendre-Fourier representations:

$$\begin{aligned} \sigma'_{rr}(r_0,p) = \sigma''_{rr}(r_0,p) &= s(p) = \sum_{n=0}^{\infty} s_n P_n(p) \\ \sigma'_{r\theta}(r_0,p) = \sigma''_{r\theta}(r_0,p) &= t(p) = \overline{p} \sum_{n=0}^{\infty} t_n P'_n(p) \\ p = \cos\theta, \quad \overline{p} &= \sin\theta. \end{aligned} \tag{4}$$

In these expressions x, y, z represent Cartesian coordinates, r, θ, ϕ are spherical polar coordinates and ξ, η, ϕ are oblate spheroidal coordinates defined in (1) of [2].

Next the displacements u''_r, u''_θ must be obtained from the solution for a spherical cavity in the infinite medium ν'', μ'' loaded at infinity as in (1) and at the surface $r = r_0$ as in (4). Also u'_r, u'_θ in (2) are obtained from the solution of the cracked sphere presented in [2].

2 The Spherical Cavity Solution. Consider the axisymmetric problem of a spherical cavity in an infinite medium defined by the boundary and regularity conditions

$$\begin{aligned} \sigma_{rr}(r_0,p) &= h(p) = \sum_{n=0}^{\infty} h_n P_n(p), \\ \sigma_{r\theta}(r_0,p) &= k(p) = \overline{p} \sum_{n=1}^{\infty} k_n P'_n(p), \end{aligned} \tag{5}$$

[1] Now at Bell Laboratories, Whippany, N.J. 07981.

Contributed by the Applied Mechanics Division for publication in the JOURNAL OF APPLIED MECHANICS.

Discussion on this paper should be addressed to the Editorial Department, ASME, United Engineering Center, 345 East 47th Street, New York, N. Y. 10017, and will be accepted until December 1, 1980. Readers who need more time to prepare a discussion should request an extension from the Editorial Department. Manuscript received by ASME Applied Mechanics Division, September, 1979; final revision, January, 1980.

and

$$\sigma_{ij} \to 0 \quad \text{as} \quad r \to \infty. \tag{6}$$

The Legendre-Fourier coefficients h_n, k_n in (5) are given in terms of $h(p)$ and $k(p)$ by

$$h_n = \frac{2n+1}{2}\int_{-1}^{1} h(p)P_n(p)dp,$$

$$k_n = \frac{(2n+1)}{2}\frac{(n-1)!}{(n+1)!}\int_{-1}^{1} \bar{p}k(p)P_n'(p)dp. \tag{7}$$

The solution of this problem is given by Sternberg, Eubanks, and Sadowsky [3] and has the following form:

$$[S] = \sum_{n=0}^{\infty} c_n[C_n] + d_n[D_n] \tag{8}$$

where $[C_n]$ are given by

$$2\mu u_r^{(n)} = -\frac{(n+1)}{r^{n+2}}P_n, \quad 2\mu u_\theta^{(n)} = -\frac{\bar{p}P_n'}{r^{n+2}} \tag{9}$$

$$\left.\begin{aligned}
\sigma_{rr}^{(n)} &= \frac{(n+1)(n+2)}{r^{n+3}}P_n \\
\sigma_{r\theta}^{(n)} &= \frac{(n+2)}{r^{n+3}}\bar{p}P_n \\
\sigma_{\theta\theta}^{(n)} &= \frac{1}{r^{n+3}}[P_{n+1}' - (n+1)(n+2)P_n] \\
\sigma_{\phi\phi}^{(n)} &= -\frac{P_{n+1}'}{r^{n+3}}
\end{aligned}\right\} \tag{10}$$

while the solutions $[D_n]$ are given by

$$\left.\begin{aligned}
2\mu u_r^{(n)} &= -\frac{(n+1)(n+4-4\nu)}{r^{n+1}}P_{n+1} \\
2\mu u_\theta^{(n)} &= -\frac{\bar{p}(n-3+4\nu)}{r^{n+1}}P_{n+1}'
\end{aligned}\right\} \tag{11}$$

$$\left.\begin{aligned}
\sigma_{rr}^{(n)} &= (n+1)[(n+1)(n+4)-2\nu]\frac{P_{n+1}}{r^{n+2}} \\
\sigma_{r\theta}^{(n)} &= (n^2+2n-1+2\nu)\bar{p}\frac{P_{n+1}}{r^{n+2}} \\
\sigma_{\theta\theta}^{(n)} &= \frac{-1}{r^{n+2}}[(n+1)(n^2-n+1-2\nu)P_{n+1} \\
&\quad -(n-3+4\nu)P_n'] \\
\sigma_{\phi\phi}^{(n)} &= \frac{-1}{r^{n+2}}[(1-2\nu)(n+1)(2n+1)P_{n+1} + (n-3+4\nu)P_n']
\end{aligned}\right\} \tag{12}$$

Application of the boundary conditions (5) at $r = r_0$ in (8) and use of (10), (12) give a system of linear algebraic equations for the coefficients of superposition in terms of h_n, k_n. The solution of this system yields

$$c_n = -\frac{[(n^2-2+2\nu)h_n - n(n^2+3n-2\nu)k_n]}{2(n+2)[n^2+n+1-(2n+1)\nu]}r_0^{n+3};$$

$$n = 0, 1, \ldots,$$

$$d_{n-1} = \frac{[h_n - (n+1)k_n]r_0^{n+1}}{2[n^2+n+1-(2n+1)\nu]}; \quad n = 1, \ldots \tag{13}$$

3 Interface Displacements From the Spherical Cavity Solution With Biaxial Loads at Infinity. Let S^0 represent the homogeneous stress-state solution corresponding to (1). Then the desired exterior solution S'' is given by

$$[S''] = [S^0] + [\hat{S}] \tag{14}$$

where $\hat{S}$ is the solution outlined in Section 2 that satisfies the boundary conditions

$$\begin{aligned}
\hat{\sigma}_{rr}(r_0,p) &= s(p) - T_2\bar{p}^2 - T_1p^2 \\
&= \sum_{n=0}^{\infty} s_nP_n(p) - \frac{1}{3}(T_1+2T_2)P_0(p) + \frac{2}{3}(T_1-T_2)P_2(p) \\
&= \sum_{n=0}^{\infty} \hat{s}_nP_n(p) \\
\hat{\sigma}_{r\theta}(r_0,p) &= t(p) + (T_1-T_2)p\bar{p} \\
&= \bar{p}\left[\sum_{n=1}^{\infty} t_nP_n'(p) + \frac{1}{3}(T_1-T_2)P_2'(p)\right] \\
&= \bar{p}\sum_{n=1}^{\infty} \hat{t}_nP_n'(p)
\end{aligned} \tag{15}$$

The displacement components from the homogeneous state S^0 are

$$u_r^0(r_0,p) = \frac{r_0(T_1+2T_1)(1-2\nu'')}{6\mu''(1+\nu'')}P_0(p) + \frac{r_0(T_1-T_2)}{3\mu''}P_2(p)$$

$$u_\theta^0(r_0,p) = \bar{p}\frac{r_0(T_2-T_1)}{6\mu''}P_2'(p) \tag{16}$$

and the corresponding displacements from the asymmetric state $\hat{S}$ are

$$\begin{aligned}
2\mu''\hat{u}_r(r_0,p) &= \sum_{n=0}^{\infty}[\hat{U}_n\hat{c}_n + \hat{V}_{n-1}\hat{d}_{n-1}]P_n(p) \\
2\mu''\hat{u}_\theta(r_0,p) &= \bar{p}\sum_{n=1}^{\infty}[\hat{X}_n\hat{c}_n + \hat{Y}_{n-1}\hat{d}_{n-1}]P_n'(p)
\end{aligned} \tag{17}$$

where

$$\hat{U}_n = -\frac{(n+1)}{r_0^{n+2}}, \quad \hat{V}_n = -\frac{(n+1)(n+4-4\nu'')}{r_0^{n+1}}$$

$$\hat{X}_n = -\frac{1}{r^{n+2}}, \quad \hat{Y}_n = -\frac{(n-3+4\nu'')}{r_0^{n+1}}$$

and $\hat{c}_n$, $\hat{d}_n$ are the coefficients of superposition determined by (13) with h_n, k_n replaced by $\hat{s}_n$, $\hat{t}_n$ of (15). With the use of (14)–(17) and (13) we can express the displacement components at the spherical surface from the solution S'' in terms of coefficients s_n, t_n of the Legendre Fourier expansion of the interface tractions as

$$\begin{aligned}
2\mu''u_r''(r_0,p) &= \frac{r_0(T_1+2T_2)(1-\nu'')}{2(1+\nu'')}P_0(p) \\
&\quad + \frac{10r_0(T_1-T_2)(1-\nu'')}{(7-5\nu'')}P_2(p) \\
&\quad + \sum_{n=0}^{\infty}(E_ns_n + F_nt_n)P_n(p) \\
2\mu''u_\theta''(r_0,p) &= \bar{p}\frac{5r_0(T_2-T_1)(1-\nu'')}{(7-5\nu'')}P_2'(p) \\
&\quad + \bar{p}\sum_{n=0}^{\infty}(G_ns_n + H_nt_n)P_n'(p)
\end{aligned} \tag{18}$$

4 Interface Displacements From the Cracked Sphere Solution. The solution to the cracked sphere problem is presented in [2]. Recall that the desired solution S' was obtained there by superposition of two solutions S^1 and S^2

$$[S'] = [S^1] + [S^2] \tag{19}$$

where S^1 and S^2 are the solutions for an axisymmetrically loaded uncracked sphere and a crack in an infinite medium, respectively. The interface displacement components corresponding to the solution S^1 are

$$\begin{aligned}
2\mu' u_r^1(r_0,p) &= \sum_{n=0}^{\infty}[U_n^1c_n^1 + V_{n+1}^1d_{n+1}^1]P_n(p) \\
2\mu' u_\theta^1(r_0,p) &= \bar{p}\sum_{n=0}^{\infty}[X_n^1c_n^1 + Y_{n+1}^1d_{n+1}^1]P_n'(p)
\end{aligned} \tag{20}$$

where c_n^1 and d_{n+1}^1 are the coefficients of superposition determined by (34) of [2] and

$$U_n^1 = nr_0^{n-1}, \quad V_n^1 = nr_0^n(n-3+4\nu') \tag{21}$$
$$X_n^1 = -r_0^{n-1}, \quad Y_n^1 = r_0^n(n+4-4\nu')$$

Likewise the interface displacements corresponding to S^2 are

$$2\mu' u_r^2(r_0,p) = \sum_{n=0}^{\infty}\sum_{m=0}^{\infty}[a_n f_1'(m,n)P_{2m+n} + c_n\{f_2'(m,n)P_{2m+n} + f_3'(m,n)P_{2m+n+2}\}]$$
$$2\mu' u_\theta^2(r_0,p) = \bar{p}\sum_{n=0}^{\infty}\sum_{m=0}^{\infty}[a_n \bar{f}_1'(m,n)P'_{2m+n}(p) + c_n\{\bar{f}_2'(m,n)P_{2m+n} + \bar{f}_3'(m,n)P'_{2m+n+2}(p)\}] \tag{22}$$

where

$$f_1'(m,n) = -n(n-1)G(n)M_m^n \frac{a^{2m+n+1}}{r_0^{2m+n+2}}(2m+n+1),$$
$$f_2'(m,n) = -\frac{(2m+n+5-4\nu')(2m+n+1)}{(4m+2n+3)} f_1'(m,n),$$
$$f_3'(m,n) = -\frac{(2m+n+5-4\nu')(2m+n+2)}{(4m+2n+3)} f_1'(m,n),$$
$$\bar{f}_1'(m,n) = -n(n-1)G(n)M_m^n \frac{a^{2m+n+1}}{r_0^{2m+n+2}},$$
$$\bar{f}_2'(m,n) = -\frac{(2m+n+1)[2m+n+1+4(1-\nu')]}{(4m+2n+3)} \bar{f}_1'(m,n),$$
$$\bar{f}_3'(m,n) = -\frac{(2m+n+1)[2m+n+2-4(1-\nu')]}{(4m+2n+3)} \bar{f}_1'(m,n). \tag{23}$$

$G(n)$ and M_m^n are defined in (41) and (43) (all of [2]). The equations (22) can be expressed as

$$2\mu' u_r^2(r_0,p) = \sum_{n=0}^{\infty}\sum_{m=0,1}^{n}[W_{nm}^1 a_m P_n(p) + W_{nm}^2 b_m P_n(p)]$$
$$2\mu' u_\theta^2(r_0,p) = \bar{p}\sum_{n=0}^{\infty}\sum_{m=0,1}^{n}[W_{nm}^3 a_m P_n'(p) + W_{nm}^4 b_m P_n'(p)] \tag{24}$$

In these equations m is even or odd according as n is even or odd, $n \geq m$. With the aid of (22), (46), and (47) (all of [2]) the equations (24) can be expressed in terms of the coefficients of the interface tractions s_n, t_n. This computation yields the form

$$2\mu' u_r^2(r_0,p) = \sum_{n=0}^{\infty}\sum_{m=0}^{\infty}[A_{nm}s_m + B_{nm}t_m]P_n(p)$$
$$2\mu' u_\theta^2(r_0,p) = \bar{p}\sum_{n=0}^{\infty}\sum_{m=0}^{\infty}[C_{nm}s_m + D_{nm}t_m]P_n'(p) \tag{25}$$

From (20), (25), and (47) of [2] we finally write the displacements corresponding to the solution S' on the surface of the cracked sphere μ', ν'.

$$2\mu' u_r'(r_0,p) = \sum_{n=0}^{\infty}\left\{J_n s_n + K_n t_n + \sum_{m=0}^{\infty}(A_{nm}s_m + B_{nm}t_m)\right\}P_n(p)$$
$$2\mu' u_\theta'(r_0,p) = \bar{p}\sum_{n=0}^{\infty}\left\{L_n s_n + N_n t_n + \sum_{m=0}^{\infty}(C_{nm}s_m + D_{nm}t_m)\right\}P_n'(p) \tag{26}$$

With these results and (18), the displacement continuity condition (2) yields the following system of algebraic equations for the coefficients of Legendre-Fourier expansion of the interface tractions:

$$(J_n - kE_n)s_n + (K_n - kF_n)t_n + \sum_{m=0}^{\infty}[A_{nm}s_m + B_{nm}t_m]$$
$$= \frac{kr_0(T_1+2T_2)}{4}\left(\frac{1-\nu''}{1+\nu''}\right)\delta_{n0} + \frac{10kr_0(T_1-T_2)(1-\nu'')}{(7-5\nu'')}\delta_{n2}$$
$$(L_n - kG_n)s_n + (N_n - kH_n)t_n + \sum_{m=0}^{\infty}[C_{nm}s_m + D_{nm}t_m] \tag{27}$$
$$= \frac{5kr_0(T_2-T_1)(1-\nu'')}{(7-5\nu'')}\delta_{n2} \quad (Cont.)$$

where $k = \mu'/\mu''$ $n = 0, 1, 2, \ldots$

It is clear that s_n, t_n determined by these equations depend on elastic constants ν', ν'', and the ratio $k = \mu'/\mu''$. Thus the same is true of the interface tractions in (4) and the entire stress field.

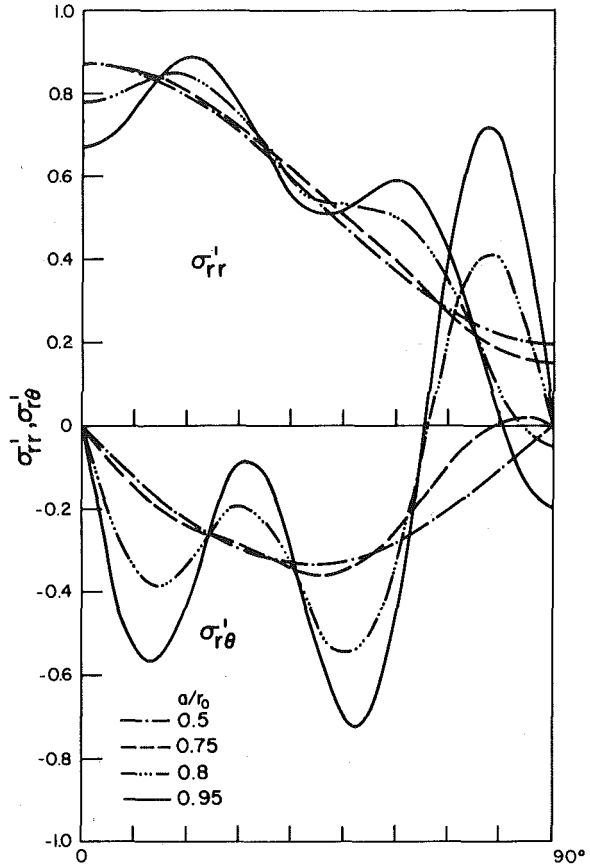

Fig. 1 The interface stresses for various values of a/r_0 ($\nu' = 0.4$, $\nu'' = 0.2$, $k = 0.5$, $r_0 = 2$, $T_1 = 1$, $T_2 = 0$)

3 Numerical Results and Discussion

The calculations implied by (27) were carried out for several composites in which ν' and ν'' were varied from 0.2 to 0.4 and $k = \mu'/\mu''$ was varied from 0.5 to 2.0. These composites were subject to the far field loading $T_1 = 1$, $T_2 = 0$. Figs. 1–4 show the interface stresses $\sigma_{rr}'(r_0, p)$ and $\sigma_{r\theta}'(r_0, p)$ for $a/r_0 = 0.5, 0.75, 0.9$, and 0.95. For each of the composites we find that these interface tractions vary only slightly from the case of uncracked sphere if $a/r_0 < 0.5$. The effect of the crack on the interface stresses becomes appreciable if $a/r_0 > 0.75$.

Fig. 5 shows the variation of the stress-intensity factor K_1 with a/r_0 for various composites. Bogy [4] has shown for plane problems that the power of the stress singularity at the crack tip, when the crack terminates at the interface varies and depends on the intersection angle and the two Dundurs [6] composite parameters defined by (for plane strain)

$$\alpha = \frac{\mu'(1-\nu'') - \mu''(1-\nu')}{\mu'(1-\nu'') + \mu''(1-\nu')}$$
$$\beta = \frac{\mu'(1-2\nu'') - \mu''(1-2\nu')}{2\mu'(1-\nu'') + 2\mu''(1-\nu')} \tag{28}$$

Here we record the values γ of the power of the singularity in the plane problem, when the crack terminates at the interface at a right angle, for the six composites shown in Fig. 5. Cases 1–3 correspond to the situations where $\gamma > -0.5$ while in Cases 4–6 $\gamma < -0.5$. Guided by the

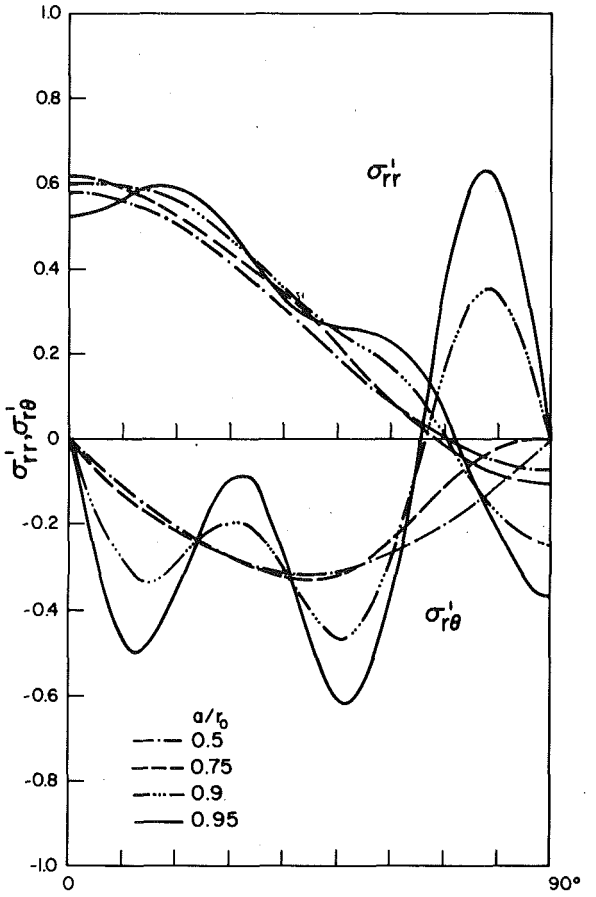

Fig. 2 The interface stresses for various values of a/r_0 ($\nu' = 0.2$, $\nu'' = 0.4$, $k = 0.5$, $r_0 = 2$, $T_1 = 1$, $T_2 = 0$)

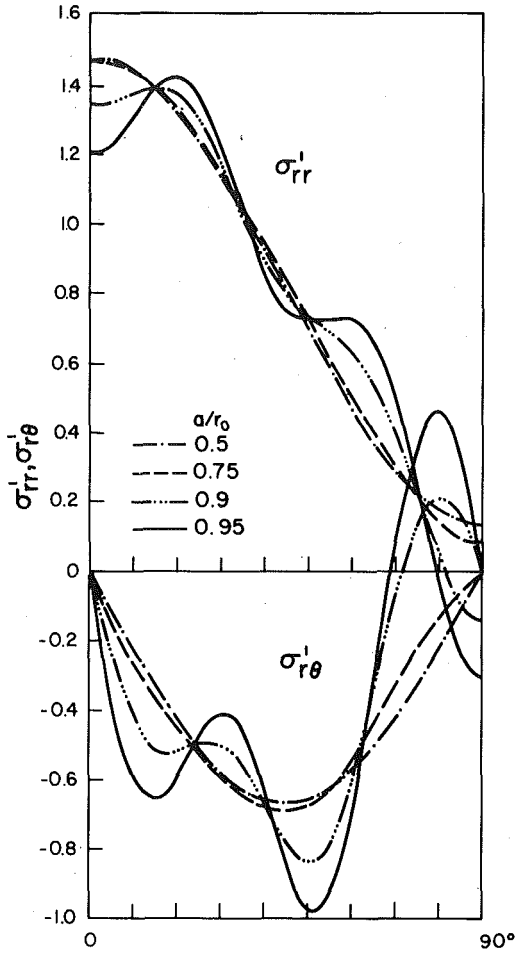

Fig. 3 The interface stresses for various values of a/r_0 ($\nu' = 0.4$, $\nu'' = 0.2$, $k = 2$, $r_0 = 2$, $T_1 = 1$, $T_2 = 0$)

plane problem we therefore expect that the stress-intensity factor should tend to zero in Cases 1–3 and to infinity in Cases 4–6, respectively, as $a/r_0 \to 1$. This trend is seen in Fig. 5 for the present spherical problem also except for the Case 3 where the stress-intensity factor appears to increase rather than decrease near $a/r_0 = 1$. No explanation for this unexpected result was found, except the possibility that the singularity is different for the spherical geometry than for cylindrical and plane geometry, even when the crack intersects the interface at a right angle in each case.

4 Energy Calculations

In this section we calculate the change in the elastic energy due to the presence of the crack in the spherical inclusion. It is easy to show that this change is given by

$$\Delta E = -\frac{1}{2}\int_c T_i^u u_i' dA, \tag{29}$$

where the integral in (29) is taken over the area of the crack, and where T_i^u are the tractions on the imagined crack surface in the uncracked inclusion, and u_i' are the displacements at the crack surface in the cracked composite.

1 Determination of Displacements at the Crack Surface. At the crack surface we have

$$u_\xi'(0,\eta) = u_z'(r,z) \quad \text{at} \quad z = 0, \quad 0 < \eta \le 1, \quad 0 \le r \le a \tag{30}$$

From (19)

$$u_z'(r,0) = u_z^1(r,0) + u_z^2(r,0). \tag{31}$$

However, $u_z^1(r,0) = 0$ since the tractions in $[S^1]$ are symmetric with respect to the plane $z = 0$ so that

$$u_z'(r,0) = u_z^2(r,0) \tag{32}$$

From (6), (7), (17), and (18) (all of [2]) we have

$$2\mu' u_z'(r,z) = \sum_{n=0}^{\infty} \{a_n n(n-1)\nabla\phi_n + b_n n(n-1)[\nabla(z\psi_n) + 4(\nu'-1)\psi_n \mathbf{k}]\}\cdot\mathbf{k} \tag{33}$$

where ϕ_n and ψ_n are defined in (4) and (5) (of [2]). At $z = 0$ the displacement $u_z'(r, z)$ becomes

$$2\mu' u_z'(r,0) = \sum_{n=0}^{\infty} 2(\nu'-1)b_n n(n-1)\frac{Q_n(i\xi)}{a\xi}P_n'(\eta)\big|_{\xi=0}$$

$$= \sum_{n=0}^{\infty} (\nu'-1)b_n n(n-1) i^{n+1} \frac{\Gamma\left(1+\frac{n}{2}\right)\sqrt{\pi}}{\Gamma\left(\frac{1}{2}+\frac{n}{2}\right)a} P_n'(\eta) \tag{34}$$

where $[Q_n(i\xi)/\xi]_{\xi=0}$ must be evaluated as the limit $\xi \to 0$ with $\xi > 0$ and $\Gamma(n)$ is the Gamma function. Also r and η are related by

$$r^2 = a^2(1-\eta^2). \tag{35}$$

In obtaining (34) we have used

$$a_n + (2\nu'-1)b_n = 0 \quad (n \text{ even}). \tag{36}$$

which can be obtained from (19) of [2] for the case when $\sigma_{\xi\eta}' = 0$ (crack is opened by normal stress only, so that $g_n = 0$).

2 Tractions at the Imagined Crack Face in the Uncracked Composite. Denote the uncracked composite solution by $[S^u]$. This

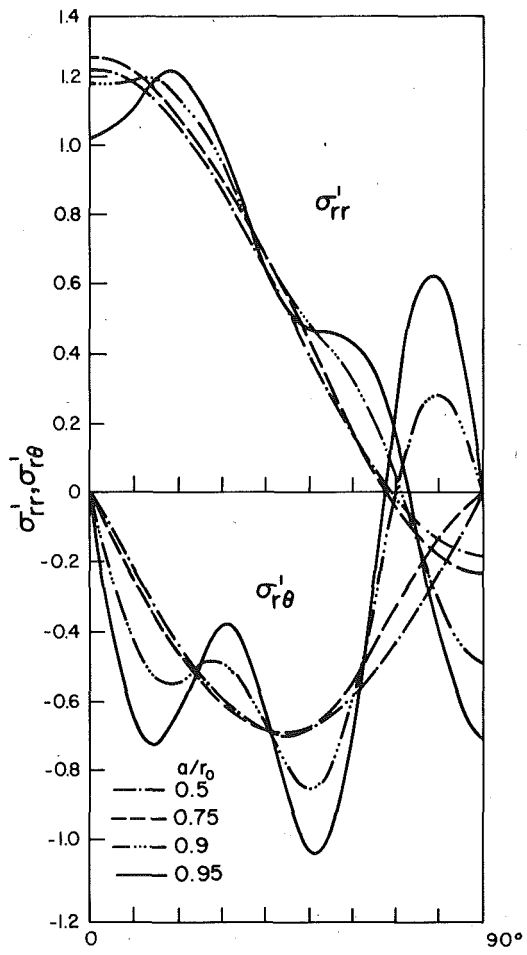

Fig. 4 The interface stresses for various values of a/r_0 ($\nu' = 0.2$, $\nu'' = 0.4$, $k = 2$, $r_0 = 2$, $T_1 = 1$, $T_2 = 0$)

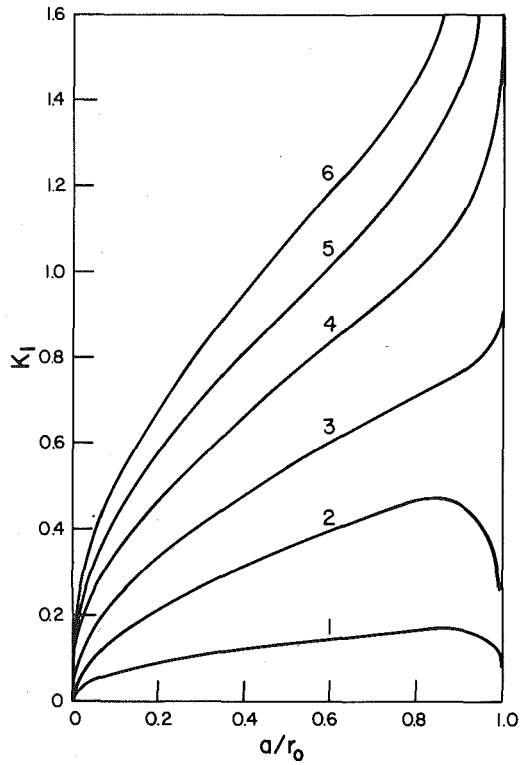

Fig. 5 Variation of the stress-intensity factor, for various composites, with a/r_0 ($r_0 = 2$); see Table 1

Table 1 The value of γ

Case No.	ν'	ν''	$\mu'/10^6$ psi	$\mu''/10^6$ psi	α	β	$-\gamma$
1	0.325	0.25	1	10	−0.8	−0.2	0.3
2	0.2	0.4	2	4	0.454	−0.227	0.38
3	0.4	0.2	2	4	−0.2	0.5	0.49
4	0.2	0.4	4	2	0.2	−0.05	0.53
5	0.4	0.2	4	2	0.454	0.091	0.60
6	0.036	0.454	10	1	0.7	0.0	0.69

solution is a special case of that given by Sternberg, Eubanks, and Sadowsky [3] or Hashin [8]. It is also a special case of the solution presented here when $a/r_0 \to 0$. In this case A_{nm}, B_{nm}, C_{nm}, D_{nm} in (25) are zero and (27) yields the result

$$s_0 = T_1\left(\frac{1-\nu''}{1+\nu''}\right)\left[\frac{k}{k+2(1-2\nu')/(1+\nu')}\right]$$

$$s_2 = -5kT_1(1-\nu'')(7-5\nu'')(7+5\nu')\{7(k+4)+5\nu'(k-8)\}/\Delta$$

$$t_2 = -\frac{1}{2}s_2$$

$$\Delta = 2k^2(7+5\nu')^2\{25(\nu'')^2 - 55\nu' - 28\}$$
$$+ (7-5\nu'')^2\{3626 - 3470\nu' - 3700(\nu')^2\}/16$$
$$-k(7+5\nu')(7-5\nu')\{375\nu''\nu' + 518\nu' - 182\nu'' - 273\}$$

$$s_n = t_n = 0, \qquad n = 1 \quad \text{and} \quad n > 2 \tag{37}$$

for the Legendre-Fourier coefficients for the interface tractions at the spherical surface of the uncracked spherical inclusion. By the use of (34) of [2] with h_n, k_n replaced by s_n, t_n in (37), the coefficients c_n, d_n in (28) of [2] determining the solution inside the uncracked sphere are

$$c_2 = -\frac{5}{2}kT_1(1-\nu'')(7-5\nu'')(7+5\nu')\{7(k+4)+5\nu'(k-8)\}/\Delta$$

$$d_1 = -\frac{1}{2}T_1\left(\frac{1-\nu''}{1+\nu''}\right)\left[\frac{k}{k+2(1-2\nu')/(1+\nu')}\right]\frac{1}{(1+\nu')} \tag{38}$$

where Δ is defined in (37), and all other c_n, d_n are zero. Use of this result together with (30) and (32) (of [2]) yields the following for the tractions on the equatorial plane:

$$\sigma^u_{\theta\theta}(r,\pi/2) = 2[c_2 - (1+\nu')d_1],$$
$$\sigma^u_{r\theta}(r,\pi/2) = 0. \tag{39}$$

With the help of (37) and (38) we can see that $\sigma^u_{\theta\theta}(r, \pi/2)$ is uniform throughout the equatorial plane. We denote

$$\sigma^u_{\theta\theta}(r,\pi/2) = p_0(\nu', \nu'', k). \tag{40}$$

Since the imagined crack surface occupies a part or all of the equatorial plane, depending upon the ratio a/r_0, the tractions on the imagined crack face are also given by (40).

Substitution of (40) and (34) into (29) yields

$$\Delta E = -\pi a p_0 \sum_{n=0}^{\infty} \frac{b_n n(n-1)(\nu'-1)i^{n+1}\Gamma(1+n/2)\sqrt{\pi}}{\mu'\Gamma\left(\frac{1}{2}+\frac{n}{2}\right)} \tag{41}$$

where we have used

$$\int_0^1 P'_n \eta d\eta = 1 \quad (n \text{ even}) \tag{42}$$

Expression (41) reduces to previously known results for the special case of a crack in the infinite medium (μ', ν') subject to uniform tension T_1 at infinity. To show this recall from (55) of [2] and (37) that in this case

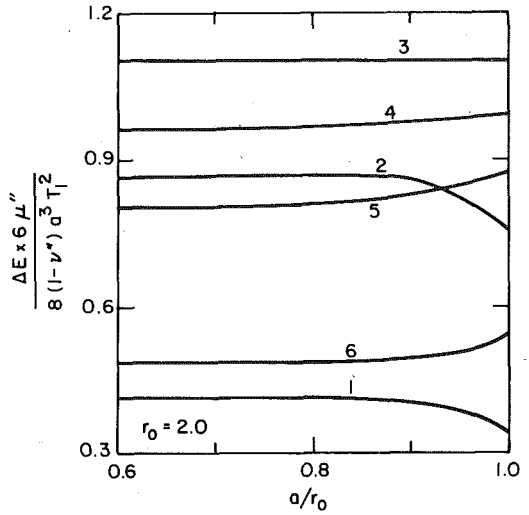

Fig. 6 Energy released (after normalization) versus $a/r_0(r_0 = 2)$ for various composites; see Table 1

$$a_2 = (1 - 2\nu')T_1a^2i/3\pi$$
$$b_2 = T_1a^2i/3\pi \tag{43}$$

and all other a_n, b_n are zero. Use of this result in (41) yields

$$\Delta E = \frac{8a^3T_1^2(1-\nu')}{6\mu'} \tag{44}$$

which agrees with Sneddon and Lowengrub [7].

Calculations implied in (41) have been carried out for several composites. Figs. 6 and 7 indicate the energy released normalized with respect to the energy released by a crack of the same radius in the infinite medium. Fig. 6 shows the normalized energy released versus $a/r_0(r_0 = 2)$. It can be seen here that this quantity is insensitive to the value of the ratio a/r_0 except for $a/r_0 \simeq 1$. It is possible to obtain a good estimate for this quantity (except for $a/r_0 \simeq 1$) by considering the limiting case $a/r_0 \to 0$. From (41) and (44) we obtain

$$\Delta E_N = -\frac{6\pi\mu''(\nu'-1)p_0}{8a^2\mu'(1-\nu'')T_1^2} \times \sum_{n=0}^{\infty} b_n n(n-1)i^{n+1}\frac{\Gamma(n/2+1)\sqrt{\pi}}{\Gamma\left(\frac{1}{2}+n/2\right)} \tag{45}$$

where ΔE_N is the energy released after normalization. When the radius of the crack is small compared to the radius of the inclusion it follows from arguments similar to Saint-Venant's principle together with (25) and Fig. 2 (both of [2]) that

$$\sigma_{rr}^2[f,g] \simeq 0, \quad \sigma_{r\theta}^2[f,g] \simeq 0 \tag{46}$$

and

$$h(p) \simeq s(p), \quad t(p) \simeq k(p) \tag{47}$$

Therefore from (25) of [2]

$$\sigma_{\xi\xi}^1[s,t] \simeq -f, \quad \sigma_{\xi\eta}^1[s,t] \simeq -g, \tag{48}$$

where $\sigma_{\xi\xi}^1[s,t]$ and $\sigma_{\xi\eta}^1[s,t]$ represent the normal and shearing stresses on the imagined crack surface when the spherical surface in $[S^1]$ of (19) is loaded with tractions $s(p)$, $t(p)$. It follows from (40) that

$$\sigma_{\xi\xi}^1[s,t] \simeq -p_0(\nu',\nu'',k), \quad \sigma_{\xi\eta}^1[s,t] \simeq 0. \tag{49}$$

In order to obtain the solution $[S']$ in (19) we must superpose on $[S^1]$ the solution $[S^2]$ subject to the boundary conditions (49). For this case we find from (20) of [2] that

$$b_2 \simeq \frac{p_0a^2i}{3\pi},$$

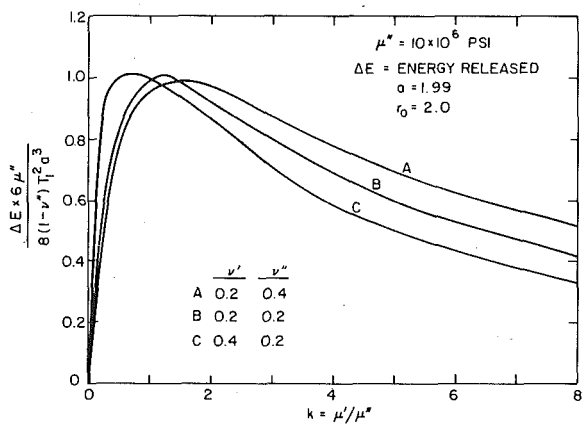

Fig. 7 Energy released (after normalization) for various composites ($a/r_0 = 0.995$, $r_0 = 2$)

$$a_2 \simeq (1 - 2\nu)p_0a^2i/3\pi. \tag{50}$$

All other a_n, b_n are negligible. Substitution of (50) into (45) yields

$$\lim_{a\to 0} \Delta E_N = \frac{p_0^2\mu''(1-\nu')}{T_1^2\mu'(1-\nu'')}. \tag{51}$$

The stress $p_0(\nu', \nu'', k)$ is given by (37)–(40). The computation implied by (51) was carried out and agrees with Fig. 6 at $a/r_0 = 0$ (it actually agrees to plotting accuracy for $0 < a/r_0 < 0.75$). In fact the expression (51) provides a good estimate of the energy released even when the inclusion is completely fractured. From Fig. 6 it also follows that the amount of energy released increases essentially as a^3 for the composite as it does for a crack in an infinite medium.

Fig. 7 shows the dependence on $k = \mu'/\mu''$ of the energy released from the composites when the inclusion is almost completely fractured. ($a = 1.99$, $r_0 = 2$). As expected no energy is released when $k = 0$. It sharply increases to a maximum near $k = 1$, then it decreases asymptotically to zero. This limit would be expected to differ from zero if the corresponding computations were made for $a/r_0 = 1$. Notice also that when $k = 1$ the curve for $\nu' = \nu''$ passes through the value 1 as it should for the crack in an infinite medium because of the normalization.

Acknowledgment

The authors wish to thank Dr. M. A. Hamstad for suggesting this problem and for his interest and helpful discussions. The support of Lawrence Livermore Laboratory is also gratefully acknowledged.

References

1 Bianchetti, R., Hamstad, M. A., and Mukherjee, A. K., "Origin of Burst-Type Acoustic Emission in Unflawed 7075-76 Aluminum," *Journal of Testing and Evaluation*, Vol. 4, No. 5, Sept. 76, pp. 313–318.

2 Kant, R. and Bogy, D. B., "The Axisymmetric Elastostatic Problem of a Cracked Sphere," ASME JOURNAL OF APPLIED MECHANICS, Vol. 47, Sept. 1980, pp. 538–544.

3 Sternberg, E., Eubanks, R. A., and Sadowsky, M. A., "On the Axisymmetric Problem of Elasticity Theory for a Region Bounded by Two Concentric Spheres," *Proceedings of the First National Conference of Applied Mechanics*, 1951, pp. 205–215.

4 Bogy, D. B., "On the Plane Elastostatic Problem of a Loaded Crack Terminating at a Material Interface," ASME JOURNAL OF APPLIED MECHANICS, Vol. 38, Dec. 1971, pp. 911–918.

5 Bogy, D. B., "Edge-Bonded Dissimilar Orthogonal Elastic Wedge Under Normal and Shear Loading," ASME JOURNAL OF APPLIED MECHANICS, Vol. 35, 1968, p. 460.

6 Dundurs, J., Discussion of [5], JOURNAL OF APPLIED MECHANICS, Vol. 36, 1969, p. 650.

7 Sneddon, I. N., and Lowengrub, M., *Crack Problems in the Classical Theory of Elasticity*, Wiley, New York, 1969.

8 Hashin, Z., "The Elastic Moduli of Heterogenous Materials," ASME JOURNAL OF APPLIED MECHANICS, Vol. 84, No. 1, 1962, pp. 143–150.

Elastodynamic Analysis of an Edge Crack

J. D. Achenbach
Professor.
Fellow ASME

L. M. Keer
Professor.
Mem. ASME

Department of Civil Engineering,
The Technological Institute,
Northwestern University,
Evanston, Ill. 60201

D. A. Mendelsohn
Senior Engineer.

Chemical Research Department,
Halliburton Services,
Duncan, Okla. 73533

Introduction

Among the crack configurations that are usually considered in fracture mechanics, the surface-breaking crack is of distinct practical interest. The simplest configuration is the two-dimensional normal edge-crack of depth d in an elastic half plane. For a broad class of static loads the stress-intensity factor for the normal edge-crack was analyzed by Koiter [1], and in a different manner by Sneddon and Das [2]. In the present paper we investigate elastodynamic fields for the edge-crack configuration.

The cracked half plane is subjected to a class of time-harmonic line loads which are applied to its free surface. The elastodynamic problem of a half plane subjected to a time-harmonic line load applied normal to the free surface is known as Lamb's problem [3]. It is well known that sufficiently far from the point of application Rayleigh surface waves dominate the elastodynamic field near the free surface. Consequently, in this paper we only consider the elastodynamic stress-intensity factors generated by surface motion.

It is assumed that the faces of the crack do not interact with each other. Thus the crack never completely closes. This is a realistic assumption if the crack is actually a thin slit of finite width, or if a static prestress is applied which tends to hold the crack in an open position. In the latter case the solution sought in this paper is an elastodynamic perturbation (caused by time-harmonic surface motion) on this static prestress.

Contributed by the Applied Mechanics Division for presentation at the Winter Annual Meeting, Chicago, Ill., November 16–21, 1980, of THE AMERICAN SOCIETY OF MECHANICAL ENGINEERS.

Discussion on this paper should be addressed to the Editorial Department, ASME, United Engineering Center, 345 East 47th Street, New York, N. Y. 10017, and will be accepted until December 1, 1980. Readers who need more time to prepare a discussion should request an extension from the Editorial Department. Manuscript received by ASME Applied Mechanics Division, August, 1979; final revision, February, 1980. Paper No. 80-WA/APM-6.

The elastodynamic response of the cracked half plane is analyzed as the superposition of the fields in the uncracked half plane and the fields generated by appropriate surface tractions on the faces of the crack in the cracked half plane. The resulting boundary-value problem for the cracked half plane is decomposed into two problems for the quarter plane, which represent the symmetric and antisymmetric motions relative to the plane of the crack, respectively. These two boundary-value problems are reduced by integral transform techniques to two uncoupled singular integral equations, which are solved numerically using a collocation scheme due to Erdogan, Gupta, and Cook [4]. The stress-intensity factors and crack opening displacements are then easily calculated from the solutions of the singular integral equations.

Mode-I and Mode-II dynamic stress-intensity factors at the crack tip and the corresponding crack opening displacements due to several combinations of line-loads applied to the feee surface are computed and plotted versus the frequency. One significant feature of these results is the existence of maxima at regularly spaced frequencies. It appears that these frequencies correspond to resonant modes of vibration of the crack faces due to constructive interference of surface motions on the crack faces.

Formulation

The two-dimensional geometry of a homogeneous, isotropic, linearly elastic half plane containing a normal edge crack of length d is shown in Fig. 1. The origin of a Cartesian coordinate system is located at the mouth of the crack.

The cracked half plane is subjected to time-harmonic excitation. In this paper the steady-state fields in the vicinity of the crack tip are investigated. By virtue of linear superposition the dynamic response of the half plane can be analyzed as the superposition of the fields in the uncracked half plane and fields in the cracked half plane generated

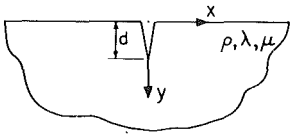

Fig. 1 Half plane containing a normal edge-crack

by appropriate surface tractions τ_x and τ_{xy} on the faces of the crack. The fields generated by surface tractions can, however, conveniently be decomposed in symmetric and antisymmetric fields relative to the plane $x = 0$. Consequently the solution sought in this paper is equivalent to the sum of two problems for the quarter plane $x \geq 0, y \geq 0$. These problems are the *symmetric* problem defined by the boundary conditions on $x = 0$

$$\tau_{xy} = 0, \qquad 0 \leq y < \infty \tag{1}$$

$$\tau_x = \tau_0(y)e^{-i\omega t}, \qquad 0 \leq y < d \tag{2}$$

$$u = 0, \qquad d \leq y < \infty \tag{3}$$

and the *antisymmetric* problem defined by the boundary conditions on $x = 0$

$$\tau_x = 0, \qquad 0 \leq y < \infty \tag{4}$$

$$\tau_{xy} = \sigma_0(y)e^{-i\omega t}, \qquad 0 \leq y < \mathrm{d} \tag{5}$$

$$v = 0, \qquad d \leq y < \infty \tag{6}$$

For both the symmetric and the antisymmeric problem the boundary conditions on $y = 0$ are

$$\tau_y = 0, \quad \tau_{yx} = 0, \quad x \geq 0 \tag{7, 8}$$

In addition it is required that the elastodynamic fields generated by these crack-face excitations represent outgoing waves, and that the singularities at the crack tip are consistent with an integrable strain-energy density.

In the sequel the term $\exp(-i\omega t)$ which is common to all field variables is omitted. Since the deformation is in plane strain the relevant stresses in terms of the displacement derivatives are

$$\tau_x = (\lambda + 2\mu)\frac{\partial u}{\partial x} + \lambda\frac{\partial v}{\partial y} \tag{9}$$

$$\tau_{xy} = \mu\left(\frac{\partial u}{\partial y} + \frac{\partial v}{\partial x}\right) \tag{10}$$

$$\tau_y = (\lambda + 2\mu)\frac{\partial v}{\partial y} + \lambda\frac{\partial u}{\partial x} \tag{11}$$

The displacement equations of motion are

$$c_L{}^2\frac{\partial^2 u}{\partial x^2} + c_T{}^2\frac{\partial^2 u}{\partial y^2} + (c_L{}^2 - c_T{}^2)\frac{\partial^2 v}{\partial x \partial y} = -\omega^2 u \tag{12}$$

$$(c_L{}^2 - c_T{}^2)\frac{\partial^2 u}{\partial x \partial y} + c_T{}^2\frac{\partial^2 v}{\partial x^2} + c_L{}^2\frac{\partial^2 v}{\partial y^2} = -\omega^2 v \tag{13}$$

where

$$c_L{}^2 = (\lambda + 2\mu)/\rho \qquad c_T{}^2 = \mu/\rho$$

In equations (9)–(13), λ and μ are the Lamé elastic constants and ρ is the mass density.

Integral Equations

In this section we derive the governing equation for the symmetric problem defined by equations (1)–(3) and equations (7)–(13) in some detail and we state the corresponding governing equation for the antisymmetric problem.

Suitable solutions to the displacement equations of motion have been given in reference [4]. They are

$$u^s(x, y) = \frac{2}{\pi}\int_0^\infty [\xi k_L{}^{-2}Ae^{-\alpha_L y} - 2\alpha_T k_T{}^{-2}Ce^{-\alpha_T y}]\sin(\xi x)d\xi + \frac{2}{\pi}\int_0^\infty [\alpha_L k_L{}^{-2}Be^{-\alpha_L x} + 2\xi k_T{}^{-2}De^{-\alpha_T x}]\cos(\xi y)d\xi \tag{14}$$

$$v^s(x, y) = \frac{2}{\pi}\int_0^\infty [\alpha_L k_L{}^{-2}Ae^{-\alpha_L y} - 2\xi k_T{}^{-2}Ce^{-\alpha_T y}]\cos(\xi x)d\xi + \frac{2}{\pi}\int_0^\infty [\xi k_L{}^{-2}Be^{-\alpha_L x} + 2\alpha_T k_T{}^{-2}De^{-\alpha_T x}]\sin(\xi y)d\xi \tag{15}$$

where k_L and k_T are the wave numbers of longitudinal and transverse waves respectively,

$$k_L = \omega/c_L, \quad k_T = \omega/c_T$$

and A, B, C, and D are undetermined functions of the transform variable ξ, while the functions α_L and α_T are given by

$$\alpha_L = (\xi^2 - k_L{}^2)^{1/2}, \quad \xi > k_L \quad \text{and} \quad \alpha_L = -i(k_L{}^2 - \xi^2)^{1/2}, \quad \xi < k_L \tag{16}$$

$$\alpha_T = (\xi^2 - k_T{}^2)^{1/2}, \quad \xi > k_T \quad \text{and} \quad \alpha_T = -i(k_T{}^2 - \xi^2)^{1/2}, \quad \xi < k_T \tag{17}$$

where ξ is real. This choice of branches for α_L and α_T, namely, that Re (α_L) and Re (α_T) be positive and that Im (α_L) and Im (α_T) be nonpositive on the contour of integration, insures the existence of the integrals in equations (14)–(15) as well as the satisfaction of the requirement of outgoing waves stated in the previous section. The stress components $\tau_x{}^s$, $\tau_{xy}{}^s$, and $\tau_y{}^s$ corresponding to equations (14)–(15) are easily calculated from equations (9)–(11) and they will not be given here.

Application of the symmetry boundary condition (1) leads to the following algebraic relation:

$$B = -(k_L{}^2/k_T{}^2)\frac{(\alpha_T{}^2 + \xi^2)}{\alpha_L \xi}D, \tag{18}$$

while the application of the free surface boundary condition (8) leads to

$$C = (k_T{}^2/k_L{}^2)\frac{\alpha_L \xi}{(\alpha_T{}^2 + \xi^2)}A, \tag{19}$$

with D and A still undetermined. Now define D in the following manner [6]:

$$D = \int_0^d b(s)\sin(\xi s)ds. \tag{20}$$

Substituting equations (18) and (20) into equation (14) and evaluating at $x = 0$, the following expression is obtained for the normal displacement on $x = 0$:

$$u^s(0, y) = \frac{2}{\pi}\int_0^d b(s)ds \int_0^\infty \xi^{-1}\sin(\xi s)\cos(\xi y)d\xi. \tag{21}$$

The inner integral in this expression is a representation of a generalized function and may be evaluated as, reference [5],

$$\int_0^\infty \xi^{-1}\sin(\xi s)\cos(\xi y)d\xi = \frac{\pi}{2}\mathrm{H}(s - y),$$

where $\mathrm{H}(s - y)$ is the Heaviside step function. This result reduces equation (21) to

$$u^s(0, y) = \int_y^d b(s)ds \quad 0 < y < d$$
$$= 0 \qquad\qquad d < y < \infty \tag{22}$$

and hence boundary conditions (3) is automatically satisfied for any choice of $b(s)$. It is also seen that $b(y)$ is proportional to the tangential derivative of the crack-opening displacement in the x-direction and hence has the physical meaning of the dislocation density.

Using equations (18)–(20) and applying the remaining free surface condition (7) yields an integral relation involving A and $b(s)$ of the form

$$\frac{2}{\pi}\int_0^\infty F(\xi)A(\xi)\cos(\xi x)d\xi = \int_0^\infty G(x,\xi)d\xi \int_0^d b(s)\sin(\xi s)ds \quad (23)$$

where F and G are known functions. Taking the Fourier cosine transform of this expression with respect to x yields the following explicit expression for A in terms of $b(s)$:

$$A(\xi) = \int_0^d \frac{(k_L{}^2/k_T{}^2)(\alpha_T{}^2+\xi^2)[F_1e^{-\alpha_L s}+F_2e^{-\alpha_T s}+F_3]b(s)ds}{4\alpha_L\alpha_T\xi^2-(\alpha_T{}^2+\xi^2)^2} \quad (24a)$$

where

$$F_1 = -\alpha_L{}^{-2}[k_T{}^2(2k_L{}^2-k_T{}^2)+4\alpha_L{}^2\xi^2] \quad (24b)$$

$$F_2 = 4\xi^2 \quad (24c)$$

$$F_3 = \alpha_L{}^{-2}k_T{}^2(2k_L{}^2-k_T{}^2). \quad (24d)$$

Having now expressed A, B, C, and D in terms of $b(s)$, the normal stress on $x = 0$ may be written as

$$\tau_x{}^s(0,y) = \frac{2\mu}{\pi k_T{}^2}\int_0^d b(s)ds \int_0^\infty \frac{[(2\alpha_L{}^2+k_T{}^2)(\alpha_T{}^2+\xi^2)e^{-\alpha_L y}-4\alpha_L\alpha_T\xi^2e^{-\alpha_T y}][F_1e^{-\alpha_L s}+F_2e^{-\alpha_T s}+F_3]d\xi}{4\alpha_L\alpha_T\xi^2-(\alpha_T{}^2+\xi^2)^2}$$
$$+\frac{2\mu}{\pi k_T{}^2}\int_0^d b(s)ds\int_0^\infty \frac{(\alpha_T{}^2+\xi^2)^2-4\alpha_L\alpha_T\xi^2}{\alpha_L\xi}\sin(\xi s)\cos(\xi y)d\xi. \quad (25)$$

The integrand of the second term in equation (25) is $O(1)$ as $\xi \to \infty$ and hence, as it stands, the integral does not converge. However, if the first term of the asymptotic expansion of the integrand for large ξ is subtracted from the exact form, the resulting integrand is $O(\xi^{-2})$ as $\xi \to \infty$ and the integral will converge. The term which must then be added to equation (25) has as its inner integral

$$\int_0^\infty \sin(\xi s)\cos(\alpha y)d\xi$$

which may also be evaluated by employing Fourier representations of generalized functions, reference [5], and is found to be

$$\frac{1}{2}\left(\frac{1}{s-y}+\frac{1}{s+y}\right).$$

Carrying out the steps previously indicated and applying the boundary condition (2) and normalizing the variables s and y with respect to the crack length d yields the following singular integral equation:

$$\int_0^1 \frac{\varphi(S)}{S-Y}dS + \int_0^1 \varphi(S)\left[\frac{1}{S+Y}+K_s(Y,S)\right]dS = \frac{\pi\kappa^2}{2\mu(\kappa^2-1)}\bar{\tau}_0(Y), \quad 0 \le Y \le 1 \quad (26)$$

where $\varphi(S)$ is defined as

$$\varphi(S) = b(Sd) \quad (27a)$$

and $K_s(Y,S)$ is given by

$$(1-\kappa^2)K_s(Y,S)D^{-1} = \int_0^\infty \left[\frac{(2\zeta^2-\kappa^2)^2-4\zeta^2\beta_L\beta_T}{\zeta\beta_L}+2(\kappa^2-1)\right]\times\sin(D\zeta S)\cos(D\zeta Y)d\zeta$$
$$+\int_0^\infty \frac{[(2\zeta^2+\kappa^2-2)(2\zeta^2-\kappa^2)e^{-\beta_L DY}-4\beta_L\beta_T\zeta^2e^{-\beta_T DY}]}{4\beta_L\beta_T\zeta^2-(2\zeta^2-\kappa^2)^2}\times[H_1e^{-\beta_L DS}+H_2e^{-\beta_T DS}+H_3]d\zeta, \quad (27b)$$

while $\bar{\tau}_0(Y)$ is defined by

$$\bar{\tau}_0(Y) = \tau_0(Yd). \quad (27c)$$

The functions H_1, H_2, H_3 are defined by

$$H_1 = -\beta_L{}^{-2}[\kappa^2(2-\kappa^2)+4\beta_L{}^2\zeta^2], \quad (27d)$$

$$H_2 = 4\zeta^2, \quad (27e)$$

$$H_3 = \beta_L{}^{-2}\kappa^2(2-\kappa^2). \quad (27f)$$

Furthermore,

$$\beta_L = (\zeta^2-1)^{1/2}, \quad \beta_T = (\zeta^2-\kappa^2)^{1/2} \quad (27g)$$

The following dimensionless variables have been used:

$$\zeta = \xi/k_L, \quad D = \omega d/c_L = k_L d, \quad S = s/d, \quad Y = y/d, \quad \kappa = c_L/c_T. \quad (27h)$$

The governing singular integral equation given as follows for the antisymmetric problem defined by equations (4)–(13) is obtained in an exactly analogous manner as that for the symmetric problem. The unknown dislocation density $a(s)$ is proportional to the tangential derivative of the crack-opening displacement in the y-direction and must satisfy,

$$\int_0^1 \frac{\psi(S)}{S-Y}dS + \int_0^1 \psi(S)\left[\frac{1}{S+Y}+K_a(Y,S)\right]dS = \frac{\pi}{2\mu(\kappa^2-1)}\bar{\sigma}_0(Y), \quad 0 \le Y \le 1 \quad (28)$$

where $\psi(S)$ is related to $a(s)$ by

$$\psi(S) = a(Sd) \quad (29a)$$

and where K_a is given by

$$\frac{1}{4}(\kappa^2-1)K_a(Y,S)D^{-1} = \int_0^\infty \left[\frac{4\beta_L\beta_T\zeta^2-(2\zeta^2-\kappa^2)^2}{4\beta_T\zeta}+\frac{1}{2}(1-\kappa^2)\right]\sin(\zeta DS)\cos(\zeta DY)d\zeta$$
$$+\int_0^\infty \frac{[(2\zeta^2-\kappa^2)^2e^{-\beta_T DY}-4\beta_T\beta_L\zeta^2e^{-\beta_L DY}}{4\beta_L\beta_T\zeta^2-(2\zeta^2-\kappa^2)^2}\times[G_1e^{-\beta_L DS}+G_2e^{-\beta_T DS}+G_3]d\zeta, \quad (29b)$$

while $\bar{\sigma}_0(Y)$ is defined by

$$\bar{\sigma}_0(Y) = \sigma_0(Yd) \quad (29c)$$

The functions G_1, G_2, and G_3 are defined as

$$G_1 = -\zeta^2 \quad (29d)$$

$$G_2 = -\beta_T{}^{-2}(\zeta^4-\kappa^2\zeta^2+\tfrac{1}{4}\kappa^4) \quad (29e)$$

$$G_3 = -\tfrac{1}{4}\beta_T{}^{-2}\kappa^4 \quad (29f)$$

Numerical Analysis

The singular integral equations given by equations (26) and (28) are solved numerically by employing the collocation scheme discussed in reference [7]. This collocation scheme is based on expansions in terms of Chebyshev polynomials.

By the inroduction of the nondimensional variables

$$\tilde{s} = 2S-1, \quad \tilde{y} = 2Y-1 \quad (30)$$

the integral equation for the symmetric problem, equation (26), may be written as

$$\int_{-1}^{1} \frac{\tilde{b}(\tilde{s})}{\tilde{s}-\tilde{y}}\,d\tilde{s} + \int_{-1}^{1} (\tilde{b}(\tilde{s}) \left[\frac{1}{(1+\tilde{s})+(1+\tilde{y})} + \tilde{K}_s(\tilde{y},\tilde{s})\right] d\tilde{s} = \frac{\pi}{2\mu(\varkappa^2-1)} \bar{\tau}_0 \left[\frac{1}{2}(1+\tilde{y})\right] \quad -1<\tilde{y}<1 \tag{31a}$$

where

$$\tilde{b}(\tilde{s}) = \varphi\left[\frac{1}{2}(1+\tilde{s})\right] = b\left[\frac{d}{2}(1+\tilde{s})\right] \tag{31b}$$

$$\tilde{K}_s(\tilde{y},\tilde{s}) = \frac{1}{2} K_s\left[\frac{1}{2}(1+\tilde{y}), \frac{1}{2}(1+\tilde{s})\right]. \tag{31c}$$

It is expedient to introduce a function $\bar{b}(\ )$ by

$$\tilde{b}(\tilde{s}) = \bar{b}(\tilde{s})(1-\tilde{s})^{-1/2}(1+\tilde{s})^{-1/2}. \tag{32}$$

Now, using the Gauss-Chebyshev formula for $\varkappa = 1$ given by equations (7.55)–(7.56) of reference [6], the following system of $m-1$ equations for m unknown values of $\bar{b}(\tilde{s})$ follows:

$$\frac{\pi}{m}\sum_{i=1}^{m} \bar{b}(\tilde{s}_i)\left[\frac{1}{\tilde{s}_i-\tilde{y}_j} + \frac{1}{(1+\tilde{s}_i)+(1+\tilde{y}_j)} + \tilde{K}_s(\tilde{y}_j,\tilde{s}_i)\right] = \frac{\pi\varkappa^2}{2\mu(\varkappa^2-1)} \bar{\tau}_0\left[\frac{1}{2}(1+\tilde{y}_j)\right] \quad j=1,\ldots,m-1 \tag{33a}$$

where

$$\tilde{s}_i = \cos\left(\pi\frac{2i-1}{2m}\right) \tag{33b}$$

$$\tilde{y}_j = \cos\left(\pi\frac{j}{m}\right). \tag{33c}$$

Since $\tilde{b}(\tilde{s})$ represents a dislocation density it must be square root singular at the crack tip $\tilde{s}=1$, $(s=d)$, hence the factor $(1-\tilde{s})^{-1/2}$ in equation (32) appears. The factor $(1+\tilde{s})^{-1/2}$ appears to impose the same singularity at the crack mouth $\tilde{s}=-1$, $(s=0)$ which is physically unreasonable. However, if $\bar{b}(\tilde{s})$ vanishes at $\tilde{s}=-1$ in such a way as to cancel the $(1+\tilde{s})^{-1/2}$ factor then $\tilde{b}(\tilde{s})$ will approach a finite value at $\tilde{s}=-1$. Therefore, since $\bar{b}(-1)$ must be zero, the mth unknown, $\bar{b}(\tilde{s}_m)$, is assumed to be zero since $\tilde{s}_m$ is the closest of the $\tilde{s}_i$ to -1. This assumption is in fact true as $m\to\infty$. Eliminating this unknown yields $m-1$ equations for the $m-1$ remaining unknowns. The kernels $\tilde{K}_s(\tilde{y}_y,\tilde{s}_i)$ are evaluated numerically in the complex ξ plane. The details of this integration are given in the Appendix. The linear algebraic system given in equation (33a), where the sum is taken only to $m-1$, is solved using Gaussian elimination for $m-1$ values of $\bar{b}(\tilde{s}_i)$.

Now, it is easily seen upon examining the boundary conditions (1)–(6) for the symmetric and antisymmetric problems, that only the symmetric problem contributes to Mode-I crack deformation and only the antisymmetric problem contributes to Mode-II deformation.

Therefore, the Mode-I stress-intensity factor at the crack tip may be expressed as

$$K_{\mathrm{I}} = \lim_{y\to d^+} (y-d)^{1/2}|\tau_x{}^s(0,y)| = \frac{\mu d^{1/2}(\varkappa^2-1)}{\varkappa^2}|\bar{b}(1)|. \tag{34}$$

The normal crack-opening displacement is also easily expressed in terms of $\bar{b}(\tilde{s})$ as

$$\Delta u\,(y) = \int_{2Y-1}^{1} \bar{b}(\tilde{s})(1+\tilde{s})^{-1/2}(1-\tilde{s})^{-1/2}d\tilde{s}. \tag{35}$$

The integral equation for the antisymmetric problem, equation (28) may be treated in an analogous manner by letting

$$\psi\left[\frac{1}{2}(1+\tilde{s})\right] = a\left[\frac{d}{2}(1+\tilde{s})\right] = \bar{a}(\tilde{s})(1+\tilde{s})^{-1/2}(1-\tilde{s})^{-1/2} \tag{36}$$

Then a linear system for $m-1$ values of $\bar{a}(\tilde{s})$ is obtained just as in the symmetric case. The Mode-II stress-intensity factor is then given by

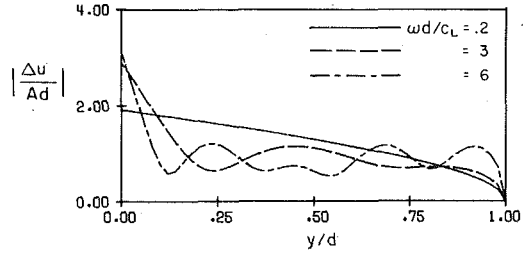

Fig. 2 Normal crack-opening displacement versus y/d for 3 values of the dimensionless frequency

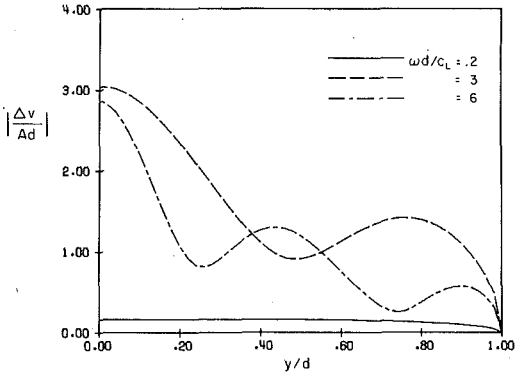

Fig. 3 Tangential crack-opening displacement versus y/d for 3 values of the dimensionless frequency

$$K_{\mathrm{II}} = \lim_{y\to d^+} (y-d)^{1/2}|\tau_{xy}{}^s(0,y)| = \frac{\mu d^{1/2}(\varkappa-1)}{2}|\bar{a}(1)| \tag{37}$$

and the tangential crack opening displacement by

$$\Delta v\,(y) = -\frac{1}{2}\varkappa^2 \int_{2Y-1}^{1} \bar{a}(\tilde{s})(1+\tilde{s})^{-1/2}(1-\tilde{s})^{-1/2}d\tilde{s}. \tag{38}$$

As a check of the kernels $\tilde{K}_s$ and $\tilde{K}_a$ and their evaluation, a convergence analysis of the collocation scheme was performed. For the range of frequencies treated in this investigation, a value of $m-1=14$ was found to be sufficient in order to achieve an accuracy of 3–4 percent. As a further verification of the analysis the crack loading represented by

$$\tau_0(y) = \frac{\mu \sin(k_L y)}{D}, \quad \sigma_0(y) = \frac{\mu \sin(k_T y)}{\varkappa D} \tag{39}$$

was considered for small D and $\varkappa D$. In the static limit these loads reduce to a linear loading on the crack faces. Numerical results for K_{I}, K_{II}, Δu_x and Δu_y from the present analysis with the foregoing loading for $k_L d = 0.05$ were compared to results from reference [2] for the static problem of linear normal and shear loading. Agreement of better than 0.5 percent was obtained for the stress-intensity factors and crack-opening displacements at the mouth of the crack.

In order to obtain the results described in the next section, the following general forms of crack-face loading which correspond to the tractions induced by an arbitrary surface disturbance in a semi-infinite medium are considered for numerical computations.

$$\tau_0(y) = -2\mu A k_R d i\left[\frac{2-2\varkappa_L{}^2+\varkappa_T{}^2}{2-\varkappa_T{}^2} e^{-(k_R{}^2-k_L{}^2)^{1/2}y} - e^{-(k_R{}^2-k_T{}^2)^{1/2}y}\right] \tag{40}$$

$$\sigma_0(y) = -\mu A k_R d\,\frac{(2-\varkappa_T{}^2)}{(1-\varkappa_T{}^2)^{1/2}}\left[e^{-(k_R{}^2-k_L{}^2)^{1/2}y} - e^{-(k_R{}^2-k_T{}^2)^{1/2}y}\right] \tag{41}$$

where k_R is the wave number of Rayleigh surface waves, $\varkappa_L = k_L/k_R$ and $\varkappa_T = k_T/k_R$. The linear system in equation (33a), where the sum

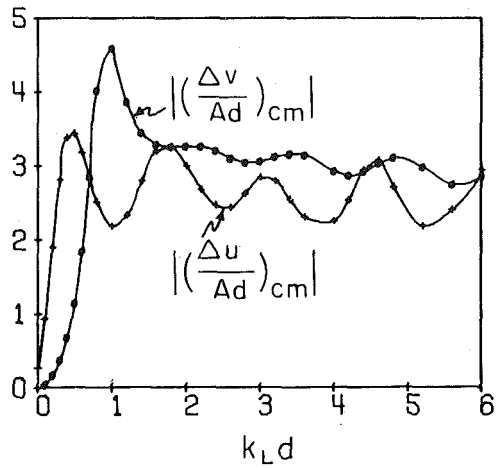

Fig. 4 Crack-opening displacements at the mouth of the crack versus the dimensionless frequency; $k_L d = D$

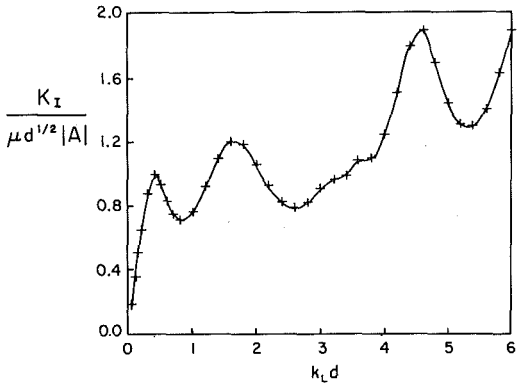

Fig. 5 Mode-I normalized dimensionless stress-intensity factor versus the dimensionless frequency; $k_L d = D$

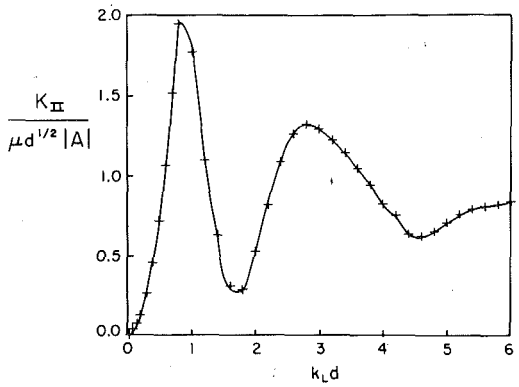

Fig. 6 Mode-II normalized dimensionless stress-intensity factor versus the dimensionless frequency; $k_L d = D$

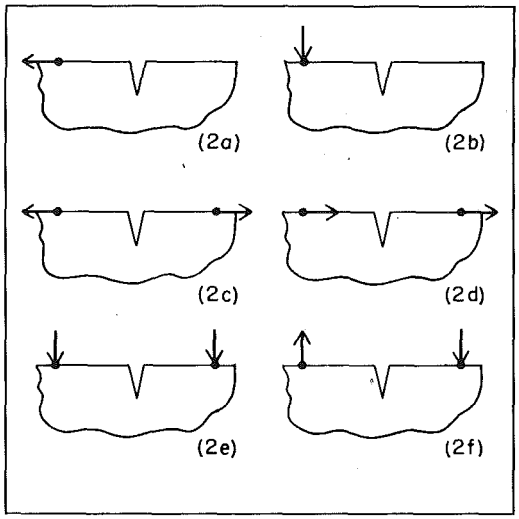

Fig. 7 Loading configurations; each arrow represents a line load of strength $T \exp(-i\omega t)$ applied in the indicated direction at the points $(-x_1, 0)$ or $(x_1, 0)$ to the left or right of the crack, respectively

is only taken up to $m - 1$, was solved for a Poisson's ration of $\frac{1}{3}$ and a frequency range corresponding to $D = 0.1$ to $D = 6.0$, using the expression in equation (40) for $\tau_0(y)$. The corresponding linear system for the antisymmetric problem with $\sigma_0(y)$ given in equation (41) was also solved over the same frequency range for a Poisson's ratio of $\frac{1}{3}$.

It should be noted that the dimensionless constant A in equations (40) and (41) is unspecified. Its value depends on the particular surface loading configuration which causes the surface disturbance. In the following section results are presented for crack-opening displacements and stress-intensity factors normalized with respect to this arbitrary constant A. To obtain the results for a particular surface loading configuration one need only multiply the computed results by the appropriate value of A. It is also noted that the crack-face loadings are proportional to the dimensionless frequency, $k_L d$, and as a result these loadings go to zero as the dimensionless frequency goes to zero.

Results

Figs. 2 and 3 show the crack-opening displacement versus y/d for a few values of the dimensionless frequency. When $\omega d/c_L$ increases the wavelength decreases, and the variation of the crack-opening displacement with y shows the formation of waves on the crack faces. The crack-opening displacements at the mouth of the crack (denoted by subscripts "cm") have been plotted versus D in Fig. 4. In this figure the peaks at certain frequencies suggest resonance effects of surface motions on the faces of the crack. The normalized nondimensional stress-intensity factors $K_I/(\mu d^{1/2}|A|)$ and $K_{II}/(\mu d^{1/2}|A|)$ have been plotted versus D in Fig. 5 and Fig. 6, respectively. Again, there are distinct peaks at resonant frequencies.

Note that the results presented in Figs. 2–6 are absolute values or amplitudes of the corresponding complex-valued quantities.

It should be noted that the results presented in Figs. 2–6 are for crack-face loadings of the general form given by equations (40) and (41), where A is an arbitrary constant. These results may now be used to assemble solutions to a family of corresponding time-harmonic loadings of a cracked half plane by appropriate choices of A.

We consider here the six loading configurations shown in Fig. 7. For each case a time-harmonic line load of strength T per unit length, whose position and direction are indicated, is applied to the surface of the half plane. It is assumed that $k_R x_1 \gg 1$, and hence only the surface motions due to these loads interact with the crack. The loadings shown in Figs. 7(a) and (b) induce traveling surface waves propagating toward the crack. The other four loads, shown in Figs. 7(c)–(e), induce standing waves all along the free surface of the half plane.

By virtue of linear superposition the field in the cracked half plane subjected to external loads consists of the sum of the field in the loaded uncracked body and the field in the cracked body when the crack faces are subjected to appropriate surface tractions. Normal crack-face loadings generate Mode-I deformations with symmetric displacement fields. Tangential crack-face loadings induce Mode-II deformations with antisymmetric displacements. The loadings shown in Figs. 7(a) and (b) cause both Mode-I and Mode-II deformations

Table 1 Definition of A for various loading cases; $k_R = \omega/c_R$, where c_R = velocity of Rayleigh waves

Loading	A
a	$i\,(T/4\mu)B_H \exp(ik_Rx_1)$
b	$(T/4\mu)B_V \exp(ik_Rx_1)$
c	$(T/2\mu)B_H \sin(k_Rx_1)$
d	$i\,(T/2\mu)B_H \cos(k_Rx_1)$
e	$-(T/2\mu)B_V \cos(k_Rx_1)$
f	$i\,(T/2\mu)B_V \sin(k_Rx_1)$

and the solution to these loadings must be composed as the sum of solutions to a symmetric and an antisymmetric problem. Due to symmetry about $x = 0$, the loadings shown in Figs. 7(c) and (e) will cause only Mode-I deformations, and their solutions are obtained from appropriate symmetric problems or normal crack-face loading. On the other hand, the loadings shown in Figs. 7(d) and (f) yield only Mode-II deformation and their solutions are obtained from appropriate antisymmetric problems of tangential crack-face loading.

The previous observations imply that the appropriate stress-intensity factors for the six loading configurations shown in Fig. 7 may be obtained from the single pair of curves shown in Figs. 5 and 6 for the normalized nondimensional stress-intensity factors. Each loading configuration induces known stresses at the position of the crack faces, of the general form given by equations (40) and (41). The amplitude constant A for each loading is given in Table 1. The coefficients B_H and B_V are defined by

$$B_H = (1 - \varkappa_T{}^2)G, \quad B_V = -\tfrac{1}{2}(1 - \varkappa_T{}^2)^{1/2}(2 - \varkappa_T{}^2)G \qquad (42)$$

where

$$G = (1 - \varkappa_L{}^2)^{1/2}(2 - \varkappa_T{}^2)[(4 - \varkappa_T{}^4)(1 - \varkappa_L{}^2)^{1/2}(1 - \varkappa_T{}^2)^{1/2} - 2(2 - 2\varkappa_L{}^2 + \varkappa_T{}^2)]^{-1} \qquad (43)$$

These coefficients are functions of Poisson's ratio only. The stress-intensity factors for the loadings shown in Fig. 7 can thus be obtained by multiplying the results of Figs. 5 and 6 by the factors A listed in Table 1.

Acknowledgment

The work reported here was carried out in the course of research sponsored by the Air Force Office of Scientific Research under Grant No. AFOSR 78-3589 to Northwestern University. Helpful discussions with Dr. F. Neerhoff and Dr. P. Burgers are gratefully acknowledged.

References

1 Koiter, W. T., "On the Flexural Rigidity of a Beam Weakened by Transverse Saw Cuts," *Proceedings, Kon. Ned. Ak. Wet.*, Amsterdam, Series B, Vol. 59, 1956, pp. 354–374.

2 Sneddon, I. N., and Das, S. L., "The Stress-Intensity Factor at the Tip of an Edge-Crack in an Elastic Half Plane," *International Journal of Engineering Sciences*, 1971, Vol. 9, pp. 25–36.

3 Lamb, H., "On the Propagation of Tremors Over the Surface of an Elastic Solid," *Philosophical Transactions of the Royal Society*, 1904, Series A, Vol. 203, pp. 1–42.

4 Luong, W. C., Keer, L. M., and Achenbach, J. D., "Elastodynamic Stress-Intensity Factors of a Crack Near an Interface," *International Journal of Solids and Structures*, Vol. 11, 1975, pp. 919–925.

5 Lighthill, M. J., *Introduction to Fourier Analysis and Generalized Functions*, Cambridge University Press, 1978, pp. 35–36.

6 Erdogan, F., and Gupta, G. D., "Layered Composites With an Interface Flaw," *International Journal of Solids and Structures*, Vol. 7, 1971, pp. 1089–1107.

7 Erdogan, F., Gupta, G. D., and Cook, T. S., "Numerical Solution of Singular Integral Equations," *Methods of Analysis and Solutions to Crack Problems*, ed., Sih, G. C., Noordhoff, 1972.

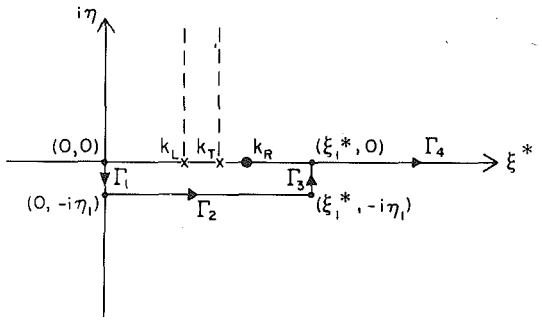

Fig. 8 Integration contour for $K_\beta(y, s)$ and $K_\beta(y, s)$ in the complex $\xi = \xi^* + i\eta$ plane; dashed lines denote branch cuts emanating from k_β to $k_\beta + i\infty$; $\beta = L$ or T

APPENDIX

The kernels given in equations (27) and (29) must be evaluated numerically to solve the integral equations, equations (26) and (28). The choice of possible integration contours in the complex ξ-plane for the kernel integrals are governed by the behavior of their integrands as $|\xi| \to \infty$ and by requiring that

$$\mathrm{Re}\,(\alpha_L) > 0, \quad \mathrm{Re}\,(\alpha_T) > 0 \qquad (44)$$

and

$$\mathrm{Im}\,(\alpha_L) \le 0, \quad \mathrm{Im}\,(\alpha_T) \le 0 \qquad (45)$$

for ξ on the integration contour. Assuming the branch cuts shown in Fig. 8 for α_L and α_T and requiring that (44) be satisfied everywhere in the ξ-plane, it is found that ξ must either lie in the 2nd or 4th quadrants or on the real axis in order that (45) be satisfied; therefore, the integration contour must lie in the 4th quadrant or on the positive real axis. Furthermore, due to the presence of the factor $\sin(\xi s)\cos(\xi y)$ in the first integral of both equations (27) and (29), $\mathrm{Im}\,(\xi)$ must be zero as $|\xi| \to \infty$ on the integration contour.

The contour, made up of Γ_1, Γ_2, Γ_3, and Γ_4 shown in Fig. 8 satisfies the aforementioned requirements and is chosen in order to avoid the numerical difficulties associated with the pole at $\xi = k_R$ in the integrands of the second integrals of equations (27) and (29).

The choice of η_1 was made on the basis of convergence properties of the numerical quadrature used to evaluate the integrals on Γ_2. An optimum value, which is independent of frequency, was found to be $\eta_1 = 1.5$. A value of $\xi_1{}^*$ was chosen sufficiently large that the pole at $\xi = k_R$ caused minimal convergence difficulties in the numerical integration. $\xi_1{}^*$ was usually taken to be approximately $1.5\,k_R$.

W. N. Sharpe, Jr.
Professor and Chairman,
Department of Mechanical Engineering,
Louisiana State University,
Baton Rouge, La. 70803
Mem. ASME

N. J. Altiero
Associate Professor,
Department of Metallurgy, Mechanics,
and Materials Science,
Michigan State University,
East Lansing, Mich.
Assoc. Mem. ASME

A. Mirmohamadsadegh
Assistant Professor,
Department of Mechanical Engineering,
University of Science and Technology,
Narmak, Tehran, Iran

Measurements of Mixed-Mode Crack Surface Displacements and Comparison With Theory

The problem of a finite-width tension specimen containing a crack oriented at various angles to the load axis is attacked from experimental and theoretical viewpoints. Displacements of an electro-machined slot, 12.5 mm long and oriented at angles of 0°, 15°, 30°, 45°, 60°, and 75°, are measured using a laser-based in-plane measuring technique. Various width specimens, ranging from a crack-length/width ratio of 0.167 to 0.794, are tested. A boundary-integral equation method is extended to deal with the presence of a sharp crack. Agreement between the two approaches is generally good except near the tips of the cracks.

1 Introduction

The general problem of mixed-mode crack extension has received relatively little attention compared to that devoted to single-mode problems. The main effort of investigators to date has been toward development of a criterion of fracture for a combination of Mode-I and Mode-II deformation. It has been proposed that this criterion should be a functional relationship between Mode-I and Mode-II stress-intensity factors which can be equated to the strain-energy release rate or strain-energy density at fracture. Practical application of such a criterion is limited by a lack of knowledge about this functional relationship for specific materials, geometries, and loadings. Thus mixed-mode fracture mechanics has reached the level at which classical fracture mechanics was 15 years ago—the level at which it is imperative that an effective method be developed for determination of the relationship required for implementation of the fracture criterion. Crack surface displacements have proven to be quite useful in Mode-I fracture analysis in that they are directly related to the strain-energy release rate and the stress-intensity factor. It is felt that similar relationships can be developed for the mixed-mode case; it is the purpose of this paper to study the crack surface displacements under mixed-mode loading by both experimental and theoretical methods.

The stress-freezing photoelasticity technique has been extremely successful in determining stress-intensity factors in various complicated three-dimensional geometries. However, an investigation into mixed load stress-intensity factors [1] discovered that the remote stresses exerted a measurable effect much closer to the crack tip than had been expected. This required that the fringe pattern be magnified by nearly two orders of magnitude in order to obtain valid fringe data. The errors resulting from such high magnification leave one with little confidence in the results. The experimental technique described in this paper makes measurements of crack opening displacements directly across thin slots electro-machined in metal specimens. The data obtained are easy to compare with theoretical calculations.

The theoretical method employed here is an "indirect" form of the boundary-integral equation (BIE) method which includes the effect of the crack in the kernal of the integral equations. Various forms of the BIE method have been applied to two-dimensional crack problems [2–7] with excellent success. The form of the method employed here is discussed further in [6–8].

The measurement technique is briefly described in Section 2. More detail can be obtained from the NASA report [8]. The theoretical approach is described in Section 3, and finally the experimental and theoretical results are compared and discussed.

2 Experimental Techniques

The crack opening displacements were measured with the interferometric strain-displacement gage (ISDG) technique. This noncontacting method has a very short gage length which permits accurate measurement of the displacement of the crack surfaces at several positions along the crack—even very near the crack tip. The principles and various applications of the ISDG are well documented, but for this research a particularly easy-to-use measuring system was developed. In addition, new techniques were developed to permit measurement of displacement parallel to the crack.

2.1 The Interferometric Strain/Displacement Gage. The

Contributed by the Applied Mechanics Division for publication in the JOURNAL OF APPLIED MECHANICS.
Discussion on this paper should be addressed to the Editorial Department, ASME, United Engineering Center, 345 East 47th Street, New York, N. Y. 10017, and will be accepted until December 1, 1980. Readers who need more time to prepare a discussion should request an extension from the Editorial Department. Manuscript received by ASME Applied Mechanics Division, October, 1979; final revision, February, 1980.

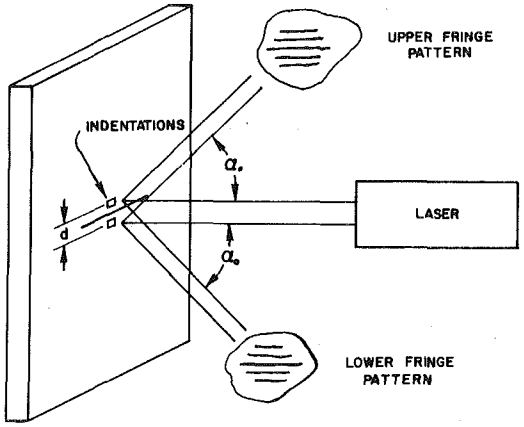

Fig. 1 Schematic of the ISDG

basic principles of the ISDG are illustrated in Fig. 1. Two very small indentations are pressed into the surface of a specimen; these are located one on each side of the crack. When coherent light impinges upon the indentations, it is diffracted back at an angle α_0 with respect to the incident beam. Since the indentations are very close together, the two diffracted beams overlap, resulting in interference fringe patterns on either side of the incident laser beam. Movement of the two indentations relative to each other causes a movement of the two fringe patterns; this fringe motion is easily related to the displacement, by

$$\delta d = \frac{\lambda}{\sin \alpha_0}\left(\frac{\Delta m_1 + \Delta m_2}{2}\right) \tag{1}$$

where λ is the wavelength of laser light, Δm_1 and Δm_2 are the fringe motions of the upper and lower fringe patterns, α_0 is defined in Fig. 1, and δd is the relative displacement of the two indentations. It is necessary to average the two fringe motions together to eliminate rigid body motion in a direction parallel to the load application. Reference [9] describes the ISDG in more detail.

Since a large number of measurements were planned for this series of experiments, it was important to have a convenient data acquisition system, and a measurement system for monitoring the motion of the two fringe patterns was developed. This consisted of two phototransistors (one for each pattern) which monitored the intensity of the fringe patterns as they moved. The output was a sinusoidal-shaped voltage signal. The signal from each fringe pattern was fed into an analog circuit that triggered a one-shot monostable multivibrator which produced a pulse every time the incoming voltage was increasing and exceeded a certain level. The pulses from the two signals were combined into a summing circuit which simply incremented the voltage output every time a pulse was received. This output was fed to the vertical channel of an X-Y plotter; the signal from the specimen load cell was applied to the other channel. The final data were then a plot of load versus displacement from which the slope could be taken to yield the crack surface displacement per unit load. The optics, physical arrangement, and electronics of this instrument are described in reference [10].

2.2 Specimens. The specimen material was type 2219 aluminum, 3.2 mm thick, furnished by NASA-Lewis. The specimens were oriented so that the rolling direction was paralled to the loading direction. Tests were run on the material to obtain the following elastic properties: elastic modulus = $70 \pm 1 \times 10^3$ MPa, Poisson's ratio = 0.33 $\pm$ 0.01.

The specimen geometry is shown schematically in Fig. 2. The slot in the center of the specimen was nominally 12.5 mm long $\times$ 300 micrometers wide. These slots were electromachined in the specimens. Six specimens were tested with angular orientations of 0°, 15°, 30°, 45°, 60°, and 75°. In addition six different widths of the specimen were tested; the width was varied by machining down the tested specimen after each series of experiments. Note from Fig. 2 that displacement

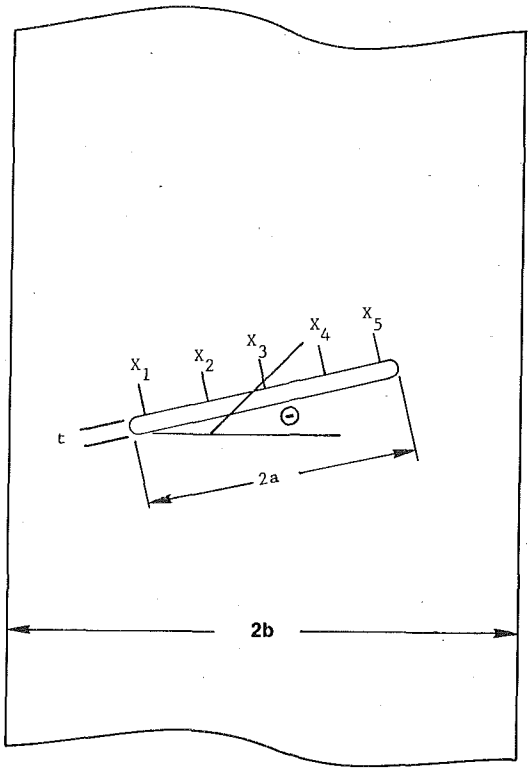

Fig. 2 Schematic of the specimens

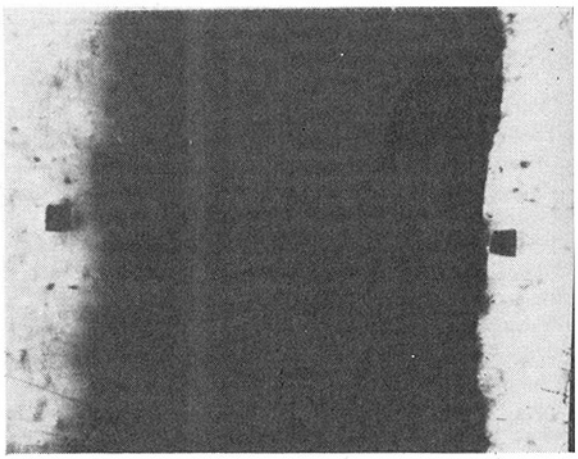

Fig. 3 Photomicrograph of a set of indentations; the slot is 290 micrometers wide

measurements were made at five positions along the slot—at the center, at two quarter points, and at the ends of the slot. The indentation at the "ends" of the slot were actually located about 650 microns from the slot tip. The slot tip was a very smooth semicircle. In other words, the indentations at the ends of the slot were actually slightly more than four radii away from the end of the slot.

Fig. 3 is a photomicrograph of a set of indentations and the specimen slot. The slot in that picture is 290 micrometers wide. Note that the indentations are close enough to the edge of the slot that one can reasonably assume that the crack surface displacements is being measured.

2.3 Data Reduction. The specimens were loaded in an Instron screw-driven testing machine. The test procedure was to apply a very slight preload to the specimen and then set a maximum load value on the test machine. While the specimen was cycled several times between the maximum and minimum load, the positions of the laser and

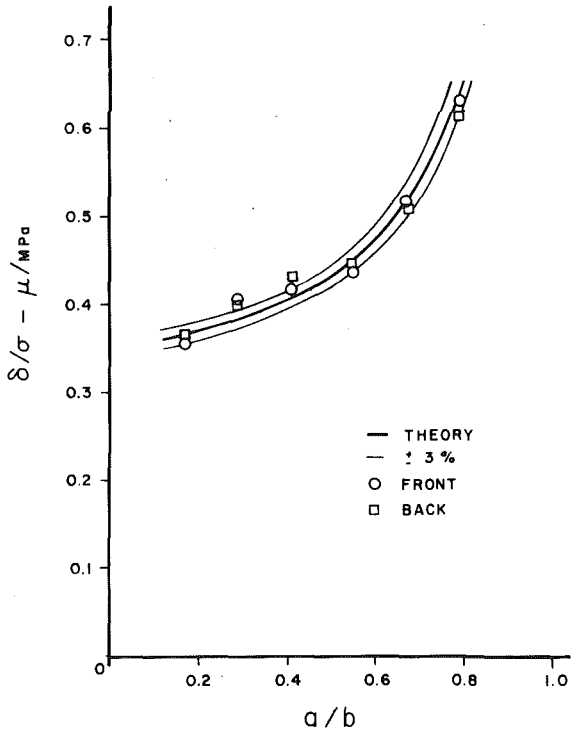

Fig. 4 Calibration plot comparing the measured displacements at the center of the 0° specimens with theoretical values; measurements were made on the front and back of the specimens

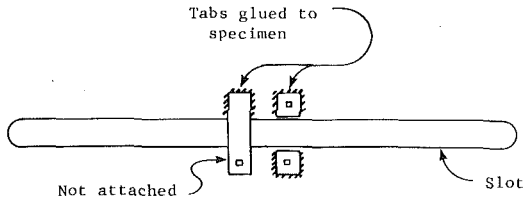

Fig. 5 Schematic of the tab arrangement for biaxial displacement measurement

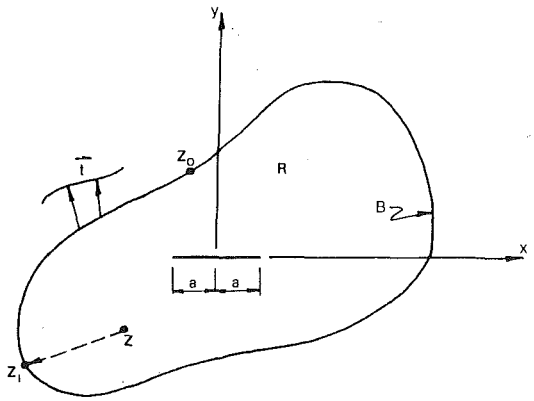

Fig. 6 Boundary-value problem involving region weakened by a sharp crack

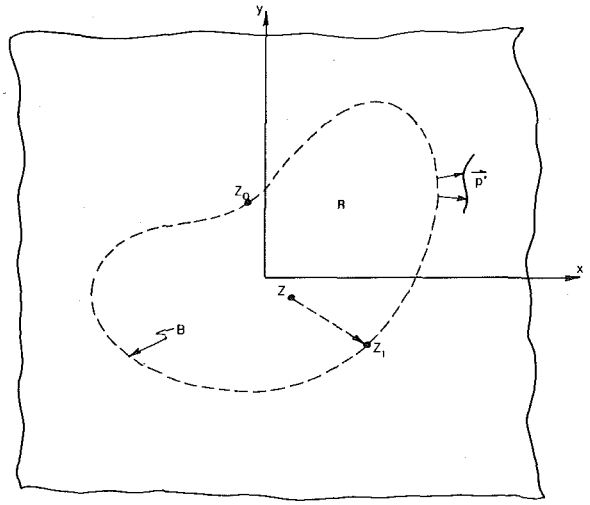

Fig. 7 Auxiliary boundary-value problem

the phototransitors was adjusted so that the fringe pattern remained bright at the phototransitor during the entire load cycle. The maximum load was chosen small enough that no plastic deformation occurred at the ends of the slots during the entire series of experiments.

After the adjustment had been completed, the data record was an X-Y plot of load versus displacement taken as the load was increasing. It had been determined early in the course of the experiments that the difference between loading "up" and "down" was negligible. The scale on the displacement plots was calibrated using the measured value of the angle α_0 in equation (1). The resulting curves were "stair-step" in appearance because of the limited sensitivity of the simple measuring curcuit. A straight line was drawn through this plot and the slope of the line computed. The total relative uncertainty of the slope measurement was 3 percent; 1 percent from the load calibration, 1 percent from the human element in drawing the straight line through the plot, and 1 percent in the measurement of the angle α_0.

To assure that the measurement system was giving accurate results, the data for specimens with a horizontal slot ($\theta = 0°$) were compared with that predicted from the existing solution [11]. Measurements were taken on both the front and the back of the specimen as it was mounted in the test machine to see if there was any bending or misalignment in the machine. The results are presented in Fig. 4 for the various widths of specimens—ranging from a crack length to specimen width ratio of 0.17 to 0.79. Fig. 4 shows that the ISDG works satisfactorily for slots of this size.

2.4 Biaxial Measurement. Special arrangements have to be made for measurement of displacement parallel to the slot. This is accomplished as shown schematically in Fig. 5. The small tabs were cut from a Pt-Rh alloy sheet, 250 micrometers thick. The nominal size of the tabs was 250 microns square for the small tabs, while the tab across the slot was 750 microns long. These tabs were glued to the specimen with Eastman 910 adhesive, and then the indentations were applied. This arrangement turns out to be a suitably small displacement transducer considering the fact that the slot is over 1200 microns long. However, the application of the tabs is a fairly delicate procedure. Note that the measurements on the front of the specimen, as shown in Fig. 4, were made using the two smaller tabs.

3 Theoretical Approach

Consider the plane linear-elastic region R of Fig. 6, bounded by contour B and containing a crack of length $2a$. The boundary contour B is subjected to a specified traction, denoted by $\mathbf{t}$. It has been shown [2–7] that this problem can be treated quite effectively by "boundary-integral" techniques and, in this section, one such technique [6–8] will be applied to the problem of interest in this paper.

We begin by considering the "auxillary" problem of Fig. 7, i.e., an infinite plane containing the crack of length $2a$, with a layer of body force $\mathbf{p}^*$ applied along contour B. If $H_{ij;q}(Z, Z_0)$ and $I_{i;q}(Z, Z_0)$ are the ijth stress component and the ith displacement component, respec-

tively, at point Z caused by a unit load in the q-direction applied at point Z_0, then by superposition the solution to the problem of Fig. 7 can be written as

$$\sigma_{ij}(Z) = \oint_B H_{ij;q}(Z, Z_0)p_q^*(Z_0)ds(Z_0)$$
$$u_i(Z) = \oint_B I_{i;q}(Z, Z_0)p_q^*(Z_0)ds(Z_0) \tag{2}$$

where s is a coordinate measured along B. The notation employed here implies summation over repeated indices. If the solutions to the problems of Figs. 6 and 7 are to be identical within R, then the stress field given by equation (2) must satisfy

$$\sigma_{ij}(Z_1)n_j(Z_1) = t_i(Z_1) \tag{3}$$

as Z approaches Z_1 from the inside of R, where $n_j(Z_1)$ is the j-component of the outward-directed unit vector normal to B at point Z_1. Inserting equation (2) into equation (3) yields

$$\tfrac{1}{2}p_i^*(Z_1) + n_j(Z_1)\oint_B H_{ij;q}(Z_1, Z_0)p_q^*(Z_0)ds(Z_0) = t_i(Z_1) \tag{4}$$

where the singularity which occurs when $Z_1 = Z_0$ has been extracted and the integral is thus to be interpreted in the principal-value sense.

An approximate solution can be obtained by discretizing the boundary and the boundary values and converting equations (2) and (4) into linear algebraic equations. A simple scheme would be to divide B into N intervals of length ΔS_k, $k = 1, \ldots, N$, and to integrate the traction of Fig. 6 and body force layer of Fig. 7 over interval ΔS_k, denoting the results as

$$P_{ik} = \int_{\Delta S_k} t_i ds$$
$$P_{ik}^* = \int_{\Delta S_k} p_i^* ds \tag{5}$$

where $i = x, y; k = 1, \ldots, N$. If the resultant loads of equation (5) are then located at the center point of interval ΔS_k, equations (2) and (4) are converted to

$$\tfrac{1}{2}P_{il}^*(Z_1) + \sum_{\substack{k=1 \\ k\neq l}}^{N} H_{ij;q}(Z_1, Z_0)P_{qk}^*(Z_0)n_j(Z_1)\Delta S_l = P_{il}(Z_1) \tag{6}$$

where $i = x, y; j = x, y; l = 1, \ldots, N$, and

$$\sigma_{ij}(Z) = \sum_{k=1}^{N} H_{ij;q}(Z, Z_0)P_{qk}^*(Z_0)$$
$$u_i(Z) = \sum_{k=1}^{N} I_{i;q}(Z, Z_0)P_{qk}^*(Z_0). \tag{7}$$

In equations (6) and (7), Z_1 is to be interpreted as the center point of boundary interval l and Z_0 as the center point of boundary interval k.

Once the $2N \times 2N$ system of equations (6) is solved for P_{ik}^*, $i = x, y, k = 1, \ldots, N$, the stress and displacement components at any point Z in R can be found by simple summation, i.e., equations (7).

The influence functions in equations (6) and (7) can be written in terms of the complex potential functions, ϕ and ψ, associated with the region of Fig. 7 subjected to a point load $P_k^*(Z_0) = P_{xk}^*(Z_0) + iP_{yk}^*(Z_0)$ applied at the point Z_0 [12]:

$$H_{xx;q}(Z, Z_0)P_{qk}^*(Z_0) = R[2\phi'(Z, Z_0) - \overline{Z}\phi''(Z, Z_0) - \psi'(Z, Z_0)]$$
$$H_{yy;q}(Z, Z_0)P_{qk}^*(Z_0) = R[2\phi'(Z, Z_0) + \overline{Z}\phi''(Z, Z_0) + \psi'(Z, Z_0)]$$
$$H_{xy;q}(Z, Z_0)P_{qk}^*(Z_0) = I[\overline{Z}\phi''(Z, Z_0) + \psi'(Z, Z_0)]$$
$$I_{x;q}(Z, Z_0)P_{qk}^*(Z_0) = \frac{1}{2\mu}R[\alpha\phi(Z, Z_0) - Z\overline{\phi'(Z, Z_0)} - \overline{\psi(Z, Z_0)}]$$
$$I_{y;q}(Z, Z_0)P_{qk}^*(Z_0) = \frac{1}{2\mu}I[\alpha\phi(Z, Z_0) - Z\overline{\phi'(Z, Z_0)} - \overline{\psi(Z, Z_0)}] \tag{8}$$

where $\alpha = (3 - \nu)/(1 + \nu)$ for plane stress and $\alpha = 3 - 4\nu$ for plane strain, μ is the shear modulus, ν is Poisson's ratio, and $Z = x + iy$, $Z_0 = x_0 + iy_0$. It is clear that the complex potential functions can be written as

$$\phi(Z, Z_0) = \phi^0(Z, Z_0) + \phi^*(Z, Z_0)$$
$$\psi(Z, Z_0) = \psi^0(Z, Z_0) + \psi^*(Z, Z_0) \tag{9}$$

where ϕ^0 and ψ^0 are the complex potential functions associated with an infinite plane, with no crack, subjected to the point load, i.e.,

$$\phi^0(Z, Z_0) = -\frac{P_k^*(Z_0)}{2\pi(\alpha + 1)}\ln(Z - Z_0)$$
$$\psi^0(Z, Z_0) = \alpha\frac{\overline{P_k^*(Z_0)}}{2\pi(\alpha + 1)}\ln(Z - Z_0) + \frac{P_k^*(Z_0)}{2\pi(\alpha + 1)}\frac{\overline{Z}_0}{Z - Z_0} \tag{10}$$

and ϕ^* and ψ^* are the complex potential functions associated with the problem of an infinite plane, containing the crack, subjected to a traction along the crack faces equal in magnitude and opposite in direction to the traction generated along an imagined crack in the problem of ϕ^0, ψ^0. It is shown in [7] that, if we introduce the mapping function

$$Z = \omega(\zeta) = \frac{a}{2}\left(\zeta + \frac{1}{\zeta}\right) \tag{11}$$

we can determine that

$$\begin{aligned}
\phi^*(Z) &= \phi_1^*(\zeta) \\
&= \frac{P_k^*(Z_0)}{2\pi(\alpha + 1)}\left[\ln\frac{r_0 - \zeta}{r_0} - \alpha\ln\frac{t_0 - \zeta}{t_0}\right] \\
&\quad + \frac{\overline{P_k^*(Z_0)}}{2\pi(\alpha + 1)}\left[\frac{\zeta^2 - Z_0\zeta + 1}{\zeta^2 - \overline{Z}_0\zeta + 1} + \frac{(t_i^2 - Z_0t_i + 1)\zeta}{t_i(t_0 - t_i)(\zeta - t_i)} - 1\right] \\
\psi^*(Z) &= \psi_1^*(\zeta) \\
&= \frac{P_k^*(Z_0)}{2\pi(\alpha + 1)}\left[\frac{\zeta^2 - \overline{Z}_0\zeta + 1}{\zeta^2 - Z_0\zeta + 1} + \frac{(r_i^2 - \overline{Z}_0r_i + 1)\zeta}{r_i(r_0 - r_i)(\zeta - r_i)}\right. \\
&\quad \left. + \frac{\zeta(\zeta^2 + 1)}{1 - \zeta^2}\left(\frac{1}{\zeta - r_0} - \frac{\alpha}{\zeta - t_0}\right) - 1\right] \\
&\quad + \frac{\overline{P_k^*(Z_0)}}{2\pi(\alpha + 1)}\left[\ln\frac{t_0 - \zeta}{t_0} - \alpha\ln\frac{r_0 - \zeta}{r_0}\right. \\
&\quad \left. + \frac{\zeta(\zeta^2 + 1)}{1 - \zeta^2}\left\{\frac{(Z_0 - \overline{Z}_0)(\zeta^2 - 1)}{(\zeta^2 - \overline{Z}_0\zeta + 1)^2} - \frac{t_i^2 - Z_0t_i + 1}{(t_0 - t_i)(\zeta - t_i)^2}\right\}\right]
\end{aligned} \tag{12}$$

provided that $Z \neq \overline{Z}_0$, where

$$r_{0,i} = \tfrac{1}{2}[Z_0 \pm (Z_0^2 - 4)^{1/2}]$$
$$t_{0,i} = \tfrac{1}{2}[\overline{Z}_0 \pm (\overline{Z}_0^2 - 4)^{1/2}] \tag{13}$$

and $a = 2$ for convenience. If $Z = \overline{Z}_0$, we have

$$\begin{aligned}
\phi^*(\overline{Z}_0) &= \phi_1^*(t_i) \\
&= \frac{P_k^*(Z_0)}{2\pi(\alpha + 1)}\left[\ln\frac{r_0 - t_i}{r_0} - \alpha\ln\frac{t_0 - t_i}{t_0}\right] \\
&\quad + \frac{\overline{P_k^*(Z_0)}}{2\pi(\alpha + 1)}\left[\frac{t_i^2 - 2t_it_0 + Z_0t_0 - 1}{(t_i - t_0)^2} - \frac{Z_0t_0 - 1}{t_0^2}\right] \\
\psi^*(\overline{Z}_0) &= \psi_1^*(t_i) \\
&= \frac{P_k^*(Z_0)}{2\pi(\alpha + 1)}\left[\frac{t_i^2 - \overline{Z}_0t_i + 1}{t_i^2 - Z_0t_i + 1} + \frac{r_i^2 - \overline{Z}_0r_i + 1}{r_i(r_0 - r_i)(t_i - r_i)}\right. \\
&\quad \left. + \frac{t_i(t_i^2 + 1)}{1 - t_i^2}\left(\frac{1}{t_i - r_0} - \frac{\alpha}{t_i - t_0}\right) - 1\right] \\
&\quad + \frac{\overline{P_k^*(Z_0)}}{2\pi(\alpha + 1)}\left[\ln\frac{t_0 - t_i}{t_0} - \alpha\ln\frac{r_0 - t_i}{r_0}\right. \\
&\quad \left. + \frac{t_i(t_i^2 + 1)}{1 - t_i^2}\frac{2(t_0^2 - Z_0t_0 + 1)}{(t_i - t_0)^3}\right]
\end{aligned} \tag{14}$$

The method is now applied to the problem of interest, shown in Fig. 8, i.e., a rectangular region, containing a centrally located sharp crack of half-length 6.40 mm and subjected to a uniaxial tension of 1 MPa.

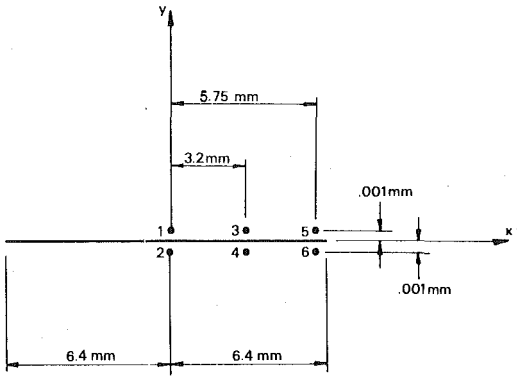

Fig. 8 Locations of field points for BIE computations

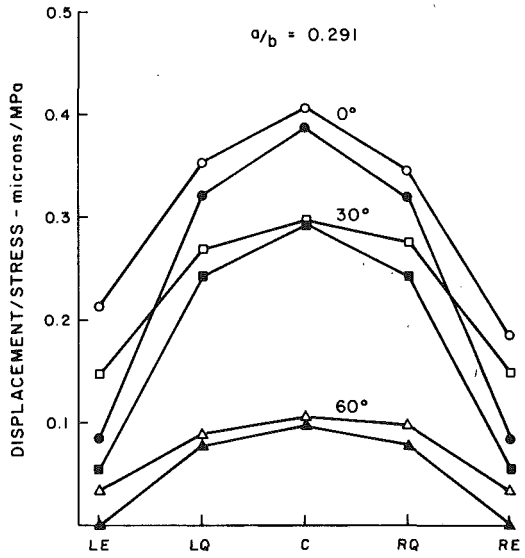

Fig. 9 Comparison of experimental and theoretical results for $a/b = 0.291$; open symbols are experimental data

Plane stress is assumed and $\nu = 0.33$, $E = 70 \times 10^3$ MPa. The following 36 cases are treated: $W = 7.62$ cm, 4.37 cm, 3.05 cm, 2.34 cm, 1.90 cm, 1.60 cm; and $\theta = 0°$, 15°, 30°, 45°, 60°, 75°. For all cases, the displacements u_x and u_y in the x and y-directions, respectively, are computed at the 6 field points shown in Fig. 8. The results for crack opening displacements at the center point, quarter point and end point and for relative transverse displacement at the center point can then be readily determined fron

$$\begin{aligned} \delta_{\text{center}} &= (u_y)_1 - (u_y)_2 \\ \delta_{\text{trans}} &= (u_x)_1 - (u_x)_2 \\ \delta_{\text{quart}} &= (u_y)_3 - (u_y)_4 \\ \delta_{\text{end}} &= (u_y)_5 - (u_y)_6. \end{aligned} \tag{15}$$

Results are presented in the next section where comparison is made with the experimental results.

For implementation of equations (6) and (7), the boundary is divided into $N = 60$ divisions, 10 on each of the loaded sides of length $\Delta S_l = W/10$, and 20 on each of the unloaded sides of length $\Delta S_l = 3W/20$. The solution of equations (6) was obtained via the Crout algorithm with equilibration and partial pivoting. Since a crack half length of $a = 2$ was assumed earlier, the problem was first scaled accordingly and the solutions were subsequently scaled back.

4 Results and Conclusions

The results for displacements perpendicular to the crack are pre-

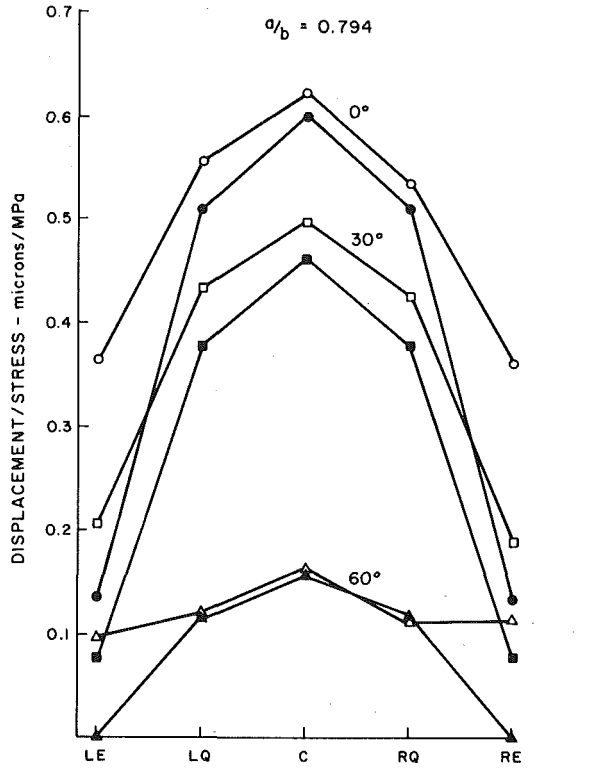

Fig. 10 Comparison of experimental and theoretical results for $a/b = 0.794$; open symbols are experimental data

Table 1 Comparison for $a/b = 0.291$ (displacements in microns)

Loct.	Center		Transverse		Quarter		End	
θ	BIE	IDG	BIE	IDG	BIE	IDG	BIE	IDG
0°	.386	.405	.000	-	.320	.349	.083	.197
15°	.360	.377	.092	.015	.299	.330	.075	.172
30°	.292	.295	.162	.165	.241	.271	.054	.148
45°	.196	.215	.189	.182	.160	.182	.025	.095
60°	.098	.105	.165	.128	.077	.094	-.003	.034
75°	.025	.024	.096	.046	.017	.023	-.023	.011

Table 2 Comparison for $a/b = 0.794$ (displacements in microns)

Loct.	Center		Transverse		Quarter		End	
θ	BIE	IDG	BIE	IDG	BIE	IDG	BIE	IDG
0°	.600	.623	.000	-	.509	.546	.135	.362
15°	.574	.620	.099	-	.483	.540	.123	.294
30°	.462	.499	.169	.168	.378	.431	.078	.199
45°	.311	.337	.212	.219	.245	.275	.032	.121
60°	.159	.163	.197	.198	.118	.116	-.003	.107
75°	.040	.033	.118	.096	.026	.041	-.024	-

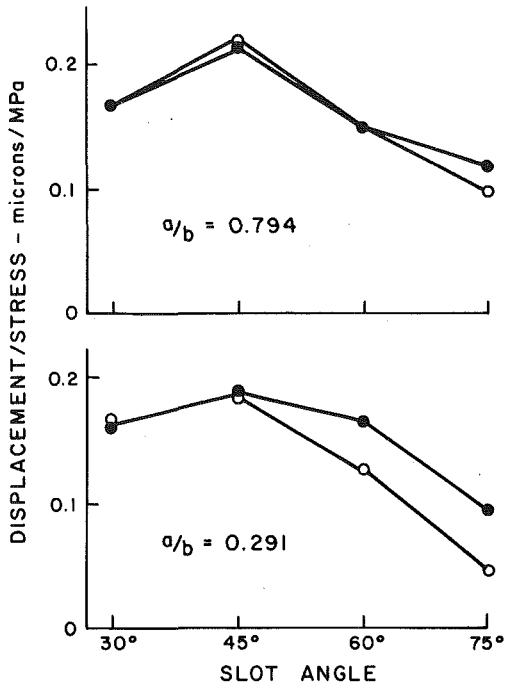

Fig. 11 Comparison of experimental and theoretical results for transverse displacements; open symbols are experimental data

sented in Figs. 9 and 10 for two selected crack-length/width (a/b) ratios. The measured values are designated as open symbols while the displacements computed from the boundary integral equation technique are represented by filled symbols. These data are also presented in Tables 1 and 2. The complete set of data for all six crack-length/wide ratios is available in reference [8].

Figs. 9 and 10 show that the agreement between the BIE technique and the experiments is in general quite good except at the end points. The fact that the two techniques don't agree for displacements near the crack tips is understandable. The BIE computations are for a sharp crack; whereas the IDG measurements were made on a finite slot. Note that the IDG values are larger—much larger at the end points. The difference between the modeled crack and the actual slot is not very significant away from the end points. Another reason for the greater disagreement at the end points is that the measured displacements are smaller and thus more susceptible to experimental error.

Transverse displacements at the center of the slot are plotted in Fig. 11 and tabulated in Tables 1 and 2. Attempts were made to make IDG measurements at $\theta = 15°$, but the displacements were so small that the data were useless. However, for larger angles the agreement is quite good. This agreement demonstrates that the elaborate technique of gluing tabs across the slot didn't distort the measurements.

Examination of Tables 1 and 2 shows that the end displacements were negative for angles of 60° and 75°. In fact, the BIE technique gave the same negative values for 60° and 75° for every crack-length/width ratio investigated. This negative displacement implies that the sharp crack surfaces cross each other—a physical impossibility. Certainly allowing these negative displacements influences the displacements at the quarter points and at the center of the crack.

The results of this extensive research program show that the theoretical and experimental techniques (both of which were developed in the course of the work) are valid for establishing crack surface displacements. The choice of method for future problems will depend on how easily the geometry and applied loads can be modeled. Where external loads can be accurately predicted and the geometry is reasonably simple, the BIE method is more appropriate. For more complicated situations, the IDG is an accurate, easy-to-use experimental technique.

Acknowledgments

The authors greatly appreciate the support of NASA-Lewis and the comments and guidance of Mr. Thomas Orange for part of the work. The very capable assistance of undergraduates Marc Smith and Thomas Payne during the experimental studies is acknowledged.

References

1 Smith, D. G., and Smith, C. W., "Photoelastic Determination of Mixed Mode Stress-Intensity Factors," *Engineering Fracture Mechanics,* Vol. 4, 1972, pp. 357–366.

2 Cruse, T. A., "Boundary-Integral Equation Fracture Mechanics Analysis," *Boundary-Integral Equation Method: Computational Applications in Applied Mechanics,* eds., Cruse, T. A., and Rizzo, F. J., ASME (AMD-Vol. 11), New York, 1975, pp. 31–46.

3 Besuner, P. M., and Snow, D. W., "Application of the Two-Dimensional Integral Equation Method to Engineering Problems," *ibid.,* 1975, pp. 101–117.

4 Snyder, M. D., and Cruse, T. A., "Boundary-Integral Equation Analysis of Cracked Anisotropic Plates," *International Journal of Fracture,* Vol. 10, 1975, pp. 315–328.

5 Cruse, T. A., "Two-Dimensional BIE Fracture Mechanics Analysis," *Recent Advances in Boundary Element Methods,* ed., Brebbia, C. A., Pentech Press, London: Plymouth, 1978, pp. 167–184.

6 Mirmohamadsadegh, A., and Altiero, N. J., "A Boundary-Integral Approach to the Problem of an Elastic Region Weakened by an Arbitrarily Shaped Hole," *Mechanics Research Communications,* Vol. 6, 1979, pp. 167–175.

7 Mirmohamadsadegh, A., and Altiero, N. J., "Solution of the Problem of a Crack in a Finite Plane Region Using an Indirect Boundary-Integral Method," *Engineering Fracture Mechanics,* Vol. 11, 1979, pp. 831–837.

8 Altiero, N. J., Jr., and Sharpe, W. N., Jr., *Measurements of Mixed-Mode Crack Surface Displacements and Comparison With Theory,* NASA-CR-157579.

9 Sharpe, W. N., Jr., "Interferometric Surface Strain Measurement," *International Journal of Nondestructive Testing,* Vol. 3, 1971, pp. 59–76.

10 Sharpe, W. N., Jr., Payne, T. S., and Smith, M. K., "A Biaxial Laser-Based Displacement Transducer," *Rev. Sci. Instr.,* Vol. 49, 1978, pp. 741–745.

11 Tada, H., Paris, P., and Irwin, G., *The Stress Analysis of Cracks Handbook,* Del Research Corp., 1973.

12 Muskhelishvili, N. I., *Some Basic Problems of the Mathematical Theory of Elasticity,* translated by J. R. M. Radok, Noordhoff Publishing, Leyden 1953.

J. Tirosh

Faculty of Mechanical Engineering,
Technion—Israel Institute of Technology,
Haifa 32000, Israel
Assoc. Mem. ASME

P. Mast
L. Beaubien
D. Mulville
S. Sutton
I. Wolock

Mechanics of Materials Branch,
Ocean Technology Division,
U.S. Naval Research Laboratory,
Washington, D.C. 20375

Fracture Criteria of Fibrous Laminated Composites Under In-Plane Multidirectional Loading

A study on the validity of various fracture criteria of angle-ply-laminated composites is presented for in-plane loading. Special emphasis is given to the vectorial presentation of the J-integral as a suitable candidate for fracture characterization of composites under general combined loading. The combined loading which is composed of a simultaneous tension, shear and in-plane bending in any desired proportion, has been produced in a highly computerized fashion by a specially devised apparatus at the U.S. Naval Research Laboratory. The fracture data of several angle ply laminates of carbon/epoxy composite (T300/5208) result from prescribing the foregoing three combined radial loading until fracture. Aided by numerical stress analysis (finite-element program) the data points are cast into more well-known descriptions; namely, crack-opening displacement versus crack-sliding displacement. Mode-I stress-intensity factor (K_I) versus Mode-II stress-intensity factor (K_{II}) and energy-release rate vector J_x versus J_y. The main outcome is that the data displayed on the J-integral plane have a highly distinctive nature of aligning the data points along straight lines, thus a clear discrimination between the fracture properties of different angle-ply laminates can be characterized by only two parameters. The ability to infer fracture conditions in subcomponents from tests on small coupons is assessed.

Introduction

The applicability of structural materials is limited in many cases by their ability to resist propagation of flaws (or implanted notches). The toughness value associated with such a property, so widely documented in isotropic materials, cannot apparently be similarly obtained in fibrous-reinforced composites. The reasons are not merely the technical difficulties of observing and controlling crack extension, but primarily because the modes of fracture in a general angle-ply laminate *are coupled* (i.e., both opening and sliding modes take place simultaneously under pure tensile loading, etc.). Neither analytical expressions nor experimental observations yet enable one to relate the remote applied load to the conventional stress-intensity factors when the process of fracture is a little more complex than just a colinear crack extension. Clearly there are particular cases in fracture of composites where modes of fracture are separated, so that linear fracture mechanics approach is transferable (i.e., reference [1, 2]), notably in unidirectional reinforcement [3, 4] but not without reservations [5, 6]. By recognizing the coupling effect between the different modes it was felt that the most reliable situation by which fracture data should be produced is by activating all possible modes of fracture; namely, by applying *simultaneously* the most general in-plane loading; tension, shear, and in-plane bending. Therefore, an experimental effort is focussed here to produce fracture data on fibrous composite materials subjected to different proportions of the previously mentioned three combined loading.

A computer controlled machine was designed at the U.S. Naval Research Laboratory to meet this demand. The global features of this machine resemble the computer-aided mechanical testing machine reported by Wu and Jerina [7] for testing thin-walled tubes, but incorporates more independent loading modes with more automation in the overall procedure. The three load-displacement histories of the three loading modes are continuously recorded, and the associated dissipated energy absorbed *in situ* by the specimen is computed on real time and displayed on a T-V screen.[1] The fracture initiation was defined as the point where abrupt dissipation of energy consumed by the loading specimen was begun. The meaning of dissipative energy is explained later. The collection of such fracture data at each angle-ply laminate of T300/5208 (30°, 45°, 60°) is analyzed in different ways in order to reveal the most convenient parameters for

Contributed by the Applied Mechanics Division for presentation at the Winter Annual Meeting, Chicago, Ill., November 16–21, 1980, of THE AMERICAN SOCIETY OF MECHANICAL ENGINEERS.

Discussion on this paper should be addressed to the Editorial Department, ASME, United Engineering Center, 345 East 47th Street, New York, N.Y. 10017, and will be accepted until December 1, 1980. Readers who need more time to prepare a discussion should request an extension from the Editorial Department. Manuscript received by ASME Applied Mechanics Division, October, 1979; final revision, March, 1980. Paper No. 80-WA/APM-9.

[1] At preselected small time increments during the test (say, a few miliseconds) measurements of loads and displacements at each actuator are continuously recorded and stored. This information is used on-line to compute the current dissipated energy (equation (1)). It is only a technical matter to display it graphically (as in Fig. 4) for visualization of the specimen behavior up to total failure.

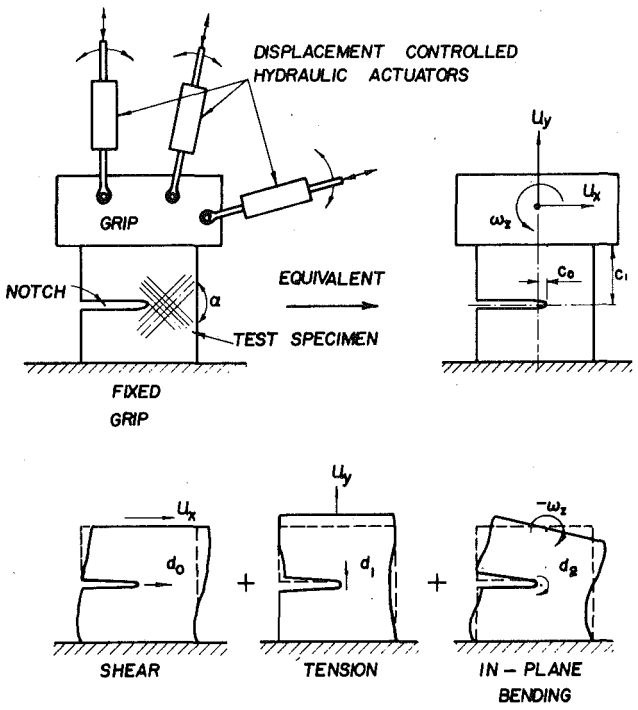

Fig. 1 Grips arrangement and loading conditions produced by in-plane loader

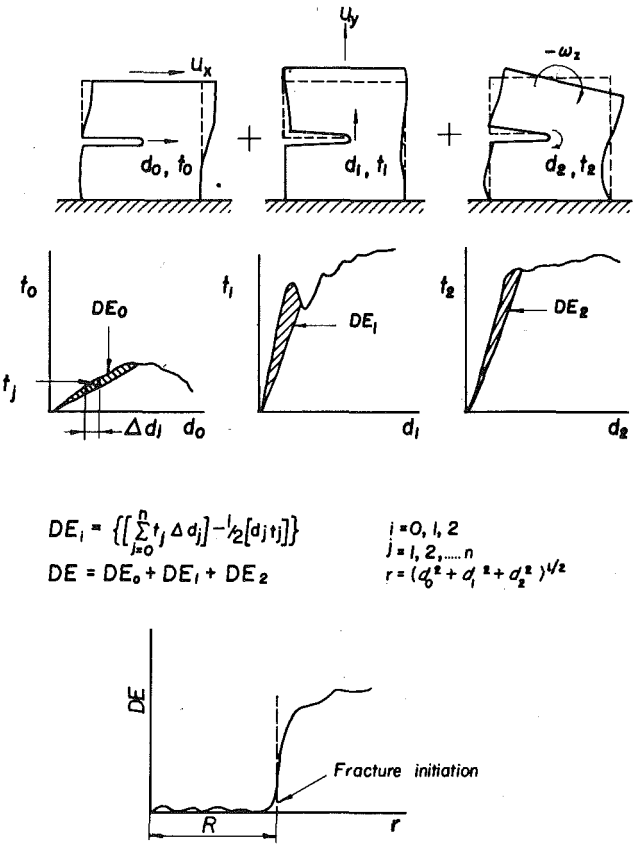

Fig. 2 Fracture initiation as indicated by the global displacement R at which a sharp increase in the total dissipative energy, DE, is observed

fracture characterization: (*a*) crack-opening displacement versus crack-sliding displacement; (*b*) Mode-I stress-intensity factor (K_I) versus Mode-II stress-intensity factor; and (*c*) energy-release rate in x-direction (J_x integral) versus energy-release rate in the y-direction (J_y integral). The main outcome is that the data displayed on the J-integral plane has a distinctive nature, not obtained in the previous presentations, *of aligning the fracture data along straight lines.* The importance of having a fracture locus as a straight line is discussed.

A Brief Description of the Test and the Analysis Procedure

The in-plane loader machine is used to test small prenotched coupons (1 in. × 0.5 in.) of graphite/epoxy (T300/5208) of angle-ply laminates with various angles. The specimen is fixed by a clamped grip at one edge and free to displace and rotate (in a plane) by a "floating" grip along the second edge, as shown in Fig. 1. The three degrees of freedom of this latter edge are controlled by the shown three (hydraulic) actuators, such that any desired combination of shear, tension, and bending is readily available via a computerized program which drives the actuators accordingly. Once the combined load is preselected the test proceeds by maintaining the proportionality[2] between the three combined loading until total separation of the specimen takes place. This proportional displacement loading path is described as a radius vector (r) in the displacement space with the coordinates d_0, d_1, and d_2, originating at the crack tip (see Fig. 1 for more details). During the displacement controlled loading, the asso-

[2] Any other history of loading can essentially be programmed as well.

Nomenclature

α = angle-ply (included angle) of fibrous composite laminate with respect to notch direction

a_{ij} = components of elastic compliances

A, B, C, E = coefficients defined in equations (9) and (10)

c_0, c_1 = geometrical parameters of the specimen

$\{d\} = (d_0, d_1, d_2)$ = displacement components (shear, tension and rotation, respectively) at the notch root which are related directly [via (4)] to the applied boundary displacement

$\left.\begin{matrix} D_x \\ D_y \end{matrix}\right\}$ = normalized crack opening displacement [equations (7) and (8)]

$[E]$ = matrix of structural stiffness

$\{f\} = (f_0, f_i, f_2)$ = boundary tractions (shear, tension, and rotation) which result from the boundary displacement

J_x, J_y = components of J-integral (13)

K_I, K_{II} = stress-intensity factors for Mode-I and Mode-II

R = generalized displacement magnitude at failure (Fig. 3).

r_i = distance from crack tip

S_1, S_2 = roots of the characteristic operation (12)

θ_1, θ_2, r = polar coordinates of displacement vector with origin at the notch tip (Fig. 3)

$\{t\} = (t_0, t_i, t_2)$ = traction components (shear, tension, and rotation) at the notch tip related directly to the boundary tractions [via (equation 3)]

$\{u\} = (u_x, u_y)$ = boundary displacement at the edge of the gripped specimen

$\hat{u}_x(r_i), \hat{u}_y(r_i)$ = displacements at point r_i

w = strain-energy density

ω_z = bending displacement produced by rotation of the grip

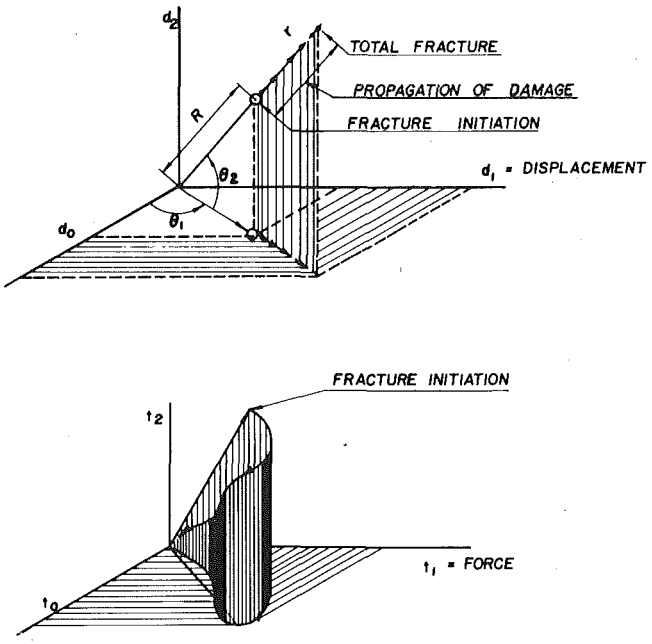

Fig. 3 A schematic description of the so-called "proportional loading" used in the tests. The displacement loading path (d_0, d_1, d_2) and the associated force path (t_0, t_1, t_2), represent the physical situation pre and postfailure (i.e., fracture initiation) of the specimen.

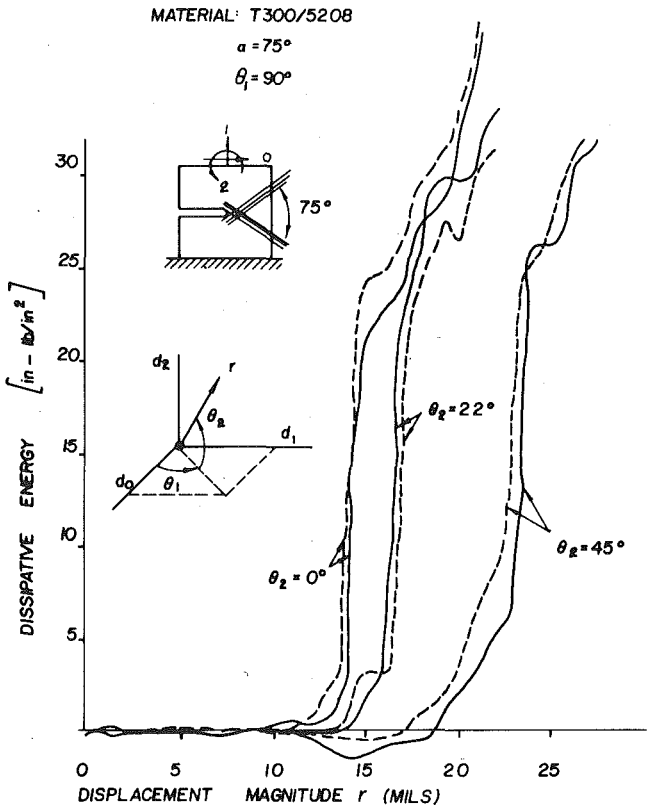

Fig. 4 Reproducibility of fracture initiation for three different combinations of loads. These graphs are taken from the T-V display during the on-line experimental results.

ciated forces (t_0, t_1, t_2)[3] are recorded versus the displacements so that the change in the three compliances is simultaneously obtained as shown in Fig. 2. It was observed that the three forces do not decrease at the same time. When the composite starts to fail not all the compliances necessarily decrease simultaneously, and load-carrying capacity may still be sustained even if some kind of damage starts to grow. After a while, as shown in Fig. 3, the increases in the displacements gradually release the loads and substantial damage is seen. A suggested measure to decide upon the critical load at which failure starts is to view the variation in the dissipative energy consumed by the coupon during its loading process. The total energy imparted to the coupon/machine system namely, the elastic one and all other irreversible dissipations which may possibly occur, is integrated on-line during the test, which is $\int_0^{d_j} t_j \delta d_j$. By subtracting the recoverable elastic energy[4] $1/2\, t_j d_j$ and summing up the contribution of the three loadings, one gets the net energy dissipated in the process by the following expression:

$$DE = \sum_{i=1}^{3} \left(\int_{d=0}^{d_j} t_j \delta d_j - \frac{1}{2}(t_j d_j) \right) \qquad (1)$$

$i = 1 \rightarrow$ shear
$i = 2 \rightarrow$ tension
$i = 3 \rightarrow$ rotation (i.e., in-plane bending)

It appears in our experiments that the sum of the three contributions as stated in equation (1) shows at a certain point a quite distinctive increase in the dissipative energy. A typical case is shown in Fig. 4. Consequently, we identify the load associated with this point as the "fracture load." The conjugate critical displacements of the moveable grip are used as boundary conditions for numerical stress analysis of the coupon at its fracture load. Various fracture surfaces are then extracted from such results as shown in Fig. 6.

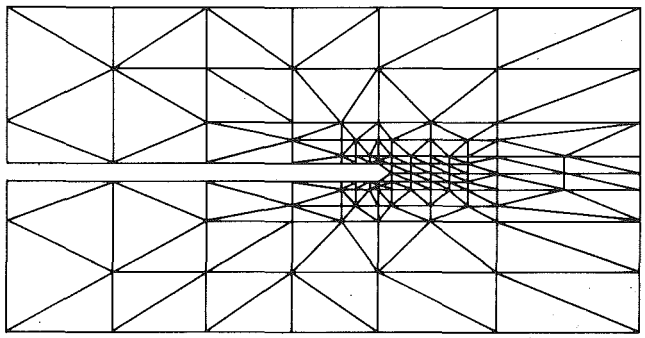

Fig. 5 Finite-element mesh used for stress analysis of the specimens at fracture initiation

Presentation of Fracture Data

The subject of this paragraph is to organize the fracture data gathered on small coupons into several forms more conceivable by designers. The computational procedures which follow are based on the displacement boundary conditions associated with the condition "at failure" as defined previously. The detailed stress and displacement fields throughout the coupon are resolved by finite-element structure analysis (Beaubien [8]) whose mesh is shown in Fig. 5. As mentioned before, the laminate appears to initiate failure without preceding substantial nonlinearities[5] as revealed by the abrupt step-rise in the dissipative energy. Consequently, one can establish

[3] The forces f_0, f_1, f_2 measured by the actuators are transformed for computational convenience, to a traction vector (t_0, t_1, t_2) located at the crack tip as explained later (equation (3)) and therefore associated to the displacement vector of the tip (d_0, d_1, d_2).

[4] Assuming that in unloading the strain resumes zero value in linear fashion.

[5] This, however, is not entirely true when compressive loading or bending in the direction which causes crack closure are used as the loading path. Our work excluded such cases.

a priori the structural stiffnesses [E] for each angle-ply laminate of the notched coupons under the three possible displacement loading u_x, u_y, and ω_z. It reads

$$\begin{Bmatrix} f_0 \\ f_1 \\ f_2 \end{Bmatrix} = \begin{vmatrix} E_{0x} & E_{0y} & E_{0z} \\ & E_{1y} & E_{1z} \\ \text{Sym} & & E_{2z} \end{vmatrix} \begin{Bmatrix} u_x \\ u_y \\ \omega_z \end{Bmatrix} \tag{2}$$

Values for [E] used in this work are tabulated in Appendix A. For simplification and convenience the generalized forces {f} which result from the prescribed displacements {u} are transformed to the notch tip location and denoted by {t} according to

$$\{f\} = [T_f]\{t\} \quad [T_f] = \begin{vmatrix} 1 & 0 & 0 \\ 0 & 1 & 0 \\ c_1 & -c_0 & 1 \end{vmatrix} \tag{3}$$

where $c(c_0, c_1)$ is the location of the load {f} with respect to the notch tip. Similarly the displacement {u} is also transformed by $[T_u]$ to the notch tip coordinate and denoted there by {d} as shown in Fig. 1 and Fig. 2. The geometrical relation is

$$\{u\} = [T_u]\{d\}, \quad [T_u] = \begin{vmatrix} 1 & 0 & -c_1 \\ 0 & 1 & c_0 \\ 0 & 0 & 1 \end{vmatrix} \tag{4}$$

It can be readily shown from (3) and (4) that the transformation matrices for forces and displacements are connected by

$$[T_u]^{-1} = [T_f] \tag{5}$$

hence, the general *Constitutive Equation* for the coupon specimen emerges from (2)–(4) by the following expression:

$$\{d\} = [T_f]^T[E]^{-1}[T_f]\{t\} \quad (\text{compliance} = [T_f]^T[E]^{-1}[T_f]) \tag{6}$$

The experiments are continuously monitored by {t} and {d}. Therefore, equation (6) serves as a computational device to find out the relative compliances (three independent compliances) of the testing machine, so vitally important for precise evaluation of experimental data. The so-called failure surfaces on the d space are plotted in a polar form[6] in Fig. 6. The fracture data on these surfaces compose the tests performed on 30°, 45°, and 60° deg of included angle (with respect to the notch). The smooth connectivity between fracture points at different proportions of shear, tension, and rotation is highly manifested. This can partially be attributed to the automatic man-free nature by which specimens are loaded and gripped in the testing machine.

Various Fracture Criteria

The goal in applying fracture mechanics concepts in composite materials is to *reduce the numbers of independent parameters* required to characterize their fracture properties. The experimental tests which depend on *three* different loading conditions, convey fracture data (Figs. 5 and 6) which are inherently three-dimensional in nature. In the following we will attempt to reduce the dimensionality of the experimental data of Fig. 6 from three to two by considering approaches which have been used successfully in the past to characterize fracture properties of isotropic materials.

Crack Opening Displacement. The concept of "crack opening displacement" is based on the premise that the displacement associated with the notch (or with the whole flank) at incipient fracture constitutes a material property and therefore can be used by a designer as fracture criterion. The question whether this holds true in composites subjected to combined loading is considered in the light of our experimental data.

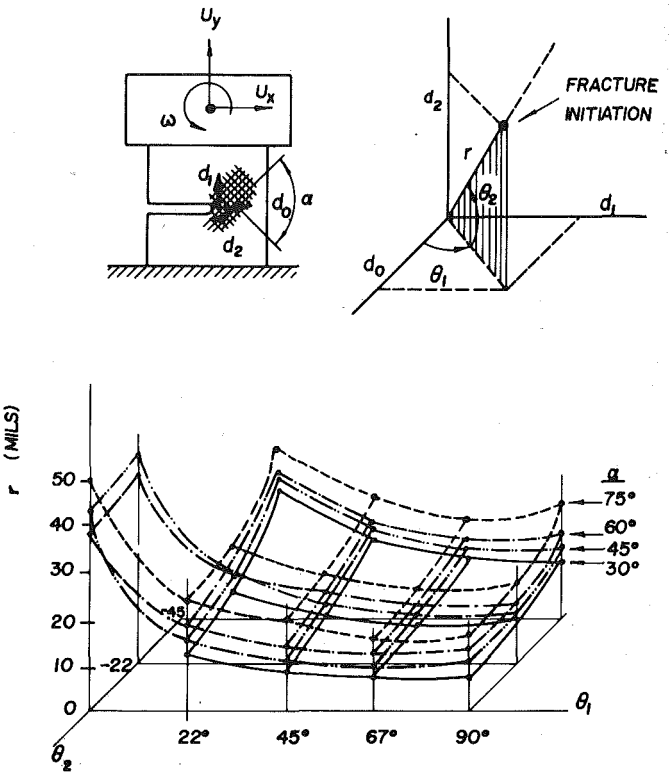

Fig. 6 Failure surfaces in polar coordinates of T300/5208 composite as produced by various loading paths; each circular black dot represents experimental failure at a given path; note the clear distinction between failure surfaces of different angle-ply laminates

For this purpose we define a normalized displacement vector (D_x, D_y) along N discrete points along the two flanks of the notch by

$$D_x{}^{(j)} = \frac{1}{N}\sum_{i=1}^{N}\frac{\hat{u}_x(r_i)}{\sqrt{r_i}} \quad D_y{}^{(j)} = \frac{1}{N}\sum_{i=1}^{N}\frac{\hat{u}_y(r_i)}{\sqrt{r_i}} \tag{7}$$

As seen in equation (7) the displacement of the flank is weighted by the corresponding distance $(1/\sqrt{r_i}$ to the tip of the notched and averaged throughout the flanks. Evaluation of equation (7) is repeated for each mode of loading ($j = 0, 1, 2$ corresponds to the three displacement loading u_x, u_y, ω_z shown in Fig. 1). As a result the total opening displacement D_x and D_y (unprimed) is obtained by adding the contributions of all the acting loading modes as expressed by

$$\begin{Bmatrix} D_x \\ D_y \end{Bmatrix} = \begin{vmatrix} D_x{}^{(0)} & D_x{}^{(1)} & D_x{}^{(2)} \\ D_y{}^{(0)} & D_y{}^{(1)} & D_y{}^{(2)} \end{vmatrix} \begin{Bmatrix} u_x \\ u_y \\ w_z \end{Bmatrix} \tag{8}$$

The critical crack opening displacement is resolved from (8) by using the values of u_x, u_y, ω_z at "incipient failure." The results shown in Fig. 7 are quite scattered without a clear topological structure required for fracture characterization. Consequently we felt that equation (7) is not a well-suited parameter for fracture criterion of angle-ply composite under combined loading.

Stress-Intensity Factors. By assuming that the notch tip is sharp and the composite is homogeneous, an analytical near-tip elastic solution [9] is valid and consequently used to evaluate the stress-intensity factors (K_I and K_{II}) at the critical loads $\{f\}^c$ in all tested combinations for the various angle-ply laminates. It is the purpose

[6] In polar form the variables d_0, d_1, d_2, are related to the three polar coordinates r, θ_1, θ_2, by

$$r = (d_0^2 + d_1^2 + d_2^2)^{1/2}$$

$$\theta_1 = \tan^{-1}(d_1/d_0)$$

$$\theta_2 = \tan^{-1}[d_2/(d_0^2 + d_1^2)]$$

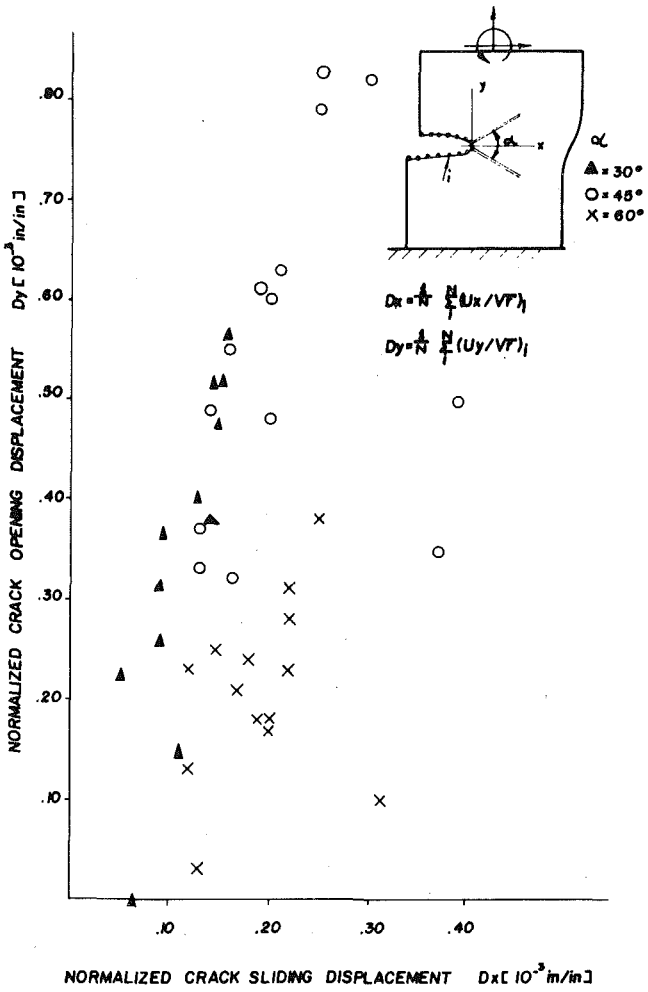

Fig. 7 Critical crack-opening displacement versus crack-sliding displacement of several angle-ply laminated composites

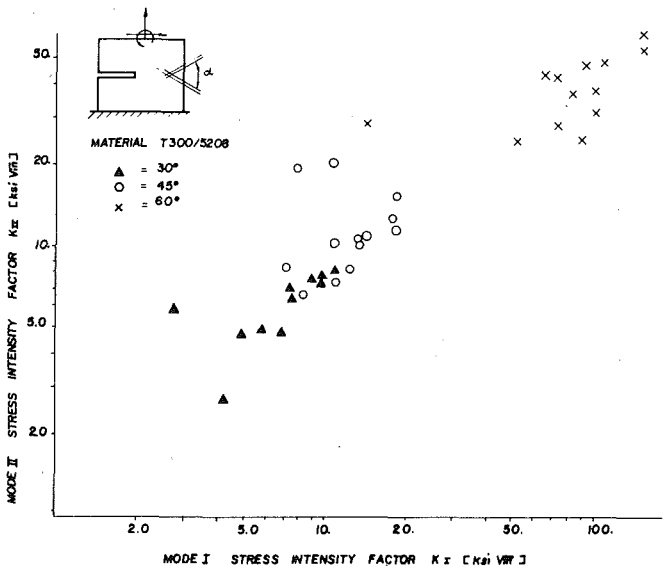

Fig. 8 Critical stress-intensity factors (K_I versus K_{II}) of several angle-ply laminated composites

of this analysis to see whether the critical stress-intensity factors can characterize the fracture behaviors of our composites.

The relation connecting the normalized opening of the crack (D_x, D_y) to the stress-intensity factors (K_I, K_{II}) in composites *are coupled* and can be generally described by the following:

$$\begin{Bmatrix} D_x \\ D_y \end{Bmatrix} = \frac{1}{\sqrt{\pi}} \begin{vmatrix} A & B \\ C & E \end{vmatrix} \begin{Bmatrix} K_I \\ K_{II} \end{Bmatrix} \tag{9}$$

The coefficients A, B, C, E are readily inferred from the analytical work of Sih and Leibowitz [9]. These coefficients consist of material elastic properties A_{ij} and the roots S_i and S_2 of the characteristic equation (12) by the following:

$$A = \mathrm{Im}\left\{\frac{S_1 p_2 - S_2 p_1}{S_1 - S_2}\right\}, \quad B = \mathrm{Im}\left\{\frac{p_2 - p_1}{S_1 - S_2}\right\}$$
$$C = \mathrm{Im}\left\{\frac{S_1 q_2 - S_2 q_1}{S_1 S_2}\right\}, \quad E = \mathrm{Im}\left\{\frac{q_2 - q_1}{S_1 - S_2}\right\} \tag{10}$$

where

$$p_1 = a_{11}S_1^2 + a_{12}, \quad p_2 = a_{11}S_2^2 + a_{12}$$
$$q_1 = \frac{a_{12}S_1^2 + a_{22}}{S_1}, \quad q_2 = \frac{a_{12}S_2^2 + a_{22}}{S_2} \tag{11}$$

The values of a_{ij} used in the experiments are tabulated in Table 1. The characteristic equation for the symmetric case used in our tests is

$$a_{11}S^4 + (2a_{12} + a_{66})S^2 + a_{22} = 0 \tag{12}$$

Table 1 Elastic compliances of T300/5208 laminates

Angle-ply T300/5208 included angle α	$a_{ij}[10^{-7}]$ psi^{-1}			
	a_{11}	a_{12}	a_{22}	a_{66}
30°	48.7	−23.4	3.20	6.45
45°	60.3	−43.0	2.96	4.74
60°	82.1	−65.0	2.60	3.73

Table 2 The roots of equation (12)

α	S_1	S_2
30°	$0.75i$	$3.42i$
45°	$0.94i$	$2.36i$
60°	$1.7 + 0.52i$	$-1.7 - 0.52i$

Using the coefficients a_{ij} from Table 1 we get the complex roots shown in Table 2.

The values of K_I and K_{II} are obtained from the inversion of equation (9) where the data of (D_x, D_y) are evaluated at incipient fracture. Results are plotted in Fig. 8. The relatively high values of the apparent toughness of the composite shown in this figure, particularly for α = 60° might have several hypothetical explanations. Since the blunting of the notch by matrix separation is most pronounced in 60° angle, a relatively high stress level for fracture is likely to result. Here again the data of Fig. 8 is not readily expressible as a convenient fracture surface (although the data seems to be a little bit more grouped along a preferred direction) and therefore, we decline to characterize fracture by critical stress-intensity factors for combined loading conditions.

The *J*-Integral Vector. The two components of the energy release rate J_x and J_y in a form of path-independent integrals, elaborated and propounded by Budiansky and Rice [10], are applicable to homogeneous bodies which can be unisotropic and nonlinear in general. Their values represent the amount of the potential energy which would be relaxed when a traction-free crack would extend (differentially) in the x and y-directions, respectively. The integrals to be

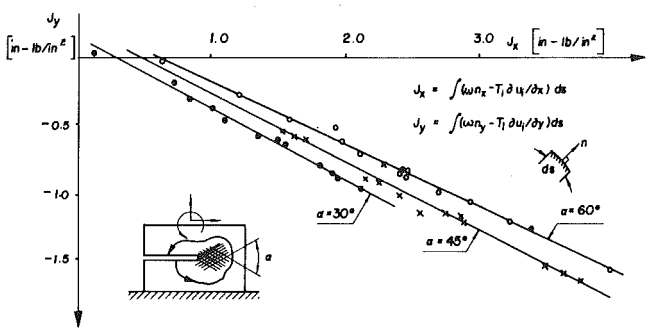

Fig. 9 Critical energy release rate (J_x versus J_y) for several angle-ply laminated composites; the appearance of fracture data of different angle-ply laminates in multidirectional loading as straight lines (i.e., only two independent parameters for each laminate) is notable

evaluated counterclockwise along arbitrary contour Γ surrounding the notch are

$$J_x = (\omega n_x - T_i \partial u_i/\partial x)ds$$
$$J_y = (\omega n_y - T_i \partial u_i/\partial y)ds \tag{13}$$

where ω is the strain-energy density (i.e., $\int \sigma_{ij} d\epsilon_{ij}$), T_i is the traction vector on Γ (i.e., $T_i = \sigma_{ij} n_j$) and ds is an element of the path Γ. Now J_x and J_y are evaluated numerically by equation (13) at incipient fracture of our coupons, the raw data of which was gathered by the in-plane loader as explained in our previous cases. The display of the fracture points for various angle-ply laminates in J_x, J_y plane is shown in Fig. 9.

It appears quite clear in this figure that the data points align themselves along straight lines; each line corresponds to a different angle-ply laminate. The main importance of such an outcome is that the distinction between the fracture properties of different angle-ply laminates (and probably between different composites as well) is reduced to just *two parameters* as for example the slope of the line and the value of J_x at the intersection with $J_y = 0$ line. In passing, it is worth reiterating that this last parameter (J_x-value at $J_y = 0$) is strictly the critical energy release rate for a notch which extends "self-similarly" (i.e., colinearly with its original position). The physical interpretation of such situations is that this single parameter coincides with the classical fracture toughness parameter G_{Ic}, or alternatively with the critical stress-intensity factor K_{Ic}. Most of the fracture study of composites up to date was restricted to such particular cases where only *one* characteristic fracture property was tested, either by classical means (i.e., [1, 2]) or by employing the J concept [6, 11, and 12].

Summary and Discussion

Reduction of dimensionality from *three* independent coordinates to *two* in describing fracture data of composite materials in multiloading case was studied. While functional relation in two-dimensional description was unsuccessful for crack-opening displacements and stress-intensity factors parameter, a *straight line relation* appears to dominate data when parametizing fracture by the corresponding critical J vector. Consequently, a clear discrimination between the fracture properties of different angle-ply laminates is achieved in terms of merely *two* parameters; the slope of the line and its intersection with the J_x-axis. As mentioned earlier this distance is identical to the well-explored toughness G_{Ic}, because J_y is zero only if the crack is propagating in a self-similar fashion. To such situations the conventional term G_{Ic} is applied. Indeed, values of G_{Ic} obtained in Fig. 5 are very close to those reported by Konish, Swedlow and Cruse [6] for the case of "crack running along the fibers" in their three-point bending tests. The slope of the fracture lines may be considered as a new parameter for fracture characterization but no profound physical interpretation has yet been attached to it besides recognizing its important role in indicating the amount of deviation from colinear crack extension. The smaller the slope the less tendency for the crack to branch away from its original position is expected. Such a trend is validated by our experiments where smaller slopes are associated with fracture of laminates composed of smaller angle-plies along which the crack was propagating.

It is still an open question whether the two-parameter fracture characterization of angle-ply composite suggested here is valid for loading conditions beyond the testing spectrum experienced by us. For example, two resulting deformation fields near a notch might differ one from the other in their details and still might yield the same values of J integrals. Therefore, fracture prediction of subcomponents via the experimental tests on small coupon necessitates the insurance that the laboratory tests from which the fracture locus is drawn, are performed on as wide combination of loadings as possible. This calls for numerous laboratory tests as a prerequisite for practical fracture prediction. Indeed, this is the main factor underlying the highly automotive and efficient nature of the multiloading test machine at the Naval Research Laboratory (NRL).

If structural subcomponents are subjected to proportional loading and prediction of fracture from an already detected flow is sought, one may take advantage of the fracture-data line by checking how far the radius vector $J(J_x, J_y)$ (emanating from the origin) which is evaluated on the subcomponent with the working load, can radially be elongated until its intersection with the experimental fracture line. This portion of the line between the current value of J and intersection point indicates the amount of the additional working load (squared) which might initiate failure in the structure. It is needless to say that the ultimate goal is to *experience such a predictor on substructure* (which is underway at NRL) before this approach is comprehensively assessed.

References

1 Mandell J. F., et al., "Stress-Intensity Factors for Anisotropic Fracture Test Specimens of Several Geometries," *Journal of Composite Materials,* Vol. 8, pp. 106–116.

2 Tirosh, J., "The Mixed Mode Fracture of Unidirectional Fibrous Composites," *Journal of Engineering Fracture Mechanics,* Vol. 13, 1980, pp. 119–127.

3 Wu, E. M., and Reuter, R. C., "Crack Extension in Fiber-Glass Reinforced Plastics," University of Illinois, TAM Report No. 275, 1965.

4 Sih, G. C., et al., "Material Characterization on the Fracture of Filament-Reinforced Composites," *Journal of Composite Materials,* Vol. 9, 1975, pp. 167–185.

5 Tirosh, J., "The Effect of Plasticity and Crack Blunting on the Stress Distribution in Orthotropic Composite Materials," ASME JOURNAL OF APPLIED MECHANICS, Vol. 40, 1973, pp. 785–790.

6 Konish, H. J., Jr., Swedlow, J. L., and Cruse, T. A., "Fracture Phenomena in Advanced Fiber Composite Materials," *AIAA Journal,* Vol. II, 1973, pp. 40–43.

7 Wu, E. M., and Jerina, K. L., "Computer Aided Mechanical Testing of Composites," *Materials Research and Standards,* MTRSTA, Vol. 12, 1972, pp. 13–18.

8 Beaubien, L., "TOTAL, Two-Dimensional Orthotropic Time Sharing Analysis Library," *Structural Mechanics Software Series,* Vol. I, University of Virginia Press, in press.

9 Sih, G. C., and Liebowitz, H., "Mathematical Theories of Brittle Fracture," *Fracture,* Vol. II, Chapter 2, H. Liebowitz, ed., Academic Press, 1969, pp. 67–190.

10 Budiansky, B., and Rice, J. R., "Conservation Laws and Energy Release Rates," ASME JOURNAL OF APPLIED MECHANICS, Vol. 40, 1973, pp. 201–203.

11 Tirosh, J., and Berg C. A., "Experimental Stress-Intensity Factor in Orthotropic Composites," *Composite Materials: Testing and Design, ASTM STP 546,* American Society for Testing and Materials, 1974, pp. 663–673.

12 Mandell, J. F., Wang, S. S., and McGarry, F. J., "The Extension of Crack-Tip Damage Zones in Fiber-Reinforced Plastic Laminates," *Journal of Composite Materials,* Vol. 9, 1975, pp. 266–287.

APPENDIX *A*

The matrix of influence coefficients $[E]$ of the cracked specimen (i.e., $[E]\{u\} = \{f\}$ as extracted from the finite-element solution.

Material T300/5208, units [lb/in.] for unit thickness

$$[E]_{\alpha=30°} = \begin{bmatrix} 18013.94 & 11.09 & 4645.92 \\ 11.10 & 28282.69 & 7633.72 \\ 4645.83 & 7674.33 & 3500.02 \end{bmatrix}$$

$$[E]_{\alpha=45°} = \begin{bmatrix} 22272.80 & 22.18 & 5743.24 \\ 22.18 & 31626.13 & 9116.33 \\ 5743.23 & 8388.92 & 4441.10 \end{bmatrix}$$

$$[E]_{\alpha=60^\circ} = \begin{bmatrix} 25959.74 & 39.78 & 6693.72 \\ 3978. & 37880.17 & 9900.68 \\ 6693.66 & 9896.17 & 5166.18 \end{bmatrix}$$

Note: The small deviation from symmetry of the foregoing matrices is the result of the numerical nature of the stress analysis (finite elements).

APPENDIX *B*

The matrix of influence coefficients $[D]$ for the crack-opening displacement vector (D_x, D_y, nondimensional)

$$[D] = \begin{vmatrix} D_x^{(0)} & D_x^{(1)} & D_x^{(2)} \\ D_y^{(0)} & D_y^{(1)} & D_y^{(2)} \end{vmatrix}$$

Material T300/5208

α = angle-ply (included angle with respect to the notch).

$\alpha = 30^\circ$

$$\begin{vmatrix} 0.601 & E-1 & -0.064 & E-3 & 0.250 & E-1 \\ 0.214 & E-2 & 0.994 & E-1 & -0.384 & E-2 \end{vmatrix}$$

$\alpha = 45^\circ$

$$\begin{vmatrix} 0.667 & E-1 & -0.478 & E-3 & 0.285 & E-1 \\ -0.713 & E-3 & 0.981 & E-1 & -0.417 & E-2 \end{vmatrix}$$

$\alpha = 60^\circ$

$$\begin{vmatrix} 0.736 & E-1 & -0.780 & E-3 & 0.322 & E-1 \\ -0.600 & E-1 & 0.991 & E-1 & 0.372 & E-2 \end{vmatrix}$$

APPENDIX *C*

The matrix of influence coefficients $[J]$ for the J-integral vector

$$\begin{vmatrix} J_x^{(0)} & J_x^{(1)} & J_x^{(2)} \\ J_y^{(0)} & J_y^{(1)} & J_x^{(2)} \end{vmatrix}$$

0 = shear displacement
1 = tensile displacement
2 = bending displacement

Material T300/5208, units [(in.-lb)/in.^{2}]

$\alpha = 30^\circ$

$$\begin{vmatrix} 161.62 & 309.44 & 10.51 \\ 5.54 & 4.12 & 10.83 \end{vmatrix}$$

$\alpha = 45^\circ$

$$\begin{vmatrix} 237.30 & 361.99 & 15.15 \\ 10.97 & 5.30 & 12.27 \end{vmatrix}$$

$\alpha = 60^\circ$

$$\begin{vmatrix} 320.82 & 455.38 & 19.93 \\ 15.00 & 6.57 & 10.54 \end{vmatrix}$$

T. Nishioka
Research Scientist.

S. N. Atluri
Regents' Professor of Mechanics.
Mem. ASME.

Center for the Advancement
of Computational Mechanics,
School of Civil Engineering,
Georgia Institute of Technology,
Atlanta, Ga. 30332

Numerical Modeling of Dynamic Crack Propagation in Finite Bodies, by Moving Singular Elements

Part 1: Formulation

An efficient numerical (finite-element) method is presented for the dynamic analysis of rapidly propagating cracks in finite bodies, of arbitrary shape, wherein linear-elastic material behavior and two-dimensional conditions prevail. Procedures to embed analytical asymptotic solutions for singularities in stresses/strains near the propagating crack-tip, to account for the spatial movement of these singularities along with the crack-tip, and to directly compute the dynamic stress-intensity factor, are presented. Numerical solutions of several problems and pertinent discussions are presented in Part 2 of this paper.

Introduction

A concise summary of the present status of the theories of dynamic crack propagation can be found in a recent article by Freund [1]. Several analytical solutions of the linear elastodynamic equations for crack propagation in unbounded plane bodies have appeared earlier. These include the works of: Yoffé; Cragg; Broberg; and Baker, for Mode-I (plane-strain opening mode) crack propagation; and the works of: Eshelby; and Achenbach, for Mode-III crack extension. All the aforementioned works are summarized and referenced in a paper by Freund [2], who considered the problem of a half-plane crack, in an elastic solid subject to time-independent loading, which is initially at rest and, at a certain instant, begins to move with either a constant velocity [2] or a nonuniform velocity [3]. The studies in [2, 3] were later extended [4] to consider stress-wave loading. However, as is usually the case, to study dynamic crack propagation in finite bodies of arbitrary geometry, it is necessary to formulate consistent numerical methods, which may capitalize on the insights, into the field behavior near propagating crack-tips, gained through the analytical solutions. A critical appraisal of several and varied numerical solution techniques in dynamic fracture mechanics was made in a 1978 paper by Kanninen [5]. Most of the dynamic finite-element methods, for fast crack-propagation analysis, reviewed in [5] use the conventional finite elements with simple polynomials for assumed displacements, and do not account for the singularity in strains near the crack-tip. Further, in these methods, the dynamic crack propagation was simulated by a "gradual" release of the restraining nodal force at a finite-element node which represents the "current" crack-tip. The dynamic stress-intensity factor is then extracted from the displacement field or from the work done in releasing the nodal force. It was concluded in [5] that the foregoing "node-release" techniques were not sufficiently accurate.

Since the appearance of [5], Bazant, et al. [6], have presented a calibrated, nonsingular, crack-tip element procedure for the dynamic analysis of running cracks. In the procedure of [6], the finite-element grid moves undeformed with the crack-tip. However, the procedure of [6] has two serious limitations:

(*i*) It is restricted to finite bodies whose surfaces and/or bimaterial interfaces are parallel to the direction of crack propagation.

(*ii*) More importantly, it cannot be applied to bodies having finite dimensions in the direction of crack propagation.

On the other hand, Aoki, et al. [7], presented a finite-element procedure wherein the singular nature of stress/strain near the *propagating* crack-tip is accounted for *a priori*. However, in [7], only when the crack-tip has reached close to the boundary of the singular element, the entire singular element is shifted, as a rigid body, to a new location. The numerical details of the procedures are still somewhat sketchy in [7]. Finally, King and Malluck [8] reported a procedure of simulating crack propagation similar to that in [7], except that the singular element used in [8] has, built within it, a large number of eigenfunction solutions corresponding to a *stationary* crack. In an attempted simulation of the well-known problem of Baker, the procedure in [8] produced spurious oscillations, of large amplitude, in the solution for dynamic stress-intensity factor, as compared to the analytical solution. Based on these results, it is suggested in [8] that the procedure in [8] may not be feasible for simulating large scale fast fracture.

In Part 1 of the present paper, a moving singular element procedure is presented for the dynamic analysis of fast crack-propagation

Contributed by the Applied Mechanics Division for publication in the JOURNAL OF APPLIED MECHANICS.

Discussion on this paper should be addressed to the Editorial Department, ASME, United Engineering Center, 345 East 47th Street, New York, N. Y. 10017, and will be accepted until December 1, 1980. Readers who need more time to prepare a discussion should request an extension from the Editorial Department. Manuscript received by ASME Applied Mechanics Division, November, 1979; final revision, February, 1980.

problems in arbitrary shaped finite bodies. In the present procedure a singular element, within which a large number of analytical eigenfunctions corresponding to a *propagating* crack are used as basis functions for displacements, may move by an arbitrary amount $\Delta\Sigma$ in each time-increment Δt of the numerical time-integration procedure (as opposed several time steps, say 6 to 8, per increment of crack growth, used in the procedures reviewed in [5]). The moving singular element, within which the crack-tip always has a fixed location, retains its shape at all times, but the mesh "regular" (isoparametric) finite elements, surrounding the moving singular element, deforms accordingly. An energy-consistent variational statement is first developed, as a basis for the foregoing moving singular element, finite-element method of dynamic crack growth analysis. The present procedure leads to a direct evaluation of dynamic stress-intensity factor(s), since they are unknown parameters in the assumed basis functions for the singular element.

In Part 2 of the paper, several numerical results for cracks propagating in finite bodies are presented and discussed.

In the following we discuss the details of formulation of a moving-singularity finite-element formulation for analyzing dynamic crack propagation.

Basis Functions for a Moving Singular Element

We consider Mode-I-type dynamic crack propagation in two-dimensional (plane-strain) linear elastic isotropic bodies of finite geometry. Let x_α ($\alpha = 1, 2$) be fixed Cartesian coordinates in the plane of the body, and x_3 be the thickness coordinate of the body such that $x_2 = 0$ defines the plane of the crack. In the context of the present numerical method, without loss of generality, we consider the case when the crack-tip is moving along x_1-axis at a constant speed v. We introduce the coordinate system (ξ, x_2) which remains fixed with respect to the moving crack-tip, such that $\xi = x_1 - vt$. Let Φ and Ψ be the dilatational and shear wave potentials, respectively; and let C_d and C_s be the corresponding wave speeds. It can then be shown [2] that Φ is governed by the equation

$$[1 - (v/C_d)^2]\frac{\partial^2\Phi}{\partial\xi^2} + \frac{\partial^2\Phi}{\partial x_2^2} = -(2v/C_d^2)\frac{\partial^2\Phi}{\partial t\,\partial\xi} + (1/C_d^2)\frac{\partial^2\Phi}{\partial t^2} \quad (1)$$

and that Ψ is governed by a similar equation, except that C_d is to be replaced by C_s. Consider the "steady-state" solution to the homogeneous part of the previous equation, that is, the solution which appears time-invariant to an observer moving with the crack-tip. This eigenfunction solution which satisfies the traction-free condition on the crack-face ($\xi < 0, x_2 = \pm 0$), can be derived easily, as for instance in [9, 10], and is given in Appendix A for the sake of completeness.

In the present procedure, a finite region (which, for convenience, is taken to be rectangular in shape) near the moving crack-tip is modeled by one finite element, in which the displacement field is assumed to be a linear-superposition of a finite number of the previously discussed eigenfunctions. However since the solution, in general, will also explictly depend on time, the undetermined parameters, β_n, are taken to be functions of time. Thus, in the singular element, we assume

$$u_1(\xi, x_2, t) = \sum_n u^*_{1n}(\xi, x_2, v)\beta_n(t) + \text{Rigid body modes} \quad (2)$$

$$u_2(\xi, x_2, t) = \sum_n u^*_{2n}(\xi, x_2, v)\beta_n(t) + \text{Rigid body modes} \quad (3)$$

where u^*_{2n}, u^*_{1n} are given in Appendix A, and, in particular, $\beta_1(t)$ is identified as the Mode-I dynamic stress-intensity factor. It can then be seen that, in the present finite-element procedure, the dynamic stress-intensity factor is an unknown parameter in the element basis-functions, and thus can be calculated directly. Representing the foregoing equations (2), (3) in the familiar matrix notation,

$$\mathbf{u}^s(\xi, x_2, t) = \underline{\mathbf{U}}(\xi, x_2, v)\boldsymbol{\beta}(t) \quad (4)$$

where bold-faced letters and a bold-faced letter with a tilde under it denote a column vector and a matrix, respectively; and $\mathbf{u}^s$ denotes the vector of displacements in the singular element. We note that the total velocity and acceleration of a material point in the singular element are given by

$$\dot{\mathbf{u}}^s = \underline{\mathbf{U}}\dot{\boldsymbol{\beta}} - v(\underline{\mathbf{U}})_{,\xi}\boldsymbol{\beta} \quad (5)$$

and

$$\ddot{\mathbf{u}}^s = \underline{\mathbf{U}}\ddot{\boldsymbol{\beta}} - 2v(\underline{\mathbf{U}})_{,\xi}\dot{\boldsymbol{\beta}} + v^2(\underline{\mathbf{U}})_{,\xi\xi}\boldsymbol{\beta} \quad (6)$$

where, a $(\cdot)$ denotes a total derivative with respect to time t, and $(\ )_{,\xi}$ denotes a partial derivative with respect to ξ.

Let the domain of the singular element in the present procedure be V_s and its boundary be ∂V_s; and let ρ_s be that part of ∂V_s where the usual isoparameteric finite elements adjoin. In order that convergence of the present finite-element method may be achieved, compatibility of displacements, velocities, and accelerations between the singular elements and surrounding regular elements, i.e., at ρ_s, is maintained in a least-squares sense as described in the following. Let the displacement, velocity, and acceleration assumption for the regular element, at ρ_s, be taken, respectively, as

$$\mathbf{u}^R = \underline{\mathbf{N}}\mathbf{q}_s; \qquad \dot{\mathbf{u}}^R = \underline{\mathbf{N}}\dot{\mathbf{q}}_s; \qquad \ddot{\mathbf{u}}^R = \underline{\mathbf{N}}\ddot{\mathbf{q}}_s \quad (7a, b, c)$$

where $\underline{\mathbf{N}}$ are functions of the boundary coordinate $\eta(x_\alpha)$ at ∂V_s, and $\mathbf{q}_s$ is the vector of displacements at nodes at ρ_s. The parameters $\boldsymbol{\beta}, \dot{\boldsymbol{\beta}}$, and $\ddot{\boldsymbol{\beta}}$ are so chosen that they minimize the error functionals

$$I_1 = \int_{\rho_s} (\mathbf{u}^s - \mathbf{u}^R)^2 d\rho; \quad I_2 = \int_{\rho_s} (\dot{\mathbf{u}}^s - \dot{\mathbf{u}}^R)^2 d\rho;$$

$$I_3 = \int_{\rho_s} (\ddot{\mathbf{u}}^s - \ddot{\mathbf{u}}^R)^2 d\rho \quad (8, 9, 10)$$

Using equations (4)–(7) in (8)–(10), and minimizing I_1, I_2, and I_3 successively with respect to $\boldsymbol{\beta}, \dot{\boldsymbol{\beta}}$, and $\ddot{\boldsymbol{\beta}}$ it can be shown that

$$\boldsymbol{\beta} = \underline{\mathbf{A}}\mathbf{q}_s; \quad \dot{\boldsymbol{\beta}} = \underline{\mathbf{A}}\dot{\mathbf{q}}_s + \underline{\mathbf{B}}\mathbf{q}_s; \quad \ddot{\boldsymbol{\beta}} = \underline{\mathbf{A}}\ddot{\mathbf{q}}_s + 2\underline{\mathbf{B}}\dot{\mathbf{q}}_s + \underline{\mathbf{C}}\mathbf{q}_s \quad (11\text{–}13)$$

where

$$\underline{\mathbf{A}} = \underline{\mathbf{H}}^{-1}\underline{\mathbf{G}}; \qquad \underline{\mathbf{B}} = (v)\underline{\mathbf{H}}^{-1}\underline{\mathbf{E}}\underline{\mathbf{A}} \quad (14, 15)$$

$$\underline{\mathbf{C}} = 2(v)\underline{\mathbf{H}}^{-1}\underline{\mathbf{E}}\underline{\mathbf{B}} - (v^2)\underline{\mathbf{H}}^{-1}\underline{\mathbf{F}}\underline{\mathbf{A}} \quad (16)$$

$$\underline{\mathbf{H}} = \int_{\rho_s} \underline{\mathbf{U}}^T\underline{\mathbf{U}}d\rho; \quad \underline{\mathbf{G}} = \int_{\rho_s} \underline{\mathbf{U}}^T\underline{\mathbf{N}}d\rho \quad (17a, b)$$

$$\underline{\mathbf{E}} = \int_{\rho_s} \underline{\mathbf{U}}^T(\underline{\mathbf{U}})_{,\xi}d\rho; \quad \underline{\mathbf{F}} = \int_{\rho_s} \underline{\mathbf{U}}^T(\underline{\mathbf{U}})_{,\xi\xi}d\rho \quad (17c, d)$$

Thus equations (4)–(6) together with (11)–(13) represent the displacements, total velocities and total accelerations in the singular element, in terms of its nodal displacements, velocities, and accelerations, $\mathbf{q}_s$, $\dot{\mathbf{q}}_s$, and $\ddot{\mathbf{q}}_s$, respectively. Thus, if $\mathbf{q}_s$ at ρ_s is determined, then $\boldsymbol{\beta}$ (and especially the Mode-I stress-intensity factor β_1), can be determined directly. Finally, it is noted that the foregoing equations (4)–(6) and (11)–(13) represent the assumptions for the relevant field variables in the singular element at any generic time t.

Now we consider the problem of dynamic crack propagation within a time increment Δt between two generic times t_1 and t_2.

Variational Principle for Dynamic Crack-Propagation Analysis

In the following, we present a variational statement for dynamically growing cracks in linear elastic solids. Consider two instants of time t_1 and t_2 ($= t_1 + \Delta t$) at which the variables of the problem are denoted by superscripts 1 and 2, respectively. At time t_1, let the volume of the solid be V_1, the external boundary of the solid where tractions $\overline{T}_i^1$ are prescribed, be $S_{\sigma 1}$; and let Σ_1^+ and Σ_1^- be, respectively, the two surfaces of the crack. Also, let $\overline{F}_i^2$ be body forces per unit volume in the body at time t_2. We assume that between time t_1 and t_2, the crack surfaces change by $\Delta\Sigma$. The orientation of $\Delta\Sigma$ to Σ, can be determined by some crack-growth direction criterion; however, for pure Mode-I, self-similar growth is assumed. The newly created crack surfaces can be traction-free, but, for the sake of generality, assume that new trac-

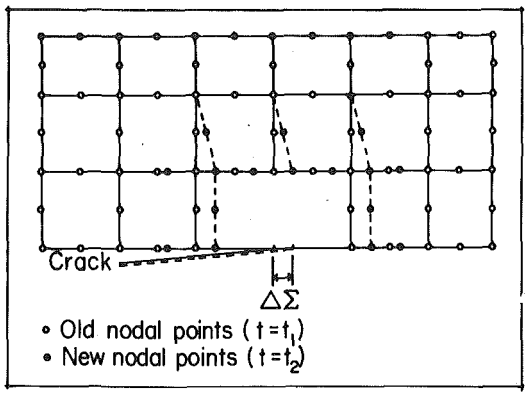

Fig. 1 Schematic representation of the movement of the singular element

tions[1] $\overline{T}_i^{2+}$ and $\overline{T}_i^{2-}$ are applied on the new crack-faces $\Delta\Sigma^+$ and $\Delta\Sigma^-$, respectively; likewise, let new tractions $\overline{T}_i^2$ act at $S_{\sigma 2}$. The principle of virtual work applied at t_2 can be written as

$$0 = \int_{V_2} (\sigma_{ij}^2 \delta\epsilon_{ij}^2 + \rho \ddot{u}_i^2 \delta u_i^2) dv - \int_{V_2} \overline{F}_i^2 \delta u_i^2 dv - \int_{S_{\sigma 2}} \overline{T}_i^2 \delta u_i^2 ds - \int_{\Sigma_1^+} (\overline{T}_i^2)^+ (\delta u_i^2)^+ ds - \int_{\Sigma_1^-} (\overline{T}_i^2)^- (\delta u_i^2)^- ds - \int_{\Delta\Sigma^+} (\overline{T}_i^2)^+ (\delta u_i^2)^+ ds - \int_{\Delta\Sigma^-} (\overline{T}_i^2)^- (\delta u_i^2)^- ds \quad (18)$$

However, for the case of cracked structures, the changes in volume and external surfaces between times t_1 and t_2, due to a change in the crack surface by $\Delta\Sigma$ alone, can be assumed to be negligible, i.e., $V_1 \simeq V_2$ and $S_{\sigma 1} \simeq S_{\sigma 2}$. It is important to note in equation (18) that $(u_i^2)^+ \neq (u_i^2)^-$ [or $(\delta u_i^2)^+ \neq (\delta u_i^2)^-$] at the initial crack surfaces Σ_1^+ and Σ_1^-, nor, more importantly, for the newly created crack-faces $\Delta\Sigma^+$ and $\Delta\Sigma^-$ during the time interval $t_2 - t_1$ $(=\Delta t)$. If similar virtual displacements (δu_i^2), such that $(\delta u_i^2)^+ \neq (\delta u_i^2)^-$ either on Σ, or on $\Delta\Sigma$, are considered in the statement of virtual work at time t_1 (prior to the creation of new crack-faces $\Delta\Sigma$); this statement can be written as

$$0 = \int_{V_2} (\sigma_{ij}^1 \delta\epsilon_{ij}^2 + \rho \ddot{u}_i^1 \delta u_i^2) dv - \int_{V_2} \overline{F}_i^1 \delta u_i^2 dv - \int_{S_{\sigma 2}} \overline{T}_i^1 \delta u_i^2 ds - \int_{\Sigma_1^+} (\overline{T}_i^1)^+ (\delta u_i^2)^+ ds - \int_{\Sigma_1^-} (\overline{T}_i^1)^- (\delta u_i^2)^- ds - \int_{\Delta\Sigma^+} (\sigma_{ij}^1 \nu_j^1)^+ (\delta u_i^2)^+ ds - \int_{\Delta\Sigma^-} (\sigma_{ij}^1 \nu_j^1)^- (\delta u_i^2)^- ds \quad (19)$$

wherein the approximations $V_2 \simeq V_1$; $S_{\sigma 2} \simeq S_{\sigma 1}$ are used and ν_j^1 is a unit normal to Σ_1. Adding equations (18) and (19), the virtual work principle governing dynamic crack propagation between times t_1 and t_2 can be written as

$$\int_{V_2} \{(\sigma_{ij}^2 + \sigma_{ij}^1)\delta\epsilon_{ij}^2 + \rho(\ddot{u}_i^2 + \ddot{u}_i^1)\delta u_i^2 - (\overline{F}_i^2 + \overline{F}_i^1)\delta u_i^2\} dv = \int_{S_{\sigma 2}} (\overline{T}_i^1 + \overline{T}_i^2)\delta u_i^2 ds + \int_{\Sigma_1^+} (\overline{T}_i^2 + \overline{T}_i^1)^+ (\delta u_i^2)^+ ds + \int_{\Sigma_1^-} (\overline{T}_i^2 + \overline{T}_i^1)^- (\delta u_i^2)^- ds + \int_{\Delta\Sigma^+} (\overline{T}_i^2 + \sigma_{ij}^1 \nu_j^1)^+ (\delta u_i^2)^+ ds + \int_{\Delta\Sigma^-} (\overline{T}_i^2 + \sigma_{ij}^1 \nu_j^1)^- (\delta u_i^2)^- ds \quad (20)$$

[1] It is noted that the element basis functions assumed in equations (2) and (3) satisfy only the traction-free conditions on the crack-face. It is, however, easy to accommodate nonzero traction conditions on the crack-face by introducing appropriate additional terms in equations (2) and (3). These additional terms are so chosen that they satisfy the nonzero crack-face traction conditions either exactly or in an average sense.

In the finite-element development, the domain V_2 can be considered to be broken into a singular element V_{2s} surrounding the crack tip (see Fig. 1), and a number, N, of regular elements V_{2Rn} $(n = 1 \ldots N)$ (thus $V_2 = V_{2s} + \sum_n V_{2Rn}$); likewise $S_{\sigma 2} = \sum_n S_{\sigma 2Rn}$. Also, as seen from Fig. 1, $\Sigma_1^+ = \Sigma_{s1}^+ + \sum_n \sigma_{1Rn}^+$. Henceforth, for simplicity, we use symbols V_s, V_{Rn}, $S_{\sigma n}$, Σ_s^+, and Σ_{Rn}^+ instead of V_{2s}, V_{2Rn}, $S_{\sigma 2Rn}$, Σ_{s1}^+, and Σ_{Rn}^+, respectively. We now restrict our attention to the Mode-I case only, i.e., when the applied loading is in a direction normal to the crack plane and is symmetric with respect to the crack plane for all times t. Thus, for the Mode-I case, using the previous notation, the virtual work equation as applicable to a system of finite elements may be written as

$$\sum_n \left[\int_{V_{Rn}} \{(\sigma_{ij}^2 + \sigma_{ij}^1)\delta\epsilon_{ij}^2 + \rho(\ddot{u}_i^2 + \ddot{u}_i^1)\delta u_i^2 - (\overline{F}_i^2 + \overline{F}_i^1)\delta u_i^2\} dv - \int_{S_{\sigma n}} (\overline{T}_i^2 + \overline{T}_i^1)\delta u_i^2 ds - \int_{\Sigma_n^+} (\overline{T}_i^2 + \overline{T}_i^1)^+ \delta u_i^{2+} ds \right] + \int_{V_s} \left\{ (\sigma_{ij}^2 + \sigma_{ij}^1)\delta\epsilon_{ij}^2 + \rho(\ddot{u}_i^2 + \ddot{u}_i^1)\delta u_i^2 - (\overline{F}_i^2 + \overline{F}_i^1)\delta u_i^2 \right\} dv - \int_{\Sigma_s^+} (\overline{T}_i^2 + \overline{T}_i^1)^+ \delta u_i^{2+} ds - \int_{\Delta\Sigma^+} (\overline{T}_i^2 + \sigma_{ij}^1 \nu_j^1)^+ \delta u_i^{2+} ds = 0 \quad (21)$$

Assuming that crack-growth occurs between times t_1 and t_2 (which can be determined by an appropriate criterion, in the so-called "application" calculations using the given material dynamic fracture toughness as an input; or is known, *a priori*, in the so-called "generation phase," i.e., in the case of simulation of known crack-tip time history data), the singular element is translated, in the Mode-I case, along the original crack axis, by an appropriate distance $\Delta\Sigma$ from its location at time t_1, as shown in Fig. 1.

It is important to note that in the present procedure, this amount $\Delta\Sigma$ is not, in any way, related to the distance between any two adjacent finite-element nodes at time t_1; as is the case with most common finite-element methods which use the node-release technique in the simulation of dynamic crack propagation. As can be seen from Fig. 1, as the singular element is translated by $\Delta\Sigma$ between t_1 and t_2, the nodal pattern of the surrounding regular elements also changes between t_1 and t_2. It is to this readjusted finite-element mesh at time t_2 that the virtual work equation in equation (21) is understood to be applied. However, it is also noted that only the nodes of the elements immediately surrounding the singular element are readjusted due to crack-growth of amount $\Delta\Sigma$ between t_2 and t_1. Thus one has to obtain data, such as displacements, velocities, and accelerations, at time t_1, at the *new* nodes of the regular elements, which are indicated by solid circles in Fig. 1. This data can be determined, using elementary interpolation techniques, from the known data, at time t_1, at the "*old*" nodes at time t_1, which are indicated by open circles in Fig. 1. The details of these interpolation techniques are omitted for simplicity and will be reported elsewhere. Thus one is in a position to know the relevant data at time t_1, at new nodes and (hence new elements) corresponding to the mesh in t_2; and to assume the appropriate basis functions for the relevant variables at time t_2 for the mesh at time t_2, as follows:

Known at t_1 for the Mode at t_2

$$\text{In } V_{Rn}: \mathbf{u}_1 = \underline{\mathbf{N}}\mathbf{q}_1; \quad \boldsymbol{\epsilon}_1 = \underline{\mathbf{B}}\mathbf{q}_1; \quad \boldsymbol{\sigma}_1 = \underline{\mathbf{E}}\underline{\mathbf{B}}\mathbf{q}_1 \quad (22\text{–}24)$$

$$\dot{\mathbf{u}}_1 = \underline{\mathbf{N}}\dot{\mathbf{q}}_1; \quad \ddot{\mathbf{u}}_1 = \underline{\mathbf{N}}\ddot{\mathbf{q}}_1 \quad (25, 26)$$

$$\text{In } V_s: \mathbf{u}_1 = \underline{\mathbf{U}}_1\beta_1; \quad \dot{\mathbf{u}}_1 = \underline{\mathbf{U}}_1\dot{\beta}_1 - v_1\underline{\mathbf{U}}_{1,\xi}\beta_1 \quad (27, 28)$$

$$\ddot{\mathbf{u}}_1 = \underline{\mathbf{U}}_1\ddot{\beta}_1 - 2v_1\underline{\mathbf{U}}_{1,\xi}\dot{\beta}_1 + v_1^2\underline{\mathbf{U}}_{1,\xi\xi}\beta_1 \quad (29)$$

$$\boldsymbol{\epsilon}_1 = \underline{\mathbf{S}}_1\beta_1; \quad \boldsymbol{\sigma}_1 = \underline{\mathbf{P}}_1\beta_1; \quad \mathbf{T}_1 = \underline{\mathbf{R}}_1\beta_1 \quad (30\text{–}32)$$

Assumed at Time t_2 for the Mesh at Time t_2

$$\text{In } V_{Rn}: \mathbf{u}_2 = \underline{\mathbf{N}}\mathbf{q}_2; \quad \boldsymbol{\epsilon}_2 = \underline{\mathbf{B}}\mathbf{q}_2; \quad \boldsymbol{\sigma}_2 = \underline{\mathbf{E}}\underline{\mathbf{B}}\mathbf{q}_2 \quad (33\text{–}35)$$

$$\dot{\mathbf{u}}_2 = \underline{\mathbf{N}}\dot{\mathbf{q}}_2; \quad \ddot{\mathbf{u}}_2 = \underline{\mathbf{N}}\ddot{\mathbf{q}}_2 \quad (36, 37)$$

$$\text{In } V_s\text{: } \mathbf{u}_2 = \underline{\mathbf{U}}_2\beta_2; \quad \dot{\mathbf{u}}_2 = \underline{\mathbf{U}}_2\dot{\beta}_2 - v_2\underline{\mathbf{U}}_{2,\xi}\beta_2 \qquad (38, 40)$$

$$\ddot{\mathbf{u}}_2 = \underline{\mathbf{U}}_2\ddot{\beta}_2 - 2v_2\underline{\mathbf{U}}_{2,\xi}\dot{\beta}_2 + v_2^2\underline{\mathbf{U}}_{2,\xi\xi}\beta_2 \qquad (41)$$

$$\boldsymbol{\epsilon}_2 = \underline{\mathbf{S}}_2\beta_2; \quad \boldsymbol{\sigma}_2 = \underline{\mathbf{P}}_2\beta_2; \quad \mathbf{T}_2 = \underline{\mathbf{R}}_2\beta_2 \qquad (42\text{–}44)$$

where the familiar vector representations for displacements, strains, stresses, and tractions, are employed as $\mathbf{u}$, $\boldsymbol{\epsilon}$, $\boldsymbol{\sigma}$ and $\mathbf{T}$, respectively. Also, v_1 and v_2 are velocities of the crack-tip at times t_1 and t_2, respectively, and the eigenfunctions $\underline{\mathbf{U}}_1$ and $\underline{\mathbf{U}}_2$ depend on v_1 and v_2, respectively.

Using equations (22)–(44) in equation (21), the finite-element equations, for arbitrary variations δq_2 and $\delta\beta_2$ can be written, as shown in Appendix B, as

$$\underline{\mathbf{K}}\mathbf{q}_2 + \underline{\mathbf{m}}\ddot{\mathbf{q}}_2 = \bar{\mathbf{Q}}_2 + \bar{\mathbf{Q}}_1 - \underline{\mathbf{K}}\mathbf{q}_1 - \underline{\mathbf{m}}\ddot{\mathbf{q}}_1 \quad \text{for} \quad V_{Rn} \quad \text{in} \quad V_2 - V_s \qquad (45)$$

$$\underline{\mathbf{K}}_s^*\mathbf{q}_{s2} + \underline{\mathbf{D}}_s^*\dot{\mathbf{q}}_{s2} + \underline{\mathbf{m}}_s^*\ddot{\mathbf{q}}_{s2} = \mathbf{Q}_s^* \quad \text{for} \quad V_s \qquad (46)$$

where $\underline{\mathbf{K}}$, $\underline{\mathbf{m}}$, $\bar{\mathbf{Q}}_2$, $\bar{\mathbf{Q}}_1$, $\underline{\mathbf{K}}_s^*$, $\underline{\mathbf{D}}_s^*$, and $\underline{\mathbf{m}}_s^*$ are defined in Appendix B, from which it can be seen that the metrices $\underline{\mathbf{K}}_s^*$ and $\underline{\mathbf{D}}_s^*$ are, unfortunately, unsymmetric, while the others are all symmetric. In equation (45), $\mathbf{q}_2$ and $\ddot{\mathbf{q}}_2$ are displacements and accelerations at t_2 at nodes everywhere in and at the boundary of the region $(V_2 - V_s)$; whereas, $\mathbf{q}_{s2}$, $\dot{\mathbf{q}}_{s2}$, and $\ddot{\mathbf{q}}_{s2}$ are displacements, velocities, and accelerations at t_2 at nodes along the boundary ∂V_s of the singular element. When equations (45), (46) are assembled, it can be seen that the resulting global "stiffness" and "damping" (which, however, is *not* a physical damping term) matrices have only a "small" degree of unsymmetry, confined to those rows and columns corresponding to nodes around the singular element. We can use the common time-integration schemes to integrate equations (45)–(46). In particular, we use the Newmark's method which can be characterized by the approximations

$$\dot{\mathbf{q}}_2 = C_1(\mathbf{q}_2 - \mathbf{q}_1) - C_2\dot{\mathbf{q}}_1 - C_3\ddot{\mathbf{q}}_1 \qquad (47)$$

$$\ddot{\mathbf{q}}_2 = C_4(\mathbf{q}_2 - \mathbf{q}_1) - C_5\dot{\mathbf{q}}_1 - C_6\ddot{\mathbf{q}}_1 \qquad (48)$$

where

$$C_1 = (\delta/\gamma\Delta t);\ C_2 = (\delta/\gamma) - 1;\ C_3 = \left(\frac{\Delta t}{2}\right)[(\delta/\gamma) - 2]$$

$$C_4 = 1/\gamma(\Delta t)^2;\ C_5 = 1/(\gamma\Delta t);\ C_6 = (1/2\gamma) - 1 \qquad (49)$$

where, in the present calculations, $\gamma = 1/4$, $\delta = 1/2$ are used. With the difference approximations in equations (47), (48), and similar ones for $\dot{\mathbf{q}}_{s2}$ and $\ddot{\mathbf{q}}_{s2}$, we reduce equations (45), (46) to

$$\hat{\underline{\mathbf{K}}}\mathbf{q}_2 = \hat{\mathbf{Q}} \quad \text{for} \quad V_2 - V_s \qquad (50)$$

$$\hat{\underline{\mathbf{K}}}_s\mathbf{q}_{s2} = \hat{\mathbf{Q}}_s \quad \text{for} \quad V_s \qquad (51)$$

$$\hat{\underline{\mathbf{K}}} = \underline{\mathbf{K}} + C_4\underline{\mathbf{m}} \qquad (52)$$

where

$$\hat{\mathbf{Q}} = \bar{\mathbf{Q}}_2 + \bar{\mathbf{Q}}_1 - \underline{\mathbf{K}}\mathbf{q}_1 - \underline{\mathbf{m}}\mathbf{q}_1 + \underline{\mathbf{m}}(C_4\mathbf{q}_1 + C_5\dot{\mathbf{q}}_1 + C_6\ddot{\mathbf{q}}_1) \qquad (53)$$

$$\underline{\mathbf{K}}_s = \underline{\mathbf{K}}_s^* + C_4\underline{\mathbf{m}}_s^* + C_1\underline{\mathbf{D}}_s^* \qquad (54)$$

$$\hat{\mathbf{Q}}_s = \mathbf{Q}_s^* + \underline{\mathbf{m}}_s^*(C_4\mathbf{q}_{s1} + C_5\dot{\mathbf{q}}_{s1} + C_6\ddot{\mathbf{q}}_{s1}) + \underline{\mathbf{D}}_s^*(C_1\mathbf{q}_{s1} + C_2\dot{\mathbf{q}}_{s1} + C_3\ddot{\mathbf{q}}_{s1}) \qquad (55)$$

where $\underline{\mathbf{K}}$ is symmetric; however, $\hat{\underline{\mathbf{K}}}_s$ is unsymmetric. When equations (50), (51) are assembled, we obtain, the final algebraic equations

$$[\hat{\underline{\mathbf{K}}}^*]\{\mathbf{q}_2^*\} = \{\mathbf{Q}^*\} \qquad (56)$$

where the stiffness matrix in equation (56) is, in general, unsymmetric, but the unsymmetry is confined mainly to the rows and columns corresponding to nodes around V_s. A rather simple technique of iterative solution of the foregoing equation, based on the decomposition of the stiffness matrix into symmetric and skew-symmetric parts, as below, was used.

$$\tfrac{1}{2}[\hat{\underline{\mathbf{K}}}^* + \hat{\underline{\mathbf{K}}}^{*T}]\{\mathbf{q}_2^{*p}\} = \{\mathbf{Q}^*\} - \tfrac{1}{2}[\hat{\underline{\mathbf{K}}}^* - \hat{\underline{\mathbf{K}}}^{*T}]\{\mathbf{q}_2^{*(p-1)}\} \qquad (57)$$

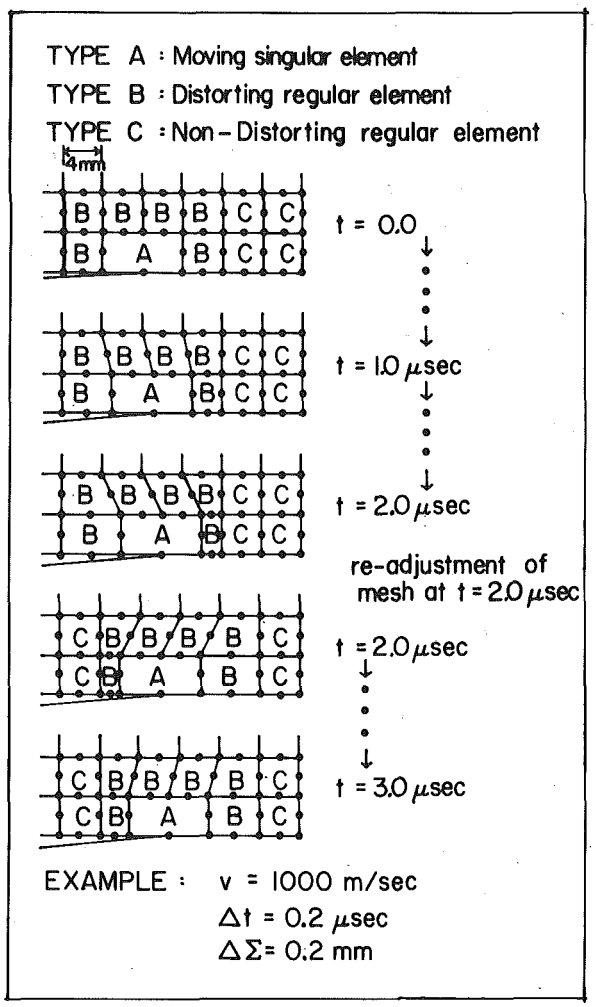

Fig. 2 Schematic representation of crack growth in a typical problem: constant crack velocity v = 1000 m/s; Δt = 0.2 μs; $\Delta\Sigma$ = 0.2 mm; the mesh of regular elements around the singular element is readjusted at t = 2.0 μs

for any pth-iteration. In all the solutions obtained, only two iterations were found to adequate. Once $\mathbf{q}_2^*$ is computed from equation (56), the solution for time $t_2 + \Delta t$ can be repeated, with the approximations for the initial values $\ddot{\mathbf{q}}_2^*$ and $\dot{\mathbf{q}}_2^*$ as

$$\ddot{\mathbf{q}}_2^* = C_4[\mathbf{q}_2^* - \mathbf{q}_1^*] - C_5\dot{\mathbf{q}}_1^* - C_6\ddot{\mathbf{q}}_1^* \qquad (58)$$

$$\dot{\mathbf{q}}_2^* = \dot{\mathbf{q}}_1^* + C_7\ddot{\mathbf{q}}_1^* + C_8\ddot{\mathbf{q}}_2^* \qquad (59)$$

where C_4, C_5, C_6 are defined earlier, and $C_7 = \Delta t\ (1 - \delta)$; and $C_8 = \delta\Delta t$ (where a value of $\delta = 1/2$ is used presently).

Once the nodal displacements $\mathbf{q}_2^*$ (and hence the corresponding displacements at the nodes of the singular element), at time t_2, are computed from equation (57), the unknown parameters $\boldsymbol{\beta}$ (and hence the dynamic stress-intensity factor β_1) in the singular element can be computed from equation (11).

Using equations (58) and (59) as initial data, the time-integration between the time steps t_2 and t_3 $(t_2 + \Delta t)$ can be carried out and, thus the process can be repeated for all subsequent time intervals. The successive growth of the crack, for a representative problem is schematically illustrated in Fig. 2.

From the example given in Fig. 2, it is seen that the singular element (A) remains its shape at all times but the regular elements (B) in the "immediate surrounding" of the singular element continually distort. However, in the previous example, at t = 2.0 μsec, elements B have distorted sufficiently so that the use of isoparametric approximations in these elements may introduce spurious numerical errors. For this

reason, as typified by the foregoing example, at $t = 2.0\ \mu s$, the regular elements B are readjusted as shown in Fig. 2. This involves a simple reinterpolation of data, in "B"-type elements from $t = 2.0 - 0\ \mu s$ to $t = 2.0 + 0\ \mu s$, the details of which are omitted for brevity. Finite-element calculations detailed earlier can be repeated for the readjusted mesh at $t = 2.0 + 0\ \mu s$ until the B-type elements become so distorted that another readjustment may be warranted. These mesh readjustments were found to be easy to accomplish in the computer coding based on the present approach.

Finally, it may be of interest to note that in the present singular element, 19 eigenfunctions[2] for a propagating crack (see Appendix A) were used along with a rigid body translation mode in x_1-direction; whereas, there are 18 degrees of freedom along the boundary ρ_s of the singular element. The regular elements were of the common 8-noded isoparametric type.

It should be remarked that the problems dealt with in the present paper are limited to the case of determining the stress-intensity factor at the crack-tip which is propagating with a prescribed velocity-time history. Thus the presently treated problem may be considered to fall in the category of "generation phase calculations" in the sense defined in [5]. The present procedure may be used to simulate the experimentally determined crack-velocity-time history in test specimens, such as the double-cantilever-beam (DCB) specimen [11], to determine the velocity-dependent dynamic fracture toughness. Using this as input data, the problem of *determining* the crack-tip motion in plane elastic bodies subject to Mode-I-type dynamic transient loading may be treated. This second phase of research, which is the so-called "application phase" in the sense defined in [5], is currently being completed, and will be the basis of a forthcoming paper.

Finally, we wish to note that once the basic features of the procedure based on the present moving singular element, with embedded propagating-crack eigenfunctions, are well understood, the numerical procedure can be further simplified. This can be accomplished, for instance, by using the well-known distorted isoparametric elements (the so-called "quarter-point elements") [12] in place of the present singular element. Even though the results from the use of a quarter-point element are not expected to be as accurate as from the use of the present singular element; such results, with a suitable calibration, may be used in analyzing large-scale fast fracture in practical situations. The results from the use of a quarter-point element, and their comparison with those reported in Part 2 of this paper (using the present singular element), will be reported on shortly. Also, since it is known [10] that the eigenfunctions for a crack propagating at constant velocity differ significantly in their behavior from those for stationary crack only at very high speeds ($v \simeq C_s$) of propagation, the present procedure can be simplified, for practical purposes, by using the stationary-crack eigenfunctions in the singular element. The results from this modification, are also to be reported shortly.

Closure

In this paper we have presented a new translating-singularity finite-element procedure, wherein use is made of analytical eigenfunctions for a two-dimensional crack whose tip propagates at a constant velocity. The procedure is capable of modeling large-scale fast crack propagation in finite two-dimensional bodies of arbitrary shape. However, the type of problems considered is limited to the case of determining the dynamic stress-intensity factor at the crack-tip which is propagating with a prescribed velocity-time history.

Implementation of the present approach and numerical example are discussed in an accompanying Part 2 of the paper.

[2] The number of eigenfunctions plus the number of rigid modes must be greater than or equal to the number of degrees of freedom at the boundary. A study of the effect of the number of eigenfunctions used, on the results was conducted, by varying this number from 17–25. The results varied only insignificantly (i.e., less than 0.4 percent), and the number of eigenfunctions was chosen to be 19 in all subsequent computations.

Acknowledgments

This work was supported by the Office of Naval Research under Contract No. N00014-78-0636 with the Georgia Institute of Technology (GIT) and by supplemental funds from G.I.T. The authors thank Dr. N. Perrone for his timely encouragement. Thanks are also expressed to Mrs. T. Rapp for her able typing of this manuscript.

References

1 Freund, L. B., "Dynamic Crack Propagation," *The Mechanics of Fracture* Erdogan, F. ed., ASME-AMD Vol. 19, ASME, New York, 1976, pp. 105–134.

2 Freund, L. B., "Crack Propagation in an Elastic Solid Subjected to General Loading—I. Constant Rate of Extension," *Journal of the Mechanics and Physics of Solids*, Vol. 20, 1972, pp. 129–140.

3 Freund, L. B., "Crack Propagation in an Elastic Solid Subjected to General Loading—II. Nonuniform Rate of Extension," *Journal of the Mechanics and Physics of Solids*, Vol. 21, 1972, pp. 141–152.

4 Freund, L. B., "Crack Propagation in an Elastic Solid Subjected to General Loading—III. Stress Wave Loading," *Journal of the Mechanics and Physics of Solids*, Vol. 21, 1973, pp. 47–61.

5 Kanninen, M. F., "A Critical Appraisal of Solution Techniques in Dynamic Fracture Mechanics," *Numerical Methods in Fracture Mechanics*, Luxmore, A. R., and Owen, D. R. J., eds., *Proceedings of a Conference*, held at Swansea, United Kingdom, Jan. 1978, pp. 612–634.

6 Bazant, Z. P., Glazik, J. L., and Achenbach, J. D., "Elastodynamic Fields Near Running Cracks by Finite Element," *Computer and Structures*, Vol. 8, 1978, pp. 193–198.

7 Aoki, S., et al., "Elastodynamic Analysis of Crack by Finite-Element Method Using Singular Element," *International Journal of Fracture*, Vol. 14, No. 11, 1978, pp. 59–68.

8 King, W. W., and Malluck, J. F., "Toward a Singular Element for Propagating Cracks," *International Journal of Fracture*, Vol. 14, 1978, pp. R7–R11.

9 Rice, J. R., "Mathematical Analysis in the Mechanics of Fracture," *Fracture*, Vol. II, Liebowitz, H., ed., Academic Press, 1968, pp. 192–308.

10 Malluck, J. F., "Crack Propagation in Finite Bodies," PhD Thesis, Georgia Institute of Technology, 1976.

11 Kalthoff, J. F., Beinert, J., and Winkler, S., "Measurements of Dynamic Stress-Intensity Factors for Fast Running and Arresting Cracks in Double Cantilever-Beam Specimens," *Fast Fracture and Crack Arrest*, ASTM STP 627, Hahn, G. T., and Kanninen, M. F., eds. American Society for Testing and Materials, 1977, pp. 161–176.

12 Gallagher, R. H., "A Review of Finite-Element Techniques in Fracture Mechanics," *Numerical Methods in Fracture Mechanics*, Owen, D. R. J., and Luxmore, A. R., eds. *Proceedings of a Conference*, held at Swansea, United Kingdom, Jan. 1978.

APPENDIX *A*

Details of basis functions for the singular element, for the Mode-I case, are given here. The eigenfunctions given here are solutions to the following equations for wave potentials Φ and Ψ:

$$[1 - (v/C_d)^2]\frac{\partial^2\Phi}{\partial\xi^2} + \frac{\partial^2\Phi}{\partial x_2^2} = 0 \tag{60}$$

with a similar equation for Ψ when C_d is replaced by C_s. For any nonzero, constant, speed of propagation, the eigenfunctions can be derived to be

$$u_1 = \sum_n u^*_{1n}\beta_n; \quad u_2 = \sum_n u^*_{2n}\beta_n; \quad \sigma_{\alpha\beta} = \sum_n \sigma_{\alpha\beta n}\beta_n; \quad \alpha, \beta = 1, 2 \tag{61–63}$$

where

$$u^*_{1n} = \frac{1}{\mu}F(\alpha_s, \alpha_d)[(n/2) + 1]\{r_1^{n/2}\cos(n\theta_1/2) - (1/2)g(n)r_2^{n/2}\cos(n\theta_2/2)\} \tag{64}$$

$$u^*_{2n} = \frac{1}{\mu}F(\alpha_s, \alpha_d)[(n/2) + 1]\{-\alpha_d r_1^{n/2}\sin(n\theta_1/2) + (1/2)[g(n)/\alpha_s]r_2^{n/2}\sin(n\theta_2/2)\} \tag{65}$$

$$\sigma_{11n} = F(\alpha_s, \alpha_d)(n/2)[(n/2) + 1]\{(2\alpha_d^2 - \alpha_s^2 + 1)r_1^{[(n/2)-1]} \times \cos[((n/2) - 1)\theta_1] - g(n)r_2^{[(n/2)-1]}\cos[((n/2) - 1)\theta_2]\} \tag{66}$$

$$\sigma_{22n} = F(\alpha_s, \alpha_d)(n/2)[(n/2) + 1]\{-(1 + \alpha_s^2)r_1^{[(n/2)-1]} \times \cos[((n/2) - 1)\theta_1] + g(n)r_2^{[(n/2)-1]}\cos[((n/2) - 1)\theta_2]\} \tag{67}$$

$$\sigma_{12n} = F(\alpha_s, \alpha_d)(n/2)[(n/2)+1]\{-2\alpha_d r_1^{[(n/2)-1]} \times \sin[((n/2)-1)\theta_1] + (1/2)[(1+\alpha_s^2)/\alpha_s]g(n) r_2^{[(n/2)-1]} \times \sin[((n/2)-1)\theta_2] \quad (68)$$

where λ, μ are the Lamé constants; C_d and C_s, respectively, the dilatational and shear wave speeds $C_d = [(\lambda+2\mu)/\rho]^{1/2}$; $C_s = (\mu/\rho)^{1/2}$; and the various parameters in the foregoing are defined as

$$\alpha_d^2 = [1-(v/C_d)^2]; \quad \alpha_s^2 = [1-(v/C_s)^2] \quad (69)$$

$$F(\alpha_d, \alpha_s) = \frac{4}{3(2\pi)^{1/2}} \frac{(1+\alpha_s^2)}{4\alpha_s\alpha_d - (1+\alpha_s^2)^2} \quad (70)$$

$$g(n) = (4\alpha_d\alpha_s)/(1+\alpha_s^2) \quad \text{when } n \text{ is odd}$$

$$= [1+\alpha_s^2] \quad \text{when} \quad n \quad \text{is even} \quad (71)$$

$$r_1 e^{i\theta_1} = \xi + i\alpha_d x_2 \quad (72)$$

$$r_2 e^{i\theta_2} = \xi + i\alpha_s x_2 \quad (73)$$

when $v = 0$, the aforementioned functions can be reduced to the usual Williams' [22] eigenfunctions.

It is interesting to note that the stress field $\sigma_{\alpha\beta}(x_\mu)$ $[\alpha, \beta, \mu = 1, 2]$, should in general case, satisfy the equations

$$\sigma_{\alpha\beta,\beta} = \left(\frac{\partial^2 u_\alpha}{\partial t^2} - 2v\frac{\partial^2 u_\alpha}{\partial\xi\partial t} + v^2\frac{\partial^2 u_\alpha}{\partial\xi^2}\right)\rho \quad (74)$$

However, it can be seen that the special eigenfunctions given in (66)–(68), corresponding to the solution of equation (60), satisfy only the equations

$$\sigma_{\alpha\beta,\beta} - \rho v^2\frac{\partial^2 u_\alpha}{\partial\xi^2} = 0 \quad (75)$$

for all values of v; thus, when $v = 0$, the correspondingly reduced eigenfunctions in equations (66)–(68), which coincide with the well-known Williams' eigenfunction, needless to say, satisfy the static equations of equilibrium, $\sigma_{\alpha\beta,\beta} = 0$.

APPENDIX *B*

Details of Finite-Element Equation Development for Dynamically Propagating Cracks

Upon substitution of equations (22)–(44), into (21), we obtain

$$0 = \sum_n \{[(\mathbf{q}_2^T\underline{\mathbf{K}}^T + \dot{\mathbf{q}}_2^T\underline{\mathbf{m}}^T - \overline{\mathbf{Q}}_2^T + \mathbf{q}_1^T\underline{\mathbf{K}}^T + \dot{\mathbf{q}}_1^T\underline{\mathbf{m}}^T - \overline{\mathbf{Q}}_1^T)]\delta\mathbf{q}_2\} + (\boldsymbol{\beta}_2^T\underline{\mathbf{K}}_{s2}^T + \dot{\boldsymbol{\beta}}_2^T\underline{\mathbf{D}}_{s2}^T + \ddot{\boldsymbol{\beta}}_2^T\underline{\mathbf{m}}_{s2}^T - \mathbf{Q}_{s2}^T + \boldsymbol{\beta}_1^T\underline{\mathbf{K}}_{s1}^T + \dot{\boldsymbol{\beta}}_1^T\underline{\mathbf{D}}_{s1}^T + \ddot{\boldsymbol{\beta}}_1^T\underline{\mathbf{m}}_{s1}^T - \overline{\mathbf{Q}}_{s1}^T)\delta\boldsymbol{\beta}_2 \quad (76)$$

where

$$\underline{\mathbf{K}} = \int_{V_{Rn}} \underline{\mathbf{B}}^T\underline{\mathbf{D}}\underline{\mathbf{B}}dv; \quad \underline{\mathbf{m}} = \int_{V_{Rn}} \rho\underline{\mathbf{N}}^T\underline{\mathbf{N}}dv \quad (77, 78)$$

$$\mathbf{Q}_2 = \int_{V_{Rn}} \underline{\mathbf{N}}^T\overline{\mathbf{F}}_2 dv + \int_{S_{\sigma n}} \underline{\mathbf{N}}^T\overline{\mathbf{T}}_2 ds \quad (79)$$

$$\mathbf{Q}_1 = \int_{V_{Rn}} \underline{\mathbf{N}}^T\overline{\mathbf{F}}_1 dv + \int_{S_{\sigma n}} \underline{\mathbf{N}}^T\overline{\mathbf{T}}_1 ds \quad (80)$$

$$\underline{\mathbf{K}}_{s2} = \int_{V_s} \underline{\mathbf{S}}_2^T\underline{\mathbf{P}}_2 dv + \rho v_2^2\int_{V_s} \underline{\mathbf{U}}_2^T(\underline{\mathbf{U}}_2)_{,\xi\xi} dv \quad (81)$$

$$\underline{\mathbf{K}}_{s1} = \int_{V_s} \underline{\mathbf{S}}_2^T\underline{\mathbf{P}}_1 dv + \rho v_1^2\int_{V_s} \underline{\mathbf{U}}_2^T(\underline{\mathbf{U}}_1)_{,\xi\xi} dv - \int_{\Delta\Sigma} \underline{\mathbf{U}}_2^T\underline{\mathbf{R}}_1 ds \quad (82)$$

$$\underline{\mathbf{m}}_{s2} = \rho\int_{V_s} \underline{\mathbf{U}}_2^T\underline{\mathbf{U}}_2 dv; \quad \underline{\mathbf{m}}_{s1} = \rho\int_{V_s} \underline{\mathbf{U}}_2^T\underline{\mathbf{U}}_1 dv \quad (83)$$

$$\underline{\mathbf{D}}_{s2} = -2\rho v_2\int_{V_s} \underline{\mathbf{U}}_2^T(\underline{\mathbf{U}}_2)_{,\xi} dv \quad (84)$$

$$\underline{\mathbf{D}}_{s1} = -2\rho v_1\int_{V_s} \underline{\mathbf{U}}_2^T(\underline{\mathbf{U}}_1)_{,\xi} dv \quad (85)$$

$$\mathbf{Q}_{s2} = \int_{V_s} \underline{\mathbf{U}}_2^T\overline{\mathbf{F}}_2 dv + \int_{\Sigma^+} \underline{\mathbf{U}}_2^T\overline{\mathbf{T}}_2 ds \quad (86)$$

$$\mathbf{Q}_{s1} = \int_{V_s} \underline{\mathbf{U}}_2^T\overline{\mathbf{F}}_1 dv + \int_{\Sigma^+} \underline{\mathbf{U}}_2^T\overline{\mathbf{T}}_1 ds$$

Now, the conditions of "least-squares" matching of displacements, velocities, and accelerations between the singular element and the surrounding regular elements, i.e., equations (11)–(13) are used to express $\boldsymbol{\beta}_2, \dot{\boldsymbol{\beta}}_2$, and $\ddot{\boldsymbol{\beta}}_2$ in terms of the respective values $\mathbf{q}_{s2}, \dot{\mathbf{q}}_{s2}, \ddot{\mathbf{q}}_{s2}$ at nodes along the boundary of V_s. Thus

$$\boldsymbol{\beta}_1 = \underline{\mathbf{A}}_1\mathbf{q}_{s1}; \quad \dot{\boldsymbol{\beta}}_1 = \underline{\mathbf{A}}_1\dot{\mathbf{q}}_{s1} + \underline{\mathbf{B}}_1\mathbf{q}_{s1};$$
$$\ddot{\boldsymbol{\beta}}_1 = \underline{\mathbf{A}}_1\ddot{\mathbf{q}}_{s1} + 2\underline{\mathbf{B}}_1\dot{\mathbf{q}}_{s1} + \underline{\mathbf{C}}_1\mathbf{q}_{s1} \quad (87)$$

$$\boldsymbol{\beta}_2 = \underline{\mathbf{A}}_2\mathbf{q}_{s2}; \quad \dot{\boldsymbol{\beta}}_2 = \underline{\mathbf{A}}_2\dot{\mathbf{q}}_{s2} + \underline{\mathbf{B}}_2\mathbf{q}_{s2};$$
$$\ddot{\boldsymbol{\beta}}_2 = \underline{\mathbf{A}}_2\ddot{\mathbf{q}}_{s2} + 2\underline{\mathbf{B}}_2\dot{\mathbf{q}}_{s2} + \underline{\mathbf{C}}_2\mathbf{q}_{s2} \quad (88)$$

We note that ($\underline{\mathbf{A}}_1$, $\underline{\mathbf{B}}_1$, and $\underline{\mathbf{C}}_1$) and ($\underline{\mathbf{A}}_2$, $\underline{\mathbf{B}}_2$ and $\underline{\mathbf{C}}_2$) are dependent on velocities of crack propagation v_1 and v_2, respectively. When equations (87), (88) are used, equation (76) can be rewritten as

$$0 = \sum_n \{(\mathbf{q}_2^T\underline{\mathbf{K}}^T + \dot{\mathbf{q}}_2^T\underline{\mathbf{m}}^T - \mathbf{Q}_2^T + \mathbf{q}_1^T\underline{\mathbf{K}}^T + \dot{\mathbf{q}}_1^T\underline{\mathbf{m}}^T - \overline{\mathbf{Q}}_1^T)\delta\mathbf{q}_2\} + [\mathbf{q}_{s2}^T\underline{\mathbf{K}}_s^{*T} + \dot{\mathbf{q}}_{s2}^T\underline{\mathbf{D}}_s^{*T} + \ddot{\mathbf{q}}_{s2}^T\underline{\mathbf{m}}_s^{*T} - \mathbf{Q}_s^{*T}]\delta\mathbf{q}_{s2} \quad (89)$$

where

$$\underline{\mathbf{K}}_s^* = [\underline{\mathbf{A}}_2^T\underline{\mathbf{K}}_{s2}\underline{\mathbf{A}}_2 + \underline{\mathbf{A}}_2^T\underline{\mathbf{D}}_{s2}\underline{\mathbf{B}}_2 + \underline{\mathbf{A}}_2^T\underline{\mathbf{m}}_{s2}\underline{\mathbf{C}}_2] \quad (90)$$

$$\underline{\mathbf{D}}_s^* = [\underline{\mathbf{A}}_2^T\underline{\mathbf{D}}_{s2}\underline{\mathbf{A}}_2 + 2\underline{\mathbf{A}}_2^T\underline{\mathbf{m}}_{s2}\underline{\mathbf{B}}_2] \quad (91)$$

$$\underline{\mathbf{m}}_s^* = \underline{\mathbf{A}}_2^T\,\underline{\mathbf{m}}_{s2}\,\underline{\mathbf{A}}_2 \quad (92)$$

$$\mathbf{Q}_s^* = \underline{\mathbf{A}}_2^T(-\underline{\mathbf{K}}_{s1}\boldsymbol{\beta}_1 - \underline{\mathbf{D}}_{s1}\dot{\boldsymbol{\beta}}_1 - \underline{\mathbf{m}}_{s1}\ddot{\boldsymbol{\beta}}_1 + \overline{\mathbf{Q}}_{s2} + \overline{\mathbf{Q}}_{s1}) \quad (93)$$

From equations (89), equations (45), (46) were derived. It can now be seen that both the singular-element matrices $\underline{\mathbf{K}}_s^*$ and $\underline{\mathbf{D}}_s^*$ are unsymmetric. The "damping" matrix $\underline{\mathbf{D}}_s^*$ is a result of the fact that the total accelerations of a material point in the singular element depend on $\dot{\boldsymbol{\beta}}_2$.

It may be of interst to note that in the evaluation of $\underline{\mathbf{K}}_{s2}$ of equation (81), the integrand will have a singularity of the type $(1/r_1)$ and $(1/r_2)$. Special numerical integration schemes to evaluate this domain integral of equation (81) directly, can be developed. Alternatively, one can use the observation that, by definition, from equations (21) and (76)

$$\boldsymbol{\beta}_2^T\underline{\mathbf{K}}_{s2}^T\delta\boldsymbol{\beta}_2 = \int_{V_s} (\sigma_{ij}^2\delta\epsilon_{ij}^2 + \rho(v_2)^2\frac{\partial^2 u_\alpha^2}{\partial\xi^2}\delta u_\alpha^2) dv \quad (94)$$

Using the divergence theorem, equation (94) can be rewritten as

$$\boldsymbol{\beta}_2^T\underline{\mathbf{K}}_{s2}^T\delta\boldsymbol{\beta}_2 = \int_{\partial V_s} \sigma_{ij}^2\nu_j^2\delta u_i^2 ds + \int_{V_s}\left(-\sigma_{ij,j}^2 + \rho(v_2)^2\frac{\partial^2 u_i^2}{\partial\xi^2}\right)\delta u_i^2 dv \quad (95)$$

the second integral on the right-hand side of equation (95) vanishes due to the special property of the eigenfunctions embedded in the singular element, as explained in equation (75). Thus one can write alternatively,

$$\underline{\mathbf{K}}_{s2}^T = \int_{\rho_s} \underline{\mathbf{R}}_2^T\underline{\mathbf{U}}_2 ds \quad (96)$$

wherein, the integrand is nonsingular along ρ_s, and no special integration schemes are necessary.

Likewise, it is seen that

$$\boldsymbol{\beta}_1^T\underline{\mathbf{K}}_{s1}^T\delta\boldsymbol{\beta}_2 = \int_{V_s} (\sigma_{ij}^1\delta\epsilon_{ij}^2 + \rho(v_1)^2\frac{\partial^2 u_\alpha^1}{\partial\xi^2}\delta u_\alpha^2)\, dv - \int_{\Delta\Sigma} \sigma_{ij}^1\nu_j^1\delta u_i^2 ds \quad (97)$$

once again, using the property, as given in equation (75), of the eigenfunctions σ_{ij}^1 in V_1, and using the divergence theorem, we write

$$\boldsymbol{\beta}_1^T \underline{\mathbf{K}}_{s1}^T \delta\boldsymbol{\beta}_2 = \int_{\partial V_s} \sigma_{ij}^1 \nu_j^1 \delta u_i^2 ds - \int_{\Delta\Sigma} \sigma_{ij}^1 \nu_j^1 \delta u_i^2 ds \tag{98}$$

It can easily be seen that the foregoing equation can be simplified to

$$\boldsymbol{\beta}_1^T \underline{\mathbf{K}}_{s1}^T \delta\boldsymbol{\beta}_2 = \int_{\rho_s} \sigma_{ij}^1 \nu_j^1 \delta u_i^2 ds \tag{99}$$

The aforementioned simplification is possible because $\partial V_s = \rho_s + \Sigma_1 + \Delta\Sigma + S_{u2}$, where ρ_s is the interface of the singular element with surrounding regular elements, and Σ_1 is assumed, without loss of generality, to be free of any applied tractions at all times, and S_{u2} is the ligament ahead of the crack-tip (along x_1-axis) in the singular element, where, for Mode-I problems, $T_1^1 = 0$, and $u_2^1 = 0$. The boundary integration as indicated by equation (99) to evaluate $\underline{\mathbf{K}}_{s1}$ may be more convenient than to directly apply equations (97) or (98).

T. Nishioka
Research Scientist.

S. N. Atluri
Regents' Professor of Mechanics.
Mem. ASME.

Center for the Advancement
of Computational Mechanics,
School of Civil Engineering,
Georgia Institute of Technology,
Atlanta, Ga.

Numerical Modeling of Dynamic Crack Propagation in Finite Bodies, by Moving Singular Elements

Part 2: Results

Using the moving-singularity finite-element method described in Part 1 of this paper, several problems of dynamic crack propagation in finite bodies have been analyzed. Discussions of the effects of wave interactions on the dynamic stress-intensity factors are presented. The obtained numerical results are compared with the corresponding infinite domain solutions and other available numerical solutions for finite domains.

Introduction

In Part 1 of the present paper [1], a "moving singular-element" procedure has been presented for the dynamic analysis of problems of fast crack propagation in arbitrarily shaped finite bodies with linear elastic material behavior. In this procedure a singular-element, within which a large number of analytical eigenfunctions corresponding to a propagating crack are used as basis functions for displacements, may be translated by an arbitrary amount $\Delta\Sigma$ in each time increment Δt of the numerical time-integration procedure. The moving singular-element, within which the crack-tip has always a fixed location, retains its shape at all times, while the mesh of "regular" (isoparametric) finite elements, surrounding the moving singular element, deforms accordingly. An energy-consistent variational statement was developed, as a basis for the foregoing moving singularity finite-element method of dynamic crack propagation analysis. It has been shown [1] that the present procedure leads to a direct evaluation of the dynamic stress-intensity factors.

In the present Part 2 of the paper several numerical studies of stationary as well as propagating cracks in finite bodies, are presented. These studies, in general, fall into the category of linear elastic dynamic fracture mechanics. These studies, in addition to illustrating the efficiency and accuracy of the present procedure, also shed light on the effects of stress-wave interactions on the stress-intensity factors for dynamically propagating cracks in finite bodies.

The presently considered examples include:

1 *Static extension of a central crack in a panel from a nonzero* initial length.

2 Self-similar, constant-velocity, propagation from a finite initial length of a central crack in a finite plane body subject to an uniform, time-independent, tensile stresses (normal to crack-axis) at the edges (which problem, is analogous to that treated by Broberg [2], and Rose [3, 4]).

3 A stationary central crack in a finite plane body subject, at its edges, to a Mode-I type uniformly distributed stress with a Heaviside step-function time-dependence (analogous to the problems of Baker [5], Sih, Embley, and Ravera [6], and Thau and Lu [7]).

4 A problem similar to that in Example 3 except that the crack-tips remain stationary until a time t_0, where upon they start propagating at a constant speed (analogous to the problems studied by Freund [8]).

5 Constant-velocity propagation of an edge-crack in a panel, with the direction of propagation being parallel to the panel-edges on which uniform displacements, normal to the edges, are prescribed (analogous to the problem treated by Nilsson [9]). All the references [2–8] deal with unbounded bodies, except [9] which deals with a finite height, but infinite width strip. Thus the presently obtained results for finite bodies are compared with those in [2–9] and the effects of finiteness of the domains are discussed. Comparisons of the present results with the numerical results of other investigators, where available, are also presented and discussed.

In the following we present results for each of the problems just cited.

1 **Static Crack Extension.** To test the accuracy of the present method of "moving singular-elements," first a *static* problem of a central-cracked square panel [$2L$ (length) = $2W$ (width)], subjected to uniform tension at edges parallel to the crack axis, was solved to obtain the static stress-intensity factor as a function of the current crack length, Σ. Thus, in the finite-element development given in Part 1 of this paper [1], velocity and acceleration effects were ignored. The eigenfunctions embedded in the singular-element reduce, when $v = 0$, to the well-known Williams' eigenfunctions as shown in Appendix A of [1]. Starting from an initial crack length value of $\Sigma_0 = 0.2W$, the

Contributed by the Applied Mechanics Division for publication in the JOURNAL OF APPLIED MECHANICS.

Discussion on this paper should be addressed to the Editorial Department, ASME, United Engineering Center, 345 East 47th Street, New York, N. Y. 10017, and will be accepted until December 1, 1980. Readers who need more time to prepare a discussion should request an extension from the Editorial Department. Manuscript received by ASME Applied Mechanics Division, November, 1979; final revision, February, 1980.

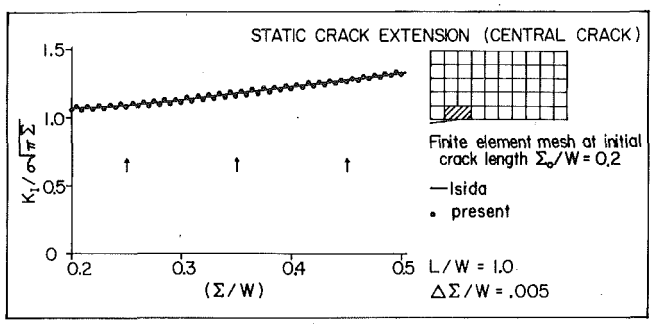

Fig. 1 Calculation of static K_I factors in a center-cracked tension specimen by the present "moving-singularity" method: $\Delta\Sigma = 0.005$; (↑) indicates the current crack length when the regular element are readjusted as shown in Fig. 2 of [1]

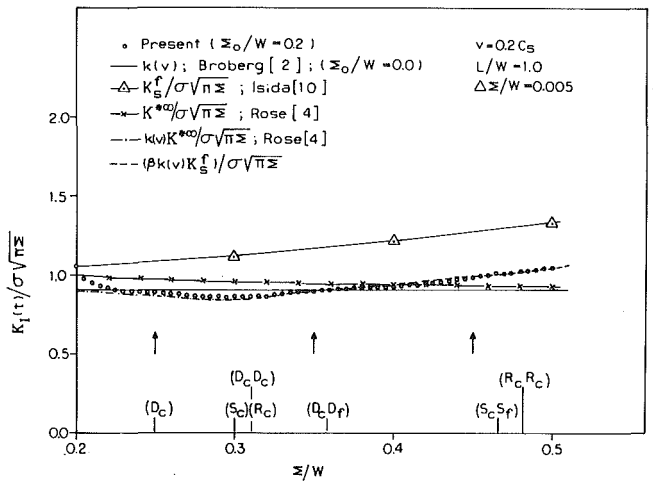

Fig. 2 Normalized dynamic stress-intensity factor for a crack starting from a finite initial length and propagating with constant velocity, $v/C_s = 0.2$

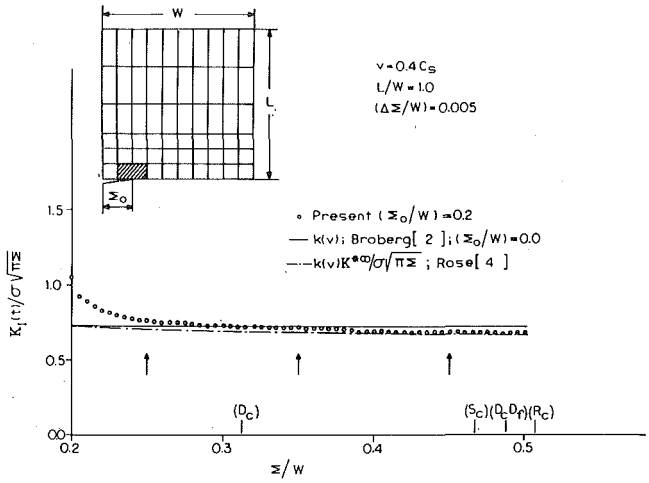

Fig. 3 Normalized dynamic stress-intensity factor, $(v/C_s) = 0.4$

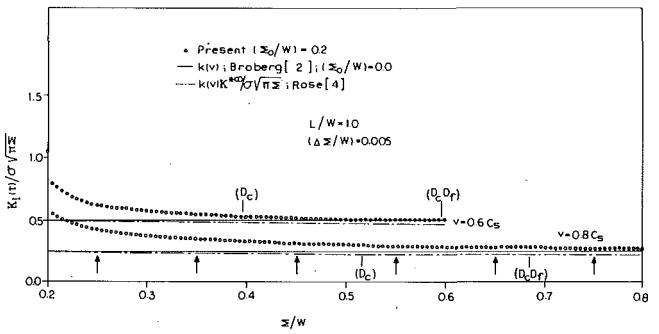

Fig. 4 Normalized dynamic stress-intensity factors for the cases $(v/C_s) = 0.6$ and 0.8

singularity element was successively translated (in Mode-I growth sense), statically (with $v = 0$) in increments of $\Delta\Sigma = 0.005W$ until a final value of crack length $\Sigma = 0.5W$ is reached. During the previous series of calculations, the externally applied uniform tension was held constant. At each current crack-length level, the stress-intensity factor is computed directly as an unknown from the finite-element equations, as described in [1]. From the normalized stress-intensity factor solutions shown in Fig. 1, it is seen that the present results agree excellently with those reported by Isida [10]. The normalized results shown in Fig. 1 may be viewed as correction factors for static stress-intensities, due to the finite size of the panel.

We note that the symbols (↑) in Fig. 1, as well as in all the subsequent figures, denote the current crack length (Σ/W) where the regular elements surrounding the moving crack-element were readjusted as described in Fig. 2 of [1].

2 Self-Similar, Constant Velocity, Crack-Propagation From a Finite Initial Length. The problem is that of a centrally cracked square panel ($L = W = 40$mm) with properties: μ (shear modulus) = 2.94×10^{10} N/m^2; ν (Poisson's ratio) = 0.286; ρ (mass density) = 2.45×10^3 Kg/m^3. A time-independent tensile stress was assumed to be acting at the edges of the specimen parralel to the crack-axis. The crack is assumed to open from an initial length $(\Sigma_0/W) = 0.2$ and to grow symmetrically with a constant velocity, v. This problem may be considered to be similar to that treated by Broberg [2] except that Broberg treated an infinite body with a crack which opens from a zero initial length. The problem was analyzed for four different values of v, namely, $(v/C_s) = 0.2, 0.4, 0.6$, and 0.8, respectively, where the shear wave speed for the present problem is $C_s = 3.4641 \times 10^6$ mm/sec. The dilatational and surface (Rayleigh) wave speeds, C_d and C_R, respectively, are such that $(C_d/C_s) = 1.8266$, and $(C_R/C_s) = 0.9238$.

In all the four considered cases of (v/C_s) ratio, the increment of crack growth in each step, $\Delta\Sigma$, was kept the same, at the value: $(\Delta\Sigma/W) = 0.005$. Thus, in each of the considered (v/C_s) cases, the time integration step, Δt, changes according as: $[(v \cdot \Delta t)/W] = 0.005$. The finite-element mesh used, at the initial crack length in each of the four cases, is shown in the inset of Fig. 3. In this figure, as well as in Figs. 1, 4, and 9, the singular-element near the crack-tip is identified by hatched markings.

As noted in the review article by Rose [3], the dynamic stress-intensity factor K may be expressed as the product of a velocity factor $k(v)$ and a static factor K^*; thus

$$K = k(v)\, K^* \tag{1}$$

The "static factor" K^* depends on the current length of the crack, the applied load, the history of crack extension, but not on the instantaneous crack speed. As also discussed in [3], K^* is, in general, not equal to the static stress-intensity factor, K_s, for a stationary crack of the same length as the moving crack. The analytical expression for $K^{*\infty}$ (in an infinite body subjected to uniform stress normal to the crack axis), as a function of the current crack length is given by Eshelby [11] and in [3], as

$$K^{*\infty} = (2/\pi)^{1/2} \int_{\Sigma_0}^{\Sigma} \sigma_{yy}(x)/(\Sigma - x)^{1/2}\, dx \tag{2}$$

where

$$\sigma_{yy}(x) = \sigma\, |x|/(x^2 - \Sigma_0^2)^{1/2}; \quad |x| > \Sigma_0 \tag{3}$$

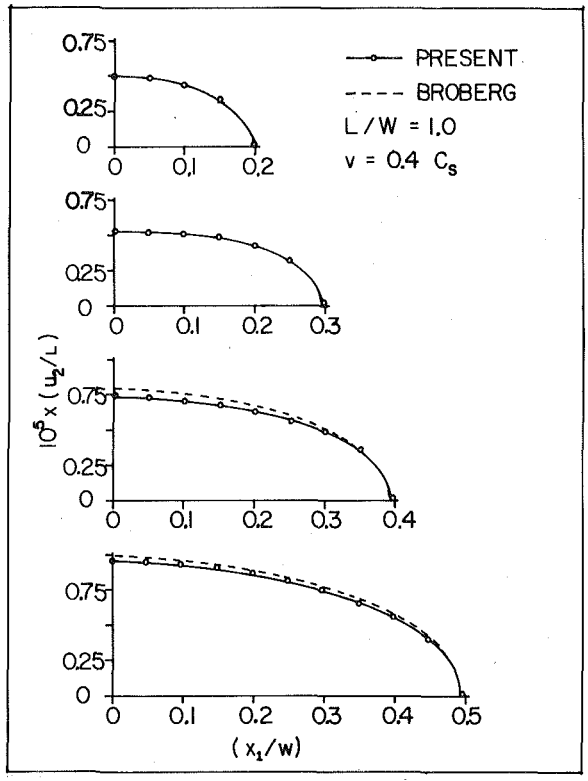

Fig. 5 Crack-face displacements at various time-instants, for a crack propagating at constant velocity, (v/C_s) = 0.4

In equations (2) and (3), σ is the applied tensile stress at infinity, $2\Sigma_0$ is the initial crack length, and x,y are Cartesian coordinates centered such that $x = \pm \Sigma(t)$ denote the current crack-tips and y is normal to crack-axis. Thus $\sigma_{yy}(x)$ in equation (2) is the initial distribution of stress along the axis of the crack, prior to its propagation. Eshelby's results for the integral in equation (2) is

$$K^{*\infty} = [\sigma(\pi\Sigma_0)^{1/2}(2/\pi)\{(2+\xi)E - F\}]/[1+(\xi/2)]^{1/2} \quad (4)$$

where $\xi = (\Sigma - \Sigma_0)/\Sigma_0$; and E and F are the complete elliptic integrals of the 2nd and 1st kind, respectively, with the modulus $[\xi/(2+\xi)]^{1/2}$. On the other hand, the static-stress-intensity factor K_s^{∞} for a crack of length 2Σ in an infinite domain is

$$k_s^{\infty} = \sigma(\pi\Sigma)^{1/2} \quad (5)$$

Thus, in general, $K^{*\infty} < K_s^{\infty}$. It is also noted that the equation (4) for $K^{*\infty}$ is valid only until the time that disturbances from one crack-tip reach the other (moving) crack-tip. However, for the case of a crack growing self-similarly from a zero initial length ($\Sigma_0 = 0$) with a constant velocity v, as in the problem studied by Broberg [2], disturbances from one crack-tip influence at all times the other moving crack-tip if $2v < c_d$, and $K^{*\infty} \equiv K_s^{\infty}$ at all times.

The normalized dynamic stress-intensity factor solution for the present problem of a crack, in a finite square panel, propagating self-similarly at a constant velocity (v/C_s) = 0.2, is shown in Fig. 2. Note that the normalization is such that a value of unity represents the normalized stress-intensity factor K_s^{∞} for a crack of length $2\Sigma(\Sigma = \Sigma_0 + vt)$ in an infinite solid with time-independent remote tension σ. Also shown in Fig. (2) are

1 The finite-size correction factor $F = K_s^f/\sigma(\pi\Sigma)^{1/2}$ for the static stress-intensity factor K_s^f in the present finite domain.

2 The normalized static factor $K^{*\infty}/\sigma(\pi\Sigma)^{1/2}$, as calculated from equation (4).

3 The velocity factor $k(v)$ for (v/C_s) = 0.2, as given by Broberg [2]. The effect of the finiteness of the domain on K^* may be accounted for, approximately, by including a finite-size correction factor in the initial stress-distribution at Σ_0, in equation (3). Thus it appears that one may write, approximately, that $K^{*f} = F(\Sigma_0)K^{*\infty}$. For the present case of (Σ_0/W) = 0.2, the finite correction factor $F(\Sigma_0) \simeq 1.055$, as seen from Fig. 1.

Also marked in Fig. 2 are several specific instants of time (or equivalently, the corresponding values of Σ) with the notations:

(*a*) D_c, S_c, and R_c are, respectively, the times taken by the dilatational, shear, and Rayleigh waves to traverse one crack-width.

(*b*) D_cD_c (or R_cR_c) denotes D_c (or R_c) plus the time for the first rescattered dilatational (or Rayleigh) waves to travel one crack-width.

(*c*) D_cD_f (or S_cS_f) denotes the time taken for the dilatational (or shear) waves emanated by one crack-tip to be reflected by the nearest free-boundary and reinteract with the crack-tip in question.

The foregoing times are calculated from the continuum relations for the respective wave speeds. However, it should be borne in mind that a "consistent-mass" representation is used in the present finite-element method.

For the case of (v/C_s) = 0.2, it is seen from Fig. 2 that the computed normalized dynamic stress-intensity factor correlates excellently with the values given by $F(\Sigma_0)K^{*\infty}k(v)/\sigma(\pi\Sigma)^{1/2}$ until roughly the time denoted by R_c. At longer times, i.e., at the times greater than R_c and D_cD_f, the computed normalized dynamic $K_I(t)$ appears to correlate excellently with the values given by $[\beta K_s^f k(v)/\sigma(\pi\Sigma)^{1/2}]$ where β is a constant. It is interesting to observe that, for the present problem, this constant β appears to be equal to $G(\Sigma_{Rc})/F(\Sigma_{Rc})$ where $F(\Sigma_{Rc})$ is the finite correction factor in the static stress intensity for a crack of length equal to the current length, Σ_{Rc}, in a dynamic problem, at which the event R_c (as defined earlier), occurs; whereas, $G(\Sigma_{Rc})$ is likewise, the ratio $[F(\Sigma_0)K^{*\infty}/\sigma(\pi\Sigma)^{1/2}]$ at $\Sigma = \Sigma_{Rc}$. The event R_c is seen to occur at the time, $\tilde{t} = (2\Sigma_0)/(C_R - v)$, and thus $\Sigma_{Rc} = \Sigma_0 + v\tilde{t}$. Both $\tilde{t}$ and (Σ_{Rc}/W) decrease as Σ_0 decreases, for given C_R and v. Thus, for smaller values of Σ_0 (and/or smaller values of v), the ratios $F(\Sigma_{Rc})$, $G(\Sigma_{Rc})$, and hence β tend to a value of unity. Thus, for cracks propagating from initial lengths such that $(\Sigma_0/W) \ll 1$, it appears that at the times greater than R_c and D_cD_f and/or after the crack has grown dynamically to a few times its initial length, the static factor K^{*f} approaches the static-stress-intensity factor for the current crack length in the finite body, namely, K_s^f.

In connection with the presently computed results shown in Fig. 2, it should be noted that the crack velocity, v, was taken to be zero at the initial crack length Σ_0. It is assumed that the crack-tip accelerates to a velocity, (v/C_s) = 0.2, during the first time increment, Δt. The convergence of the present numerical results to the analytically predicted ones, at small times, $t \ll D_c$ in the present case of (v/C_s) = 0.2, could have been studied by altering this time step Δt in which the crack-tip accelerates from (v/C_s) = 0 to (v/C_s) = 0.2. However, this was not attempted.

The computed normalized dynamic stress-intensity factor solution for the case (v/C_s) = 0.4 is shown in Fig. 3, wherein the times D_c, S_c D_cD_f, and R_c, as defined earlier, are also marked. Once again, it is seen that until significant interaction of the waves from the other crack-tip and the free surface takes place (i.e., for time $t < R_c$ or D_cD_f), the computed dynamic K-factor for the finite body correlates excellently with the value predicted by the approximate function: $[K^{*f}k(v)]$.

Finally, the results for the cases (v/C_s) = 0.6 and 0.8, respectively, are shown in Fig. 4, wherein only the times D_c, and D_cD_f are also marked. The values of R_c and S_c are greater than the time for which the solution is obtained. Once again, it is seen that the computed dynamic K-factor correlates well with the approximate prediction, $K^{*f}k(v)$. Moreover, the convergence of the computed solution, to that analytically predicted, is slow, at these higher crack-speeds. A possible reason for this may be the initial conditions at Σ_0 used in the present study, as explained earlier.

The crack-mouth opening displacements at various instants of time (or equivalently, at corresponding crack-lengths), for the case of (v/C_s) = 0.4, are shown in Fig. 5. Also shown in Fig. 5 are the corresponding analytical results by Broberg [2], who considers constant velocity crack-propagation starting from a zero initial crack-length. An excellent correlation between the present results and those of [2] is

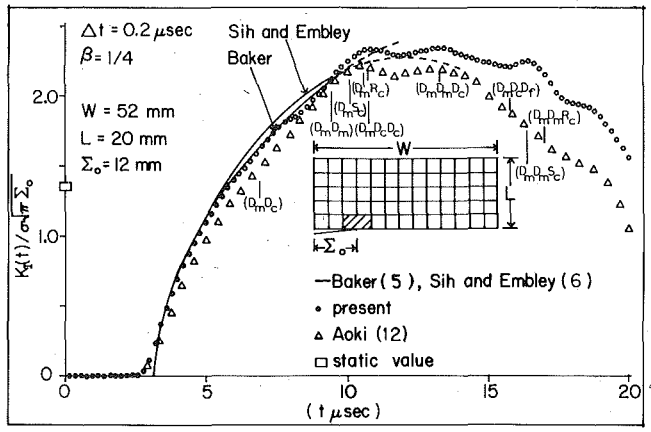

Fig. 6 Time-dependence of dynamic stress-intensity factor for a center-cracked rectangular plate subjected to Heaviside step-function normal stress

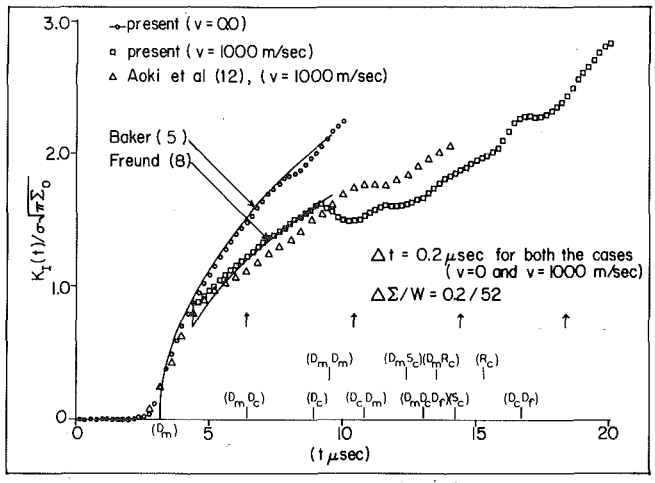

Fig. 7 Time-dependence of dynamic stress-intensity factor for a center-cracked rectangular plate subject to a step-function normal stress; crack remains stationary until t_0 and then propagates with a constant velocity

noted. A similar correlation was also noted for the other considered cases of (v/C_s) ratio, but are not shown here.

(3) Stress-Wave Loading of a Stationary Crack in a Finite Body. The problem is that of a rectangular panel $[(W/L) = 2.6]$ with a centrally located crack of length $(\Sigma_0/W) = (3/13)$. The material properties are taken to be: μ (shear modulus) $= 2.94 \times 10^{10}$ N/m^2; $\nu = 0.286$; and $\rho = 2.45 \times 10^3$ kg/m^3. Uniformly distributed uniaxial tensile stresses, with a Heaviside step-function time-dependence, were assumed to act at the edges of the panel parallel to the crack-axis. The crack is assumed to be stationary under the action of this time-dependent loading.

Due to symmetry, only a quadrant of the panel is modeled by finite elements, as shown in Fig. 6. Also marked in Fig. 6 are specific instants of time, calculated by using continuum wave speeds, with the notations:

(*a*) D_m is the time taken by the dilatational waves to travel the distance from the boundary, where time-dependent tractions are applied, to the crack-tip.

(*b*) D_mD_c, D_mS_c and D_mR_c are, respectively, equal to D_m plus the time taken by the first scattered dilational, shear, and Raleigh waves to reach from one crack-tip to the other.

(*c*) $D_mD_cD_c$ is equal to D_mD_c plus the time taken by the first rescattered dilatational wave to travel one crack-width.

(*d*) $D_mD_cD_f$ is equal to D_m plus the time taken by the scattered longitudinal waves to travel from the crack-tip to the nearest free boundary surface and back to the same crack-tip.

(*e*) D_mD_m is the time taken by the dilational waves to travel the length of the bar, reflect from the boundary surface on the opposite and return back to the crack-tip.

(*f*) $D_mD_mD_c$, $D_mD_mS_c$ and $D_mD_mR_c$ are, respectively, equal to D_mD_m plus the time for the rescattered dilatational, shear, and surface waves to travel one crack-width.

The presently computed normalized dynamic stress-intensity factor solution is shown in Fig. 6. Also shown in Fig. 6 are the analytical solutions by Baker [5], Sih, Embley, and Ravera [6], for infinite domains, and the numerical solution by Aoki, et al. [12], for a finite domain identical to the one considered here. During the time interval D_m to D_mD_c, when no wave interaction takes place, the results for the present problem must agree with the results of Baker [5] and this can be seen to be the case with the present results. The solution at longer times is found to be in good agreement with that of Sih, et al. [6]. It is noted that the overshoot in the k-factor at the time instant D_mR_c in the present solution, as compared to the solution by Sih, et al. [6], is analogous to that in a recent solution by Kim [13]. It is also seen from Fig. 6, that the present solution is higher than that of Aoki, et al. [12], at all times. However, the solution of Aoki, et al., appears to be lower than that by Baker [5] even for times less than D_mD_c.

Finally, it is of interest to note that even though the time for the longitudinal wave to arrive from the loaded boundary to the crack, as computed from continuum wave speeds, is D_m as marked in Fig. 6, a nonzero stress intensity is observed at the crack-tip even at times lower than D_m in the finite-element solution. This is due to the inertia-coupling that exists between the finite-element nodes (especially those of the singular-element) when a consistent mass-matrix, as in the present, is used.

(4) Crack-Propagation at Constant Speed: Stress-Wave Loading. We consider the problem wherein the geometry, material properties and the time-dependent loading are all identical to those described under Case (*iii*) in the foregoing. In this problem, the crack with an initial length of $(\Sigma_0/W) = 3/13$ remains stationary until a time $t_0 = 4.4$ μs and then propagates with a constant velocity $v = 1000$ m/sec. The finite-element breakdown at the initial crack length, Σ_0, is identical to that in Fig. 6. In modeling the crack propagation, the regular elements are periodically readjusted as indicated in Fig. 2 of [1]. The instants of time (or equivalently the value of Σ) at which these readjustments are done, are marked, by (↑) in Fig. 7.

Also marked in Fig. 7 are several specific instants of time, calculated by using continuum wave speeds, with the notations:

(*a*) D_m is the time for the dilatational waves to travel from the boundary, where a Heaviside step function tension is applied, to the stationary crack-tip.

(*b*) D_mD_c, D_mS_c and D_mR_c are, respectively, equal to D_m plus the time taken by the dilatational, shear, and surface waves first scattered by the stationary crack-tip to reach the other crack-tip.

(*c*) D_c, S_c, R_c are, respectively, equal to t_0 (when the crack-tips begin to propagate) plus the time taken by the dilatational, shear, and surface waves emanated by crack-tip at t_0 to reach the other crack-tip.

(*d*) D_mD_m is the time taken by the longitudinal waves to travel the length of the panel to the opposite side and return to a (moving) crack-tip.

(*e*) D_cD_m is the time taken for the dilatational waves emanating from a crack-tip at t_0 travel to the nearest boundary (which in this case is the one where tractions are applied) and back to the same crack-tip.

(*f*) $D_mD_cD_f$ is equal to D_m plus the time taken by the dilatational waves first scattered by the stationary crack-tip to travel to the nearest free-boundary and back to the same crack-tip, which is now propagating.

(*g*) D_cD_f is equal to t_0 plus the time taken by the dilatational waves emanating from the crack-tip at t_0 to travel to the nearest *free* boundary and back to the same crack-tip.

The presently computed results for the dependence of the dynamic

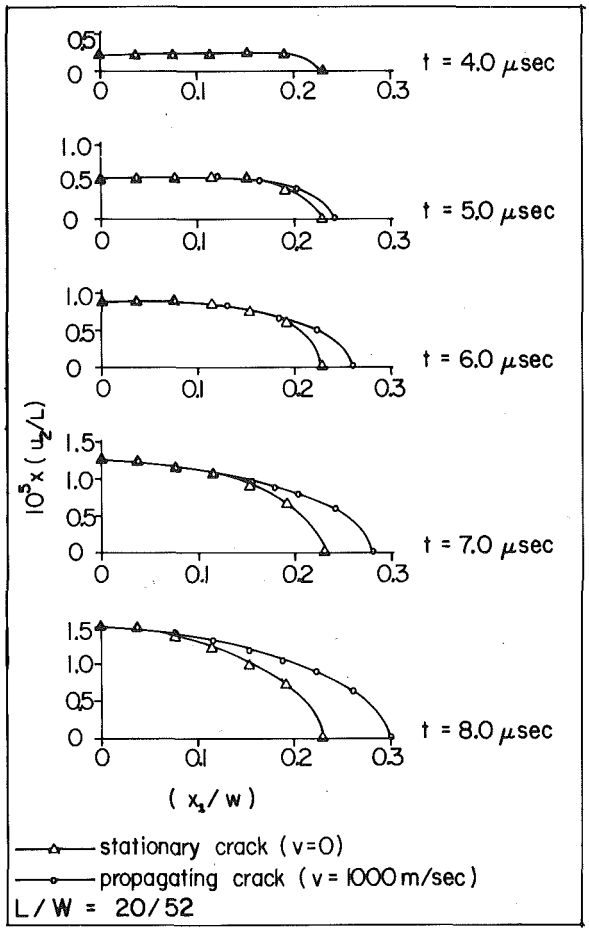

Fig. 8 Crack-face profiles for a stationary as well as propagating crack at various times

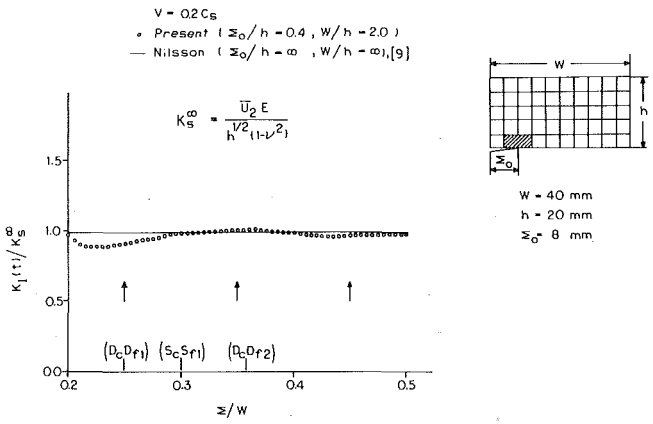

Fig. 9 Dynamic stress-intensity factor for an edge cracked square sheet subject to constant normal displacement: (v/C_s) = 0.2

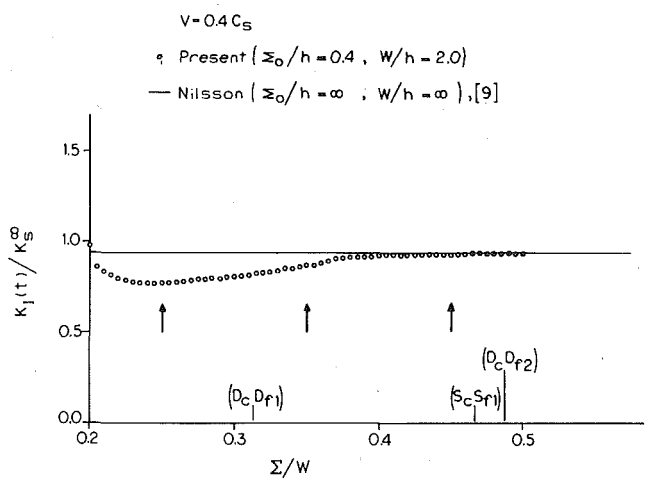

Fig. 10 Dynamic stress-intensity factor for an edge cracked square sheet subject to constant normal displacement: (v/C_s) = 0.4

stress-intensity factor on time are indicated in Fig. 7, along with the comparison (analytical) results by Freund [8] and Baker [5], and the (numerical) results by Aoki, et al. [12]. As noted earlier, the correlation of the present stationary crack results with those of Baker [5], until wave interaction takes place, is excellent. In the case when the crack propagates suddenly at the time t_0 (= 4.4 μs in Fig. 7), the infinite domain results by Freund [8] are seen to correlate excellently with the present results, until significant interaction of waves emanating from one crack-tip with the other crack-tip takes place. It is noted that in [8] the crack-tip velocity is assumed to change from zero to "v" in zero time, whereas, in the present numerical study, this transition is assumed to take place over a finite time-step Δt. For a closer comparison with the results of [8], it would be interesting to vary the size of Δt over which the aforementioned transition occurs; but this is not pursued in the present study. It is seen that the comparison results by Aoki, et al. [12], are somewhat lower than those in [8] even until the time that the solution in [8] may be considered valid. Further, the results in [12] are higher than the present, after this time.

The crack-face opening displacements at various time intervals for the propagating crack, as well as similar results at corresponding times for a stationary crack are shown in Fig. 8. It is interesting to note that at sufficient distances away from the propagating crack-tip, the crack-mouth opening displacements are nearly the same for the stationary as well as propagating cracks.

(5) Constant Velocity Crack-Propagation in a Strip With Prescribed Boundary Displacements. The problem considered is that of the constant velocity propagation of an edge crack in a square sheet whose edges parrallel to the direction of crack-propagation are subject to uniform displacements $\bar{u}_2$ in the direction normal to that of crack-propagation. This problem is analogous to that treated by Nilsson [9] who obtained an analytical solution for the steady-state stress-intensity factor for the constant velocity propagation of semi-infinite crack in a finite-height (normal to crack-axis), infinite-width, strip.

In the present problem the following geometry and material parameters are used: $(2h/W) = 1.0$ (see inset of Fig. 9), $\nu = 0.286$; $\mu = 2.94 \times 10^{10}$ N/m^2, and $\rho = 2.45 \times 10^3$ Kg/m^3. The crack is assumed to start to propagate from an initial length of $(\Sigma_0/h) = 0.4$.

Three different cases of constant velocity propagation, $(v/C_s) = 0.2$; 0.40, and 0.60, respectively, are considered.

The results for the dynamic stress-intensity factor for the case $(v/C_s) = 0.2$ are shown in Fig. 9 along with the analytical solutions by Nilsson [9]. The results in Fig. 9 are normalized with respect to the plane-strain, static ($v = 0$) stress-intensity factor for the semi-infinite crack in a finite-height, infinite-width strip, namely, $K_s^{\infty} = \bar{u}_2 E/h^{1/2}(1 - \nu^2)$. Also shown in Fig. 9 are certain specific instants of time, with the notations:

(a) D_cD_{f1}, S_cS_{f1}, are, respectively, the times taken by the dilational, and shear waves, emanated by the moving crack-tip to be reflected from the nearest free-boundary and travel back to the crack-tip.

(b) D_cD_{f2} is the time taken by the dilatational waves emanated from the crack-tip to be reflected by the second free-boundary ($x = W$) and travel back to the crack-tip.

It is seen from Fig. 9 that, the correlation between the present and Nilsson's [9] results is excellent. It may be of interest to note that in an analysis using the "node-release" technique, Malluck and King

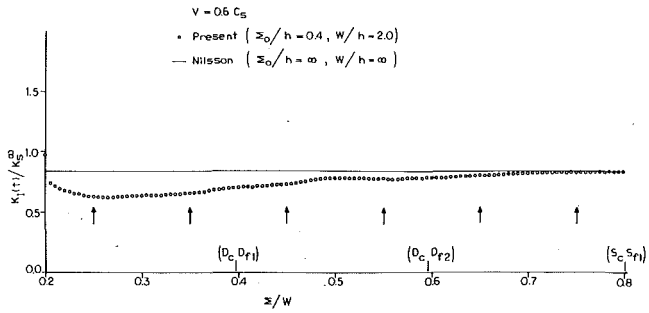

Fig. 11 Dynamic stress-intensity factor for an edge cracked square sheet subject to constant normal displacement: (v/C_s) = 0.6

[14] found, for the case of $(v/C_s) = 0.325$, that their computed results for the energy-release rate for a similar problem were about 20% lower than that predicted by Nilsson [9], as steady-state conditions are reached. This may indicate the relative efficiency of the present numerical method as compared to the familiar "node-release" techniques.

Finally the computed results for the cases $(v/C_s) = 0.4$ and 0.6 are shown in Figs. 10 and 11, respectively. The times noted in Figs. 10 and 11 have the same meanings on those indicated in Fig. 9. From Figs. 10 and 11 it is once again seen that the present results agree excellently with those in [9].

Closure

The procedure of a moving singular element, within which a large number of eigenfunctions for a propagating crack are embedded, has been applied to study several problems of dynamic crack propagation in finite bodies. The numerical results have been found to correlate well with the available analytical solutions, for corresponding problems in infinite domains, during the time for which these analytical solutions may be considered as valid. The computed solutions beyond these times, and the knowledge of the times involved for wave-interaction in finite bodies, indicate both qualitatively and quantitatively the effects of stress-wave interactions on dynamic stress-intensity factors for cracks propagating in finite bodies.

The use of the presented numerical procedure in the simulation of experimental data from dynamic fracture test specimens, as well as in predicting crack-propagation history in dynamically loaded cracked bodies, are the subjects of a forthcoming paper.

Acknowledgments

This work was supported by the Office of Naval Research under Contract No. N0004-78-0636 with the Georgia Institute of Technology. The authors thank Dr. N. Perrone for his encouragement. Thanks are also expressed to Mrs. T. Rapp for her able typing of this manuscript.

References

1 Nishioka, T., and Atluri, S. N., "Numerical Modeling of Dynamic Crack Propagation in Finite Bodies, by Moving Singular Elements—Part 1: Formulation," ASME JOURNAL OF APPLIED MECHANICS, Vol. 47, Sept. 1980, pp. 570–576.

2 Broberg, K. B., "The Propagation of a Brittle Crack," *Arkiv För Fysik*, Band 18, No. 10, 1960, pp. 159–192.

3 Rose, L. R. F., "Review Article, Recent Theoretical and Experimental Results on Fast Brittle Fracture," *International Journal of Fracture*, Vol. 12, No. 6, 1976, pp. 799–813.

4 Rose, L. R. F., "On the Initial Motion of a Griffith Crack," *International Journal of Fracture*, Vol. 12, No. 6, 1976, pp. 829–841.

5 Baker, B. R., "Dynamic Stresses Created by a Moving Crack," ASME JOURNAL OF APPLIED MECHANICS, Vol. 29, 1962, pp. 449–545.

6 Sih, G. C., Embley, G. T., and Ravera, R. S., "Impact Response of a Finite Crack in Plane Extension," *International Journal of Solids and Structures*, Vol. 8, 1972, pp. 977–993.

7 Thau, S. A., and Lu, T. H., "Transient Stress-Intensity Factors for Finite Crack in an Elastic Solid Caused by a Dilational Wave," *International Journal of Solids and Structures*, Vol. 7, 1971, pp. 731–750.

8 Freund, L. B., "Crack-Propagation in an Elastic Solid Subjected to General Loading—III. Stress Wave Loading," *Journal of the Mechanics and Physics of Solids*, Vol. 21, 1973, pp. 47–61.

9 Nilsson, F., "Dynamic Stress-Intensity Factors for Finite Strip Problems," *International Journal of Fracture*, Vol. 8, No. 4, 1972, pp. 403–411.

10 Isida, M., "Effect of Width and Length on Stress-Intensity Factors of Internally Cracked Plates Under Various Boundary Conditions," *International Journal of Fracture*, Vol. 7, No. 3, 1971, pp. 301–306.

11 Eshelby, J. D., "The Elastic Field of a Crack Extending Nonuniformly Under General Antiplane Loading," *Journal of the Mechanics and Physics of Solids*, Vol. 17, 1969, pp. 177–199.

12 Aoki, S., et al., "Elastodynamic Analysis of Crack by Finite-Element Method Using Singular Element," *International Journal of Fracture*, Vol. 14, No. 11, 1978, pp. 59–68.

13 Kim, K. S., "Dynamic Propagation of a Finite Crack," *International Journal of Solids and Structures*, Vol. 15, 1979, pp. 685–699.

14 Malluck, J. F., and King, W. W., "Fast Fracture Simulated By a Finite-Element Analysis Which Accounts for Crack-Tip Energy Dissipation," *Numerical Methods in Fracture Mechanics*, eds., Luxmore and Owen, University College, Swansea, 1978, pp. 648–659.

J. W. Nicholson
Assistant Professor,
Department of Applied Mathematics
and Computer Science,
University of Virginia,
Charlottesville, Va. 22901

M. R. Bradley
Senior Scientist,
Planning Systems Incorporated,
Slidell, La. 70458

C. K. Carrington
Graduate Student,
Department of Engineering Science
and Mechanics,
Virginia Polytechnic Institute
and State University,
Blacksburg, Va. 24061

Asymptotic Evaluation of a Combined Stress-Intensity Factor for a Pressurized Cylindrical Shell Containing a Longitudinal Crack

Sanders' path-independent energy-release-rate integral I for a cracked shallow shell is used to compute the asymptotic form of the combined stress-intensity factor for a pressurized elastically isotropic cylindrical shell containing a longitudinal crack. The combined stress-intensity factor is expressible in terms of the conventional stretching and bending stress-intensity factors and is a function of Poisson's ratio ν and a dimensionless crack length λ. When λ is small the shell is nearly flat and when λ is large the shell is very thin. Asymptotic formulas for I when λ is small or large are obtained. A numerical solution for $\lambda = 0(1)$ is also obtained.

Introduction

Nicholson and Simmonds [1] have specialized Sanders' path-independent, energy-release-rate integral I [2] to an arbitrarily loaded elastically isotropic shallow shell containing a stress-free void. I can be interpreted physically as the flow of potential energy from the shell to the void (to create new surface area if the void expands). When the void is a crack one form of I is expressible in terms of the conventional bending and stretching stress-intensity factors, B and S, respectively. Another form reduces to an integral along the crack. Both forms of I are nondimensional and depend on Poisson's ratio ν and the dimensionless crack length

$$\lambda = \left[\frac{3}{4}(1-\nu^2)\right]^{1/4} \frac{c}{\sqrt{Rh}},$$

where c is the crack half length, h is the shell thickness, and R is the minimum radius of curvature.

To interpret λ we hold c fixed. Thus $\lambda \ll 1$ implies the shell is nearly flat and $\lambda \gg 1$ implies the shell is very thin.

In [1] a bent cylindrical shell with a longitudinal crack was analyzed and a combined stress-intensity factor $C(\lambda, \nu)$ calculated for $0 \leq \lambda < \infty$. In this paper we will use the path-independent integral I to determine $C(\lambda, \nu)$ for a pressurized cylindrical shell containing a finite length crack. The ratio c/R is assumed small so that shallow shell theory applies. For symmetrical stress and displacement fields the combined stress-intensity factor is related to I and S and B by

$$I(\lambda, \nu)/2\pi = C^2(\lambda, \nu) = S^2(\lambda, \nu) + \frac{B^2(\lambda, \nu)}{(3+\nu)(1-\nu)}. \tag{1}$$

Thus the determination of I yields $C(\lambda, \nu)$.

Our analysis is split into three parts. First, for $\lambda \ll 1$, a perturbation expansion in λ is obtained for C. For moderate values of λ, $0 < \lambda < 40$, we must turn to numerical methods. Finally, for $\lambda \gg 1$, an asymptotic solution is given.

Sanders' Energy-Release-Rate Integral

The derivation and nondimensionalization of I for linear shallow shells is contained in [1] and will not be repeated here. For a cylindrical shell of radius R under internal pressure p and containing a crack of length $2c$, the nondimensional governing equations are

$$N_{\alpha\beta,\beta} = 0 \tag{2a}$$

$$M_{\alpha\beta,\alpha\beta} + 4\lambda^2(z_{,\alpha\beta}N_{\alpha\beta} + p) = 0, \tag{2b}$$

$$\tfrac{1}{2}(u_{\alpha,\beta} + u_{\beta,\alpha}) - 4\lambda^2 z_{,\alpha\beta} w = (1+\nu)N_{\alpha\beta} - \nu\delta_{\alpha\beta}N_{\gamma\gamma}, \tag{2c}$$

$$M_{\alpha\beta} = -(1-\nu)w_{,\alpha\beta} - \nu\delta_{\alpha\beta}w_{,\gamma\gamma}, \tag{2d}$$

where

$$z_{,11} = 0, \quad z_{,12} = 0, \quad z_{,22} = 1. \tag{3}$$

Since the governing equations are linear, the analysis of the cracked shell reduces to the analysis of the uncracked shell and the analysis of a shell with a crack subject to stresses that are equal and opposite

Contributed by the Applied Mechanics Division for publication in the JOURNAL OF APPLIED MECHANICS.
Discussion on this paper should be addressed to the Editorial Department, ASME, United Engineering Center, 345 East 47th Street, New York, N. Y. 10017, and will be accepted until December 1, 1980. Readers who need more time to prepare a discussion should request an extension from the Editorial Department. Manuscript received by ASME Applied Mechanics Division, January, 1980; final revision, March, 1980.

to those in the uncracked shell, the so-called residual problem. The nonzero stresses and displacements for the uncracked shell subject to internal pressure are

$$N_{22}^{\circ} = 1, \quad u_1^{\circ} = -\nu, \quad w^{\circ} = -(4\lambda^2)^{-1}. \tag{4}$$

Thus, noting equations (45,) (46), (76)–(81) of [1], we obtain

$$I = 2\pi C^2(\lambda, \nu) = \tfrac{1}{2} \int_{-1}^{1} [2u_2 + \lambda \dot{u}_2](x)dx, \tag{5}$$

where a dot denotes differentiation with respect to λ and the brackets denote the jump across the crack of the enclosed quantity, i.e.,

$$[f](x) = \lim \{f(x, \epsilon) - f(x, -\epsilon)\} \quad \text{as} \quad \epsilon \to 0.$$

The Residual Problem

The residual boundary-value problem is given by equations (2)–(3) with boundary conditions

$$N_{22}(x_1, \pm 0) = -1, \quad |x_1| \leq 1 \tag{6a}$$

$$N_{21}(x_1, \pm 0) = 0, \quad |x_1| \leq 1 \tag{6b}$$

$$w_{,22}(x_1, \pm 0) + \nu w_{,11}(x_1, \pm 0) = 0, \quad |x_1| \leq 1 \tag{6c}$$

$$(2 - \nu)w_{,112}(x_1, \pm 0) + w_{,222}(x_1, \pm 0) = 0, \quad |x_1| \leq 1. \tag{6d}$$

Furthermore all stresses must vanish as $r^2 = x_1^2 + x_2^2 \to \infty$. We have expressed the moment boundary conditions in terms of the midsurface normal displacement w.

Equations (2), (3), and (6) can be reduced to singular integral equations using the results of [3]. Thus we obtain

$$\int\!\!\!\!\!\!-_{-1}^{1} H_{11}(\lambda x - \lambda t)F_1(t;\lambda, \nu)dt + \int_{-1}^{1} H_{12}(\lambda x - \lambda t; \nu)F_2(t; \lambda, \nu)dt = -1, \tag{7}$$

$$\int_{-1}^{1} H_{12}(\lambda x - \lambda t; \nu)F_1(t; \lambda, \nu)dt + \int\!\!\!\!\!\!-_{-1}^{1} H_{22}(\lambda x - \lambda t; \nu)F_2(t; \lambda, \nu)dt = 0, \tag{8}$$

where $|x| < 1$, $\int\!\!\!\!\!\!-$ denotes the Cauchy principle value,

$$F_1 = \int_0^{x_1} [N_{11,2}]dt, \quad F_2 = -[w_{,12}] \tag{9}$$

and the H_{ij} are given by equations (63)–(65) of [1].

As pointed out in [1] the solutions of (5) and (6) have the form

$$F_\alpha(t; \lambda, \nu) = (1 - t^2)^{1/2}G_\alpha(t; \lambda, \nu), \quad |t| < 1, \quad \lambda \geq 0, \quad \alpha = 1, 2, \tag{10}$$

where the G_α are continuous for $t \epsilon [-1, 1]$.

I in Terms of the Unknown F_1

For a cylindrical shell one can show that

$$u_{1,12} = N_{11,2} + \nu N_{12,1}, \tag{11}$$

$$\tfrac{1}{2}(u_{1,2} + u_{2,1}) = (1 + \nu)N_{12}. \tag{12}$$

Evaluating the jump across the crack and using the boundary conditions (6) yields

$$[u_{1,12}] = [N_{11,2}], \tag{13}$$

$$[u_{1,2}] + [u_{2,1}] = 0. \tag{14}$$

Differentiating (14) we obtain

$$[u_{1,21}] + [u_{2,11}] = 0. \tag{15}$$

Thus

$$[u_{2,11}] = -[N_{11,2}]. \tag{16}$$

Integrating (16) with respect to x_1, we obtain

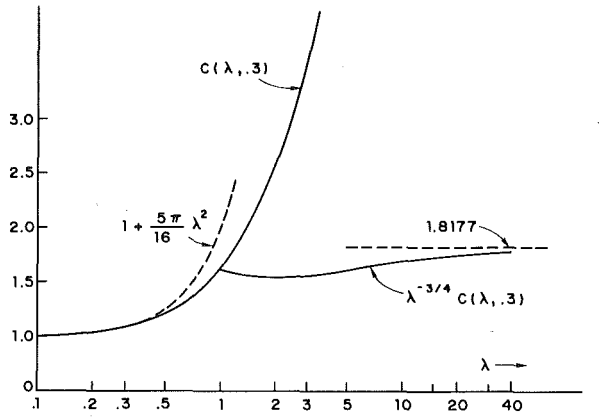

Fig. 1 Combined stress-intensity factor versus λ

$$[u_{2,1}] = -\int_0^{x_1} [N_{11,2}]dt = -F_1(x_1; \lambda, \nu). \tag{17}$$

Hence

$$\int_{-1}^{1} [u_2](t)dt = -\int_{-1}^{1} t[u_{2,1}]dt = \int_{-1}^{1} tF_1(t; \lambda, \nu)dt \tag{18}$$

and (5) becomes

$$I = \frac{1}{2} \int_{-1}^{1} t\{2F_1(t; \lambda, \nu) + \lambda \dot{F}_1(t; \lambda, \nu)\}dt. \tag{19}$$

Approximate Solutions of the Integral Equations

The integral equations (7) and (8) need to be solved to determine I. We obtain approximate solutions for the ranges $\lambda \ll 1, 0 < \lambda < 40$, and $\lambda \gg 1$.

For $\lambda \ll 1$ a perturbation solution may be obtained. Following the same procedure spelled out in detail in [3 or 4], we find that

$$F_1(x; \lambda, \nu) = \frac{4x}{(1 - x^2)^{1/2}} \left[1 + \frac{5\pi}{16}\lambda^2 + \ldots\right]. \tag{20}$$

Hence

$$C(\lambda, \nu) = 1 + \frac{5\pi}{16}\lambda^2 + \ldots. \tag{21}$$

For $\lambda = 0(1)$ we have obtained numerical solutions for (7) and (8) by noting (10) and using the Lobatto-Chebyshev integration method of Theocaris and Ioakimidis [5]. The results for λ up to 40 (a significant improvement in the range of λ over Copley and Sanders' numerical solutions [6]) are shown in Fig. 1. There $\nu = 0.3$.

For $\lambda \gg 1$ Bradley has obtained an asymptotic solution to (7) and (8). The details may be found in [4]. The method used there is due to Latta and was also used in the analysis of a bent cylindrical shell [7]. From [4]

$$F_1(x; \lambda, \nu) \sim B\lambda^{3/2}(1 - x^2)^{1/4}[4x \cos \theta(x) - 2D \sin \theta(x)] \quad \text{as} \quad \lambda \to \infty, \tag{22}$$

where

$$B = \frac{8\sqrt{2}(1 + \sqrt{2})}{3\sqrt{\pi}},$$

$$D = \frac{4}{\pi} \ln \left[\frac{1 + \sqrt{1 + \sqrt{2}}}{2^{1/4}}\right],$$

$$\theta(x) = \frac{1}{\pi} \ln \left[\frac{1 + \sqrt{1 + \sqrt{2}}}{2^{1/4}}\right] \ln \left[\frac{1 - x}{1 + x}\right].$$

To obtain the asymptotic form of I as $\lambda \to \infty$ we replace F_1 in (19) by the right-hand side of (22) and integrate. We find

$$I \sim 20.7590\lambda^{3/2}. \tag{23}$$

Thus, from (1),

$$C(\lambda, \nu) \sim 1.8177\, \lambda^{3/4} \quad \text{as} \quad \lambda \to \infty. \tag{24}$$

Fig. 1 is a graph of $C(\lambda, 0.3)$ and $\lambda^{-3/4}C(\lambda, 0.3)$ as determined from a numerical solution of the exact integral equations (7) and (8) and as determined from the small and large λ asymptotic solutions (21) and (24).

Conclusion

We have used Sanders' path-independent energy-release rate integral, as derived for a cracked shallow shell by Nicholson and Simmonds [1], to compute the asymptotic behavior of a combined stress-intensity factor for a pressurized cylindrical shell containing a longitudinal crack. This result along with that of [1] extends (and completes) the work of Copley and Sanders[6].

Acknowledgment

We wish to thank Prof. J. G. Simmonds for his help during the completion of this project.

References

1 Nicholson, J. W., and Simmonds, J. G., "Sanders' Energy-Release-Rate Integral for Arbitrarily Loaded Shallow Shells and Its Asymptotic Evaluation for a Cracked Cylinder," ASME JOURNAL OF APPLIED MECHANICS, Vol. 47, June 1980, pp. 363–369.

2 Sanders, J. L., Jr., "On the Griffith-Irwin Fracture Theory," ASME JOURNAL OF APPLIED MECHANICS, Vol. 27, 1960, pp. 352–353.

3 Simmonds, J. G., Bradley, M. R., and Nicholson, J. W., "Stress-Intensity Factors for Arbitrarily Oriented Cracks in Shallow Shells," ASME JOURNAL OF APPLIED MECHANICS, Vol. 45, 1978, pp. 135–141.

4 Bradley, M. R., "Cracks in Shells," PhD Dissertation, University of Virginia, Charlottesville, Va., 1977.

5 Theocaris, P. S., and Ioakimidis, N. I., "Numerical Integration Methods for the Solution of Singular Integral Equations," *Quarterly Journal of Applied Mathematics,* Vol. 35, 1977, pp. 173–183.

6 Copley, L. G., and Sanders, J. L., Jr., "A Longitudinal Crack in a Cylindrical Shell Under Internal Pressure," *International Journal of Fracture Mechanics,* Vol. 5, 1969, pp. 117–131.

7 Nicholson, J. W., "Asymptotic Evaluation of Stress-Intensity Factors in Cracked Shells Via a Path-Independent Integral," PhD Dissertation, University of Virginia, Charlottesville, Va., 1979.

E. Reissner

Department of Applied Mechanics and Engineering Sciences, University of California, San Diego, La Jolla, Calif. 92093
Fellow ASME

On the Influence of a Rigid Circular Inclusion on the Twisting and Shearing of a Shallow Spherical Shell[1]

Known results for plates with rigid inclusions are complemented by explicit asymptotic solutions of the corresponding problems for sufficiently thin spherical shells. An important element of the analysis is recognition of the fact that in addition to the distinction between interior and edge zone solution contributions there is a significant distinction between near-field and far-field behavior of the interior solution, with the nature of this distinction depending on the nature of the boundary conditions which are prescribed. In the event that near-field behavior is of the membrane type and far-field behavior of the inextensional bending type, or vice versa, much higher stress concentrations occur than without such change in interior solution behavior.

Introduction

In what follows we complement a recent analysis of the effect of a small circular hole in a shallow spherical shell on the states of stress which without the hole would be states of uniform transverse twisting [3] or of uniform membrane shear [4], by a consideration of the related problems which are given upon assuming a rigid inclusion in place of the circular hole. We find, as before, that the solution of the problems as stated depends on the value of Possion's ratio and on the value of the dimensionless parameter a^2/Rh, where a is the radius of the inclusion, R the radius of the shell, and h the wall thickness of the shell. When $a^2/Rh = 0$ the results for the two problems are well-known classical results of the theory of elastic plates. While our formulation shows the possibility of an explicit closed-form solution for all values of a^2/Rh, as previously observed for the problem of the circular hole, we are limiting ourselves here to determine the solution for values of a^2/Rh which are large enough to permit the application of an asymptotic procedure. The essence of this procedure, for a class of thin-shell problems which include the present two problems, consists of the successive determination of interior and edge zone solution contributions [1, 2].

Our earlier work for the problem of the shell with circular hole led to results which it was easy to consider as reasonable for the problem of transverse twisting, but which seemed somewhat paradoxical for the problem of the effect of the hole on the state of uniform membrane shear. It is one of the remarkable conclusions of the present analysis that an exactly opposite state of affairs prevails for the case of the shell with rigid circular inclusion. To wit, we now obtain a "reasonable" result for the membrane shear problem and a "paradoxical" result for the transverse twisting problem.

A rationalization of the occurrence of paradoxical results as indicated, which emerged in the course of the present analysis, is as follows. Our reasonable results are associated with interior solution contributions which are of the inextensional-bending type or of the membrane-theory type *throughout* the "interior" domain. Our paradoxical results are associated with interior solution contributions which change character, from inextensional-bending behavior in a far-field domain, to membrane-theory behavior in a near-field domain, or vice versa, because of a conflict between the effects of the boundary conditions at infinity and the effects of the boundary conditions at the edge of the circular hole or inclusion.

Differential Equations and Boundary Conditions

The middle surface equation of the shallow spherical shell, with reference to base plane polar coordinates r and θ, is given by $z = H - r^2/2R$. The basic differential equations, for a uniform isotropic shell, are of the form

$$RB\nabla^2\nabla^2K - \nabla^2w = 0, \quad RD\nabla^2\nabla^2w + \nabla^2K = 0. \tag{1}$$

In this, $\nabla^2 = (\ )_{,rr} + r^{-1}(\ )_{,r} + r^{-2}(\ )_{,\theta\theta}$, D and $1/B$ are bending and stretching stiffness factors, and w and K are transverse displacement and Airy's stress function, respectively.

In what follows, use is made of the relations

$$N_{rr} = r^{-1}K_{,r} + r^{-2}K_{,\theta\theta}, \quad N_{\theta\theta} = K_{,rr}, \tag{2}$$

[1] Supported by the Office of Naval Research.

Contributed by the Applied Mechanics Division for presentation at the Winter Annual Meeting, Chicago, Ill., November 16–21, 1980, of THE AMERICAN SOCIETY OF MECHANICAL ENGINEERS.

Discussion on this paper should be addressed to the Editorial Department, ASME, United Engineering Center, 345 East 47th Street, New York, N. Y. 10017, and will be accepted until December 1, 1980. Readers who need more time to prepare a discussion should request an extension from the Editorial Department. Manuscript received by ASME Applied Mechanics Division, August, 1979; final revision, March, 1980. Paper No. 80-WA/APM-5.

and

$$M_{rr} = -D[w_{,rr} + \nu(r^{-1}w_{,r} + r^{-2}w_{,\theta\theta})],$$
$$M_{\theta\theta} = -D[r^{-1}w_{,r} + r^{-2}w_{,\theta\theta} + \nu w_{,rr}], \tag{3}$$

for normal stress resultants and couples, and of the fact that the solutions of (1) may be written in the form

$$w = \phi + \chi, \quad K = \psi - RD\nabla^2\chi, \tag{4}$$

where ϕ and ψ are harmonic functions and χ is subject to the equation $\nabla^4\chi + \lambda^4\chi = 0$ with $\lambda^4 = 1/R^2BD$.

We furthermore need to make use of expressions for tangential displacement components u_r and u_θ which have earlier been shown [2] to be expressible, except for terms which do not arise for the problems considered in what follows, in the form

$$u_r = -(1+\nu)BK_{,r} - R^{-1}\int \phi dr,$$
$$u_\theta = -(1+\nu)Br^{-1}K_{,\theta} + rR^{-1}\int(\int \phi_{,\theta}dr)r^{-2}dr, \tag{5}$$

It is important to observe that equations (5) are derived subject to the restriction $R < \infty$ and that the transition to the corresponding expressions for the limiting case $R = \infty$ is of a subtle nature.

The boundary conditions at infinity are for the problem of *transverse twisting* due to concentrated corner forces $\pm P$

$$r \to \infty; \qquad w \to \frac{Pr^2 \sin 2\theta}{4(1-\nu)\mathrm{D}}, \qquad K \to 0, \tag{6}$$

and for the problem of *membrane shear*

$$r \to \infty; \qquad w \to 0, \qquad K \to -\tfrac{1}{2}Sr^2 \sin 2\theta. \tag{7}$$

The boundary conditions corresponding to a rigid insert of radius a are the four conditions

$$r = a; \qquad w = w_{,r} = u_r = u_\theta = 0. \tag{8}$$

Closed-Form Solutions

We have, as for the corresponding two problems of the shell with a circular hole, as expressions for w and K,

$$\phi = -\frac{Pa^2 \sin 2\theta}{2(1-\nu)D}\left(\frac{1}{2}\frac{r^2}{a^2} + c_1\frac{a^2}{r^2}\right), \quad \psi = \frac{Pa^2 \sin 2\theta}{2(1-\nu)\sqrt{DB}}c_2\frac{a^2}{r^2}, \tag{9}$$

for transverse twisting, and

$$\phi = Sa^2\sqrt{\frac{B}{D}}c_1\frac{a^2}{r^2}\sin 2\theta, \ \psi = -Sa^2\left(\frac{1}{2}\frac{r^2}{a^2} + c_2\frac{a^2}{r^2}\right)\sin 2\theta, \tag{10}$$

for the problem of membrane shear, with the function χ for these two cases being of the form

$$\chi = -\frac{Pa^2 \sin 2\theta}{2(1-\nu)D}(c_3 \ker_2 \lambda r + c_4 \mathrm{kei}_2 \lambda r) \tag{11}$$

and

$$\chi = Sa^2\sqrt{\frac{B}{D}}(c_3 \ker_2 \lambda r + c_4 \mathrm{kei}_2 \lambda r)\sin 2\theta, \tag{12}$$

respectively.

Equations (9)–(12) are such that the boundary conditions at infinity are automatically satisfied, with the four remaining conditions for $r = a$ serving to determine the values of the four constants of integration c_n.

Associated with these solutions we have as reference values for stress couples and stress resultants

$$M_{rr}(\infty, \tfrac{1}{4}\pi) = \tfrac{1}{2}P, \qquad N_{rr}(\infty, \tfrac{1}{4}\pi) = S, \tag{13}$$

and we are interested, in particular, in the values of stress-concentration factors which are, for the problem of the rigid insert

$$k_b = \frac{M_{rr}(a, \frac{1}{4}\pi)}{\frac{1}{2}P}, \qquad k_m = \frac{hN_{rr}(a, \frac{1}{4}\pi)}{3P}, \tag{14}$$

and

$$k_m = \frac{N_{rr}(a, \frac{1}{4}\pi)}{S}, \qquad k_b = \frac{6M_{rr}(a, \frac{1}{4}\pi)}{hS}, \tag{15}$$

respectively. For the present problems, just as for the corresponding problems of the shell with a circular hole, these stress-concentration factors depend on Poisson's ratio and on a shell parameter $\mu = \lambda a$ which, for the case of a homogeneous shell, with $D = Eh^3/12(1-\nu^2)$ and $B = 1/Eh$, is of the form $\mu = \sqrt{12(1-\nu^2)}\, a/\sqrt{Rh}$.

Known classical results for the values of k_m and k_b concern the case $\mu = 0$ of a flat plate. The results for $\mu = 0$ are

$$k_b = 2(1-\nu)^{-1}, \qquad k_m = 0, \tag{16}$$

for the problem of transverse (plate) twisting, and

$$k_m = 8(3-\nu)^{-1}, \qquad k_b = 0 \tag{17}$$

for the problem of membrane (plane stress) shearing.

In what follows we complement these results for $\mu = 0$ by asymptotic results, which apply when the parameter μ is sufficiently large compared to unity, say larger than about ten, with the determination of results in the intermediate range depending on the evaluation of the exact solution, in accordance with equations (8)–(12).

Asymptotic Solution

The boundary conditions (8) are now written in the form

$$\phi + \chi = 0, \qquad \phi_{,r} + \chi_{,r} = 0, \tag{18}$$

$$-(1+\nu)BR\psi_{,r} - \lambda^{-4}(\nabla^2\chi)_{,r} + \int \phi dr = 0, \tag{19}$$

$$-(1+\nu)BRr^{-1}\psi_{,\theta} - \lambda^{-4}r^{-1}(\nabla^2\chi)_{,\theta} + r\int(\int \phi_{,\theta}dr)r^{-2}dr = 0, \tag{20}$$

for $r = a$.

In order to derive an asymptotic solution for sufficiently large values of $\mu = \lambda a$ we take account of the order-of-magnitude relations

$$\phi_{,r} = O(a^{-1}\phi), \qquad \int \phi dr = O(a\phi), \qquad \chi_{,r} = O(\lambda\chi), \tag{21}$$

and we consider that the first of the two relations in (18) implies that, necessarily,

$$\chi = O(\phi). \tag{22}$$

A use of (21) and (22) in (19) and (20) indicates that the terms with χ in these equations are of relative order μ^{-1} and μ^{-2}, respectively, compared to the terms with ϕ. Accordingly, we may, for sufficiently large values of μ, omit these terms and have then that the interior solution contributions ϕ and ψ may be determined from the *abbreviated* tangential displacement boundary conditions

$$(1+\nu)B\psi_{,r} - \frac{\int \phi dr}{R} = 0, \ (1+\nu)B\frac{\psi_{,\theta}}{r} - \frac{r}{R}\int\frac{\int \phi_{,\theta}dr}{r^2}dr = 0, \tag{23}$$

for $r = a$.

Having ϕ we *subsequently* determine χ by means of two boundary conditions which follow from the transverse displacement conditions (18), upon consideration of (22) and (21), in the form

$$\chi = -\phi, \qquad \chi_{,r} = 0, \tag{24}$$

for $r = a$.

Having ϕ, ψ, and χ we find stress resultants and couples from (2) and (3), in conjunction with (4) in the asymptotic form

$$N_{rr} = \frac{\psi_{,r}}{r} + \frac{\psi_{,\theta\theta}}{r} - RD\frac{(\nabla^2\chi)_{,r}}{r}, \quad N_{\theta\theta} = \psi_{,rr} - RD(\nabla^2\chi)_{,rr}, \tag{25}$$

$$M_{rr} = -D\left[\phi_{,rr} + \nu\frac{\phi_{,r}}{r} + \nu\frac{\phi_{,\theta\theta}}{r} + \chi_{,rr}\right],$$
$$M_{\theta\theta} = -D\left[\frac{\phi_{,r}}{r} + \frac{\phi_{,\theta\theta}}{r} + \nu\phi_{,rr} + \nu\chi_{,rr}\right]. \tag{26}$$

In this it is consistent to use as expression for χ,

$$\chi = k\exp\left(-\lambda\frac{r-a}{\sqrt{2}}\right)\left(c_3\cos\lambda\frac{r-a}{\sqrt{2}} + c_4\sin\lambda\frac{r-a}{\sqrt{2}}\right)\sin 2\theta. \tag{27}$$

where $k = -Pa^2/2(1-\nu)D$ for the problem of twisting, and $k = Sa^2\sqrt{B/D}$ for the problem of shearing.

Results for the Problem of Transverse Twisting

An introduction of ϕ and ψ as given in (9) into the interior solution boundary conditions (23) reduces these to the form

$$2\frac{1+\nu}{\mu^2}c_2+\frac{1}{6}-c_1=0, \qquad 2\frac{1+\nu}{\mu^2}+\frac{1}{6}+c_1=0, \tag{28}$$

so that

$$c_1=0, \qquad c_2=-\frac{1}{12}\frac{\mu^2}{1+\nu}. \tag{29}$$

Therewith, the two edge zone solution boundary conditions (24) give

$$c_3=c_4=\tfrac{1}{2} \tag{30}$$

and then

$$\phi=-\frac{Pa^2\sin 2\theta}{4(1-\nu)D}\frac{r^2}{a^2}, \qquad \psi=-\frac{Pa^2\mu^2\sin 2\theta}{24(1-\nu^2)\sqrt{DB}}\frac{a^2}{r^2}, \tag{31}$$

$$\chi=-\frac{Pa^2\sin 2\theta}{4(1-\nu)D}\exp\left(-\lambda\frac{r-a}{\sqrt{2}}\right)\left(\cos\lambda\frac{r-a}{\sqrt{2}}+\sin\lambda\frac{r-a}{\sqrt{2}}\right). \tag{32}$$

With (31) we obtain from equations (25) and (26) for the distribution of stress outside the edge zone, that is in the interior domain

$$M_{rr}{}^i=-M_{\theta\theta}{}^i=\tfrac{1}{2}P\sin 2\theta, \tag{33}$$

$$N_{rr}{}^i=-N_{\theta\theta}{}^i=\frac{P\mu^2\sin 2\theta}{4(1-\nu^2)\sqrt{DB}}\frac{a^4}{r^4}. \tag{34}$$

Inside the edge zone these expressions are complemented by the contribution of the χ-function, as given by (32). We limit ourselves here to the calculation of the edge values of resultants and couples at the most highly stressed location, that is for $r=a$ and $\theta=\pi/4$.

We find from (25) that except for terms of relative order $1/\mu$,

$$N_{rr}(a,\tfrac{1}{4}\pi)=N_{rr}{}^i(a,\tfrac{1}{4}\pi), \tag{35}$$

$$N_{\theta\theta}(a,\tfrac{1}{4}\pi)=\nu N_{rr}{}^i(a,\tfrac{1}{4}\pi). \tag{36}$$

Equation (26) gives for the edge values of M_{rr} and $M_{\theta\theta}$, except for terms of relative order $1/\mu^2$,

$$M_{rr}\left(a,\frac{\pi}{4}\right)=\frac{P}{4}\frac{\mu^2}{1+\nu}, \qquad M_{\theta\theta}\left(a,\frac{\pi}{4}\right)=\nu\frac{P}{4}\frac{\mu^2}{1+\nu}. \tag{37}$$

We conclude from equations (33) and (34) that it is appropriate to distinguish two subdomains of the interior domain, which may be designated as the "far field" and the "near field." The far-field solution, which is valid when $\mu \ll r^2/a^2$, is an inextensional bending solution, while the near-field solution, which holds when $r^2/a^2 \ll \mu$, is a membrane solution, with the bending stresses in this near-field being small of relative order $1/\mu$ compared with the membrane stresses.

Next, equations (35)–(37) indicate that in the edge zone membrane stresses and bending stresses are of one and the same order or magnitude, with the membrane stresses retaining their order of magnitude in the passage across the edge zone and with the bending stresses decaying from their value for $r=a$ to practically zero in the course of this passage.

Equations (35) and (37), in conjunction with (14), give as asymptotic expressions for stress-concentration factors

$$k_b=\frac{1}{2}\frac{\mu^2}{1+\nu}, \qquad k_m=\frac{\mu^2}{\sqrt{12(1-\nu^2)}}. \tag{38}$$

Equation (38) indicates the remarkable fact that for large values of μ the concentration of stress due to the rigid inset in the transversely twisted shell comes out to be much larger than the corresponding concentration for the analogous problem of the flat plate.

Results for the Problem of Tangential Shearing

We introduce ϕ and ψ as given in (10) into the boundary conditions (23) so as to obtain the relations

$$(1+\nu)(1-2c_2)+c_1\mu^2=0, \quad (1+\nu)(1+2c_2)+c_1\mu^2=0. \tag{39}$$

It follows from this that now

$$c_1=-(1+\nu)\mu^2, \qquad c_2=0. \tag{40}$$

The two boundary conditions (24) for χ then give for the constants c_3 and c_4 in equation (27)

$$c_3=c_4=(1+\nu)\mu^{-2}, \tag{41}$$

and therewith, altogether,

$$\phi=-Sa^2\sqrt{\frac{B}{D}}\frac{1+\nu}{\mu^2}\frac{a^2}{r^2}\sin 2\theta, \qquad \psi=-\frac{1}{2}Sa^2\frac{r^2}{a^2}\sin 2\theta, \tag{42}$$

$$\chi=Sa^2\sqrt{\frac{B}{D}}\frac{1+\nu}{\mu^2}\exp\left(-\frac{r-a}{\sqrt{2}}\right)\left(\cos\lambda\frac{r-a}{\sqrt{2}}+\sin\lambda\frac{r-a}{\sqrt{2}}\right)\sin 2\theta. \tag{43}$$

We now find from equations (42), (25), and (26) as expressions for interior resultant and couple distributions

$$N_{rr}{}^i=-N_{\theta\theta}{}^i=S\sin 2\theta, \tag{44}$$

$$M_{rr}{}^i=-M_{\theta\theta}{}^i=6S\sqrt{BD}\frac{1-\nu^2}{\mu^2}\frac{a^4}{r^4}. \tag{45}$$

Again, these expressions are complemented inside the edge zone by a χ-contribution which is now given by (43). We limit ourselves again to a determination of resultants and couples for $r=a$ and $\theta=\pi/4$ and find now, except for terms which are small of higher order in μ,

$$N_{rr}(a,\tfrac{1}{4}\pi)=N_{rr}{}^i(a,\tfrac{1}{4}\pi) \tag{46}$$

$$N_{\theta\theta(a,\frac{1}{4}\pi)}=\nu N_{rr}{}^i(a,\tfrac{1}{4}\pi) \tag{47}$$

$$M_{rr}(a,\tfrac{1}{4}\pi)=(1+\nu)S\sqrt{BD} \tag{48}$$

$$M_{\theta\theta}(a,\tfrac{1}{4}\pi)=\nu(1+\nu)S\sqrt{BD} \tag{49}$$

It may be concluded from (44) and (45) that now there is no distinction between near-field and far-field behavior in the interior domain, with the entire interior solution contribution representing a membrane state, effectively.

As concerns the edge zone state, membrane and bending stresses again come out to be of one and the same order of magnitude. Membrane stresses retain their order of magnitude in the passage across the edge zone and bending stresses decay from their edge value to practically zero.

Equations (46) and (48), in conjunction with (15), give as asymptotic expressions for stress-concentration factors

$$k_m=1, \qquad k_b=\sqrt{\frac{3+3\nu}{1-\nu}}, \tag{50}$$

with k_m and k_b now both being of the same order of magnitude as the value of k_m for the corresponding problem of the flat plate.

References

1 Reissner, E., "A Note on Membrane and Bending Stresses in Spherical Shells," *Journal of the Society of Industrial and Applied Mathematics*, Vol. 4, 1956, pp. 230–240.

2 Reissner, E., "On the Determination of Stresses and Displacements for Unsymmetrical Deformations of Shallow Spherical Shells," *Journal of Mathematics and Physics*, Vol. 38, 1959, pp. 16–35.

3 Reissner, E., "On the Transverse Twisting of Shallow Spherical Ring Caps," ASME JOURNAL OF APPLIED MECHANICS, Vol. 47, 1980, pp. 101–105.

4 Reissner, E., "On the Effect of a Small Circular Hole on States of Uniform Membrane Shear in Spherical Shells," ASME JOURNAL OF APPLIED MECHANICS, Vol. 47, 1980, pp. 430–431.

S. D. Hassan
Professor of Aeronautical Engineering,
College of Engineering,
Cairo University,
Egypt

S. S. El-Ghabaty
Associate Professor,
Department of Mathematics,
University of Riyadh,
Riyadh, Saudi Arabia

Perturbation Analysis of Buckling of Circular Rings Under Nonuniform Normal Pressures

Perturbation solutions are found for buckling of thin elastic circular rings under nonuniform pressures. The solution leads to the same results obtained before by numerical methods. Two cases of pressure distribution of the form $p = p_0(1 + \epsilon \cos 2m\theta)$ *and* $p = p_0[1 + \epsilon(\cos 2\theta + \nu \cos 4\theta)]$ *are considered. The analysis yields equations to determine the ring curvature at any angle and pressure.*

Introduction

A problem of interest, as well as of practical application, is the nonlinear behavior of an elastic circular ring under nonuniform pressure. The loads are taken to be doubly symmetric and always remain normal to the ring. The applied pressure is assumed to be of the form

$$p = p_0[1 + \epsilon f(\theta)], \tag{1}$$

where ϵ is a nonuniformity parameter, and $f(\theta)$ is periodic and doubly symmetric. The ring is considered to be an inextensible elastica of constant stiffness EI, for which the curvature change is proportional to the applied bending moment. The governing equations for this problem are given by [1]

$$\frac{d^2U}{d\theta^2} + \frac{1}{2}U^3 + CU = \bar{p} \tag{2}$$

and

$$C = \bar{p}_0 - \frac{1}{4\pi}\int_0^{2\pi} U^3 d\theta, \tag{3}$$

where $U = R/\rho$ is the ratio of the ring radius R before deformation and the radius of curvature ρ at the same arc length after deformation, $\bar{p} = pR^3/EI$ is the nondimensional pressure parameter, and $\bar{p}_0$ is the average pressure parameter for the ring circumference.

Seide and Jamjoom [1] carried out a numerical investigation of this nonlinear integro-differential equation for the particular case where $f(\theta) = \cos 2\theta$. Their numerical results are given by a set of curves which show the curvature ratio U at $\theta = 0$ and $\theta = \pi/2$ versus $\bar{p}_0$ for various cases of the parameter ϵ. They obtained also the deflected ring shapes when $\epsilon = 0.0001$ and $\epsilon = 1.0$ for different values of the applied pressure $\bar{p}_0$.

In the present paper, a perturbation analysis of this problem is worked out. An asymptotic solution is obtained for the buckling shape as function of $\bar{p}_0$ and ϵ. The perturbation method used here reproduces exactly the same results as the numerical solution given by Seide and Jamjoom [1]. The analysis and results will be presented for two cases of the nonuniformity distribution function $f(\theta)$. In one case we take $f(\theta) = \cos 2m\theta$, and the other $f(\theta) = \cos 2\theta + \nu \cos 4\theta$.

Analysis When $f(\theta) = \cos 2m\theta$

To seek a perturbation solution for equations (2) and (3), we assume the following expansions:

$$U = 1 + \eta v_1 + \eta^2 v_2 + \eta^3 v_3 + \ldots \tag{4}$$

$$\epsilon\bar{p}_0 = \eta A_1 + \eta^2 A_2 + \eta^3 A_3 + \ldots \tag{5}$$

where the A's are constants and the v's are functions of θ which are periodic and doubly symmetric. Inserting these expansions (4) and (5) into equations (2) and (3) and equating different powers of η to zero, one gets

$$v_1'' + (\bar{p}_0 + 1)v_1 = A_1 \cos 2m\theta \tag{6}$$

$$v_2'' + (\bar{p}_0 + 1)v_2 = \frac{3}{2}(\alpha - v_1^2) + A_2 \cos 2m\theta \tag{7}$$

$$v_3'' + (\bar{p}_0 + 1)v_3 = \frac{1}{2}\beta + 3\gamma + \frac{3}{2}\alpha v_1 - \frac{1}{2}v_1^3 - 3v_1v_2 + A_3 \cos 2m\theta \tag{8}$$

where

$$\alpha = \frac{1}{2\pi}\int_0^{2\pi} v_1^2 d\theta, \quad \beta = \frac{1}{2\pi}\int_0^{2\pi} v_1^3 d\theta, \quad \gamma = \frac{1}{2\pi}\int_0^{2\pi} v_1 v_2 d\theta \tag{9}$$

Equation (6) gives

$$A_1 = -4m^2 + \bar{p}_0 + 1 \tag{10}$$

Contributed by the Applied Mechanics Division for publication in the JOURNAL OF APPLIED MECHANICS.
Discussion on this paper should be addressed to the Editorial Department, ASME, United Engineering Center, 345 East 47th Street, New York, N.Y. 10017, and will be accepted until December 1, 1980. Readers who need more time to prepare a discussion should request an extension from the Editorial Department. Manuscript received by ASME Applied Mechanics Division, April, 1979; final revision, January, 1980.

$$v_1 = \cos 2m\theta \tag{11}$$

In equation (7), we require v_2 to be orthogonal to v_1, hence we must set

$$A_2 = 0, \tag{12}$$

and v_2 will thus be

$$v_2 = \frac{3\cos 4m\theta}{4(16m^2 - \bar{p}_0 - 1)} \tag{13}$$

From equation (8), the orthogonality condition of v_3 to v_1 and v_2 then leads to

$$A_3 = -\frac{3(16m^2 - \bar{p}_0 - 4)}{8(16m^2 - \bar{p}_0 - 1)} \tag{14}$$

Here, it should be mentioned that further calculations indicate that there is no need to find v_3. To account for the nonlinear term in equation (2), $\epsilon\bar{p}_0$ is calculated up to third order in η and U is determined up to second order. Hence the solution is given by

$$\epsilon\bar{p}_0 = (-4m^2 + \bar{p}_0 + 1)\eta - \frac{3(16m^2 - \bar{p}_0 - 4)}{8(16m^2 - \bar{p}_0 - 1)}\eta^3 \tag{15}$$

$$U = 1 + \eta\cos 2m\theta + \eta^2\frac{3\cos 4m\theta}{4(16m^2 - \bar{p}_0 - 1)} \tag{16}$$

From these equations, one can find U at any angle θ by setting first a value for $\bar{p}_0$ then solving the cubic equation (15) for η. For the special case treated by Seide and Jamjoom [1], one has $m = 1$; and our results from equations (15) and (16) are

$$\epsilon\bar{p}_0 = (\bar{p}_0 - 3)\eta - \frac{3(12 - \bar{p}_0)}{8(15 - \bar{p}_0)}\eta^3 \tag{17}$$

$$U = 1 + \eta\cos 2\theta + \eta^2\frac{3\cos 4\theta}{4(15 - \bar{p}_0)} \tag{18}$$

Here, it is worth mentioning that equations (17) and (18) reproduce exactly the curves given by Seide and Jamjoom [1] for U against $\bar{p}_0$. For later discussion and comparison, we consider also the special case with $m = 2$, the results are

$$\epsilon\bar{p}_0 = (\bar{p}_0 - 15)\eta - \frac{3(60 - \bar{p}_0)}{8(63 - \bar{p}_0)}\eta^3 \tag{19}$$

$$U = 1 + \eta\cos 4\theta + \eta^2\frac{3\cos 8\theta}{4(63 - \bar{p}_0)} \tag{20}$$

Analysis When $f(\theta) = \cos 2\theta + \nu\cos 4\theta$

The analysis of the present case is quite similar to the preceding one. In equations (6)–(8), $\cos 2m\theta$ is now replaced by $\cos 2\theta + \nu\cos 4\theta$ and this leads to the following results:

$$A_1 = x, \quad A_2 = \frac{3\nu x}{2y}, \quad A_3 = -\frac{3}{8}\left[1 + \frac{3}{y}\left(1 + \frac{64\nu^2 x}{yz}\right)\right] \tag{21}$$

$$v_1 = \cos 2\theta + \frac{\nu x}{y}\cos 4\theta \tag{22}$$

$$v_2 = -\frac{3}{4y}\left[\left(1 - \frac{2\nu^2 x}{y}\right)\cos 4\theta + \frac{2\nu x}{z}\cos 6\theta + \frac{\nu^2 x^2}{yt}\cos 8\theta\right] \tag{23}$$

where

$$x = \bar{p}_0 - 3, \quad y = \bar{p}_0 - 15, \quad z = \bar{p}_0 - 35, \quad t = \bar{p}_0 - 63 \tag{24}$$

The solution is therefore given by

$$\epsilon\bar{p}_0 = x\eta + \frac{3\nu x}{2y}\eta^2 - \frac{3}{8}\left[1 + \frac{3}{y}\left(1 + \frac{64\nu^2 x}{yz}\right)\right]\eta^3 \tag{25}$$

$$U = 1 + \eta v_1 + \eta^2 v_2 \tag{26}$$

Results and Discussion

The main results of this paper are equations (15) and (16) for $f(\theta) = \cos 2m\theta$ and equations (25) and (26) for $f(\theta) = \cos 2\theta + \nu\cos 4\theta$. We consider first the particular case when $f(\theta) = \cos 2\theta$ which was solved numerically be Seide and Jamjoom [1]. From equations (17) and (18), we have plotted U at $\theta = 0$ versus $\bar{p}_0$ in Fig. 1 for different values of ϵ. By comparing this figure and Fig. 4(*b*) in reference [1], one finds that corresponding curves are identical even when $\epsilon = 1$. This is encouraging in favor of the perturbation method used here to deal with the type of problems as the present one. From Fig. 1, it is clear that uniform loading ($\epsilon = 0$) on the ring causes no deformation until $\bar{p}_0$ reaches the value $\bar{p}_0 = 3$. On the other hand when $\epsilon > 0$, the ring deformation starts from the moment the load is applied and increases rapidly when $\bar{p}_0$ is in the vicinity of the value $\bar{p}_0 = 3$.

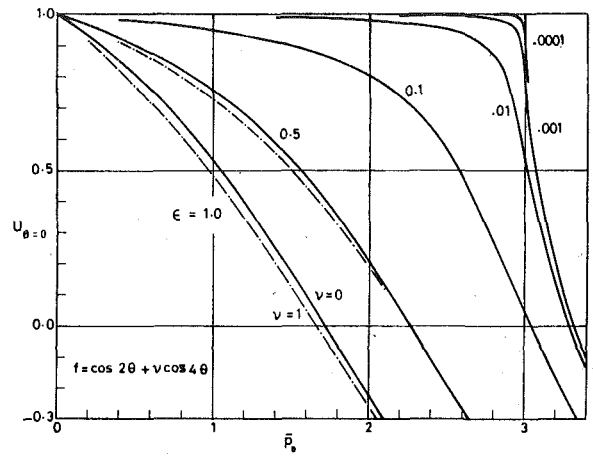

Fig. 1 Variation of ring curvature with applied pressure

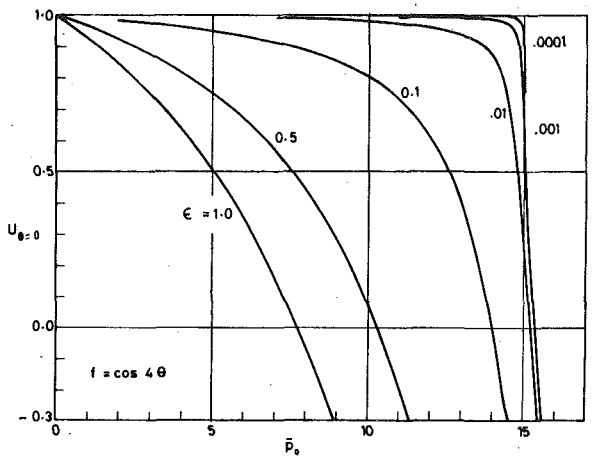

Fig. 2 Variation of ring curvature with applied pressure

Now we consider another particular case when $f(\theta) = \cos 4\theta$. From equations (19) and (20), we plotted the curves of U versus $\bar{p}_0$ in Fig. 2, and it is interesting to notice that these curves behave almost the same way as in the previous case with $f(\theta) = \cos 2\theta$. But, we should remark that uniform loading in this case causes no deformation until $\bar{p}_0$ reaches the value $\bar{p}_0 = 15$.

Finally, when $f(\theta) = \cos 2\theta + \nu\cos 4\theta$, curves of U versus $\bar{p}_0$ can be plotted from equations (25) and (26). One may expect to find these curves somewhere between those in Figs. 1 and 2 of the foregoing two cases. The results however show that the term $\nu\cos 4\theta$ does not affect much the situation have we had $\nu = 0$. In Fig. 1, we plotted dashed curves of $\nu = 1$ and solid ones for $\nu = 0$. We notice that curves for $f(\theta) = \cos 2\theta + \cos 4\theta$ are slightly away from those for $f(\theta) = \cos 2\theta$ and only when ϵ is not very small.

Reference

1 Seide, P., and Jamjoom, T. M. M., "Large Deformations of Circular Rings Under Nonuniform Normal Pressures," ASME JOURNAL OF APPLIED MECHANICS, Vol. 41, 1974, pp. 192–196.

J. Tani

Assistant Professor,
Institute of High Speed Mechanics,
Tohoku University,
Sendai, Japan
Mem. ASME

Elastic Instability of an Annular Plate Under Uniform Compression and Lateral Pressure

The elastic instability of a thin clamped annular plate which has suffered a finite axisymmetric deformation due to simultaneous loading of uniform compression and lateral pressure is studied by examining the asymmetric small free vibration in the neighborhood of the nonlinear axisymmetric equilibrium state. The problem is solved by applying a finite-difference method to the dynamic version of the nonlinear von Karman plate theory. The numerical results indicate that there are the ranges of the magnitude of combined loads under which the axisymmetric deformation of the plate becomes unstable.

Introduction

The nonlinear axisymmetric bending and postbuckling of thin circular plates have been studied by numerous researchers [1–7]. In addition, the secondary buckling or wrinkling, i.e., the branching of asymmetric equilibrium states from nonlinear axisymmetric ones of the circular plate has been investigated by Morozov [8], Yanowitch [9], and Cheo and Reiss [10, 11]. On the other hand, the axisymmetric postbuckling behavior of thin annular plates has been studied by Pal [7], Huang [12, 13], and Uthgenannt and Brand [14]. The present author referred to the secondary buckling of the heated annular plate [15].

In the present paper, the elastic instability of thin clamped annular plates subjected to simultaneous loading of uniform compression and lateral pressure is studied theoretically. The dynamic version of the nonlinear von Karman plate theory is employed. Equations describing the asymmetric small free vibration of the plate which has suffered a finite axisymmetric deformation are solved by means of a finite-difference method. By examining a continuous variation of the asymmetric frequency as a function of the load parameters, one may detect the unstable axisymmetric equilibrium state. The ranges of the combined loads under which the axisymmetric deformation of the plate becomes unstable are clarified through a numerical example.

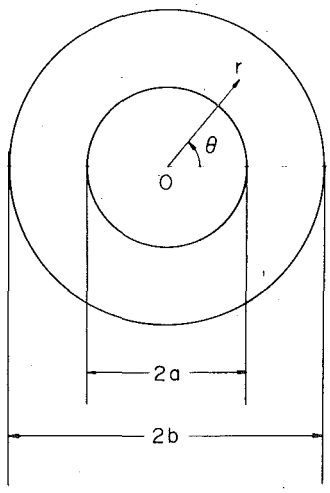

Fig. 1 Dimensions and coordinate system of the annular plate

Basic Equations and Method of Solution

Let us consider that a uniform, radial, compressive, edge thrust T and a uniform lateral pressure p are applied simultaneously to a thin, isotropic, clamped annular plate with thickness h, inner radius a, outer radius b, Young's modulus E, Poisson's ratio ν, and the mass density ρ. Taking the coordinate system as shown in Fig. 1, the transverse displacement of the midplane and the stress function for stress resultants are denoted by W and F, respectively. As a basis for the analysis of the asymmetric small vibration of the plate in the neighborhood of an nonlinear axisymmetric equilibrium state, we use the dynamic version of von Karman's equations. These equations and

Contributed by the Applied Mechanics Division for publication in the JOURNAL OF APPLIED MECHANICS.

Discussion on this paper should be addressed to the Editorial Department, ASME, United Engineering Center, 345 East 47th Street, New York, N. Y. 10017, and will be accepted until December 1, 1980. Readers who need more time to prepare a discussion should request an extension from the Editorial Department. Manuscript received by ASME Applied Mechanics Division, November, 1979; final revision, April, 1980.

the boundary conditions are given in nondimensional form as follows:

$$\nabla^4 f = -\frac{12}{x}\left(w_{,x} + \frac{1}{x}w_{,\theta\theta}\right)w_{,xx} + \frac{12}{x^2}\left(w_{,x\theta} - \frac{1}{x}w_{,\theta}\right)^2 \tag{1}$$

$$\nabla^4 w = \frac{1}{x}\left(f_{,x} + \frac{1}{x}f_{,\theta\theta}\right)w_{,xx} + \frac{1}{x}f_{,xx}\left(w_{,x} + \frac{1}{x}w_{,\theta\theta}\right) - 2\left(\frac{1}{x}f\right)_{,x\theta}\left(\frac{1}{x}w\right)_{,x\theta} + \bar{p} - w_{,\tau\tau} \tag{2}$$

$$w = w_{,x} = f = 0, \quad f_{,x} = -\lambda x \quad \text{at} \quad x = \gamma, 1 \tag{3}$$

where subscripts following a comma stand for partial differentiation and

$$\nabla^2 = \frac{\partial^2}{\partial x^2} + \frac{1}{x}\frac{\partial}{\partial x} + \frac{1}{x^2}\frac{\partial^2}{\partial \theta^2}$$

In these equations, the nondimensional quantities are related to the corresponding physical ones through the following relations:

$$x = \frac{r}{b}, \quad \gamma = \frac{a}{b}, \quad w = \frac{\sqrt{1-\nu^2}}{h}W, \quad f = \frac{F}{D}$$

$$\tau = \frac{t}{b^2}\sqrt{\frac{D}{\rho h}}, \quad \lambda = \sqrt{1-\nu^2}\,\frac{Tb^2}{2\pi Dh}, \quad \bar{p} = \sqrt{1-\nu^2}\,\frac{pb^4}{Dh} \tag{4}$$

in which γ is a ratio of inner to outer radii, $D = Eh^3/12(1-\nu^2)$ is the flexural rigidity of the plate and t is time.

Denoting the time-independent, nonlinear axisymmetric deformation state by $w_0(x)$ and $f_0(x)$, the relevant equations are obtained from equations (1)–(3).

$$x\left[\frac{1}{x}(x\eta)_{,x}\right]_{,x} = -6\zeta^2 \tag{5}$$

$$x\left[\frac{1}{x}(x\zeta)_{,x}\right]_{,x} = \eta\zeta + \frac{1}{2}x^2\bar{p} \tag{6}$$

$$\zeta = 0, \quad \eta = -\lambda x \quad \text{at} \quad x = \gamma, 1 \tag{7}$$

where

$$\eta = f_{0,x}, \qquad \zeta = w_{0,x}$$

In order to analyze the asymmetric small free vibration of the plate in the vicinity of an axisymmetric equilibrium state, we express w and f in the form

$$\begin{aligned} w &= w_0(x) + w_1(x)\cos N\theta e^{i\omega\tau} \\ f &= f_0(x) + f_1(x)\cos N\theta e^{i\omega\tau} \end{aligned} \tag{8}$$

where N and ω are the number of circumferential waves and a circular frequency, while w_1 and f_1 are infinitesimal quantities.

The equations governing the asymmetric small free vibration of the plate in the neighborhood of the axisymmetric equilibrium state are obtained by substituting equations (8) into (1)–(3), subtracting the equations of axisymmetric deformation from resulting equations and retaining only the linear terms in the infinitesimal quantities. This leads to

$$\nabla_1{}^4 f_1 = -\frac{12}{x}\left[\zeta w_{1,xx} + \left(w_{1,x} - \frac{N^2}{x}w_1\right)\zeta_{,x}\right] \tag{9}$$

$$\nabla_1{}^4 w_1 = \frac{1}{x}\left[\zeta f_{1,xx} + \left(f_{1,x} - \frac{N^2}{x}f_1\right)\zeta_{,x} + \eta w_{1,xx} + \left(w_{1,x} - \frac{N^2}{x}w_1\right)\eta_{,x}\right] + \omega^2 w_1 \tag{10}$$

$$w_1 = w_{1,x} = f_1 = f_{1,x} = 0 \quad \text{at} \quad x = \gamma, 1 \tag{11}$$

where

$$\nabla_1{}^2 = \frac{d^2}{dx^2} + \frac{1}{x}\frac{d}{dx} - \frac{N^2}{x^2}$$

We solve the foregoing nonlinear axisymmetric and eigenvalue problems by means of the numerical method employed in reference [16]. An outline of our application of this procedure is presented here.

The system of nonlinear differential equations (5)–(7) governing the axisymmetric deformation is solved by Newton's method, which replaces these equations with a system of linear correctional equations. This latter system of equations is in turn approximated by a system of finite-difference equations using central difference formulas

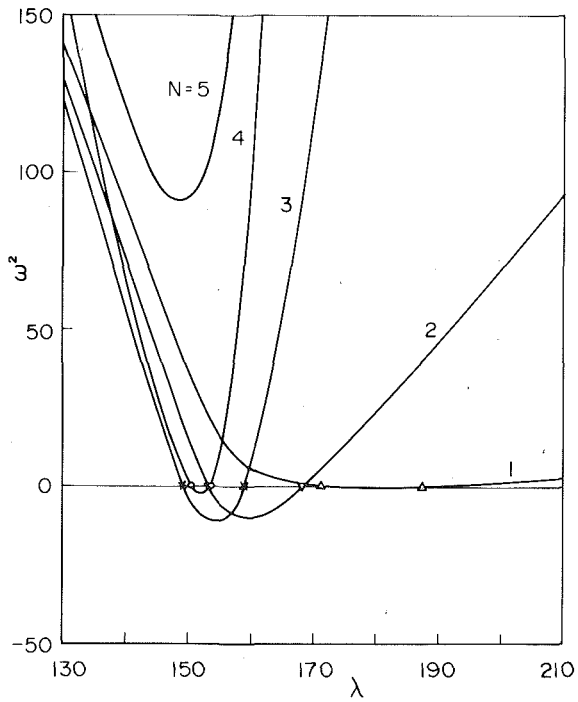

Fig. 2 Relations between thrust and the square of frequency: $\bar{p} = 100$

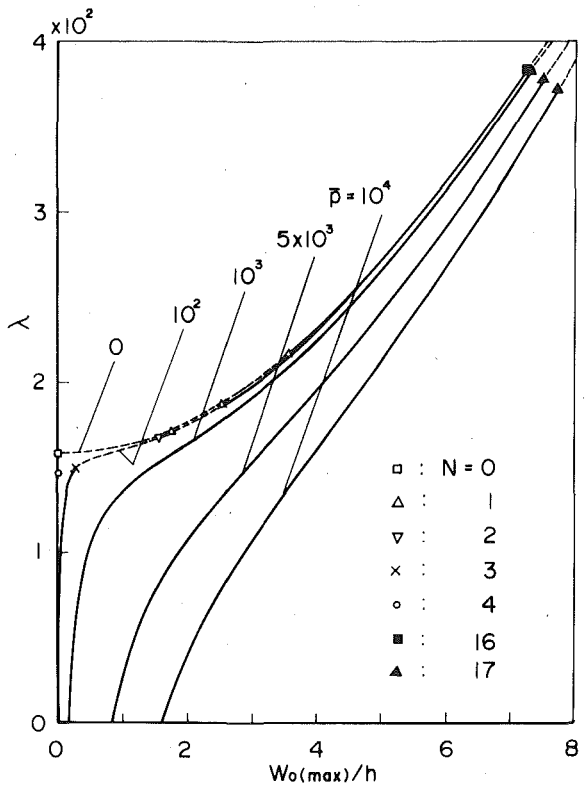

Fig. 3 Relations between thrust and the maximum value of axisymmetric deflection

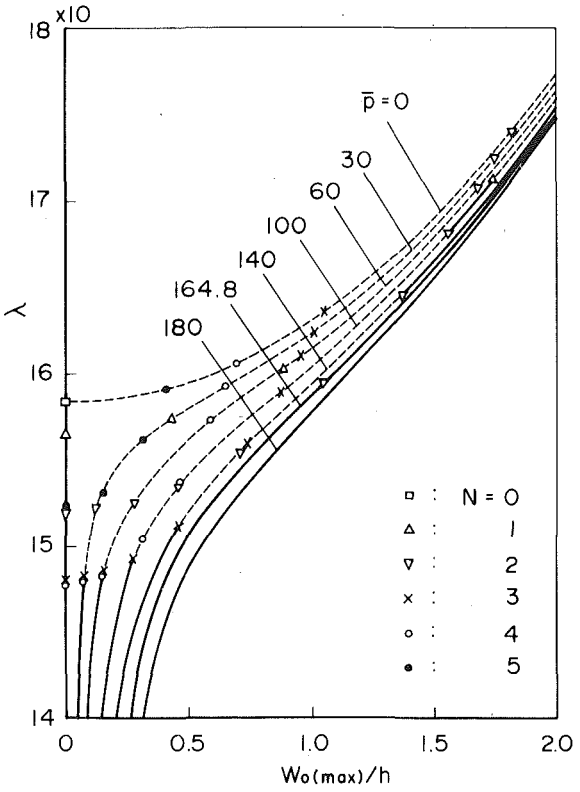

Fig. 4 Relations between thrust and the maximum value of axisymmetric deflection

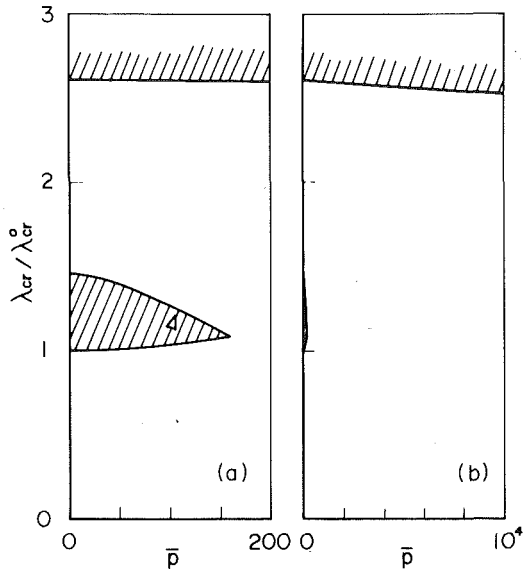

Fig. 5 Instability regions

for the derivatives and solved by the application of Potters' algorithm [17]. The solution with sufficient accuracy can be obtained by repeating the foregoing procedure until the condition $|\delta y^{(n)}/y^{(n)}| \leqq 10^{-4}$ is satisfied, where $\delta y^{(n)}$ and $y^{(n)}$ correspond to the values of correction term and solution of n iteration at each point, respectively. The eigenvalue problem posed by equations (9)–(11) is replaced by the finite-difference analog and solved by Potters' algorithm in the same way as the foregoing statement. A mesh of 100 points on the interval of $(1 - \gamma)$ was considered in the finite-difference method.

When the values of the ratio γ, Poisson's ratio ν, and the load parameters λ and $\bar{p}$ are given, we can determine the eigenvalues, i.e., the natural frequencies ω for each value of the circumferential mode N. If the square of a particular frequency of the asymmetric vibration in the neighborhood of the axisymmetric deformation is negative, the axisymmetric deformation is unstable. The branching of the asymmetric equilibrium states from the axisymmetric one may occur at the point which the particular frequency vanishes.

Numerical Results and Discussion

As a numerical example, we take an annular plate with $\gamma = 0.5$ and $\nu = 0.3$.

The variation of the square of the first order of natural frequencies corresponding to $N = 1, 2, 3, 4$, and 5 for $\bar{p} = 10^2$ as a function of the compressive thrust λ is shown in Fig. 2. From this figure, it can be seen that there are the ranges in which the square of the natural frequencies corresponding to $N = 1, 2, 3$, and 4 becomes negative. Hence, the axisymmetric deformation is unstable between $\lambda = 149.2$ and 168.3, and between $\lambda = 171.1$ and 187.5. The branching of the asymmetric equilibrium states with $N = 1, 2$, and 3 from the axisymmetric one may occur at these four points $\lambda_{cr} = 149.2$, etc.

Fig. 3 shows the relations between the thrust and the maximum value of the axisymmetric deflection for various values of pressure. Fig. 4 shows a part of Fig. 3 after magnification. In these figures, circles, triangles, squares, etc., denote the branching points, while broken lines correspond to the unstable axisymmetric equilibrium states in which the square of the natural frequency of the asymmetric small vibration is negative. The bifurcation buckling with the indicated wave number N may occur practically at the branching points of the ends of the broken lines. The following may be observed from these figures. The asymmetric bifurcation buckling of the annular plate without pressure occurs at the point with $\lambda^0_{cr} = 147.7$ and $N = 4$. For the case with $\bar{p} \leq 164.8$, the axisymmetric deformation is unstable near λ^0_{cr}. When the thrust is approximately 2.6 times the asymmetric buckling one λ^0_{cr} of the annular plate without pressure, the bifurcation buckling with $N = 17$ occurs and the axisymmetric deformation is always unstable.

According to Figs. 3 and 4, the relation between thrust and pressure is shown in Figs. 5. Fig. 5(a) shows a part of Fig. 5(b) after magnification. In these figures, the shaded ranges show the values of the combined loads destabilizing the axisymmetric deformation. It can be seen that the lateral pressure reduces the bifurcation buckling thrust λ_{cr} with the large value. The small stability region exists in the instability region near λ^0_{cr}.

Figs. 6 and 7 show (a) the axisymmetric deflection, (b) the axisymmetric radial and circumferential stress resultants, N_{r0} and $N_{\theta 0}$, just before bifurcation buckling, and (c) the buckling deflection in the cases with $\bar{p} = 10^2$, 10^4, and 0. In these figures, 0.5 and 1 in the abscissa correspond to the inner and outer edges of the annular plate, while N^0_{r0} stands for the axisymmetric compressive radial stress resultant just before buckling with $N = 4$ of the annular plate under only uniform compression. From these figures, it can be seen that the bifurcation buckling at the large thrust is caused by the large circumferential stress and that the corresponding buckling deflection has many waves in the circumferential direction, three half waves in the radial direction and the maximum value near the outer edge.

Conclusions

On the basis of the dynamic version of the nonlinear von Karman theory, a theoretical analysis is performed on the elastic instability of a thin annular plate subjected to simultaneous loading of uniform edge thrust and lateral pressure. The problem is solved by applying a finite-difference method to the equations describing the asymmetric small free vibrations of the plate in the neighborhood of the finite axisymmetric equilibrium state. The present study has led to the following conclusions:

The combination of uniform radial compression and lateral pressure destabilizing the axisymmetric deformation of the annular plate exists always for the large thrust. The annular plate under small

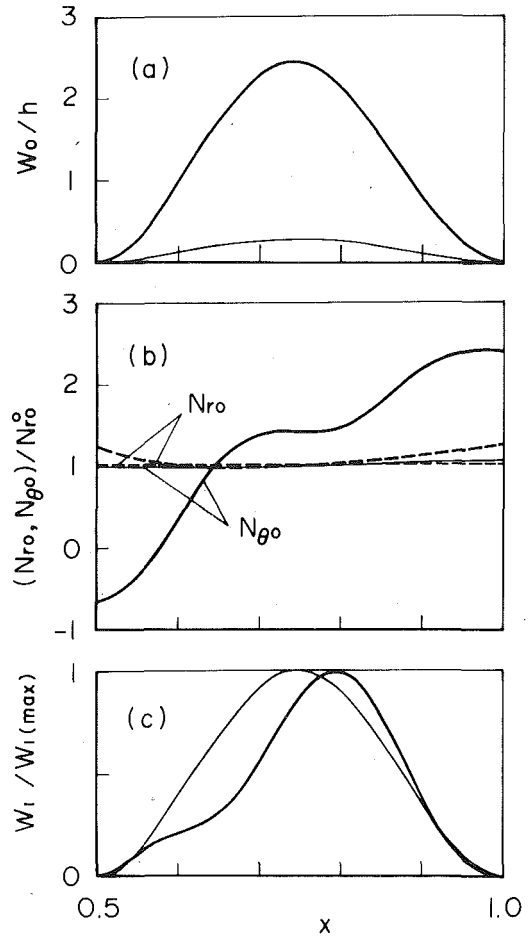

Fig. 6 Distributions of (*a*) axisymmetric deflection, (*b*) axisymmetric radial and hoop stress resultants just before buckling, and (*c*) buckling deflection: $\bar{p} = 100$, ----; $\lambda_{cr} = 187.5$, $N = 1$, ----; $\lambda_{cr} = 149.2$, $N = 3$

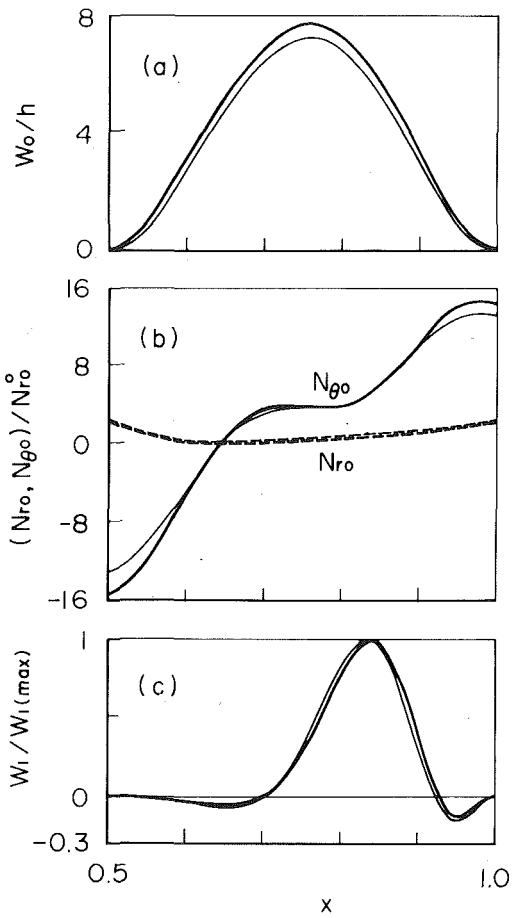

Fig. 7 Distributions of (*a*) axisymmetric deflection, (*b*) axisymmetric radial and hoop stress resultants just before buckling, and (*c*) buckling deflection: ----; $\bar{p} = 10^4$, $\lambda_{cr} = 372.8$, $N = 17$, ----; $\bar{p} = 0$, $\lambda_{cr} = 385.2$, $N = 16$

pressure becomes unstable due to the small thrust which gives rise to the buckling of the annular plate without pressure. The bifurcation buckling, i.e., the branching of the asymmetric equilibrium state from the axisymmetric one occurs at the boundary between the stability and instability regions in the space of combined loads. The bifurcation buckling at the large thrust is caused by the large hoop stress and this buckling load is about 2.6 times that of the annular plate without pressure.

Acknowledgment

The author is especially grateful to the associate editor, Prof. G. A. Wempner and the reviewers for their helpful and important comments. The author also wishes to express his appreciation to Prof. N. Yamaki, Tohoku University, for many valuable suggestions. The generous financial support of Prof. H. Abe, Tohoku University, are gratefully acknowledged.

References

1 Friedrichs, K. O., and Stoker, J. J., "The Nonlinear Boundary-Value Problem of the Buckled Plate," *American Journal of Mathematics,* Vol. 63, 1941, pp. 839–888.

2 Friedrichs, K. O., and Stoker, J. J., "Buckling of the Circular Plate Beyond the Critical Thrust," ASME JOURNAL OF APPLIED MECHANICS, Vol. 9, 1942, pp. A7–A14.

3 Bodner, S. R., "The Postbuckling Behavior of a Clamped Circular Plate," *Polytechnic Institute of Brooklyn,* Vol. XII, No. 4, 1955, pp. 397–401.

4 Keller, H. B., and Reiss, E. L., "Nonlinear Bending and Buckling of Circular Plates," *Proceedings of the 3rd U.S. National Congress of Applied Mechanics,* 1958, pp. 375–385.

5 Keller, H. B., Keller, J. B., and Reiss, E. L., "Buckled States of Circular Plates," *Quarterly of Applied Mechanics,* Vol. 20, 1961, pp. 55–65.

6 Wolkowisky, J. H., "Existence of Buckled States of Circular Plates," *Communications on Pure and Applied Mathematics,* Vol. 20, 1967, pp. 549–560.

7 Pal, M. C., "Large Deflections on Heated Circular Plates," *Acta Mechanica,* Vol. 8, Nos. 1–2, 1969, pp. 82–103.

8 Morozov, N. F., "Investigation of a Circular Symmetric Compressible Plate With a Large Boundary Load," *Izv. Vyssh. Ucheb. Zav.,* Vol. 34, 1963, pp. 95–97.

9 Yanowitch, M., "Nonlinear Buckling of Circular Elastic Plates," *Communications on Pure and Applied Mathematics,* Vol. IX, 1956, pp. 661–672.

10 Cheo, L. S., and Reiss, E. L., "Unsymmetric Wrinkling of Circular Plates," *Quarterly of Applied Mathematics,* Vol. 31, No. 1, 1973, pp. 75–91.

11 Cheo, L. S., and Reiss, E. L., "Secondary Buckling of Circular Plates," *SIAM Journal of Applied Mathematics,* Vol. 26, No. 3, 1974, pp. 490–495.

12 Huang, C. L., "Postbuckling of an Annulus," *American Institute of Aeronautics and Astronautics Journal,* Vol. 11, No. 12, 1973, pp. 1608–1612.

13 Huang, C. L., "On Postbuckling of Orthotropic Annular Plates," *International Journal of Nonlinear Mechanics,* Vol. 10, No. 1, 1975, pp. 63–74.

14 Uthgenannt, E. B., and Brand, R. S., "Postbuckling of Orthotropic Annular Plates," ASME JOURNAL OF APPLIED MECHANICS, Vol. 40, No. 2, 1973, pp. 559–564.

15 Tani, J., "Thermal Buckling of an Annular Plate With Axisymmetric Initial Deflection," ASME JOURNAL OF APPLIED MECHANICS, Vol. 45, No. 3, 1978, pp. 693–695.

16 Tani, J., "Influence of Prebuckling Deformations on the Buckling of Truncated Conical Shells Under Axial Compression," *Transactions of the Japan Society of Aeronautical and Space Sciences,* Vol. 16, No. 34, 1973, pp. 232–245.

17 Potters, M. L., "A Matrix Method for the Solution of a Second-Order Difference Equation in Two Variables," *Report MR19, Mathematical Centrum,* Amsterdam, The Netherlands, 1955.

J. Tani
Assistant Professor.
Mem. ASME

T. Nakamura
Assistant.

Institute of High Speed Mechanics,
Tohoku University,
Sendai, Japan

Dynamic Stability of Annular Plates Under Pulsating Torsion

The dynamic stability of annular plates under periodic torsion is analyzed by means of the Galerkin method in conjunction with Hsu's procedure. The instability regions associated with both principal and combination parametric resonances are clarified for relatively low frequency ranges. It is found that under the purely periodic torsion only the combination instability region exists, while under the simultaneous action of the static torsion the principal instability region exists also. The circumferential phase difference of two vibration modes excited simultaneously at the resonance is also found to change remarkably the relative width of the instability region.

Introduction

The dynamic stability of flat plates subjected to periodic in-plane forces is a problem of technical importance which has received a great deal of attention in the last decade. For example, Bolotin [1], Hutt and Salan [2], Duffield and Willems [3], Merritt and Willems [4], Reckling [5], and Popescu [6] investigated the principal and secondary regions of instability for various plates by means of Bolotin's method. The instability regions for both principal and combination resonances of square and rectangular plates were examined by Jagadish [7], and Yamaki and Nagai [8], respectively. Recently, the principal and combination instability regions of annular plates under periodic radial loads were studied by Tani and Nakamura [9, 10]. However, to the best of our knowledge, the dynamic stability of annular plates under pulsating torsion has not been investigated yet.

This paper examines theoretically the dynamic stability of clamped thin annular plates subjected to both static and periodic torsion. The Galerkin method is used to reduce the problem to that for a finite degree-of-freedom system, the instability regions of which are determined by utilizing Hsu's result [11] for coupled Hill's equations. Through detailed calculations, the instability regions of practical importance, associated with both principal and combination resonances, are clarified for relatively low frequency ranges. It is found that the circumferential phase difference of two modes, having the same circumferential wave number, of vibration excited simultaneously at the resonance has an important role in the principal and combination resonance. The principal resonance is also found to depend sensitively on the simultaneous action of the static torsion.

Problem Formulation

Consider that a periodic torsion $Q = q_0 + q_1 \cos \Omega t$ acts on the circumferential edges of a thin, isotropic, annular plate with thickness h, inner radius a and outer radius b. The coordinate system is taken as shown in Fig. 1. When the problem is restricted to relatively low frequency ranges where flexural vibrations of the plate are dominant, effects of transverse shear deformation and in-plane as well as rotatory inertia forces can be neglected. The effect of damping is assumed to be negligible. Hence, in the unperturbed motion, the plate executes a simple in-plane vibration with the stress resultants as given by

$$N_{r0} = N_{\theta 0} = 0, \qquad N_{r\theta 0} = (q_0 + q_1 \cos \Omega t)/2\pi r^2 \tag{1}$$

where q_0 is a static load, while q_1 and Ω are an amplitude and an exciting frequency of dynamic load, respectively.

Next, with W denoting the small incremental deflection just after

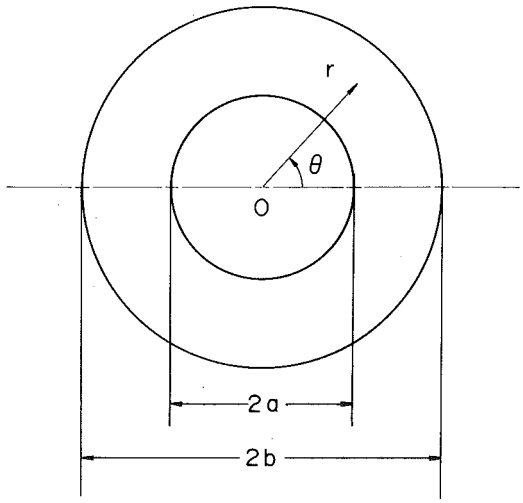

Fig. 1 Geometry of an annular plate

Contributed by the Applied Mechanics Division for publication in the JOURNAL OF APPLIED MECHANICS.

Discussion on this paper should be addressed to the Editorial Department, ASME, United Engineering Center, 345 East 47th Street, New York, N. Y. 10017, and will be accepted until December 1, 1980. Readers who need more time to prepare a discussion should request an extension from the Editorial Department. Manuscript received by ASME Applied Mechanics Division, November, 1979.

the plate loses its stability, the equation governing the perturbed motion of plate is

$$\rho h W_{,tt} + D\nabla^4 W - 2N_{r\theta 0}\left(\frac{1}{r}W_{,\theta}\right)_{,r} = 0 \tag{2}$$

where

$$D = \frac{Eh^3}{12(1-\nu^2)}, \qquad \nabla^2 = \frac{\partial^2}{\partial r^2} + \frac{1}{r}\frac{\partial}{\partial r} + \frac{1}{r^2}\frac{\partial^2}{\partial \theta^2}$$

In the foregoing, D is the flexural rigidity of the plate, E, ν, ρ, and t are Young's modulus, Poisson's ratio, mass density of the plate, and time, respectively, while subscripts following a comma stand for partial differentiation.

As for the boundary conditions, we will consider the case of both edges clamped as follows:

$$W = W_{,r} = 0 \quad at \quad r = a, b \tag{3}$$

Here we introduce the following notations for convenience:

$$x = \log\frac{r}{b}, \quad \tau = \frac{t}{b^2}\sqrt{\frac{D}{\rho h}}, \quad w = \frac{W}{h}$$

$$(\bar{q}_0, \bar{q}_1) = \frac{1}{q_{cr}}(q_0, q_1), \quad q_{cr} = 2\pi D k_s$$

$$\omega = \Omega b^2\sqrt{\frac{\rho h}{D}}, \quad \gamma = \frac{a}{b} \tag{4}$$

In the notations, γ is the ratio of inner to outer radii and q_{cr} is the buckling load with the relevant parameter k_s. Further, $\bar{q}_0$ and $\bar{q}_1$ are the static and periodic load intensities normalized by q_{cr}, respectively, while ω is nondimensional parameter relating to exciting frequency. With these notations, equations (2) and (3) can be rewritten as follows:

$$L(w) \equiv w_{,\tau\tau} + e^{-4x}\bar{\nabla}^4 w - 2k_s(\bar{q}_0 + \bar{q}_1\cos\omega\tau)e^{-4x}(w_{,x\theta} - w_{,\theta}) = 0 \tag{5}$$

$$w = w_{,x} = 0 \quad \text{at} \quad x = 0, \log\gamma \tag{6}$$

where

$$\bar{\nabla}^4 = \frac{\partial^4}{\partial x^4} - 4\frac{\partial^3}{\partial x^3} + 4\frac{\partial^2}{\partial x^2} + \frac{\partial^2}{\partial\theta^2}\left(2\frac{\partial^2}{\partial x^2} - 4\frac{\partial}{\partial x} + 4 + \frac{\partial^2}{\partial\theta^2}\right)$$

Under given boundary conditions, equation (5) has, in general, only bounded solutions for w and the unperturbed motion is stable. However, under specific combinations of $\bar{q}_0$, $\bar{q}_1$, and ω_1 the governing equation has the solution increasing indefinitely with time, leading to the dynamic instability of the plate. The problem consists in determining the boundaries dividing the stability and instability regions in the space of $\bar{q}_1$ and ω, when the values of the static load $\bar{q}_0$ and the ratio γ are prescribed.

Method of Solution

Considering the boundary condition (6), we put a solution of equation (5) as

$$w = \sum_m (c_{m-1} - c_{m+1})[a_m(\tau)\cos N\theta + b_m(\tau)\sin N\theta]$$

$$c_m = \cos(m\beta x), \quad \beta = \pi/\log\gamma, \quad (m = 1, 2, 3, \ldots) \tag{7}$$

where $a_m(\tau)$ and $b_m(\tau)$ are unknown time functions and N is the number of circumferential waves. With this expression, we apply the Galerkin method to (5), which leads to the following conditions:

$$\int_0^{2\pi}\int_0^{\log\gamma} L(w)(c_{n-1} - c_{n+1})\begin{pmatrix}\cos N\theta \\ \sin N\theta\end{pmatrix} e^{2x}dx d\theta = 0, \quad (n = 1, 2, 3, \ldots) \tag{8}$$

Performing the foregoing integration, we obtain the following set of equations for $a_m(\tau)$ and $b_m(\tau)$:

$$\sum_m [M_{nm}a_{m,\tau\tau} + R_{nm}a_m + k_s(\bar{q}_0 + \bar{q}_1\cos\omega\tau)P_{nm}b_m] = 0$$

$$\sum_m [M_{nm}b_{m,\tau\tau} + R_{nm}b_m - k_s(\bar{q}_0 + \bar{q}_1\cos\omega\tau)P_{nm}a_m] = 0$$

$$(m, n = 1, 2, 3, \ldots) \tag{9}$$

where

$$M_{nm} = [1 - (-1)^{n+m}\gamma^2](\Phi_{n,m-1} - \Phi_{n,m+1})$$

$$R_{nm} = -[1 - (-1)^{n+m}\gamma^{-2}][E_{m-1}\Phi_{n,m-1} - E_{m+1}\Phi_{n,m+1} - 2\beta^2(H_{m-1}\Psi_{n,m-1} - H_{m+1}\Psi_{n,m+1})]$$

$$P_{nm} = -2N[1 - (-1)^{n+m}\gamma^{-2}]\{\Phi_{n,m-1} - \Phi_{n,m+1} + \frac{1}{2}\beta^2[(m-1)\Psi_{n,m-1} - (m+1)\Psi_{n,m+1}]\}$$

$$\Phi_{n,m} = I_{m+n-1} + I_{m-n+1} - I_{m+n+1} - I_{m-n-1}, \quad I_l = 1/(4 + \beta^2 l^2)$$

$$\Psi_{n,m} = J_{m+n-1} + J_{m-n+1} - J_{m+n+1} - J_{m-n-1}, \quad J_l = lI_l$$

$$E_m = \beta^4 m^4 + 2\beta^2 m^2(N^2 - 2) + N^2(N^2 - 4)$$

$$D_m = \beta^2 m^2 + N^2, \quad H_m = mD_m \tag{10}$$

In the foregoing, the coefficients M_{nm}, R_{nm}, and P_{nm} depend on the ratio γ as well as the wave number N and are symmetric with respect to indices n and m. Equations (9) represent a set of coupled Mathieu equations.

Upon omitting the inertia terms as well as those with periodic coefficients, and putting $a_m(\tau) \equiv \bar{a}_m$, $b_m(\tau) \equiv \bar{b}_m$, and $\bar{q}_0 = 1$, equations (9) become

$$\sum_m (R_{nm}\bar{a}_m + k_s P_{nm}\bar{b}_m) = 0$$

$$\sum_m (R_{nm}\bar{b}_m - k_s P_{nm}\bar{a}_m) = 0 \quad (m, n = 1, 2, 3, \ldots) \tag{11}$$

In order that these homogeneous equations have nontrivial solutions in $\bar{a}_m$ and $\bar{b}_m$, the determinant of the coefficients should vanish, from which the value of k_s can be obtained for the assigned value of N. The minimum value of k_s will be determined by successively changing the value of N, which gives the value of k_s corresponding to the buckling load q_{cr}, together with the buckling wave number N_s.

Next, upon omitting the terms with periodic coefficients and putting $a_m(\tau) \equiv \tilde{a}_m\cos\omega\tau$ and $b_m(\tau) \equiv \tilde{b}_m\cos\omega\tau$, equations (9) become

$$\sum_m [(R_{nm} - \omega^2 M_{nm})\tilde{a}_m + k_s\bar{q}_0 P_{nm}\tilde{b}_m] = 0$$

$$\sum_m [(R_{nm} - \omega^2 M_{nm})\tilde{b}_m - k_s\bar{q}_0 P_{nm}\tilde{a}_m] = 0 \quad (m, n = 1, 2, 3, \ldots) \tag{12}$$

Equating to zero the determinant of the coefficients of these equations, we obtain, for each prescribed value of N, the nondimensional natural frequencies and the corresponding modes of vibration, under the effect of the static torsion $\bar{q}_0$. The natural frequencies thus obtained may be denoted by $\omega_i (i = 1, 2, 3, \ldots)$ in order of smallness and the corresponding eigenvectors by $\phi_{ij} (i, j = 1, 2, 3, \ldots)$. The subscript i defines the order of radial modes of vibration, which represents the number of half waves in the radial direction.

Here, one should note that in addition to $\tilde{a}_1 = 1$, the other condition is required to determine the eigenvectors ϕ_{ij}, because of the assumption of the solution (7). Hence, the following condition is added:

$$w_{,xx} = 0 \quad \text{at} \quad x = \gamma, \quad \theta = \theta_0 \tag{13}$$

This condition corresponds to that a nodal line of vibration mode in the radial direction develops from the position (γ, θ_0) on the inner edge of the plate. Further this condition makes it possible to designate

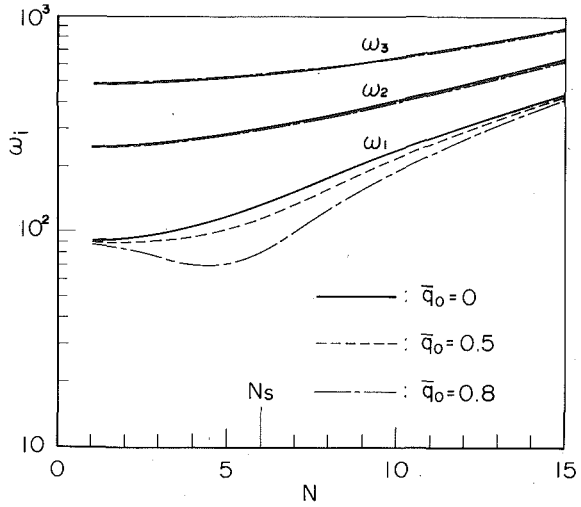

Fig. 2 Effect of static torque $\bar{q}_0$ on the natural frequencies ω_i in the case with $\gamma = 0.5$

the circumferential phase difference of two modes, having the same circumferential wave number, of vibration excited simultaneously at the resonance.

Now, it is well known that under certain combinations of $\bar{q}_0$, $\bar{q}_1$, and ω, equations (9) have the solution $a_m(\tau)$ and $b_m(\tau)$ growing with time indefinitely, leading to the parametric instability of the system. To clarify the stability boundaries, it is convenient to rewrite (9) in the standard form. For this purpose, one transforms the generalized coordinates a_m and b_m to the normal coordinates d_i by making use of the eigenvectors ϕ_{ij}, which leads to the following set of coupled Mathieu equations in the standard form:

$$d_{i,\tau\tau} + \omega_i{}^2 d_i + \bar{q}_1 \cos \omega\tau \sum_j S_{ij} d_j = 0$$

$$S_{ij} = S_{ji} = k_s \sum_k \sum_l \psi_{ki} P_{kl} \psi_{lj}$$

$$\psi_{ji} = \phi_{ij} \left(\sum_k \sum_l \phi_{ik} M_{kl} \phi_{il}\right)^{-1/2}; \quad (i, j, k, l = 1, 2, 3, \ldots) \tag{14}$$

For the stability of these equations, detailed studies have been made by Hsu [11]. According to his results, equations (14) have instability regions of combination resonance type when ω is in the neighborhood of $\omega_i + \omega_j$, and the first approximations for the stability boundaries are given by

$$\frac{\omega}{\omega_{ij}} = 1 \pm \theta_{ij} \bar{q}_1, \quad (i, j = 1, 2, 3, \ldots)$$

$$\omega_{ij} = \omega_i + \omega_j, \quad \theta_{ij} = \frac{|S_{ij}|}{2\omega_{ij}\sqrt{\omega_i \omega_j}} \tag{15}$$

In the foregoing, ω_{ij} and θ_{ij} stand for the central frequency and the relative width parameter of the instability region, respectively. The numerous instability regions closely distributed can be represented easily by using of ω_{ij} and θ_{ij}. At the combination resonance, it is to be noted that two modes of vibration, having different radial modes i and j but having the same circumferential wave number N, are excited simultaneously, and that these modes may have a phase difference in the circumferential direction. Equations (14) have also principal instability regions when ω is almost twice the natural frequency ω_i, the boundaries of which are given by putting $i = j$ in (15). In this case, only the mode corresponding to ω_i is excited.

By means of the higher approximations [12], we may obtain many secondary instability regions with small relative openness. Under small exciting forces, however, the occurrence of the secondary instability will be prevented by inevitable small damping. Hence, the consideration of the secondary instability will be omitted in the following.

Table 1 Torsion buckling load parameter k_s and the corresponding wave number N_s in each case

	Present		Dean [13]	
γ	k_s	N_s	k_s	N_s
0.2	36.00	3	35.99	3
0.5	186.1	6	186.1	6
0.8	1780	17	1780	17

Buckling Load and Natural Frequencies

On the basis of (11) with 20 terms for each unknown parameter $\bar{a}_m$ and $\bar{b}_m$, the buckling parameter k_s and the corresponding wave number N_s in the cases with $\gamma = 0.2$, 0.5, and 0.8 are determined with the results listed in Table 1. Accurate results obtained by Dean [13] are also shown. Excellent agreement will be noticed.

Next, on the basis of (12) with 20 terms for each unknown parameter $\tilde{a}_m$ and $\tilde{b}_m$, and k_s as given in Table 1, the natural frequencies $\omega_i (i = 1, 2, 3)$ in the case with $\gamma = 0.5$ are determined for each wave number N, with the effect of the static torsion $\bar{q}_0$ taken into consideration. The results are illustrated in Fig. 2. The following will be observed from this figure. The first order of natural frequencies decreases with an increase in the static torsion. This tendency is most pronounced when N is in the vicinity of buckling wave number N_s. The effect of the static torsion on the second and third orders of natural frequencies is very small.

The effect of the static torsion on the first and second natural modes of vibration can be also examined. The typical results for the case with $\gamma = 0.5$, $N = 6 (= N_s)$, and $\theta_0 = \pi/2N$ are shown in Fig. 3, with the contour lines with the maximum amplitude of the deflection w taken as unity. It will be seen that, with the application of static torque, the radial nodal lines are obliquely rotated in the loading direction and that the first natural mode of vibration almost agrees with that of the static buckling.

Instability Regions

First, the variation of the relative openness θ_{ij} of instability regions with the circumferential phase difference α of two vibration modes is examined for the case with $\gamma = 0.5$ and $\bar{q} = 0.5$ by using the eigenvectors ϕ_{ij} obtained along with the calculation of natural frequencies ω_i. This is because two vibration modes, having the same circumferential wave number but having the different phase in the circumferential direction, may be excited simultaneously at the resonance. The results with $\theta_{ij} \geqq 10^{-2}$ are shown in Fig. 4, from which the following is observed. The relative openness of the combination instability region is widest when the value of the circumferential phase difference α is in the vicinity of $\pi/2N$. On the other hand, that of the principal instability region is widest when the value of α is equal to 0 and π/N. The value of the relative width parameter θ_{ij} depends on the circumferential wave number N which two vibration modes simultaneously excited have equally.

Next, to examine the effect of the static torsion, the instability regions for the cases with $\bar{q}_0 = 0$, 0.25, 0.5, 0.75 and $\gamma = 0.5$ are determined with the results shown in Fig. 5. In this figure and the following, the relative width parameter θ_{ij} represents the maximum value with respect to the circumferential phase difference. Only the instability regions with $\theta_{ij} \geqq 10^{-2}$ have been considered for natural frequencies up to third order of radial modes. From Fig. 5, one can easily find the location and the openness of the instability regions, together with the wave number as well as the modes of the excited vibration. The following observations can be made. Under purely periodic torque without the static one, one has only the instability regions of combination resonance type. To judge from the magnitudes of the relative widths θ_{ij}, the instability regions associated with (i, j) as (1, 2) are of

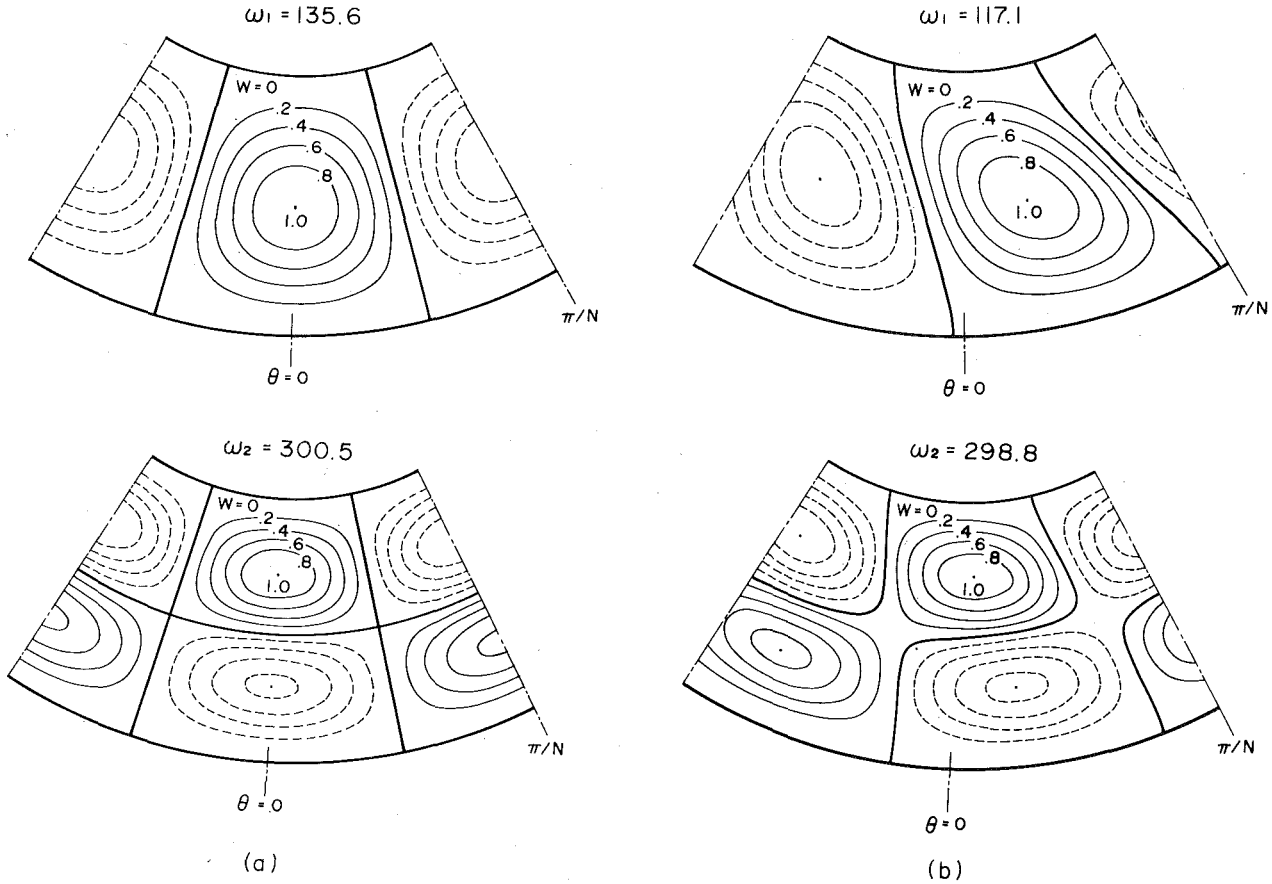

Fig. 3 Waveforms of the natural modes of vibration: $\gamma = 0.5$, $N = 6$; (*a*) $\bar{q}_0 = 0$; (*b*) $\bar{q}_0 = 0.5$

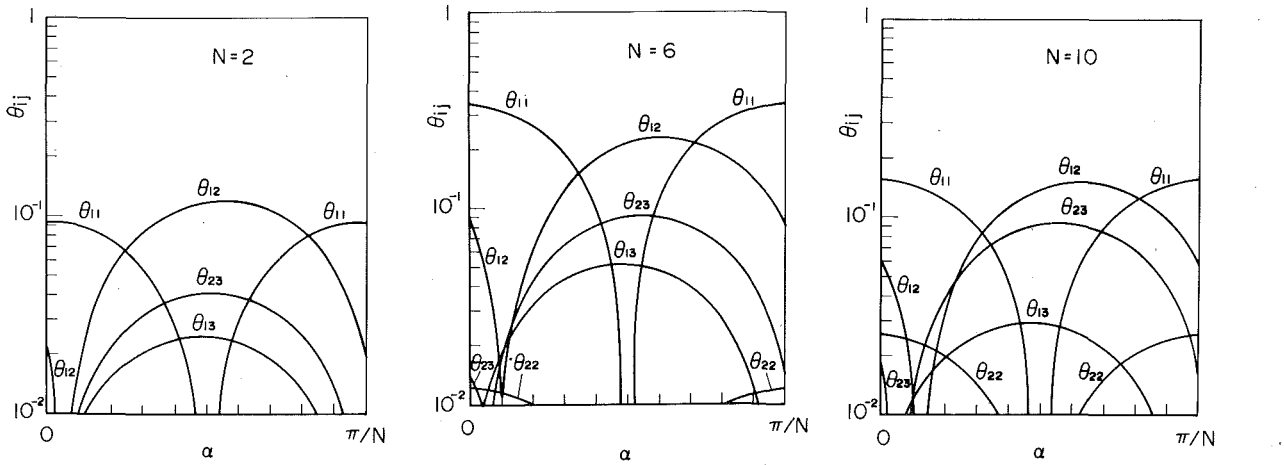

Fig. 4 Relation between relative openness θ_{ij} and circumferential phase difference α in the case with $\gamma = 0.5$ and $\bar{q}_0 = 0.5$

most importance. The relative width θ_{12} has a maximum when N is near the buckling wave number N_s. Under the simultaneous action of the static torque, one has the principal instability regions, besides the combination instability regions. With an increase in the static torque, the relative widths θ_{ii} of the principal instability regions, especially θ_{11}, grow rapidly, while those for the combination type θ_{ij} ($i \neq j$) remain almost unchanged. When the static torque exceeds one half of the buckling load, the principal instability region of the lowest order, associated with the wave number around N_s, is of most importance. The central frequency of each instability region is shifted toward the lower frequency with the static torque.

To check the effect of the radial ratio γ, the instability regions for the cases with $\gamma = 0.2$ and 0.8 are also determined with the results shown in Figs. 6 and 7. It can be seen from these figures that the increase of the radial ratio raises the central frequency and reduces the variations of the central frequency and the relative width with the

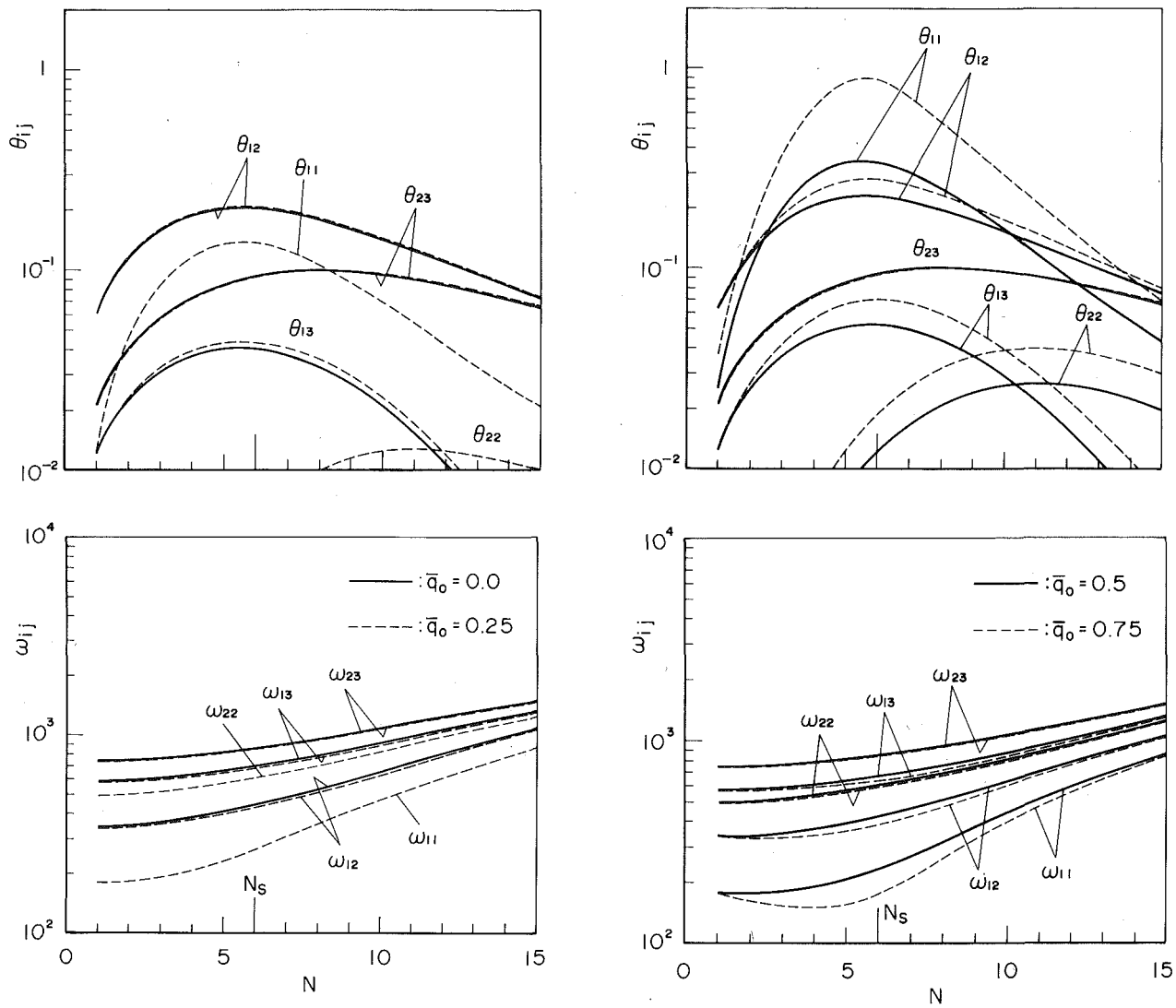

Fig. 5(a)

Fig. 5(b)

Fig. 5 Effect of static torque $\bar{q}_0$ on the central frequency ω_{ij} and the relative openness θ_{ij} of the instability regions: $\gamma = 0.5$

wave number. The large change of the central frequency with the radial ratio is obviously due to the variation in the natural frequency.

Conclusions

The dynamic stability of annular plates subjected to both static and periodic torsion has been theoretically studied within relatively low frequency ranges. The main results obtained may be summarized as follows:

1 Under the purely periodic torque only the instability regions of combination resonance type exist, while the simultaneous action of the static torque gives rise to the principal instability regions.

2 With the increase in the static torque, the relative widths of the principal instability regions, especially θ_{11}, grow rapidly, while those for the combination type remain almost unchanged. When the static torque exceeds one half of the buckling load, the principal instability region of the lowest order, associated with the wave number around the buckling one becomes most significant.

3 The relative openness of the instability regions depends sensitively on the circumferential phase difference of two vibration modes excited simultaneously at the resonance with the same circumferential wave number.

4 With the increase in the static torque and/or the decrease in the radial ratio, the central frequency of each instability region is shifted toward the lower frequency, due to the variation in the natural frequency.

Acknowledgment

The authors express their sincere appreciation to Prof. N. Yamaki, Tohoku University, for his instructive suggestions and discussions on the present study. The authors also wish to thank Prof. C. S. Hsu for his valuable advice.

References

1 Bolotin, V. V., *The Dynamic Stability of Elastic Systems*, Holden-Day, Inc., 1964.

2 Hutt, J. M., and Salam, A. E., "Dynamic Stability of Plates by Finite Elements," *Journal of the Engineering Mechanics Division, Trans. ASCE*, Vol. 97, No. EM3, 1971, pp. 879–899.

3 Duffield, R. C., and Willems, N., "Parametric Resonance of Stiffened Rectangular Plates," ASME JOURNAL OF APPLIED MECHANICS, Vol. 39, Mar. 1972. pp. 217–226.

4 Merritt, R. G., and Willems, N., "Parametric Resonance of Skew Stif-

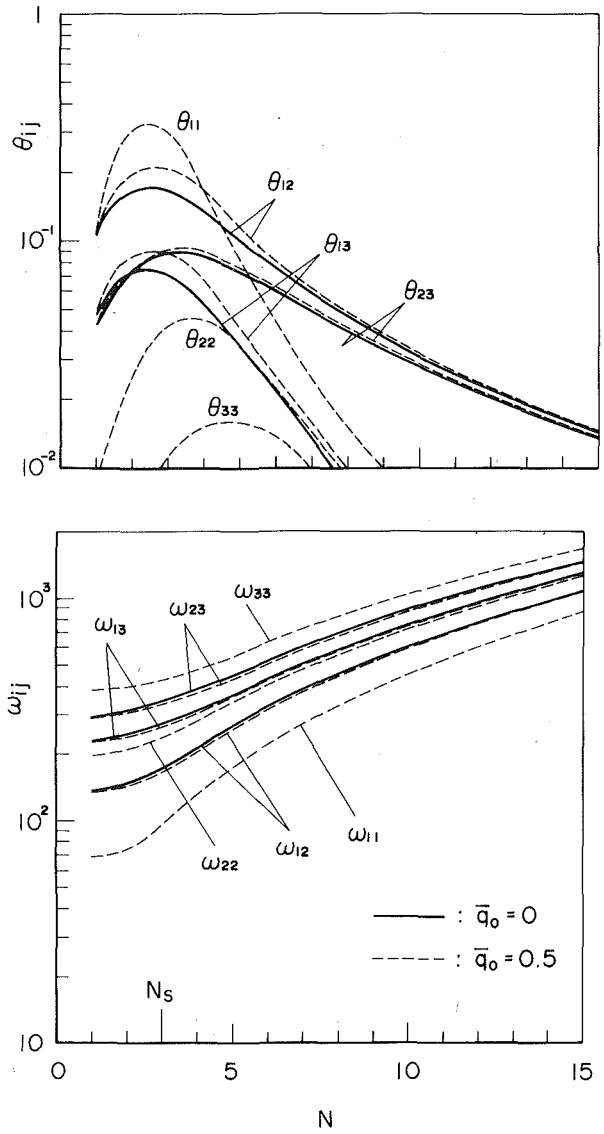

Fig. 6 Central frequency and the relative openness of the instability regions: $\gamma = 0.2$

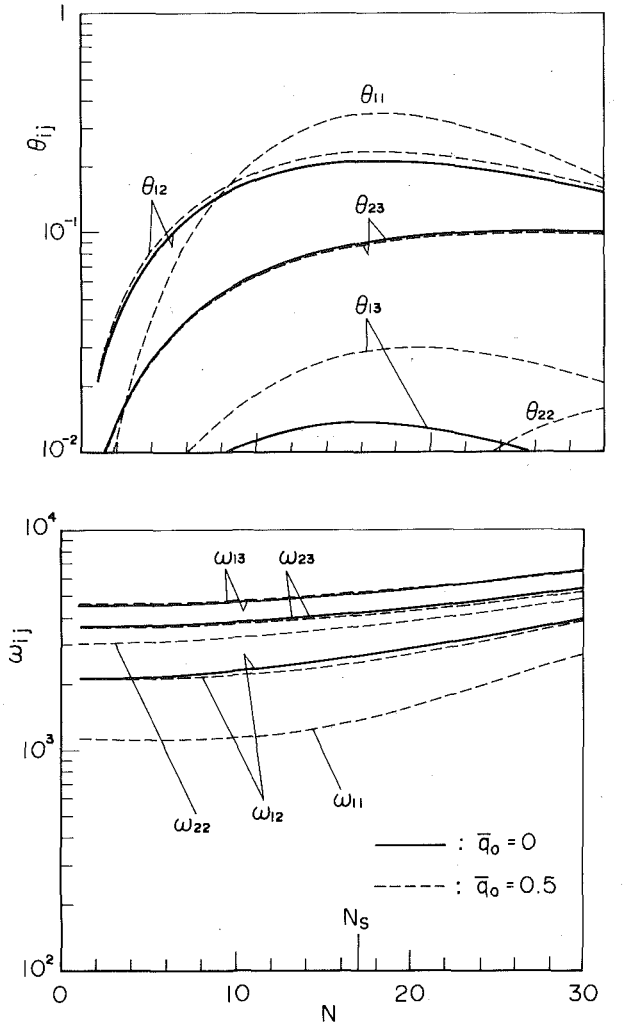

Fig. 7 Central frequency and the relative openness of the instability regions: $\gamma = 0.8$

fened Plates," ASME JOURNAL OF APPLIED MECHANICS, Vol. 40, June 1973, pp. 439–444.

5 Reckling, K. A., "Die dünne Kreisplatte mit pulsierender Randbelastung in ihrer Mittelebene also Stabilitätsproblem," *Ingenieur-Archiv,* Vol. 21, No. 2, 1953, pp. 141–147.

6 Popescu, N. O., "Die dynamische Stabilität Kreisförmiger, der Wirkung periodisch veranderlicher Krafte ausgesetzter Platten," *Forschung aus dem Gebiete des Ingenieur-wesens,* Vol. 36, No. 5, 1970, pp. 148–159.

7 Jagadish, K. S., "The Dynamic Stability of Degenerate Systems Under Parametric Excitation," *Ingenieur-Archiv,* Vol. 43, No. 4, 1974, pp. 240–246.

8 Yamaki, N., and Nagai, K., "Dynamic Stability of Rectangular Plates Under Periodic Compressive Forces," *The Reports of the Institute of High Speed Mechanics, Tohoku University,* Vol. 32, No. 288, 1975, pp. 103–127.

9 Tani, J., and Nakamura, T., "Dynamic Stability of Annular Plates Under Periodic Loads," *Journal of the Acoustical Society of America,* Vol. 64, No. 3, 1978, p. 827–831.

10 Tani, J., and Nakamura, T., "Parametric Resonance of Annular Plates Under Pulsating Uniform Internal and External Loads With Different Periods," *Journal of Sound and Vibration,* Vol. 60, No. 2, 1978, pp. 289–297.

11 Hsu, C. S., "On the Parametric Excitation of a Dynamic System Having Multiple Degrees of Freedom," ASME JOURNAL OF APPLIED MECHANICS, Vol. 30, Sept. 1963, pp. 367–371.

12 Struble, R. A., *Nonlinear Differential Equations,* McGraw-Hill, New York, 1976.

13 Dean, W. R., "The Elastic Stability of an Annular Plate," *Proceedings of the Royal Society,* London, Vol. 106, 1924, pp. 268–284.

E. R. Johnson

Assistant Professor,
Department of Engineering Science and Mechanics,
Virginia Polytechnic Institute and State University,
Blacksburg, Va. 24061

The Effect of Damping on Dynamic Snap-Through

Dynamic snap-through criteria are compared for an impulsively loaded shallow circular arch modeled as a Kelvin-Voigt material. The Budinasky-Roth criterion is used in conjunction with direct numerical integration of an approximate set of motion equations to obtain critical magnitudes of the load as a function of small viscous damping and the spatial distribution of the load. These critical magnitudes are compared to a lower bound estimate which is independent of the load distribution and damping. This lower bound is a stability-sufficiency condition formulated by Hsu. The presence of small damping significantly increases the critical magnitudes with respect to the undamped results for nonsymmetric loading, and thus indicates the conservative nature of the lower bound.

Introduction

In a recent paper [1] the effect of the spatial distribution of an impulsive load on dynamic snap-through of a shallow circular arch was discussed. A spatially independent lower bound on the critical magnitude of the impulsive load required for snap-through was compared to a criterion based on direct integration of the equations of motion. This latter criterion, then, accounted for the spatial distribution. The lower bound is a sufficient condition for dynamic stability formulated by Hsu [2], and the criterion used to determine critical magnitudes by direct integration is due to Budinasky and Roth [3]. The Budiansky-Roth criterion was used to obtain critical magnitudes for snap-through occurring on the initial oscillation of the response, termed immediate snap-through, and for snap-through occurring at any time of the finite integration period, termed finite time snap-through. For most spatial distributions considered, the lower bound was a considerably less conservative estimate of finite time snap-through than for immediate snap-through. The present paper considers the effect of small material damping on this conclusion, since it is anticipated that finite time snap-through will be significantly affected by small damping whereas immediate snap-through will not.

The influence of damping on dynamic snapping of a simply supported sinusoidal arch subject to a timewise step pressure with sinusoidal spatial distribution was addressed by Lock [4], Hegemier and Tzung [5], and Huang and Nachbar [6]. Both Lock and Hegemier and Tzung consider energy dissipation by external damping (simulating an arch on a viscous foundation), whereas Huang and Nachbar use material viscous damping for energy dissipation. Lock found that damping had an appreciable effect on the critical pressures required for "indirect" snap-through (analogous to finite time snap-through in the present work). Further, Lock found no significant numerical difference between dynamic and static critical pressures for large arch rises and for a value of the viscous damping coefficient γ equal to 1 percent of critical damping of the fundamental symmetric mode. Huang and Nachbar also observed that dynamic buckling loads equaled static buckling loads for damped arches with large rises. However, Hegemier and Tzung state this is true as $\gamma \to 0+$, and moreover that there is a discontinuity between the critical pressure as $\gamma \to 0+$ and the critical pressure determined from a purely elastic response ($\gamma = 0$). In their concluding remarks, Hegemier and Tzung go on to state that for the arch subject to impulsive loading and sufficiently small disturbances, only symmetric snapping is possible because small asymmetric disturbances will be damped out. Considering step pressure loading and axisymmetric deformations of a spherical cap, Mescall and Tsui [7] do not obtain dynamic response characteristics suggested by Hegemier and Tzung. Instead they find dynamic critical pressures to be about one-half the static values and a smooth increase in the dynamic critical pressures with increasing damping.

Basic Equations

In dimensionless form the equations governing the nonlinear planar vibrations of the shallow circular shell (or arch) modeled as a Kelvin-Voigt material (see Fig. 1) are

$$\ddot{\phi} + \lambda^{-4}(\phi'''' + \gamma\dot{\phi}'''') - (1 + \phi'')(\eta + \gamma\dot{\eta}) = 0 \tag{1}$$

$$\eta = -(1/2)\int_{-1}^{+1} [\phi - (1/2)(\phi')^2]d\Gamma \tag{2}$$

where $\beta^2\eta$ is the spatially uniform circumferential strain of the midsurface and[1]

$$\phi = w/a\beta^2, \quad \lambda^2 = \sqrt{12}(\beta^2 a/h) \simeq \sqrt{48}(H_0/h) \tag{3}$$

Contributed by the Applied Mechanics Division for publication in the JOURNAL OF APPLIED MECHANICS.

Discussion on this paper should be addressed to the Editorial Department, ASME, United Engineering Center, 345 East 47th Street, New York, N. Y. 10017, and will be accepted until December 1, 1980. Readers who need more time to prepare a discussion should request an extension from the Editorial Department. Manuscript received by ASME Applied Mechanics Division, March, 1979.

[1] It is noted that equation (3) in [1] is missing a square root sign.

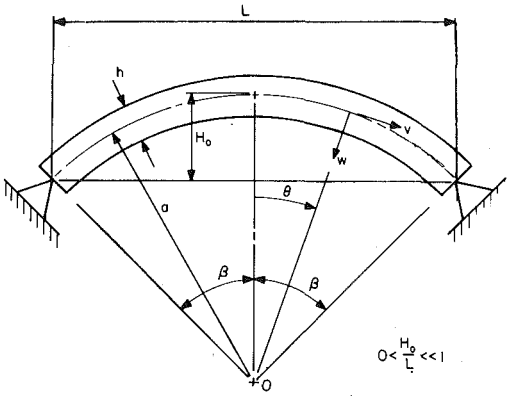

Fig. 1 Shallow circular arch

in which w is the radial displacement, a is the midsurface radius, H_0 is the maximum arch rise, h is the arch thickness, and β is the semi-opening angle of the arch. The dot and prime indicate partial derivatives with respect to dimensionless time τ and scaled polar angle Γ, respectively, where

$$\tau = ct/a, \quad c^2 = E/\rho(1-\nu^2), \quad \Gamma = \theta/\beta \tag{4}$$

in which t is real time, E and ν are the usual elastic constants, ρ is mass density, and θ is the polar angle. The dimensionless damping coefficient γ is given by

$$\gamma = (\zeta/a)[(1-\nu^2)/E\rho]^{1/2} \tag{5}$$

In (5), ζ is the actual damping coefficient in the Kelvin-Voigt constitutive equation

$$\sigma = \frac{E}{1-\nu^2}e + \zeta\frac{\partial e}{\partial t}, \tag{6}$$

where σ and e refer to the normal stress and strain, respectively, in the circumferential direction for a surface parallel to the midsurface.

The shallow circular shell equations (1) and (2) for a Kelvin-Voigt material model may be obtained from the shallow arch equations derived in [6]. In [6], one must specialize the initial shape to be circular (equivalent to a parabolic shape for a shallow arch), and substitute $E/(1-\nu^2)$ for E_0 to obtain (1) and (2).

The boundary conditions associated with (1) and (2) for a pinned-end arch are

$$\phi(\pm 1,\tau) = 0, \quad \phi''(\pm 1,\tau) = 0, \quad \tau > 0 \tag{7}$$

The initial conditions are taken as

$$\phi(\Gamma,0) = 0, \quad \dot{\phi}(\Gamma,0) = \epsilon u(\Gamma), \quad |\Gamma| < 1 \tag{8}$$

These initial conditions are equivalent to imparting a very short-duration impulsive load to the arch at the initial instant having a spatial distribution $u(\Gamma)$. It is convenient to normalize this spatial distribution by requiring

$$\langle u,u\rangle = 1, \tag{9}$$

where the scalar product of two functions is defined as

$$\langle u,v\rangle = \int_{-1}^{+1} u(\Gamma)v(\Gamma)d\Gamma \tag{10}$$

In this manner the dimensionless magnitude ϵ of the initial velocity in (8) can be related to the dimensionless initial kinetic energy $\tilde{T}(0)$ imparted to the arch by the impulsive load. The dimensionless kinetic energy of the arch is

$$\tilde{T} = (1/2)\lambda^4\langle\dot{\phi},\dot{\phi}\rangle \tag{11}$$

where

$$\tilde{T} = 12a(1-\nu^2)(\beta E h^3)^{-1}T \tag{12}$$

in which T is the actual kinetic energy per unit arch width. It follows from (8), (9), and (11) that

$$\tilde{T}(0) = (1/2)\lambda^4\epsilon^2 \tag{13}$$

Approximate Solution

An exact solution to (1) and (2) subject to conditions (7) and (8) is not available, so an approximate solution is sought. Here we use Galerkin's method and expand $\phi(\Gamma,\tau)$ as

$$\phi(\Gamma,\tau) = \sum_{n=1}^{\infty}[\zeta_n(\tau)\tilde{Z}_n(\Gamma) + \xi_n(\tau)\overline{Z}_n(\Gamma)] \tag{14}$$

The functions $\tilde{Z}_n(\Gamma)$ and $\overline{Z}_n(\Gamma)$ are the symmetric and antisymmetric mode shapes, respectively, of the free, undamped, infinitesimal vibrations of the arch about its undeformed configuration. These mode shapes are orthonormal and are given in the appendix of [1]. Coefficients $\zeta_n(\tau)$ and $\xi_n(\tau)$, then, represent the symmetric and antisymmetric generalized displacements. Substituting (14) into (1) and (2), and using Galerkin's method, results in the following ordinary differential equations for the generalized coordinates:

$$\ddot{\zeta}_i + \gamma\tilde{\mu}_i^2\dot{\zeta}_i + \tilde{\mu}_i^2\zeta_i + Q_{i2}(\zeta_l,\dot{\zeta}_l) + Q_{i3}(\zeta_l,\dot{\zeta}_l) + \pi^2 Q_{i1}(\zeta_l)\sum_k k^2\xi_k^2 + 2\gamma\pi^2[Q_{i1}(\zeta_l)]\sum_k k^2\xi_k\dot{\xi}_k = 0$$

$$\ddot{\xi}_i + \gamma\bar{\mu}_i^2\dot{\xi}_i + \bar{\mu}_i^2\xi_i + (i\pi)^2[S(\zeta_l) + \gamma\dot{S}(\zeta_l)]\xi_i + (i^2\pi^4/4)\left[\sum_j j^2\xi_j^2 + 2\gamma\sum_j j^2\xi_j\dot{\xi}_j\right]\xi_i = 0 \tag{15}$$

The parameters $\tilde{\mu}_i$ and $\bar{\mu}_i$ represent the symmetric and antisymmetric eigenfrequencies, respectively, and the polynomials in the symmetric displacements are

$$Q_{i1} = \eta_i/2 + (1/4)\sum_j P_{ij}\zeta_j$$

$$Q_{i2} = \sum_j\sum_k[(\eta_i P_{jk}/2 + \eta_k P_{ij})\zeta_j\zeta_k + \gamma(\eta_i P_{jk} + \eta_k P_{ij})\zeta_j\dot{\zeta}_k]$$

$$Q_{i3} = (1/4)\sum_j\sum_k\sum_l[(P_{ij}P_{kl})\zeta_j\zeta_k\zeta_l + 2\gamma(P_{ij}P_{kl})\zeta_j\zeta_k\dot{\zeta}_l]$$

$$S = \sum_j\eta_j\zeta_j + (1/4)\sum_j\sum_k P_{jk}\zeta_j\zeta_k \tag{16}$$

The coefficients η_i and P_{ij} are

$$\eta_i = -(1/2)\langle\tilde{Z}_i,1\rangle, \quad P_{ij} = \langle\tilde{Z}_i',\tilde{Z}_j'\rangle \tag{17}$$

Initial conditions on the generalized displacements are

$$\zeta_i(0) = \xi_i(0) = 0$$
$$\dot{\zeta}_i(0) = \epsilon\langle u,\tilde{Z}_i\rangle, \quad \dot{\xi}_i(0) = \epsilon\langle u,\overline{Z}_i\rangle \tag{18}$$

For numerical integration of (15), the series representation (14) was truncated to the first two symmetric modes and the first antisymmetric mode. Constraining the motion to a three-dimensional configuration subspace sacrifices quantitative accuracy but, as discussed in [1], this simplified model exhibits the qualitative features inherent to snap-through. The reduced set of equations (15) were integrated numerically using a Hamming Predictor-Corrector method for a specific arch rise of λ equal to five.

To specify various spatial distributions of the initial velocity consistent with (9), one may select

$$u(\Gamma) = [\tilde{Z}_1 + \tilde{\nu}\tilde{Z}_2 + \bar{\nu}(1+\tilde{\nu}^2)^{1/2}\overline{Z}_1]/D \tag{19}$$

where

$$D = [(1+\tilde{\nu}^2)(1+\bar{\nu}^2)]^{1/2} \tag{20}$$

such that initial conditions (18) become

$$\dot{\zeta}_1(0) = \epsilon/D, \quad \dot{\zeta}_2(0) = \tilde{\nu}\epsilon/D, \quad \dot{\xi}_1(0) = \bar{\nu}(1 + \tilde{\nu}^2)^{1/2}\epsilon/D \qquad (21)$$

The parameters $\tilde{\nu}$ and $\bar{\nu}$ represent initial direction parameters of the motion trajectory in the three-dimensional configuration space. If $\bar{\nu}$ vanishes, the spatial distribution (18) is symmetric and equations of motion (15) admit a purely symmetric response ($\xi_i = 0, \tau > 0$). Thus $\tilde{\nu}$ is interpreted both as a symmetric initial direction parameter and a symmetric spatial distribution parameter. Consequently the parameter $\bar{\nu}$ represents an asymmetric initial direction (distribution) parameter.

For specific values of γ, $\tilde{\nu}$, and $\bar{\nu}$ the equations of motion (15) were integrated for many values of ϵ. Each integration was carried out for 48 nondimensional time units. This corresponds to three periods of the lowest frequency mode which, for λ equal to five, is the antisymmetric mode. As discussed in [1], an extended integration time of five periods (80 nondimensional time units) did not significantly alter the critical magnitudes determined for finite time snap-through. Thus the three periods of the lowest frequency mode appeared an adequate length of time for numerical integration.

For each value of ϵ the displacement norm was obtained over the finite time integration period. This norm is defined as

$$R(\tau) = (\zeta_1^2 + \zeta_2^2 + \xi_1^2)^{1/2} \qquad (22)$$

The peak value of R on its initial oscillation and its maximum value during the entire period were recorded for each ϵ so the dependence of $R_{\max}$ on ϵ for both immediate and finite time snap-through could be determined and subsequently plotted. These plots are called response curves. According to the Budiansky-Roth criterion, critical magnitudes for both immediate and finite time snap-through correspond to "jumps" in these response curves.

To facilitate an understanding of the dynamic results and establish the lower bound estimate of ϵ_c, the results of the static analysis of equations (15) given in [1] are summarized here. The static equilibrium solutions of (15) are the critical points in the three-dimensional configuration space. The origin of this space represents the undeformed symmetric arch. For λ equal to five there are four additional symmetric equilibrium configurations and a pair of asymmetric configurations. The asymmetric pair have identical symmetric displacements and equal in magnitude, but opposite in sign, antisymmetric displacements. Of the seven critical points in the configuration space, only two are stable with respect to infinitesimal disturbances. These are the origin and a symmetric critical point whose norm R is near unity. The latter critical point corresponds to the static snap-through configuration. The asymmetric pair of critical points have the same potential energy, and it is the smallest potential energy of all the unstable critical points. Either of this pair, then, represents the "nearest" critical point to the origin in the sense of Hsu [2]. Here the one with a positive antisymmetric displacement is selected as nearest. Equating the potential energy of this nearest critical point to the initial kinetic energy (13) imparted to the arch gives the lower bound on the critical magnitude necessary for dynamic snap-through. For λ equal to five this value of ϵ is 0.1276. Hence the dynamic motion is stable against snap-through for any spatial distribution of the initial velocity if $\epsilon < 0.1276$.

Discussion of Numerical Results

In addition to a fixed arch rise with λ equal to five, the present results are limited to a specific value of 0.848404 for the symmetric component $\tilde{\nu}$ of the initial velocity distribution. This particular value of $\tilde{\nu}$ is the symmetric direction component of the nearest critical point to the origin of the configuration space. Values chosen for the asymmetric distribution parameter $\bar{\nu}$ range from zero to 0.40. This includes the particular value of $\bar{\nu} = 0.183666$ which is the asymmetric direction component of the nearest critical point. Thus increasing values of $\bar{\nu}$ imply increasing amounts of asymmetry in the initial velocity distribution, and the particular distribution with $\bar{\nu} = 0.183666$ starts the motion trajectory in the configuration space toward the nearest critical point.

Values selected for the damping parameter γ are 0, 0.005, 0.01, and 0.05. Undamped results are also given in [1] and are represented here with some refinements. The largest value of the damping parameter considered is approximately 1 percent of critical damping for the linear vibrations of the antisymmetric mode (lowest frequency mode for λ equal to five). Also, these values of γ seem physically reasonable. For example, damping coefficients determined from vibration tests of double cantilevered aluminum beams [8], as reported in [9], result in values of γ within the range used, for realistic arch radii in (5).

Some of the response curves obtained are shown in Figs. 2(*a*)–(*h*). Only the purely symmetric response ($\bar{\nu} = 0$) and nearly symmetric response ($\bar{\nu} = 0.025$) are shown for each value of γ. The jump criterion for the purely symmetric response is very distinct for both immediate and finite time snap-through. The critical magnitudes ϵ_c for immediate snap-through are slightly larger than for finite time snap-through. This difference decreases with increased damping and for $\gamma = 0.05$ it vanishes (i.e., snap-through occurs on the initial oscillation). For finite time snap-through and $\bar{\nu} = 0$, the critical magnitude increases from 0.189 at $\gamma = 0$ to 0.198 at $\gamma = 0.05$ (a 4.8 percent increase).

A small amount of asymmetry ($\bar{\nu} = 0.025$) in the initial velocity's spatial distribution causes dramatic changes in the response curves with respect to those of the purely symmetric response, as shown in Figs. 2(*b*), (*d*), and (*f*). The finite time snap-through curves exhibit alternating jumps to snap-through and back with increasing ϵ. The initial jump in $R_{\max}$ to snap-through ($R_{\max}$ near unity) occurs at a substantially lower magnitude of ϵ than for the purely symmetric results. This alternating pattern in the finite time response curves for $\bar{\nu} = 0.025$ persists for $\gamma = 0.005$ and 0.01, but is damped out for $\gamma = 0.05$. Contrary to the assertion of Hegemier and Tzung [5] that only symmetric snapping is possible if $\gamma \neq 0$, the present results show a strong influence of small asymmetric perturbations on dynamic snapping, even in the presence of small damping, as evidenced by comparing Figs. 2(*c*) and (*d*). Apparently the qualitative character of the finite time snapping phenomenon for small damping is the same as in the undamped case.

Although not presented here, the time histories of the individual displacements imply that the symmetric response is unstable with respect to asymmetric perturbations. For small asymmetric perturbations, the symmetric motion parametrically excites the growth of the asymmetric displacement, which in turn reacts with the symmetric motion. This instability may or may not lead to dynamic snap-through, as the alternating pattern of the response curves show. Parametrically induced snap-through was used as an explanation by Lock [4] for dynamic critical step pressure loads exceeding the static critical pressure loads for sufficiently large arch rises. A recent paper [10] reviews other current literature on snap-through by parametric excitation.

The immediate snap-through response curves in Figs. 2(*b*), (*d*), and (*f*) do not exhibit a large jump as they do for the purely symmetric results shown in Figs. 2(*a*), (*c*), and (*e*). Consequently, the Budiansky-Roth criterion is quite subjective. This gradual rise in the response curves was also noted for centrally distributed step pressure loads applied to spherical caps [11].

The critical magnitudes ϵ_c determined from the response diagrams are plotted versus the distribution (direction) parameter $\bar{\nu}$ in Figs. 3(*a*)–(*d*). Also shown in each of these figures is the lower bound estimate of ϵ_c determined by Hsu's criterion. The critical magnitudes for undamped finite time snap-through in Fig. 3(*a*) decrease very rapidly for small increases in $\bar{\nu}$ from $\bar{\nu} = 0$, and remain relatively close to the lower bound.[2] The "jump-in-response" criterion is very distinct for most finite time results and hence critical magnitudes were easily determined for Figs. 3(*a*)–(*d*). An exception is shown in Fig. 3(*d*) for

[2] Fig. 3(*a*) is a refinement of Fig. 5 in [1]. In the present work many values of ϵ for each distribution in the undamped case were used to generate more precise response curves like Fig. 2(*b*). Thus the determination of the critical magnitudes for finite time snap-through is more precise.

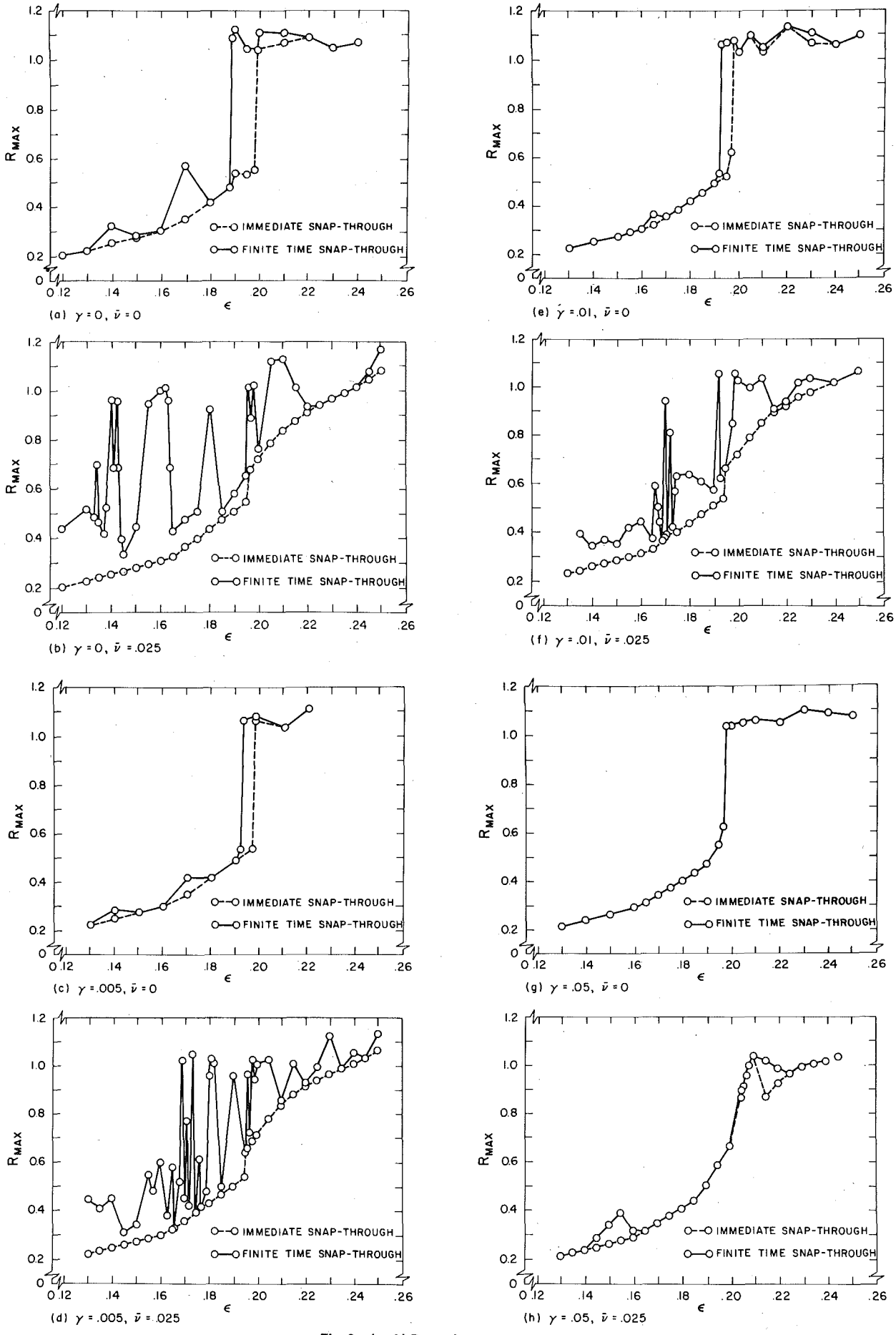

Fig. 2 (*a–h*) Dynamic response curves

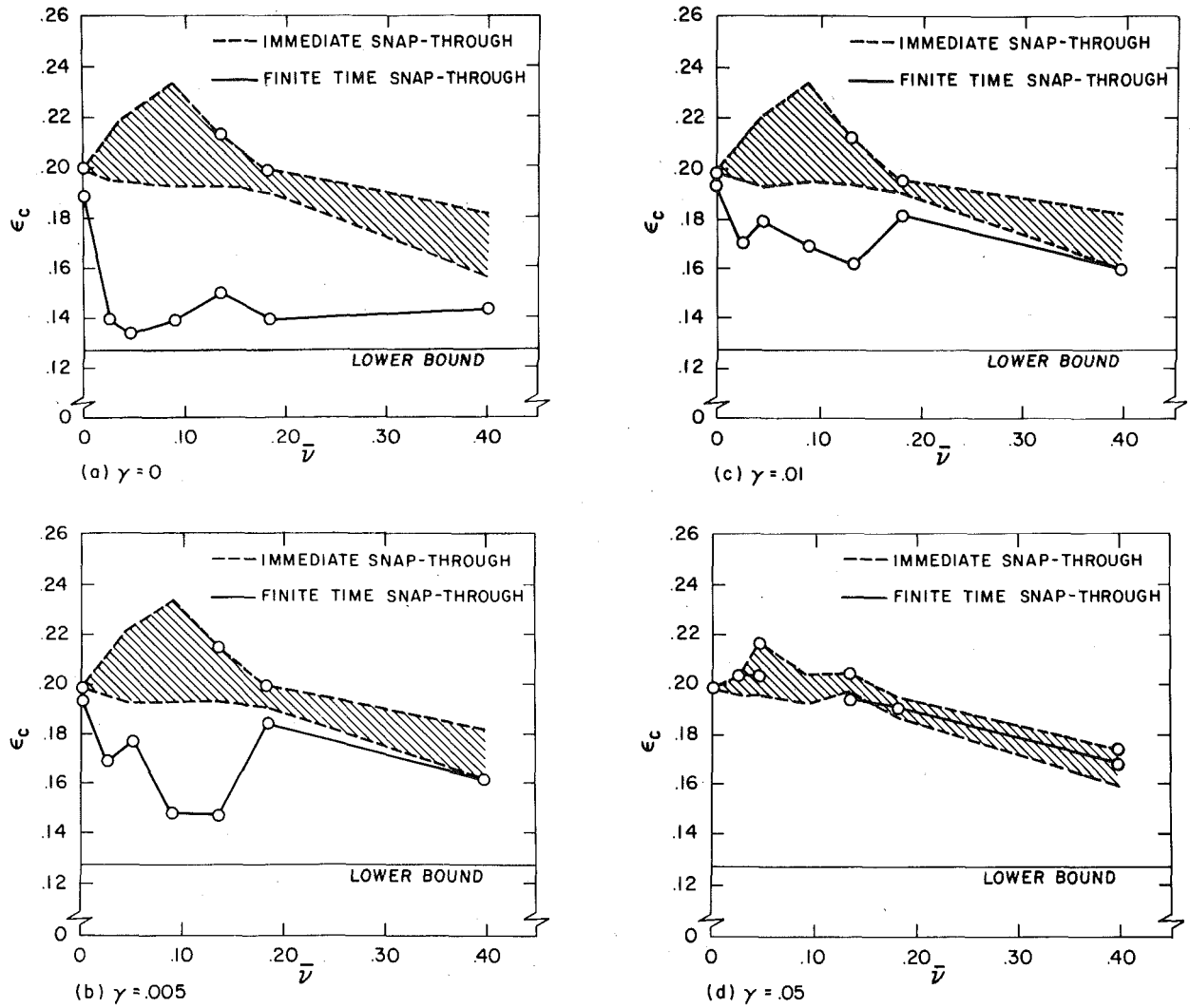

Fig. 3 (*a–d*) Critical magnitude versus distribution

$\bar{\nu} = 0.09$ and $\gamma = 0.05$ where no distinct jump in the finite time response existed so the critical magnitude was not defined. Figs. 3(*b*)–(*d*) show that small amounts of damping significantly affect the finite time critical magnitudes for all distributions considered. As the damping increases, these critical magnitudes approach those of immediate snap-through. As the damping decreases, there appears to be a smooth decrease in critical magnitudes to their undamped ($\gamma = 0$) values.

In most cases where $\bar{\nu} \neq 0$, the immediate snap-through critical magnitudes could not be determined, since no distinct jumps in the response curves occurred. Instead, a range of critical magnitudes is shown, based on R_{max} varying from 0.6 to 0.862. The latter value is the norm of the nearest critical point. The larger this range is for a given $\bar{\nu}$, the more gradual is the increase in R_{max} on the initial oscillation with increasing ϵ. If a distinct jump in R_{max} greater than 0.2 occurred for immediate snap-through results, this value of ϵ is circled in Figs. 3(*a*)–(*d*).

Concluding Remarks

Critical magnitudes of the initial velocity, determined by direct time integration and the Budiansky-Roth criterion, are a function of the initial velocity's spatial distribution and material viscous damping. For the elastic response (see Fig. 3(*a*)) the critical magnitudes for finite time snap-through are appreciably reduced for nonsymmetric distributions ($\bar{\nu} \neq 0$) of the load. For these same distributions, the undamped critical magnitudes for immediate snap-through are not precisely defined by the Budiansky-Roth criterion. This subjectivity is reflected in a range of ϵ determined for each distribution which results in a R_{max} value varying from 0.60 to 0.862 on the initial oscillation of the response. The critical magnitudes are compared to a lower bound estimate formulated by Hsu [2] which is independent of the spatial distribution and damping. This lower bound is a good estimate of the undamped finite time critical magnitudes for nonsymmetric distributions, but is a very conservative estimate of the range of undamped critical magnitudes for immediate snap-through.

Small viscous damping significantly increases the finite time critical magnitudes (see Figs. 3(*b*)–(*d*)). Immediate snap-through critical magnitudes remain subjective and their range is essentially unaffected for damping coefficients γ of 0.005 and 0.01. For $\gamma = 0.05$ finite time and immediate snap-through critical magnitudes approximately coincide, and the range of subjectivity for immediate snap-through is appreciably decreased. It is apparent, then, that the lower bound estimate becomes quite conservative when small dissipation is included. However, it remains precise. For $\gamma = 0.05$ the critical magnitude is approximately 69 percent higher than the lower bound for a distribution with small asymmetry ($\bar{\nu} = 0.045$), and is 33 percent high for a distribution with larger asymmetry ($\bar{\nu} = 0.40$).

References

1 Johnson, E. R., and McIvor, I. K., "The Effect of Spatial Distribution on Dynamic Snap-Through," ASME JOURNAL OF APPLIED MECHANICS, Vol. 45, No. 3, Sept. 1978, pp. 612–618.

2 Hsu, C. S., "On Dynamic Stability of Elastic Bodies With Prescribed

Initial Conditions," *International Journal of Engineering Science,* Vol. 4, 1966, pp. 1–21.

3 Budiansky, B., and Roth, R. S., "Axisymmetric Dynamic Buckling of Clamped Spherical Caps," NASA TN D-1510, Dec. 1962, pp. 597–606.

4 Lock, M. H., "Snapping of a Shallow Sinusoidal Arch Under a Step Pressure Load," *AIAA Journal,* Vol. 4, No. 7, July 1966, pp. 1249–1256.

5 Hegemier, G. A., and Tzung, F., "Influence of Damping on the Snapping of a Shallow Arch Under a Step Pressure Load," *AIAA Journal,* Vol. 7, No. 8, Aug. 1969, pp. 1494–1499.

6 Huang, N. C., and Nachbar, W., "Dynamic Snap-Through of Imperfect Viscoelastic Shallow Arches," ASME JOURNAL OF APPLIED MECHANICS, Vol. 35, No. 2, June 1968, pp. 289–296.

7 Mescall, J., and Tsui, T., "Influence of Damping on Dynamic Stability of Spherical Caps Under Step Pressure Loading," *AIAA Journal,* Vol. 9, No. 7, July 1971, pp. 1244–1248.

8 Granick, N., and Stern, J. E., "Material Damping of Aluminum by a Resonant-Dwell Technique," NASA TN D-2893, Aug. 1965.

9 Lazan, B. J., *Damping of Materials and Members in Structural Mechanics,* Pergamon Press, 1968, p. 208.

10 Holzer, S. M., "Dynamic Snap-Through of Shallow Arches and Spherical Caps," *The Shock and Vibration Digest,* Vol. 11, No. 3, Mar. 1979, pp. 3–6.

11 Stephens, W. B., and Fulton, R. E., "Axisymmetric Static and Dynamic Buckling of Spherical Caps Due to Centrally Distributed Pressures," *AIAA Journal,* Vol. 7, No. 11, Nov. 1969, pp. 2120–2126.

D. Hui
Doctoral Research Assistant.
Assoc. Mem. ASME

J. S. Hansen
Assistant Professor.
Institute of Aerospace Studies,
University of Toronto,
Downsview,
Ontario, Canada M3H 5T6

Two-Mode Buckling of an Elastically Supported Plate and Its Relation to Catastrophe Theory

Classical buckling and initial postbuckling of a geometrically imperfect infinite plate on a nonlinear elastic foundation under two independent applied compressive loads are analyzed. The plate is assumed to have imperfections of the same form as the buckling modes. It is found that single mode behavior occurs when the two independent loads N_x and N_y are unequal. A two-mode case occurs when the two applied loads are equal and the form of the instability falls into the category of the parabolic umbilic type one or type two, depending on the quadratic and cubic spring constants. The importance of the contribution of the quartic term and imperfection-sensitivity is examined. The analysis is studied within the context of Koiter's general theory of multimode postbuckling behavior.

Introduction

Catastrophe theory [1] and the theory of elastic stability [2–5] are two independently developed theories which deal with the stability analysis of physical systems which evolve as a function of certain prescribed parameters. As such, these theories are closely related to one another and have resulted in a number of papers [6–8] which provide comparative studies. It is evident from the foregoing that catastrophe theory is effective in the classification of the forms of instability which may occur while the task of actually providing a method of analysis of physical systems has been taken up in the theory of elastic stability.

Thompson and Hunt [6] were among the first to investigate the similarity between the theory of elastic stability and catastrophe theory and they provided a comparative study of the various types of instability mechanisms. Sewell [7] provided a series of examples which demonstrated various forms of the elementary catastrophes while Huseyin [8] considered the comparison between the theory of multiple-parameter systems and catastrophe theory. Further, a general analysis of two-mode buckling problems and their relation to the hyperbolic and elliptic catastrophes were presented in [9]. In addition, the parabolic umbilic catastrophe was first analyzed in depth in terms of the theory of elastic stability in [10] and was then applied to the two-mode buckling problem of an imperfection-sensitive externally pressurized spherical shell. Further applications to various simple structures can also be found in [11, 12].

Contributed by the Applied Mechanics Division for publication in the JOURNAL OF APPLIED MECHANICS.

Discussion on this paper should be addressed to the Editorial Department, ASME, United Engineering Center, 345 East 47th Street, New York, N. Y. 10017, and will be accepted until December 1, 1980. Readers who need more time to prepare a discussion should request an extension from the Editorial Department. Manuscript received by ASME Applied Mechanics Division, February, 1979; final revision, October, 1979.

The present paper deals with the two-mode initial postbuckling analysis of an infinite plate resting on a nonlinear elastic foundation. It is found that the resulting form of the potential energy falls into the category of the parabolic umbilic model of catastrophe theory. This represents an extension of a paper by Reissner [13] in which he showed that this problem is qualitatively similar to the two-mode buckling problem of an externally pressurized spherical shell [14] in that the expanded potential energy takes a similar form. A Koiter style analysis is used and the problem is attacked using a UVW displacement formulation.

The analysis considers the case of two independent compressive in-plane loads N_x and N_y and it is shown that in general there exists a unique eigenvalue for the buckling problem. However, in the particular situation that $N_x = N_y$, an infinite number of buckling modes are involved. In the present case, the analysis is focused on a two-mode interaction problem and it is shown that this leads to a stability problem which takes the form of the parabolic umbilic catastrophe. Critical load-imperfection results are obtained and it is demonstrated that the inclusion of two independent load parameters, as specified by catastrophe theory, can significantly alter the results. In addition, the results show that higher-order terms of the potential energy for the present two-mode plate buckling problem cannot always be neglected in this type of asymptotic analysis.

Potential Energy

The potential energy of a plate resting on a nonlinear elastic foundation can be expressed as

$$\text{P.E.} = U_m + U_b + U_F - U_W \tag{1}$$

where U_m is the membrane strain energy, U_b is the bending strain energy, U_F is the strain energy of the elastic foundation, and U_W is the work done (positive for compessive loads) by the applied load. The aforementioned quantities are given by

$$U_m = \frac{Et}{2(1-\nu^2)} \iint \left\{ \left[U_{,x} + \frac{1}{2} W^2_{,x} + V_{,y} + \frac{1}{2} W^2_{,y} \right]^2 - 2(1-\nu) \left[\left(U_{,x} + \frac{1}{2} W^2_{,x} \right) \left(V_{,y} + \frac{1}{2} W^2_{,y} \right) - \frac{1}{4} \left(U_{,y} + V_{,x} + W_{,x} W_{,y} \right)^2 \right] \right\} dxdy \quad (2)$$

$$U_b = \frac{Et^3}{24(1-\nu^2)} \iint \left[\left(W_{,xx} + W_{,yy} \right)^2 - 2(1-\nu) \left(W_{,xx} W_{,yy} - W^2_{,xy} \right) \right] dxdy \quad (3)$$

$$U_F = \frac{Et}{2(1-\nu^2)} \iint \left[\frac{1}{2} k_1 W^2 + \frac{1}{3} k_2 W^3 + \frac{1}{4} k_3 W^4 \right] dxdy \quad (4)$$

and

$$U_W = \int\int N_x U_{,x} dxdy + \int\int N_y V_{,y} dxdy \quad (5)$$

In the foregoing, E is Young's modulus, t is the thickness of the plate, ν is Poisson's ratio, (U, V, W) is the displacement vector of the middle plane of the plate, k_2, k_2, k_3 are related to the linear, quadratic, and the cubic spring constants of the elastic foundation, respectively, and N_x, N_y are the in-plane, applied loads in the x,y-directions respectively.

The prebuckling state of a plate is composed of end shortening in the two in-plane directions with no out-of-plane displacement. Therefore, the total displacement takes the form

$$U = c_1 x + u, \quad V = c_2 y + v, \quad W = w \quad (6)$$

where c_1 and c_2 are functions of the applied loads and u, v, w are incremental displacements which are zero prior to buckling.

Substituting the total displacement into the potential energy expression and then grouping the terms according to the powers of the incremental displacements, the potential energy may be expressed as

$$P^\lambda[u] = P_1{}^\lambda[u] + P_2{}^\lambda[u] + P_3{}^\lambda[u] + P_4{}^0[u] + \ldots \quad (7)$$

where $P_i{}^\lambda[u]$ is a function of the ith degree in the perturbed displacements and u represents the vector of displacements $[u, v, w]^T$. The superscript λ indicates that the functional contains terms which depend on the applied loads and the superscript 0 implies that the functional is independent of the applied loads.

Explicit values for c_1 and c_2 are obtained from the requirement that $P_1{}^\lambda[u]$ must vanish in order that the prebuckling state be an equilibrium state. Using this condition yields

$$c_1 = -\frac{1}{Et}[N_x - \nu N_y]; \quad c_2 = -\frac{1}{Et}[N_y - \nu N_x] \quad (8)$$

The remaining quantities $P_2{}^0[u]$, $P_2{}'[u]$, $P_2{}^*[u]$, and $P_4{}^0[u]$ are

$$P_2{}^0[u] = \frac{Et}{2(1-\nu^2)} \iint \left\{ u^2_{,x} + v^2_{,y} + \frac{1}{2}(1-\nu)(u_{,y} + v_{,x})^2 + 2\nu(u_{,x} v_{,y}) + \left(\frac{t^2}{12} \right) [w^2_{,xx} + w^2_{,yy} + 2\nu w_{,xx} w_{,yy} + 2(1-\nu) w^2_{,xy}] + \frac{1}{2} k_1 w^2 \right\} dxdy \quad (9)$$

$$P_2{}'[u] = -\iint \frac{1}{2} w^2_{,x} dxdy \quad (10)$$

$$P_2{}^*[u] = -\iint \frac{1}{2} w^2_{,y} dxdy \quad (11)$$

$$P_3{}^0[u] = \frac{Et}{2(1-\nu^2)} \iint u_{,x} w^2_{,x} + v_{,y} w^2_{,y} + \nu(u_{,x} w^2_{,y}) + (v_{,y} w^2_{,x}) + (1-\nu)(u_{,y} + v_{,x})(w_{,x} w_{,y}) + \frac{1}{3} k_2 w^3 dxdy \quad (12)$$

$$P_4{}^0[u] = \frac{Et}{2(1-\nu^2)} \iint \frac{1}{4}(w^2_{,x} + w^2_{,y})^2 + \frac{1}{4} k_3 w^4 dxdy \quad (13)$$

where

$$P_2{}'[u] = \frac{\partial}{\partial N_x} P_2{}^\lambda[u] \quad \text{and} \quad P_2{}^*[u] = \frac{\partial}{\partial N_y} P_2{}^\lambda[u]$$

In the foregoing, it may be noted that $P_3{}^0[u]$ has replaced $P_3{}^\lambda[u]$. This results because of the linearity of the prebuckling problem.

Classical Buckling Load

The classical critical load is determined from the condition that the first and second variations of the quadratic terms in the potential energy must vanish. These calculations take the form of an eigenvalue problem in terms of N_x and N_y, with the set of minimum values corresponding to the locus of classical critical loads.

The eigenfunctions are easily found as

$$u_{k_x k_y} = 0; \quad v_{k_x k_y} = 0$$

$$w_{k_x k_y} = \begin{matrix} \sin \\ \cos \end{matrix} \left(k_x \frac{x}{q} \right) \begin{matrix} \sin \\ \cos \end{matrix} \left(k_y \frac{y}{q} \right)$$

with the corresponding eigenvalues defined by

$$\lambda_x k_x{}^2 + \lambda_y k_y{}^2 = \frac{1}{2}[(k_x{}^2 + k_y{}^2)^2 + 1] \quad (14)$$

In obtaining these results the nondimensional quantities λ_x, λ_y have been introduced as

$$(\lambda_x, \lambda_y) = \frac{6(1-\nu^2)q^2}{Et^3}(N_x, N_y)$$

where $q = [t^2/6k_1]^{1/4}$. In addition, k_x, k_y are the wave numbers in the x, y-directions, respectively.

The classical critical load is obtained as the least value of this expression when it is minimized with respect to the wave numbers $k_x{}^2$ and $k_y{}^2$. Also, since λ_x and λ_y are assumed to be independent, there is a locus of values of λ_x and λ_y which defines the classical critical load. This locus of values may be determined in a number of ways; however, in the present case it is determined by assuming a prescribed relationship between λ_x and λ_y and another parameter λ, and then determining the least value of λ. Doing so yields

$$\lambda_x \equiv \alpha\lambda; \quad \lambda_y \equiv \beta\lambda$$

where α and β (not both zero) take the values $0 \le (\alpha, \beta) \le 1$. Thus the eigenvalue equation can be rewritten as

$$\lambda = \frac{(k_x{}^2 + k_y{}^2)^2 + 1}{2(\alpha k_x{}^2 + \beta k_y{}^2)} \quad (15)$$

For the case $0 \le \beta < \alpha$ it may be shown that the minimum eigenvalues are

$$\lambda_{x_{cl}} = 1; \quad 0 \le \lambda_{y_{cl}} < 1 \quad (16)$$

where

$$\lambda_{y_{cl}} = \left(\frac{\beta}{\alpha} \right)$$

corresponding to the wave numbers

$$k_x{}^2 = 1; \quad k_y{}^2 = 0 \quad (17)$$

A second possibility $0 \le \alpha < \beta$ follows in a parallel manner and yields identical results with the interchange of $\lambda_{x_{cl}}$ and $\lambda_{y_{cl}}$ as well as k_x and k_y in the aforementioned. The third possibility which arises is that due to the uniform compression case $\alpha = \beta$. For this situation the least eigenvalue is

$$\lambda_{x_{cl}} = 1; \quad \lambda_{y_{cl}} = 1 \quad (18)$$

corresponding to the critical wave numbers

$$k_x{}^2 + k_y{}^2 = 1 \quad (19)$$

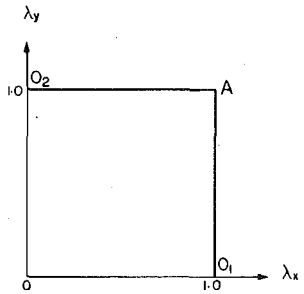

Fig. 1 Interaction of the critical loads $\lambda_{x_{cl}}$ and $\lambda_{y_{cl}}$

The previous eigenvalue will be designated as λ_{cl} or in dimensional form

$$N_{cl} = \frac{Et^3}{6(1-\nu^2)q^2}$$

These results, which yield the buckling load interaction for the independent applied loads N_x and N_y, are presented in Fig. 1. The interaction curves are obtained as the straight lines O_1A and O_2A, respectively. Excluding the point A, any point which lies on the line O_1A implies a state of single mode buckling. Similarly, any point on the line O_2A leads to a state of single mode buckling. The point A represents the case when the applied loads are of equal magnitude and for which multimode buckling occurs as there exist more than one set of wave numbers k_x and k_y which satisfy the condition for a minimum eigenvalue.

From this point on, the analysis will concentrate on the two-mode buckling problem which results when the critical wave numbers are given by

$$k_x = 1, \quad k_y = 0 \quad \text{First mode}$$
$$k_x = \frac{1}{2}, \quad k_y = \frac{\sqrt{3}}{2} \quad \text{Second mode} \tag{20}$$

or by the identical situation when k_x and k_y are interchanged. The specification of this particular combination of k_x and k_y may seem rather arbitrary and quite restricitve; however, it represents an important stepping stone to the multiple mode buckling situations. That is, for the possibilities involving $\lambda_{x_{cl}} \neq \lambda_{y_{cl}}$, single mode buckling occurs which has been adequately treated elsewhere. In addition, for the situation $\lambda_{x_{cl}} = \lambda_{y_{cl}}$, the foregoing combinations of k_x and k_y lead to the only two-mode problem which has nontrivial cubic terms in the potential energy. Thus, since higher-order instabilities contain the lower-order ones as special cases, it is appropriate to obtain a complete understanding of the lower-order problem. This has not been considered previously.

Initial Postbuckling of a Two-Mode System

Following Koiter's method of analysis [2], the potential energy of a two-mode system can be expanded in a Taylor's series about the classical critical load of the perfect system. Upon expansion, the approximation to the potential energy becomes

$$PE = (N_x - N_{cl})P_2'[u_c] + (N_y - N_{cl})P_2^*[u_c] + P_3^0[u_c] + \ldots + N_xP_{11}'[u_c, \bar{u}] + N_yP_{11}^*[u_c, \bar{u}] + \ldots \tag{21}$$

where $\bar{u}$ are initial imperfections which are taken in the same form as the buckling modes. The two sets of wave numbers given in the last section yields the critical modes

$$u_c^1 = [u_c^1, v_c^1, w_c^1]^T = t\xi_1[0, 0, \cos(x/q)]^T$$
$$u_c^2 = [u_c^2, v_c^2, w_c^2]^T = t\xi_2[0, 0, \cos(x/2q)\cos(\sqrt{3}y/2q)]^T \tag{22}$$

Upon substitution of the eigenvectors into the potential energy and carrying out the appropriate integration, the quadratic terms become

$$P_2'[u_c] = -\frac{1}{4}\left(\xi_1^2 + \frac{\xi_2^2}{8}\right)S_0\left(\frac{t}{q}\right)^2$$
$$P_2^*[u_c] = -\frac{1}{4}\left(\frac{3}{8}\xi_2^2\right)S_0\left(\frac{t}{q}\right)^2 \tag{23}$$

The terms involving the initial imperfections are

$$P_{11}'[u_c, \bar{u}] = -\frac{1}{2}\left(\xi_1\bar{\xi}_1 + \frac{1}{8}\xi_2\bar{\xi}_2\right)S_0\left(\frac{t}{q}\right)^2$$
$$P_{11}^*[u_c, \bar{u}] = -\frac{1}{2}\left(\frac{3}{8}\xi_2\bar{\xi}_2\right)S_0\left(\frac{t}{q}\right)^2 \tag{24}$$

where $\bar{\xi}_1\bar{\xi}_2$ are the imperfection amplitudes. The cubic contribution is given by

$$P_3^0[u_c] = \frac{Et}{2(1-\nu^2)}\iint\frac{1}{3}k_2(w_c^1 + w_c^2)^3 dx\,dy,$$

which can be expressed as

$$P_3^0[u_c] = P_3^0[u_c^1] + P_{21}^0[u_c^1, u_c^2] + P_{12}^0[u_c^1, u_c^2] + P_3^0[u_c^2]$$

Upon evaluation, the various terms become

$$P_{12}^0[u_c^1, u_c^2] = \frac{Et}{2(1-\nu^2)}(\xi_1\xi_2^2)(t^3k_2/8)S_0$$
$$P_3^0[u_c^1] = P_{21}^0[u_c^1, u_c^2] = P_3^0[u_c^2] = 0 \tag{25}$$

The fact that the last three terms vanish leads to the requirement [10] that higher-order quantities must be retained in the first approximation to the potential energy. The appropriate quantity for the present problem is a quartic and with the inclusion of this term the problem falls into the classification of the parabolic umbilic catastrophe. The additional term which is required is $P_4^0[u_c^1] - P_2^\lambda[u_2]$ where

$$P_4^0[u_c^1] = \frac{Et}{2(1-\nu^2)}\left[\frac{3}{32}\right][1 + q^4k_3]\left[\frac{t}{q}\right]^4\xi_1^4S_0 \tag{26}$$

and where $u_2 = [u_2, v_2, w_2]^T$ is the solution of the second-order perturbation problem. Following Koiter [2], u_2 is given by the solution of

$$P_{11}^\lambda[u_2, \delta u_2] = -P_{21}^0[u_c^1, \delta u_2] \tag{27}$$

subject to the appropriate orthogonality conditions for u_2. The set of differential equations for u_2, v_2, w_2 is then obtained as

$$2u_{2,xx} + (1+\nu)v_{2,xy} + (1-\nu)u_{2,yy} = -\xi_1^2\frac{t^2}{q^3}\sin\left(\frac{2x}{q}\right)$$
$$2v_{2,yy} + (1+\nu)u_{2,xy} + (1-\nu)v_{2,xx} = 0 \tag{28}$$
$$\frac{t^2}{6}[w_{2,xxxx} + 2w_{2,xxyy} + w_{2,yyyy}] + k_1w_2 + \frac{2(1-\nu^2)}{Et}[N_xw_{2,xx} + N_yw_{2,yy}] = -\frac{1}{2}\xi_1^2t^2k_2\left(1 + \cos\frac{2x}{q}\right)$$

and where it is noted that the influence of the boundary conditions has been omitted and are replaced by a periodicity requirement.

The solution of the aforementioned differential equations is of the form

$$u_2 = (s_1)(\xi_1^2)\left(\sin\frac{2x}{q}\right)$$
$$v_2 = s_2$$
$$w_2 = s_3\xi_1^2 + s_4\xi_1^2\cos\frac{2x}{q} \tag{29}$$

Since only derivatives of v_2 appear in $P_2^\lambda[u_2]$ then s_2 need not be

evaluated. Thus, substituting the expressions for u_2 and w_2 into the differential equations, the constants s_1, s_3, and s_4 can be evaluated. Doing so yields

$$s_1 = \frac{t^2}{8q}, \quad s_3 = -\frac{t^2}{2}\frac{k_2}{k_1}, \quad s_4 = -\frac{t^2}{18}\frac{k_2}{k_1}$$

and therefore the desired modification to the quartic term is

$$-P_2^{\lambda}[u_2] = \frac{Et}{2(1-\nu^2)}\left(\frac{t}{q}\right)^4\left\{-\frac{1}{32} - \frac{19q^4}{144}\frac{(k_2)^2}{k_1}\right\}\xi_1^4 S_0 \tag{30}$$

Now, assembling the results from equations (23)–(26) and (30), the approximation to the potential energy becomes

$$PE = \frac{Et}{2(1-\nu^2)}\left(\frac{t}{q}\right)^4 S_0\left\{\frac{1}{12}(1-\lambda_x)\left(\xi_1^2 + \frac{1}{8}\xi_2^2\right) + \frac{1}{12}(1-\lambda_y)\frac{3}{8}\xi_2^2 + \frac{1}{8}K_2\xi_1\xi_2^2 + C_{40}\xi_1^4 - \frac{1}{6}\lambda_x(\bar{\xi}_1\xi_1 + \frac{1}{8}\bar{\xi}_2\xi_2) - \frac{1}{6}\lambda_y\left(\frac{3}{8}\bar{\xi}_2\xi_2\right)\right\} \tag{31}$$

where

$$C_{40} = \frac{1}{16}\left[1 + \frac{3}{2}K_3 - \frac{38}{3}(K_2)^2\right] \tag{32}$$

and where $K_2 = (q^4/t)\,k_2$, $K_3 = q^4 k_3$ are nondimensional spring constants. The equilibrium equations and stability determinant for the foregoing may now be obtained directly as

$$(1-\lambda_x)\xi_1 + \frac{3}{4}K_2\xi_2^2 + 24C_{40}\xi_1^3 = \lambda_x\bar{\xi}_1$$

$$\left[\frac{1}{8}(1-\lambda_x) + \frac{3}{8}(1-\lambda_y)\right]\xi_2 + \frac{3}{2}K_2\xi_1\xi_2 = \frac{1}{8}(\lambda_x + 3\lambda_y)\bar{\xi}_2 \tag{33}$$

and

$$\begin{bmatrix} (1-\lambda_x) + 72C_{40}\xi_1^2 & \frac{3}{2}K_2\xi_2 \\ \frac{3}{2}K_2\xi_2 & \left[\frac{1}{8}(1-\lambda_x) + \frac{3}{8}(1-\lambda_y) + \frac{3}{2}K_2\xi_1\right] \end{bmatrix} \tag{34}$$

respectively.

Transformation to Standard Form

The previously obtained potential energy expression can be transformed to the standard form of the parabolic umbilic by introducing the nondimensional quantities x, y, L_1, L_2, ϵ_1, and ϵ_2 (x and y not to be confused with coordinates of plate). The appropriate expressions are

$$x = C^*\xi_1, \quad y = [K_2/8C^*]^{1/2}\xi_2$$

$$L_1 = \frac{1}{12}(1-\lambda_x)/C^{*2} \quad L_2 = \frac{1}{12}[(1-\lambda_x) + 3(1-\lambda_y)][C^*/K_2]$$

$$\epsilon_1 = \frac{1}{6}[\lambda_x/C^*]\bar{\xi}_1 \quad \epsilon_2 = \frac{1}{6}(\lambda_x + 3\lambda_y)\sqrt{C^*/8K_2}\,\bar{\xi}_2$$

where

$$C^* = \sqrt[4]{|C_{40}|}.$$

Thus, after division by a constant, the potential energy is transformed to the form

$$PE = \pm x^4 + xy^2 + L_1x^2 + L_2y^2 - \epsilon_1 x - \epsilon_2 y$$

where the "+" or "−" signs correspond to C_{40} being positive or negative, respectively. The stability problem is therefore characterized by four control parameters (L_1, L_2, ϵ_1, ϵ_2) which are defined by the loads λ_x and λ_y and the initial geometric imperfections $\bar{\xi}_1$ and $\bar{\xi}_2$. The two cases defined by a positive or negative coefficient C_{40} result in distinctive stability problems and these are termed the parabolic umbilic types one and two, respectively. Fig. 2 shows the range of parameters K_2, K_3 which lead to either of these possibilities. Here, the hatched region corresponds to the type one case, the line represents a singular case when C_{40} vanishes (which is not treated in the context of the present analysis) and the remainder is the type two case.

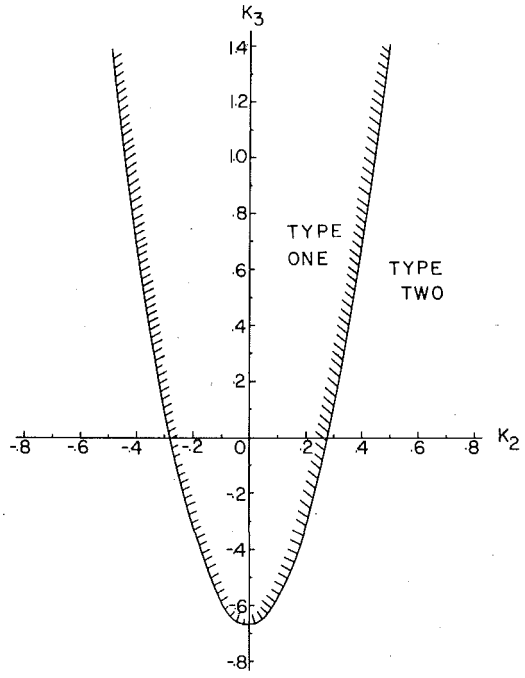

Fig. 2 Range of spring constants K_2 and K_3 which leads to the parabolic umbilic type one and type two models

Results

In order to show the influence of the quartic term as well as that of independent loads a series of representative curves demonstrating these parameters has been evaluated. The results are for the particular two-mode case corresponding to the modes of equation (22) and in the form of selected critical load-initial imperfection curves resulting from the stability problem described by equations (33) and (34). For the purposes of illustration K_2 and K_3 have been chosen as $K_2 = 0.133$, $K_3 = -0.4375$ and -0.5955 which yield $\frac{3}{4}K_2 = 0.1$ and $24C_{40} = \pm 0.177$ and where the type one and type two cases occur for positive and negative values of C_{40}, respectively. Further, for comparison purposes, in Fig. 3 the results for $C_{40} = 0$ are also presented. It is felt that the foregoing choice of coefficients yields the possibility of obtaining an unbiased parameter study for the present problem.

Fig. 3 demonstrates the differences in imperfection sensitivity for the type one and type two cases and a further comparison curve when the quartic term is omitted is also evaluated. It is noted that the applied loads are constrained to be equal ($\lambda_x = \lambda_y$). Of importance in this figure are the changes in imperfection sensitivity even for small imperfections and perhaps more importantly the existence of a critical load curve only in the type two case for positive values of the imperfection. Thus, if the quartic term is omitted in the analysis, there are fundamental changes in the critical load behavior of the type two case, even in an asymptotic sense.

Figs. 4 and 5 are denoted to an evaluation of the applied loads, λ_x and λ_y, being independent. This feature manifests itself in the factor ϵ. For the situation presented in Fig. 4 it may be appreciated that there

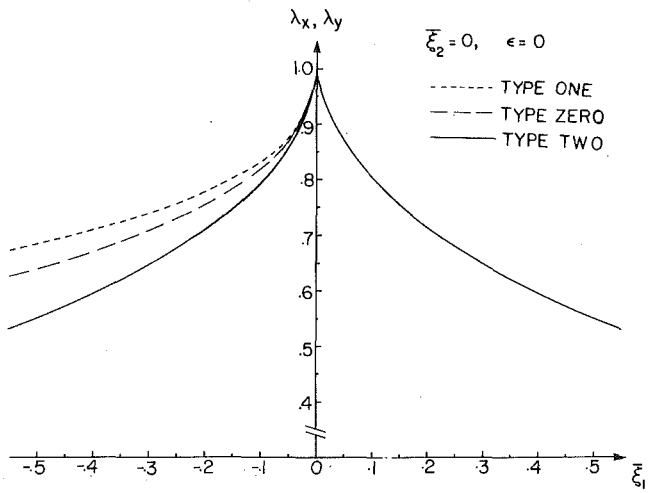

Fig. 3 Critical load-imperfection curves for equal applied loads ($\lambda_x = \lambda_y$) and $\bar{\xi}_2 = 0$

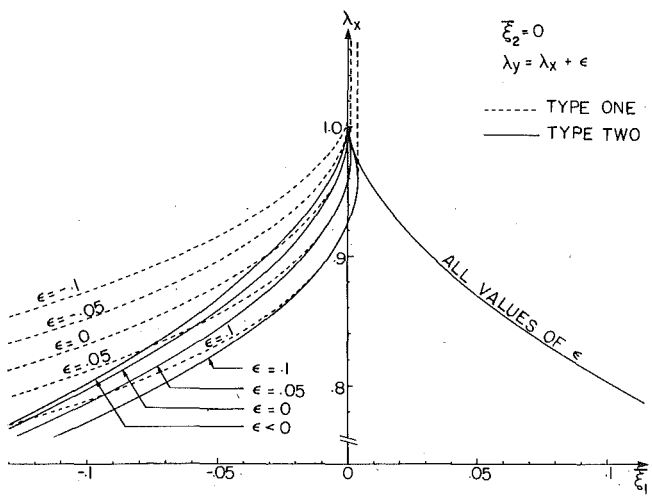

Fig. 4 Critical load-imperfection curves for unequal applied loads ($\lambda_y = \lambda_x + \epsilon$) and $\bar{\xi}_2 = 0$

are indeed changes in the critical loads as a function of ϵ, this change being quite uniform. The most interesting aspect is that for ϵ positive the critical load curve intersects the vertical axis. This implies a decrease in $\lambda_{x_{cr}}$ even for $\bar{\xi}_1 = 0$ and in addition that the type one situation becomes imperfection sensitive to positive $\bar{\xi}_1$ which was not the case for equal applied loads ($\lambda_x = \lambda_y$). Thus, although it is true for only very small positive $\bar{\xi}_1$, there has been a fundamental asymptotic change in the critical load-initial imperfection result. It is further noted in Fig. 4 that the type one and type two cases yield asymptotically similar results for negative $\bar{\xi}_1$ although the results do show different trends even for small imperfections. Fig. 5 considers the case when $\bar{\xi}_1 = 0$ and $\bar{\xi}_2$ varies. The features which are predominant are that the type one and type two problems yield essentially similar trends and that the parameter ϵ causes a quite uniform shift in the critical load-imperfection curve.

Summary and Conclusions

This paper has presented the initial postbuckling analysis of a plate loaded under the action of two independent in-plane loads. It has been noted that in general terms single mode buckling occurs if the applied loads are of unequal magnitude and multiple mode buckling occurs for equal magnitude loads. One particular aspect of the multiple mode case has been investigated. That is, a two mode case which results from the lowest order coupling in the problem. It has been further noted that for this situation the problem takes the form of the parabolic umbilic catastrophe and thus for a complete representation of the initial postbuckling behavior, a higher-order quartic term in the potential energy as well as independence of the applied loads must be permitted. The influence of these factors are then investigated and it is fair to say that the inclusion or exclusion of the quartic term can alter the postbuckling behavior completely while the variability of the applied loads results in some not unimportant changes in the overall as well as asymptotic character of the critical load-initial imperfection results.

Two additional factors related to this presentation should be mentioned. First, the two mode analysis considered is only part of a more complex multimode situation; however, the coupling terms for the more general case are of fourth order or higher. In addition, the present problem will always exist as a reduction of the more general case. Second, the form of the cubic terms in the potential energy $\alpha\xi_1\xi_2^2$ obtained in the present analysis leads directly to a consideration of the parabolic umbilic. This is not the most general situation as the same results will occur if the cubic terms are of a more complete form $A\xi_1^3 + B\xi_1^2\xi_2 + C\xi_1\xi_2^2 + D\xi_3^3$ where the coefficients A, B, C, D are related such that this cubic form has two equal roots. Thus higher-order terms in the potential energy as well as independence of applied loads may play a role even when the cubic terms in the potential energy are apparently quite complete.

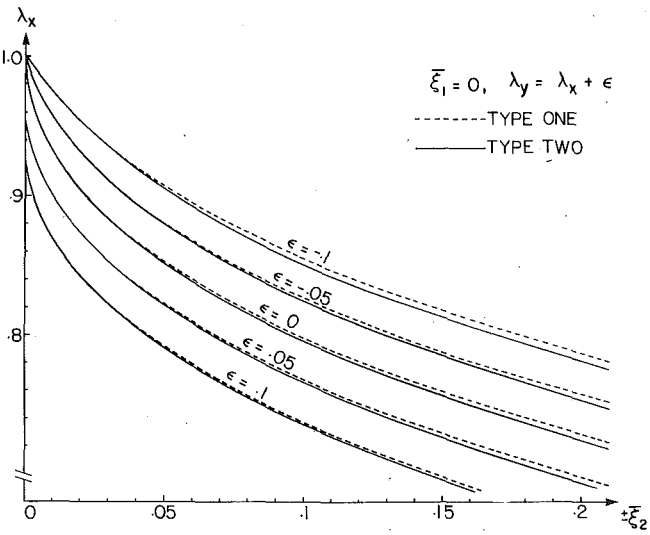

Fig. 5 Critical load-imperfection curves for unequal applied loads ($\lambda_y = \lambda_x + \epsilon$) and $\bar{\xi}_1 = 0$

References

1 Thom, R., *Structural Stability and Morphogenesis*, W. A. Benjamin Inc., 1975.

2 Koiter, W. T., "On the Stability of Elastic Equilibrium," Thesis, Delft, H. J. Paris, Amsterdam, 1945, English translation: NASA TT F-10, 833, 1967, and AFFDL-TR-70-25, 1970.

3 Thompson, J. M. T., and Hunt, G. W., *A General Theory of Elastic Stability*, Wiley, 1973.

4 Budiansky, B., and Hutchinson, J. W., "Dynamic Buckling of Imperfection-Sensitive Structures," *Proceedings of the 11th International Congress of Applied Mechanics*, Munich, Germany, 1964, pp. 636–651; ed., Gortler, H., Springer-Verlag, 1966.

5 Huseyin, K., *Nonlinear Theory of Elastic Stability*, Noordhoff International Publishing, Leyden, 1975.

6 Thompson, J. M. T., and Hunt, G. W., "Toward a Unified Bifurcation Theory," *Journal of Applied Mathematics and Physics, ZAMP*, 1975, pp. 581–604.

7 Sewell, M. J., "Some Mechanical Examples of Catastrophe Theory," *The Institute of Mathematics and Its Applications*, June 1976, pp. 163–172.

8 Huseyin, K., "The Multiple-Parameter Stability Theory and Its Relation

to Catastrophe Theory," *Proceedings of the Interdisciplinary Conference on Problem Analysis in Science and Engineering*, Branin, F., and Huseyin, K., Academic Press, 1977, pp. 229–255.

9 Hansen, J. S., "Some Two-Mode Buckling Problems and Their Relation to Catastrophe Theory," *AIAA Journal*, Vol. 15, No. 11, 1977, pp. 1638–1644.

10 Hui, D., "The Parabolic Umbilic Catastrophe and Its Application in the Theory of Elastic Stability," MASc Thesis, University of Toronto, Jan. 1977.

11 Hui, D., and Hansen, J. S., "The Swallowtail and Butterfly Cuspoids and Their Applications in a Beam on a Nonlinear Foundation," *Quarterly of Applied Mathematics*, to appear.

12 Hilton, P., ed., "Structural Stability, The Theory of Catastrophes, and Applications in the Sciences," *Proceedings of the Conference*, held at Battelle Research Center, 1975, *Lecture Notes in Mathematics*, Vol. 525, Springer-Verlag, 1977.

13 Reissner, E., "On Postbuckling Behavior and Imperfection Sensitivity of Thin Elastic Plates on a Nonlinear Elastic Foundation," *Studies in Applied Mathematics*, Vol. XLIX, No. 1, Mar. 1970, pp. 45–57.

14 Hutchinson, J. W., "Imperfection Sensitivity of Externally Pressurized Spherical Shells," ASME JOURNAL OF APPLIED MECHANICS, Vol. 34, 1967, pp. 49–55.

V. Tvergaard[1]
Visiting Associate Professor

A. Needleman
Associate Professor.
Mem. ASME

Division of Engineering,
Brown University,
Providence, R. I. 02912

On the Localization of Buckling Patterns

The possibility of localization of a buckling pattern is investigated for a class of structures in which the initial buckling mode is periodic. A simple model indicates that the basic mechanism of localization involves a bifurcation at the maximum load point. This model also illustrates a clear analogy between localization of a buckling pattern in a structure under compressive loading and the phenomenon of necking in a bar under tensile loading. An analysis of the bifurcation that leads to localization, carried out for the more realistic structural model of a column on a softening foundation, demonstrates a delay between the maximum load point and the bifurcation point. A finite-element analysis of an elastic-plastic plate strip under axial compression shows the development of localization for a low hardening material, whereas localization does not occur in a plate made of a high hardening material for which no maximum load is reached.

Introduction

A frequent observation in structural buckling is that the final buckled configuration of the structure involves a localized deformation pattern, in contrast with the periodic deformation pattern associated with the critical buckling mode. The structures prone to this type of localization have the common property that the applied load-deflection curve achieves a maximum. For example, Moxham [1] has observed the behavior illustrated in Fig. 1 in over 100 tests carried out on steel plates and has used a model based on an assembly of single plates hinged together to argue that continued growth of all buckles is not stable beyond the maximum load [2].

In the present paper such localization of buckling patterns is discussed in a broad perspective. First, for a simple model we show that the basic mechanism of localization is a bifurcation at the maximum load point. This type of model reveals that localization of a buckling pattern is in various ways analogous to necking in tensile bars.

Next, for an elastic column on a softening foundation, the bifurcation, at which the initial periodic buckling pattern loses uniqueness, is analyzed in detail. In particular, we show, again analogous to the situation prevailing in tensile necking, that in a realistic structural model there is a delay between the maximum load point and the point of bifurcation that leads to localization. For this structure, the effect of geometric and material parameters on this delay is explored.

Finally, we carry out a finite-element analysis of a long simply supported rectangular plate made of a strain-hardening elastic-plastic material. For a particular plate geometry the bifurcation point, at which the initial periodic buckling pattern loses uniqueness, is determined. However, here, primary emphasis is given to analyzing the development of localization.

Simplified Models

The basic mechanism involved in the localization of a buckling pattern is revealed by a simple bar model (Fig. 2) which can be regarded as a one-dimensional model of a long periodically buckled structure under compressive loading.

Consider a homogeneous axially compressed bar constrained to remain straight, but free to slide in the axial direction (Fig. 2*a*). The axial stress-strain curve is taken to be a nonlinear function of the strain. This constitutive law models the axial force versus average axial strain dependence in a structure, such as a long simply supported plate strip, including the effects of any periodic buckling pattern which has developed. Thus we take the effects of both geometric and material nonlinearities to be incorporated into the nonlinear stiffness of the bar.

For a bar of length L, the end displacements are taken to be prescribed at $x = 0, L$. The incremental relation between the axial force N and strain ϵ is

$$\dot{N} = C\,\dot{\epsilon} \qquad \dot{\epsilon} = \dot{u}_{,x} \tag{1}$$

where C is the instantaneous modulus and u is the axial displacement. We have used a small strain formulation since in the buckling problems of interest here the strains do remain small.

Bifurcation away from a uniformly strained state is governed by the variational equation

$$\delta I = 0 \qquad I = \int_0^L C\bar{\epsilon}\bar{\epsilon}\,dx \tag{2}$$

[1] Permanent Address, Department of Solid Mechanics, The Technical University of Denmark, 2800 Lyngby, Denmark.

Contributed by the Applied Mechanics Division for publication in the JOURNAL OF APPLIED MECHANICS.

Discussion on this paper should be addressed to the Editorial Department, ASME, United Engineering Center, 345 East 47th Street, New York, N. Y. 10017, and will be accepted until December 1, 1980. Readers who need more time to prepare a discussion should request an extension from the Editorial Department. Manuscript received by ASME Applied Mechanics Division, November, 1979; final revision, February, 1980.

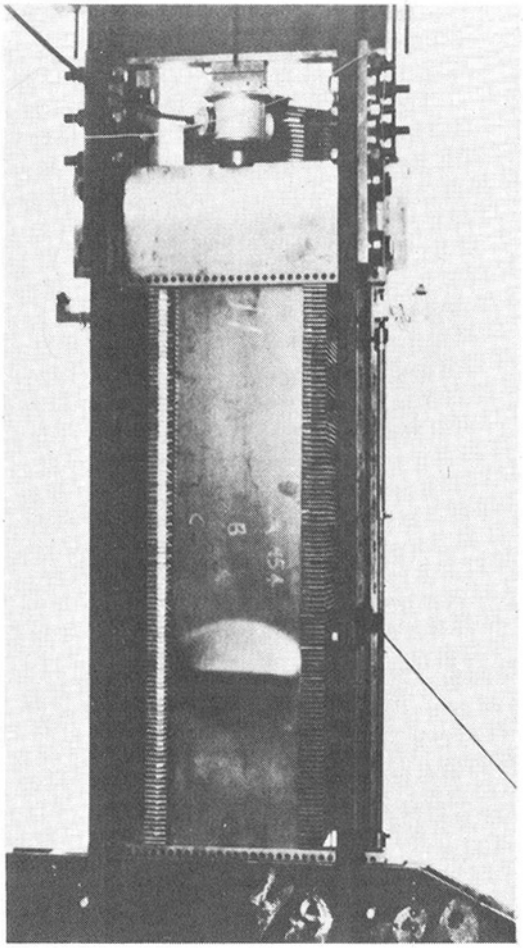

Fig. 1 Final collapse mode of an axially compressed steel plate strip, from Moxham [1]

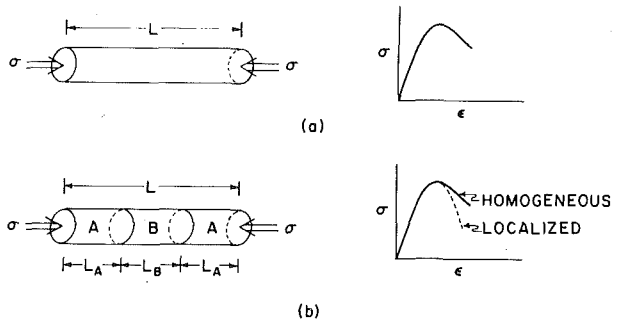

Fig. 2 Axially compressed bar model; (*a*) a homogeneous bar with its stress-strain curve; (*b*) a bar undergoing localization. In (*b*), the stress-strain curve in the localized mode (- - -) is contrasted with that for a homogeneous bar (——)

where (˜) denotes the difference between two solutions corresponding to the same prescribed end displacements. Bifurcation modes of the form

$$\tilde{u} = \sin \frac{n\pi x}{L} \qquad n = 1, 2, 3 \ldots \tag{3}$$

are all critical simultaneously for $C = 0$, i.e., at the maximum load. If no maximum is reached, bifurcation does not occur. Note that in this very simple model the classical bifurcation of a geometrically perfect structure into a periodic buckling pattern effects the stiffness C, but within the context of this model is not a bifurcation, since the average axial strain ϵ remains uniform.

The same conclusion can be reached by a different analysis. Consider incremental deformations from the homogeneous state. We investigate whether a localized region (B in Fig. 2(b)) can undergo incremental straining different from that in the surrounding material (A in Fig. 2(b)).

Incremental equilibrium requires

$$\dot{\sigma}_A = \dot{\sigma}_B \tag{4}$$

where ($\dot{}$) denotes an increment and subscripts A and B denote quantities associated with the corresponding regions in Fig. 2(b).

Since

$$\dot{\sigma}_A = C\dot{\epsilon}_A \qquad \dot{\sigma}_B = C\dot{\epsilon}_B \tag{5}$$

Incremental equilibrium implies

$$C(\dot{\epsilon}_B - \dot{\epsilon}_A) = 0 \tag{6}$$

Hence, such an alternative deformation state is possible only when $C = 0$, i.e., at the maximum load point.

These analyses are quite analogous to the similar one-dimensional analyses of necking in a tensile bar. As for the tensile bar [3, 4], the extent of the region of localized deformation is determined by factors not incorporated into the one-dimensional model. For example, in an axially compressed plate strip with a periodic buckling pattern, σ can be associated with the axial load and ϵ with the node-to-node shortening divided by the distance between nodes. The localized deformation pattern then covers at least one buckle in the fundamental periodic pattern.

The postlocalization behavior can readily be determined within the context of this simple bar model. We let L denote the total length of the bar and $\dot{\epsilon}$ denote the total strain increment. Hence, as shown in Fig. 2(b)

$$L = 2L_A + L_B \tag{7}$$

and

$$\dot{\epsilon} = (1 - \rho)\,\dot{\epsilon}_A + \rho\,\dot{\epsilon}_B \tag{8}$$

where $\rho = L_B/L$.

Incremental equilibrium (4) then gives

$$\dot{\epsilon} = \frac{\dot{\sigma}}{C_B}\left[\rho + (1 - \rho)\frac{C_B}{C_A}\right] \tag{9}$$

At bifurcation $C_B = 0$ (implying a smooth stress-strain curve at bifurcation for this model), while C_B is negative after the maximum load. As long as C_A is algebraically larger than C_B, the stress-strain curve corresponding to localization will lie below the one corresponding to homogeneous deformation, as shown in Fig. 2(b). Note that for a given C_B/C_A, the smaller ρ is, the more rapidly the load drops. If the bar in Fig. 2 is considered as a model of an axially compressed plate strip, then (9) gives the load-end shortening curve that emerges from Moxham's model [2].

In addition to the axially compressed plate strip this simple bar model also has a bearing on other buckling problems. Among these are a column supported by an elastic or elastic-plastic foundation, a column continuous over several constantly spaced supports, which are free to move in the axial direction, and a stiffened panel continuous over several bays. In these cases a maximum load may be reached due to elastic-plastic material behavior or, in the panel, due to geometric nonlinearities [5, 6].

A similar simple model can also be used for the problem of tube bending that has attracted some interest in recent years [7–9]. In tube bending a maximum moment is reached due to the ovalization of the cross section (the Brazier effect), and possible buckling into a short-wave pattern on the compressed side of the tube will further decrease the bending stiffness. If the tube yields plastically, much less ovalization is needed before the maximum moment is reached.

Consider the tube as a uniform bar of length L bent into a circular shape with current radius R (Fig. 3). The current angle θ between the

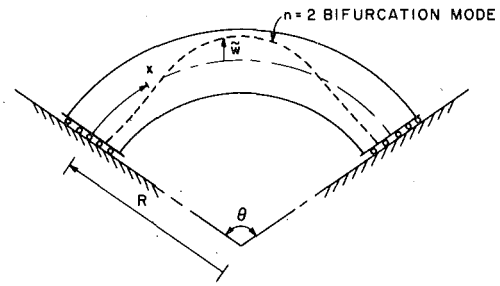

Fig. 3 Tube bent into a circular shape with current radius R, by prescribing the angle θ

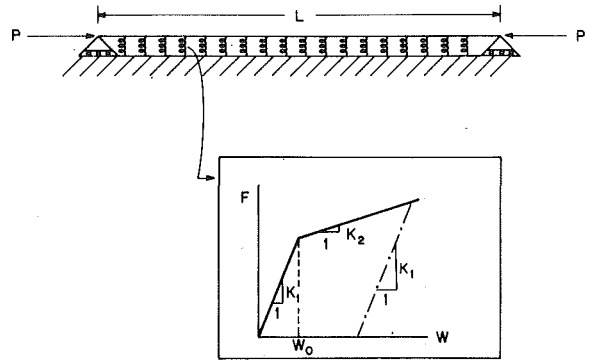

Fig. 4 Column on a softening foundation; the insert shows the piecewise linear force-deflection curve of the foundation

end cross sections at $x = 0$, L is taken to be prescribed, but otherwise the ends can slide freely. Referred to the current neutral axis of the bar the incremental relations between the bending moment M, the axial force N, the bending strain κ, and the axial strain ϵ are

$$\dot{M} = D\dot{\kappa} \quad \dot{\kappa} = \dot{w}_{,xx}$$
$$\dot{N} = C\dot{\epsilon} \quad \dot{\epsilon} = \dot{u}_{,x} + \frac{\dot{w}}{R} \tag{10}$$

where D and C are instantaneous moduli and shallow arch expressions are used for the strains in terms of the tangential and radial displacements u and w. Bifurcation is governed by the variational equation

$$\delta I = 0 \quad I = \int_0^L (C\tilde{\epsilon}\tilde{\epsilon} + D\tilde{\kappa}\tilde{\kappa} + N\tilde{w}_{,x}\tilde{w}_{,x})\, dx \tag{11}$$

and with $N = 0$, $C > 0$ bifurcation into modes of the form

$$\tilde{w} = a_1 \cos\frac{n\pi x}{L} \quad \tilde{u} = a_2 \sin\frac{n\pi x}{L} \quad n = 1, 2, 3 \ldots . \tag{12}$$

is critical for $D = 0$, i.e., at the point of maximum bending moment. This means that even for prescribed edge rotations the circular shape is unstable beyond the point of maximum moment. The symmetric $n = 2$ mode, sketched in Fig. 3, leads to the well-known final collapse mode, in which the tube forms a sharp kink. Higher-order modes would lead to more kinks.

We note that equations paralleling (4)–(9) can also be written down for this tube bending problem.

Elastic Column on a Softening Foundation

The structure considered is a linear elastic column of length L, having bending stiffness EI and subjected to an axial load P as shown in Fig. 4. The column rests on a foundation that provides a restoring force per unit length F.

In the presence of an initial imperfection $\overline{W}(X)$, the governing differential equation takes the form

$$EI\frac{d^4W}{dX^4} + P\frac{d^2W}{dX^2} + F = -P\frac{d^2\overline{W}}{dX^2} \tag{13}$$

Here $W(X)$ is the lateral displacement of the column in addition to the initial deviation from the straight configuration measured by $\overline{W}(X)$.

The restoring force provided by the foundation is a piecewise linear function of the additional displacement $W(X)$, as sketched in Fig. 4, so that

$$F = \begin{cases} K_1 W & |W| \leq W_0 \\ \pm K_1 W_0 + K_2(W \mp W_0) & |W| > W_0 \end{cases} \tag{14}$$

with the upper sign taken for $W > 0$ and the lower for $W < 0$ and $K_1 > K_2$ for a softening foundation.

Here, the displacement W_0 is termed the yield point of the foundation. We introduce the nondimensional quantities

$$x = (K_1/EI)^{1/4} X \quad w = W/W_0 \quad \overline{w} = \overline{W}/W_0$$
$$\beta = K_2/K_1 \qquad \lambda = \frac{1}{2} P/(K_1 EI)^{1/2} \tag{15}$$

where, since $K_1 > K_2$, $\beta < 1$. Substituting (14) and (15) into (13) gives

$$\begin{aligned} w'''' + 2\lambda w'' + w &= -2\lambda\overline{w}'' && |w| \leq 1 \\ w'''' + 2\lambda w'' + \beta w &= -2\lambda\overline{w}'' \mp (1-\beta) && |w| > 1 \end{aligned} \tag{16}$$

where $(\ )'$ denotes $d(\ )/dx$.

The column is taken to be simply supported at its ends so that

$$w(0) = w(l) = 0 \quad w''(0) = w''(l) = 0 \tag{17}$$

with $l \equiv (K_1/EI)^{1/4} L$.

For a perfect column, $\overline{w} \equiv 0$, the initial bifurcation mode $\tilde{w}$ and the corresponding bifurcation load are

$$\tilde{w} = \sin\frac{n\pi x}{l} \quad \lambda_c = \frac{1}{2}\left[\left(\frac{n\pi}{l}\right)^2 + \left(\frac{n\pi}{l}\right)^{-2}\right] \tag{18}$$

where n is the integer that minimizes λ_c. For convenience, we focus attention on columns with length $l = n\pi$, for which

$$\tilde{w} = \sin x \quad \lambda_c = 1 \tag{19}$$

Now, consider a column with an imperfection, of amplitude δ, in the shape of the critical bifurcation mode (19). The solution to (16) is simply

$$w(x) = \frac{\lambda\delta}{1-\lambda}\sin x \tag{20}$$

so long as $\lambda\delta \leq 1 - \lambda$. For larger deflections, the softening branch of (14) will be activated. One solution has, as does (20), n half waves over the length of the column. The locations of the yield point, i.e., the positions at which $|w| = 1$, are given by $(k - 1/2)\,\pi - \gamma$ and $(k - 1/2) \times \pi + \gamma$ for each half wave, $k = 1, 2 \ldots n$. The parameter γ is determined by the analysis.

Due to symmetry, we can focus on the quarter wave for which $0 \leq x \leq \pi/2$. In this interval the solution to (16) is

$$w(x) = \begin{cases} w_1(x) & 0 \leq x \leq \pi/2 - \gamma \\ w_2(x) & \pi/2 - \gamma \leq x \leq \pi/2 \end{cases} \tag{21}$$

Here,

$$w_1(x) = 2\,\mathrm{Re}\{c_1 \sinh sx\} + \frac{\lambda\delta}{1-\lambda}\sin x \tag{22}$$

$$w_2(x) = r_1 \cos p(x - \pi/2) + r_2 \cos q(x - \pi/2) + \frac{\lambda\delta}{\dfrac{\beta+1}{2} - \lambda}\sin x + \left(1 - \frac{1}{\beta}\right) \tag{23}$$

where

$$p^2 = \lambda - \sqrt{\lambda^2 - \beta} \quad q^2 = \lambda + \sqrt{\lambda^2 - \beta} \quad s^2 = -\lambda + i\sqrt{1 - \lambda^2} \tag{24}$$

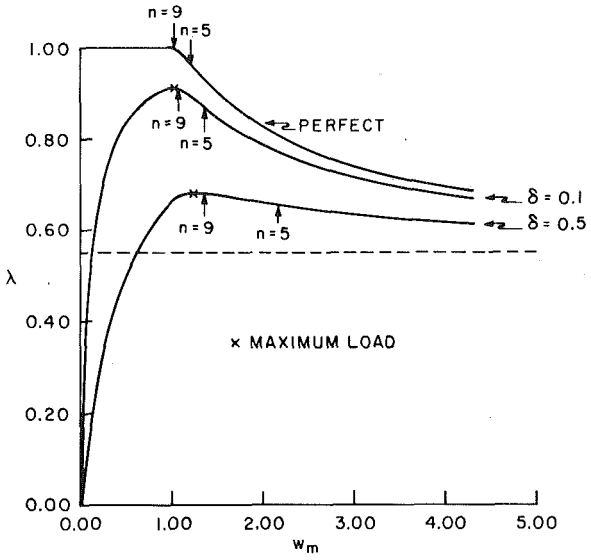

Fig. 5 Load versus lateral deflection amplitude for a column on a softening foundation with $\beta = 0.1$

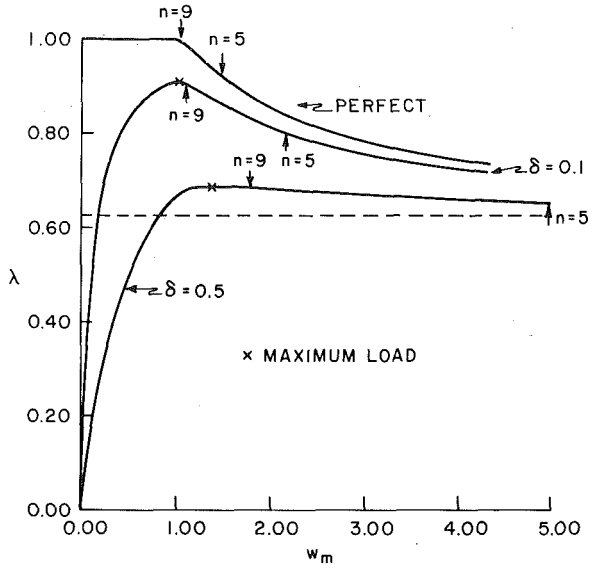

Fig. 6 Load versus lateral deflection amplitude for a column on a softening foundation with $\beta = 0.25$

with $i = \sqrt{-1}$ and Re{ } denoting the real part of a complex quantity. The form of $w_2(x)$ displayed in (23) presumes $\lambda^2 > \beta$, which holds for the range of parameters of interest here.

The complex constant c_1 and the two real constants r_1 and r_2 are determined from the requirement that the deflection, the rotation, the bending moment, and the shear force are continuous at $x = \pi/2 - \gamma$. In terms of the functions $w_1(x)$ and $w_2(x)$, these conditions become

$$w_1 = w_2 \quad w_1' = w_2' \quad w_1'' = w_2'' \quad w_1''' = w_2''' \tag{25}$$

for $x = \pi/2 - \gamma$. In addition, for consistency, there is the requirement that

$$w(\pi/2 - \gamma) = 1 \tag{26}$$

The relations (25) give four equations for the four coefficients; the real part of c_1, the imaginary part of c_1, r_1, and r_2. The subsidiary condition (26) fixes λ for a given γ.

These equations are solved by a straightforward numerical procedure. Figs. 5 and 6 display the results in terms of curves of load λ versus the lateral deflection amplitude w_m where

$$w_m = \left| w\left\{\left(k - \frac{1}{2}\right)\pi\right\}\right| \quad k = 1, 2, \ldots n \tag{27}$$

In Fig. 5, β is taken as 0.1 while in Fig. 6 results for a somewhat stiffer foundation $\beta = 0.25$, are illustrated. In each figure, the dotted lines denote the limiting value of the load for large w_m, namely, $(\beta + 1)/2$, and results are displayed for a perfect column $\delta = 0$, and for imperfection amplitudes δ, of 0.1 and 0.5. Of course, in this periodic mode, the load-lateral deflection curves are independent of the length of the column.

Bifurcation from this state is possible when there exists a solution to the homogeneous version of (16), which satisfies the boundary conditions (17) and the continuity conditions (25) at each

$$(k - 1/2)\,\pi \pm \gamma, k = 1, 2 \ldots n.$$

Since each of (16) is a constant coefficient fourth-order ordinary differential equation, the homogeneous solution can be expressed as the sum of four complex exponentials, there being two pairs of complex conjugate exponentials. For a column of length $n\pi$, the homogeneous solution to (16) contains $2(2n + 1)$ arbitrary constants. At each of the $2n$ locations $(k - 1/2)\,\pi \pm \gamma, k = 1, 2 \ldots n$, the four continuity conditions (25) must be satisfied. Additionally, the homogeneous boundary conditions (17) at each end of the column give four

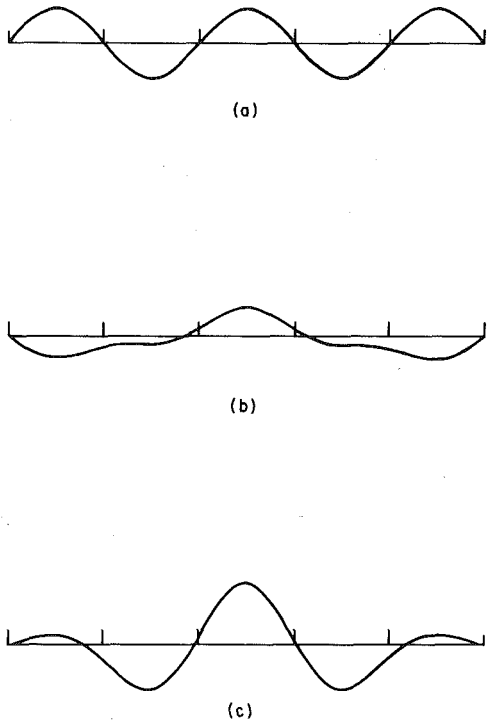

Fig. 7 (*a*) The periodic lateral deflection pattern for $\beta = 0.1$ and $\delta = 0$ at the bifurcation point for $l = 5\pi$. (*b*) The bifurcation mode. (*c*) An arbitrary linear combination of the periodic mode and the bifurcation mode, illustrating the tendency to localization

equations. Thus there are $8n + 4$ homogeneous equations to be satisfied by $4n + 2$ complex constants. When the determinant of the coefficients of the equivalent system of $(8n + 4) \times (8n + 4)$ real equations vanishes, a nontrivial solution exists to the bifurcation equations.

Since the load λ is taken as the prescribed quantity, this determinant necessarily vanishes at the maximum load point. However, the corresponding eigenmode is not a bifurcation mode, but is some arbitrary multiple of the solution (21)–(23). The agreement between this trivial mode and (21)–(23) served as a check on the numerical procedures.

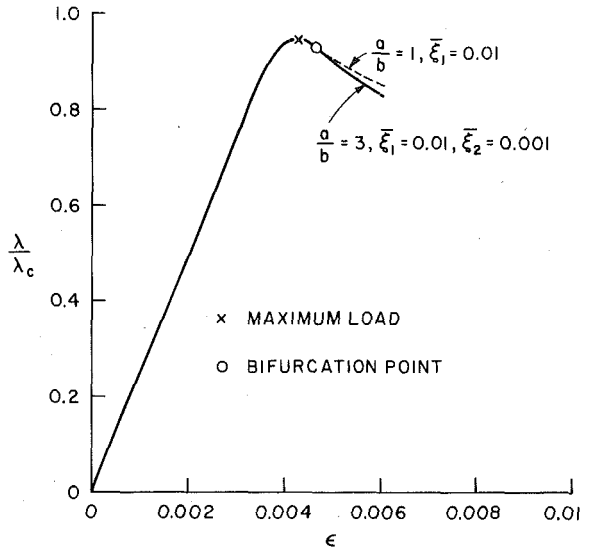

Fig. 8 Load versus average axial strain for a rectangular plate with $n = 10$, $\sigma_y/E = 0.00337$, $h/b = 0.035$, $\nu = 0.3$

A straightforward numerical search procedure was employed to determine the value of the lateral deflection amplitude at bifurcation from the configuration described by (21)–(23) for various column lengths $n\pi$. For a perfect column this is a secondary bifurcation point.

As will be discussed in conjunction with Fig. 7 subsequently, the bifurcation mode has a number of half waves different from n, so that a linear combination of the primary periodic mode and the bifurcation mode can result in preferential growth of one of the buckles. However, to distinguish between mode snapping to the wavenumber of the bifurcation mode and localization involves postbifurcation considerations. If the springs are elastic-plastic, in the sense that unloading occurs with stiffness K_1 in (14) (the dash-dot line in Fig. 4), then localization rather than mode snapping is anticipated. In this case unloading initiates at bifurcation and the relative amplitudes of the periodic mode and the localized mode, at bifurcation, are set by the Shanley condition [10, 11, 13].

Bifurcation points for various values of n are shown in Figs. 5 and 6. The bifurcation modes are constrained to be symmetrical about the center of the column $x = n\pi/2$. For the boundary conditions employed here, bifurcation modes antisymmetrical about $x = n\pi/2$ occur somewhat before the ones shown.

In Fig. 5, where $\beta = 0.1$, the bifurcation points for column lengths of 9π ($n = 9$) and 5π ($n = 5$) are shown. As the length of the column increases, the bifurcation point approaches the maximum load point which is the bifurcation point according to the simple model discussed in the previous section. This is analogous to necking in a tensile bar [3, 4] where for a finite length bar the onset of necking is somewhat delayed beyond the maximum load point. In Fig. 6 where the foundation is somewhat stiffer, $\beta = 0.25$, bifurcation occurs at larger deflections, w_m, than in Fig. 5 where $\beta = 0.1$. For a fixed column length, it can be seen that the bifurcation point occurs further beyond the maximum load point as the harmonic imperfection amplitude δ increases.

Fig. 7 shows, for $\beta = 0.1$ and $l = 5\pi$, the periodic deflection pattern, the bifurcation mode and an arbitrary linear combination of these indicating the tendency to localization. For the antisymmetric bifurcation mode, which occurs somewhat earlier, localization would occur at one end of the column. In the analysis of the onset of necking in tensile bars [4] an analogous situation is encountered in that under the idealized boundary conditions employed in that analysis, the neck is predicted to form at one end of the bar, unless symmetry about the midplane of the bar is imposed.

Elastic-Plastic Plates

The rectangular plates considered in this section have length a and width b in the x_1 and x_2-directions, respectively, and the thickness is h. Using von Karman plate theory the in-plane components of the Lagrangian strain tensor are approximated by

$$\eta_{\alpha\beta} = \epsilon_{\alpha\beta} + x_3\,\kappa_{\alpha\beta}$$
$$\epsilon_{\alpha\beta} = \frac{1}{2}(u_{\alpha,\beta} + u_{\beta,\alpha} + w_{,\alpha}\,w_{,\beta}), \quad \kappa_{\alpha\beta} = -w_{,\alpha\beta} \tag{28}$$

where u_α are the in-plane displacements and w is the lateral displacement of the plate middle surface. The coordinate normal to the middle surface is x_3 and $(\ )_{,\alpha}$ denotes partial differentiation with respect to the in-plane coordinates.

The theory of plasticity employed is small strain J_2-flow theory with isotropic hardening, using a uniaxial stress-strain behavior represented by the following piecewise power law

$$\epsilon = \begin{cases} \dfrac{\sigma}{E}, & \text{for} \quad \sigma < \sigma_y \\ \dfrac{\sigma_y}{E}\left[\dfrac{1}{n}\left(\dfrac{\sigma}{\sigma_y}\right)^n - \dfrac{1}{n} + 1\right], & \text{for} \quad \sigma \geq \sigma_y \end{cases} \tag{29}$$

Here σ and ϵ are the uniaxial stress and strain, E is Young's modulus, σ_y is the initial yield stress, and n is the strain-hardening exponent. At each stage of the computation the membrane stress tensor $N_{\alpha\beta}$ and the moment tensor $M_{\alpha\beta}$ are determined from the stresses by integrating through the thickness, and the incremental principle of virtual work is used as the basis for a numerical solution. The details of the equations are given in [12] and shall not be repeated here.

The plates are taken to be simply supported at all four edges

$$w = 0, M_{11} = 0 \quad \text{at} \quad x_1 = 0, a$$
$$w = 0, M_{22} = 0 \quad \text{at} \quad x_2 = 0, b \tag{30}$$

The loaded edges are constrained to remain straight, whereas the other two edges are free to pull in

$$u_1(0, x_2) = -u_1(a, x_2) = U$$
$$N_{22} = 0 \quad \text{at} \quad x_2 = 0, b$$
$$N_{12} = 0 \quad \text{at} \quad x_1 = 0, a \quad \text{and} \quad x_2 = 0, b \tag{31}$$

Here, U is the prescribed edge displacement and in the following the parameter λ is taken to be proportional with the resultant axial force. Furthermore, only deflections symmetric about the lines $x_1 = a/2$ and $x_2 = b/2$ are considered here, so that symmetry conditions are prescribed along these two lines and only one quarter of the plate needs be considered in the numerical solution.

Imperfections in the initial stress-free state of the plate are specified in the form of an initial deflection

$$\bar{w} = h(\bar{\xi}_1 + \bar{\xi}_2 e^{-[(2x_1-a)/b]^2}) \sin\frac{m\pi x_1}{a} \sin\frac{\pi x_2}{b} \tag{32}$$

where $\bar{\xi}_1$ is the amplitude of an imperfection in the shape of the bifurcation mode and $\bar{\xi}_2$ represents the amplitude of a localized imperfection. Thus the total lateral deflection w is the sum of the initial deflection $\bar{w}$ and the further deflection due to the loading.

The thickness to width ratio $h/b = 0.035$ and material parameters $\sigma_y/E = 0.00337$, $\nu = 0.3$, and $n = 10$ used in [12] are also chosen here. Furthermore, $a/b = 3$ is chosen with $m = 3$ in (32), corresponding to square buckles; even though the minimum bifurcation load in this case is obtained for buckles 0.814 times as long as the plate width. A reason for this choice is that the bifurcation load for square buckles is only 2.5 percent above that for the critical wavelength, and square buckles grow faster prior to plastic yielding.

Numerical solutions of the incremental equilibrium equation are obtained by dividing one quarter of the plate into 6×2 rectangular conforming finite elements. Within an element each displacement component is approximated by products of Hermitian cubics in the x_1 and x_2-directions, and integrals over the middle surface are evaluated by 4×4 point Gaussian quadrature, with 7 point Simpson integration through the thickness.

Fig. 8 shows a plot of the load parameter λ normalized by the critical value λ_c for square buckles versus the average axial strain $\epsilon = 2U/a$.

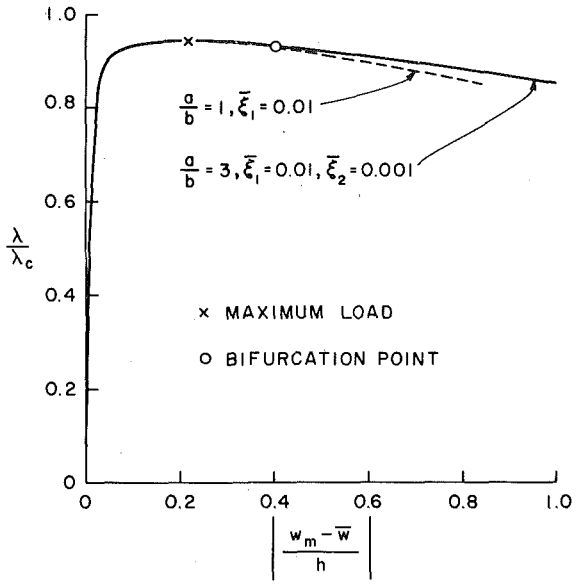

Fig. 9 Load versus maximum lateral deflection amplitude for a rectangular plate with $n = 10$, $\sigma_y/E = 0.00337$, $h/b = 0.035$, $\nu = 0.3$

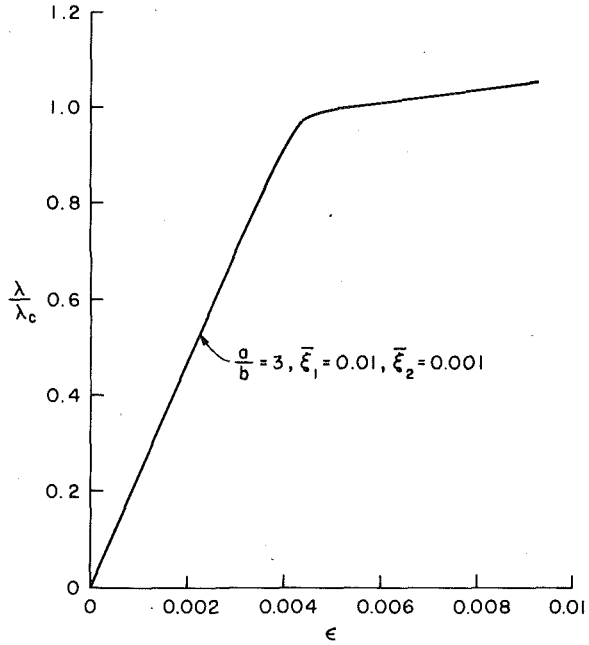

Fig. 10 Load versus average axial strain for a rectangular plate with $n = 2.5$, $\sigma_y/E = 0.00337$, $h/b = 0.035$, $\nu = 0.3$

Fig. 9 shows λ versus the maximum displacement $w_m = w(a/2, b/2)$. For $\bar{\xi}_1 = 0.01$ and $\bar{\xi}_2 = 0$ three equal buckles grow in a stable manner until a bifurcation point is reached a little after the point of maximum axial force. The bifurcation point is characterized by a nonzero solution of the variational equation

$$\delta I = 0 \quad I = \int_A \{\tilde{N}_{\alpha\beta}\tilde{\epsilon}_{\alpha\beta} + \tilde{M}_{\alpha\beta}\tilde{\kappa}_{\alpha\beta} + N_{\alpha\beta}\tilde{w}_{,\alpha}\tilde{w}_{,\beta}\}\, dA = 0 \quad (33)$$

for fixed edge displacements. Thus, at this point, the uniqueness of the periodic solution is lost in agreement with the prediction of the simplified bar model and with the behavior of the elastically supported column.

Now in order to follow the process of localization a slightly nonuniform imperfection is considered with $\bar{\xi}_1 = 0.01$ and $\bar{\xi}_2 = 0.001$. In Figs. 8 and 9, the result is compared with the prebifurcation solution obtained by considering a square plate with just one buckle ($a/b = 1$, $\bar{\xi}_1 = 0.01$). Near the bifurcation point the deformations suddenly concentrate in the central buckle with rather little deformation of the other two buckles. At the same time the $\lambda - \epsilon -$ curve (Fig. 8) starts to decay more rapidly, and, as for the simple bar model, it is evident that a longer plate localizing into a single buckle will give a stronger decay of this curve. The load-deflection curve in Fig. 9 would not at all be affected by localization, if the plate had straight frictionless hinges built in between buckles at the initial nodal lines as in the model problem considered by Moxham [2]. However, in the real plate a clamping effect from the neighboring plate material will oppose localization into a single buckle, resulting in the slower decay after the bifurcation point shown in Fig. 9.

The behavior of an initially perfect plate, $\bar{w} \equiv 0$, has not been analyzed here. However, prior to any localization it is well known [12, 13] that the plate will remain flat up to the critical bifurcation point, at which sinusoidal deflections start to grow. On the postbifurcation path a maximum load is reached at small but finite deflections [12, 13], so according to the simple model this point offers the earliest possibility of a secondary bifurcation and subsequent localization. As for the model of a column on a softening foundation, it is expected that the delay between the maximum load point and the bifurcation point is somewhat greater for an imperfect plate (Figs. 8 and 9) than for a perfect plate.

As shown in [12], a maximum load point and the corresponding imperfection-sensitivity for rectangular plates occur only for low strain hardening. Therefore, the previous computation with imperfections $\bar{\xi}_1 = 0.01$ and $\bar{\xi}_2 = 0.001$ is repeated for a high hardening material, $n = 2.5$. The load versus axial compression curve is shown in Fig. 10. Here no localization occurs, which is expected, as no maximum load point is reached. The difference is most clearly illustrated by the plots in Fig. 11 of the ratio between the maximum deflection $w_m = w(a/2, b/2)$ and the deflection $w_1 = w\,(a/6, b/2)$ at the center of the first buckle. Initially this ratio is close to 1.1, due to the imperfections chosen, but as the buckles grow with increasing load the ratio approaches unity. For $n = 2.5$, where no maximum is reached, this tendency of stable uniform growth continues, whereas for $n = 10$ the ratio starts to increase rapidly at the bifurcation point a little beyond the maximum.

The stable uniform growth of all buckles found for $n = 2.5$ agrees with the behavior of elastic plates. It is of interest to note here though that long elastic plates can experience a secondary bifurcation in the advanced postbuckling region [14, 15]. However, this bifurcation leads to snapping into a periodic mode with a higher axial wave number, which then grows for increasing load.

The elastic-plastic plates considered here have the particular aspect ratio $a/b = 3$ and only symmetric modes are accounted for. It is expected that, as for the column on a softening foundation, considering longer plates and including nonsymmetric bifurcation modes would result in bifurcation more closely following the maximum load point.

The occurrence of a bifurcation just after the maximum load does not, of course, effect the load-carrying capacity of a perfect plate or of a plate with a periodic imperfection. However, for a plate with a localized as well as a periodic imperfection, there is a possibility that some imperfection-sensitivity associated with the localization bifurcation might accelerate the growth of the nonuniformity of the buckling pattern and result in a reduced maximum load. It is therefore of interest to notice in Fig. 11 that, on the contrary, up to the maximum load the tendency is to smooth out the initial nonuniformity in the deflection pattern.

Concluding Remarks

A wide variety of structures, for which the applied-load deflection curve achieves a maximum, are susceptible to the type of localization discussed here. The basic mechanism of localization involves a bifurcation, subsequent to the maximum load point, at which the initial deformation pattern loses uniqueness. Thus, as illustrated in Fig. 1, the final collapse mode in a structure prone to localization bears no resemblance to the deformation pattern prevailing at the maximum load point. However, it is the prelocalization deformation pattern

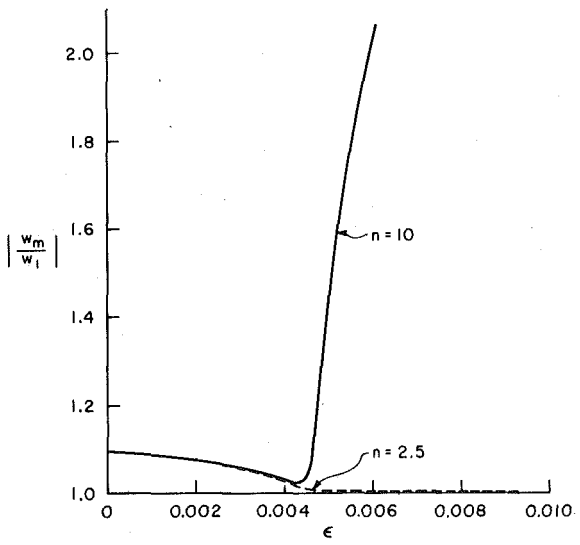

Fig. 11 Ratio between lateral deflection amplitudes at the central buckle and at the first buckle versus average axial strain for $a/b = 3$, $\bar{\xi}_1 = 0.01$, $\bar{\xi}_2 = 0.001$, $\sigma_y/E = 0.00337$, $h/b = 0.035$, $\nu = 0.3$

which determines the maximum load point. Furthermore, at least for the plate strip analyzed here, small localized imperfections do not significantly effect the structure's load-carrying capacity. Hence, the fact that localization occurs does not invalidate an analysis directed toward determining the maximum support load which restricts attention to periodic modes and imperfections. On the other hand, there are applications, such as shock-absorbing devices, in which the final collapse mode is a significant concern.

Acknowledgment

We are grateful to the Division of Engineering, Brown University, for supporting this work. We are also indebted to Dr. K. E. Moxham for permission to use Fig. 1.

References

1 Moxham, K. E., "Buckling Tests on Individual Welded Steel Plates in Compression," Cambridge University Engineering Department, Report CUED/C—Struct/TR.3 (1971).

2 Moxham, K. E., "Theoretical Prediction of the Strength of Welded Steel Plates in Compression," Cambridge University Engineering Department, Report CUED/C—Struct/TR. 2 (1971).

3 Needleman, A., "A Numerical Study of Necking in Circular Cylindrical Bars," *Journal of the Mechanics and Physics of Solids,* Vol. 20, 1972, pp. 111–127.

4 Hutchinson, J. W., and Miles, J. P., "Bifurcation Analysis of the Onset of Necking in an Elastic-Plastic Cylinder Under Uniaxial Tension," *Journal of the Mechanics and Physics of Solids,* Vol. 22, 1974, pp. 61–77.

5 Tvergaard, V., and Needleman, A., "Buckling of Eccentrically Stiffened Elastic-Plastic Panels on Two Simple Supports or Multiply Supported," *International Journal of Solids and Structures,* Vol. 11, 1975, pp. 647–663.

6 Koiter, W. T., and Pignataro, M., "An Alternative Approach to the Interaction Between Local and Overall Buckling in Stiffened Panels," *Buckling of Structures,* ed., Budiansky, B., Springer-Verlag, Berlin, 1976, pp. 133–148.

7 Fabian, O., "Collapse of Cylindrical, Elastic Tubes Under Combined Bending, Pressure, and Axial Loads," *International Journal of Solids and Structures,* Vol. 13, 1977, pp. 1257–1270.

8 Gellin, S., "The Plastic Buckling of Long Cylindrical Shells Under Pure Bending," *International Journal of Solids and Structures,* Vol. 16, 1980, pp. 397–407.

9 Reddy, B. D., "An Experimental Study of the Plastic Buckling of Circular Cylinders in Pure Bending," *International Journal of Solids and Structures,* Vol. 15, 1979, pp. 669–683.

10 Shanley, F. R., "Inelastic Column Theory," *Journal of Aeronautical Sciences,* Vol. 14, 1947, pp. 261–267.

11 Hill, R., "A General Theory of Uniqueness and Stability in Elastic-Plastic Solids," *Journal of the Mechanics and Physics of Solids,* Vol. 7, 1958, pp. 209–225.

12 Needleman, A., and Tvergaard, V., "An Analysis of the Imperfection Sensitivity of Square Elastic-Plastic Plates Under Axial Compression," *International Journal of Solids and Structures,* Vol. 12, 1976, pp. 185–207.

13 Hutchinson, J. W., "Plastic Buckling," *Advances in Applied Mechanics,* ed., Yih, C. S., Vol. 14, Academic Press, New York, 1974, pp. 67–144.

14 Koiter, W. T., "Introduction to the Postbuckling Behavior of Flat Plates," *Colloque sur le comportement Postcritique des Plaques utilisées en Construction Metallique,* Liege, Novembre 1962, pp. 17–35; *Mémoires de la Société Royale des Sciences de Liege,* 5mé sêrie, tome VIII, fascicule 5, 1963.

15 Nakamura, T., and Uetani, K., "The Secondary Buckling and Postsecondary Buckling Behaviours of Rectangular Plates," *International Journal of Mechanical Sciences,* Vol. 21, 1979, pp. 265–286.

K. Nagaya[1]

Associate Professor,
Department of Mechanical Engineering,
Faculty of Engineering,
Yamagata University,
Yonezawa, Japan

Dynamic Response of a Plate With Arbitrary Shape

This paper is concerned with a method for solving dynamic response problems of a thin plate with arbitrary shape based on the classical plate theory. The result for an arbitrarily shaped plate subjected to general transient loads is obtained by utilizing the Fourier expansion collocation method. As an example, the dynamic response of a truncated elliptical plate subjected to a uniformly distributed exponentially decaying impact load is investigated. To verify the present method, numerical calculations are also carried out for a circular plate, and the results obtained are compared with the exact ones.

1 Introduction

A variety of structures used in land, sea, air, and space vehicles is subjected to dynamic loads. Various plates are used as elements of structures, and many researches on the dynamic problem of circular, rectangular, and elliptical plates have been reported based on the exact analysis. For the plates with arbitrary shape, general approximate methods such as the finite-element, finite-difference and point-matching methods have been used [1–3]. These methods have many advantages for solving eigenvalue problems of a plate with irregular boundaries. However, in such methods, a large-size digital computer is required, and in general, there exist many computational difficulties to obtain good results in cases of higher mode vibration and dynamic response problems [4]. Recently the more rigorous methods have been given by Laura, et al. [5, 6], and the author [7, 8]. In those studies there are some restrictions to the shape of the boundaries, and in general, the analysis must be developed on each problem. Therefore it seems to be important to give a more direct method from which the results with reasonable accuracy being obtained easily using a minicomputer. This paper is concerned with a direct method for dealing with dynamic response problems of a plate with arbitrary shape. The method developed in the author's previous report [9] concerning dynamic response problems of a membrane of arbitrary shape is expanded into this problem. In the analysis, the curved boundaries are divided into small segments, and the boundary conditions are satisfied directly using the Fourier expansion collocation method. To verify the present method, the results obtained are compared with exact ones for a circular plate. Numerical calculations are carried out for a truncated elliptical plate subjected to a uniformly distributed exponentially decaying impact load.

2 General Formulation of a Plate With Arbitrary Shape

When the origin of polar coordinates r and θ is taken at an arbitrary point in a plate, the equation of motion of the thin plate, in the coordinates r, θ, is

$$D\nabla^2\nabla^2 w + \rho h \partial^2 w/\partial t^2 = q \tag{1}$$

where w is the transverse displacement, ∇^2 is the two-dimensional Laplacian operator, ρ is the mass density, h is the thickness, $D = Eh^3/12(1-\nu^2)$ is the flexural rigidity, E is Young's modulus, ν is Poisson's ratio, t is the time, and q is the applied dynamic load. By applying Laplace transformation $\bar{f}(r, \theta, s) = \int_0^\infty f(r, \theta, t)e^{-st}dt$ to equation (1), the solution for a solid plate, under the assumption of all initial conditions being zero, is obtained as [7]

$$\bar{w} = (1/D)\sum_{l=1}^{2}\sum_{n=0}^{\infty}\epsilon_n\Big[A_{ln}J_n(\alpha r) + B_{ln}I_n(\alpha r) + (\pi/4\alpha^2)\int_0^r \bar{q}_{ln}\Big\{J_n(\alpha r)Y_n(\alpha\xi) - Y_n(\alpha r)J_n(\alpha\xi) + (2/\pi)[I_n(\alpha r)K_n(\alpha\xi) - K_n(\alpha r)I_n(\alpha\xi)]\Big\}\xi d\xi\Big]\Phi_{ln} \tag{2}$$

where

$$\bar{q}_{ln} = (1/\pi)\int_0^{2\pi}\bar{q}(r, \theta, s)\Phi_{ln}d\theta, \quad \alpha^4 = -s^2\rho h/D$$

$$\epsilon_n = 1/2 \quad \text{for} \quad n = 0 \quad \epsilon_n = 1 \quad \text{for} \quad n \geqq 1, \quad \Phi_{1n} = \cos n\theta, \quad \Phi_{2n} = \sin n\theta \tag{3}$$

The coefficients A_{ln} and B_{ln} are constants of integration to be determined from the boundary conditions, $J_n(\alpha r)$ and $Y_n(\alpha r)$ are the complex Bessel functions of first and second kinds of order n, and $I_n(\alpha r)$ and $K_n(\alpha r)$ are the modified Bessel functions.

The boundary conditions for the plate with arbitrary shape are

[1] After April 1, 1980, Department of Mechanical Engineering, Faculty of Engineering, Gunma University, Kiryu 376, Gunma, Japan.

Contributed by the Applied Mechanics Division for publication in the JOURNAL OF APPLIED MECHANICS.

Discussion on this paper should be addressed to the Editorial Department, ASME, United Engineering Center, 345 East 47th Street, New York, N.Y. 10017, and will be accepted until December 1, 1980. Readers who need more time to prepare a discussion should request an extension from the Editorial Department. Manuscript received by ASME Applied Mechanics Division, October, 1979; final revision, February, 1980.

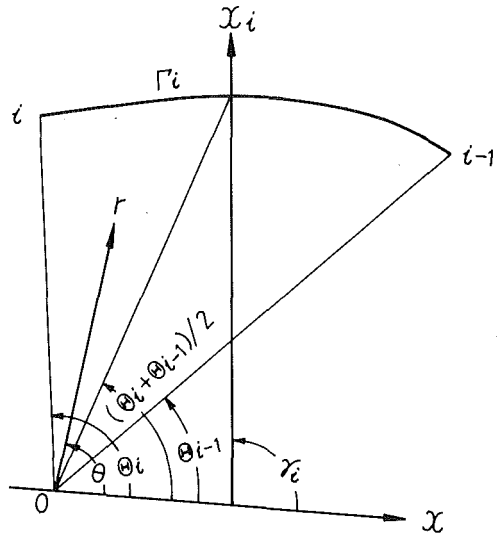

Fig. 1 Geometry of *i*th segment of curved boundaries of arbitrary shape

$$\left.\begin{aligned}(\overline{w})_\Gamma = (\partial\overline{w}/\partial z)_\Gamma = 0 \quad &\text{for the clamped edge}\\ (\overline{w})_\Gamma = (\overline{M}z)_\Gamma = 0 \quad &\text{for the simply supported edge}\\ (\overline{M}z)_\Gamma = (\overline{V}z)_\Gamma = 0 \quad &\text{for the free edge}\end{aligned}\right\} \tag{4}$$

where z is the coordinate normal to the boundary. We consider the case of the most complex plate of which boundary is consisted of both curved and straight lines. It is difficult to find the transformed expressions of the bending slope $\partial\overline{w}/\partial z$, Kirchhoff's shear V_z and the bending moment M_z in the direction normal to the boundary curve in the case of arbitrarily shaped plates. In this paper, to obtain the general transformed expressions, the curved boundary is divided into small segments as shown in Fig. 1. For treating the curved boundaries of arbitrary shape, the variation of the directions of the bending slope, the bending moment and the shearing force along the small segment of the boundary curve is neglected. Then each direction of these is assumed to be a constant although each magnitude of these varies along the segment. The following relations can be obtained from Fig. 1 for the ith segment: $dr = dx_i \cos(\theta - \gamma_i)$, $d\theta = -(dx_i/r)\sin(\theta - \gamma_i)$. By making use of the assumption as just mentioned, the general transformed expressions of $\partial\overline{w}/\partial x_i$ and M_{xi} in the direction x_i normal to the segment are obtained as

$$\left.\begin{aligned}\partial\overline{w}/\partial x_i &= (\partial\overline{w}/\partial r)\cos(\theta-\gamma_i) - (\partial\overline{w}/r\partial\theta)\sin(\theta-\gamma_i)\\ \overline{M}_{xi} &= -D\{(\partial^2\overline{w}/\partial r^2)[\cos^2(\theta-\gamma_i) + \nu\sin^2(\theta-\gamma_i)]\\ &\quad - 2(\partial^2\overline{w}/r\partial\theta\partial r)(1-\nu)\sin(\theta-\gamma_i)\cos(\theta-\gamma_i)\\ &\quad + (\partial\overline{w}/r\partial r)[\sin^2(\theta-\gamma_i) + \nu\cos^2(\theta-\gamma_i)]\\ &\quad + 2(\partial\overline{w}/r^2\partial\theta)(1-\nu)\sin(\theta-\gamma_i)\cos(\theta-\gamma_i)\\ &\quad + (\partial^2\overline{w}/r^2\partial\theta^2)[\sin^2(\theta-\gamma_i) + \nu\cos^2(\theta-\gamma_i)]\}\end{aligned}\right\} \tag{5}$$

where γ_i is the angle between the normal and the x-axis which has a constant value in a small segment under the assumption as just mentioned (see Fig. 1). Substituting equation (2) into equations (5), one obtains

$$\left.\begin{aligned}\overline{w} &= (1/D)\sum_{l=1}^{2}\sum_{n=0}^{\infty}\epsilon_n[A_{ln}J_n(\alpha r)\Phi_{ln} + B_{ln}I_n(\alpha r)\Phi_{ln} + F_{ln}{}^1]\\ \partial\overline{w}/\partial x_i &= (\alpha/D)\sum_{l=1}^{2}\sum_{n=0}^{\infty}\epsilon_n(A_{ln}X_{ln}{}^1 + B_{ln}X_{ln}{}^2 + F_{ln}{}^2)\\ M_{xi} &= -\alpha^2\sum_{l=1}^{2}\sum_{n=0}^{\infty}\epsilon_n(A_{ln}m_{ln}{}^1 + B_{ln}m_{ln}{}^2 + F_{ln}{}^3)\end{aligned}\right\} \tag{6}$$

where $X_{\ln}{}^1 = X_{\ln}{}^1(r,\theta)$, $X_{\ln}{}^2 = X_{\ln}{}^2(r,\theta)$, ... are given by

$$\begin{aligned}X_{1n}{}^1(r,\theta) &= [J_{n-1}(\alpha r) - (n/\alpha r)J_n(\alpha r)]\cos(\theta-\gamma_i)\cos n\theta\\ &\quad + (n/\alpha r)J_n(\alpha r)\sin(\theta-\gamma_i)\sin n\theta\\ X_{1n}{}^2(r,\theta) &= [I_{n-1}(\alpha r) - (n/\alpha r)I_n(\alpha r)]\cos(\theta-\gamma_i)\cos n\theta\\ &\quad + (n/\alpha r)I_n(\alpha r)\sin(\theta-\gamma_i)\sin n\theta\\ m_{1n}{}^1(r,\theta) &= \{(n^2+n)(1-\nu)[\cos 2(\theta-\gamma_i)\cos n\theta\\ &\quad - \sin 2(\theta-\gamma_i)\sin n\theta]/\alpha^2r^2 - [\cos^2(\theta-\gamma_i)\\ &\quad + \nu\sin^2(\theta-\gamma_i)]\cos n\theta\}J_n(\alpha r)\\ &\quad - \{(1-\nu)[\cos 2(\theta-\gamma_i)\cos n\theta - n\sin 2(\theta-\gamma_i)\\ &\quad \times \sin n\theta]/\alpha r\}J_{n-1}(\alpha r)\\ m_{1n}{}^2(r,\theta) &= \{(n^2+n)(1-\nu)[\cos 2(\theta-\gamma_i)\cos n\theta\\ &\quad - \sin 2(\theta-\gamma_i)\sin n\theta]/\alpha^2r^2\\ &\quad + [\cos^2(\theta-\gamma_i) + \nu\sin^2(\theta-\gamma_i)]\cos n\theta\}I_n(\alpha r)\\ &\quad - \{(1-\nu)[\cos 2(\theta-\gamma_i)\cos n\theta\\ &\quad - n\sin 2(\theta-\gamma_i)\sin n\theta]/\alpha r\}I_{n-1}(\alpha r)\\ F_{1n}{}^1(r,\theta) &= (\pi/4\alpha^2)\int_0^r \overline{q}_{\ln}\{J_n(\alpha r)Y_n(\alpha\xi) - Y_n(\alpha r)J_n(\alpha\xi)\\ &\quad + (2/\pi)[I_n(\alpha r)K_n(\alpha\xi) - K_n(\alpha r)I_n(\alpha\xi)]\}\xi d\xi\cos n\theta\\ F_{1n}{}^2(r,\theta) &= (1/\alpha)[\cos(\theta-\gamma_i)\partial F_{1n}{}^1/\partial r - \sin(\theta-\gamma_i)\\ &\quad \partial F_{1n}{}^1/r\partial\theta]\\ F_{1n}{}^3(r,\theta) &= (1/\alpha^2)\{(\partial^2F_{1n}{}^1/\partial r^2)[\cos^2(\theta-\gamma_i)\\ &\quad + \nu\sin^2(\theta-\gamma_i)]\\ &\quad - (2\partial^2F_{1n}{}^1/r\partial r\partial\theta)(1-\nu)\sin(\theta-\gamma_i)\cos(\theta-\gamma_i)\\ &\quad + (\partial F_{1n}{}^1/r\partial r)[\sin^2(\theta-\gamma_i) + \nu\cos^2(\theta-\gamma_i)]\\ &\quad + (2\partial F_{1n}{}^1/r^2\partial\theta)(1-\nu)\sin(\theta-\gamma_i)\cos(\theta-\gamma_i)\\ &\quad + (\partial^2F_{1n}{}^1/r^2\partial\theta^2)[\sin^2(\theta-\gamma_i) + \nu\cos^2(\theta-\gamma_i)]\end{aligned} \tag{7}$$

The expressions for $l = 2$ have the same forms as equations (7), but $\cos n\theta$ is replaced by $\sin n\theta$ and also $\sin n\theta$ is replaced by $-\cos n\theta$. The transformed expressions for the straight line boundary are also the same as equations (6), but the angle γ_i has a constant value.

The boundary conditions along the whole range of the boundary cannot be satisfied directly. To satisfy the boundary conditions, the Fourier expansion is performed to the equations of the boundary conditions along the boundary line. For the present case, one straight line is considered to be one segment, while one curved line must be divided into many segments according to the convergence of the solution. The Fourier coefficients are therefore obtained by the addition of those for the separately considered boundaries. When the plate is symmetric about an axis, the analysis can be separated into symmetric and antisymmetric cases. Hence when the coordinate θ is taken from the axis of symmetry and the series are truncated to $N+1$, the simultaneous equations for finding the unknown constants A_{ln} and B_{ln} can be obtained, as

$$\begin{bmatrix}\\ \Delta_1(\lambda)\\ \\ \end{bmatrix}\begin{bmatrix}A_{10}\\ \vdots\\ A_{1N}\\ B_{10}\\ \vdots\\ B_{1N}\end{bmatrix} = \begin{bmatrix}\sum_{n'=0}^{N}P_{n'0}{}^{11}\\ \vdots\\ \sum_{n'=0}^{N}P_{n'N}{}^{11}\\ \sum_{n'=0}^{N}P_{n'0}{}^{21}\\ \vdots\\ \sum_{n'=0}^{N}P_{n'N}{}^{21}\end{bmatrix} \tag{8a}$$

$$\begin{bmatrix} \\ \Delta_2(\lambda) \\ \\ \end{bmatrix} \begin{bmatrix} A_{21} \\ \vdots \\ A_{2N} \\ B_{21} \\ \vdots \\ B_{2N} \end{bmatrix} = \begin{bmatrix} \sum_{n'=1}^{N} P_{n'1}{}^{12} \\ \vdots \\ \sum_{n'=1}^{N} P_{n'N}{}^{12} \\ \sum_{n'=1}^{N} P_{n'1}{}^{22} \\ \vdots \\ \sum_{n'=1}^{N} P_{n'N}{}^{22} \end{bmatrix} \tag{8b}$$

where

$$|\Delta_1(\lambda)| = \begin{vmatrix} S_{00}^{11} & \cdots & S_{N0}^{11} & S_{00}^{21} & \cdots & S_{N0}^{21} \\ \vdots & & \vdots & \vdots & & \vdots \\ S_{0N}^{11} & \cdots & S_{NN}^{11} & S_{0N}^{21} & \cdots & S_{NN}^{21} \\ S_{00}^{31} & \cdots & S_{N0}^{31} & S_{00}^{41} & \cdots & S_{N0}^{41} \\ \vdots & & \vdots & \vdots & & \vdots \\ S_{0N}^{31} & \cdots & S_{NN}^{31} & S_{0N}^{41} & \cdots & S_{NN}^{41} \end{vmatrix} \tag{9a}$$

$$|\Delta_2(\lambda)| = \begin{vmatrix} S_{11}^{12} & \cdots & S_{N1}^{12} & S_{11}^{22} & \cdots & S_{N1}^{22} \\ \vdots & & \vdots & \vdots & & \vdots \\ S_{1N}^{12} & \cdots & S_{NN}^{12} & S_{1N}^{22} & \cdots & S_{NN}^{22} \\ S_{11}^{32} & \cdots & S_{N1}^{32} & S_{11}^{42} & \cdots & S_{N1}^{42} \\ \vdots & & \vdots & \vdots & & \vdots \\ S_{1N}^{32} & \cdots & S_{NN}^{32} & S_{1N}^{42} & \cdots & S_{NN}^{42} \end{vmatrix} \tag{9b}$$

$$\left.\begin{aligned} S_{nm}^{kl} &= (2\epsilon_n/\pi) \sum_{i=1}^{I} \int_{\Theta_{i-1}}^{\Theta_i} Z_{ln}^{ik} \psi_{lm} d\theta \quad \text{for} \quad k = 1, 2, 3, 4 \\ \psi_{1m} &= \cos m\theta, \qquad \psi_{2m} = \sin m\theta \end{aligned}\right\} \tag{10}$$

and where

$$\left.\begin{aligned} Z_{ln}{}^{i1} &= J_n(\alpha R_i)\Phi_{ln}, \quad Z_{ln}{}^{i2} = I_n(\alpha R_i)\Phi_{ln}, \\ Z_{ln}{}^{i3} &= X_{ln}{}^{1}(R_i, \theta), \quad Z_{ln}{}^{i4} = X_{ln}{}^{2}(R_i, \theta) \\ P_{nm}{}^{1l} &= -(2\epsilon_n/\pi) \sum_{i=1}^{I} \int_{\Theta_{i-1}}^{\Theta_i} F_{ln}{}^{1}(R_i, \theta)\psi_{lm} d\theta \\ P_{nm}{}^{2l} &= -(2\epsilon_n/\pi) \sum_{i=1}^{I} \int_{\Theta_{i-1}}^{\Theta_i} F_{ln}{}^{2}(R_i, \theta)\psi_{lm} d\theta \end{aligned}\right\} \tag{11a}$$

for the clamped edge, and

$$\left.\begin{aligned} Z_{ln}{}^{i1} &= J_n(\alpha R_i)\Phi_{ln}, \quad Z_{ln}{}^{i2} = I_n(\alpha R_i)\Phi_{ln}, \\ Z_{ln}{}^{i3} &= m_{ln}{}^{1}(R_i, \theta), \quad Z_{ln}{}^{i4} = m_{ln}{}^{2}(R_i, \theta) \\ P_{nm}{}^{1l} &= -(2\epsilon_n/\pi) \sum_{i=1}^{I} \int_{\Theta_{i-1}}^{\Theta_i} F_{ln}{}^{1}(R_i, \theta)\psi_{lm} d\theta, \\ P_{nm}{}^{2l} &= -(2\epsilon_n/\pi) \sum_{i=1}^{I} \int_{\Theta_{i-1}}^{\Theta_i} F_{ln}{}^{3}(R_i, \theta)\psi_{lm} d\theta \end{aligned}\right\} \tag{11b}$$

for the simply supported edge. I is the number of the segments including the straight line boundaries in the range $\theta = 0$ to $\theta = \pi$ and R_i is the coordinate r at ith boundary which is expressed as a function of θ.

The frequency equation is obtained by putting the determinant of the coefficients of the simultaneous equation to zero

$$|\Delta_l(\lambda)| = 0 \tag{12}$$

The displacement of the plate is found from the Laplace transform inversion integral $f(r, \theta, t) = (1/2\pi j) \int_{Br} \bar{f}(r, \theta, s) e^{st} ds$, where $j = \sqrt{-1}$. The Laplace transform inversion integral is evaluated by the residue theroem. It is difficult to obtain the analytical values for the residues because, in general, the integration in equations (10) and (11) cannot be found analytically for arbitrarily shaped plates. Therefore the integration for finding the Fourier coefficients and the differentiation of the determinant of the coefficients of the simultaneous equations for finding the residues are performed numerically. The displacement w as a function of time is then shown to be

$$w(r, \theta, t) = \sum \text{Res}\ (\bar{w} e^{st}) \tag{13}$$

where ΣRes shows the sum of the residues.

3 Dynamic Response of Arbitrarily Shaped Plates to Exponentially Decaying Impact Loads

As an example, we consider a plate subjected to a uniformly distributed exponentially decaying impact load $q = q_0 \exp(-\beta t)$, where q_0 is the intensity of the load and β is the time decay parameter. By applying the Laplace transform. one has $\bar{q} = q_0/(s + \beta)$. Hence $F_{1n}{}^{1}$ through $F_{1n}{}^{3}$ in equations (7) become

$$\left.\begin{aligned} F_{10}{}^{1} &= (\pi/2\alpha^3)[q_0 r/(s + \beta)]\{J_0(\alpha r)Y_1(\alpha r) - Y_0(\alpha r)J_1(\alpha r) \\ &\quad - (2/\pi)[I_0(\alpha r)K_1(\alpha r) + K_0(\alpha r)I_1(\alpha r)]\} \\ F_{1n}{}^{1} &= 0 \quad \text{for} \quad n \geq 1, \qquad F_{1n}{}^{2} = F_{1n}{}^{3} = 0 \end{aligned}\right\} \tag{14}$$

Substituting equations (14) into equation (11a) yield

$$P_{0m}{}^{11} = \pi b^4 q_0 P_{0m}{}^{*}/2\lambda^2(s + \beta), \qquad P_{0m}{}^{21} = 0 \tag{15}$$

where

$$\left.\begin{aligned} P_{0m}{}^{*} &= -(1/\pi) \sum_{i=1}^{I} \int_{\Theta_{i-1}}^{\Theta_i} \alpha^* R_i^* \{J_0(\alpha^* R_i^*)Y_1(\alpha^* R_i^*) \\ &\quad - Y_0(\alpha^* R_i^*)J_1(\alpha^* R_i^*) - (2/\pi)[I_0(\alpha^* R_i^*)K_1(\alpha^* R_i^*) \\ &\quad + K_0(\alpha^* R_i^*)I_1(\alpha^* R_i^*)]\} \cos m\theta d\theta, \ \alpha^* = \alpha b, \\ \lambda &= (\alpha^*)^2 = -js(\rho h b^4/D)^{1/2}, \ R_i^* = R_i/b, \quad r^* = r/b \end{aligned}\right\} \tag{16}$$

and where b is the reference length which is introduced to make the expressions to nondimensional forms. The constants A_{1n} and B_{1n} are obtained from equation (8a) as

$$A_{1n} = \pi b^4 q_0 A_{1n}{}^{*}/2\lambda^2(s + \beta), \quad B_{1n} = \pi b^4 q_0 B_{1n}{}^{*}/2\lambda^2(s + \beta) \tag{17}$$

where

$$A_{1n}{}^{*} = H_{n+1}(\lambda)/|\Delta_1(\lambda)|, \quad B_{1n}{}^{*} = H_{n+N+2}(\lambda)/|\Delta_1(\lambda)| \tag{18}$$

$H_{n+1}(\lambda)$ or $H_{n+N+2}(\lambda)$ is the determinant shown in equation (9a), but in which the elements of $(n + 1)$th or $(n + N + 2)$th column is replaced by $(P_{00}{}^{*}, P_{01}{}^{*}, \ldots P_{0N}{}^{*}, 0, \ldots 0)$, respectively. Substituting equation (17) into (6), $\bar{w}$ is obtained as

$$\begin{aligned} \bar{w}(r, \theta, s) = [\pi b^4 q_0/2\lambda^2(s + \beta)D] \Bigg[\sum_{n=0}^{N} \epsilon_n \{ & [H_{n+1}(\lambda)J_n(\alpha^* r^*) \\ & + H_{n+N+2}(\lambda)I_n(\alpha^* r^*)]/|\Delta_1(\lambda)|\} \cos n\theta \\ & + 0.5\alpha^* r^* [J_0(\alpha^* r^*)Y_1(\alpha^* r^*) \\ & - Y_0(\alpha^* r^*)J_1(\alpha^* r^*)] - (\alpha^* r^*/\pi)[I_0(\alpha^* r^*)K_1(\alpha^* r^*) \\ & + K_0(\alpha^* r^*)I_1(\alpha^* r^*)] \Bigg] \end{aligned} \tag{19}$$

The displacement as a function of time is found from equation (13).

---

[2] In reference (7), $H_{n+N+1}(\lambda^*)$ should read $H_{n+N+2}(\lambda^*)$, and equation (26) also should read

$$W_2 = \sum_{P} \sum_{n=0}^{N} \{[\epsilon_n/(\lambda^* - i\beta^*)][H_{n+1}(\lambda^*)J_n(\alpha^*\eta) + H_{n+N+2}(\lambda^*)I_n(\alpha^*\eta)]/(d\Delta(\lambda^*)/d\lambda^*)\}_{\lambda^*=\lambda_p{}^*} \exp(i\lambda_p{}^* T) \cos n\theta'$$

Numerical calculations in reference (7) have been carried out, of course, using the corrected expressions.

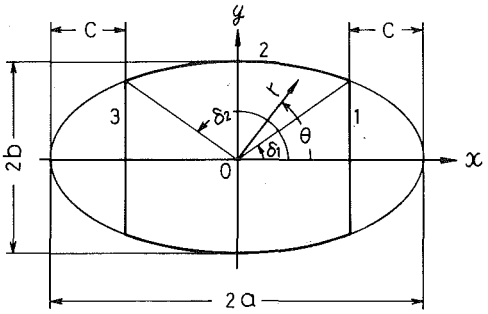

Fig. 2 Geometry of truncated elliptical plates

For the present case, one of the poles of the integrand is given by $s = -\beta$ or $\lambda = j\beta(\rho h b^4/D)^{1/2}$ and the other poles by the roots of the frequency equation. One has the conjugate poles from the frequency equation (12), hence the displacement $w(r, \theta, t)$ can be evaluated by the residue theorem, in a nondimensional form[2]

$$w^* = Dw/b^4 q_0 = W_1 + W_2 \tag{20}$$

where

$$W_1 = (-\pi/2\beta^{*2}) \left[\sum_{n=0}^{N} \epsilon_n \{ [H_{n+1}(\lambda) J_n(\alpha^* r^*) + H_{n+N+2}(\lambda) I_n(\alpha^* r^*)]/ |\Delta_1(\lambda)| \} \cos n\theta + 0.5\alpha^* r^* [J_0(\alpha^* r^*) Y_1(\alpha^* r^*) - Y_0(\alpha^* r^*) J_1(\alpha^* r^*)] - (\alpha^* r^*/\pi)[I_0(\alpha^* r^*) K_1(\alpha^* r^*) + K_0(\alpha^* r^*) I_1(\alpha^* r^*)] \right]_{\lambda = j\beta^*} \exp(-\beta^* T)$$

$$W_2 = R_e \left[\sum_{P} \{ [\pi/\lambda^2(\lambda - j\beta^*)] \sum_{n=0}^{N} \epsilon_n [H_{n+1}(\lambda) J_n(\alpha^* r^*) + H_{n+N+2}(\lambda) I_n(\alpha^* r^*)] \cos n\theta / (d|\Delta_1(\lambda)|/d\lambda) \}_{\lambda = \lambda_P} \exp(j\lambda_P T) \right]$$

$$\beta^* = \beta(\rho h b^4/D)^{1/2}, \quad T = t(D/\rho h b^4)^{1/2} \tag{21}$$

and where R_e denotes the real part of the expression and λ_P is the coordinate of the pth pole in a right half λ-plane which is obtained from the frequency equation.

3.1 Example 1: Circular Plates. First, we consider a circular plate of radius a subjected to a uniformly distributed exponentially decaying load. For the present case, the reference length b is taken as the radius of the plate, i.e., $b = a$, in the previous equations. Hence one has the following relations:

$$R_i^* = R_i/a = 1, \qquad \gamma_i = \Theta_i^* \tag{22}$$

where $\Theta_i^* = (\Theta_{i-1} + \Theta_i)/2$.

3.2 Example 2: Truncated Elliptical Plates. As an example of arbitrarily shaped plates, we consider a truncated elliptical plate as shown in Fig. 2. For this case, the boundary curve is separated into two straight lines (boundary 1, 3) and one elliptical curve (boundary 2). The equation of the elliptical curve of major axis $2a$ and minor axis $2b$ is

$$x^2/a^2 + y^2/b^2 = 1, \qquad x = R_i \cos\theta, \qquad y = R_i \sin\theta \tag{23}$$

From which one obtains $dy/dx = -(b/a)^2(x/y)$. Hence R_i^* and γ_i are denoted by

$$\left.\begin{aligned} R_i^* &= R_i/b = (a/b)/[\cos^2\theta + (a^2/b^2)\sin^2\theta]^{1/2} \\ \gamma_i &= \pi/2 - \tan^{-1}[(b/a)^2/\tan\Theta_i^*] \quad \text{for} \quad \Theta_i^* < \pi/2, \\ \gamma_i &= \pi/2 \quad \text{for} \quad \Theta_i^* = \pi/2 \\ \gamma_i &= \pi/2 + \tan^{-1}[(b/a)^2/|\tan\Theta_i^*|] \quad \text{for} \quad \Theta_i^* > \pi/2 \end{aligned}\right\} \tag{24}$$

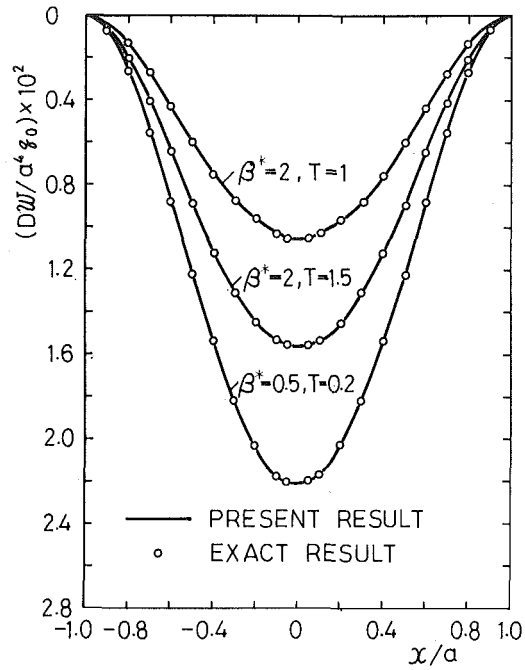

Fig. 3 Comparison between present and exact results for a clamped solid circular plate subjected to a uniformly distributed exponentially decaying impact load

for the boundary 2. The following relations can be obtained easily for the boundary 1 as

$$\gamma_i = 0, \qquad R_i^* = (a - c)/b\cos\theta \tag{25}$$

and for the boundary 3 as

$$\gamma_i = \pi, \qquad R_i^* = -(a - c)/b\cos\theta \tag{26}$$

The angles δ_1 and δ_2 are

$$\delta_1 = \tan^{-1}\{[b/(a - c)][1 - (a - c)^2/a^2]^{1/2}\}, \quad \delta_2 = \pi - \delta_1 \tag{27}$$

By substituting the expressions for R_i and γ_i into equations (11a) and (11b), $Z_{ln}{}^{ik}$ and $P_{0m}{}^*$ are expressed as a function of θ only. Hence the integration can be performed numerically, and the displacement $w(r, \theta, t)$ is evaluated from equation (20) directly.

The results for the other plates can be obtained easily only by obtaining the expressions for R_i and γ_i as in the same way as previously. If the Mindlin plate theory is utilized instead of the classical plate theory used in this analysis, the solution for the thick plate can be given by the similar technique developed in this paper.

4 Numerical Examples

In this paper the boundary conditions are satisified approximately by using the Fourier series although the solution satisfies the equation of motion exactly. Therefore the results obtained must be investigated with respect to both the convergence and the errors of calculation. In the numerical calculation, first three residues are added up and $N = 4$ or $N = 7$ is included according to the convergence of the series. Poisson's ratio is taken as 0.3 and the curved boundary is divided into 20 segments.

To verify the present results, both present and exact results (see the Appendix) are compared with each other for a solid circular plate as shown in Fig. 3. In the figure, the present results with $N = 4$ are denoted by the solid line and the exact ones by the small circle. It can be noted that the present result coincides with the exact one. As a numerical example, vibrations and the dynamic response of a truncated elliptical plate as shown in Fig. 2 are investigated. Tables 1 and 2 depict the nondimensional natural frequencies $\alpha b = (\omega^2 b^4 \rho h/D)^{1/4}$ of the clamped and simply supported truncated elliptical plates for

Table 1 Nondimensional natural frequencies $\alpha b(=\omega^2 b^4 \rho h/D)^{1/4}$ of clamped truncated elliptical plates (ω represents the circular frequency, * denotes Sato's exact result [10, 11])

		c/a						
a/b	Mode No.	0	0.1	0.2	0.3	0.4	0.5	0.6
1.0	1	3.197(3.196*)	3.279	3.479	3.787	4.252	4.962	6.072
	2	4.611	4.826	5.252	5.869	6.422	6.861	7.740
1.2	1	2.953(2.953*)	3.002	3.131	3.350	3.697	4.248	5.143
	2	4.055	4.201	4.521	5.006	5.709	6.396	6.976
1.4	1	2.809(2.809*)	2.835	2.919	3.074	3.334	3.765	4.496
	2	3.692	3.786	4.030	4.412	4.986	5.846	6.535
2.0	1	2.616(2.616*)	2.619	2.640	2.695	2.805	3.018	3.426
	2	3.142	3.163	3.259	3.452	3.777	4.307	5.184
2.5	1	2.551(2.550*)	2.551	2.555	2.579	2.635	2.757	3.011
	2	2.939	2.945	2.980	3.087	3.291	3.655	4.299
3.0	1	2.512(2.512*)	2.512	2.514	2.522	2.552	2.623	2.787
	2	2.824	2.821	2.835	2.887	3.016	3.270	3.748

Table 2 Nondimensional natural frequencies αb of simply suppoted truncated elliptical plates with $\nu = 0.3$ (* denotes Sato's exact result [10, 11])

		c/a						
a/b	Mode No.	0	0.1	0.2	0.3	0.4	0.5	0.6
1.0	1	2.222(2.222*)	2.299	2.463	2.682	3.006	3.482	4.209
	2	3.728	3.920	4.271	4.771	5.424	5.662	6.092
1.4	1	1.955(1.953*)	1.987	2.079	2.213	2.408	2.708	3.195
	2	2.937	3.042	3.272	3.597	4.065	4.762	5.485
2.0	1	1.817(1.818*)	1.821	1.858	1.929	2.036	2.206	2.497
	2	2.432	2.464	2.591	2.790	3.077	3.519	4.233
3.0	1	1.735(1.735*)	1.734	1.737	1.759	1.807	1.891	2.041
	2	2.111	2.112	2.140	2.237	2.395	2.641	3.060

various aspect ratios, respectively. The results for a solid elliptical plate can be calculated when the truncated sides are removed in this analysis. The calculated frequencies in such a special case of c/a being zero are in very good agreement with the exact ones given by Sato [10, 11]. However as the aspect ratio a/b becomes significantly large, the convergence of the series becomes poor, so that it is difficult to obtain the good results for such slender plates.

For the case of truncated plates, the convergence of the series becomes poor as compared with the circular plates. Comparisons between the displacements $(Dw/b^4q_0) \times 10^2$ along the x-axis of a truncated elliptical plate subjected to the impact load with $a/b = 2$, $c/a = 0.2$, $\beta^* = 0.5$, and $T = 0.2$ for $N = 5$ and $N = 7$ are as follows:

	$x/a = 0.05$	0.2	0.4	0.6	0.8	
$(Dw/b^4q_0) \times 10^2$	= 2.699	2.467	1.792	0.827	0.197	for $N = 5$
	= 2.620	2.385	1.718	0.746	0.089	for $N = 7$

It can be observed that the results with reasonable accuracy can be obtained when up to eight terms are included in the numerical calculation. Figs. 4 and 5 show the displacements $w^* = Dw/q_0b^4$ along the x and y-axis for the truncated circular ($a = b$) and the truncated elliptical plates ($a/b = 2$) subjected to the impact loads $q = q_0 \exp(-\beta t)$. Since the boundary conditions are satisfied approximately in the present analysis, the calculated result has a small error and the displacement at the boundary does not vanish exactly as shown in the figures. However the errors are significantly small, so that we can conclude that the present method gives reliable results for dynamic

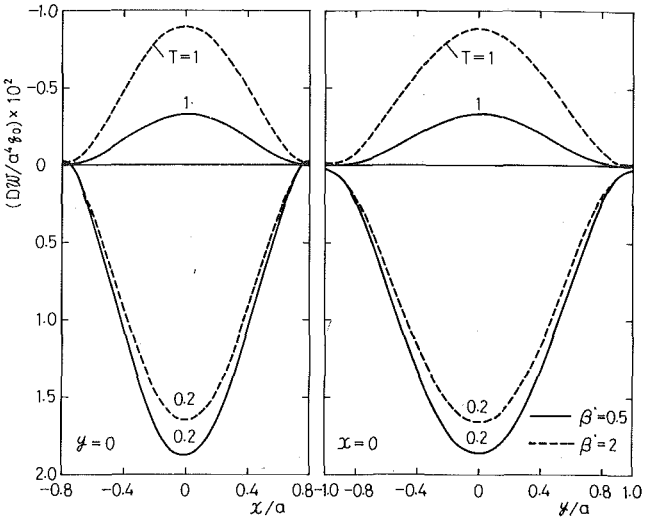

Fig. 4 Displacments along the x and y-axis of a clamped truncated circular plate subjected to a uniformly distributed exponentially decaying impact load with $a/b = 1$ and $c/a = 0.2$

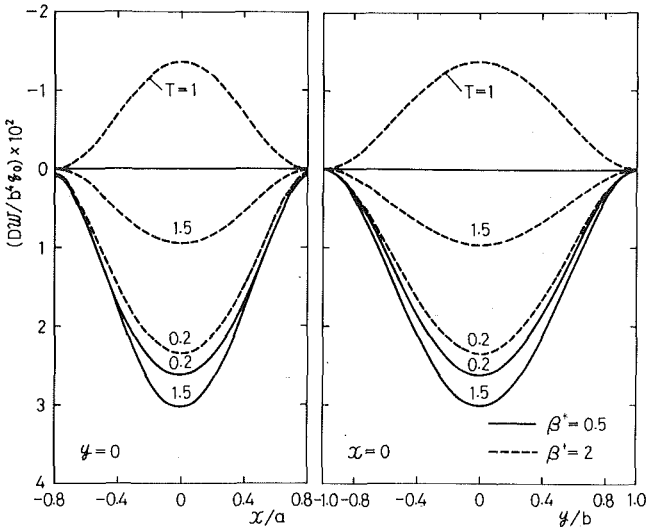

Fig. 5 Displacements along the x and y-axis of a clamped truncated elliptical plate subjected to a uniformly distributed exponentially decaying impact load with $a/b = 2$ and $c/a = 0.2$

response problems of arbitrarily shaped plates. Fig. 6 depicts the response curves of the displacements for the truncated elliptical plate with $a/b = 2$, $c/a = 0.2$.

5 Conclusions

In this paper a direct method for solving dynamic response problems of an arbitrarily shaped plate has been presented. Numerical calculations have been carried out for a circular or a truncated elliptical plate subjected to a uniformly distributed exponentially decaying impact load. The comparison between present and exact results for typical plates such as the circular and the elliptical plates shows good agreement. The method developed in this paper is straightforward and the numerical results can be obtained easily for arbitrarily shaped plates by using a minicomputer. It seems therefore the present method has advantages as compared with the other general approximate methods.

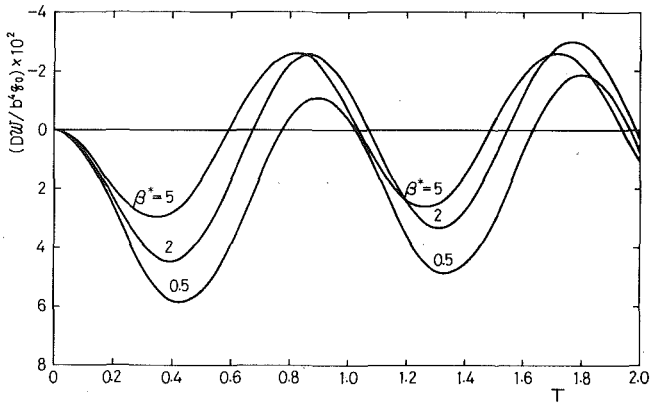

Fig. 6. Displacements at $x/a = 0.05$, $y = 0$ versus the time for a clamped truncated elliptical plate subjected to a uniformly distributed exponentially decaying impact load with $a/b = 2$ and $c/a = 0.2$

Acknowledgments

The author wishes to thank heartily Prof. Y. Hirano, Yamagata University, for his kind guidance. The author is also indebted to Mr. J. Nakamura for his various contributions throughout the progress of the present investigation.

References

1 Conway, H. D., "The Bendings and Flexural Vibrations of Simply Supported Polygonal Plates by Point-Matching," ASME JOURNAL OF APPLIED MECHANICS, Vol. 28, 1960, pp. 281–291.

2 Conway, H. D., and Farnham, K. A., "The Flexural Vibrations of Triangular, Rhombic and Parallelogram Plates and Some Analogies," *International Journal of Mechanical Sciences*, Vol. 7, 1965, pp. 811–816.

3 Hegarty R. F., and Ariman, T., "Elasto-Dynamic Analysis of Rectangular Plates With Circular Holes," *International Journal of Solids and Structures*, Vol. 11, 1975, pp. 895–906.

4 Hirano, Y., and Okazaki, K., "Vibration of a Circular Plate Having Partly Clamped or Partly Simply Supported Boundary," *Bulletin of the JSME*, Vol. 19, 1976, pp. 610–618.

5 Laura, P. A. A., Discussion to "The Eigenvalue Problem for Two-Dimensional Regions With Irregular Boundaries," ASME JOURNAL OF APPLIED MECHANICS, Vol. 35, 1968, p. 198.

6 Shahady, P. A., Passarelli, R., and Laura, P. A. A., "Application of Complex Variable Theory to the Determination of the Fundamental Frequency of Vibrating Plates," *Journal of the Acoustical Society of America*, Vol. 42, 1967, pp. 806–809.

7 Nagaya, K., "Dynamics of Viscoelastic Plates With Curved Boundaries of Arbitrary Shape," ASME JOURNAL OF APPLIED MECHANICS, Vol. 45, 1978, pp. 629–635.

8 Nagaya, K., "Vibrations of a Plate With an Elastic Constraint of Eccentric Circular Part," *Journal of the Acoustical Society of America*, Vol. 66, 1979, pp. 185–191.

9 Nagaya, K., "Dynamic Response of Membranes With Both Curved and Straight Line Boundaries," ASME JOURNAL OF APPLIED MECHANICS, Vol. 46, 1979, pp. 667–671.

10 Sato, K., "Free Flexural Vibrations of an Elliptical Plate With Simply Supported Edge," *Journal of the Acoustical Society of America*, Vol. 52, 1971, pp. 919–922.

11 Sato, K., "Free Flexural Vibrations of an Elliptical Plate With an Elastically Supported Edge," *Transactions of the Japan Society of Mechanical Engineers* (in Japanese), Vol. 41, 1975, pp. 1996–2001.

APPENDIX

By taking the terms of $n = 0$ only in equation (2), the displacement of a circular plate subjected to a uniformly distributed exponentially decaying impact load is found to be

$$\bar{w} = (1/2D)\Big[A_0 J_0(\alpha r) + B_0 I_0(\alpha r) + [\pi q_0 r/2\alpha^3(s+\beta)]\{J_0(\alpha r)Y_1(\alpha r) - Y_0(\alpha r)J_1(\alpha r) - (2/\pi)[I_0(\alpha r)K_1(\alpha r) + K_0(\alpha r)I_1(\alpha r)]\}\Big] \quad (28)$$

The boundary conditions for the clamped circular plate are $(\bar{w})_{r=a} = (\partial\bar{w}/\partial r)_{r=a} = 0$. One can obtain the unknown constants A_0 and B_0, and the displacement $\bar{w}$ then can be expressed as

$$D\bar{w}/q_0 a^4 = [\pi/4\alpha^3 a^3(s+\beta)]\Big[-[J_0(\alpha r)I_1(\alpha a) + J_1(\alpha a)I_0(\alpha r)]\{J_0(\alpha a)Y_1(\alpha a) - Y_0(\alpha a)J_1(\alpha a) - (2/\pi)[I_0(\alpha a)K_1(\alpha a) + K_0(\alpha a)I_1(\alpha a)]\}/ \quad (29)$$

$$[J_0(\alpha a)I_1(\alpha a) + J_1(\alpha a)I_0(\alpha a)]$$
$$+ (r/a)\{J_0(\alpha r)Y_1(\alpha r) - Y_0(\alpha r)J_1(\alpha r)$$
$$- (2/\pi)[I_0(\alpha r)K_1(\alpha r) + K_0(\alpha r)I_1(\alpha r)]\}\Big]_{\lambda=j\beta^*} \quad (29)$$
(Cont.)

By applying the Laplace transform inversion integral to equation (29), the displacement as a function of time is obtained in a nondimensional form

$$w^* = Dw(r, \theta, t)/q_0a^4 = W_1^* + W_2^* \quad (30)$$

where

$$W_1^* = \Big[-(\pi/4\alpha^{*3})[J_0(\alpha^* r^*)I_1(\alpha^*) + J_1(\alpha^*)I_0(\alpha^* r^*)]$$
$$\times \{J_0(\alpha^*)Y_1(\alpha^*) - Y_0(\alpha^*)J_1(\alpha^*) - (2/\pi)[I_0(\alpha^*)K_1(\alpha^*)$$
$$+ K_0(\alpha^*)I_1(\alpha^*)]\}/[J_0(\alpha^*)I_1(\alpha^*) + J_1(\alpha^*)I_0(\alpha^*)]$$
$$+ (\pi/4\alpha^{*3})(r/a)\{J_0(\alpha^* r^*)Y_1(\alpha^* r^*) - Y_0(\alpha^* r^*)J_1(\alpha^* r^*)$$
$$- (2/\pi)[I_0(\alpha^* r^*)K_1(\alpha^* r^*) + K_0(\alpha^* r^*)I_1(\alpha^* r^*)]\}\Big]_{\lambda=j\beta^*} \exp(-\beta^* T) \quad (31)$$

$$W_2^* = R_e \sum_P \left[\frac{-\pi \exp(j\lambda T)}{\lambda(\lambda - j\beta^*)} \right.$$
$$\times \left. \frac{[J_0(\alpha^* r^*)I_1(\alpha^*) + J_1(\alpha^*)I_0(\alpha^* r^*)]\{J_0(\alpha^*)Y_1(\alpha^*) - Y_0(\alpha^*)J_1(\alpha^*) - (2/\pi)[I_0(\alpha^*)K_1(\alpha^*) + K_0(\alpha^*)I_1(\alpha^*)]\}}{2J_0(\alpha^*)I_0(\alpha^*) - (1/\alpha^*)[J_0(\alpha^*)I_1(\alpha^*) + J_1(\alpha^*)I_0(\alpha^*)]} \right]_{\lambda=\lambda_P}$$

and where λ_p is the pth axisymmetric modal frequency for the solid circular plate.

D. E. Beskos
Associate Professor,
Department of Civil and Mineral Engineering,
University of Minnesota,
Minneapolis, Minn. 55455
Mem. ASME

B. A. Boley
Dean,
The Technological Institute,
Northwestern University,
Evanston, Ill. 60201
Fellow ASME

Critical Damping in Linear Discrete Dynamic Systems

Free viscously damped vibrations of linear discrete systems are studied. The amount of damping varies among the various elements of the system resulting in several critical damping possibilities. A general method is developed for determining the "critical damping surfaces" of a system. These surfaces represent the loci of combinations of damping values corresponding to critically damped motions, and thus separate regions of partial or complete underdamping from those of overdamping. The dimension of a critical damping surface is equal to the number of independent amounts of damping present in the system. Three examples presented in detail illustrate the proposed technique and some of the important characteristics of critical damping surfaces.

Introduction

Critical damping studies, apart from being theoretically interesting, are also important in the design of sensitive instruments which must have high amounts of damping (usually critical damping) to avoid resonant amplitude distortion.

When the viscous damping in a linear dynamic system, expressed as a percentage of the critical damping, is everywhere the same or is given in modal form, the problem of determining the amount of critical damping and thus characterize the system as underdamped or overdamped is essentially one-dimensional and presents no difficulties.

However, for the more realistic model of a linear dynamic system with viscous damping varying among its elements the problem of determining critical damping becomes much more difficult since there are many critical and partially critical damping possibilities corresponding to different critical element damping value combinations. The importance of this problem lies in the fact that introduces the possibility of controlling the dynamic response more easily and with a greater flexibility by differently varying the damping of a number of elements.

Characterization of the free motion of a discrete linear dynamic system with different amounts of viscous damping in its elements can be accomplished by determining the roots of the determinantal equation of the system. Thus real, complex or purely imaginary roots characterize the motion as overdamped, underdamped or undamped, respectively. This is what is usually mentioned in the literature without consideration of the case of critical damping or the case of coexistence of all kinds of the foregoing roots. The only exceptions appear to be Crafton [1] and Bishop and Johnson [2] who have considered two-degrees-of-freedom spring-mass-damper systems and studied the behavior of the frequencies for different amounts of damping. However, their method of characterization of the motion is not convenient for design purposes, since it requires a complete root determination for every combination of element damping values assumed.

The present paper presents a detailed study of the effect of damping distributed in an arbitrary manner throughout the structural elements on the free motion of the system. A general method is first proposed to determine the critical damping surfaces of a viscously damped linear discrete dynamic system; these are the loci, in "damping space," of amounts of damping leading to critically damped motions. Three examples are then presented in detail which illustrate the proposed method and lead to some interesting and unexpected results.

Critical Damping Surfaces

Consider a viscously damped linear discrete dynamic system of n degrees of freedom characterized by the mass matrix $[M]$, the stiffness matrix $[K]$, and the damping matrix $[C]$, where the elements of $[C]$ are combinations of the m different damping coefficients c_k ($k = 1,2, \ldots m$) of the various elements of the system. The number m can be greater, equal or smaller than n. The determinantal equation of this system is

$$\det [\lambda^2[M] + \lambda[C] + [K]] = | \lambda^2[M] + \lambda[C] + [K] | = | D(\lambda) | = 0, \tag{1}$$

an algebraic equation of order $2n$ in λ.

For partial (complete) overdamping or critical damping some (all) of the roots of (1) are of the form

$$\lambda = -b, \qquad b > 0 \tag{2}$$

and in this case (1) becomes

Contributed by the Applied Mechanics Division for publication in the JOURNAL OF APPLIED MECHANICS.

Discussion on this paper should be addressed to the Editorial Department, ASME, United Engineering Center, 345 East 74th Street, New York, N.Y. 10017, and will be accepted until December 1, 1980. Readers who need more time to prepare a discussion should request an extension from the Editorial Department. Manuscript received by ASME Applied Mechanics Division, October, 1979; final revision, February, 1980.

$$| b^2 [M] - b[C] + [K] | = | D(b,c_k) | = 0. \quad (3)$$

In the m-dimensional space with coordinates c_k ($k = 1,2, \ldots ,m$), equation (3) represents a family of m-dimensional surfaces S_b. Each member of the family corresponds to overdamping or critical damping and is characterized by its own value of b, which is a function of the c_k's. The problem is to determine that b which corresponds to the "critical damping surface," i.e., the locus of combinations of c_k leading to critically damping motion and thus separating regions of partial or complete underdamping from those of overdamping. There are actually q ($q \leqslant n$) critical damping surfaces since there are at most as many partial critical damping possibilities as the number of the pairs of roots λ in (1) with zero imaginary part. Since critical damping represents the threshold between overdamping and underdamping, one can conclude that among the S_b surfaces, the critical surface S_{cr} is the one for which the damping will be a minimum, i.e.,

$$(d/db) | D(b,c_k) | = (\partial/\partial b) | D(b,c_k) | + \sum_k (\partial/\partial c_k) | D(b,c_k) | (\partial c_k/\partial b) = 0, \quad (4)$$

$$(\partial c_k/\partial b) = 0, \qquad k = 1,2, \ldots ,m.$$

An alternative derivation of (3) and (4) is the following: Consider equation (1) with $\lambda = -R + jI$, ($R > 0, I$ = real, $j = \sqrt{-1}$), i.e.,

$$\Delta(\lambda) = \Delta(-R,jI) = | D(-R + jI) | = 0. \quad (5)$$

Expansion of $\Delta(\lambda)$ in Taylor series about the point $\lambda_0 = (-R,0)$ yields

$$\Delta(-R,jI) = \Delta(-R,0) + (jI)\left.\frac{\partial\Delta}{\partial\lambda}\right|_{(-R,0)} + \frac{1}{2!}(-I^2)\left.\frac{\partial^2\Delta}{\partial\lambda^2}\right|_{(-R,0)} + \frac{1}{3!}(-jI^3)\left.\frac{\partial^3\Delta}{\partial\lambda^3}\right|_{(-R,0)} + \ldots, \quad (6)$$

which in view of (5) reduces to

$$\Delta(-R,0) - \frac{1}{2!}I^2\left.\frac{\partial^2\Delta}{\partial\lambda^2}\right|_{(-R,0)} + \ldots = 0,$$
$$\left.\frac{\partial\Delta}{\partial\lambda}\right|_{(-R,0)} - \frac{1}{3!}I^2\left.\frac{\partial^3\Delta}{\partial\lambda^3}\right|_{(-R,0)} + \ldots = 0. \quad (7)$$

For critical damping, for which $I = 0$, equations (7) lead to equations

$$\Delta(-R,0) = 0, \qquad (\partial\Delta/\partial\lambda)\,|_{(-R,0)} = 0 \quad (8)$$

which are the same as (3) and (4).

In principle, one can solve (4) for b and obtain its critical value b_{cr} as a function of the c_k's. Thus the equation of critical damping surfaces will be given by (3) with $b = b_{cr}$, i.e., by

$$| b^2_{cr}[M] - b_{cr}[C] + [K] | = 0. \quad (9)$$

In practice, however, the nonlinear system of (3) and (4) has to be solved numerically. Thus provided that differentiations in (4) can be done analytically, one determines numerically a finite number of groups of $m + 1$ values for b_{cr} and $c_{k\,cr}$ satisfying (3) and (4) simultaneously, and one is then able to represent critical damping surfaces in the m-dimensional c_k space as sets of points with coordinates $c_{k\,cr}$. Eventhough the previous method of determining critical damping surfaces is quite general and applicable, in principle, to a n-degrees-of-freedom system, the fact that, to the authors knowledge, there is no presently available efficient numerical treatment of the differentiations in (4), limits the range of applicability of the method to small-order systems.

However, the particular point $c_1 = c_2 = \ldots c_m = c$ of a critical damping surface can be very easily obtained for the special case in which $[C]_{c_k=c}$ is of the Rayleigh type, i.e., of the form

$$[C]_{c_k=c} = a_1 [M] + a_2 [K], \quad (10)$$

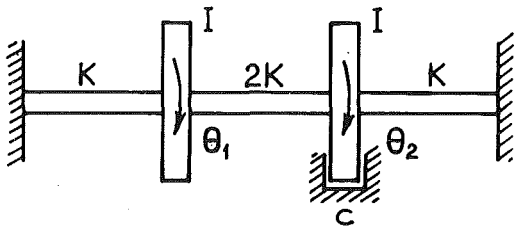

Fig. 1 The two-degrees-of-freedom system of Example 2

where a_1 and a_2 are constants. For this case and for the i th ($i = 1,2, \ldots ,n$) mode with underdamping, (1) yields

$$(\lambda_i^2 + a_1\lambda_i)/(1 + a_2\lambda_i) = -w_{oi}^2, \quad (11)$$

where w_{oi} is the ith natural frequency of the system.

Equation (11) can be solved for λ_i and give

$$\lambda_i = -b_i \pm jw_i, \quad (12)$$

where

$$b_i = 1/2(a_1 + a_2 w_{oi}^2), \quad w_i^2 = w_{oi}^2 - b_i^2, \quad a_1 + a_2 w_{oi}^2 \geqslant 0, \quad j = \sqrt{-1}. \quad (13)$$

It is apparent then, in view of (12) and (13), that at critical damping one has

$$b_{i\,cr} = w_{oi}, \quad (14)$$

with a_1 and a_2 satisfying the relation

$$a_{2\,cr}\, w_{oi}^2 - 2w_{oi} + a_{1\,cr} = 0, \quad (15)$$

where $a_{1\,cr}$ and $a_{2\,cr}$ are their values at critical damping. Equations (14) and (15) therefore represent the solution of (4) for the particular surface point $c_1 = c_2 = \ldots c_m = c$ and for systems obeying (10). This solution is unique if one of the a_1 and a_2 is zero. Once the $b_{i\,cr}$'s have been computed from (14), a numerical evaluation of the left-hand side of (9) for a sequence of values of c leads to the determination of the common value c of the c_k's which satisfies (9) for every i. One important result of this analysis is that, as equation (14) clearly demonstrates, for systems obeying (10), one has $q = n$, i.e., as many critical damping surfaces as there are degrees of freedom in the system.

Examples

Example 1. For the single-degree-of-freedom system $m = n = 1$ so that there exists only one critical damping surface of dimension one, i.e., a point. The condition (3) reduces to

$$mb^2 - bc + K = 0. \quad (16)$$

Use of (4) provides $b_{cr} = c_{cr}/2m$ which, in conjunction with (16) leads to

$$c_{cr} = 2mw_o, \qquad w_o = (K/m)^{1/2}, \quad (17)$$

which is the well-known condition of critical damping for this system.

Example 2. Consider the two-degrees-of-freedom system of Fig. 1 consisting of a variable torsional stiffness shaft with two flywheels and one viscous damper and being in free torsional vibration. This system has been taken from reference [2, p. 507] which studies the way in which the free motion of the system changes as the damping is increased from zero to infinity by determining the roots of the determinantal equation for a sequence of values of the amount of damping present. Here the results of reference [2] will be verified by applying the proposed method for determining critical damping.

The determinantal equation (1) for this system takes the form [2]

$$\Lambda^4 + 2\alpha\Lambda^3 + 6\Lambda^2 + 6\alpha\Lambda + 5 = 0, \quad (18)$$

where

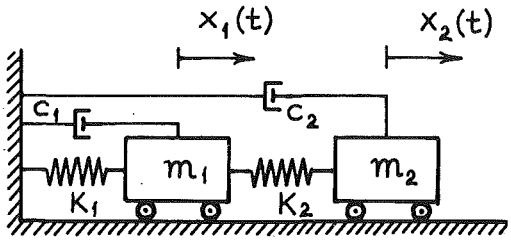

Fig. 2 The two-degrees-of-freedom system of Example 3

$$\Lambda = \lambda/w_1, \quad \alpha = c/2Iw_1, \quad w_1^2 = K/I, \tag{19}$$

and where I, c, and K stand for the mass moment of inertia of the flywheel, the damping coefficient, and the torsional stiffness of the shaft, respectively. Use of (3), (4), and (18) with $\Lambda = -B = -b/w_1$ yields

$$\alpha = 2B(3 + B^2)/3(1 + B^2), \quad B^6 + 3B^4 + 3B^2 - 15 = 0. \tag{20}$$

The only one real positive root of $(20)_2$ is $B = 1.233$ for which $(20)_1$ yields the equation of the only existing here critical damping surface—a point, as

$$\alpha_{cr} = 1.474, \tag{21}$$

a value which is identical to that obtained in [2].

The existence of just one critical damping surface for this two-degrees-of-freedom system indicates that this actually corresponds to partial critical damping. For $0 < \alpha < 1.474$ the system is underdamped, for $\alpha = 1.474$ it is partially critically damped, and for $\alpha > 1.474$ it is partially underdamped. Thus no matter how great the damping parameter α may be, there is no way to reach complete overdamping, exactly because there is no other critical damping surface for $\alpha > 1.474$

Example 3. Consider the two-degrees-of-freedom spring-dashpot-mass system shown in Fig. 2, where K_i, c_i, and m_i $(i = 1,2)$ stand for spring constants, coefficients of viscous damping and masses, respectively, and x_1 and x_2 represent the two translational degrees of freedom of the system. Notice that for $c_1 = 0$ one has a case similar to that treated in Example 2. For this system, equation (1) becomes

$$\lambda^4 + 2(\beta_1 + \beta_2)\lambda^3 + (w_1^2 + w_2^2 + w_{12}^2 + 4\beta_1\beta_2)\lambda^2 + 2(\beta_1 w_2^2 + \beta_2 w_1^2 + \beta_2 w_{12}^2)\lambda + w_1^2 w_2^2 = 0, \tag{22}$$

where

$$w_1^2 = K_1/m_1, \quad w_2^2 = K_2/m_2, \quad w_{12}^2 = K_2/m_1, \quad \beta_1 = c_1/2m_1, \quad \beta_2 = c_2/2m_2, \tag{23}$$

while equation (3) takes the form

$$b^4 - 2(\beta_1 + \beta_2)b^3 + (w_1^2 + w_2^2 + w_{12}^2 + 4\beta_1\beta_2)b^2 - 2(\beta_1 w_2^2 + \beta_2 w_1^2 + \beta_2 w_{12}^2)\, b + w_1^2 w_2^2 = 0. \tag{24}$$

The conditions of critical damping described by (4) yield

$$b^4 - (3/2)(\beta_1 + \beta_2)b^2 + (1/2)(w_1^2 + w_2^2 + w_{12}^2 + 4\beta_1\beta_2)b - (1/2)(\beta_1 w_2^2 + \beta_2 w_1^2 + \beta_2 w_{12}^2) = 0. \tag{25}$$

Thus the critical damping surfaces of this system are curves in the (β_1,β_2) plane described by (24) with $b = b_{cr}$ being a function of β_1 and β_2 which can be obtained by solving (25). Construction of these curves can, in general, be accomplished by computing the left-hand sides of (24) and (25) for all possible combinations of a finite number of values for β_1,β_2, and b, and selecting those combinations that simultaneously satisfy (24) and (25); these combinations provide the points $(\beta_{1\,cr},\beta_{2\,cr})$ of the critical damping curves. In this case, however, the construction of the critical damping curves can be done more easily by solving explicitly the cubic algebraic equation (25) for b in terms of β_1 and β_2.

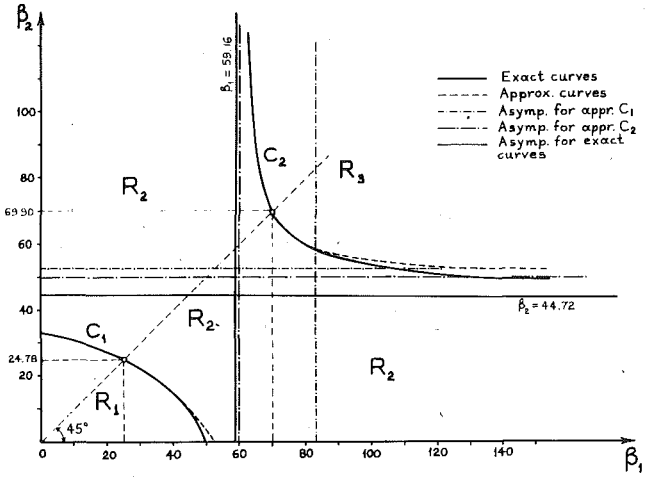

Fig. 3 Critical damping curves for the system of Fig. 2

Fig. 3 shows the two critical damping curves C_1 and C_2 of the two-degrees-of-freedom system of Fig. 2 in the (β_1,β_2) plane for the following numerical data:

$$K_1 = 3000 \text{ lb/ft} = 43{,}779.528 \text{ N/m}, \quad K_2 = 4000 \text{ lb/ft} = 58{,}372.703 \text{ N/m}, \tag{26}$$

$$m_1 = m_2 = 1 \text{ lb sec}^2/\text{ft} = 14.593 \text{ N sec}^2\text{m}, \quad (1 \text{ ft} = 0.3048 \text{ m}, \quad 1 \text{ lb} = 4.448 \text{ N}).$$

The two critical damping curves were constructed with the aid of a computer by both the purely numerical method and the one based on the solutions of the cubic equation. For $\beta_1 = \beta_2 = \beta$, condition (10) is satisfied with $\alpha_1 = 2\beta$ and $\alpha_2 = 0$, $q = n = 2$ and (14) and (15) lead to

$$b_{i\,cr} = \beta_{cr} = w_{oi}, \quad (i = 1,2). \tag{27}$$

The critical damping curves C_1 and C_2 divide the plane (β_1,β_2) into the regions R_1, R_2, and R_3, as shown in Fig. 3. Curve C_1 defines a state of partial critical damping and separates a region of complete underdamping (region R_1) from a region of partial underdamping (region R_2). Curve C_2 defines a state of complete critical damping and separates a region of partial underdamping (region R_2) from a region of complete overdamping (region R_3). The results of Fig. 3 were also verified numerically by determining on the computer all the four roots of equation (22) with the aid of Newton's iterative method for quite a number of possible combinations of numerical values of β_1 and β_2.

The interesting thing in this example is the fact that region R_2 is unbounded and that even for values of β_1 or β_2 (but not both) approaching infinity there is still partial underdamping, while one might expect to achieve overdamping if one of the β's is large enough. This phenomenon is the two-dimensional counterpart of that of Example 2 and is amenable to the following physical explanation: At the limit, as β_1, for example, approaches infinity, the mass m_1 becomes essentially locked, x_1, approaches zero, the system becomes a single-degree-of-freedom one, and one can obtain

$$\beta_{2\,cr} = w_2 = 44.72. \tag{28}$$

Similarly, for β_2 approaching infinity, one can obtain

$$\beta_{1\,cr} = \sqrt{w_1^2 + \omega_{12}^2} = 59.16. \tag{29}$$

Equations (28) and (29) are equations for the asymptotes of the critical damping curves and indicate that even for infinite values of $\beta_1(\beta_2)$ there are values of $\beta_2(\beta_1)$ in region R_2, which are less than their critical values, for which there is partial underdamping.

One can approximately construct the curves C_1 and C_2 by assuming that (27) holds true not only for the points $\beta_1 = \beta_2 = \beta$ of the curves

but for any point of them. Thus (24) with $b_{i\,cr} = w_{oi}$ finally becomes

$$\beta_2 = \frac{A_i\beta_1 - B_i}{E_i\beta_1 - D_i}, \tag{30}$$

where

$$\begin{aligned} A_i &= 2w_{oi}\,(w_2^2 + w_{oi}^2), \\ B_i &= w_{oi}^4 + w_1^2\,w_2^2 + w_{oi}^2\,(w_1^2 + w_2^2 + w_{12}^2), \\ E_i &= 4w_{oi}, \\ D_i &= 2w_{oi}\,(w_1^2 + w_{12}^2 + w_{oi}^2), \quad i = 1,2. \end{aligned} \tag{31}$$

It is evident from (30) that the approximate critical damping curves are two equilateral hyperbolas with two branches each and asymptotes $\beta_1 = D_i/E_i$ and $\beta_2 = A_i/E_i$. Out of the two branches only that for which $\beta_1 = \beta_2 = w_{oi}$ represents a critical damping curve.

A plot of the approximate critical damping curves on the basis of the numerical data (26) is shown in Fig. 3. The approximate curves of course coincide with the exact curves at $\beta_1 = \beta_2$, and they slightly depart from them more and more as the β's increase. Such approximate critical damping curves can be very useful for rapid design calculations, although, unfortunately, no general extensions of their validity can be presented here.

Conclusions

The following remarks can be made on the basis of the preceding developments about the free vibrations of linear discrete systems with viscous damping varying among their elements:

1 There exist critical damping surfaces for every system representing the loci of combinations of damping leading to partial or complete critically damped motion and thus separating regions of partial or complete underdamping from those of overdamping.

2 A general method is proposed for determining the equations of these critical damping surfaces. The determination of the surface point corresponding to equal amounts of damping is considerably simplified for systems which, on the assumption that all amounts of damping are equal, possess a damping matrix of the Rayleigh type.

3 The dimension of these critical damping surfaces is equal to the number of the independent damping values in the system, while their number is less or equal than the number of the system degrees of freedom. For a n-degrees-of-freedom system with a damping matrix reducible to Rayleigh type for equal amounts of damping, there are at most one completely underdamped region, one completely overdampled region and n-2 partially underdamped regions.

Acknowledgments

The authors acknowledge the support of the University of Minnesota Computer Center. The second author also acknowledges the support of the Office of Naval Research.

References

1. Crafton, P. A., *Shock and Vibration in Linear Systems,* Harper and Brothers, New York, 1961.
2. Bishop, R. E. D., and Johnson, D. C., *The Mechanics of Vibration,* Cambridge University Press, 1960.

C. H. J. Fox[1]
Department of Mechanical Engineering,
Nottingham University,
Nottingham NG7 2RD, England

J. S. Burdess
Department of Mechanical Engineering,
University of Newcastle upon Tyne,
Newcastle upon Tyne NE1 7RU,
England

The Rotating Beam Gyroscope

This paper investigates the dynamics of a novel "multisensor" comprising a two-axis gyroscope and a single-axis linear accelerometer. The theoretical analysis indicates that the gyroscope has two modes of operation, untuned and tuned, offering, respectively, angular rate and angular displacement measurement capability, depending on the damping and mistuning present. In addition to the sensing of two-axis angular motion, the instrument is capable of measuring linear acceleration along a third axis. Experimental tests on a prototype instrument show generally good agreement with the theory giving confidence of the development potential of the instrument.

Introduction

This paper introduces a novel instrument of extremely simple basic design, which can be used simultaneously as a two-axis gyroscope and a linear acceleration transducer. The instrument is based on a simple rotating cantilever beam, mounted as shown in Fig. 1 with the root and tip of the beam situated on opposite sides of the spin axis. In a previously published paper [1] the authors investigated the dependence of the natural frequencies of such a beam on the ratio $R = r/L$, of root offset r, to beam length L, and on the spin frequency n. In particular it was shown that for values of $r/L = R$ greater than approximately 0.067 the effect of the centrifugal loading is such that it is possible to select a value of spin frequency that coincides with the fundamental natural frequency of the cantilever. In this condition the cantilever is said to be tuned to the spin frequency. For $R < 0.067$ tuning is not possible because the effect of centrifugal loading is to stiffen the cantilever so that the fundamental natural frequency is always greater than the spin frequency. The present paper investigates the possibility of using a rotating cantilever as the basis for a sensitive gyroscope [2], which may be used to measure angular rates of turn or angular displacements depending on the conditions of tuning and damping, and linear acceleration irrespective of the condition of tuning.

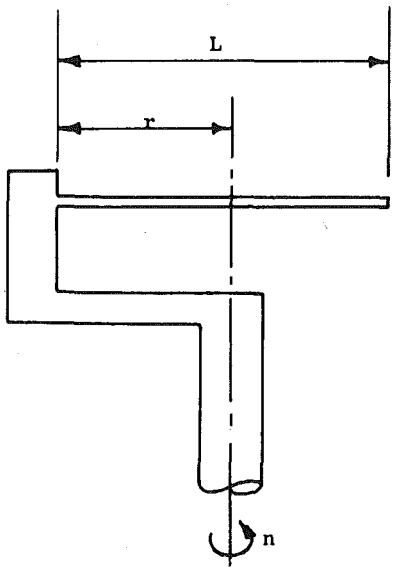

Fig. 1 Cantilever root offset

Analysis

Equations of Motion. The main elements of the instrument and appropriate frames of reference are shown schematically in Fig. 2. Axes $OXYZ$ are fixed in the instrument casing which houses the drive motor. A rigid drive member is mounted on the motor shaft and rotates at high speed about OZ with constant angular velocity n, relative to the casing. $Oxyz$ rotate with the drive member and their position relative to $OXYZ$ is defined by rotation nt about OZ. The sensitive element consists of a thin uniform elastic cantilever attached to the drive member at $y = -r$ as shown. The center line of the undeflected cantilever lies along Oy so that it's tip is situated at $y = L - r$ where L is the cantilever length.

It is assumed that the center line of the undeflected cantilever is perpendicular to the spin axis and that only linear vibration parallel to the spin axis can occur. Rotatory inertia, which can be shown to have no effect on the fundamental operation of the instrument, has been neglected together with shear deformation and axial extension of the beam due to centrifugal loading. Input rotations to the instrument can be defined with considerable generality in terms of an applied rotation $\phi_X(t)$ about the case fixed axis OX. It is assumed that $\dot{\phi}_X \ll n$.

[1] Formerly, University of Newcastle upon Tyne, Newcastle upon Tyne, England.

Contributed by the Applied Mechanics Division for publication in the JOURNAL OF APPLIED MECHANICS.

Discussion on this paper should be addressed to the Editorial Department, ASME, United Engineering Center, 345 East 47th Street, New York, N.Y. 10017, and will be accepted until December 1, 1980. Readers who need more time to prepare a discussion should request an extension from the Editorial Department. Manuscript received by ASME Applied Mechanics Division, October, 1979; final revision, February, 1980.

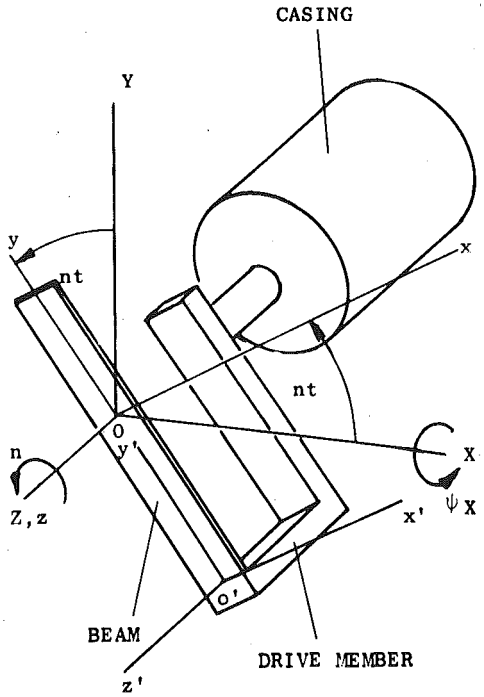

Fig. 2 Schematic and reference axes

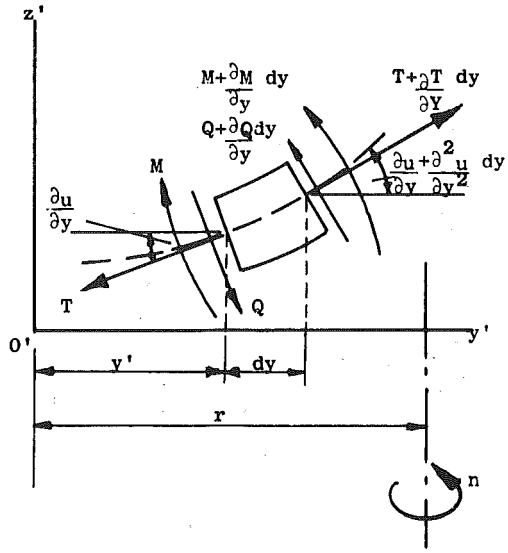

Fig. 3 Beam element

The equation of motion for the beam is derived in the usual manner by considering the equilibrium of an element of length dy, situated at distance y' from the root of the cantilever as shown in Fig. 3. The acceleration of such an element in direction OZ may be written to first-order terms as

$$a_Z = L\frac{\partial^2 Z}{\partial t^2} - L(R-\xi)[\ddot{\phi}_X \cos nt - 2n\dot{\phi}_X \sin nt] + a_c(t)$$

where $Z = z/L$; $\xi = y'/L$, $R = r/L$, and a_c is the acceleration of the instrument casing in direction OZ. Note that R is taken as positive for the beam configuration shown in Fig. 1, but would be negative in the case where the root and tip were situated on the same side of the spin axis with the cantilever directed radially outward as, for example, in the case of an aeroplane propeller.

The equation of motion follows as

$$\frac{\partial^2 Z}{\partial t^2} + \frac{c}{\mu}\frac{\partial Z}{\partial t} + \frac{EI}{\mu L^4}\frac{\partial^4 Z}{\partial \xi^4} - n^2\frac{\partial}{\partial \xi}\left[T(\xi)\frac{\partial Z}{\partial \xi}\right] = (R-\xi)[\ddot{\phi}_X \cos nt - 2n\dot{\phi}_X \sin nt] - \frac{a_c}{L} \quad (1)$$

where

$$T(\xi) = \tfrac{1}{2}[\xi(2R-\xi) - (2R-1)] \quad (2)$$

represents the centrifugal loading in the cantilever due to the spin. EI is the flexural rigidity, μ the mass per unit length, and c is the viscous damping coefficient per unit length, all assumed to be constant.

The boundary conditions associated with equation (1) are

At $\xi = 0$

$$Z = \frac{\partial Z}{\partial \xi} = 0;$$

At $\xi = 1$

$$\frac{\partial^2 Z}{\partial \xi^2} = \frac{\partial^3 Z}{\partial \xi^3} = 0 \quad (3)$$

Solution of Equations of Motion. The presence of the centrifugal loading term $T(\xi)$ precludes an exact analytical solution of equation (1) in terms of known functions. An approximate solution will therefore be constructed using Galerkin's method [3]. A series solution of the form

$$Z_n = \sum_{j=1}^{n} q_k(t)\phi_k(\xi) \quad (4)$$

is assumed where $q_k(t)$ are a finite set of generalized coordinates, to be determined, and $\phi_k(\xi)$ are the normal modes of the corresponding nonrotating cantilever.

In [1], where the free vibration of an undamped beam was studied, a series containing two terms was assumed. In the present paper we are primarily interested in the dynamical characteristics of the beam at values of spin in the vicinity of the fundamental frequency where the motion is predominantly at the first mode. To simplify the analysis a series solution of only one term will be assumed. While this results in a small loss in numerical accuracy of computed results in the region of the tuning frequency, this is felt to be justified by the fact that all the main dynamical features can be illustrated simply.

The fundamental mode of the corresponding nonrotating cantilever is given in [4] as

$$\phi(Y) = \cosh(\lambda\xi) - \cos(\lambda\xi) - \sigma[\sinh(\lambda\xi) - \sin(\lambda\xi)] \quad (5)$$

where $\lambda = 1.8751$ and $\sigma = 0.7341$.

Free Motion and Tuning. The equation of motion for this case is equation (1) with $\ddot{\phi}_X = \dot{\phi}_X = a_c = 0$. Following Galerkin's method, substitution of the assumed solution (5) in equation (1) yields the following equation for q:

$$\ddot{q} + \frac{c}{\mu}\dot{q} + q(p_{01}^2 + n^2 a_{11}) = 0 \quad (6)$$

where

$$a_{11} = \int_0^1 T(\xi)\left(\frac{\partial \phi}{\partial \xi}\right)^2 d\xi$$

and $p_{01} = \lambda(EI/\mu L^4)^{1/2}$ is the fundamental frequency of the corresponding nonrotating beam.

The fundamental natural frequency p, of an undamped cantilever, follows from equation (6) and may be expressed as

$$p^2 = p_{01}^2 + n^2 a_{11} \quad (7)$$

If $R = r/L > 0.067$, it has been shown in [1] that $a_{11} < 1$ and tuning to the spin frequency is possible.

Tuning occurs when $p = n = n_t$ and is achieved when

$$n_t^2 = \frac{p_{01}^2}{(1 - a_{11})} \tag{8}$$

Response to a Constant Applied Rate of Turn. The potential usefulness of the device as an angular motion sensor is best illustrated by considering its response to a constant rate of turn, $\dot{\phi}_X = \Omega = \text{const}$, $a_c = 0$. Appropriate substitution of equation (4) in equation (1) then yields

$$\ddot{q} + 2\nu p\dot{q} + p^2 q = -2n\Omega F \sin nt \tag{9}$$

where

$$F = \int_0^1 (R - \xi)\phi d\xi \quad \text{and} \quad \nu = c/2\mu p.$$

p and a_{11} are as defined for equations (6) and (7).

Consider first the special case of an undamped beam, tuned according to equation (8). In this case equation (9) reduces to

$$\ddot{q} + n^2 q = -2n\Omega F \sin nt \tag{10}$$

The particular integral now takes the special form associated with resonance and the general solution of equation (10) may be expressed as

$$q = q_0 \sin (nt + \alpha_0) + F\Omega t \cos nt \tag{11}$$

where q_0 and α_0 are initial condition constants.

For a step input of magnitude $\phi_X = \Omega$

$$q = \dot{q} = 0 \quad \text{at} \quad t = 0, \tag{12}$$

from which $\alpha_0 = 0$ and $q_0 = -F\Omega/n$. The general solution is thus

$$q = -(F\Omega/n) \sin nt + F\Omega t \cos nt \tag{13}$$

For values of $t \gg 1/n$ (typically $1/n \sim 10^{-3}$ sec) the second term on the right-hand side of equation (13) predominates and the amplitude of the response is governed chiefly by the total applied turn Ωt. A precisely tuned and undamped instrument would therefore operate as an angular displacement measuring device until the amplitude of beam vibration reached a level where the linear approximation theory became invalid. Furthermore, since the orientation of the axes OXY is arbitrary, the phase of the beam vibration relative to a suitable case fixed reference determines the axis about which the input rate is applied. The instrument therefore operates essentially as a two-axis device. Physically, the motion of the beam in this case is such that an element of the beam, for example, the tip, moves on a path in space that is essentially circular, the plane of the circle deviating from the initial plane by an angle which increases linearly with time. The axis about which the plane of the circle rotates determines the axis of the input rate. The motion of the beam is thus akin to that of a free rotor which maintains a fixed direction in space.

The response as given by equation (13) represents the response of an ideal gyroscope. In practice however, damping will inevitably be present and the instrument will not be operated *precisely* at the tuning frequency. It is therefore more realistic to consider the general case where damping and mistuning are present. The response in this case follows directly from equation (9) and takes the form:

$$q = e^{-\nu pt}[P \sin p_d t + Q \cos p_d t] \times \frac{-2n\Omega F}{[(p^2 - n^2) + (2\nu np)^2]^{1/2}} \sin (nt - \gamma) \tag{14}$$

where

$$\gamma = \tan^{-1}\left[\frac{2\nu np}{p^2 - n^2}\right], \quad p_d = p(1 - \nu^2)^{1/2}$$

and P and Q are initial condition constants. For a step input Ω in applied rate of turn at time $t = 0$ the initial conditions are given by equation (12) and P and Q take the values

$$P = \frac{2nF\Omega}{p_d} \frac{[n \cos \gamma - \nu p \sin \gamma]}{[(p^2 - n^2)^2 + (2\nu np)^2]^{1/2}} \tag{15}$$

$$Q = \frac{-2nF\Omega \sin \gamma}{[(p^2 - n^2)^2 + (2\nu np)^2]^{1/2}} \tag{15 (Cont.)}$$

If the mistuning and damping are both small, as they may be in practice, we may write

$$p_d \approx p = n(1 + \eta)$$

where $\eta(\ll 1)$ represents the amount of mistuning. Equations (14) and (15) may then be rearranged as

$$q = \frac{F\Omega\eta}{n(\eta^2 + \nu^2)}[e^{-\nu nt} \cos \eta nt - 1] \sin nt + \frac{F\Omega\nu}{n(\eta^2 + \nu^2)}[1 - e^{-\nu nt} \cos \eta nt] \cos nt + \frac{F\Omega e^{-\nu nt}}{n(\eta^2 + \nu^2)}[\eta \cos nt + \nu \sin nt] \sin \eta nt - \frac{F\Omega\nu^2}{n(\eta^2 + \nu^2)} e^{-\nu nt}[\cos \eta nt \sin nt + \sin \eta nt \cos nt] \tag{16}$$

For small intervals of times such that $\nu nt \ll 1$, $\eta nt \ll 1$ equation (16) simplifies and the response is given by

$$q \approx \frac{-F\Omega\nu^2 \sin nt}{n(\eta^2 + \nu^2)} - F\Omega t \cos nt \tag{17}$$

Comparison of equation (17) with equation (13) shows that for small intervals of time the response of the damped mistuned instrument is substantially the same as that of a tuned undamped instrument, and is governed by the total applied turn Ωt.

For longer time periods such that νnt, $\eta nt \gg 1$ equation (16) may be expressed with good approximation as

$$q = \frac{-F\Omega}{n(\eta^2 + \nu^2)^{1/2}} \sin (nt - \gamma) \tag{18}$$

with $\gamma = \tan^{-1}(\nu/\eta)$ and the steady-state response is proportional to the applied rate of turn Ω. Thus the damping and mistuning limit the length of time for which the instrument acts as an angular displacement sensor and strongly affect the sensitivity of the instrument as a rate sensor. Furthermore, equation (18) indicates that phase of the output signal is critically dependent on the relative magnitudes of the mistuning and damping. This means that, if the damping and mistuning were of the same order, a significant error could occur in determining the input axis (about which the input rate is applied) from the relative phase of the output vibration. Thus, if the instrument were to be used as a rate sensor, one would probably choose $\eta \gg \nu$ so that $\gamma \to 0$. The selection of the mistuning parameter would therefore involve a tradeoff between sensitivity and accuracy.

Response to Applied Acceleration. Consider the case where $\dot{\phi}_X = \ddot{\phi}_X = 0$ and the instrument is subjected to an applied acceleration $a_c(t)$ in direction OZ. Following Galerkin's method appropriate substitution of equation (4) in equation (1) yields

$$\ddot{q} + 2\nu p\dot{q} + p^2 q = -F_1 a_c(t) \tag{19}$$

where

$$F_1 = \frac{1}{L}\int_0^1 \phi d\xi.$$

Without deriving specific solutions, the following points of interest may be noted in relation to the response to linear acceleration.

The steady-state response of the beam will be proportional to a_c. The beam therefore acts as a linear acceleration transducer in addition to acting as a two-axis angular motion sensor. Since the useful response to applied rotation is always at spin frequency n, it is a straightforward matter to discriminate between the response to applied rotation and the response to applied linear acceleration unless the applied acceleration has a component at frequency n which will excite the beam in the same manner as an applied rate of turn. However, the bandwidth of $a_c(\pm 3d\beta)$ will be much less than the natural frequency p and in practical applications in which a combined gyro/

accelerometer might be used, only low frequency components of acceleration would be of interest. Thus it will be possible to discriminate useful acceleration information simply on a frequency basis.

Response to Angular Vibration. It is important to consider the response of the instrument to angular vibration since it is known to give rise to measurement errors in other tuned gyroscopes such as the oscillogyro [4] and the Hooke's joint gyro [5]. Consider the response of the instrument to an angular vibratory input $\dot{\phi}_X = \Omega \sin \omega t$, $a_c = 0$. Following Galerkin's method, equation (1) yields

$$\ddot{q} + 2\nu p\dot{q} + p^2 q = \frac{F\Omega}{2}\left|(2n + \omega)\cos(\omega + n)t - (2n - \omega)\cos(\omega - n)t\right| \quad (20)$$

where ν, F, and p are as previously defined. The general solution of equation (20) for an untuned instrument may be expressed as

$$q = e^{-\nu pt}[A \cos p_d t + B \sin p_d t] + \frac{F\Omega}{2}\{R_1 \cos[(\omega - n)t - \alpha_1] + R_2 \cos[(\omega + n)t - \alpha_2]\} \quad (21)$$

where

$$R_1 = [2n - \omega]/\{[p^2 - (\omega - n)^2]^2 + [2\nu p(\omega - n)]^2\}^{1/2}$$

$$R_2 = [2n + \omega]/\{[p^2 - (\omega + n)^2]^2 + [2\nu p(\omega + n)]^2\}^{1/2}$$

$$\alpha_1 = \tan^{-1}\{2\nu p(\omega - n)/[p^2 - (\omega - n)^2]\}$$

$$\alpha_2 = \tan^{-1}\{2\nu p(\omega + n)/[p^2 - (\omega + n)^2]\}$$

A and B are initial condition constants and p and p_d are as defined previously.

In general, the steady-state response, which is represented by the second term on the right-hand side of equation (21) contains two frequency components, $(\omega - n)$ and $(\omega + n)$. For the untuned instrument ($p \neq n$) the input vibration frequencies which cause resonance depend on whether the spin frequency is above or below the tuning frequency. Below the tuning frequency ($n < p$) resonance occurs for values of ω in the region of $p + n$ in the first component and $p - n$ in the second component. Above the tuning frequency ($n > p$) resonance occurs only in the first component when ω is in the region of $n + p$ and $n - p$.

The response of the tuned instrument ($n = p$) is of special interest. For an ideal tuned undamped beam the particular integral solution of equation (20) follows on simplification of (21) as

$$q = \frac{F\Omega}{2\omega}[\cos(\omega - n)t - \cos(\omega + n)t] \quad (22)$$

As $\omega \to 0$, resonance occurs in both the first and second components of response and the limiting case when $\omega = 0$ corresponds to the response to a constant applied rate of turn.

In the case where $\omega = 2n$ the low frequency component of response for the ideal instrument takes the form

$$q = \frac{F\Omega}{4n}\cos nt \quad (23)$$

This should be compared with equation (13) which expresses the corresponding response to a constant rate of turn. It can be seen that equation (22) is essentially different from the predominant second term on the right-hand side of equation (13).

In the presence of damping R_1 is zero when $\omega = 2n$ irrespective of the state of tuning and the beam exhibits a null response in the low frequency component.

Thus the instrument is immune to twice spin frequency angular vibration in both the angular displacement and angular rate modes of operation.

A further point of interest arises when the excitation frequency ω and the spin frequency n are equal. In this case $\omega - n = 0$ and the low frequency component of steady-state response as expressed by equation (21) becomes

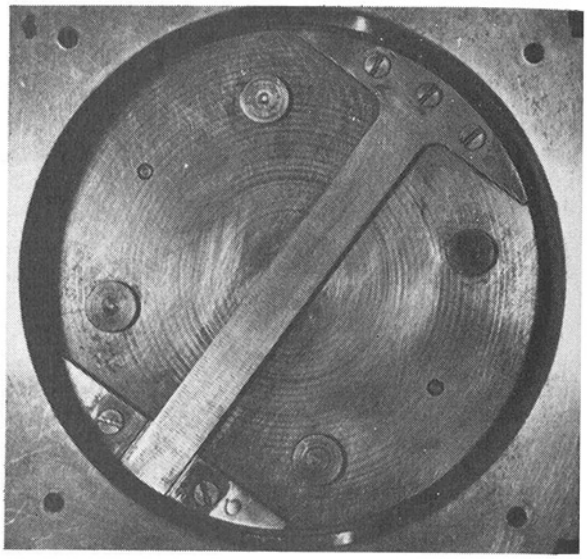

Fig. 4(*a*) Detail of beam of test gyro

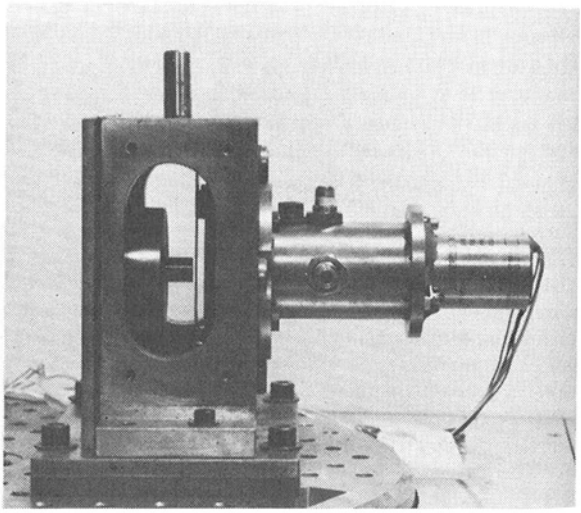

Fig. 4(*b*) General view of test gyro

$$q = \frac{F\Omega n}{2p^2} \quad (24)$$

so that the beam adopts a steady offset from the original undeflected position. While this response does not affect the angular motion sensing capability of the device, it could be interpreted as a constant applied acceleration in direction OZ if the instrument were used as an accelerometer as explained in the previous section.

Experiments

The Experimental Gyroscope. A prototype beam gyroscope was manufactured so that the main theoretical predictions could be tested. The design was extremely simple and used commercially available "off the shelf" components where possible.

The main elements of the experimental instrument are shown in Fig. 4. The sensitive element consisted of a steel cantilever beam, nominally 86.5 mm long, 10 mm wide, and 0.75 mm thick, mounted diametrally across the drive plate so that the root offset r was 38.1 mm. The drive plate and beam were spun by means of an externally mounted hysteresis motor, the speed of which was controlled by the electrical supply frequency. The drive plate and beam were enclosed in a casing which could be evacuated to reduce drag on the rotating elements.

The deflection of the beam was measured by means of a stationary

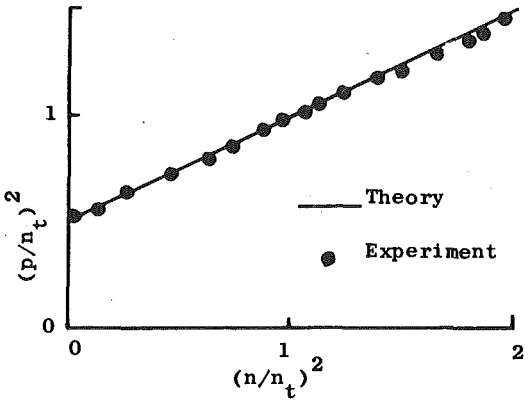

Fig. 5 Variation of first natural frequency p with spin n

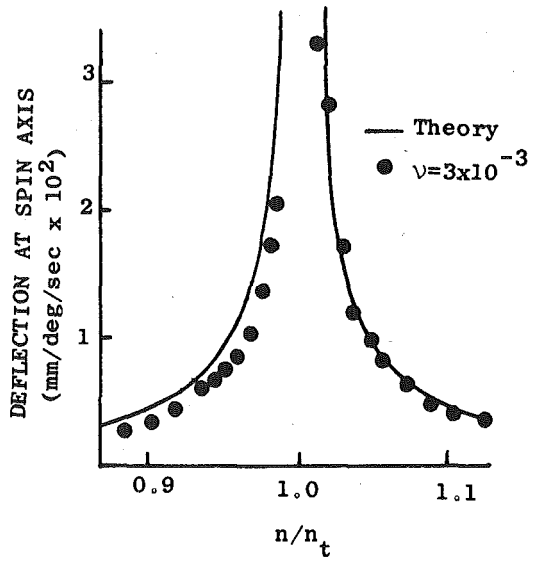

Fig. 6(a) Response to constant rate input; steady-state amplitude versus spin frequency

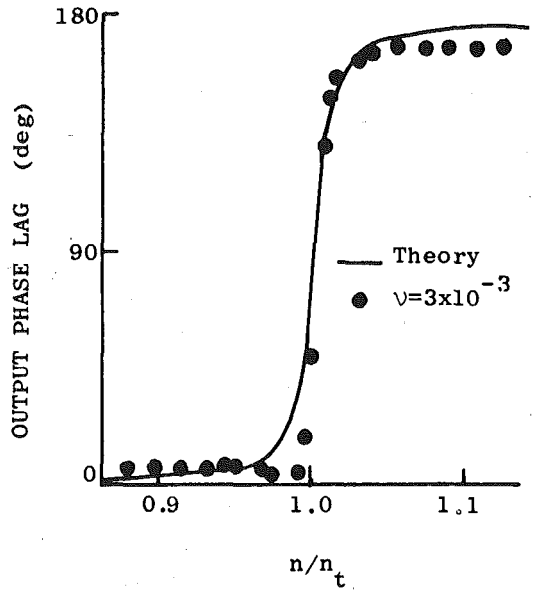

Fig. 6(b) Response to constant rate input; phase lag versus spin frequency

inductive proximity transducer mounted in the casing on the spin axis. Phase reference signals, used in resolving the pickoff signal into perpendicular components, were generated by two inductive proximity transducers acting against an eccentric on the drive shaft. The pickoff signals were filtered where necessary so that appropriate components of output could be observed.

During manufacture particular attention was given to heat-treatment of the sensitive element in an attempt to minimize internal damping in the steel. In practice it was found that the air pressure in the instrument casing did not significantly affect the damping of the beam vibration. It was therefore concluded that hysteretic damping in the beam material was the principal cause of energy dissipation.

When manufacture was completed the rotating elements were dynamically balanced to minimize vibration levels.

Constant rate inputs were applied to the test gyroscope by means of test tables which were capable of providing stabilized rates of turn in a range between a minimum of earth's rate (15°/hr) and a maximum of 60°/sec. Angular vibratory inputs were generated by means of a special angular vibration test table.

Three main series of tests were conducted. The first related to the tuning condition, the second investigated the response to constant applied rates of turn and the third examined the response to angular vibration.

Free Vibration and Tuning. The (approximate) theoretical variation of undamped natural frequency with spin is given by equation (7) and tuning is achieved when the spin frequency is chosen to satisfy equation (8). Experimentally, p and the damping ratio ν were measured by applying an impulse to the casing and recording the resulting free vibration. The measured damping ratio ν with the casing evacuated and the spin frequency approximately equal to the tuning frequency was found to be of the order of 3×10^{-3}. As mentioned earlier, variation of the absolute air pressure in the casing between 350 mm Hg and 60 mm Hg did not significantly affect the damping ratio.

In view of the low damping ratio, the undamped natural frequency was sensibly equal to the frequency of the damped vibration. Fig. 5 shows the theoretical relationship between p and n as expressed by equation (7), together with experimentally measured points, for a range of spin frequencies including the tuning frequency. Satisfactory agreement between theory and experiment is demonstrated.

Constant Rate Input. The steady-state response of the damped untuned instrument to a constant rate of turn is expressed by the second term on the right-hand side of equation (14). Figs. 6(a) and (b) show a comparison of the theoretical steady-state vibration amplitude and phase lag, respectively, with representative experimental measurements of these quantities, taken over a range of spin frequencies including the tuning frequency. Although there is some discrepancy between predicted and measured response amplitude, the predicted trend is nevertheless adequately confirmed. Fig. 7 compares the theoretical and experimentally determined sensitivity of the gyro to a constant rate input for a range of spin frequencies near the tuning speed. In this case also the theoretical trend is confirmed and reasonable linearity is displayed. With a mistuning factor of the order $\eta \sim 0.01$, the minimum detectable applied rate of turn was of the order $\Omega \sim 10^{-3}$ rad/sec. These results tend to confirm the feasibility of using the untuned beam gyro as a two-axis open-loop rate gyro. The sensitivity would increase for $\eta < 0.01$ but in the prototype instrument the problem discussed in the following paragraph was encountered as the tuning condition was approached.

It was not possible, with the prototype instrument, to make any experimental measurements at the tuning condition. This was because the beam was found to resonate when the tuning condition was reached, due to a cause other than the applied rate of turn. The most likely source of excitation producing the resonance was considered to be either the spin axis bearings or the housings in which they were mounted. Any imperfection in this area could cause the drive shaft

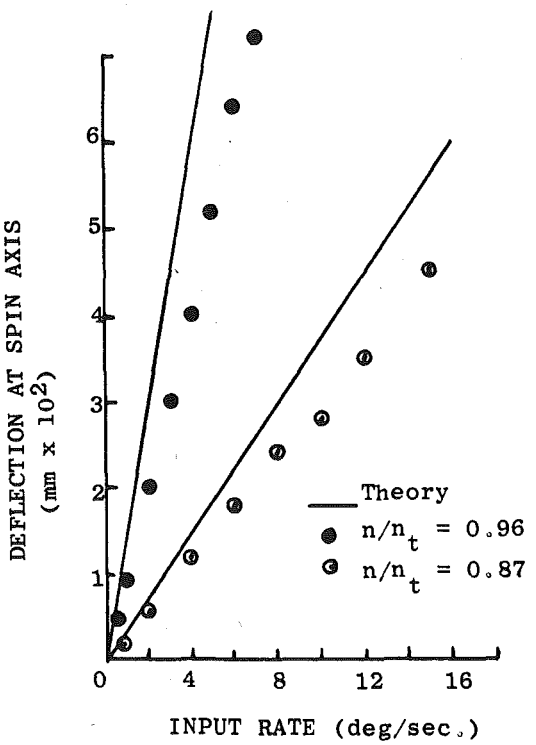

Fig. 7 Response to constant rate input; steady-state amplitude versus input rate

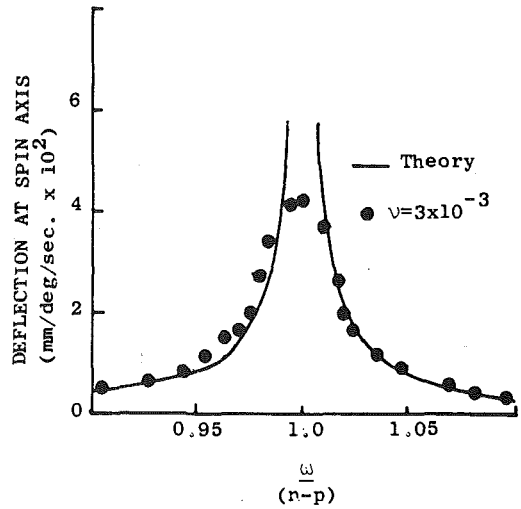

Fig. 8(*a*) Response to angular vibration, $n/n_t = 1.37$; resonance in low frequency component when $\omega = n - p$

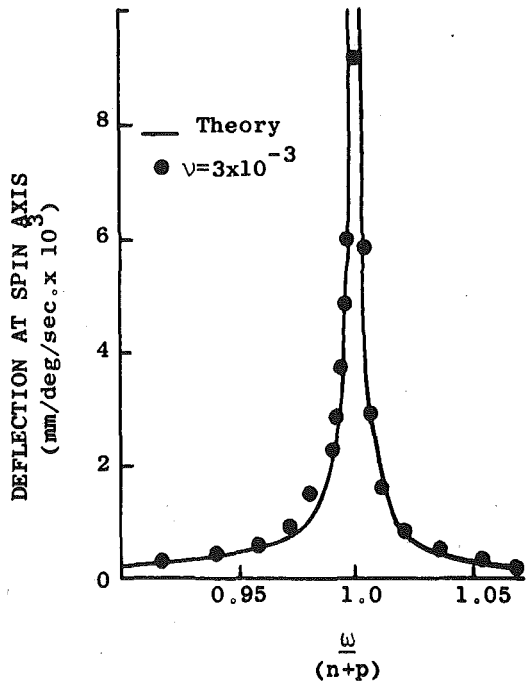

Fig. 8(*b*) Response to angular vibration; $n/n_t = 1.37$; resonance in low frequency component when $\omega = n + p$

to oscillate along its axis with a component at spin frequency, and in fact accelerometer measurements of casing vibration indicated a component of axial vibration at the spin frequency. As discussed in the section "Response to Applied Acceleration," the beam is very sensitive to linear vibration at a natural frequency, which at tuning coincides with the spin frequency. It is felt that this effect, which was exaggerated by the relative crudity of the prototype gyro, resulting from the limited manufacturing facility available, could be minimized by appropriately high precision manufacture of the drive system.

Response to Angular Vibration. The theoretical response of the instrument to angular vibration is expressed by equation (21) which reveals that the steady-state response consists of two components having frequencies equal to the difference and sum, respectively, of the spin and input frequencies. The amplitude of each component becomes large when its frequency coincides with a natural frequency of the beam. Note that because the mathematical model adopted in this paper effectively considers the instrument to have only one degree of freedom, resonances are only predicted for frequency combinations equal to the first natural frequency of the beam. In practice resonances associated with the second and higher natural frequencies are also to be expected.

Experimentally, the spin frequency was set at each of a number of fixed values, above and below the tuning frequency, and the input frequency was varied over the appropriate range. In each case the pickoff output was found to consist of the predicted frequency components. As the input frequency was varied the predicted two resonances were observed, both occurring in the low frequency component when $n > n_t$ and one in each component when $n < n_t$. Theoretical response curves and representative experimental points for values of $n > n_t$ are shown in Figs. 8(*a*) and (*b*), for ranges of input frequencies in the region of the two resonances. These show close agreement between theory and experiment, which was also found for values of $n < n_t$.

Conclusions

A novel "multisensor" comprising a two-axis gyroscope and single-axis linear accelerometer has been proposed, and its fundamental dynamical characteristics have been investigated. The gyroscope has two possible modes of operation, namely, tuned and untuned. In the untuned mode the instrument behaves, in steady state, as a two-axis rate gyroscope and may, for short intervals of time, be used as an angular displacement sensor. In the tuned mode the instrument offers potential as an angular displacement sensor, its performance as such being limited by the amount of damping and the degree of mistuning which are inevitably present in a practical instrument.

In addition to its two-axis angular motion sensing capability, the instrument is capable of simultaneously measuring linear acceleration along a third (perpendicular) axis.

Experimental evaluation of a prototype instrument has demonstrated the practicability of the device as an open-loop two-axis rate sensor in the untuned mode. Good agreement has been obtained between theoretical prediction and experimental measurement, which

gives confidence that the instrument is capable of development to achieve higher levels of performance.

Acknowledgments

The authors acknowledge with thanks the support of the Science Research Council (U.K.).

References

1 Fox, C. H. J., and Burdess, J. S., "The Natural Frequencies of a Thin Rotating Cantilever With Offset Root," *Journal of Sound and Vibration,* Vol. 65, No. 2, July 1979, pp. 152–158.

2 U.K. Patent Application 7702/78, Feb. 1978.

3 Timoshenko, Young, and Weaver, *Vibration Problems in Engineering,* 4th ed., Wiley, New York, 1974, 468 pp.

4 Ormandy, D., and Maunder, L., "Dynamics of the Oscillogryo," *Journal of Mechanics and Engineering Science,* Vol. 15, No. 3, 1973, pp. 210–217.

5 Craig, R. J. G., "Theory of Errors of a Multigimbal Elastically Supported Gyroscope," *I.E.E.E. Transactions on Aerospace and Electronic Systems,* Vol. AES-8, No. 3, May 1972, pp. 289–297.

F. C. Moon

Associate Professor,
Department of Theoretical and Applied Mechanics,
Cornell University,
Ithaca, N. Y. 14853., Mem. ASME

Experiments on Chaotic Motions of a Forced Nonlinear Oscillator: Strange Attractors[1]

The forced vibrations of a buckled beam show nonperiodic, chaotic behavior for forced deterministic excitations. Using magnetic forces to buckle the beam, two and three stable equilibrium positions for the postbuckling state of the beam are found. The deflection of the beam under nonlinear magnetic forces behaves statically as a butterfly catastrophe and dynamically as a strange attractor. The forced nonperiodic vibrations about these multiple equilibrium positions are studied experimentally using Poincare plots in the phase plane. The apparent chaotic motions are shown to possess an intricate but well-defined structure in the Poincare plane for moderate damping. The structure of the strange attractor is unravelled experimentally by looking at different Poincare projections around the toroidal product space of the phase plane and phase angle of the forcing function. An experimental criterion on the forcing amplitude and frequency for strange attractor motions is obtained and compared with the Holmes-Melnikov criterion and a heuristic formula developed by the author.

Introduction

There has been growing interest in nonperiodic, steady-state solutions of nonlinear differential equations in applications to atmospheric dynamics [1], electrical circuits [2], and elastic structures [3, 4]. The equations governing these systems are deterministic while for certain control parameters chaotic motions appear. The importance of these motions is twofold. First, conventional methods for finding steady-state solutions to nonlinear differential equations such as perturbation schemes, and averaging techniques must be abandoned or modified since they assume periodic solutions. The second point is that in many physical systems observation of chaotic behavior is often ascribed to some randomness in the problem parameters. The existence of strange attractor motions of deterministic systems may obviate the need for the existence of random "demons" in certain dynamical problems.

Mathematicians have used the name "strange attractor" to denote bounded, chaotic, nonperiodic solutions of deterministic, nonlinear differential equations in contrast to more predictable motions such as those near equilibrium points and limit cycles. Strange attractor oscillations have been found for third-order autonomous differential equations by Lorenz [1] in developing an atmospheric dynamics model. Strange attractor solutions have been found in analog computer simulations of Duffing's equation by Ueda [2, 5] and Holmes [3, 4]. Ueda, [2], has also observed chaotic behavior in analog computer solutions of a forced Van der Pol oscillator.

Mechanical examples of continuous, nonperiodic, bounded motions in deterministic systems can be found in the vibrations of buckled or curved plates and beams. These motions occur when the vibration amplitude becomes large enough to cause the beam or plate to "snap-through." Tseng and Dugundji [6] have studied the nonlinear vibrations of a buckled beam with fixed ends and observed both periodic and nonperiodic motions. They refer to the latter as continuous, "intermittent" snap-through under harmonic excitations. In a recent paper, the author and Holmes [7] examined the nonlinear forced vibrations of a cantilevered beam which is buckled by magnetic forces. The harmonic excitation of this model exhibited chaotic snap-through behavior similar to strange attractor motions found in analog computer studies. In [6, 7], the Galerkin approximation was used to reduce the nonlinear beam equations to Duffing's equation with harmonic excitation.

The work of Tseng and Dugundji [6] was an extension of previous work by Cummings [8], and Eisley [9] on large amplitude vibrations of buckled and curved plates. Cummings treated the snap-through

[1] Research supported in part by a grant from the National Science Foundation, Engineering Mechanics Division, Grant No. 76-23627.

Contributed by the Applied Mechanics Division for presentation at the Winter Annual Meeting, Chicago, Ill., November 16–21, 1980, of The AMERICAN SOCIETY OF MECHANICAL ENGINEERS.

Discussion on this paper should be addressed to the Editorial Department, ASME, United Engineering Center, 345 East 47th Street, New York, N. Y. 10017, and will be accepted until December 1, 1980. Readers who need more time to prepare a discussion should request an extension from the Editorial Department. Manuscript received by ASME Applied Mechanics Division, May, 1979; final revision, January, 1980. Paper No. 80-WA/APM-2.

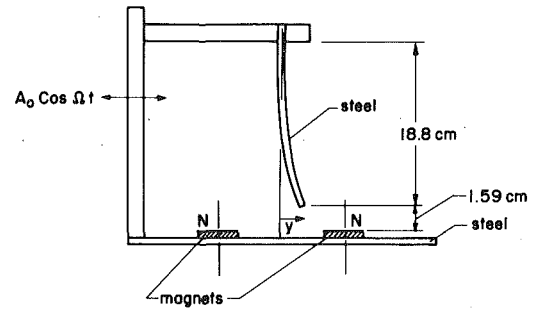

Fig. 1 Sketch of experimental apparatus

problem under a pulsed load but did not examine the intermittent snap-through discussed in [6].

The present paper is an extension of the work of Moon and Holmes [7] on the chaotic vibrations of a cantilevered beam buckled by magnetic forces. Although there are potential applications for the study of magnetically buckled structures, such as in fusion reactors (see, e.g., [10]), its main interest in this paper is as one of the simplest mechanical examples of strange attractor motions which can be easily studied experimentally. In the previous work analysis of the magnetic and elastic forces led to a Duffing-type equation for the first mode approximation. Briefly, the beam was assumed to have a magnetization $\mathbf{M}$ induced by the magnetic field of external magnets $\mathbf{B}^0$. The magnetic field acting on the beam creates distributed magnetic forces and couples

$$\mathbf{F} = \mathbf{M} \cdot \nabla \mathbf{B}^0$$

$$\mathbf{C} = \mathbf{M} \times \mathbf{B}^0 \tag{1}$$

When a one mode Galerkin approximation is used, a magnetic energy potential can be found in terms of $\mathbf{M}$, $\mathbf{B}^0$

$$\mathcal{W} = -\frac{1}{2} \int \mathbf{M} \cdot \mathbf{B}^0 dv \tag{2}$$

This potential is nonlinear in the modal amplitude "a" and is expanded in a Taylor series in "a;"

$$\mathcal{W} = \frac{1}{2}\gamma a^2 + \frac{1}{4}\beta a^4 + \frac{1}{6}\eta a^6. \tag{3}$$

The resulting nonlinear modal magnetic forces when added to linear modal elastic forces lead to a nonlinear differential equation of the form,

$$\ddot{a} + \delta\dot{a} + \alpha a + \beta a^3 + \eta a^5 = \Omega^2 A_0 \cos \Omega t \tag{4}$$

where a is the modal amplitude of the first bending mode of the cantilevered beam, A_0 is the vibration amplitude of the forced support motion, and Ω is the frequency of the support motion. Structural damping is represented by δ. The control parameters in this problem are the spacing of the magnets, damping, forcing amplitude, and frequency. As a static problem only the spacing of the magnets is relevant. The elastic bending stiffness, magnet field strength, and positions of the magnets relative to the beam form a four parameter system which admit one to five equilibrium positions of the tip. For a given beam stiffness, the locus of points in the plane of magnet spacing parameters for which the number of equilibrium points changes is known as a butterfly catastrophe, [11], and is shown in Fig. 2. For the three equilibrium state case only two are stable and the governing nondimensionalized differential equation takes the form

$$\ddot{A} + \gamma\dot{A} - \frac{1}{2}(1 - A^2)A = f \cos \omega t \tag{5}$$

where the following nondimensional groups are noted:

$$\gamma = \delta/\omega_0, \quad A = a/x_0$$

$$f = \frac{\Omega^2 A_0}{\omega_0^2 x_0}$$

$$\omega = \Omega/\omega_0$$

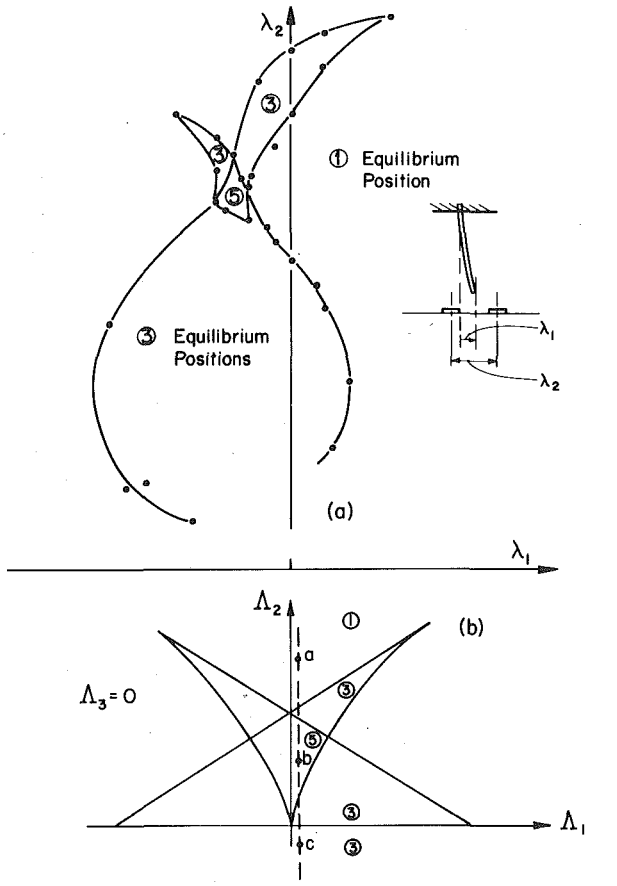

Fig. 2 (a) **Equilibrium state regions in the plane of magnet spacing parameters; experimental data.** (b) **Ideal "butterfly" catastrophe set for a potential** $\mathcal{V} = a^6 + \Lambda_4 a^4 + \Lambda_3 a^3 + \Lambda_2 a^2 + \Lambda_1 a$ **with** $\Lambda_3 = 0$, $\Lambda_4 < 0$

The amplitude is normalized by x_0 and the time by $2\pi/\omega_0$ where x_0 is the static position of the beam tip and ω_0 is the frequency for small vibrations about the buckled position.

For fixed damping and frequency the motion for small forcing amplitudes is periodic but for larger amplitudes becomes chaotic with the beam tip jumping from one equilibrium position to the other as shown in Fig. 3. A phase plane picture is shown in Fig. 4 and it is clear that a continuous history of the motion has very little structure.

In this paper experiments are described which attempt to characterize the behavior of this chaotic motion and to determine the critical parameters for which one might expect chaotic behavior from a second-order, single-degree-of-freedom system. Theoretical attempts have been made recently to determine the nature of the attracting set. In [4] Holmes has developed a necessary criterion for strange attractor motions which determines the minimum forcing amplitude as a function of forcing frequency. This criterion is compared with experimentally determined parameters as well as another theoretical criterion posited by the author. Experimental Poincare plots in the phase plane are used to partially unravel the strange attractor.

Description of Experimental Apparatus

The apparatus consisted of a steel (ferromagnetic) cantilevered beam suspended vertically. The clamped end was attached to a vibration shaker, (Fig. 1) while permanent magnets, 2.54 cm (1 in.) in diameter, were placed below the free end of the beam. The dimensions of the beam were 18.8 cm (7.4 in.) long, 9.5 mm (3/8 in.) wide, and 0.23 mm (0.009 in.) thick. The magnets had a 0.18 Tesla magnetic field normal to the magnet face and rested on a steel base.

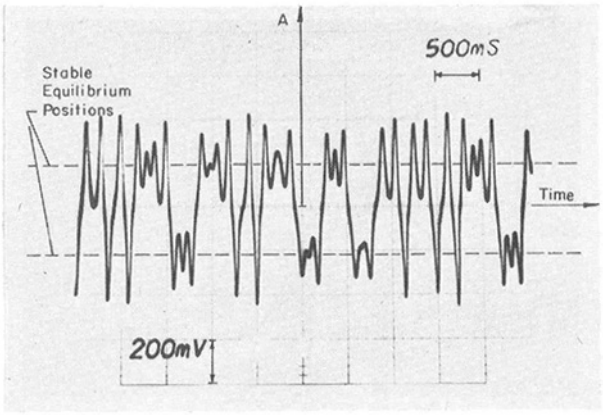

Fig. 3 Bending strain versus time for forced chaotic vibrations of the buckled beam

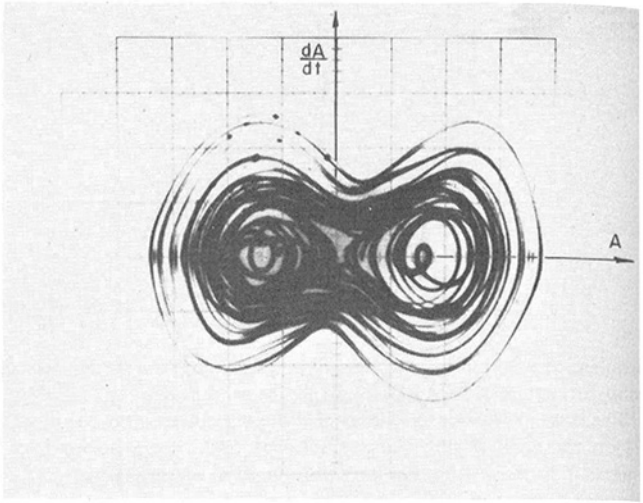

Fig. 4 Phase plane motion for the chaotic motion in Fig. 3; bending strain, horizontal axis and time rate of strain, vertical axis

Strain gages were attached to the beam near the clamped end while a linear variable differential transformer was attached to the shaker platform to measure the forced vibration amplitude of the beam base. Data were recorded on a storage oscilloscope.

To display motion in the phase plane and to perform a Poincare map, a differentiator was used. In order to avoid spurious differentiation from high frequency noise, a low pass active filter was built (Bessel filter) with a 3 db drop in amplitude at 40 hz and less than 1 percent error in phase shift in the operating region. The experiments were performed at driving frequencies below 15 hz. With no magnets the beam had natural frequencies of 4.6, 26.6, and 73.6 hz. The amplitude and phase shift of the differentiator was checked carefully over the range of driving frequencies.

To perform a Poincare map, a storage oscilloscope was used. The scope trace intensity was modulated by a pulse triggered by the vibration shaker amplitude. The bending strain was displayed on the horizontal axis of the scope while the time rate of strain controlled the vertical displacement of the scope trace. By modulating the trace intensity in synchronization with a particular phase of the vibrator motion, a dot would appear with every cycle and the set of dots over time would provide a Poincare map or section of the motion.

Results

A number of different experimental methods were used to characterize the nonperiodic motion of the beam including time histories, Fourier analysis, zero crossing times distribution, Poincare maps, and determination of chaotic motion threshold for driving amplitude and frequency.

Static Bifurcations. Static buckling experiments were done as reported in [7] to determine the critical values of magnet spacing λ_2 and magnetic offset λ_1 at which the number of equilibrium positions changed (Fig. 2(a)). The locus of points in the λ_1, λ_2 plane where the *number* of equilibrium solutions changes is known as a *catastrophe* set, [11]. In classic symmetric buckling problems this set is simply a point, namely, the buckling load. However when one allows other parameters to vary, such as geometric imperfections, the set becomes a curve, surface, or hypersurface in the parameter space. The dimension of the hyperspace depends on the potential energy function.

For this problem the magnetic potential (3) implies that four parameters will be sufficient to describe all the possible bifurcations. The theoretical set is called a butterfly catastrophe, [11], and a two-dimensional section is shown in Fig. 2(b), for the potential,

$$\mathcal{V} = a^6 + \Lambda_4 a^4 + \Lambda_3 a^3 + \Lambda_2 a^2 + \Lambda_1 a \qquad (6)$$

The projection shown in Fig. 2(b) is for $\Lambda_3 = 0$, $\Lambda_4 < 0$. The number of equilibrium positions in each region is shown by the circled numbers.

Comparison of the experimental and theoretical catastrophe sets shows good qualitative agreement. One can imagine a change of parameters $\Lambda_1(\lambda_1, \lambda_2)$ and $\Lambda_2(\lambda_1, \lambda_2)$ which will transform the experimental "rabbit" catastrophe Fig. 2(a), into the topologically identical butterfly set, Fig. 2(b).

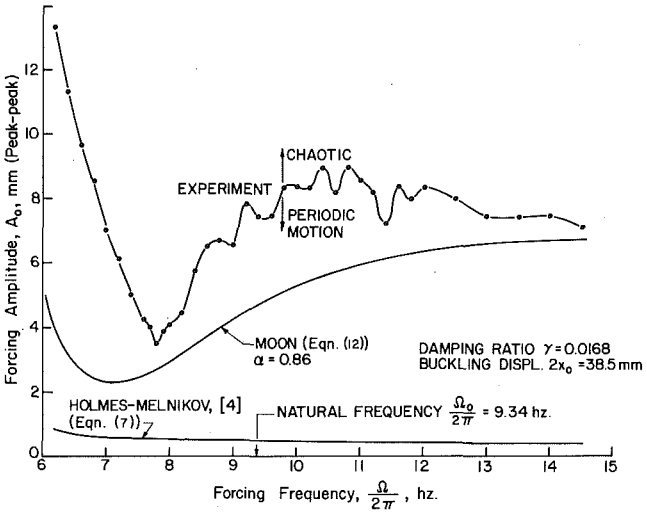

Fig. 5 Experimental and theoretical thresholds for spontaneous chaotic motion-moderate damping, $\gamma = 0.0168$

Most of the dynamic experiments were run in the three equilibria regimes in the λ_1, λ_2 plane with two stable and one unstable equilibria. However a few tests were performed for the five point case. In the latter case, three are stable equilibria while two are saddle-type points and are unstable.

Experimental Criteria for Chaotic Motions. Next the range of vibration base amplitudes and frequencies for chaotic motions was determined. These data were obtained by fixing the frequency and varying the shaker amplitude. For small motions periodic orbits of period one would occur. For larger amplitudes, period one, two, three, four, or more times the driving period might occur. At a sufficiently high amplitude, chaotic motions would occur. Such motions might not persist. Thus, if a periodic motion were disturbed by deflection of the beam, a chaotic motion like that in Fig. 4 might appear and decay to the periodic orbit. However a threshold would occur where the beam would spontaneously jump out of periodic motion into nonperiodic or chaotic motions.

This threshold amplitude of shaker motion is shown in Fig. 5 for different shaker frequencies and damping. The lowest amplitude for

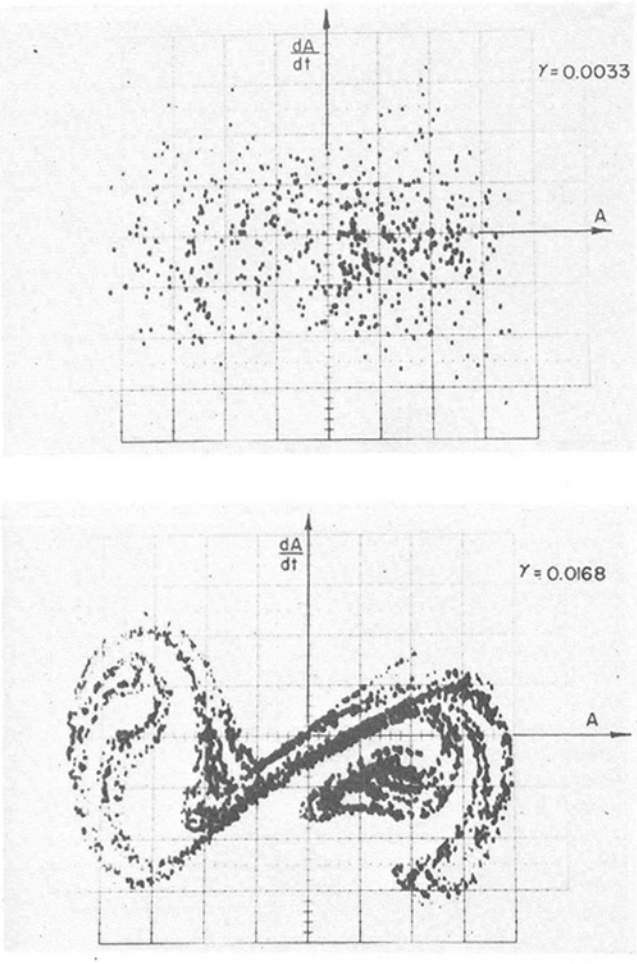

Fig. 6 Experimental Poincare map of chaotic motion for low damping; experimental Poincare map of chaotic motion for moderate damping

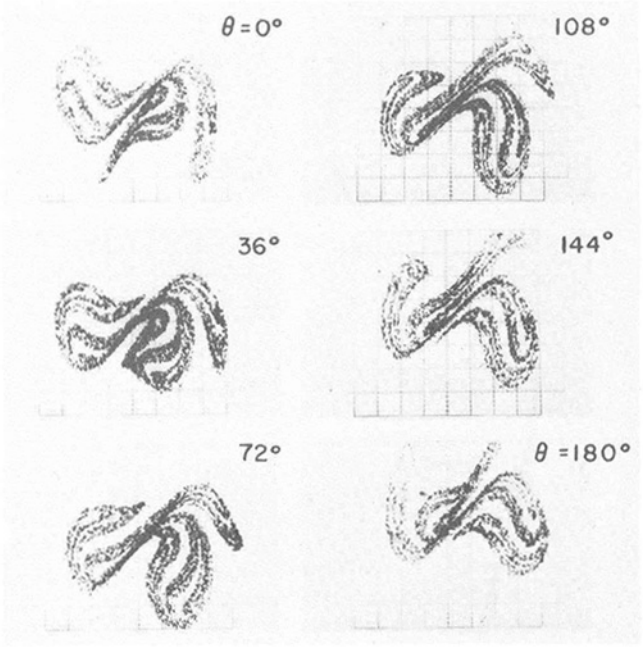

Fig. 7 Poincare maps of a strange attractor for different phase synchronization with forcing function

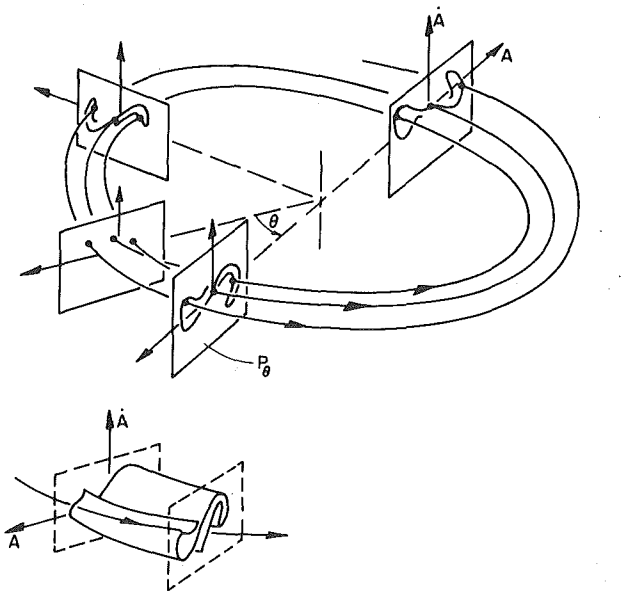

Fig. 8 Sketch of strange attractor surfaces in the product space of Poincare plane and forcing amplitude phase

chaos occurs at a forcing frequency below the natural frequency of the linearized buckled beam. A comparison of the experimental criteria with theoretical predictions is discussed in a later section of this paper.

There is some belief that an upper criterion exists where the forced motion changes from nonperiodic to periodic, [4], but this was not observed within the range of shaker amplitudes available to the author.

Poincare Plots. A time history of the bending strain for nonperiodic motions is shown in Fig. 3. This oscilloscope trace shows vibration about the two stable equilibrium positions, the transition between them, and oscillations about all three equilibrium positions. A phase plane portrait of this motion is shown in Fig. 4. Motion about the left, right, and all three equilibrium points can be seen but it is clear that the plane will become dense with these traces, making any characterization of the motion difficult to interpret. Instead of looking at the motion for all times, one can choose to observe the position in the phase plane at certain multiples of periods of the forcing motion. A sequence of points or dots on the oscilloscope will appear called a Poincare map.

A period one Poincare map is shown in Fig. 6(a) for low damping. One can see that there appears to be little global structure, though locally small clusters of straight lines of dots can be seen. Thus the forced nonperiodic motions of the near Hamiltonian system do not reveal much structure or order in the Poincare map.

To increase the damping, a 0.05 mm (0.002 in.) thick stainless steel strip was glued to the beam which increased the damping from $\gamma = 0.0033$ to $\gamma = 0.0168$.

The Poincare map for the moderate damping case is shown in Fig. 6(b). Here one can see that the period one Poincare map shows a great deal of order resembling a line wrapped back and forth on itself. In analog computer studies [3], Holmes has shown that this parallel line structure continues to exist when local regions of the phase plane are magnified, suggesting the property of a Cantor set.

The Poincare map in Fig. 6(b) depends on the phase angle of the driving motion, θ. For the symmetric problem examined here, the map should invert itself when $\theta \rightarrow \theta + \pi$. The change of shape of the strange attractor for different θ where $0 \leq \theta \leq \pi$, is shown in Fig. 7. One can see that although the figure at $\theta = \pi$ appears to be rotated, the evolution of this change shows that the "arms" of the attracting set deform in such a way as to invert the shape.

It should be noted that the motion of the beam must pierce all of these maps so that the lines in the Poincare plane become sheets in

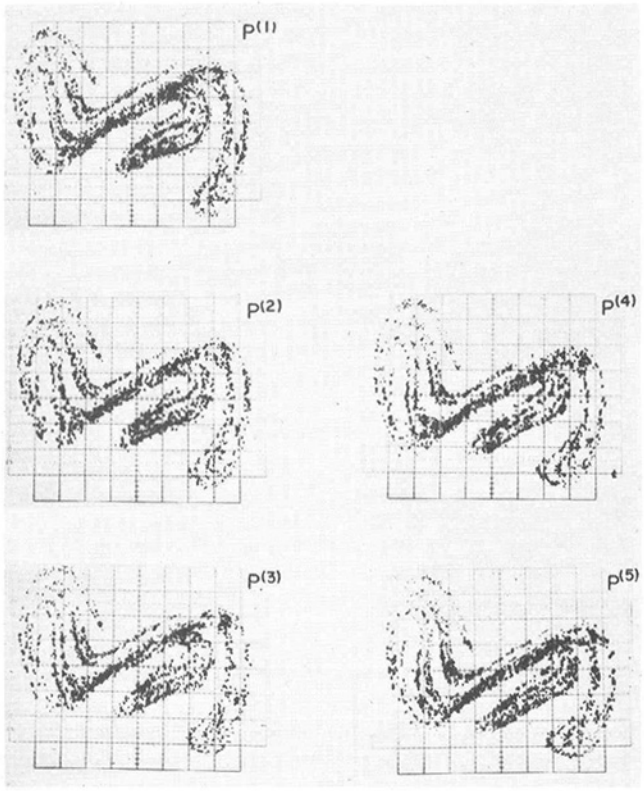

Fig. 9 Experimental multiperiod Poincare maps of the same chaotic motion

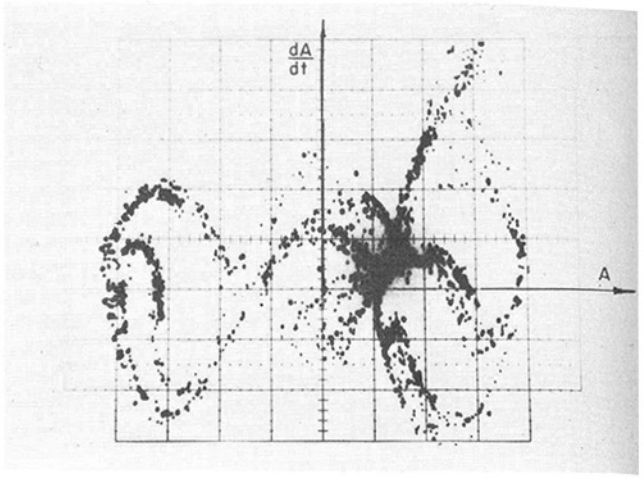

Fig. 10 Experimental strange attractor in the Poincare plane for the five equilibria case

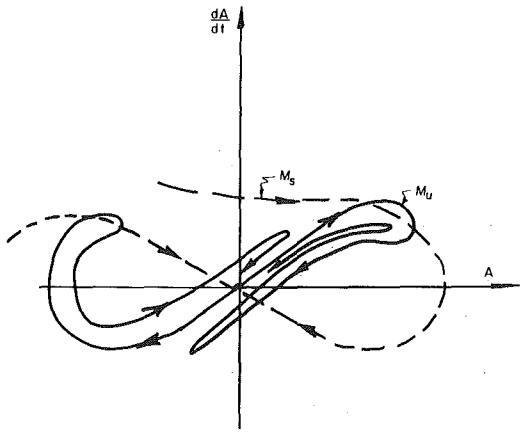

Fig. 11 Intersection of the stable manifold M_s and unstable manifold M_u of the Poincare map in the phase plane (see [4])

the toroidal product space of the Poincare plane and forcing phase θ, Fig. 8.

It is remarkable that a Poincare map synchronized with the forcing motion appears to organize what appears to be chaotic behavior. It should be clear that if the map is slightly unsynchronized, points from different P_θ maps of the synchronized maps will project onto the unsynchronized map. The resulting attracting set will appear as a blur and the structure will be lost.

One of course can obtain multiperiod Poincare maps $P^{(n)}$ defined by

$$\left\{x, \dot{x} \mid \theta = \frac{2n\pi}{\omega}, \frac{4n\pi}{\omega} \ldots\right\}.$$

We note that the maps $P^{(n)}$, $n \geq 2$ are contained in the P^1 map but the question arises as to whether the structure of the strange attractor as seen in the higher period maps will look like that of the P^1 map. Experiments were carried out for $n = 2, 3, 4, 5$ and indeed the structure of the attractor looks identical to the P^1 map as shown in Fig. 9. For example, the only difference between $P^{(5)}$ and P^1 is that $P^{(5)}$ took 20 min to obtain, while P^1 took around four minutes of data. This illustrates again that although the motion appears to be chaotic in continuous observations, stroboscopic, or P^n maps reveal highly structured features of this motion.

"Butterfly" Strange Attractor. While most of the experiments were carried out for the single saddle and double sink or three equilibrium point case, a few experiments were performed for the double saddle or five equilibria case. As had been discussed by Holmes [4] and Ueda [2], the strange attracting set in the Poincare plane seems to be organized about the unstable manifold of the saddle point. When two saddles are present in the phase plane of the unforced motion, one would expect two organizing centers to appear in the Poincare map for the chaotic motions. Experimentally this has been observed as can be seen in Fig. 10.

Fourier Analysis. Frequency analyses of these chaotic motions were carried out by digitizing the data and using a fast Fourier transform [7]. The chaotic motions exhibit a continuous spectrum of frequencies below the driving frequencies, including subharmonics. Similar results were reported earlier by Ueda [5] and Holmes [4] for a forced Duffing's equation.

Threshold Criteria for Chaotic Motions

Various qualitative analyses have demonstrated the existence and characteristics of chaotic motions in deterministic nonlinear systems. However there is at present no theory to predict for what range of parameters these chaotic motions will occur. The engineer would like a chaotic "Reynolds number" or an equivalent parameter below which periodic motions would be insured and above which chaotic, nonperiodic motions would occur in the forced nonlinear oscillator.

In [4] Holmes has presented a necessary criteria for the strange attractor based on the work of Melnikov [12]. For chaotic motions to occur, the forcing amplitude, driving frequency, and damping in (5) must satisfy the relation

$$f_1 = \frac{\gamma\sqrt{2}}{3\pi\omega}\cosh\left(\frac{\pi\omega}{\sqrt{2}}\right). \tag{7}$$

In [4] Holmes showed that the Poincare map itself has a saddle point and that as the forcing amplitude is increased the stable and unstable manifolds of the saddle of the Poincare map intersect, giving rise to infinitely many intersections or homoclinic points as shown in Fig. 11. It has been shown in [4] that two arbitrarily close points in

the Poincare phase plane can be widely separated under iterations of the Poincare map.

Comparison of the Holmes-Melnikov criterion with experimental thresholds in the driving amplitude-frequency plane for fixed damping is shown in Fig. 5. While the theoretical threshold (7) gives a lower bound it does not compare well with measurements for low damping. Also it predicts that the minimum forcing amplitude occurs at a driving frequency greater than the natural frequency while experiments indicate that for low damping the minimum occurs below the natural frequency. There is evidence however that this criterion may give good results for high damping ($\gamma > 0.1$), [4].

It should be pointed out that the experimental thresholds were for "spontaneous" departure from forced periodic motion about a buckled state to chaotic motions. Experiments have shown that under certain initial conditions chaotic motion can occur below the spontaneous threshold. Thus it is possible that initial conditions could be found for which chaotic motion could occur near the Holmes-Melnikov criterion.

As just mentioned, it has been predicted and observed experimentally that multiperiod subharmonic forced oscillations are often precursors to the strange attractor behavior. Thus a better criterion may be found by studying the stability of subharmonic motions as has been reported by Hayashi [13]. Unfortunately the stability criterion as reported in [13] does not use f and ω as parameters and it is difficult to determine if a subharmonic stability criterion will compare well with the threshold in Fig. 5. But this seems to be a worthwhile direction to go in.

Finally, we propose a hueristic criterion based in part on a perturbation solution for forced periodic motion, and experimental observations. First we observe that the criterion sought governs the transition from forced periodic to nonperiodic motion. Thus, before chaotic motions occur, the response amplitude and velocity are known functions of forcing amplitude and frequency, i.e., $\langle x^2 \rangle = g(f, \omega)$, where $\langle\ \rangle$ indicates time averaged. If a critical amplitude of $\langle x^2 \rangle$ or $\langle \dot{x}^2 \rangle$ can be found, then f and ω can be related when chaotic motion is incipient.

To find the response function we write (5) about the buckled position $A = 1$ or -1. If we denote the motion about $A = 1$ by

$$A - 1 = X/x_0$$

where x_0 is the static deflected position of the tip of the beam, then the equation of motion takes the form

$$\ddot{X} + \gamma\dot{X} + X\left(1 + \frac{3}{2}\mu X + \frac{1}{2}\mu^2 X^2\right) = x_0 f \cos(\omega t + \phi_0) \tag{8}$$

where $\mu = 1/x_0$. The parameter μ will act as a perturbation parameter, while the phase angle ϕ_0 will be adjusted so that the first-order motion is proportional to $\cos \omega t$. Then using either Duffing's method, or Linstedt's perturbation method [13], [14] one assumes a solution of the form

$$X = C_0 \cos \omega t + \mu(C_1 + C_2 \cos \omega t) + \mu^2 X_1 \tag{9}$$

The resulting force-response relation is found to be

$$\left(\frac{C_0}{x_0}\right)^2 \left\{\left[(1 - \omega^2) - \frac{3}{2}\left(\frac{C_0}{x_0}\right)^2\right]^2 + \gamma^2\omega^2\right\} = f^2 \tag{10}$$

Finally, it has been observed that over a limited range of frequencies close to the natural frequency in the post buckled state, the periodic motion seems to change to chaotic at a *critical velocity*. This velocity was not measured. However we hazard a guess that the critical velocity is near the maximum velocity on the separatrix for the phase plane motion of the undamped, unforced oscillator. This is certainly a guess, but this velocity is a characteristic of the beam and independent of the force. In nondimensional units $(dA/dt)_{\max} = \frac{1}{2}$. Thus we assume that near the chaotic threshold

$$\frac{\omega C_0}{x_0} = \frac{\alpha}{2} \tag{11}$$

where α is near but less than unity. These assumptions lead to a criterion of the form

$$f_1 = \frac{\alpha}{2\omega}\left\{\left[(1 - \omega^2) - \frac{3}{8}\frac{\alpha^2}{\omega^2}\right]^2 + \gamma^2\omega^2\right\}^{1/2} \tag{12}$$

The constant α gives us a "cheat" factor with which to fit the data. However what is remarkable, at least to the author, is that with reasonable values of α (near unity) the criterion compares very well with the experimental data both qualitatively and quantitatively as shown in Fig. 5. In Fig. 5 the dimensional forcing frequency and amplitude are given by

$$\Omega = \omega_0\omega, \quad A_0 = x_0 f \omega_0^2/\Omega^2.$$

It is left to theoreticians to determine whether the assumptions implicit in (12) are at all related to the subharmonic stability criterion of Hayashi or the Holmes-Melnikov equation (7), or whether (12) is simply a fortuitous guess.

Summary

The experiments reported here show that a simple mechanical structure can exhibit nonperiodic or chaotic motions even when the forcing inputs are highly deterministic. The results are consistent with qualitative analysis and analog computer solutions of a deterministic forced Duffing's equation. In both the mechanical structure and the analog studies reported earlier, the nonperiodic motion exhibits a remarkable mathematical structure in the Poincare plane, resembling a sheet folded infinitely many times about the saddle point with properties of a Cantor set. This structure is preserved in higher-order maps of period two or higher. However the maps must be exactly synchronized with the phase of the driving motion or else this organized structure will be blurred or washed out. Experimentally the structure of the strange attracting set is more readily observed in moderate to highly damped systems.

The attempt by Holmes [4] to develop a dynamical "catastrophe" set of parameters for which strange attractor motions will occur seems to give a lower bound for the driving force. An ad-hoc criterion developed in this paper gives a set of driving amplitudes and frequencies closer to the experimental set. However the effects of other parameters such as initial conditions have yet to be explored.

The extension of this work to other nonlinear and multistate mechanical systems should reveal similar phenomena. In experiments on the dynamics of a magnetically levitated model on a rotating guidance track the author has observed similar chaotic behavior [15]. Lateral "rattling" motions of trains may also fall into this class of problems.

Whatever the specific example however, it is clear from these experiments and those of others that what appears to be "random" or chaotic motion in many mechanical systems may be governed by deterministic mathematical models and controlled by nonrandom parameters.

Strange attractor dynamics in other engineering systems such as chemical reactors and aerospace applications have been reported in [16], including a two-dimensional mechanical oscillator with chaotic behavior [17].

Acknowledgment

The author wishes to thank Prof. P. Holmes and Prof. R. Rand of Cornell University and Prof. Ueda of Kyoto University for helpful discussions. Thanks are also due to Stephen King, research engineer, Cornell University for the design of some of the electronic equipment.

References

1 Lorenz, E. N., "Deterministic Nonperiodic Flow," *Journal of the Atmospheric Sciences*, Vol. 20, 1963, pp. 130–141.

2 Ueda, Y., Hayashi, C., and Akamatsu, N., "Computer Simulation of Nonlinear Ordinary Differential Equations and Nonperiodic Oscillations," *Electronics and Communications in Japan*, Vol. 56-A, No. 4, 1973.

3 Holmes, P. J., "Strange Phenomena in Dynamical Systems and Their Physical Implications," *Applied Mathematical Modelling*, Vol. 1 (7), 1977, pp. 362–366.

4 Holmes, P. J., "A Nonlinear Oscillator With a Strange Attractor," *Philosophical Trans. of Royal Society*, London, Vol. 292, No. 1394, Oct. 1979, pp. 419–448.

5 Ueda, Y., "Randomly Transitional Phenomena in the System Governed by Duffing's Equation," *Journal of Statistical Physics*, Vol. 20, 1979, pp. 181–196.

6 Tseng, W.-Y., and Dugundji, "Nonlinear Vibrations of a Buckled Beam Under Harmonic Excitation, ASME JOURNAL OF APPLIED MECHANICS, Vol. 38(2), 1971, pp. 467–476.

7 Moon, F. C., and Holmes, P. J., "A Magnetoelastic Strange Attractor," *Journal of Sound and Vibration*, Vol. 65(2), 1979, pp. 276–296.

8 Cummings, B. E., "Large Amplitude Vibration and Response of Curved Panels," *AIAA Journal*, Vol. 2(4) Apr. 1964, pp. 709–716.

9 Eisley, J. G., "Large Amplitude Vibration of Buckled Beams and Rectangular Plates," *AIAA Journal*, Vol. 2(12), Dec. 1964, pp. 2207–2209.

10 Moon, F. C., "Problems in Magnetosolid Mechanics," *Mechanics Today*, Vol. 4, Chapter 5, 1978.

11 Poston, T., and Stewart, I., *Catastrophe Theory and Applications*, Pitman, London, 1978.

12 Mel'nikov, V. K., "On the Stability of the Center for Time Periodic Perturbations," *Trans. Moscow Math. Soc.*, Vol. 12(1), 1963, pp. 1–57.

13 Hayashi, C., *Nonlinear Oscillations in Physical Systems*, McGraw-Hill, New York, 1964.

14 Stoker, J. J., *Nonlinear Vibrations in Mechanical and Electrical Systems*, Interscience Publ., N.Y., 1950.

15 Moon, F. C., "Static and Dynamic Instabilities in Mag-Lev Model Experiments," *Proceedings of the Conference on Noncontacting Suspension and Propulsion Systems for Advanced Ground Transportation*, M.I.T., Sept. 1977, Wormley, D., ed., printed by the U.S. Dept. of Transportation.

16 Holmes, P., ed., *New Approaches to Nonlinear Problems*, SIAM Publishing, to appear.

17 Moon, F. C., "Strange Attractor Vibrations in One and Two-Degree-of-Freedom Elastic Systems", to appear in reference [16].

L. A. Month
Assistant Professor,
Department of Mechanical Engineering,
University of California,
Berkeley, Calif. 94720

R. H. Rand
Associate Professor,
Department of Theoretical
and Applied Mechanics,
Cornell University,
Ithaca, N. Y. 14853
Mem. ASME

An Application of the Poincaré Map to the Stability of Nonlinear Normal Modes

The stability of periodic motions (nonlinear normal modes) in a nonlinear two-degree-of-freedom Hamiltonian system is studied by deriving an approximation for the Poincaré map via the Birkhoff-Gustavson canonical transofrmation. This method is presented as an alternative to the usual linearized stability analysis based on Floquet theory. An example is given for which the Floquet theory approach fails to predict stability but for which the Poincaré map approach succeeds.

Introduction

This paper is concerned with certain periodic motions, called nonlinear normal modes (NNM's), which have been shown to occur in a wide class of coupled oscillators [24, 18, 10]. In particular we shall be interested in the stability of NNM's. As usual in discussing the stability of periodic motions in a nonlinear system, we shall be concerned only with orbital (and not Liapunov) stability [4].

The usual procedure for determining stability of a periodic motion in a nonlinear system involves perturbing the solution whose stability is to be studied, and then linearizing the perturbed equations. The resulting linear system of equations has periodic coefficients and lies in the realm of Floquet theory; e.g., for small amplitudes of vibration the stability problem is often reduced to consideration of the Mathieu equation [28, 22, 16]. The question of the stability of a given NNM will often depend upon the values of the system parameters (e.g., spring constants, geometry, etc.) The parameter space is typically decomposed into stable and unstable regions separated by a codimension 1 "transition" surface. (e.g., in the case of the Mathieu equation $\ddot{x} + (\delta + \epsilon \cos t)x = 0$ the $\delta - \epsilon$ parameter plane has regions of stability separated from regions of instability by transition curves [12].) In a particular problem, analytical expressions may be obtained for the transition surfaces by perturbation methods [26, 21].

It is our purpose in this paper to provide an alternate procedure for determining the stability of NNM's in autonomous two-degree-of-freedom Hamiltonian systems. The procedure is based on using the Birkhoff-Gustavson (B-G) canonical transformation to obtain an approximation for the Poincaré map. We believe that this method offers some advantage over the usual Floquet theory approach just described. Specifically, the procedure does not require linearization in the neighborhood of any particular motion and hence it yields a global picture of the flow. Thus it not only permits conclusions to be drawn about the stability of NNM's, but it also provides insight into the dynamical structure of the system.

Moreover, there exist systems for which the Floquet theory approach simply fails to predict stability for a given NNM! We will describe such a system in this paper. The failure of Floquet theory in this case is related to the essentially *nonlinear* nature of the stability problem. We will show that the method based on the B-G transformation and the Poincaré map does, however, predict stability for this problem.

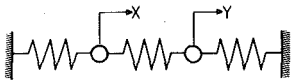

Fig. 1 The system *S*

The System

Consider a nonlinear autonomous two-degree-of-freedom Hamiltonian system S which consists of two unit masses constrained to move along a straight line and restrained by two anchor springs and a coupling spring, Fig. 1. The positions of the masses are given by generalized coordinates x and y, both of which are taken to be zero when the springs are unstretched. We assume that the restoring force F for the identical anchor springs is given by $F = d + kd^3$, while for the

Contributed by the Applied Mechanics Division for presentation at the Winter Annual Meeting, Chicago, Ill., November 16–21, 1980, of THE AMERICAN SOCIETY OF MECHANICAL ENGINEERS.

Discussion on this paper should be addressed to the Editorial Department, ASME, United Engineering Center, 345 East 47th Street, New York, N. Y. 10017, and will be accepted until December 1, 1980. Readers who need more time to prepare a discussion should request an extension from the Editorial Department. Manuscript received by ASME Applied Mechanics Division, September, 1979; final revision, February, 1980. Paper No. 80-WA/APM-4.

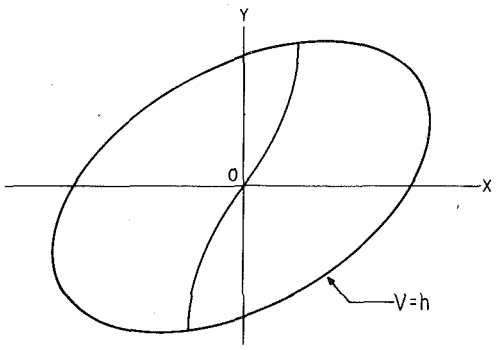

Fig. 2 A nonlinear normal mode (NNM)

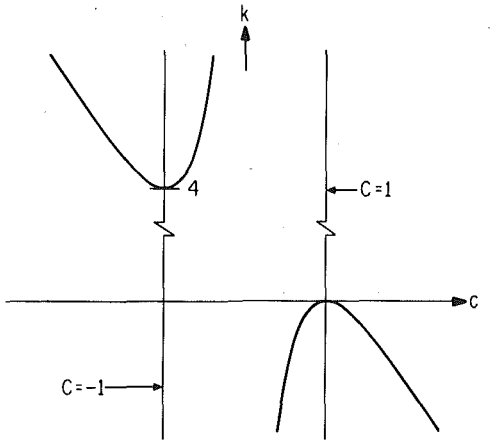

Fig. 3 Bifurcation of SNM's ($y = Cx$) for system S

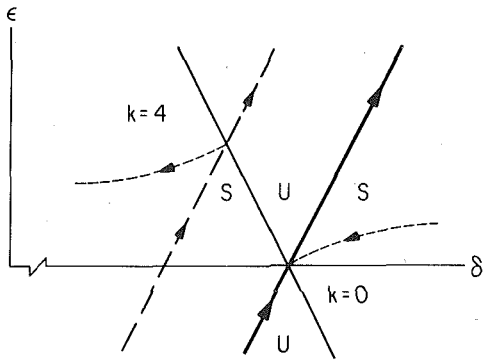

Fig. 4 Stability results from Floquet theory. The stability chart is for the Mathieu equation $\ddot{x} + (\delta + \epsilon \cos t)x = 0$ (S = stable, U = unstable). Solid lines represent transition curves, $\delta = 1/4 \pm \epsilon/2 + O(\epsilon^2)$. The location of the SNM's for varying k is displayed as follows: The dashed line corresponds to the out-of-phase mode $y = -x$; the dark solid line corresponds to the in-phase mode $y = x$ (which lies on the transition curve); the dotted lines correspond to the pairs of bifurcating modes. Arrows indicate direction of increasing k.

coupling spring, $F = d^3$. Here d is the spring deformation and k is a parameter.

The equations of motion for the system S are

$$\ddot{x} = -\frac{\partial V}{\partial x}, \quad \ddot{y} = -\frac{\partial V}{\partial y} \tag{1}$$

where the potential energy $V(x, y)$ is given by

$$V = \frac{1}{2}(x^2 + y^2) + \frac{k}{4}(x^4 + y^4) + \frac{1}{4}(x - y)^4. \tag{2}$$

The system S possesses a first integral corresponding to the conservation of energy,

$$H(x, y, \dot{x}, \dot{y}) = \frac{1}{2}(\dot{x}^2 + \dot{y}^2) + V(x, y) = h \tag{3}$$

where $H(x, y, \dot{x}, \dot{y})$ is the Hamiltonian.

In a previous work [23] it has been shown that the system S possesses bifurcating NNM's. In a manner similar to Rosenberg [24] we take NNM's to be periodic motions which pass through the origin 0 and which have precisely two rest points, Fig. 2. NNM's which project onto the xy-plane as straight lines have been called similar normal modes (SNM's) [24].

The system S possesses SNM's, $y = Cx$, where

$$C = 1, -1, 1 - \frac{k}{2} \pm \frac{\sqrt{k(k-4)}}{2}. \tag{4}$$

When $0 \le k \le 4$ there are only two SNM's, $y = \pm x$. An additional pair of SNM's bifurcates out of the $y = -x$ mode when $k > 4$, and out of the $y = x$ mode when $k < 0$, Fig. 3.

The stability of the $y = -x$ out-of-phase mode and of the two SNM's which bifurcate out of it has been investigated in a previous work [16]. Results were obtained using a linearized stability analysis and Floquet theory. The stability analysis, valid for small energies h, was shown to finally reduce to the study of a single Mathieu equation. This Mathieu equation governs perturbations which are orthogonal to the SNM under investigation, and therefore the stability being considered is orbital stability [15].

It was shown [16] that upon bifurcation at $k = 4$ the two new periodic motions enter as stable, while the existing $y = -x$ periodic motion changes from stable to unstable. See Fig. 4 which shows the location of the SNM's for varying k on a Mathieu equation stability chart.

The same analysis can also be used to investigate the stability of the modes which bifurcate out of the $y = x$ in-phase mode when $k = 0$. It has been shown that these modes enter as stable [15], Fig. 4.

However, this same kind of linear stability analysis *fails* to predict stability for the $y = x$ in-phase mode [16]. In this case the SNM lies along a transition curve in the associated Mathieu equation stability chart, Fig. 4.

In what follows we present an alternate method of stability analysis which will be shown to yield stability information for the $y = x$ mode of system S.

The Poincaré Map

In this section we will discuss a powerful technique for analyzing two-degree-of-freedom problems, the Poincaré map. Its purpose is to provide a two-dimensional description of a flow which is occurring in a four-dimensional phase space.

Let us consider an autonomous two-degree-of-freedom Hamiltonian system. Although the phase space $(x, y, \dot{x}, \dot{y})$ is four-dimensional, the first integral $H = h$, equation (3), restricts the motion to a three-dimensional surface. If another independent first integral exists then the energy manifold, $H = h$, is fibered by invariant two-dimensional tori. These may be pictured in three-dimensional space as a family of concentric tori, Fig. 5.

Now consider the two-dimensional surface Σ which results from "slicing" the three-dimensional energy manifold $H = h$ with a plane, say $x = 0$, Fig. 6. Σ, which looks locally like a two-dimensional plane, will in general intersect a particular motion infinitely often. A motion beginning on Σ returns to Σ after making a circuit around the torus. This produces a mapping of Σ onto itself. This map is known as the Poincaré map [20, 9, 2, 1], and the two-dimensional surface $\Sigma = \{x = 0\} \cap \{H = h\}$ is called a surface of section. We will choose $y, \dot{y}$ as coordinates on Σ and will project Σ down onto the $y - \dot{y}$-plane for convenience.

In order to insure that the Poincaré map gives a realistic picture of the flow in the neighborhood of a given motion, we require that the motion intersect the surface of section Σ transversally (nontangen-

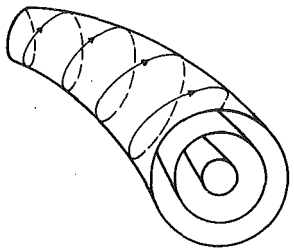

Fig. 5 In a two-degree-of-freedom Hamiltonian system, the existence of a first integral which is independent of the Hamiltonian implies that the three-dimensional energy manifold will be fibered into invariant tori; a given motion remains on a single torus for all time

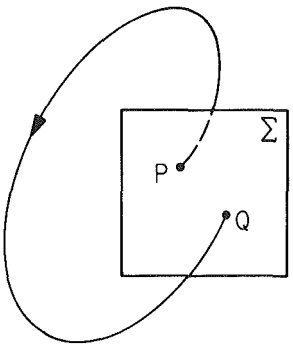

Fig. 6 A motion starting at P on the surface of section $\Sigma = \{x = 0\} \cap \{H = h\}$ reintersects Σ at Q producing a Poincaré map

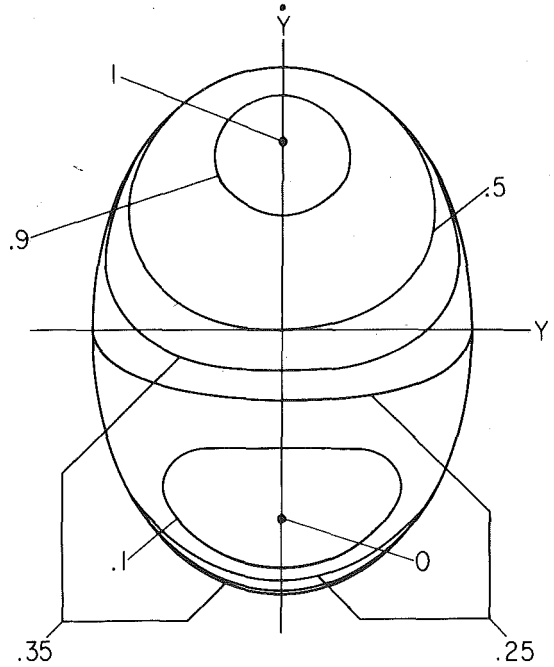

Fig. 7 The Poincaré map for the linear system L for $h = 1$; each invariant curve is associated with a value of c

tially) [5]. A motion will fail to intersect Σ transversally whenever the normal to the "slicing" surface (i.e., $x = 0$) is perpendicular to the tangent of the motion. The normal to the surface $x = 0$ is $(1, 0, 0, 0)$ and the tangent to the motion $(x, y, \dot{x}, \dot{y})$ is $(\dot{x}, \dot{y}, \ddot{x}, \ddot{y})$. Thus transversality is violated whenever $(\dot{x}, \dot{y}, \ddot{x}, \ddot{y}) \cdot (1, 0, 0, 0) = 0$ or $\dot{x} = 0$. We impose the additional restriction that $\dot{x} > 0$ when $x = 0$ in order to insure that the motion always pierces Σ from the "same side." Therefore successive intersections of a motion with the $y, \dot{y}$ surface of section Σ lie inside the region $\dot{x}(y, \dot{y}, h) \geq 0$. This region is bounded by the curve $\dot{x}(y, \dot{y}, h) = 0$, obtained by solving the equation $H(0, y, \dot{x}, \dot{y}) = h$ equation (3), for $\dot{x}$.

Periodic motions which pierce the surface of section Σ once per cycle appear as fixed points of the Poincaré map. More complicated periodic oribts may appear as n-cycles of the map, i.e., as fixed points of the map composed with itself n times.

Suppose a periodic motion which corresponds to a fixed point of the Poincaré map is stable. Then in phase space the closed curve which corresponds to the periodic motion will be enclosed by tori which contain neighboring motions. The Poincaré map will reveal the fixed point to be surrounded by concentric closed curves. Thus stable periodic motions become centers in the $y - \dot{y}$-plane. Similarly unstable periodic motions appear as saddle points in $y - \dot{y}$-plane. It is important to recognize that the dynamic on the $y - \dot{y}$-plane is that of a map and not of a flow, and although we speak of centers and saddles these must not be confused with the singular points associated with the flows of phase plane analysis (cf. [14]).

The Poincaré map can be found analytically as follows: Let $f(x, y, \dot{x}, \dot{y}) = c$ be a first integral which is independent of the energy integral $H = h$. The intersection of the $f = c$ surface with the surface of section Σ represents the invariant curves of the Poincaré map. For fixed energy h these invariant curves may be written

$$\bar{f}(y, \dot{y}) = f(0, y, \dot{x}(y, \dot{y}, h), y) = c. \tag{5}$$

Note that if no such independent first integral $f = c$ exists then the energy manifold will not, in general, be fibered by invariant tori, and the motion may even be ergodic.

To familiarize the reader with the Poincaré map we will now consider a well-known integrable two-degree-of-freedom linear system L. The system L consists of two unit masses which are constrained to move along a straight line and which are restrained by two linear anchor springs and a linear coupling spring. All three springs have a spring constant of unity.

Choosing generalized coordinates x, y as in Fig. 1, the potential energy for L becomes

$$V(x, y) = x^2 + y^2 - xy. \tag{6}$$

The general solution to the equations of motion (1) consists, of course, of a superposition of the two linear normal modes: here the $x = y$ in-phase mode has frequency 1 and the $x = -y$ out-of-phase mode has frequency $\sqrt{3}$ [6. p. 370].

In addition to the conservation of energy for the entire system, $H = h$, equation (3), the system L possesses an independent first integral corresponding to conservation of energy in either mode alone. Taking the $x = y$ in-phase mode, conservation of energy gives

$$\tfrac{1}{2}\dot{u}^2 + \tfrac{1}{2}u^2 = c \tag{7}$$

where $u = (1/\sqrt{2})(x + y)$. That is,

$$f(x, y, \dot{x}, \dot{y}) = \tfrac{1}{4}(\dot{x} + \dot{y})^2 + \tfrac{1}{4}(x + y)^2 = c. \tag{8}$$

To generate the Poincaré map, set $x = 0$ in equations (3) and (6) and solve for $\dot{x}(y, \dot{y}, h)$:

$$\dot{x} = (2h - 2y^2 - \dot{y}^2)^{1/2}. \tag{9}$$

Then set $x = 0$ in equation (8) and use equation (9) to obtain

$$\bar{f}(y, \dot{y}) = \tfrac{1}{4}[(2h - 2y^2 - \dot{y}^2)^{1/2} + \dot{y}]^2 + \tfrac{1}{4}y^2 = c. \tag{10}$$

For fixed h, say $h = 1$, equation (10) represents a one-parameter family of invariant curves with c as parameter, Fig. 7. These curves fill the interior of the region in the $y - \dot{y}$ plane bounded by the ellipse

$$2y^2 + \dot{y}^2 = 2h \tag{11}$$

obtained by setting $\dot{x} = 0$ in equation (9).

From Fig. 7 we see that the system L exhibits two stable periodic

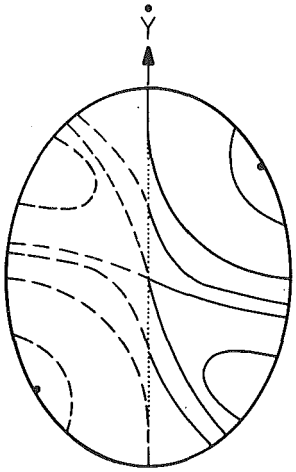

Fig. 8 The surface of section Σ for system L is topologically equivalent to a 2-sphere. Here we see a "side" view of Σ (the y-axis is directed into the paper). Solid lines are invariant curves which lie on the $\dot{x} > 0$ ("front") side of Σ. Dashed lines lie on the $\dot{x} < 0$ ("rear") side of Σ. Dotted lines represents $\dot{x} = 0$.

motions, $c = 0$ ($x = -y$) and $c = 1$ ($x = y$). There are no other periodic motions since the natural frequencies are incommensurable. For $0 < c < 0.25$ the invariant curves are closed and surround the out-of-phase mode $c = 0$, while for $0.5 < c < 1$, they surround the in-phase mode $c = 1$. However for $0.25 < c < 0.5$ the invariant curves are composed of two disconnected pieces. Nevertheless the motions which correspond to these disconnected curves are not qualitatively different from the other nonperiodic motions of the system. Their disconnected appearance is due to the topology of the energy manifold $H = h$, equation (3). We offer the following description of this situation.

The energy manifold $H = h$ for the system L is topologically equivalent to a 3-sphere. By slicing it with the 3-plane $x = 0$ we produce a surface of section Σ which is topologically equivalent to a 2-sphere. The Poincaré map of Fig. 7 is a projection of this surface onto the $y - \dot{y}$-plane. The front half of Σ corresponds to $\dot{x} > 0$ while the rear half corresponds to $\dot{x} < 0$. Since we have taken $\dot{x} > 0$ in equation (9) we see only the front half of Σ in Fig. 7. The bounding curve $\dot{x} = 0$ separates the front half of Σ from the rear half. As mentioned previously, any motion which intersects Σ at $\dot{x} = 0$ does so nontransversally. Thus every disconnected invariant curve in Fig. 7 has a motion associated with it which intersects Σ nontransversally.

In fact any such disconnected invariant curve in Fig. 7 forms a closed connected curve on Σ. Such a curve includes points on both the front and rear halves of Σ. Due to the symmetry of the system L, the invariant curves on Σ are symmetric with respect to the origin. Therefore the rear half of Σ ($\dot{x} < 0$) looks just like the front half ($\dot{x} > 0$) turned upside-down, Fig. 8.

The stability of a periodic motion follows directly from the nature of the invariant curves in the neighborhood of a fixed point of the Poincaré map. It has been shown that stability results which are obtained from a linear stability analysis and Floquet theory are equivalent to results obtained by expanding the Poincaré map about a fixed point and neglecting cubic and higher-order terms [15, 8, 13, 19]. In cases where Floquet theory fails to predict stability (e.g., system S), the Poincaré map will still give stability results if higher-order terms are retained in expansions about a fixed point. We will return to this point when we find the Poincaré map for system S. First, however, we will use the B-G transformation to determine an approximate first integral for the system S.

The Birkhoff-Gustavson Transformation

In this section we will use an approximate method developed by Birkhoff [3] and extended by Gustavson [7]. The idea of the method is to choose new dependent variables via a generating function in order to simplify the form of the Hamiltonian. Although the method can be continued to all orders of accuracy, we shall neglect terms of 0(6), i.e., terms of the form $x^\alpha y^\beta \dot{x}^\gamma \dot{y}^\delta$ where $\alpha, \beta, \gamma, \delta$ are non negative integers and $\alpha + \beta + \gamma + \delta \geq 6$. As a result, our conclusions will only be valid for small energies h. In order to simplify the notation in this section, we will write

$$x = x_1, \quad y = x_2, \quad \dot{x} = \dot{x}_1, \quad \dot{y} = \dot{x}_2. \tag{12}$$

The Hamiltonian for system S, equation (3), may be written

$$H = H(x_j, \dot{x}_j) = H^{(2)} + H^{(4)} \tag{13}$$

where $H^{(n)}$ is a homogeneous polynomial of degree n. We first transform variables from $(x_j, \dot{x}_j)$ to (ξ_j, η_j) by a near-identity canonical transformation based on the generating function $x_1\eta_1 + x_2\eta_2 + W^{(4)}(x_i, \eta_i)$;

$$\xi_j = x_j + \frac{\partial W^{(4)}}{\partial \eta_j}, \quad \dot{x}_j = \eta_j + \frac{\partial W^{(4)}}{\partial x_j}, \quad j = 1, 2. \tag{14}$$

Substituting (14) into (13) we find, neglecting terms of 0(6).

$$H^{(2)}(x_j, \dot{x}_j) = \frac{1}{2}\sum_{j=1}^{2} x_j^2 + \dot{x}_j^2$$

$$= \frac{1}{2}\sum_{j=1}^{2} \xi_j^2 + \eta_j^2 + DW^{(4)}(\xi_j, \eta_j) \tag{15}$$

where

$$D \equiv \sum_{j=1}^{2} \eta_j \frac{\partial}{\partial \xi_j} - \xi_j \frac{\partial}{\partial \eta_j} \tag{16}$$

and

$$H^{(4)}(x_j, \dot{x}_j) = H^{(4)}(\xi_j, \eta_j). \tag{17}$$

Note that the replacement of x_j by ξ_j in the argument of $W^{(4)}$ is valid to 0(6).

Before judiciously selecting $W^{(4)}$, we perform a second canonical transformation which will simplify the operator D. We transform from (ξ_j, η_j) to (q_j, p_j):

$$\xi_j = (q_j + ip_j)/\sqrt{2}, \quad \eta_j = (iq_j + p_j)/\sqrt{2} \tag{18}$$

where $i = \sqrt{-1}$. The transformed Hamiltonian $K(q_j, p_j)$ becomes

$$K(q_j, p_j) = K^{(2)}(q_j, p_j) + EW^{(4)}(q_j, p_j) + K^{(4)}(q_j, p_j) \tag{19}$$

where

$$K^{(2)}(q_j, p_j) = H^{(2)}(\xi_j, \eta_j) = i\sum_{j=1}^{2} p_j q_j$$

$$EW^{(4)}(q_j, p_j) = DW^{(4)}(\xi_j, \eta_j)$$

$$= i\sum_{j=1}^{2}\left(q_j \frac{\partial}{\partial q_j} - p_j \frac{\partial}{\partial p_j}\right)$$

and where $K^{(4)}(q_j, p_j)$ is $H^{(4)}(\xi_j, \eta_j)$ transformed to q, p variables.

We now choose $W^{(4)}$ so that the transformed Hamiltonia K has a simple form which will yield a first integral. A typical term of $W^{(4)}$ is $C_{\alpha\beta\gamma\delta} q_1^\alpha q_2^\beta p_1^\gamma p_2^\delta$, where $\alpha + \beta + \gamma + \delta = 4$. It will be more convenient to work with $W^{(4)}$ as a column vector, which we may do in view of the isomorphism between the space of homogeneous polynomials ofsdegree four and R^{35}, see Table 1.

From equation (19) we would like to choose $W^{(4)}$ so that

$$EW^{(4)} = -K^{(4)}. \tag{20}$$

Here E is a 35×35 *diagonal* matrix with typical diagonal term $i(\alpha + \beta - \gamma - \delta)$, $W^{(4)}$ is a 35-column vector whose elements are to be determined, and $K^{(4)}$ is a 35-column vector with known elements.

It if were possible to choose $W^{(4)}$ to satisfy equation (20) then equation (19) would be immediately integrable. However, the matrix E is singular. There are nine diagonal terms of E which vanish. They correspond to the following values of $\alpha, \beta, \gamma, \delta$:

Table 1 Isomorphism between the space of homogeneous polynomials of degree four and R^{35}. A basis vector in the former space may be written $q_1^{\alpha}q_2^{\beta}p_1^{\gamma}p_2^{\delta}$ where $\alpha + \beta + \gamma + \delta = 4$, and is represented in the table by $(\alpha\beta\gamma\delta)$. The corresponding basis vector in R^{35} is $\bar{e}_n = (0, 0, \ldots, 0, 1, 0, \ldots, 0)$, in which the nth element is unity and all others are zero. $\bar{e}_n$ is represented in the table simply by n.

n	$(\alpha\beta\gamma\delta)$	n	$(\alpha\beta\gamma\delta)$	n	$(\alpha\beta\gamma\delta)$
1	(0004)	13	(0301)	25	(1300)
2	(0013)	14	(0310)	26	(2002)
3	(0022)	15	(0400)	27	(2011)
4	(0031)	16	(1003)	28	(2020)
5	(0040)	17	(1012)	29	(2101)
6	(0103)	18	(1021)	30	(2110)
7	(0112)	19	(1030)	31	(2200)
8	(0121)	20	(1102)	32	(3001)
9	(0130)	21	(1111)	33	(3010)
10	(0202)	22	(1120)	34	(3100)
11	(0211)	23	(1201)	35	(4000)
12	(0220)	24	(1210)		

$$(\alpha\beta\gamma\delta) = (0202),\ (0211),\ (0220),\ (1102),\ (1111),\ (1120),\ (2002),\ (2011),\ (2020). \tag{21}$$

Thus equation (20) has no solution for a general $K^{(4)}$.

Nevertheless we may choose $W^{(4)}$ to simplify the transformed Hamiltonian K, equation (19), as much as possible. We proceed as follows:

Since E is a diagonal matrix, its null space and range are complementary spaces. Let P be a projection operator onto the range of E and let Q be a projection operator onto the null space of E. Then we may write

$$K^{(4)} = PK^{(4)} + QK^{(4)}. \tag{22}$$

Now instead of equation (20) we may choose $W^{(4)}$ so that

$$EW^{(4)} = -PK^{(4)}. \tag{23}$$

The general solution to equation (23) is not unique, since any vector in the null space of E may be appended to a given solution. However if we require $W^{(4)}$ to lie in the range of E then a unique solution emerges. (The transformation which maps the right-hand side of equation (23) into $W^{(4)}$ is called the *pseudo-inverse* of E, [25]). It is to be noted that any first integral which is independent of the Hamiltonian H is never unique since, e.g., functional combinations of H and itself may be added to it. The nonuniqueness of $W^{(4)}$ reflects this fact.

If $W^{(4)}$ is chosen so as to satisfy equation (23), then equation (19) becomes

$$K = K^{(2)} + QK^{(4)}. \tag{24}$$

By direct computation for system S we obtain the following expression for the projection of $K^{(4)}$ onto the null space of E (i.e., the space spanned by the basis vectors of equation (21)),

$$QK^{(4)} = c_1q_2^2p_2^2 + c_2q_2^2p_1p_2 + c_3q_2^2p_1^2 + c_4q_1q_2p_2^2 + c_5q_1q_2p_1p_2 + c_6q_1q_2p_1^2 + c_7q_1^2p_2^2 + c_8q_1^2p_1p_2 + c_9q_1^2p_1^2 \tag{25}$$

where

$$c_1 = c_9 = -3(k+1)/8$$

$$c_2 = c_4 = c_6 = c_8 = 3/4$$

$$c_3 = c_7 = -3/8$$

$$c_5 = -1/2.$$

To determine a first integral corresponding to the approximate Hamiltonian K, we note that

$$EK^{(2)} = 0 \tag{26}$$

and therefore, using equation (24),

$$EK = EK^{(2)} + EQK^{(4)} = 0. \tag{27}$$

Next we note that

$$\dot{K}^{(2)}(q_j, p_j) = i\sum_{j=1}^{2}(\dot{p}_jq_j + p_j\dot{q}_j) = i\sum_{j=1}^{2}\left(-\frac{\partial K}{\partial q_j}q_j + \frac{\partial K}{\partial p_j}p_j\right) = -EK. \tag{28}$$

From equations (27) and (28) we see that $\dot{K}^{(2)} = 0$ and therefore $K^{(2)}$ = constant is a first integral. Moreover, since K = constant is also a first integral, we may with greater convenience choose the difference $K - K^{(2)} = QK^{(4)}$ = constant as a first integral corresponding to the system based on the approximate Hamiltonian K. As far as the original system S is concerned, $QK^{(4)}$ = constant is an approximate first integral valid when terms of 0(6) are neglected.

Using the inverse of the canonical transformation (18) and again neglecting terms of 0(6), we may transform the expression (25) for $QK^{(4)}$ back to the original variables. In this way we find the approximate first integral to be

$$f(x, y, \dot{x}, \dot{y}) = (1+k)[(x^2+\dot{x}^2)^2 + (y^2+\dot{y}^2)^2] + 4(x^2+\dot{x}^2)(y^2+\dot{y}^2) - 4(x^2+\dot{x}^2+y^2+\dot{y}^2)(xy+\dot{x}\dot{y}) + 2(x^2-\dot{x}^2)(y^2-\dot{y}^2) + 8xy\dot{x}\dot{y} = c. \tag{29}$$

A simple computation shows that $df/dt = 0$ if terms of 0(6) are neglected.

As a check, we note that system S is integrable when $k = 0$. Setting $u = (1/\sqrt{2})(x+y)$ and $v = (1/\sqrt{2})(-x+y)$ uncouples the two equations of motion (1) in this case. It turns out that for $k = 0$

$$F(x, y, \dot{x}, \dot{y}) = x^2 + \dot{x}^2 + y^2 + \dot{y}^2 - 2(xy + \dot{x}\dot{y}) + (x-y)^4 = \text{constant} \tag{30}$$

is an *exact* first integral independent of the energy integral (3). If we set $k = 0$ in our approximate first integral (29), we find that

$$f = F^2 + 0(6) \tag{31}$$

which confirms that f is a first integral to 0(6).

Note that we did not have to find $W^{(4)}$ in order to obtain the approximate first integral (29). This situation usually occurs only for the low-order 1:1 or 3:1 resonance cases, i.e., for systems in which the linearized normal modal frequencies are in the ratio 1:1 or 3:1. (System S has a 1:1 resonance.) In all other cases the B-G method proceeds in a slightly different manner. There follows a brief outline of the B-G procedure for such cases.

In systems without 1:1 or 3:1 resonances, the transformed Hamiltonian K of equation (19) has been shown by Birkhoff [3] to be a function only of the product terms $\pi_1 = p_1q_1$ and $\pi_2 = p_2q_2$. This result implies that π_1 and π_2 are two independent first integrals, since

$$\dot{p}_j = -\frac{\partial K}{\partial q_j} = -p_j\frac{\partial K}{\partial \pi_j} \tag{32}$$

and

$$\dot{q}_j = \frac{\partial K}{\partial p_j} = q_j\frac{\partial K}{\partial \pi_j} \tag{33}$$

and therefore

$$\dot{\pi}_j = \dot{p}_jq_j + p_j\dot{q}_j = 0. \tag{34}$$

Thus, for such systems π_1 and π_2 are chosen as the two independent first integrals. They represent the energies in each of the approximately uncoupled oscillators. In this case, however, $W^{(4)}(\xi_j, \eta_j)$ is needed in order to transform back to the original variables x_j, $\dot{x}_j$ to

0(6). We note that since $\dot{K}^{(2)} = 0$, we could again choose $QK^{(4)} = K - K^{(2)}$ as an approximate first integral to 0(6). Here, however $QK^{(4)}$ could be zero, whereas it is generally not zero in the 1:1 and 3:1 resonance cases.

Application

In this section we will use the approximate first integral (29) to obtain an approximate Poincaré map (valid for small energies h) for the system S.

To generate the Poincaré map, set $x = 0$ in equations (2) and (3) and solve for $\dot{x}(y, \dot{y}, h)$:

$$\dot{x} = \left[2h - y^2 - \left(\frac{k+1}{2}\right)y^4 - \dot{y}^2\right]^{1/2} > 0. \tag{35}$$

Then set $x = 0$ in equation (29) to obtain

$$\begin{aligned}\tilde{f}(y, \dot{y}) &= (1+k)[\dot{x}^4 + (y^2 + \dot{y}^2)^2] + 2\dot{x}^2(y^2 + 3\dot{y}^2) \\ &\quad -4\dot{x}\dot{y}(\dot{x}^2 + y^2 + \dot{y}^2) \\ &= c\end{aligned} \tag{36}$$

in which $\dot{x} = \dot{x}(y, \dot{y}, h)$ is given by equation (35). For fixed h, k, equation (36) represents a one-parameter family of invariant curves with c as parameter. These curves fill the interior of the region of the $y - \dot{y}$-plane bounded by the curve

$$y^2 + \left(\frac{k+1}{2}\right)y^4 + \dot{y}^2 = 2h \tag{37}$$

obtained by setting $\dot{x} = 0$ in equation (35).

NNM's appear as fixed points of the Poincaré map which lie on the $\dot{y}$-axis ($y = 0$). This follows from the requirement that a NNM pass through the origin ($x = 0, y = 0$). At any fixed point, the level curves $\tilde{f}(y, \dot{y}) = c$ possess a singularity. Thus, for a NNM, we require

$$\frac{\partial \tilde{f}}{\partial y}(0, \dot{y}) = 0, \quad \frac{\partial \tilde{f}}{\partial \dot{y}}(0, \dot{y}) = 0 \tag{38}$$

From equations (35) and (36) we see that $\tilde{f}(y, \dot{y}) = \tilde{f}(-y, \dot{y})$ so that the first condition of (38) is satisfied identically. The second condition of (38) gives, after some algebra,

$$\dot{y} = \pm\sqrt{h}, \quad \dot{y}^2 = h\left(1 \pm \frac{\sqrt{k(k-4)}}{|k-2|}\right). \tag{39}$$

These values of $\dot{y}$, together with the condition $y = 0$, give the position on the Poincaré map of all the NNM's which occur in system S. The in-phase mode $y = x$ corresponds to $\dot{y} = \sqrt{h}$, the out-of-phase mode $y = -x$ corresponds to $\dot{y} = -\sqrt{h}$, and the bifurcating modes of equation (4) correspond to the last two values of $\dot{y}$ in equation (39). This analysis proves that system S possesses no other NNM's than the SNM's referred to in equation (4) (subject to the assumption that h is small.)

In order to investigate the stability of these NNM's, we will examine the nature of the invariant curves of the Poincaré map in the neighborhood of the corresponding singular points.

First we move the origin to the fixed points by substituting

$$w = \dot{y} - \dot{y}_0 \tag{40}$$

in the expression for $\tilde{f}$, equation (36), where $\dot{y}_0$ is one of the NNM values of equation (39). Then we expand $\tilde{f}$ in a Taylor series about $y = 0$, $w = 0$, and neglect cubic and higher-order terms.

For the out-of-phase mode $y = -x$ this procedure gives

$$(k-4)w^2 - y^2 = \frac{c - c_0}{8h} \tag{41}$$

where $c_0 = 2h^2(k+8)$ is the value of c at the fixed point. For $k < 4$, equation (41) is a family of ellipses while for $k > 4$ it is a family of hyperbolas. Thus the out-of-phase mode is stable for $k < 4$ and unstable for $k > 4$, a result which is in agreement with the Floquet theory approach, cf. Fig. 4.

For the in-phase mode $y = x$, however, the same procedure gives

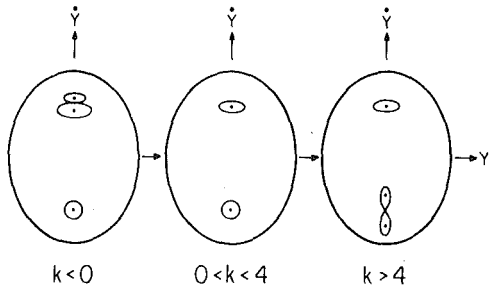

Fig. 9 Sketches of the Poincaré map for system S for different ranges of the bifurcation parameter k; the upper (lower) fixed points correspond to the in-phase (out-of-phase) mode and to the modes which bifurcate from it

$$kw^2 = \frac{c - c_0}{8h} \tag{42}$$

where now $c_0 = 2h^2k$. Thus the invariant curves in the neighborhood of the fixed point appear to be parallel lines and therefore equation (42) fails to predict stability. This result agrees with Floquet theory which also failed to predict stability for this mode.

In the case of the Poincaré map, however, we may consider the effect of nonlinear perturbations about the periodic motion in the following manner. As noted previously, equations (35) and (36) show that $\tilde{f}(y, \dot{y})$ is an even function of y. We therefore set

$$z = y^2 \tag{43}$$

and substitute (40) and (43) into (35) and (36). Expanding $\tilde{f}$ in a Taylor series about $z = 0$, $w = 0$ and neglecting higher-order terms, we obtain

$$8hkw^2 + 8\sqrt{h}kwz + [2k + 1 - hk(1+k)]z^2 = c - c_0 \tag{44}$$

The nature of this conic section depends upon the sign of the discriminant of (44) which equals

$$-32hk + O(h^2) \tag{45}$$

To $O(h^2)$, when $k < 0$ the discriminant is positive, the conics (44) are hyperbolas and the singularity in $w - z$ coordinates is a saddle. The two separatrices of this saddle for $z \geqslant 0$ map into two separatrices in $w - y$ coordinates and hence in $w - y$ coordinates the singularity is a (nonlinear) saddle. For $k > 0$ the discriminant is negative and the conics (44) in $w - z$ coordinates are ellipses. In $w - y$ coordinates this singularity becomes a (nonlinear) center. Therefore the Poincaré map predicts that the in-phase mode is unstable for $k < 0$ and stable for $k > 0$.

The stability of the bifurcating NNM's may be investigated in a similar fashion. Sketches of the Poincaré map for various values of k are given in Fig. 9.

Conclusion

We have investigated the dynamical structure of a pair of nonlinear coupled oscillators S by generating an approximation for the Poincaré map via the B-G canonical transformation. In particular we investigated the existence and stability of NNM's and found that the system S admits only 2 or 4 NNM's, depending upon the value of the parameter k. The bifurcating modes enter as stable while the mode from which they bifurcated changes from stable to unstable upon bifurcation.

It is to be noted that all these results are valid only for small h. This is not only because the B-G method is a perturbation method valid for small h, but also because KAM (Kolmogorov-Arnold-Moser) theory tells us that the invariant tori generally do not fill the energy manifold $H = h$ in systems which are not integrable [17, 1]. The set of motions which lie on invariant tori typically have decreasing measure as h is increased. For large enough h the Poincaré map (ob-

tainable by numerical integration) loses all semblance of order and appears to be filled with "noise," i.e., with motions which seem to be ergodic.

It is also to be noted that although we used the B-G method to generate the approximate Poincaré map, it could have been obtained by other equivalent methods. We mention Whittaker's adelphic integral [27] and the method of Lie transforms [11] and refer the reader to [15] where all three methods are compared and are shown to be equivalent to lowest-order terms.

Finally, we note that for negative k system S admits additional equilibrium points besides the origin $x = y = 0$ [15]. In order that the energy manifold $H = h$ be compact (i.e., closed and bounded) for negative k, it is necessary to restrict the energy h to be smaller than a limiting value dependent on k. If the energy manifold is not compact, the bounding curve for the Poincaré map will generally possess branches which reach to infinity. In such a case the system S will not be physically realistic.

Acknowledgment

The authors wish to thank Don Lewis for helpful discussions.

References

1 Arnold, V. I., *Mathematical Methods of Classical Mechanics,* Springer, 1978.

2 Arnold, V. I., and Avez, A., *Ergodic Problems of Classical Mechanics,* Benjamin, 1968.

3 Birkhoff, G. D., *Dynamical Systems,* AMS Colloquium 9, 1927.

4 Cesari, L., *Asymptotic Behavior and Stability Problems in Ordinary Differential Equations,* 3rd ed., Springer, 1971.

5 Chillingworth, D. R. J., *Differential Topology With a View to Applications,* Pitman, 1976.

6 Greenberg, M. D., *Foundations of Applied Mathematics,* Prentice Hall, 1978.

7 Gustavson, F. G., "On Constructing Formal Integrals of a Hamiltonian System Near an Equilibrium Point," *Astronomical Journal,* Vol. 71, 1963, pp. 670–686.

8 Hartman, P., *Ordinary Differential Equations,* Wiley, 1964.

9 Hirsch, M. W., and Smale, S., *Differential Equations, Dynamical Systems and Linear Algebra,* Academic Press, 1974.

10 Johnson, T. L., and Rand, R. H., "On the Existence and Bifurcation of Minimal Normal Modes," *International Journal of Non-Linear Mechanics,* Vol. 14, 1979, pp. 1–12.

11 Kamel, A. A., "Perturbation Theory Based on Lie Transforms," NASA Contractor Report 1622, 1970.

12 Kauderer, H., *Nichtlineare Mechanik,* Springer, 1958.

13 Lefschetz, S., *Differential Equations: Geometric Theory,* 2nd ed., Dover, 1977.

14 Minorsky, N., *Nonlinear Oscillations,* Van Nostrand, 1962.

15 Month, L. A., "On Approximate First Integrals of Hamiltonian Systems With an Application to Nonlinear Normal Modes in a Two-Degree-of-Freedom Nonlinear Oscillator," PhD Thesis, Cornell University, 1979.

16 Month, L. A., and Rand, R. H., "The Stability of Bifurcating Periodic Solutions in a Two-Degree-of-Freedom Nonlinear System," ASME JOURNAL OF APPLIED MECHANICS, Vol. 44, 1977, pp. 782–784.

17 Moser, J., "Stable and Random Motions in Dynamical Systems," *Annals of Mathematical Studies,* Vol. 77, Princeton University Press, 1973.

18 Pak, C. H., and Rosenberg, R. M., "On the Existence of Normal Mode Vibrations in Nonlinear Systems," *Quarterly of Applied Mathematics,* Vol. 26, 1968, pp. 403–416.

19 Pecelli, G., and Thomas, E. S., "Normal Modes, Uncoupling, and Stability for a Class of Nonlinear Oscillators," SUNY Albany Report No. 461, 1978.

20 Poincaré, H., "New Methods of Celestial Mechanics," Vol. 3, NASA Technical Translation TT F-452, 1967.

21 Rand, R. H., "On the Stability of Hill's Equation With Four Independent Parameters," ASME JOURNAL OF APPLIED MECHANICS, Vol. 36, 1969, pp. 885–886.

22 Rand, R. H., and Tseng, S. F., "On the Stability of a Differential Equation With Application to the Vibrations of a Particle in the Plane," ASME JOURNAL OF APPLIED MECHANICS, Vol. 36, 1969, pp. 311–313.

23 Rand, R., and Vito, R., "Nonlinear Vibrations of Two-Degree-of-Freedom Systems With Repeated Linarized Natural Frequencies," ASME JOURNAL OF APPLIED MECHANICS, Vol. 39, 1972, pp. 296–297.

24 Rosenberg, R. M., "On Nonlinear Vibrations of Systems With Many Degrees of Freedom," *Advances in Applied Mechanics,* Academic Press, 1966, pp. 155–242.

25 Stackgold, I., "Branching of Solutions of Nonlinear Equations," *SIAM Review,* Vol. 13, 1971, pp. 289–332.

26 Stoker, J. J., *Nonlinear Vibrations,* Interscience, 1950.

27 Whittaker, E. T., *A Treatise on the Analytical Dynamics of Particles and Rigid Bodies,* 4th ed., Cambridge University Press, 1937.

28 Yang, T. L., and Rosenberg, R. M., "On the Vibrations of a Particle in the Plane," *International Journal of Nonlinear Mechanics,* Vol. 2, 1967, pp. 1–25.

Journal of Applied Mechanics

Design Data and Methods

Natural Frequencies of Mindlin Circular Plates

T. Irie,[1] G. Yamada,[2] and S. Aomura[3]

The natural frequencies of vibration based upon the Mindlin plate theory are tabulated for uniform circular plates with free, simply supported, and clamped edges for the first several tens modes.

The natural frequencies of uniform thin circular plates of a homogeneous isotropic material are usually calculated by the classical plate theory, in which the rotatory inertia and shear deformation are not considered. Leissa [1] have presented the numerical values in his monograph and, recently, Itao and Crandall [2] have also presented the values for the first 701 modes of vibration of circular plates with free edges. However, the numerical values obtained by the classical theory cannot present accurate values for the higher modes' vibration. For obtaining more accurate values, one should calculate numerically on the basis of the Mindlin plate theory in which both of the rotatory inertia and shear deformation of plate are taken into consideration.

The design data present the natural frequencies (the dimensionless frequency parameters) of uniform Mindlin circular plates with several plate thickness under free, simply supported, and clamped edge conditions up to the higher modes.

The equations of free vibration of a Mindlin circular plate are written as [3, 4]

$$\frac{\partial M_r}{\partial r}+\frac{1}{r}\frac{\partial M_{r\theta}}{\partial \theta}+\frac{M_r-M_\theta}{r}-Q_r+\omega^2\frac{\rho h^3}{12}\psi_r=0$$
$$\frac{\partial M_{r\theta}}{\partial r}+\frac{1}{r}\frac{\partial M_\theta}{\partial \theta}+\frac{2M_{r\theta}}{r}-Q_\theta+\omega^2\frac{\rho h^2}{12}\psi_\theta=0$$
$$\frac{\partial Q_r}{\partial r}+\frac{1}{r}\frac{\partial Q_\theta}{\partial \theta}+\frac{Q_r}{r}+\omega^2\rho h W=0 \tag{1}$$

where ρ is the mass per unit volume, h is the plate thickness, and ω is the radian frequency. The components of the moments and shearing forces are

$$M_r=D\left\{\frac{\partial \psi_r}{\partial r}+\frac{\nu}{r}\left(\psi_r+\frac{\partial \psi_\theta}{\partial \theta}\right)\right\} \tag{2}$$
$$M_\theta=D\left\{\frac{1}{r}\left(\psi_r+\frac{\partial \psi_\theta}{\partial \theta}\right)+\nu\frac{\partial \psi_r}{\partial r}\right\}$$
$$M_{r\theta}=\frac{D}{2}(1-\nu)\left\{\frac{1}{r}\left(\frac{\partial \psi_r}{\partial \theta}-\psi_\theta\right)+\frac{\partial \psi_\theta}{\partial r}\right\} \tag{2 (Cont.)}$$

and

$$Q_r=\kappa^2 Gh\left(\psi_r+\frac{\partial W}{\partial r}\right)$$
$$Q_\theta=\kappa^2 Gh\left(\psi_\theta+\frac{1}{r}\frac{\partial W}{\partial \theta}\right) \tag{3}$$

in terms of the transverse deflection W and the angular rotations ψ_r and ψ_θ of the normal to the neutral surface in radial and circumferential directions, respectively. E is Young's modulus, ν is Poisson's ratio, and D is the flexural rigidity of the plate expressed by $D = Eh^3/12(1-\nu^2)$. G is the shear modulus and $\kappa^2 = \pi^2/12$ is the shear coefficient. The appropriate solutions of (1)–(3) have been obtained for the deflection and rotations by Mindlin and Deresiewicz [3, 4] as follows:

$$\psi_r=(\sigma_1-1)\frac{\partial w_1}{\partial r}+(\sigma_2-1)\frac{\partial w_2}{\partial r}+\frac{1}{r}\frac{\partial w_3}{\partial \theta}$$
$$\psi_\theta=(\sigma_1-1)\frac{1}{r}\frac{\partial w_1}{\partial \theta}+(\sigma_2-1)\frac{1}{r}\frac{\partial w_2}{\partial \theta}-\frac{\partial w_3}{\partial r}$$
$$W=w_1+w_2 \tag{4}$$

using the functions

$$w_1=A_1 J_n\left(\delta_1\frac{r}{a}\right)\quad\cos\quad n\theta$$
$$w_2=A_2 J_n\left(\delta_2\frac{r}{a}\right)\quad\cos\quad n\theta$$
$$w_3=A_3 J_n\left(\delta_3\frac{r}{a}\right)\quad\sin\quad n\theta \tag{5}$$

where A_i are arbitrary constants and $J_n(x)$ expresses Bessel function of the first kind. For simplicity of the analysis, the following dimensionless parameters have been introduced:

$$\delta_1^2,\ \delta_2^2=\frac{1}{2}\lambda^4[R+S\pm\{(R-S)^2+4\lambda^{-4}\}^{1/2}]$$
$$\delta_3^2=2(R\lambda^4-S^{-1})/(1-\nu)$$
$$\sigma_1,\ \sigma_2=(\delta_2^2,\ \delta_1^2)\,(R\lambda^4-S^{-1})^{-1}$$
$$R=(h/a)^2/12,\quad S=D/\kappa^2 Ga^2h=\{2/\pi^2(1-\nu)\}(h/a)^2 \tag{6}$$

[1] Professor of Mechanical Engineering, Faculty of Engineering, Hokkaido University, North-13, West-8, Sapporo 060, Japan.

[2] Associate Professor of Mechanical Engineering, Faculty of Engineering, Hokkaido University, North-13, West-8, Sapporo 060, Japan.

[3] Graduate Student, Faculty of Engineering, Hokkaido University, North-13, West-8, Sapporo 060, Japan.

Mansucript received by ASME Applied Mechanics Division, December, 1979; final revision, March, 1980.

Table 1 Frequency parameters $\lambda_{ns}{}^2$ of uniform Mindlin circular plates with free edge; $\nu = 0.3$

		h/a					
n	s	0	0.05	0.1	0.15	0.2	0.25
0	1	9.003	8.969	8.868	8.710	8.505	8.267
	2	38.443	37.787	36.041	33.674	31.111	28.605
	3	87.750	84.443	76.676	67.827	59.645	52.584
	4	156.818	146.758	126.274	106.397	90.059	76.936
1	1	20.475	20.260	19.711	18.917	17.978	16.979
	2	59.812	58.215	54.257	49.341	44.434	39.948
	3	118.957	112.984	99.935	86.235	74.331	64.462
	4	197.872	182.271	152.750	126.047	105.033	88.312
2	0	5.358	5.330	5.278	5.205	5.114	5.008
	1	35.260	34.598	33.033	30.942	28.668	26.427
	2	84.366	81.185	73.875	65.510	57.722	50.956
	3	153.306	143.557	123.771	104.471	88.530	75.651
3	0	12.439	12.311	12.064	11.722	11.314	10.866
	1	53.008	51.537	48.227	44.116	39.960	36.110
	2	111.945	106.405	94.531	81.930	70.862	61.613
	3	190.692	175.921	147.991	122.486	102.270	86.155
4	0	21.835	21.492	20.801	19.871	18.816	17.724
	1	73.543	70.799	64.891	58.043	51.545	45.819
	2	142.431	133.628	115.957	98.446	83.801	71.918
	3	231.031	209.863	172.453	140.255	115.568	96.464
5	0	33.495	32.766	31.270	29.334	27.255	25.221
	1	96.755	92.172	82.722	72.464	63.253	55.458
	2	175.735	162.643	137.951	114.962	96.513	81.864
	3	274.252	245.198	197.055	157.766	128.421	102.979
6	0	47.378	46.031	43.255	39.831	36.351	33.113
	1	122.570	115.473	101.480	87.201	74.982	64.981
	2	211.789	193.265	160.361	131.416	108.984	91.436
	3	320.299	281.762	221.721	175.011	140.806	112.962

As a frequency parameter

$$\lambda^4 = \rho h a^4 \omega^2 / D \tag{7}$$

is adopted here.

The boundary conditions at the edge $r = a$ are written as

$$\begin{aligned} &M_r = M_{r\theta} = Q_r = 0 && \text{for a free edge} \\ &M_r = M_{r\theta} = W = 0 && \text{for a simply supported edge} \\ &\psi_r = \psi_\theta = W = 0 && \text{for a clamped edge} \end{aligned} \tag{8}$$

By eliminating the coefficients A_i of (5) from the equation which is obtained by substituting (2)–(5) into the boundary conditions (8), one can obtain the frequency equation

$$\begin{vmatrix} C_{11} & C_{12} & C_{13} \\ C_{21} & C_{22} & C_{23} \\ C_{31} & C_{32} & C_{33} \end{vmatrix} = 0 \tag{9}$$

Elements of the determinant of (9) are

$$\begin{aligned} C_{1i} &= (\sigma_i - 1)\{J_n''(\delta_i) + \nu J_m'(\delta_i) - \nu n^2 J_n(\delta_i)\} \\ C_{2i} &= -2n(\sigma_i - 1)\{J_n'(\delta_i) - J_n(\delta_i)\} \\ C_{3i} &= \sigma_i J_n'(\delta_i) \\ C_{13} &= n(1-\nu)\{J_n'(\delta_3) - J_n(\delta_3)\} \\ C_{23} &= -\{J_n''(\delta_3) - J_n'(\delta_3) + n^2 J_n(\delta_3)\} \\ C_{33} &= n J_n(\delta_3) \end{aligned} \tag{10}$$

for a circular plate with free edge,

$$\begin{aligned} C_{1i} &= (\sigma_i - 1)\{J_n''(\delta_i) + \nu J_n'(\delta_i) - \nu n^2 J_n(\delta_i)\} \\ C_{2i} &= -2n(\sigma_i - 1)\{J_n'(\delta_i) - J_n(\delta_i)\} \\ C_{3i} &= J_n(\delta_i) \\ C_{13} &= n(1-\nu)\{J_n'(\delta_3) - J_n(\delta_3)\} \\ C_{23} &= -\{J_n''(\delta_3) - J_n'(\delta_3) + n^2 J_n(\delta_3)\} \\ C_{33} &= 0 \end{aligned} \tag{11}$$

Table 2 Frequency parameters λ_{ns}^2 of uniform Mindlin circular plates with simply supported edge; $\nu = 0.3$

		h/a					
n	s	0	0.05	0.1	0.15	0.2	0.25
0	0	4.935	4.925	4.894	4.844	4.777	4.696
	1	29.720	29.323	28.240	26.715	24.994	23.254
	2	74.156	71.756	65.942	59.062	52.514	46.775
	3	138.318	130.349	113.574	96.775	82.766	71.603
1	0	13.898	13.784	13.510	13.109	12.620	12.080
	1	48.479	47.411	44.691	41.174	37.537	34.127
	2	102.773	98.238	87.994	76.847	66.946	58.701
	3	176.801	164.109	139.270	116.170	97.873	83.782
2	0	25.613	25.215	24.313	23.079	21.687	20.270
	1	70.117	67.875	62.552	56.212	50.126	44.751
	2	134.298	126.681	110.658	94.501	80.950	70.104
	3	218.203	199.363	165.020	135.120	112.427	95.391
3	0	39.957	39.023	36.962	34.319	31.547	28.900
	1	94.549	90.509	81.526	71.610	62.675	55.147
	2	168.675	156.897	133.769	111.999	94.597	81.102
	3	262.485	235.948	190.767	153.683	126.530	*
4	0	56.842	55.034	51.158	46.495	41.908	37.762
	1	121.702	115.122	101.372	87.219	75.137	65.341
	2	205.851	188.707	157.198	129.327	107.940	91.772
	3	309.607	273.713	216.469	171.904	140.254	*
5	0	76.203	73.097	66.647	59.358	52.587	46.738
	1	151.518	141.537	121.898	102.941	87.491	75.354
	2	245.778	221.944	180.844	146.480	121.018	103.101
	3	359.532	312.522	242.091	189.820	153.646	*
6	0	97.995	93.072	83.214	72.724	63.462	55.757
	1	183.948	169.592	142.951	118.708	99.729	85.204
	2	288.414	256.460	204.632	163.458	133.865	112.182
	3	412.221	352.249	267.612	207.460	165.852	*

Table 3 Frequency parameters λ_{ns}^2 of uniform Mindlin circular plates with clamped edge; $\nu = 0.3$

		h/a					
n	s	0	0.05	0.1	0.15	0.2	0.25
0	0	10.216	10.145	9.941	9.629	9.240	8.807
	1	39.771	38.855	36.479	33.393	30.211	27.253
	2	89.104	84.995	75.664	65.551	56.682	49.420
	3	158.184	146.400	123.319	102.089	85.571	73.054
1	0	21.260	21.002	20.232	19.116	17.834	16.521
	1	60.829	58.827	53.890	48.002	42.409	37.550
	2	120.079	112.976	97.907	82.861	70.473	60.748
	3	199.053	181.210	148.698	120.840	100.115	84.801
2	0	34.877	34.258	32.406	29.890	27.214	24.670
	1	84.583	80.933	72.368	62.929	54.557	47.650
	2	153.815	142.684	120.551	100.008	83.937	71.715
	3	242.721	217.303	174.049	139.223	114.238	96.109
3	0	51.030	49.782	46.178	41.618	37.109	33.083
	1	111.021	105.028	91.712	78.077	66.667	57.624
	2	190.304	173.973	143.504	117.018	97.152	82.414
	3	289.180	254.556	199.359	157.302	128.023	*
4	0	69.666	67.420	61.272	54.038	47.340	41.657
	1	140.108	130.948	111.742	93.368	78.733	67.493
	2	229.519	206.693	166.686	133.899	110.161	92.895
	3	338.411	292.845	224.611	175.119	141.525	*
5	0	90.739	87.022	77.454	66.960	57.793	50.331
	1	171.803	158.532	132.309	108.747	90.747	77.264
	2	271.428	240.698	190.029	150.657	122.988	*
	3	390.390	332.051	249.791	192.703	155.783	*
6	0	114.213	108.445	94.527	80.252	68.396	59.063
	1	206.071	187.627	153.295	124.172	102.698	86.939
	2	316.002	275.853	213.483	167.294	135.650	*
	3	445.089	372.068	274.887	210.074	160.619	*

for a plate with simply supported edge, and

$$C_{1i} = (\sigma_i - 1)\, J_n'(\delta_i), \qquad C_{2i} = n(\sigma_i - 1)\, J_n(\delta_i)$$
$$C_{3i} = J_n(\delta_i), \qquad C_{13} = nJ_n(\delta_3), \qquad C_{23} = J_n'(\delta_3)$$
$$C_{33} = 0 \qquad i = 1, 2 \tag{12}$$

for a clamped plate.

Though the values of δ_1^2 are always positive in sign, the values of δ_2^2 and δ_3^2 become negative and hence δ_2 and δ_3 have imaginary values for $\lambda^4 < 1/RS$. Within this range of λ, the function $J_n(x)$ in the preceding equations should be replaced with modified Bessel function $I_n(x)$ of the first kind.

Tables 1–3 present the frequency parameters λ_{ns}^2 obtained by the Mindlin theory for uniform circular plates of Poisson's ratio $\nu = 0.3$ with several thickness ratios h/a. In the columns marked with an asterisk, many intricate frequencies appear under the influence of the rotatory inertia and shear deformation of plate. When the thickness ratio h/a tends to zero, the quantities R, S; σ_1, σ_2 are all zero, and $\delta_1 \to \lambda_1, \delta_2 \to j\lambda$ ($j = \sqrt{-1}$) and δ_3 becomes an infinite imaginary number of the order of $1/S$. In this case, (9) reduces to the determinant with 2×2 elements representing the frequency equation [1] of thin plate derived by the classical plate theory where the rotatory inertia and shear deformation are not taken into account. The eigenvalues of thin plate are also written on the left-most columns of Tables 1–3 for reference.

One can quote the natural frequencies of circular plates which given boundary conditions and dimensions from the tables.

References

1 Leissa, A. W., "Vibration of Plates," NASA SP-160, U.S. Gov't. Printing Office, 1969, pp. 7–36.

2 Itao, K., and Crandall, S. H., "Natural Modes and Natural Frequencies of Uniform, Circular, Free-Edge Plates," ASME JOURNAL OF APPLIED MECHANICS, Vol. 46, 1979, pp. 448–453.

3 Mindlin, R. D., and Deresiewicz, H., "Thickness-Shear and Flexural Vibrations of a Circular Disk," *Journal of Applied Physics*, Vol. 25, 1954, pp. 1329–1332.

4 Deresiewicz, H., and Mindlin, R. D., "Axially Symmetric Flexural Vibrations of a Circular Disk," ASME JOURNAL OF APPLIED MECHANICS, Vol. 22, 1955, pp. 86–88.

Journal of Applied Mechanics

Design Data and Methods

Effect of Blunt Chamfers on Contact Pressure Distribution and Elastic Limit

H. A. Francis[1]

The interfacial pressure profile is derived analytically, and the elastic load limit is evaluated numerically, for plane strain frictionless elastic contact between a flat surface and a symmetric trapezoidal body whose obtuse corners are replaced by tangent circular arcs. The shape of the pressure distribution depends only on plateau and arc widths. The results enable design of radiused chamfers to give peak-to-mean pressure ratios as low as 1.2 and elastic mean pressure limits up to 1.5 times the yield stress. Conversely, the pressure peak and elastic limit can be predicted for any microscopically blunt chamfer.

Introduction

In many engineering applications it is desirable to be able to control or predict the contact pressure distribution within an interface between two solid bodies. For example, interfacial pressure peaks could be beneficial in reducing fluid leakage, but detrimental in terms of wear and fretting processes. It is often necessary to insure that a pressure-dependent variable such as thermal or electrical contact conductance per unit area is reasonably uniform over the interface. Finally, subsurface regions of high deviatoric stress are associated with contact pressure peaks, and these may be undesirable with regard to plastic flow, creep, cracking, or fatigue.

For any frictionless elastic contact region on an initially plane surface, there will be a pressure singularity (infinite spike) at the contact periphery wherever the opposing surface has a sharp edge, 90° or greater [1]. At the other extreme, for the same contact region, there is always some shape of opposing surface which will give a uniform contact pressure distribution. However, the required surface geometry is, in general, difficult to machine accurately. As a practical means of avoiding contact stress concentrations, a chamfer (bevel) or a "radius" (circular segment) is usually designed to replace a 90° edge, since they are both easy to machine. Goodier and Loutzenheiser [2] derived the pressure distribution for plane strain elastic contact between a plane surface and a flat surface with radiused edges. However there has been no comparable analysis of chamfers. A survey of six common mechanical engineering handbooks yielded no guidance on the design of chamfers or radii.

It may be inferred from the elastic contact behavior of a wedge [3] that a perfectly sharp chamfer, or indeed any slope discontinuity, within an elastic contact will produce a pressure singularity. However, in practice the pressure spike will have a finite maximum because (*a*) a machined chamfer will be blunt at some small scale, and (*b*) a sufficiently sharp chamfer will effectively be blunted by local plastic flow in one or both surfaces during the first loading of the contact. Thus every real chamfer is bridged by a curved segment, whether by design or accident.

This paper presents an analytic solution for the plane strain, elastic, frictionless contact between a semi-infinite flat body and a symmetric body whose profile consists of a plateau, each end of which is connected with continuous slope to a straight chamfer by a convex circular segment. These results can be used to design a radius-chamfer profile which will give a required pressure distribution or elastic limit, or else to predict the contact mechanics of an existing chamfered part, using the circular segment to approximate the measured microscopic apex profile. Contact with a blunt wedge emerges as a special case. It should be noted that a completely analogous derivation could be carried out for the axisymmetric case (i.e., the contact of the end of a radiused and chamfered cylinder) using a method devised by Sneddon [4]. Similar efforts, using iterative numerical techniques, have been applied to the problem of predicting the contact pressure distribution for an axisymmetric roller of specified profile loaded radially against a flat surface [5–7].

Derivation

Consider a plane strain frictionless contact between two elastic bodies which can be approximated as half spaces. The z-axis is normal to the interface, and all displacement is in the xz-plane ($\epsilon_{yy} = 0$). Let the contact region be $-a < x < +a$, and let $\xi = x/a$. Let $w(x)$ be the overlap of the undeformed surfaces ($\partial w/\partial y = 0$), and define the dimensionless shape function $\Phi(\xi) = [w(\xi) - w(1)]/h$, where $h = w(0) - w(1)$. Muskhelishvili [8] has shown that provided the end pressures $p(-1)$ and $p(+1)$ are not infinite, the contact pressure distribution is given by

$$\frac{p(\xi)}{E^*} = \frac{h}{a}\frac{(1-\xi^2)^{1/2}}{4\pi}\int_{-1}^{+1}\frac{-\Phi'(s)ds}{(s-\xi)(1-s^2)^{1/2}} \tag{1}$$

and the mean pressure is given by

$$\frac{\bar{p}}{E^*} = \frac{1}{2}\int_{-1}^{+1}\frac{p(\xi)}{E^*}d\xi = \frac{h}{a}\frac{1}{8}\int_{-1}^{+1}\frac{-s\Phi'(s)\,ds}{(1-s^2)^{1/2}} \tag{2}$$

where $\Phi'(\xi) = d\Phi/d\xi$, $1/E^* = \frac{1}{2}[(1-\nu_1^2)/E_1 + (1-\nu_2^2)/E_2]$, and E_1, E_2, ν_1, ν_2 are the Young's moduli and Poisson's ratios of the two bodies.

Fig. 1 shows the undeformed overlap geometry $w(x)$ for the symmetric plateau-radius-chamfer contact. The two Regions I ($|x| < x_1$) constitute the flat plateau, the two Regions II ($x_1 < |x| < x_2$) are circular segments of radius R, and the two Regions III ($x_2 < |x| < a$) are straight chamfers of slope G. The surface slope is continuous at the junctions x_1, x_2. For most practical cases, the circular segment can be approximated by a parabolic segment of apex radius R; for $G < 0.20$, the errors in segment dimensions are less than 1 percent. The undeformed surface dimensions are then related by the expression

[1] The Charles Stark Draper Laboratory, Inc., 555 Technology Square, Cambridge, Mass. 02139.

Manuscript received by ASME Applied Mechanics Division, February, 1980; final revision, March, 1980.

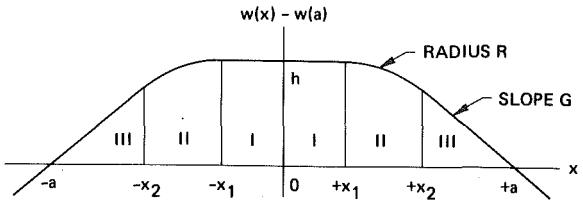

Fig. 1 Overlap profile $w(x)$ of the two undeformed surfaces; the plateau (I) and chamfer (III) are both tangent to the circular segment (II)

$x_1 - x_2 = GR$. Table 1 lists the various contact configurations which constitute special cases of the general symmetric six region geometry. Note that the contact mechanics, as described by equations (1) and (2), depends only on the shape of the overlap $w(x)$, thus one surface does not necessarily have to be flat.

The integrals in equations (1) and (2) can each be written as the sum of five definite integrals, with $\Phi'(\xi)$ taking the forms

$$\begin{aligned} &{}^{-\xi_2}_{-1}[\Phi' = C_{1'}, \quad {}^{+1}_{+\xi_2}[\Phi' = -C_{1'}, \quad {}^{+\xi_1}_{-\xi_1}[\Phi' = 0, \\ &{}^{-\xi_1}_{-\xi_2}[\Phi' = C_2(-\xi - \xi_1), \quad {}^{+\xi_2}_{+\xi_1}[\Phi' = -C_2(\xi - \xi_1), \end{aligned} \tag{3}$$

where

$$C_1 = \frac{aG}{h} = \frac{1}{1 - \frac{1}{2}(\xi_1 + \xi_2)} \tag{4}$$

$$C_2 = \frac{a^2}{Rh} = \frac{1}{(\xi_2 - \xi_1)[1 - \frac{1}{2}(\xi_1 + \xi_2)]} \tag{5}$$

Introducing the complementary variable $\eta = (1 - \xi^2)^{1/2}$, the resulting formulas are

$$\frac{p(\xi)}{E^*} = \frac{h}{a}\frac{C_2}{4\pi}\left[\xi_2 \ln\left|\frac{\eta + \eta_2}{\eta - \eta_2}\right| - \xi_1 \ln\left|\frac{\eta + \eta_1}{\eta - \eta_1}\right| + \xi \ln\left|\frac{(\xi\eta_1 + \xi_1\eta)(\xi\eta_2 - \xi_2\eta)}{(\xi\eta_1 - \xi_1\eta)(\xi\eta_2 + \xi_2\eta)}\right| + 2\eta \arcsin(\xi_2\eta_1 - \xi_1\eta_2)\right] \tag{6}$$

$$\frac{\bar{p}}{E^*} = \frac{h}{a}\frac{C_2}{8}[\xi_2\eta_2 - \xi_1\eta_1 + \arcsin(\xi_2\eta_1 - \xi_1\eta_2)] \tag{7}$$

In computing $p(\xi)$, singularities may be avoided using the following rules:

1 When $\xi = \xi_1$, set $\xi\eta_1 - \xi_1\eta = 1$ and set $\eta - \eta_1 = \xi_1$.
2 When $\xi = \xi_2$, set $\xi\eta_2 - \xi_2\eta = 1$ and set $\eta - \eta_2 = \xi_2$.
3 When $\xi = \xi_1 = 0$, all ln terms are zero.
4 When $\xi = \xi_2 = 1$, $p = 0$.

Equations (5) and (6) show that the shape of the contact pressure distribution (which is symmetric about $\xi = 0$) depends only on the two quantities $\xi_1 = x_1/a$ and $\xi_2 = x_2/a$, while the magnitude is set by ξ_1, ξ_2, and the aspect ratio $h/2a$ of the undeformed overlap of the surfaces (Fig. 1). However, it is important to note that for a given surface geometry (specified by any three of x_1, x_2, G, R), ξ_1 and ξ_2 are not constants and will decrease as the load per unit y length Q, the contact half-width a, and the ratio h/a simultaneously increase. From equations (5) and (7), Q $(= 2a\bar{p})$ can be expressed as a function of a, and the resulting equation can be solved numerically to give the value of a for a given load. Equation (4) then gives the value of h/a needed to evaluate $p(\xi)$.

Plastic flow commences in the softer body 1 when the maximum value (with respect to position) of a stress quantity denoted by Y_J reaches the value of the uniaxial yield stress Y_1 of material 1. For the von Mises yield criterion, in plane strain,

$$Y_J = [\tfrac{1}{2}(\sigma_{zz} - \sigma_{xx})^2 + \tfrac{1}{2}(\sigma_{zz} - \sigma_{yy})^2 + \tfrac{1}{2}(\sigma_{xx} - \sigma_{yy})^2 + 3\tau_{xz}{}^2]^{1/2} \tag{8}$$

$$\sigma_{yy} = \nu_1(\sigma_{zz} + \sigma_{xx}) \tag{9}$$

For each contact geometry, the stresses σ_{xx}, σ_{zz}, τ_{xz} were evaluated on a grid of subsurface points using the formulation of Bell, et al. [9], in the plane strain limit, for a 200 point piecewise linear approximation to $p(\xi)$. This provided the value of the critical yield stress $(Y_J)_{\max}$, and its location $(\pm\xi_Y, \zeta_Y)$, where $\zeta = z/a$ and z is the depth coordinate.

Results

The most convenient way to plot the results for all practical com-

Table 1 Special cases of the general symmetric plateau-arc-chamfer contact shown in Fig. 1

Surface Profile w(x)	Regions	$\xi_1 = x_1/a$	$\xi_2 = x_2/a$	Pressure Singularities
Rectangle with sharp corners	I	$\xi_1 = 1$	$\xi_2 = 1$	$\lim_{\varepsilon\to 0} p(1-\varepsilon) \propto \varepsilon^m$ $(-1/2 < m < 0)$ [1]
Wedge with sharp apex	III	$\xi_1 = 0$	$\xi_2 = 0$	$\lim_{\varepsilon\to 0} p(\pm\varepsilon) \propto -\ell n\lvert\varepsilon\rvert$ [3]
Trapezoid with sharp corners	I + III	$0 < \xi_1 = \xi_2 < 1$		$\lim_{\varepsilon\to 0} p(\xi_1 \pm \varepsilon) \propto -\ell n\lvert\varepsilon\rvert$
Parabola (Hertzian cylinder)	II	$\xi_1 = 0$	$\xi_2 = 1$	None
Rectangle with rounded corners	I + II	$0 < \xi_1 < 1$	$\xi_2 = 1$	None
Wedge with rounded apex	II + III	$\xi_1 = 0$	$0 < \xi_2 < 1$	None
Trapezoid with rounded corners	I + II + III	$0 < \xi_1 < \xi_2 < 1$		None

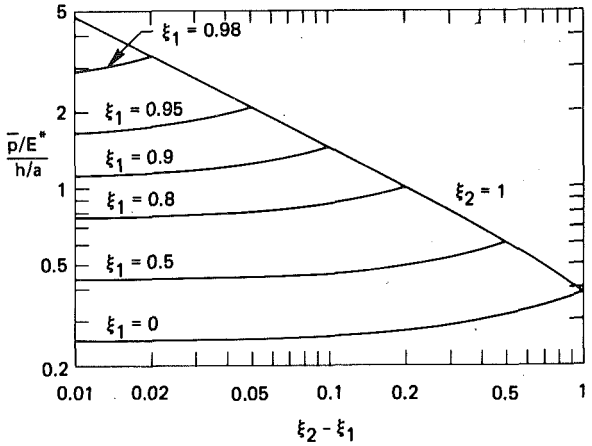

Fig. 2 Ratio of dimensionless mean contact pressure $\bar{p}/E^*$ to the overlap variable h/a, plotted against arc width $\xi_2 - \xi_1$ for various values of plateau half width ξ_1

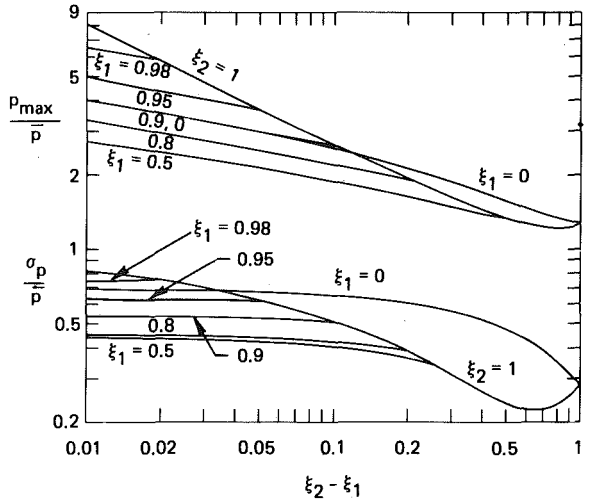

Fig. 3 Dimensionless peak value $p_{max}/\bar{p}$ and standard deviation $\sigma_p/\bar{p}$ of contact pressure, plotted against arc width $\xi_2 - \xi_1$ for various contact configurations

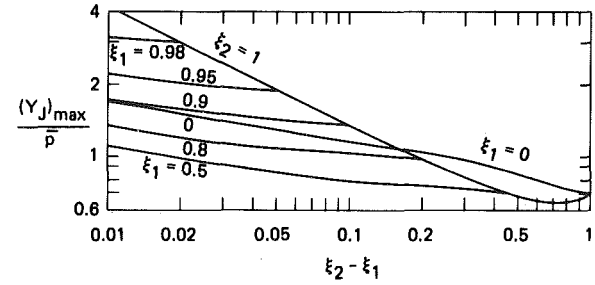

Fig. 4 Dimensionless critical yield stress $(Y_J)_{max}/\bar{p}$ plotted against arc width $\xi_2 - \xi_1$ for various surface geometries, taking $\nu_1 = 0.3$; the softer body 1 deforms elastically as long as $(Y_J)_{max} < Y_1$

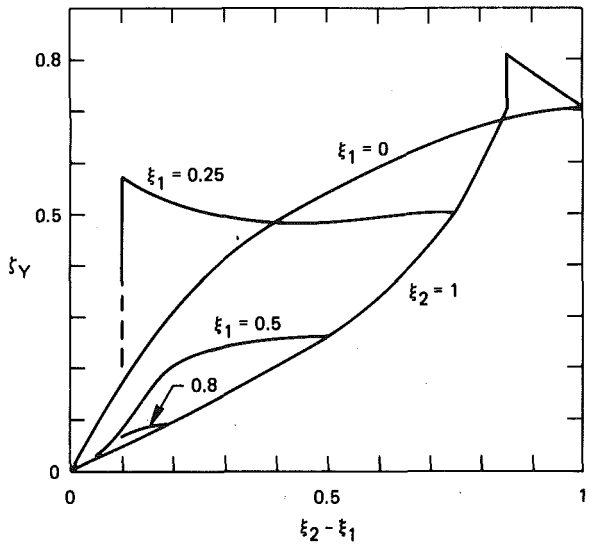

Fig. 5 Depth ζ_Y of the positions of maximum Y_J, where plastic flow initiates, plotted against arc width $\xi_2 - \xi_1$ for selected values of ξ_1

binations of ξ_1 and ξ_2 is to take as abscissa the dimensionless projected arc width $\xi_2 - \xi_1 = (x_2 - x_1)/a$, a measure of the bluntness of the chamfer. In Fig. 2, the ratio of dimensionless mean pressure $\bar{p}/E^*$ to the deformation variable h/a is plotted as a function of $\xi_2 - \xi_1$ for various cases. The plot shows that for a given h/a, $\bar{p}$ increases with plateau width $2\xi_1$, and that as arc width decreases, $\bar{p}$ approaches a constant value, except when there are no chamfers within the contact ($\xi_2 = 1$).

Two measures of the nonuniformity of the pressure distribution $p(\xi)$ are the ratios $p_{max}/\bar{p}$ and $\sigma_p/\bar{p}$, where σ_p is the standard deviation of $p(\xi)$, defined as $\sigma_p{}^2 = \int_0^1 [p(\xi) - \bar{p}]^2 d\xi$. Both quantities are plotted against $\xi_2 - \xi_1$ in Fig. 3. For $\xi_2 - \xi_1 < 0.1$, the relative pressure variation $\sigma_p/\bar{p}$ is effectively independent of $\xi_2 - \xi_1$ (excepting the curve $\xi_2 = 1$), while the relative height of the two identical pressure spikes increases with decreasing arc width according to $p_{max}/\bar{p} \propto (\xi_2 - \xi_1)^{-1/2}$ for $\xi_2 = 1$ (no chamfer) and weaker power laws for $\xi_2 < 1$. The flattest pressure profile that can be achieved with radii and/or chamfers obtains for the case $\xi_2 = 1$ and $0.2 < \xi_1 < 0.5$, i.e., no chamfers and wide arcs in contact. This optimum geometry offers a small improvement, in terms of pressure uniformity, over a plane strain Hertzian contact ($\xi_1 = 0$, $\xi_2 = 1$). A perfectly flat pressure distribution ($p_{max}/\bar{p} = 1$, $\sigma_p/\bar{p} = 0$) for plane strain contact would be given by the symmetric transcendental profile shape function [10]

$$\Phi(\xi) = 1 - \frac{1}{2 \ln 2}[(1 + \xi) \ln (1 + \xi) + (1 - \xi) \ln (1 - \xi)] \quad (-1 < \xi < +1) \quad (10)$$

for which $p/E^* = 0.567\, h/a$.

In Fig. 4, the dimensionless critical yield stress $(Y_J)_{max}/\bar{p}$ is plotted against $\xi_2 - \xi_1$, and the curves have the same general configuration as $p_{max}/\bar{p}$ in Fig. 3. The surface geometry giving the lowest pressure peaks permits loading up to $\bar{p} = 1.5 Y_1$ before plastic flow nucleates in the softer body 1. Figs. 5 and 6 show the coordinates $(\zeta_Y, \pm\xi_Y)$ of the two symmetric positions of maximum Y_J, and the location $\pm\xi_p$ of the two interfacial pressure maxima, for the various contact geometries specified by ξ_1, ξ_2. Fig. 5 shows that as the arc width $\xi_2 - \xi_1$ decreases to zero, ζ_Y also goes to zero, i.e., plastic flow nucleates nearer the interface. Fig. 6 shows that for $\xi_2 - \xi_1 < 0.8$, the lateral positions of $(Y_J)_{max}$ and p_{max} are both near the center of the arc, $\frac{1}{2}(\xi_1 + \xi_2)$. There is only one pressure peak (at $\xi_p = 0$) when $\xi_1 = 0$ (rounded wedge), and there is only one initial yield position ($\xi_Y = 0$, $\zeta_Y > 0$) when either $\xi_1 = 0$ or $\xi_2 - \xi_1 > 0.85$.

Applicability of the Results

The results presented in this paper for an infinite strip interface can be applied to finite rectangular, annular, and cylindrical contact interfaces provided the conditions of plane strain and half-space geometry are adequately satisfied. The specific geometric limits imposed by these conditions could be found only by a full three-dimensional finite-element solution for a particular pair of finite bodies in contact,

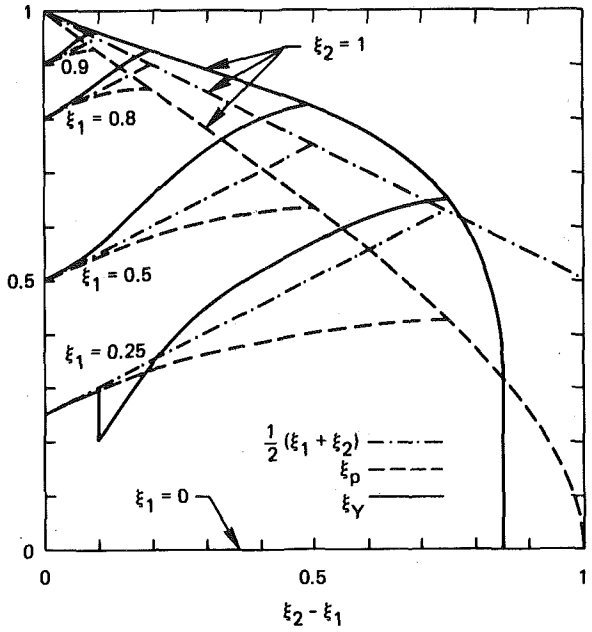

Fig. 6 Lateral coordinates of the symmetric positions of initial yield, $\pm\xi_Y$, the contact pressure peaks, $\pm\xi_p$, and the arc midpoints, $\pm\frac{1}{2}(\xi_1 + \xi_2)$, all three plotted against arc width $\xi_2 - \xi_1$ for various plateau widths $2\xi_1$

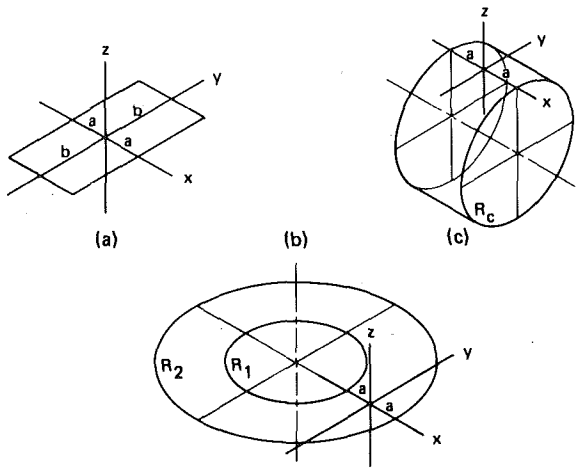

Fig. 7 Three finite interface geometries for which the infinite strip contact results are applicable: (*a*) rectangular, (*b*) annular, (*c*) cylindrical contact regions

however the general requirements can be stated semiquantitatively without analysis.

Consider first the conditions for plane strain for each of the three contact regions shown in Fig. 7, using the coordinate system defined earlier. For a rectangular contact area, Fig. 7(*a*), it is obvious that all displacement lies in the xz-plane if the y dimension of both bodies is $2b$ everywhere in the xz-plane. If one body extends beyond $y = \pm b$, then there will be pressure singularities along $y = \pm b$. In this case the deviation of the stresses and displacements from the plane strain solution will be smallest on the x-axis and will decrease as a/b decreases. For an axially symmetric annular contact, Fig. 7(*b*), the plane strain solution will be a good approximation if the contact width $2a$ is sufficiently less than the inner radius R_1. For the full cylindrical contact surface of Fig. 7(*c*) (e.g., a sleeve shrink-fitted onto a shaft), again plane strain contact will be approached in the limit $a/R_c \rightarrow 0$.

Now consider the requirement that the two bodies extend far enough from the interface in the xz-plane for the contact mechanics to be close to the half-plane solution. Suppose that for body 1 two chamfers of slope G terminate at "cliffs" $x = \pm L_x$, while body 2 is semi-infinite. As L_x/a decreases, or as G increases, the loss of the elastic material outside these free surfaces will reduce the constraint to displacement of the contact surface in body 1, thus lowering the value of the function $\overline{p}/E^*$ versus h/a. Hence *both* a/L_x and G must be sufficiently small not to alter appreciably the deformation behavior.

Conclusions

Relationships have been derived and illustrated which enable quantitative design of a symmetric, continuous-slope, plateau-radius-chamfer surface profile which, when loaded against a flat surface under conditions approximating plane strain, will give nearly any required degree of contact pressure uniformity. Conversely, the results can be used to predict the contact pressure distribution for a given blunt chamfer profile. In addition, the stress analysis results, Figs. 4–6, can be used to design the contact geometry so as to prevent plastic flow near the pressure peaks. Provided specific geometric conditions are met, the results are applicable to finite rectangular, annular, and cylindrical contact interfaces between finite bodies.

The symmetric shape of the pressure distribution (and hence the symmetric shape of the subsurface stress distribution) is determined solely by the width and position of the two curved segments within the contact interface, while the mean pressure $\overline{p}$ depends additionally on the slenderness $h/2a$ of the undeformed overlap profile. The critical yield stress $(Y_J)_{\max}$, which is the minimum value of yield stress Y_1 for which plastic flow will not occur, depends on the contact configuration in the same general manner as does the pressure peak height $p_{\max}$. By maintaining arcs wider than $0.3a$ in the contact, it is possible to keep the two pressure peaks below the value $1.5\overline{p}$, to keep the RMS pressure deviation below $0.3\overline{p}$, and to load up to $\overline{p} = 1.4Y_1$ without plastic flow. As the arc width decreases, the two pressure peaks and the two symmetric positions at which yield initiates move toward the center of each arc.

References

1 Dundurs, J., and Lee, M. S., "Stress Concentration at a Sharp Edge in Contact Problems," *Journal of Elasticity*, Vol. 2, 1972, pp. 109–112.

2 Goodier, J. N., and Loutzenheiser, C. B., "Pressure Peaks at the Ends of Plane Strain Rigid Die Contacts (Elastic)," ASME JOURNAL OF APPLIED MECHANICS, Vol. 32, 1965, pp. 462–463.

3 Sneddon, I. N., "Two-Dimensional Stress Systems," *Fourier Transforms*, McGraw-Hill, New York, 1951, pp. 436–438.

4 Sneddon, I. N., "The Relation Between Load and Penetration in the Axisymmetric Boussinesq Problem for a Punch of Arbitrary Profile," *International Journal of Engineering Science*, Vol. 3, 1965, pp. 47–56.

5 Nayak, L., and Johnson, K. L., "Pressure Between Elastic Bodies Having a Slender Area of Contact and Arbitrary Profiles," *International Journal of Mechanical Science*, Vol. 21, 1979, pp. 237–247.

6 Koshy, M., and Gohar, R., "Pressure Distribution on Radially Loaded Rollers," *Proceedings of the 18th International Machine Tool Design Research Conference*, 1977, pp. 595–604.

7 Hartnett, M. J., "The Analysis of Contact Stresses in Rolling Element Bearings," ASME *Journal of Lubrication Technology*, Vol. 101, 1979, pp. 105–109.

8 Muskhelishvili, N. I., "Boundary Problems for the Half Plane," *Some Basic Problems of the Mathematical Theory of Elasticity*, 3rd ed., Noordhoff, 1953, pp. 471–483.

9 Bell, J. C., et al., *User's Manual for FRAC3D: Supplement to Report on Stress Analysis for Structures With Surface Cracks*, NASA Report CR-159401, 1978, pp. A20–A28.

10 Timoshenko, S. P., and Goodier, J. N., "Two-Dimensional Problems in Polar Coordinates," *Theory of Elasticity*, 3rd ed., McGraw-Hill, New York, 1970, pp. 104–109.

Journal of Applied Mechanics

Brief Notes

A Brief Note is a short paper which presents a specific solution of technical interest in mechanics but which does not necessarily contain new general methods or results. A Brief Note should not exceed 1500 words *or equivalent* (a typical one-column figure or table is equivalent to 250 words; a one line equation to 30 words). Brief Notes will be subject to the usual review procedures prior to publication. After approval such Notes will be published as soon as possible. The Notes should be submitted to the Technical Editor of the JOURNAL OF APPLIED MECHANICS. Discussions on the Brief Notes should be addressed to the Editorial Department, ASME, United Engineering Center, 345 East 47th Street, New York, N. Y. 10017, or to the Technical Editor of the JOURNAL OF APPLIED MECHANICS. Discussions on Brief Notes appearing in this issue will be accepted until two months after publication. Readers who need more time to prepare a Discussion should request an extension of the deadline from the Editorial Department.

Wave Propagation in a Plate With Periodic Structure: Antiplane Strain Model

M. Dravinski[1]

Introduction

Wave motion in a periodic layered medium may be of considerable interest in problems involving nondestructive testing of composite materials [1, 2]. However, most of the analytical studies deal with waves in an infinite elastic medium [3, 4]. In this work, the wave motion in a plate of finite thickness and infinite length, with periodic structure, is considered. The main objectives of the present analysis are

1 To establish a simple, general method to determine the dispersion relations for wave in periodically layered plates.

2 To determine the influence of the basic cell upon the overall dispersion relation for the plate.

Each layer is assumed to be linearly elastic, isotropic, and homogeneous. Perfect bonding between the layers is understood. The method employed in this work is essentially due to Haskell [5], and is used frequently in geophysics and earthquake engineering.

Statement of Problem

A plate of infinite length ($|x| < \infty; 0 \le z \le z_{mn}$) consist of n identical cells. The fundamental cell is composed of m different layers. Perfect bonding is assumed between the layers and the cells; therefore, the sandwich structure consists of $n \times m$ layers of infinite extent along the y-axis. The steady-state wave motion is assumed to be of the antiplane-strain type with the displacement field specified by $u_x = u_z = 0$ and $u_y = v(x, z, \omega)$. Each layer in the unit cell is characterized by the density, ρ_j, the shear velocity, β_j, and the thickness, h_j, $j = 1, 2, \ldots, m$.

The steady-state wave motion is governed by

$$\left(\frac{\partial^2}{\partial x^2} + \frac{\partial^2}{\partial z^2} + \frac{\omega^2}{\beta^2}\right) v(x, z, \omega) = 0, \tag{1}$$

where ω represents the circular frequency and β denotes the shear wave velocity. The upper and lower faces of the plate are either stress-free, or fixed. The former case implies the following type of the nonmixed boundary conditions:

$$\sigma_{yz}(x, 0, \omega) = 0, \quad \sigma_{yz}(x, z_{mn}, \omega) = 0, \quad z_{mn} = n \sum_{j=1}^{m} h_j \tag{2}$$

Solution of Problem

For waves in the plate, the following form of displacement field $v(x, z, \omega)$ is assumed:

$$v(x, z, \omega) = \phi(z) e^{ikx}, \tag{3}$$

where k represents the wave number in the x-direction and the factor $e^{-i\omega t}$ is understood. Substituting (5) into the equation of motion (1), the displacement and stress field in the jth layer of the fundamental cell are given by

$$v_j(x,z,\omega) \equiv (a_j \cos q_j z + b_j \sin q_j z) e^{ikx}, \tag{4}$$

$$\sigma_{yz}{}^j(x, z, \omega) \equiv \mu_j q_j [-a_m \sin q_j z + b_m \cos q_j z] e^{ikx}. \tag{5}$$

with

$$q_j{}^2 = \frac{\omega^2}{\beta_j{}^2} - k^2, \quad j = 1, 2, \ldots, m. \tag{6}$$

An elastodynamic state, $\mathbf{V}_r$, is introduced [6], associated with the interface $z = z_r$: $\mathbf{V}_r{}^T \equiv [v, \sigma_{yz}]_{z = z_r \pm}$, $r = 0, 1, 2, \ldots, m \cdot n$, where superscripts $\pm$ denote that z approaches z_r from above or below, respectively. The two elastodynamic states for the rth layer are related through [5]

$$\mathbf{V}_r = \mathbf{A}_r \mathbf{V}_{r-1}, \quad r = 1, 2, \ldots, m, \cdot n, \tag{7}$$

where the matrix $\mathbf{A}_r$ is defined by

$$\mathbf{A}_r \equiv \begin{bmatrix} \cos q_r h_r & \dfrac{\sin q_r h_r}{\mu_r q_r} \\ -\mu_r q_r \sin q_r h_r & \cos q_r h_r \end{bmatrix}, \quad r = 1,2, \ldots, m \cdot n. \tag{8}$$

Similarly, the elastodynamic states at the top and bottom of the $(r-1)$th layer are related by

$$\mathbf{V}_{r-1} = \mathbf{A}_{r-1} \mathbf{V}_{r-2}, \quad r = 1, 2, \ldots, m \cdot n. \tag{9}$$

The continuity of the displacement and stress fields at each interface implies $\mathbf{V}_r{}^+ = \mathbf{V}_r{}^-$, so for the elastodynamic states $\mathbf{V}_r$ and $\mathbf{V}_{r-1}$ it follows that

[1] Research Associate, Department of Civil Engineering, University of Southern California, Los Angeles, Calif. 90007.

Manuscript received by ASME Applied Mechanics, November, 1979; final revision, March, 1980.

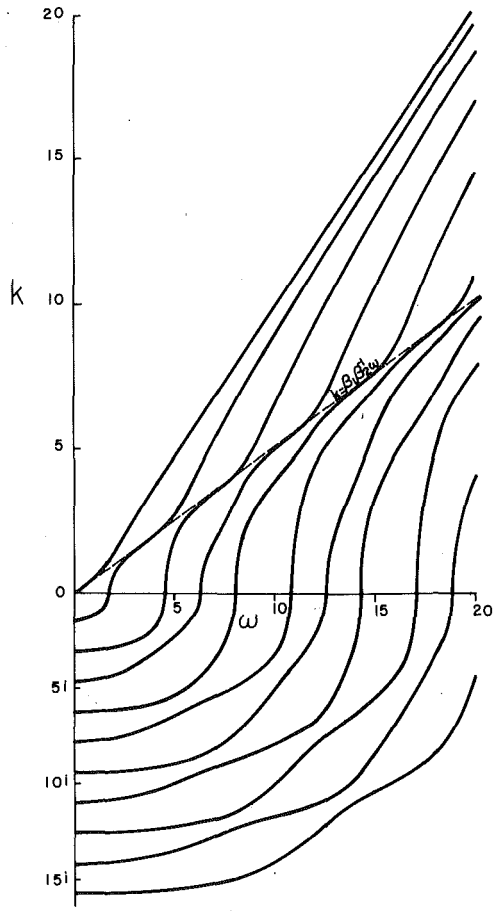

Fig. 1 Dispersion curves for stress-free boundary conditions: single two-layer cell; $\beta_1 = \rho_1 = h_1 = h_2 = 1$, $\beta_2 = \rho_2 = 2$

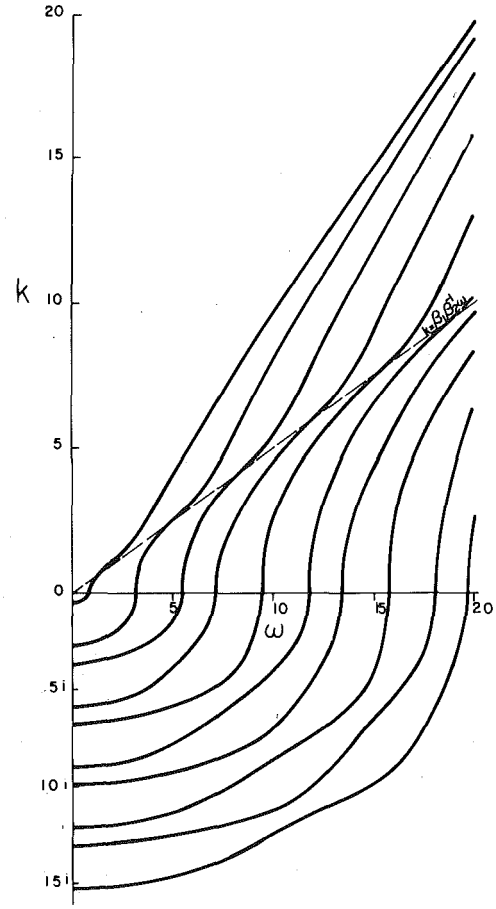

Fig. 2 Dispersion curves for stress-free boundary conditions: double two-layer cell; $\beta_1 = \rho_1 = h_1 = h_2 = 1$, $\beta_2 = \rho_2 = 2$.

$$\mathbf{V}_r = \mathbf{A}_r\mathbf{A}_{r-1}\mathbf{V}_{r-1}, \quad r = 1, 2, \ldots, m \cdot n. \tag{10}$$

The elastodynamic states at the top and the bottom of the sandwich plate are related by

$$\mathbf{V}_{m\cdot n} = \mathbf{A}_{m\cdot n}\mathbf{A}_{m\cdot n-1}\mathbf{A}_{m\cdot n-2}\ldots\mathbf{A}_{m(n-1)}\mathbf{A}_{m(n-1)-2}\ldots\mathbf{A}_{m(n-2)}\ldots \mathbf{A}_m\mathbf{A}_{m-1}\ldots\mathbf{A}_1\mathbf{V}_0 \tag{11}$$

Due to periodicity in the structure of the plate, equation (11) can be replaced by

$$\mathbf{V}_{m\cdot n} = \mathbf{A}^n\mathbf{V}_o, \quad \mathbf{A} = \mathbf{A}_m\mathbf{A}_{m-1}\mathbf{A}_{m-2}, \ldots, \mathbf{A}_1, \tag{12}$$

where $\mathbf{A}$ is a characteristics matrix of a fundamental cell. Using the boundary conditions (2), it follows from (11) that the corresponding dispersion equation is

$$\mathcal{A}_{21} = 0, \tag{13}$$

where the $\mathcal{A}_{ij}$, $i, j = 1, 2$, represents elements of the matrix $\mathcal{A}$ defined by $\mathcal{A} \equiv \mathbf{A}^n$. Using the indicial notation, the dispersion relations (13) can be expressed through

$$A_{2i}A_{ij}A_{jk}\ldots A_{rs}A_{s1} = 0, \quad i, j, \ldots, = 1, 2, \tag{14}$$

where, if not stated differently, summation over the repeated indices is understood and the left-hand side of (14) consists of n matrices $\mathbf{A}$. For example, a sandwich plate which consists of one, two, three, etc., fundamental cells, the dispersion equations that follow from (14) are

$$n = 1, A_{21} = 0 \tag{15a}$$

$$n = 2, A_{21}A_{kk} = 0 \tag{15b}$$

$$n = 3, A_{21}(A_{1r}A_{r1} + A_{22}A_{kk}) = 0 \tag{15c}$$

$$n = 4, A_{21}[A_{1r}A_{rs}A_{s1} + A_{22}(A_{1r}A_{r1} + A_{22}A_{kk})] = 0 \tag{15d}$$

$$n = 5, A_{21}\{A_{1r}A_{rs}A_{st}A_{t1} + A_{22}[A_{1r}A_{rs}A_{s1} + A_{22}(A_{1r}A_{r1} + A_{22}A_{kk})]\} = 0. \tag{15e}$$

It is evident from (15) that the dispersion relation of a fundamental cell can be factored out. Similar results follow for the fixed-fixed plate. Therefore, to find the roots (the wave numbers) of the dispersion equation for any number of cells, one evaluates first the roots for the single cell and proceeds with the roots associated with the presence of additional cells.

For a given frequency ω, there are, in general, several wave numbers k which satisfy the frequency equations (14). The wave numbers form the normal modes of propagation in the $k - \omega$ space for the model under consideration. The frequency equation (15) imply that the modes of a single cell are "preserved" in a multicell plate for nonmixed boundary conditions (2). Thus the normal modes for a plate composed of several fundamental cells consists of modes associated with a single cell and the modes which account for the presence of supplementary cells.

Evaluation of Results

As an illustration, plates which consist of two-layered fundamental cells are studied in more detail. The top layer is taken to be of unit thickness, with shear wave velocity, β, and density, ρ, all equal to one. Dimensionless shear wave velocity, density, and thickness for the bottom layer of the cell are assumed to be $\beta_2 = 2$, $\rho_2 = 2$, and $h_2 = 1$. The characteristics matrix $\mathbf{A}$ (equation (12)) is given by $\mathbf{A} = \mathbf{A}_2\mathbf{A}_1$,

where $\mathbf{A}_2$ and $\mathbf{A}_1$ are defined by (8). From (8) and (12), the characteristics matrix follows explicitly. Substitution of the elements of the matrix $\mathbf{A}$ into (15) provides the dispersion relations for the sandwich plate which consists of one, two, three, etc., number of cells.

The roots of the frequency equation (the dimensionless wave numbers k) are assumed to be either real or pure imaginary; the former implying progressing type of waves in elastic medium, while the latter describes locally standing waves [6] which exponentially decay with increasing x.

For plates that consist of one and two fundamental cells and the stress-free boundary conditions (2), the dispersion relations are presented by Figs. 1 and 2. The results depicted in Fig. 1 demonstrate progressing and the locally standing waves for a one cell plate. It can be seen that at each frequency ω there exists a finite number of progressing modes and an infinite number of locally standing modes (for the sake of illustration, only the first few modes are presented). This is an analogy compared to the case of a single layer plate, where the progressing modes reduce to the family of hyperbolae, and the locally standing modes to the family of circles [6]. For a sandwich plate, which consists of two fundamental cells, part of the dispersion curves are presented by Fig. 2. This is only the part due to factor A_{kk} in (15). A complete set of dispersion relations is obtained by superposition of the results presented by Figs. 1 and 2.

The lines $k = \omega$ and $k = \beta_1/\beta_2\omega$ separate the dispersion curves for progressing waves in the k-ω space into two physically different regions (see Figs. 1 and 2):

1 $\beta_1/\beta_2\omega < k$.

2 $k < \beta_1/\beta_2\omega$.

For values of (k, ω) in Region 1, the z dependence of the displacement field in the top (bottom) layer can be expressed in terms of circular (hyperbolic) functions (see equations (3)–(6)). For the wave numbers in Region 2, the z dependence of the displacement field in both layers is of the sinusoidal character.

The fact that the dispersion equation for a single cell can be factored out provides a significant advantage in the evaluation of dispersion relations numerically. For a high number of layers in a cell, often the lower modes are very close to each other at higher frequencies. However, factorization of the dispersion equation for a one cell plate simplifies the procedure considerably by allowing evaluation of the two factors of the dispersion equation separately (see (15)).

Acknowledgments

The author expresses appreciation to Profs. M.D. Trifunac and F. E. Udwadia for critical reading of the paper.

References

1 Krautkrämer, J., and Krautkrämer, H., *Ultrasonic Testing of Materials,* Springer-Verlag, New York, 1969.

2 Aveyard, S., and Sharpe, R. S., "Application of Ultrasonic Pulse Interference," *Proceedings of the 4th International Conference on Nondestructive Testing,* Butterworth, London, 1964.

3 Delph, T. J., Herrmann, G., and Kaul, R. K., "Harmonic Wave Propagation in a Periodically Layered, Infinite Elastic Body: Antiplane Strain," ASME JOURNAL OF APPLIED MECHANICS, Vol. 45, 1978, pp. 343–349.

4 Delph, T. J., Herrmann, G., and Kaul, R. K., "Harmonic Wave Propagation in a Periodically Layered, Infinite Elastic Body: Plane Strain, Analytical Results," ASME JOURNAL OF APPLIED MECHANICS, Vol. 46, 1973, pp. 113–118.

5 Haskell, N. A., "The Dispersion of Surface Waves on Multilayered Media," *Bulletin Seism. Soc. Amer.,* Vol. 43, 1953, pp. 17–34.

6 Achenbach, J.D., *Wave Propagation in Elastic Solids,* North-Holland, Amsterdam, 1973.

Shear and Rotatory Inertia Effects on the Large Amplitude Vibration of the Initially Imperfect Plates

Z. Celep[1]

In this paper, the free flexural vibration of an elastic rectangular plate having initial imperfection is investigated including the effects of transverse shear and rotatory inertia. It is assumed that the vibration occurs with large amplitudes which leads to nonlinear differantial equations. On the basis of an assumed vibration mode, the modal equation of the plate is obtained and solved numerically.

Introduction

Chu and Herrmann [1] studied the free vibration of a rectangular plate with hinged and immovable edge. The effect of large amplitudes on both free and forced vibrations of the rectangular and circular plates having a variety of boundary conditions were investigated by Yamaki [2]. A similar study was made by Hung [3] who used the method of successive approximations. Vendhan [4] applied the higher-order Galerkin's approximation to the solutions of these vibration problems. Recently, Prathap and Varadan [5] have investigated the nonlinear vibrations of rectangular plates using an averaging technique which helps to satisfy some of the boundary conditions.

The classical plate theory neglects the effects of shear deformation and rotatory inertia. Mindlin [6] extended this theory to cover these effects on the dynamic behavior of the plates. Kumbasar [7] suggested the inclusion of these effects by using equations of three-dimensional theory of elasticity and gave a solution to the free vibration of simply supported rectangular plates. Iyengar and Raman [8] and the author [9] studied the effects of shear deformation and rotatory inertia on the vibration of rectangular and circular plates by applying the method of initial functions. The large amplitude vibration of rectangular plates including the transverse shear and rotatory inertia effects was investigated by Singh, Das, and Sundararajan [10] and Sathyamoorthy [11].

Further, the classical theory is based on the assumption that the plane has no imperfections. The statical and dynamical behavior of imperfect plates is very much dependent on the size of the initial imperfection. This dependence becomes important in plates having large initial imperfection. The first attempt to investigate the free vibration of such plates was made by the author [12, 13].

There is a close similarity between the governing equations of initially imperfect plates and those of shallow shells, when the in-plane displacements of the shell are neglected. Reissner [14, 15] studied the vibration of shallow shells assumming that the vibration takes place principally in the direction of the shell normal. Grossman, Koplik, and Yu [16] derived the variational equation for axisymmetric vibration of spherical shells. A more general investigation was presented by Singh, Sundararajan, and Das [17] for moderately thick, straight, and curved elements in a unified way. Further, they included the transverse shear and rotatory inertia effects.

In the present Note the influence of transverse shear and rotatory inertia on the large amplitude vibration of plates having large initial imperfection is studied. A similar investigation was carried out by the author [18] using a simple generalization of Timoshenko's beam theory.

Governing Equations

Consider a plate of rectangular shape having an initially imperfection $w_0 = w_0(x,y)$ as shown in Fig. 1. u, v, and w are used to represent the displacement components of the plate. In order to consider the effects of transverse shear deformation and rotatory inertia in the

[1] Department of Civil Engineering, The Technological Institute, Northwestern University, Evanston, Ill. 60201.

Manuscript received by ASME Applied Mechanics Division, July, 1979; final revision, October, 1979.

where $\mathbf{A}_2$ and $\mathbf{A}_1$ are defined by (8). From (8) and (12), the characteristics matrix follows explicitly. Substitution of the elements of the matrix $\mathbf{A}$ into (15) provides the dispersion relations for the sandwich plate which consists of one, two, three, etc., number of cells.

The roots of the frequency equation (the dimensionless wave numbers k) are assumed to be either real or pure imaginary; the former implying progressing type of waves in elastic medium, while the latter describes locally standing waves [6] which exponentially decay with increasing x.

For plates that consist of one and two fundamental cells and the stress-free boundary conditions (2), the dispersion relations are presented by Figs. 1 and 2. The results depicted in Fig. 1 demonstrate progressing and the locally standing waves for a one cell plate. It can be seen that at each frequency ω there exists a finite number of progressing modes and an infinite number of locally standing modes (for the sake of illustration, only the first few modes are presented). This is an analogy compared to the case of a single layer plate, where the progressing modes reduce to the family of hyperbolae, and the locally standing modes to the family of circles [6]. For a sandwich plate, which consists of two fundamental cells, part of the dispersion curves are presented by Fig. 2. This is only the part due to factor A_{kk} in (15). A complete set of dispersion relations is obtained by superposition of the results presented by Figs. 1 and 2.

The lines $k = \omega$ and $k = \beta_1/\beta_2\omega$ separate the dispersion curves for progressing waves in the k-ω space into two physically different regions (see Figs. 1 and 2):

1 $\beta_1/\beta_2\omega < k$.

2 $k < \beta_1/\beta_2\omega$.

For values of (k, ω) in Region 1, the z dependence of the displacement field in the top (bottom) layer can be expressed in terms of circular (hyperbolic) functions (see equations (3)–(6)). For the wave numbers in Region 2, the z dependence of the displacement field in both layers is of the sinusoidal character.

The fact that the dispersion equation for a single cell can be factored out provides a significant advantage in the evaluation of dispersion relations numerically. For a high number of layers in a cell, often the lower modes are very close to each other at higher frequencies. However, factorization of the dispersion equation for a one cell plate simplifies the procedure considerably by allowing evaluation of the two factors of the dispersion equation separately (see (15)).

Acknowledgments

The author expresses appreciation to Profs. M.D. Trifunac and F. E. Udwadia for critical reading of the paper.

References

1 Krautkrämer, J., and Krautkrämer, H., *Ultrasonic Testing of Materials,* Springer-Verlag, New York, 1969.

2 Aveyard, S., and Sharpe, R. S., "Application of Ultrasonic Pulse Interference," *Proceedings of the 4th International Conference on Nondestructive Testing,* Butterworth, London, 1964.

3 Delph, T. J., Herrmann, G., and Kaul, R. K., "Harmonic Wave Propagation in a Periodically Layered, Infinite Elastic Body: Antiplane Strain," ASME JOURNAL OF APPLIED MECHANICS, Vol. 45, 1978, pp. 343–349.

4 Delph, T. J., Herrmann, G., and Kaul, R. K., "Harmonic Wave Propagation in a Periodically Layered, Infinite Elastic Body: Plane Strain, Analytical Results," ASME JOURNAL OF APPLIED MECHANICS, Vol. 46, 1973, pp. 113–118.

5 Haskell, N. A., "The Dispersion of Surface Waves on Multilayered Media," *Bulletin Seism. Soc. Amer.,* Vol. 43, 1953, pp. 17–34.

6 Achenbach, J.D., *Wave Propagation in Elastic Solids,* North-Holland, Amsterdam, 1973.

Shear and Rotatory Inertia Effects on the Large Amplitude Vibration of the Initially Imperfect Plates

Z. Celep[1]

In this paper, the free flexural vibration of an elastic rectangular plate having initial imperfection is investigated including the effects of transverse shear and rotatory inertia. It is assumed that the vibration occurs with large amplitudes which leads to nonlinear differantial equations. On the basis of an assumed vibration mode, the modal equation of the plate is obtained and solved numerically.

Introduction

Chu and Herrmann [1] studied the free vibration of a rectangular plate with hinged and immovable edge. The effect of large amplitudes on both free and forced vibrations of the rectangular and circular plates having a variety of boundary conditions were investigated by Yamaki [2]. A similar study was made by Hung [3] who used the method of successive approximations. Vendhan [4] applied the higher-order Galerkin's approximation to the solutions of these vibration problems. Recently, Prathap and Varadan [5] have investigated the nonlinear vibrations of rectangular plates using an averaging technique which helps to satisfy some of the boundary conditions.

The classical plate theory neglects the effects of shear deformation and rotatory inertia. Mindlin [6] extended this theory to cover these effects on the dynamic behavior of the plates. Kumbasar [7] suggested the inclusion of these effects by using equations of three-dimensional theory of elasticity and gave a solution to the free vibration of simply supported rectangular plates. Iyengar and Raman [8] and the author [9] studied the effects of shear deformation and rotatory inertia on the vibration of rectangular and circular plates by applying the method of initial functions. The large amplitude vibration of rectangular plates including the transverse shear and rotatory inertia effects was investigated by Singh, Das, and Sundararajan [10] and Sathyamoorthy [11].

Further, the classical theory is based on the assumption that the plane has no imperfections. The statical and dynamical behavior of imperfect plates is very much dependent on the size of the initial imperfection. This dependence becomes important in plates having large initial imperfection. The first attempt to investigate the free vibration of such plates was made by the author [12, 13].

There is a close similarity between the governing equations of initially imperfect plates and those of shallow shells, when the in-plane displacements of the shell are neglected. Reissner [14, 15] studied the vibration of shallow shells assumming that the vibration takes place principally in the direction of the shell normal. Grossman, Koplik, and Yu [16] derived the variational equation for axisymmetric vibration of spherical shells. A more general investigation was presented by Singh, Sundararajan, and Das [17] for moderately thick, straight, and curved elements in a unified way. Further, they included the transverse shear and rotatory inertia effects.

In the present Note the influence of transverse shear and rotatory inertia on the large amplitude vibration of plates having large initial imperfection is studied. A similar investigation was carried out by the author [18] using a simple generalization of Timoshenko's beam theory.

Governing Equations

Consider a plate of rectangular shape having an initially imperfection $w_0 = w_0(x,y)$ as shown in Fig. 1. u, v, and w are used to represent the displacement components of the plate. In order to consider the effects of transverse shear deformation and rotatory inertia in the

[1] Department of Civil Engineering, The Technological Institute, Northwestern University, Evanston, Ill. 60201.

Manuscript received by ASME Applied Mechanics Division, July, 1979; final revision, October, 1979.

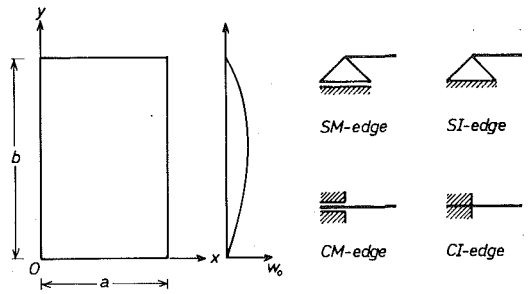

Fig. 1 Coordinate system and supporting types of the rectangular plate

plate theory, the displacement components for a point off the middle surface are taken in the following form:

$$u(x,y,z,t) = u_0(x,y,t) + z\alpha(x,y,t),$$
$$v(x,y,z,t) = v_0(x,y,t) + z\beta(x,y,t),$$
$$w(x,y,z,t) = w(x,y,t) \tag{1}$$

where u_0 and v_0 represent the displacement of the middle surface and, α and β stand for the bending slope in the x and y-directions. The strain components of the plate are

$$\epsilon_x = \epsilon_{x0} + z\alpha_{,x}, \quad \epsilon_y = \epsilon_{y0} + z\beta_{,y}, \quad \epsilon_z = 0,$$
$$\gamma_{xy} = \gamma_0 + z(\alpha_{,y} + \beta_{,x}), \quad \gamma_{yz} = \beta + w_{,y}, \quad \gamma_{xz} = \alpha + w_{,x}, \tag{2}$$

where ϵ_{x0}, ϵ_{y0}, and γ_0 denote the strains of the middle surface of the plate and they are defined as

$$\epsilon_{x0} = u_{0,x} + 0.5[(w_0 + w)_{,x}]^2 - 0.5(w_{0,x})^2,$$
$$\epsilon_{y0} = v_{0,y} + 0.5[(w_0 + w)_{,y}]^2 - 0.5(w_{0,y})^2,$$
$$\gamma_0 = u_{0,y} + v_{0,x} + (w_0 + w)_{,x}\,(w_0 + w)_{,y} - w_{0,x}\,w_{0,y}.$$

The stress-strain relations on the middle surface become

$$\sigma_{x0} = E(\epsilon_{x0} + \mu\epsilon_{y0}), \quad \sigma_{y0} = E(\epsilon_{y0} + \mu\epsilon_{x0}), \quad \tau_0 = G\gamma_0, \tag{3}$$

where σ_{x0}, σ_{y0}, and τ_0 denote the normal and shear stresses of the middle surface. E, G, and μ are the usual material constants. The relations between the moment and shear resultants and the strains are taken as follows:

$$M_x = D(\alpha_{,x} + \beta_{,y}), \quad M_y = D(\beta_{,y} + \mu\alpha_{,x}),$$
$$M_{xy} = 0.5D(1 - \mu)(\alpha_{,y} + \beta_{,x}),$$
$$Q_x = kGh(\alpha + w_{,x}), \quad Q_y = kGh(\beta + w_{,y}), \tag{4}$$

where k and h denote the well-known shear coefficient and the thickness of the plate, respectively. The equations for free vibration of the plate become

$$M_{x,x} + M_{xy,y} - Q_x - \frac{\rho h^3}{12}\ddot{\alpha} = 0, \quad M_{xy,x} + M_{y,y} - Q_y - \frac{\rho h^3}{12}\ddot{\beta} = 0,$$
$$Q_{x,x} + Q_{y,y} + \sigma_{x0}h(w_0 + w)_{,xx} + \sigma_{y0}h(w_0 + w)_{,yy} + 2\tau_0 h(w_0 + w)_{,xy} - \rho h\ddot{w} = 0. \tag{5}$$

Neglecting the in-plane inertia of the plate, and assuming a potential function as

$$\sigma_{x0} = \phi_{,yy}, \quad \sigma_{y0} = \phi_{,xx}, \quad \tau_0 = -\phi_{,xy}, \tag{6}$$

the in-plane equilibrium equations of the plate are fulfilled identically. Using the compatibility equation, the following four equations are obtained from the foregoing equations for the unknown functions ϕ, w, α, and β:

$$\Delta\Delta\phi + EL(w_0, w) + 0.5EL(w,w) = 0, \tag{7}$$

and

$$D\alpha_{,xx} + 0.5D(1 - \mu)\alpha_{,yy} + 0.5D(1 + \mu)\beta_{,xy} - 0.5\frac{khE}{1 + \mu}(\alpha + w_{,x}) - \frac{\rho h^3}{12}\ddot{\alpha} = 0,$$
$$D\beta_{,yy} + 0.5D(1 - \mu)\beta_{,xx} + 0.5D(1 + \mu)\alpha_{,xy} - 0.5\frac{khE}{1 + \mu}(\beta + w_{,y}) - \frac{\rho h^3}{12}\ddot{\beta} = 0,$$
$$L(\phi, w_0 + w) + \frac{kE}{2(1 + \mu)}(\alpha_{,x} + \beta_{,y} + \Delta w) - \rho\ddot{w} = 0, \tag{8}$$

where L is a nonlinear operator and defined as

$$L(\phi, w) = \phi_{,xx}\,w_{,yy} - 2\phi_{,xy}w_{,xy} + \phi_{,yy}w_{,xx}$$

The equations of the perfect plate are obtained, if the initial imperfection vanishes in equations (7). Eliminating α and β from equations (8), it follows:

$$\frac{D}{h}\Delta\Delta w = \frac{\rho h^2}{12}\Delta\ddot{w} + \square[L(w_0,\phi) + L(w,\phi) - \rho\ddot{w}], \tag{9}$$

where

$$\square = 1 + \frac{2(1 + \mu)}{khE}\left(\frac{\rho h^3}{12}\frac{\partial^2}{\partial t^2} - D\Delta\right).$$

The nonlinear vibration of the initially imperfect plates with large amplitudes is controlled by equations (7) and (9) which have been obtained by the author [18] by generalizing Timoshenko's beam theory for initially imperfect plates. If one assumes that the amplitudes and imperfection are small, then equation (7) is satisfied identically and equation (9) appears as

$$\frac{D}{h}\Delta\Delta w + \frac{2(1 + \mu)}{khE}\left(\frac{\rho h^3}{12}\frac{\partial^2}{\partial t^2} - D\Delta\right)\rho\ddot{w} - \frac{\rho h^2}{12}\Delta\ddot{w} + \rho\ddot{w} = 0,$$

which was deduced by Mindlin [6] and by the author [9] by using two different methods.

Boundary Conditions

Two types of boundary conditions are considered for the deflection function $w(x,y,t)$, as well as for the stress function $\phi(x,y,t)$. The conditions for the deflection function are as follows:

(1) Plate Having All Edges Simply Supported

$$\text{and} \quad \begin{matrix} w = 0, & w_{,xx} = 0, & \text{along} & x = 0 & \text{and} & x = a, \\ w = 0, & w_{,yy} = 0, & \text{along} & y = 0 & \text{and} & y = b, \end{matrix}$$

(2) Plate Having All Edges Clamped

$$\text{and} \quad \begin{matrix} w = 0, & w_{,x} = 0, & \text{along} & x = 0 & \text{and} & x = a, \\ w = 0, & w_{,y} = 0, & \text{along} & y = 0 & \text{and} & y = b. \end{matrix}$$

The boundary conditions for the stress function ϕ are as follows:

(1) Plate Having Movable Edges

$$\int_0^a \phi_{,xx}\,dx = 0, \quad \int_0^b \phi_{,yy}dy = 0,$$

which means that the resultant forces at the edges have to vanish,

(2) Plate Having Immovable Edges

$$\int_0^a \{\phi_{,yy} - \mu\phi_{,xx} - 0.5E[(w_0 + w)_{,x}]^2 + 0.5E(w_{0,x})^2\}dx = 0,$$
$$\int_0^b \{\phi_{,xx} - \mu\phi_{,yy} - 0.5E[(w_0 + w)_{,y}]^2 + 0.5E(w_{0,y})^2\}dy = 0.$$

The combination of these boundary conditions gives four types of supporting conditions for the plate as shown in Fig. 1. They are simply supported plate with movable edges (*SM*-plate), simply supported plate with immovable edges (*SI*-plate), clamped plate with movable edges (*CM*-plate), and clamped plate with immovable edges (*CI*-plate).

Approximate Solution

The solution of the coupled nonlinear governing equations (7) and

(9) under the given boundary conditions is a difficult task, if not impossible. Therefore $w(x,y,t)$ and $\phi(x,y,t)$ are selected in such a way that equation (7) and at the same time the supporting conditions are satisfied. Then, Galerkin's method is applied to equation (9) in order to eliminate the spatial coordinates of the problem. To illustrate the solution procedure, a plate having an initial imperfection

$$w_0(x,y) = \theta_0 R(x,y)$$

is considered, where the shape function are

$$R(x,y) = \sin \alpha_0 x \cdot \sin \beta_0 y, \quad \text{for } SM \text{ and } SI \text{ plates,}$$
$$R(x,y) = \sin^2 \alpha_0 x \cdot \sin^2 \beta_0 y, \quad \text{for } CM \text{ and } CI \text{ plates,}$$

where $\alpha_0 = \pi/a$ and $\beta_0 = \pi/b$. The deflection of the plate is assumed to be $w(x,y,t) = \theta(t)R(x,y)$, where θ_0 and $\theta(t)$ indicate the initial imperfection of the plate and the deflection of the middle of the plate. The stress function ϕ is determined using equation (7) and the corresponding supporting conditions as

$$\frac{\phi}{E} = \frac{\alpha_0^2\beta_0^2}{32}(\theta^2 + 2\theta_0\theta)\left(\frac{\cos 2\alpha_0 x}{\alpha_0^4} + \frac{\cos 2\beta_0 y}{\beta_0^4}\right) + \frac{P_x y^2}{2E} + \frac{P_y x^2}{2E},$$

for SM and SI plates,

$$\frac{\phi}{E} = (\theta^2 + 2\theta_0\theta)\left\{\frac{1}{32}\left(\frac{\beta_0^2}{\alpha_0^2}\cos 2\alpha_0 x + \frac{\alpha_0^2}{\beta_0^2}\cos 2\beta_0 y\right)\right.$$
$$- \frac{1}{512}\left(\frac{\beta_0^2}{\alpha_0^2}\cos 4\alpha_0 x + \frac{\alpha_0^2}{\beta_0^2}\cos 4\beta_0 y\right) + \frac{\alpha_0^2\beta_0^2}{32}\left[\frac{1}{(4\alpha_0^2 + \beta_0^2)^2}\right.$$
$$\times \cos 4\alpha_0 x \cdot \cos 2\beta_0 y + \frac{1}{(\alpha_0^2 + 4\beta_0^2)^2}\cos 2\alpha_0 x \cdot \cos 4\beta_0 y\Big]$$
$$\left. - \frac{\alpha_0^2\beta_0^2}{16(\alpha_0^2 + \beta_0^2)^2}\cos 2\alpha_0 x \cdot \cos 2\beta_0 y\right\} + \frac{P_x y^2}{2E} + \frac{P_y x^2}{2E},$$

for CM and CI plates,

where the average values of the normal stresses obtained using the supporting conditions are

$$\frac{P_x}{E} = \frac{\kappa(\theta^2 + 2\theta_0\theta)}{1-\mu^2}(\alpha_0^2 + \mu\beta_0^2), \quad \frac{P_y}{E} = \frac{\kappa(\theta^2 + 2\theta_0\theta)}{1-\mu^2}(\beta_0^2 + \mu\alpha_0^2),$$

where $\kappa = 0$ for SM and CM plates, $\kappa = 1/8$ for SI plates and $\kappa = 3/32$ for CI plates. It remains to determine $\theta(t)$ by satisfying equation (9) as accurately as possible. Applying Galerkin's method to equation (9) as

$$\int_0^a \int_0^b \left\{\frac{D}{h}\Delta\Delta w - \frac{\rho h^2}{12}\Delta\ddot{w} - \square[L(w_0,\phi) + L(w,\phi)] - \rho\ddot{w}\right\} w\, dx\, dy = 0.$$

With the nondimensional parameters

$$\zeta_0 = \frac{\theta_0}{h}, \quad \zeta = \frac{\theta}{h}, \quad \tau = \sqrt{\frac{D}{\rho h}}\frac{t}{a^2}, \quad \lambda = \frac{a}{b}, \quad r = \frac{h}{a}$$

the following modal equation which governs the nonlinear vibration of SM and SI plates is obtained

$$\left[1 + \frac{\pi^2 r^2}{12}(1+\lambda^2)\right]\frac{d^2\zeta}{d\tau^2} +$$
$$\pi^4(1+\lambda^2)^2\zeta + 12\pi^2(1-\mu^2)(\overline{Q}_x + \lambda^2\overline{Q}_y)(\zeta_0 + \zeta)$$
$$+ \frac{1+\mu}{6k}\left\{\frac{r^4}{12(1-\mu^2)}\frac{d^4\zeta}{d\tau^4} + \pi^2 r^4\frac{d^2}{d\tau^2}[(\overline{Q}_x + \lambda^2\overline{Q}_y)(\zeta_0 + \zeta)]\right.$$
$$+ \frac{\pi^2 r^2}{1-\mu^2}(1+\lambda^2)\frac{d^2\zeta}{d\tau^2}$$
$$+ 3\pi^6\lambda^2 r^2(1+\lambda^2)(\zeta_0 + \zeta)(\zeta^2 + 2\zeta_0\zeta)$$
$$\left. + 12\pi^4 r^2(1+\lambda^2)(\overline{Q}_x + \lambda^2\overline{Q}_y)(\zeta_0 + \zeta)\right\} = 0, \quad (10a)$$

where

$$\overline{Q}_x = \frac{\pi^2}{16}(\zeta^2 + 2\zeta_0\zeta) + q_x, \qquad \overline{Q}_y = \frac{\pi^2\lambda^2}{16}(\zeta^2 + 2\zeta_0\zeta) + q_y.$$

While q_z and q_y vanish for SM plates, and for SI plates they are

$$q_x = \pi^2\frac{\zeta^2 + 2\zeta_0\zeta}{8(1-\mu^2)}(1+\mu\lambda^2), \quad q_y = \pi^2\frac{\zeta^2 + 2\zeta_0\zeta}{8(1-\mu^2)}(\mu + \lambda^2).$$

A similar modal equation is obtained for CM and CI plates as follows:

$$\left[1 + \frac{\pi^2 r^2}{9}(1+\lambda^2)\right]\frac{d^2\zeta}{d\tau^2} + \frac{16\pi^4}{9}[3(1+\lambda^4) + 2\lambda^2]\zeta$$
$$+ 16\pi^2(1-\mu^2)(\overline{Q}_x + \lambda^2\overline{Q}_y)(\zeta_0 + \zeta)$$
$$- \frac{4}{3}\pi^4\lambda^4(1-\mu^2)\left[\frac{1}{(4+\lambda^2)^2} + \frac{1}{(1+4\lambda^2)^2}\right.$$
$$\left. + \frac{2}{(1+\lambda^2)^2}\right](\zeta_0 + \zeta)(\zeta^2 + 2\zeta_0\zeta) + \frac{1+\mu}{6k}\left\{\frac{r^4}{12(1-\mu^2)}\frac{d^4\zeta}{d\tau^4}\right.$$
$$+ \frac{4}{3}\pi^2 r^4\frac{d^2}{d\tau^2}[(\overline{Q}_x + \lambda^2\overline{Q}_y)(\zeta_0 + \zeta)]$$
$$- \frac{\pi^4}{9}\lambda^4 r^4\left[\frac{1}{(4+\lambda^2)^2} + \frac{1}{(1+4\lambda^2)^2}\right.$$
$$\left. + \frac{2}{(1+\lambda^2)^2}\right]\frac{d^2}{d\tau^2}[(\zeta_0 + \zeta)(\zeta^2 + 2\zeta_0\zeta)]$$
$$+ \frac{4}{3}\frac{\pi^2 r^2}{1-\mu^2}(1+\lambda^2)\frac{d^2\zeta}{d\tau^2} + \frac{\pi^6}{3}\lambda^2 r^2\left[24\lambda^4\left(\frac{1}{4+\lambda^2} + \frac{1}{1+4\lambda^2}\right)\right.$$
$$- \frac{4\lambda^4(5\lambda^2+18)}{(4+\lambda^2)^2} - \frac{4\lambda^4(5+18\lambda^2)}{(4\lambda^2+1)^2} + 9\lambda^2(1+\lambda^2)$$
$$\left. + 17(1+\lambda^6)](\zeta^2 + 2\zeta_0\zeta)\right.$$
$$\left. + \frac{64}{3}\pi^4 r^2(1+\lambda^2)(\overline{Q}_x + \lambda^2\overline{Q}_y)(\zeta_0 + \zeta)\right\} = 0, \quad (10b)$$

where

$$\overline{Q}_x = \frac{\pi^2}{3}(\zeta^2 + 2\zeta_0\zeta)\left\{\frac{17}{64} + \frac{\lambda^4}{4}\left[\frac{1}{(4\lambda^2+1)^2} + \frac{1}{2(4+\lambda^2)^2}\right]\right.$$
$$\left. + \frac{\lambda^4}{2(1+\lambda^2)^2}\right\} + q_x,$$
$$\overline{Q}_y = \frac{\pi^2}{3}(\zeta^2 + 2\zeta_0\zeta)\left\{\frac{17\lambda^2}{64} + \frac{\lambda^2}{4}\left[\frac{1}{(4+\lambda^2)^2} + \frac{1}{2(1+4\lambda^2)^2}\right]\right.$$
$$\left. + \frac{\lambda^2}{2(1+\lambda^2)^2}\right\} + q_y.$$

The quantities q_x and q_y vanish for CM plates, and for CI plates they denote

$$q_x = 3\pi^2\frac{\zeta^2 + 2\zeta_0\zeta}{32(1-\mu^2)}(1+\mu\lambda^2), \quad q_y = 3\pi^2\frac{\zeta^2 + 2\zeta_0\zeta}{32(1-\mu^2)}(\mu + \lambda^2).$$

Numerical Results and Conclusions

To obtain the period of the flexural vibration of the plate, equation (10) has been solved numerically on the B3700 Computer at the Computer Center of the Technical University, Istanbul, Turkey. The numerical solution is carried out for the square plate, i.e., for $\lambda = 1$, using the method of Runge-Kutta and assuming $k = 5/6$ and $\mu = 0.3$. Moreover, the fourth derivatives with respect to time in equation (10) have not been taken into account because of the negligible effect on the period. The initial conditions of the free vibration are assumed to be $\zeta(\tau = 0) = \zeta_s$, $\dot{\zeta}(\tau = 0) = 0$, where ζ_s represents the initial amplitude of the plate. The results of the numerical calculation are plotted in Figs. 2 which give only the variation of the nondimensional period of the SI plates versus the initial amplitude, i.e., $\tau_0 = \tau_0(\zeta_s)$, where τ_0 denotes the period of the initially imperfect plate relative to the period of the corresponding perfect plate at the small ampli-

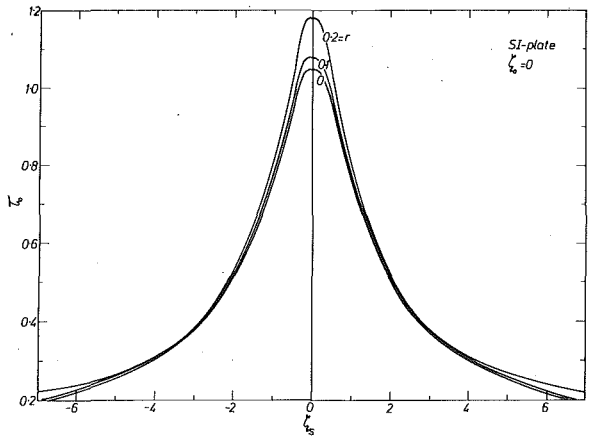

Fig. 2(*a*) $\zeta_0 = 0$

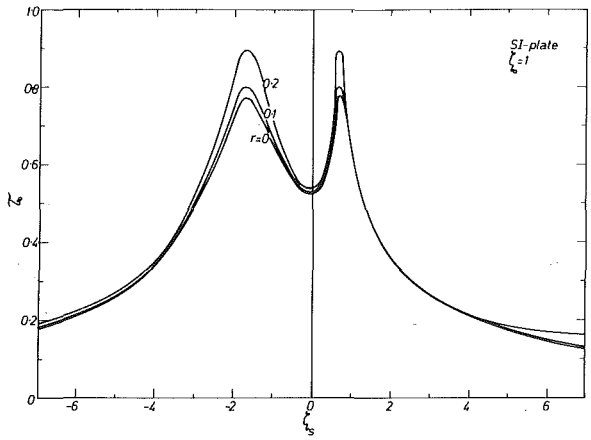

Fig. 2(*b*) $\zeta_0 = 1$

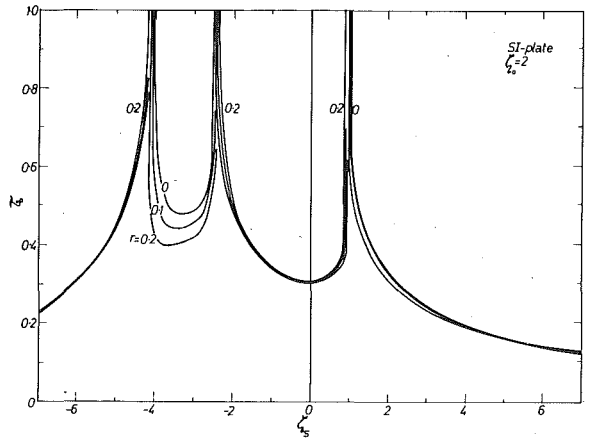

Fig. 2(*c*) $\zeta_0 = 2$

Fig. 2 Variation of the period versus the initial amplitude of the *SI*-plate having an initial imperfection of Figs. 2(*a–c*)

tudes. The curves on the figures illustrate the effects of transverse shear and rotatory inertia. As it is seen, three values are considered for the thickness-length ratio r. The vanishing ratio corresponds to the thin plate for which shear and rotatory inertia effects are neglected. The results of the perfect thin plate are the same as those of Chu and Herrmann [1], Hung [3], and Yamaki [2]. Further, the results of the perfect plate having a nonvanishing thickness-length ratio r agree with those of Singh, Das, and Sundararajan [10]. The figures concerning initial imperfections with nonvanishing thickness-length ratio are new. They represent the effects of the initial imperfection and that of the thickness-length ratio on the period of the plate. When the plate has no initial imperfection, the curve of the period is symmetrical and the period decreases with the increasing initial amplitude as Fig. 2(*a*) shows. The presence of rotatory inertia and shear effects are more pronounced at small amplitudes, where the period increases with the thickness-length ratio, but make only slight changes in the period at large amplitudes. If the plate has an initial imperfection, the curves change dramatically. The symmetry of the curves vanishes, and the maxima becomes a minima surrounded by two adjacent maxima as seen in Fig. 2(*b*). The effects of transverse shear and rotatory inertia become more pronounced at the maximas, and the period increases with the thickness-length ratio. The maximas increase with increasing imperfection, and they become two asymptotes of the curve for a certain value of the imperfection. With further increase of the initial imperfection, the curve changes and one more asymptote will appear as seen in Fig. 2(*c*). The thickness-length ratio makes slight changes in the curve of the period, and it becomes more effective at about the asymptotes of the curve. While the asymptotes correspond to the unstable equilibrium positon and to the positions having equal potential energy level with the unstable equilibrium positon, the minimas represent the stable equilibrium positions. Only the stable equilibrium position of the perfect plate corresponds to a maxima. Similar curves were obtained by Singh, Sundararajan, and Das [17] for large amplitude vibration of some moderately thick and doubly curved shells. The behavior of the initially imperfect plates at the free vibration without considering the effects of shear and rotatory inertia was explained [12] and an analogy was presented by the author [13].

References

1 Chu, H. N., and Herrmann, G., "Influence of Large Amplitudes on Free Flexural Vibrations of Rectangular Elastic Plates," ASME JOURNAL OF APPLIED MECHANICS, Vol. 23, 1956, pp. 532–540.

2 Yamaki, N., "Influence of Lage Amplitudes on Flexural Vibrations of Elastic Plates," *Zeitschrift für Angewandte Mathematik und Mechanik,* Vol. 41, 1961, pp. 501–510.

3 Hung, N., "Die Biegeschwingungen von Rechteckplatte mit grossen Amplituden," *Zeitschrift für Angewandte Mathematik und Mechanik,* Vol. 49, 1969, pp. 459–470.

4 Vendhan, C. P., "Modal Equations Applied to the Nonlinear Flexural Vibrations of the Plates," *American Institute of Aeronautics and Astronautics Journal,* Vol. 13, 1975, pp. 1092–1094.

5 Prathap, G., and Varadan, T. K., "On the Nonlinear Vibrations of Rectangular Plates," *Journal of Sound and Vibration,* Vol. 56, 1978, pp. 521–530.

6 Mindlin, R. D., "Influence of Rotatory Inertia and Shear on Flexural Motions of Isotropic Elastic Plates," ASME JOURNAL OF APPLIED MECHANICS, Vol. 18, 1951, pp. 31–38.

7 Kumbasar, N., *Investigation of the Free Vibration of Simply Supported Rectangular Plates by the Theory of Elasticity,* Faculty of Civil Engineering, Technical University, Istanbul, Turkey, 1968.

8 Iyengar, K. T. S. R., and Raman, P. V., "Free Vibration of Rectangular Plates of Arbitrary Thickness," *Journal of Sound and Vibration,* Vol. 54, 1977, pp. 229–236.

9 Celep, Z., "On the Axially Symmetric Vibration of Thick Circular Plates," *Ingenieur-Archiv,* Vol. 47, 1978, pp. 411–420.

10 Singh, P. N., Das, Y. C., and Sundararajan, V., "Large-Amplitude Vibration of Rectangular Plates," *Journal of Sound and Vibration,* Vol. 17, 1971, pp. 235–240.

11 Sathyamoorthy, M., "Effects of Large Amplitude, Shear and Rotatory Inertia on Vibration and Rectangular Plates," *Journal of Sound and Vibration,* Vol. 63, 1979, pp. 161–167.

12 Celep, Z., "Free Flexural Vibration of Initially Imperfect Thin Plates With Large Elastic Amplitudes," *Zeitschrift für Angewandte Mathematik und Mechanik,* Vol. 56, 1976, pp. 423–428.

13 Celep, Z., "An Analogy Between Free Vibration of a Plate and of a Particle of Mass," *Journal of Sound and Vibration,* Vol. 53, 1977, pp. 323–331.

14 Reissner, E., "On Transverse Vibration of Thin Shallow Elastic Shells," *Quarterly Journal of Applied Mathematics,* Vol. 13, 1955, pp. 169–176.

15 Reissner, E., "On Axisymmetrical Vibration of Shallow Spherical Shells," *Quarterly Journal of Applied Mathematics,* Vol. 13, 1955, pp. 279–290.

16 Grossman, P. L., Koplik, B., and Yu, Y., "Nonlinear Vibrations of Shallow Spherical Shells," ASME JOURNAL OF APPLIED MECHANICS, Vol. 36, 1969, pp. 451–458.

17 Singh, P. N., Sundararajan, V., and Das, Y. C., "Large Amplitude Vibration of Some Moderately Thick Structural Elements," *Journal of Sound and Vibration*, Vol. 36, 1974, pp. 375–387.

18 Celep, Z., *Flexural Vibration of Initially Imperfect Thin Plates*, Faculty of Engineering and Architecture, Technical University, Istanbul, 1976.

A Note on the Flow of a Viscoelastic Liquid Near an Oscillating Infinite Porous Plate

D. N. Mukhopadhyay[1] and T. K. Chaudhury[2]

Introduction

In view of the growing importance in chemical industries, different models of viscoelastic fluids have engaged attention of many investigators. Stress-relaxing liquid of Oldroyd [1] is a rate-type model satisfying the condition of material frame-in-difference [2]. In the approximation of very short relaxation time, this model reduces to the second-order fluid model of Coleman and Noll [3]. The present problem considers the unsteady flow of a viscoelastic liquid of Oldroyd near an infinite porous plate oscillating in its own plane. The purpose of the study is to gain some information about the influence of relaxation time in the presence of mass transfer through the surface. The corresponding problem for a second-order fluid is governed by a differential equation of third-order with two boundary conditions and can only be solved by a method of successive approximation developed by Beard and Walters [4]. However for an Oldroyd fluid, with a particular solution for one normal stress component consistent with the second-order fluid model, the differential equation obtained is of second-order and can be completely solved. This solution gives the solution for a second-order fluid as an approximation and we believe that our solution is a more general one in respect of the stress-relaxation property of the fluid. The most interesting feature of our solution is that for the mass transfer parameter within a certain range there exists a critical-relaxation parameter beyond which the role of the stress-relaxation property of the fluid is reversed.

Formulation and Solution of the Problem

The constitutive equation for a viscoelastic fluid of Oldroyd [1] has the form

$$P_{ij} = -p\delta_{ij} + T_{ij}$$

$$T_{ij} + \lambda_1\left(\frac{\partial T_{ij}}{\partial t} + V_k T_{ij,k} - V_{i,k}T_{kj} - V_{j,k}T_{ik}\right) = 2\eta_0 e_{ij} \qquad (1)$$

where P_{ij} and e_{ij} are, respectively, stress tensor and rate-of-strain tensor, V_i is the velocity component, λ_1 is the relaxation time, and η_0 is the viscosity coefficient. With x-axis along the plate parallel to the direction of motion and y-axis perpendicular to it directed into the fluid, the velocity components for the problem are taken as $(u, -v_0, 0)$ where $u = u(y, t)$ and $-v_0$ is the constant suction.

The differential equation for u will be obtained by elimination of stress component T_{xy} between (1) and the momentum equation. This elimination is affected by taking the particular solution $T_{yy} = 0$, which means vanishing normal stress T_{yy} at the line of entry (or exit) of the fluid through pores of the boundary.

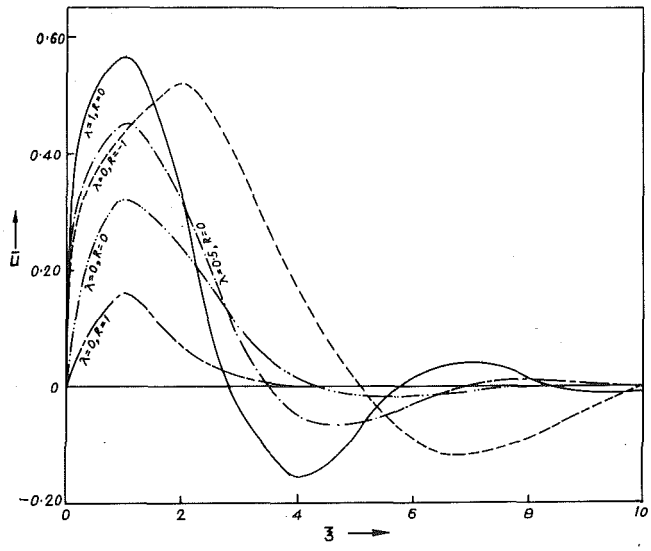

Fig. 1 Velocity profiles of Newtonian and viscoelastic fluid near an oscillating porous plate for $\tau = \pi/2$ (Case 1)

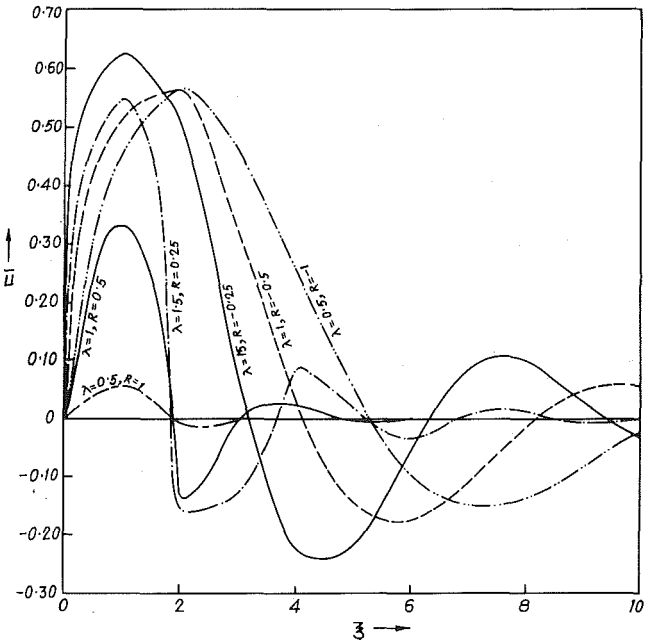

Fig. 2 Velocity profiles of a viscoelastic fluid near an oscillating porous plate for $\tau = \pi/2$ (Case 1)

We assume the motion to be entirely due to the oscillation $U_0 e^{i\omega t}$ (real part) of the plate. Now introudcing the nondimensional quantities $\bar{u} = u/U_0$, $\xi = y\sqrt{\omega/\nu}$, $\tau = \omega t$, $R = V_0/\sqrt{\omega\nu}$, $\lambda = \lambda_1\omega$, where R is the mass transfer parameter, λ is the relaxation parameter, and $\nu = \eta_0/\rho$, we have for $\bar{u}$ the equation

$$\frac{\partial \bar{u}}{\partial \tau} - R\frac{\partial \bar{u}}{\partial \xi} + \lambda\frac{\partial^2 \bar{u}}{\partial \tau^2} - 2\lambda R\frac{\partial}{\partial \tau}\left(\frac{\partial \bar{u}}{\partial \xi}\right) = (1 - \lambda R^2)\frac{\partial^2 \bar{u}}{\partial \xi^2} \qquad (2)$$

and the boundary conditions $\bar{u}(0, \tau) = e^{i\tau}$, $\bar{u} = 0$ when $\xi \to \infty$. It is evident from (2) that this flow problem divides itself into three cases, namely, $\lambda R^2 \gtrless 1$. In the first case, i.e., when the relaxation time $\lambda_1 < \nu/V_0^2$, the flow considered is possible for both blowing and suction at the oscillating plate; while in the second case, i.e., when $\lambda_1 = \nu/V_0^2$, the flow is possible only for blowing. In the remaining case, i.e., when $\lambda_1 > \nu/V_0^2$, no solution is possible for suction while for blowing the problem is indeterminate in the sense that the boundary conditions cannot determine the arbitrary constants uniquely.

[1] Department of Mathematics, Burdwan University, Burdwan, West Bengal, India.

[2] Reader, Department of Mathematics, Burdwan University, Burdwan, West Bengal, India.

Manuscript received by ASME Applied Mechanics Division, June, 1979; final revision, March, 1980.

16 Grossman, P. L., Koplik, B., and Yu, Y., "Nonlinear Vibrations of Shallow Spherical Shells," ASME JOURNAL OF APPLIED MECHANICS, Vol. 36, 1969, pp. 451–458.

17 Singh, P. N., Sundararajan, V., and Das, Y. C., "Large Amplitude Vibration of Some Moderately Thick Structural Elements," *Journal of Sound and Vibration*, Vol. 36, 1974, pp. 375–387.

18 Celep, Z., *Flexural Vibration of Initially Imperfect Thin Plates*, Faculty of Engineering and Architecture, Technical University, Istanbul, 1976.

A Note on the Flow of a Viscoelastic Liquid Near an Oscillating Infinite Porous Plate

D. N. Mukhopadhyay[1] and T. K. Chaudhury[2]

Introduction

In view of the growing importance in chemical industries, different models of viscoelastic fluids have engaged attention of many investigators. Stress-relaxing liquid of Oldroyd [1] is a rate-type model satisfying the condition of material frame-in-difference [2]. In the approximation of very short relaxation time, this model reduces to the second-order fluid model of Coleman and Noll [3]. The present problem considers the unsteady flow of a viscoelastic liquid of Oldroyd near an infinite porous plate oscillating in its own plane. The purpose of the study is to gain some information about the influence of relaxation time in the presence of mass transfer through the surface. The corresponding problem for a second-order fluid is governed by a differential equation of third-order with two boundary conditions and can only be solved by a method of successive approximation developed by Beard and Walters [4]. However for an Oldroyd fluid, with a particular solution for one normal stress component consistent with the second-order fluid model, the differential equation obtained is of second-order and can be completely solved. This solution gives the solution for a second-order fluid as an approximation and we believe that our solution is a more general one in respect of the stress-relaxation property of the fluid. The most interesting feature of our solution is that for the mass transfer parameter within a certain range there exists a critical-relaxation parameter beyond which the role of the stress-relaxation property of the fluid is reversed.

Formulation and Solution of the Problem

The constitutive equation for a viscoelastic fluid of Oldroyd [1] has the form

$$P_{ij} = -p\delta_{ij} + T_{ij}$$

$$T_{ij} + \lambda_1\left(\frac{\partial T_{ij}}{\partial t} + V_k T_{ij,k} - V_{i,k}T_{kj} - V_{j,k}T_{ik}\right) = 2\eta_0 e_{ij} \qquad (1)$$

where P_{ij} and e_{ij} are, respectively, stress tensor and rate-of-strain tensor, V_i is the velocity component, λ_1 is the relaxation time, and η_0 is the viscosity coefficient. With x-axis along the plate parallel to the direction of motion and y-axis perpendicular to it directed into the fluid, the velocity components for the problem are taken as $(u, -v_0, 0)$ where $u = u(y, t)$ and $-v_0$ is the constant suction.

The differential equation for u will be obtained by elimination of stress component T_{xy} between (1) and the momentum equation. This elimination is affected by taking the particular solution $T_{yy} = 0$, which means vanishing normal stress T_{yy} at the line of entry (or exit) of the fluid through pores of the boundary.

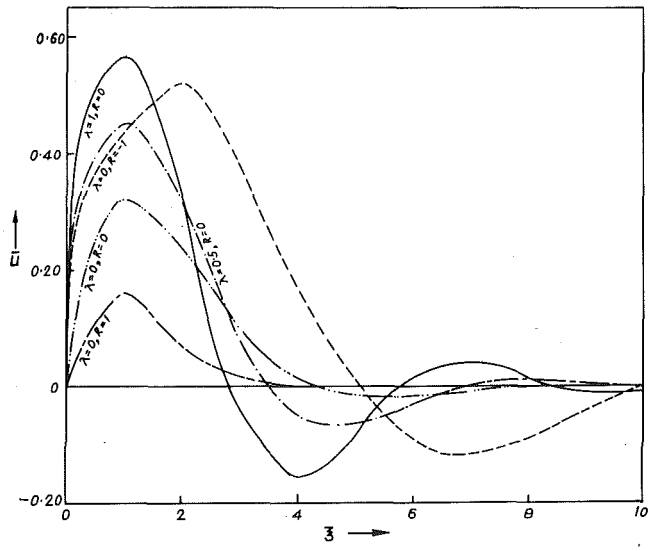

Fig. 1 Velocity profiles of Newtonian and viscoelastic fluid near an oscillating porous plate for $\tau = \pi/2$ (Case 1)

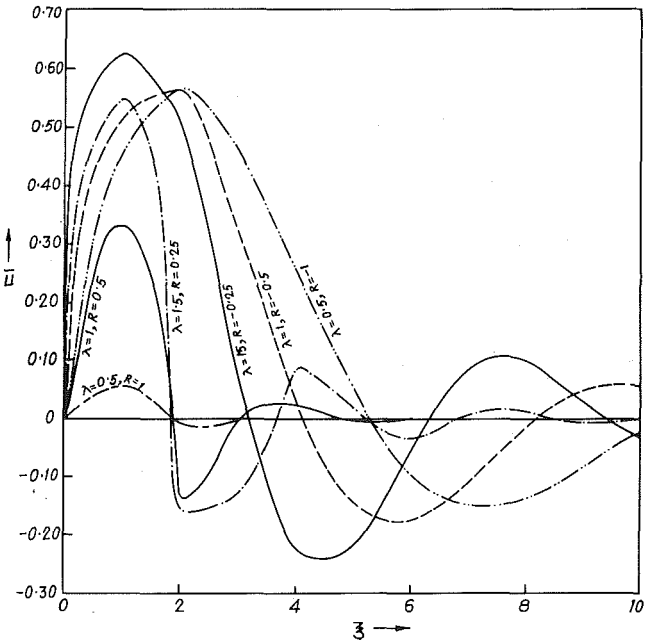

Fig. 2 Velocity profiles of a viscoelastic fluid near an oscillating porous plate for $\tau = \pi/2$ (Case 1)

We assume the motion to be entirely due to the oscillation $U_0 e^{i\omega t}$ (real part) of the plate. Now introudcing the nondimensional quantities $\bar{u} = u/U_0$, $\xi = y\sqrt{\omega/\nu}$, $\tau = \omega t$, $R = V_0/\sqrt{\omega\nu}$, $\lambda = \lambda_1\omega$, where R is the mass transfer parameter, λ is the relaxation parameter, and $\nu = \eta_0/\rho$, we have for $\bar{u}$ the equation

$$\frac{\partial \bar{u}}{\partial \tau} - R\frac{\partial \bar{u}}{\partial \xi} + \lambda\frac{\partial^2 \bar{u}}{\partial \tau^2} - 2\lambda R\frac{\partial}{\partial \tau}\left(\frac{\partial \bar{u}}{\partial \xi}\right) = (1 - \lambda R^2)\frac{\partial^2 \bar{u}}{\partial \xi^2} \qquad (2)$$

and the boundary conditions $\bar{u}(0, \tau) = e^{i\tau}$, $\bar{u} = 0$ when $\xi \to \infty$. It is evident from (2) that this flow problem divides itself into three cases, namely, $\lambda R^2 \gtrless 1$. In the first case, i.e., when the relaxation time $\lambda_1 < \nu/V_0^2$, the flow considered is possible for both blowing and suction at the oscillating plate; while in the second case, i.e., when $\lambda_1 = \nu/V_0^2$, the flow is possible only for blowing. In the remaining case, i.e., when $\lambda_1 > \nu/V_0^2$, no solution is possible for suction while for blowing the problem is indeterminate in the sense that the boundary conditions cannot determine the arbitrary constants uniquely.

[1] Department of Mathematics, Burdwan University, Burdwan, West Bengal, India.

[2] Reader, Department of Mathematics, Burdwan University, Burdwan, West Bengal, India.

Manuscript received by ASME Applied Mechanics Division, June, 1979; final revision, March, 1980.

For $\lambda R^2 < 1$,

$$\bar{u} = e^{-A\xi} \cos(\tau - B\xi), \tag{3}$$

where

$$A = \frac{\sqrt{2}\,R + S}{2\sqrt{2}\,(1 - \lambda R^2)}, \quad B = \frac{4 + 2\sqrt{2}\,\lambda RS}{2\sqrt{2}\,S(1 - \lambda R^2)},$$

$$S = \sqrt{r + R^2 - 4\lambda}, \quad r = \sqrt{(R^2 - 4\lambda)^2 + 16}.$$

For $\lambda R^2 = 1$ and $R < 0$,

$$\bar{u} = e^{-A^*\xi} \cos(\tau - B^*\xi), \tag{4}$$

where

$$A^* = -\frac{\lambda}{R(1 + 4\lambda^2)}, \quad B^* = -\frac{1 + 2\lambda^2}{R(1 + 4\lambda^2)}.$$

If we take Coleman and Noll's second-order fluid the governing differential equation of the present problem will be

$$\frac{\partial \bar{u}}{\partial \tau} - R\frac{\partial \bar{u}}{\partial \xi} = \frac{\partial^2 \bar{u}}{\partial \xi^2} - \lambda \frac{\partial^2}{\partial \xi^2}\left(\frac{\partial \bar{u}}{\partial \tau} - R\frac{\partial \bar{u}}{\partial \xi}\right), \tag{5}$$

where now $\lambda = -\nu_0\omega/\eta_0$, ν_0 being the coefficient of viscoelasticity. By successive approximation (5) gives the solution

$$\bar{u} = R_e\left(1 + \lambda\xi\frac{m^2(Rm + i)}{R - 2m}\right)e^{i\tau - m\xi} \quad \text{to the first power in } \lambda, \tag{6}$$

where

$$m = \frac{R + \sqrt{R^2 + 4i}}{2}$$

It can be easily seen that the solution (6) may be obtained from our solution (3) by taking λ to be small and retaining terms upto the first power in λ.

Discussion

It is found from computation of $\partial A/\partial\lambda$ that for blowing ($R < 0$) the amplitude of velocity increases with the increase of λ while for suction ($R > 0$) the amplitude at first increases with λ but after critical value of $\lambda(= \lambda_c)$ it begins to decrease with λ. This critical value of λ decreases as R (i.e., suction) increases and for $R > 0.5958 = R_1^*$, λ_c becomes negative. Therefore, when $R > R_1^*$ the amplitude decreases with λ within the entire range of validity of the solution.

Similarly, from the computation of $\partial B/\partial\lambda$ it is found that for suction ($R > 0$) B increases, i.e., the phase lag with respect to the plate motion increases with the increase of λ; while for blowing ($R < 0$) the phase lag at first decreases with λ but after a critical value of $\lambda(= \lambda_c')$ it increases with λ. This critical value of λ decreases as $R(<0)$ increases (i.e., $-R$ decreases) and for $R > -0.5366 = R_2^*$, λ_c' becomes negative. Therefore, when $0 > R > R_2^*$, the phase lag increases with λ within the entire range of validity of the solution. From computation, we find: for $R = 0.25$, $\lambda_c = 3.9212$; for $R = 0.5$, $\lambda_c = 0.6317$; and for $R = -1$, $\lambda_c' = 0.7468$. Thus, for small suction, the amplitude of the velocity increases with the increase of the relaxation time of the fluid but when relaxation time exceeds certain value, the stress-relaxation property of the fluid begins to dampen the amplitude. For large suction the stress-relaxation property of the fluid always acts as a damping agent. For blowing, however, this stress-relaxation property of the fluid always behaves as an amplifying agent. The critical-relaxation parameter does not arise if mass transfer is not involved. It is further observed from computation that although the two cases $\lambda R^2 < 1$ and $\lambda R^2 = 1$ are governed by two entirely different differential equations, the solution in the first case smoothly changes over to that of the second case in the valid region.

Acknowledgment

The first author is thankful to the University of Burdwan for granting him a research scholarship.

References

1 Oldroyd, J. G., "On the Formulation of Rheological Equations of State," *Proceedings of the Royal Society*, London, Series A, Vol. 200, No. 1063, 1950, p. 523.

2 Truesdell and Noll, *Encyclopedia of Physics*, Vol. III/3, 1965.

3 Coleman, B. D., and Noll. W., "An Approximation Theorem on Functionals With Application in Continuum Mechanics," *Arch. Rational Mech. Anal.*, Vol. 6, 1960, pp. 355–370.

4 Beard, D. W., and Walters, K. "Elastico-Viscous Boundary Layer Flows. Part 1—Two-Dimensional Flow Near a Stagnation Point," *Proceedings of the Cambridge Philosophical Society*, Vol. 60, 1964, pp. 667–674.

Axisymmetric Plume Flow in a Vertical Uniform Free Stream

A. V. Appalaswamy[1] and Y. Jaluria[2]

Introduction

The axisymmetric plume that arises from a point heat source has been studied [1, 2]. In many systems of practical interest, however, the plume flow does not occur in a quiescent ambient medium but is affected by the existence of an externally induced flow. This paper considers the circumstance when the external flow is aligned with the plume flow and aids or opposes the natural convection mechanisms. This problem is of interest in heat removal from heated elements, such as electronic components, where an external flow is generated in addition to the natural convection flow in order to restrict the temperature level attained by these elements [3].

The effect of mixed convection on the heat transfer, for various flow circumstances, has been considered [4, 5]. These studies determined the effect of natural convection mechanisms on a dominant forced convection circumstance and vice versa. The present study considers the effect of an external flow on the plume flow, for the two Prandtl number values of 7.0 and 0.7 and at various levels of external flow. Of particular interest was the effect on the velocity field, on the center-line temperature and on the boundary-layer thicknesses.

Analysis

The boundary-layer equations that govern the flow, in an axisymmetric plume above a point heat source, are written in terms of the vertical and radial velocity components u and v, temperature t, the vertical coordinate from the point source x, and the radial distance y, from the axis of symmetry, as

$$\frac{\partial}{\partial x}(yu) + \frac{\partial}{\partial y}(yv) = 0 \tag{1a}$$

$$u\frac{\partial u}{\partial x} + v\frac{\partial u}{\partial y} = \frac{\nu}{y}\frac{\partial}{\partial y}\left(y\frac{\partial u}{\partial y}\right) + g\beta\,(t - t_\infty) \tag{1b}$$

$$u\frac{\partial t}{\partial x} + v\frac{\partial t}{\partial y} = \frac{\alpha}{y}\frac{\partial}{\partial y}\left(y\frac{\partial t}{\partial y}\right) \tag{1c}$$

where g is the gravitational acceleration, β the coefficient of thermal expansion, ν the kinematic viscosity, α the thermal diffusivity, and t_∞ the temperature of the ambient fluid. In the foregoing equations, Boussinesq approximations have been employed and the pressure and viscous dissipation terms in the energy equation have been neglected.

Consider a steady thermal input Q_0 at $x = 0$ and $y = 0$ in an extensive ambient medium at temperature t_∞. Then the thermal energy $Q(x)$ convected in the resulting plume must be the same for all $x > 0$ and equal to Q_0, since there are no sources or sinks in the plume. The center-line temperature is denoted by $t_0(x)$. Employing the similarity

[1] Tata Consulting Engineers, Carnac, Bombay, India.

[2] Department of Mechanical Engineering, Indian Institute of Technology, Kanpur 208016, India. Mem. ASME.

Manuscript received by ASME Applied Mechanics Division, May, 1979; final revision, November, 1979.

For $\lambda R^2 < 1$,

$$\bar{u} = e^{-A\xi} \cos(\tau - B\xi), \tag{3}$$

where

$$A = \frac{\sqrt{2}\,R + S}{2\sqrt{2}\,(1 - \lambda R^2)}, \quad B = \frac{4 + 2\sqrt{2}\,\lambda RS}{2\sqrt{2}\,S(1 - \lambda R^2)},$$

$$S = \sqrt{r + R^2 - 4\lambda}, \quad r = \sqrt{(R^2 - 4\lambda)^2 + 16}.$$

For $\lambda R^2 = 1$ and $R < 0$,

$$\bar{u} = e^{-A^*\xi} \cos(\tau - B^*\xi), \tag{4}$$

where

$$A^* = -\frac{\lambda}{R(1 + 4\lambda^2)}, \quad B^* = -\frac{1 + 2\lambda^2}{R(1 + 4\lambda^2)}.$$

If we take Coleman and Noll's second-order fluid the governing differential equation of the present problem will be

$$\frac{\partial \bar{u}}{\partial \tau} - R\frac{\partial \bar{u}}{\partial \xi} = \frac{\partial^2 \bar{u}}{\partial \xi^2} - \lambda\frac{\partial^2}{\partial \xi^2}\left(\frac{\partial \bar{u}}{\partial \tau} - R\frac{\partial \bar{u}}{\partial \xi}\right), \tag{5}$$

where now $\lambda = -\nu_0\omega/\eta_0$, ν_0 being the coefficient of viscoelasticity. By successive approximation (5) gives the solution

$$\bar{u} = R_e\left(1 + \lambda\xi\frac{m^2(Rm + i)}{R - 2m}\right)e^{i\tau - m\xi} \quad \text{to the first power in } \lambda, \tag{6}$$

where

$$m = \frac{R + \sqrt{R^2 + 4i}}{2}$$

It can be easily seen that the solution (6) may be obtained from our solution (3) by taking λ to be small and retaining terms upto the first power in λ.

Discussion

It is found from computation of $\partial A/\partial\lambda$ that for blowing ($R < 0$) the amplitude of velocity increases with the increase of λ while for suction ($R > 0$) the amplitude at first increases with λ but after critical value of $\lambda(= \lambda_c)$ it begins to decrease with λ. This critical value of λ decreases as R (i.e., suction) increases and for $R > 0.5958 = R_1^*$, λ_c becomes negative. Therefore, when $R > R_1^*$ the amplitude decreases with λ within the entire range of validity of the solution.

Similarly, from the computation of $\partial B/\partial\lambda$ it is found that for suction ($R > 0$) B increases, i.e., the phase lag with respect to the plate motion increases with the increase of λ; while for blowing ($R < 0$) the phase lag at first decreases with λ but after a critical value of $\lambda(= \lambda_c')$ it increases with λ. This critical value of λ decreases as $R(<0)$ increases (i.e., $-R$ decreases) and for $R > -0.5366 = R_2^*$, λ_c' becomes negative. Therefore, when $0 > R > R_2^*$, the phase lag increases with λ within the entire range of validity of the solution. From computation, we find: for $R = 0.25$, $\lambda_c = 3.9212$; for $R = 0.5$, $\lambda_c = 0.6317$; and for $R = -1$, $\lambda_c' = 0.7468$. Thus, for small suction, the amplitude of the velocity increases with the increase of the relaxation time of the fluid but when relaxation time exceeds certain value, the stress-relaxation property of the fluid begins to dampen the amplitude. For large suction the stress-relaxation property of the fluid always acts as a damping agent. For blowing, however, this stress-relaxation property of the fluid always behaves as an amplifying agent. The critical-relaxation parameter does not arise if mass transfer is not involved. It is further observed from computation that although the two cases $\lambda R^2 < 1$ and $\lambda R^2 = 1$ are governed by two entirely different differential equations, the solution in the first case smoothly changes over to that of the second case in the valid region.

Acknowledgment

The first author is thankful to the University of Burdwan for granting him a research scholarship.

References

1 Oldroyd, J. G., "On the Formulation of Rheological Equations of State," *Proceedings of the Royal Society*, London, Series A, Vol. 200, No. 1063, 1950, p. 523.

2 Truesdell and Noll, *Encyclopedia of Physics*, Vol. III/3, 1965.

3 Coleman, B. D., and Noll. W., "An Approximation Theorem on Functionals With Application in Continuum Mechanics," *Arch. Rational Mech. Anal.*, Vol. 6, 1960, pp. 355–370.

4 Beard, D. W., and Walters, K. "Elastico-Viscous Boundary Layer Flows. Part 1—Two-Dimensional Flow Near a Stagnation Point," *Proceedings of the Cambridge Philosophical Society*, Vol. 60, 1964, pp. 667–674.

Axisymmetric Plume Flow in a Vertical Uniform Free Stream

A. V. Appalaswamy[1] and Y. Jaluria[2]

Introduction

The axisymmetric plume that arises from a point heat source has been studied [1, 2]. In many systems of practical interest, however, the plume flow does not occur in a quiescent ambient medium but is affected by the existence of an externally induced flow. This paper considers the circumstance when the external flow is aligned with the plume flow and aids or opposes the natural convection mechanisms. This problem is of interest in heat removal from heated elements, such as electronic components, where an external flow is generated in addition to the natural convection flow in order to restrict the temperature level attained by these elements [3].

The effect of mixed convection on the heat transfer, for various flow circumstances, has been considered [4, 5]. These studies determined the effect of natural convection mechanisms on a dominant forced convection circumstance and vice versa. The present study considers the effect of an external flow on the plume flow, for the two Prandtl number values of 7.0 and 0.7 and at various levels of external flow. Of particular interest was the effect on the velocity field, on the center-line temperature and on the boundary-layer thicknesses.

Analysis

The boundary-layer equations that govern the flow, in an axisymmetric plume above a point heat source, are written in terms of the vertical and radial velocity components u and v, temperature t, the vertical coordinate from the point source x, and the radial distance y, from the axis of symmetry, as

$$\frac{\partial}{\partial x}(yu) + \frac{\partial}{\partial y}(yv) = 0 \tag{1a}$$

$$u\frac{\partial u}{\partial x} + v\frac{\partial u}{\partial y} = \frac{\nu}{y}\frac{\partial}{\partial y}\left(y\frac{\partial u}{\partial y}\right) + g\beta\,(t - t_\infty) \tag{1b}$$

$$u\frac{\partial t}{\partial x} + v\frac{\partial t}{\partial y} = \frac{\alpha}{y}\frac{\partial}{\partial y}\left(y\frac{\partial t}{\partial y}\right) \tag{1c}$$

where g is the gravitational acceleration, β the coefficient of thermal expansion, ν the kinematic viscosity, α the thermal diffusivity, and t_∞ the temperature of the ambient fluid. In the foregoing equations, Boussinesq approximations have been employed and the pressure and viscous dissipation terms in the energy equation have been neglected.

Consider a steady thermal input Q_0 at $x = 0$ and $y = 0$ in an extensive ambient medium at temperature t_∞. Then the thermal energy $Q(x)$ convected in the resulting plume must be the same for all $x > 0$ and equal to Q_0, since there are no sources or sinks in the plume. The center-line temperature is denoted by $t_0(x)$. Employing the similarity

[1] Tata Consulting Engineers, Carnac, Bombay, India.

[2] Department of Mechanical Engineering, Indian Institute of Technology, Kanpur 208016, India. Mem. ASME.

Manuscript received by ASME Applied Mechanics Division, May, 1979; final revision, November, 1979.

variable η, the generalized temperature $\phi(\eta)$ and the dimensionless stream function $f(\eta)$ are

$$\phi = \frac{t - t_\infty}{t_0 - t_\infty}, \quad \psi = xf(\eta), \quad \eta = \frac{y}{x}(\mathrm{Gr}_x)^{1/4} \tag{2}$$

with $yu = \psi_y$, $yv = -\psi_x$, and $\mathrm{Gr}_x = g\beta x^3 (t_0 - t_\infty)/\nu^2$

The total convected thermal energy at any location is given by

$$Q(x) = \int_0^\infty \rho C_p (t - t_\infty) u 2\pi y dy$$

$$= 2\pi\nu\rho C_p (t_0 - t_\infty)\, x \int_0^\infty \phi f' d\eta = Q_0 \tag{3}$$

where ρ is the density of the fluid and C_p the specific heat at constant pressure. Therefore, the center-line temperature varies as x^{-1} for an axisymmetric plume and is given as

$$t_0 - t_\infty = \frac{Q_0}{2\pi\mu C_p I x} \quad \text{where} \quad I = \int_0^\infty f'\phi d\eta \tag{4}$$

The governing differential equations for $t_0 - t_\infty = N/x$, where N is a constant, are obtained as

$$f''' + (f - 1)\left(\frac{f'}{\eta}\right)' + \eta\phi = 0 \tag{5a}$$

$$(\eta\phi')' + \mathrm{Pr}\,(f\phi)' = 0 \tag{5b}$$

where the primes denote differentiation with respect to η.

The velocity components are obtained as

$$u = \frac{\nu}{x}\sqrt{\mathrm{Gr}_x}\left(\frac{f'}{\eta}\right) \quad \text{and} \quad v = -\frac{\nu}{x}(\mathrm{Gr}_x)^{1/4}\left(\frac{f}{\eta} - \frac{f'}{2}\right) \tag{6}$$

The five independent boundary conditions for the aforementioned system of equations can be shown to be [2]

$$\phi'(0) = f(0) = f'(0) = 1 - \phi(0) = \frac{f'}{\eta}(\infty) = 0 \tag{7}$$

Let us now consider a laminar vertical stream flow past an axisymmetric plume. The problem then concerns a steady thermal input Q_0 at $x = 0$ and $y = 0$ in an extensive laminar vertical stream flow at velocity u_∞ and temperature t_∞. The boundary-layer equations are the same as those previously given, equation (1). However, the boundary condition pertaining to the vertical velocity in the ambient medium is altered.

$$\frac{\nu}{x}\sqrt{\mathrm{Gr}_x}\left(\frac{f'}{\eta}\right) \to \pm u_\infty \text{ as } \eta \to \infty$$

This gives

$$\frac{f'}{\eta} \to \pm \frac{\mathrm{Re}_x}{\sqrt{\mathrm{Gr}_x}} = \pm\epsilon(x) \text{ as } \eta \to \infty \tag{8}$$

where

$$\mathrm{Re}_x = \frac{u_\infty x}{\nu}$$

The foregoing parameter, $\mathrm{Re}_x/\sqrt{\mathrm{Gr}_x}$, indicates the relative magnitude of the forced convection effects, compared to the natural convection mechanisms. The plus sign refers to aiding flow and the negative to opposing flow. Since this parameter, denoted as $\epsilon(x)$, is obtained as a function of x for the vertical surface, similarity solutions can not be obtained.

However, in the present case, an interesting circumstance arises. As has been shown by Fujii [1] and others, the center-line velocity is not a function of x in an axisymmetric plume but is a constant. This result arises because of the fact that Gr_x varies with x as x^2, the temperature dependence on x being x^{-1}, and this results in u being independent of x from equation (6). The external velocity u_∞ is also taken as independent of x. The relative magnitude of forced convection compared to natural convection is, therefore, expected to be independent of x. Since ϵ is independent of x, the constancy of $Q(x)$ downstream is maintained for a linear decrease in the center-line temperature.

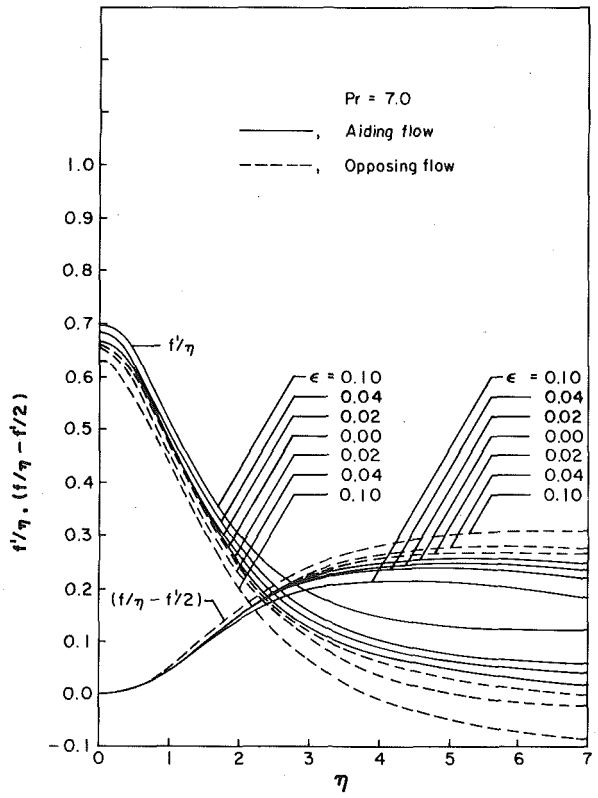

Fig. 1 Axial and radial velocity profiles for aiding and opposing flows at Pr = 7.0

Therefore, the problem of the axisymmetric plume flow in the presence of the perturbing effect of an external laminar stream is governed by equation (5), along with the boundary conditions

$$\phi'(0) = f(0) = f'(0) = 1 - \phi(0) = 0,$$

and

$$\frac{f'}{\eta}(\infty) = \pm\epsilon \tag{9}$$

where ϵ is a constant. A perturbing effect is considered so that the basic natural convection mechanisms dominate. Numerical solution was obtained by means of the fourth-order Runge-Kutta integration scheme and the results obtained are discussed as follows.

Numerical Results

Results were obtained for Prandtl number values of 7.0 and 0.7, which correspond essentially to water and air, and at various values of the forced convection parameter ϵ. Fig. 1 shows the corresponding profiles for Pr = 7.0. The axial velocity component approaches the free-stream velocity outside the boundary layer and the radial velocity component rises from its value of zero at the center line, due to symmetry, to indicate the entrainment at the edge of the boundary layer. With aiding forced convection effects, a positive free-stream velocity is present and with opposing a negative one. The center-line velocity is found to increase with aiding effects and to decrease with opposing effects. Opposing flow tends to curb the vertically rising natural convection flow and thus cause a thickening of the boundary layer.

A very similar behavior is seen in Fig. 2 for Pr = 0.7. The effect on the center-line velocity is, however, found to be essentially negligible in this case. This is obviously related to the larger viscous effects in the case of the higher Prandtl number. The effect on the temperature field is shown for Pr = 7.0 in Fig. 3. The effect is obviously quite small over the range of ϵ considered. An aiding flow, with a narrower boundary layer and a more effective heat transfer mechanism, gives rise to lower temperatures in the boundary layer.

The percentage effect on the center-line velocity and temperature,

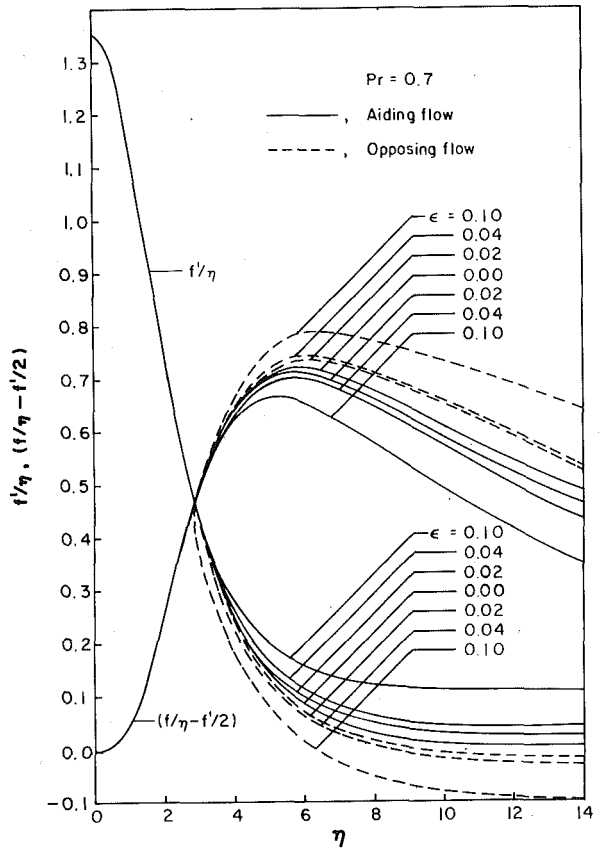

Fig. 2 Axial and radial velocity profiles for aiding and opposing flows at Pr = 0.7

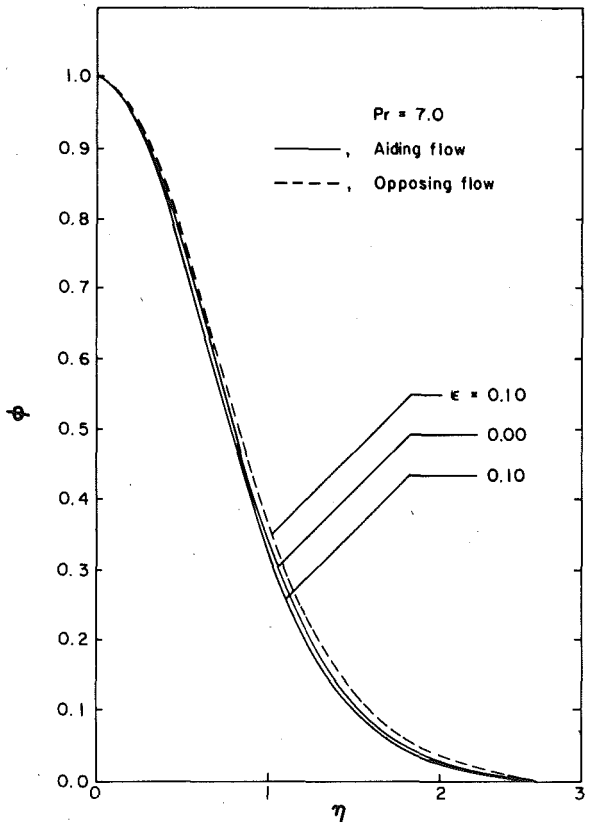

Fig. 3 Temperature profiles for aiding and opposing flows at Pr = 7.0

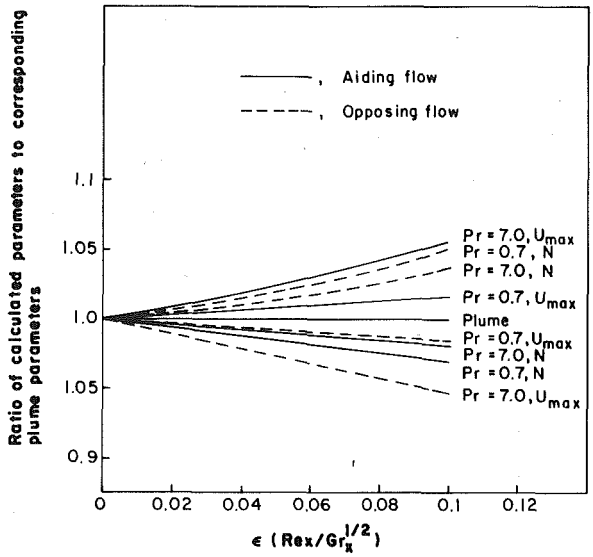

Fig. 4 Comparison of the computed values of N and U_{max}, for the present problem, to those of an axisymmetric plume, as functions of ϵ

as compared to those for an axisymmetric plume, is shown as a function of ϵ in Fig. 4. Aiding flow increases the center-line velocity, U_{max}, by about 5 percent for Pr = 7.0 at $\epsilon = 0.1$, whereas the effect is only about 1 percent for Pr = 0.7. Opposing flow decreases the center-line velocity in a similar manner. The center-line temperature given in terms of N, where $t_0 - t_\infty = N/x$, indicates an increase of about 5 percent at Pr = 0.7 for opposing flow at $\epsilon = 0.1$. The effect is smaller at Pr = 7.0. Similarly, aiding flow decreases the center-line temperature as just discussed. This study, therefore, indicates the effect of an externally induced flow on the plume flow parameters and determines the resulting profiles as a function of the mixed convection parameter ϵ, for circumstances where the external flow is a small perturbation on the natural convection flow.

Acknowledgments

The authors acknowledge the support of the Council of Scientific and Industrial Research, India, for this work.

References

1 Fujii, T., "Theory of Steady Laminar Natural Convection Above a Horizontal Line Heat Source and a Point Heat Source," *International Journal of Heat and Mass Transfer*, Vol. 6, 1963, pp. 597–606.

2 Mollendorf, J. C., and Gebhart, B., "Axisymmetric Natural Convection Flows Resulting From the Combined Buoyancy Effects of Thermal and Mass Diffusion," Fifth International Heat Transfer Conference, Tokyo, 1974.

3 Seely, J. H., and Chu, R. C., *Heat Transfer in Microelectronic Equipment: A Practical Guide*, Marcel Dekker, 1972.

4 Merkin, J. H., "The Effect of Buoyancy Forces on the Boundary Layer Flow Over a Semi-Infinite Vertical Plate in a Uniform Free Stream," *Journal of Fluid Mechanics*, Vol. 35, 1969, pp. 439–450.

5 Mollendorf, J. C., and Gebhart, B., "Thermal Buoyancy in Round Laminar Vertical Jets," *International Journal of Heat and Mass Transfer*, Vol. 16, 1973, pp. 735–745.

A Note on Optimal Conical Shells

R. Reiss[1]

Introduction

A least weight criterion for thin sandwich conical shells of circular

[1] Associate Professor, Department of Mechanical Engineering, Howard University, Washington, D.C. 20059. Assoc. Mem. ASME.

Manuscript received by ASME Applied Mechanics Division, October, 1979.

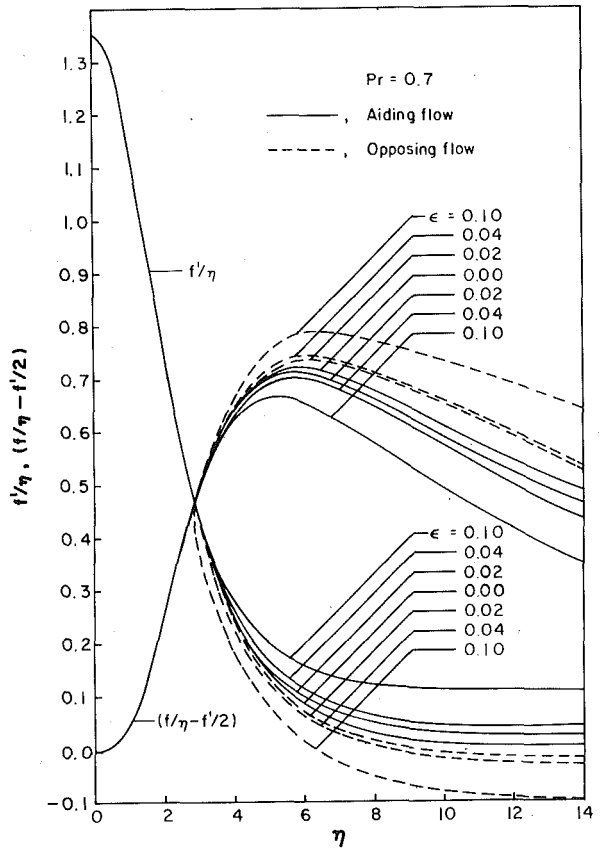

Fig. 2 Axial and radial velocity profiles for aiding and opposing flows at Pr = 0.7

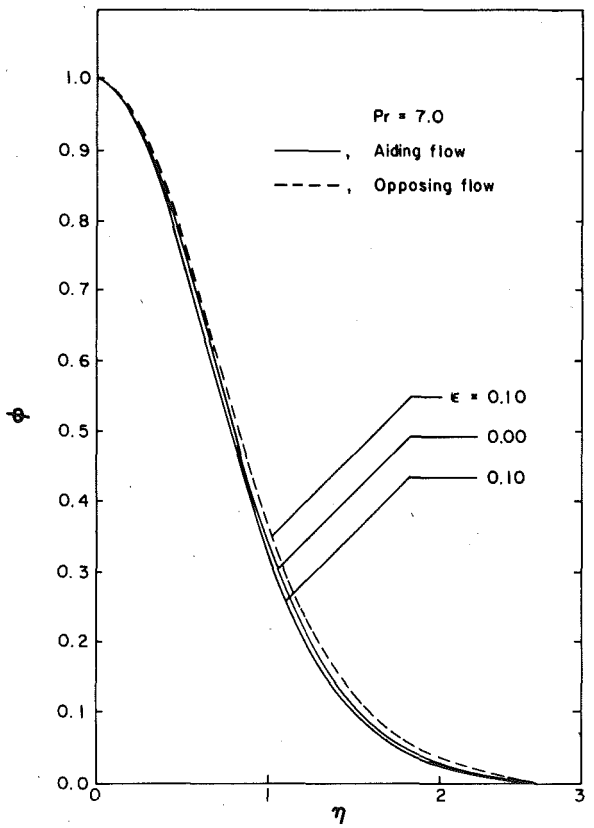

Fig. 3 Temperature profiles for aiding and opposing flows at Pr = 7.0

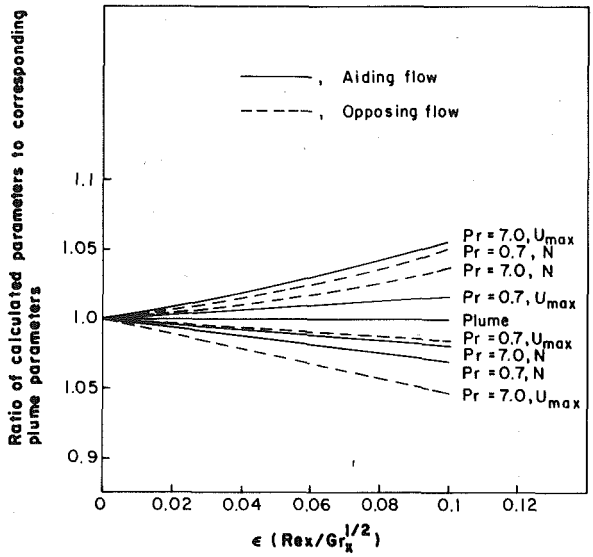

Fig. 4 Comparison of the computed values of N and U_{max}, for the present problem, to those of an axisymmetric plume, as functions of ϵ

as compared to those for an axisymmetric plume, is shown as a function of ϵ in Fig. 4. Aiding flow increases the center-line velocity, U_{max}, by about 5 percent for Pr = 7.0 at $\epsilon = 0.1$, whereas the effect is only about 1 percent for Pr = 0.7. Opposing flow decreases the center-line velocity in a similar manner. The center-line temperature given in terms of N, where $t_0 - t_\infty = N/x$, indicates an increase of about 5 percent at Pr = 0.7 for opposing flow at $\epsilon = 0.1$. The effect is smaller at Pr = 7.0. Similarly, aiding flow decreases the center-line temperature as just discussed. This study, therefore, indicates the effect of an externally induced flow on the plume flow parameters and determines the resulting profiles as a function of the mixed convection parameter ϵ, for circumstances where the external flow is a small perturbation on the natural convection flow.

Acknowledgments

The authors acknowledge the support of the Council of Scientific and Industrial Research, India, for this work.

References

1 Fujii, T., "Theory of Steady Laminar Natural Convection Above a Horizontal Line Heat Source and a Point Heat Source," *International Journal of Heat and Mass Transfer*, Vol. 6, 1963, pp. 597–606.

2 Mollendorf, J. C., and Gebhart, B., "Axisymmetric Natural Convection Flows Resulting From the Combined Buoyancy Effects of Thermal and Mass Diffusion," Fifth International Heat Transfer Conference, Tokyo, 1974.

3 Seely, J. H., and Chu, R. C., *Heat Transfer in Microelectronic Equipment: A Practical Guide*, Marcel Dekker, 1972.

4 Merkin, J. H., "The Effect of Buoyancy Forces on the Boundary Layer Flow Over a Semi-Infinite Vertical Plate in a Uniform Free Stream," *Journal of Fluid Mechanics*, Vol. 35, 1969, pp. 439–450.

5 Mollendorf, J. C., and Gebhart, B., "Thermal Buoyancy in Round Laminar Vertical Jets," *International Journal of Heat and Mass Transfer*, Vol. 16, 1973, pp. 735–745.

A Note on Optimal Conical Shells

R. Reiss[1]

Introduction

A least weight criterion for thin sandwich conical shells of circular

[1] Associate Professor, Department of Mechanical Engineering, Howard University, Washington, D.C. 20059. Assoc. Mem. ASME.

Manuscript received by ASME Applied Mechanics Division, October, 1979.

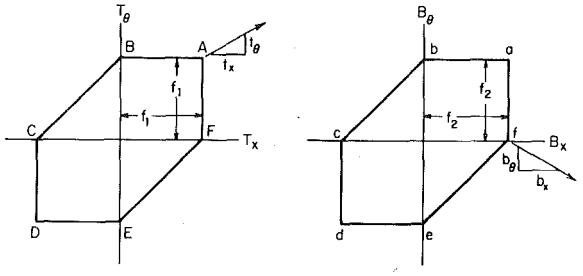

Fig. 1 Tresca yield condition

cross section, whose rigid-plastic face sheets obey the Tresca yield condition, was recently presented [1]. The optimality criterion, a generalization of the constant energy dissipation theorem [2], was developed by allowing the thickness of each face sheet to vary independently, and applied to a conical frustrum with rollers at its outer edge and constrained against rotation at its inner edge.

In the present Note, the theory [1] 1s applied to conical frustrums with hinged and clamped outer edges.

Basic Equations

For axisymmetric loading, the nondimensionalized[2] equations of equilibrium are

$$d(rT_x)/dr - T_\theta + r(p_x + s) = d(rB_x)/dr - B_\theta + r(p_x - s) = 0,$$
$$T_x + B_x + 4s = 4w/r. \tag{1}$$

To equations (1), we adjoin the compatibility conditions on the generalized strain rates

$$t_x - d(rt_\theta)/dr = b_x - d(rb_\theta)/dr = r(t_\theta - b_\theta)/4, \tag{2}$$

and the optimality conditions

$$T_x t_x + T_\theta t_\theta = f_1, \quad B_x b_x + B_\theta b_\theta = f_2. \tag{3}$$

With the adoption of the Tresca yield condition (Fig. 1), Euler's theorem for homogeneous functions, flow law, and equation (3) may be used to show that

$$t_i = \partial f_1/\partial T_i, \quad b_i = \partial f_2/\partial B_i \quad (i = x, \theta) \tag{4}$$

Equations (1)–(4), subject to continuity of T_x, B_x, t_θ, and b_θ are solved by assuming that appropriate stress regimes apply for certain regions of the shell. For example, the stress regime (A, d), together with equations (2) and (3) will yield a solution for the strain rates. If the resulting strain rates satisfy the normality requirements imposed by equations (4) and if the stresses obtained from equations (1) lead to non-negative thicknesses, then the solution obtained will be optimal.

It has been previously established [1] that the only stress regimes compabible with equation (4) are:

1 Any combination of corners, excluding B and E.
2 Side $CD(AF)$ and corner $c(f)$.
3 Side $bc(ef)$ and corner $C(F)$.

Examples

In each of the following examples, it is assumed that a central boss is rigidly attached to the shell's inner edge, and that the load $w(r)$ is non-negative.

Hinged Outer Edge. The boundary conditions at the inner radius r_a are $t_\theta = b_\theta = 0$. Equations (2), evaluated at r_a implies $t_\theta t_x \geq 0$ and $b_\theta b_x \geq 0$ near r_a. Therefore, the appropriate regime must consist of the corners A or D and a or d. Anticipating that $N_x \geq 0$, $M_x \leq 0$ and $\epsilon_\theta = b_\theta + t_\theta \leq 0$, where ϵ_θ is the strain rate associated with N_θ, it follows that the regime for the inner region $r_a \leq r \leq r_1$ is (A,d), hence equations (2) furnish

$$t_{\theta,x} = (r^2 \mp r_a{}^2)/2r^2 \mp (r + 2r_a)(r - r_a)^2/12r^2 \geq 0,$$
$$b_{\theta,x} = -(r^2 \mp r_a{}^2)/2r^2 \mp (r + 2r_a)(r - r_a)^2/12r^2 \leq 0. \tag{5}$$

It can easily be shown that these inequalities are satisfied provided

$$r_1 \leq r^* = 3 - r_a/2 + [(r_a/2 + 3)^2 + 2r_a{}^2]^{1/2}, \tag{6}$$

where r^* satisfies $t_\theta(r^*) = 0$ and $b_\theta(r^*) < 0$.

Since equations (5) require $\epsilon_\theta < 0$ for $r_a \leq r \leq r_1$, the kinematic condition at the hinged outer edge $b_\theta(r_b) + t_\theta(r_b) = 0$ can be satisfied only if the solution consists of at least one more regime. At the outer edge M_x vanishes and N_x is positive. Thus, both T_x and B_x are positive near r_b so that the only admissible regimes are (A or F; a or f). Assuming the solution consists of but two regimes, $b_\theta(r_1) < 0$ and $\epsilon_\theta(r_b) = 0$ requires that $t_\theta(r_b) \geq 0$. This suggests choosing (A,f) for the outer region $r_1 \leq r \leq r_b$, so that

$$t_\theta = r^{-1}[C_1 I_2(\sqrt{r}) + C_2 K_2(\sqrt{r})] \geq 0, \quad t_x = 1 - t_\theta \geq 0,$$
$$-1 \leq b_\theta = r^{-1}[-4 + C_1 I_0(\sqrt{r}) + C_2 K_0(\sqrt{r})] \leq 0, \quad b_x \equiv 1, \tag{7}$$

where I_n and K_n are modified Bessel functions of the first and second kind, respectively. The constants C_1 and C_2, determined from the continuity requirements on t_θ and b_θ, are

$$C_1 = -r_1[\xi r_1 K_0(\sqrt{r_1}) + (\eta r_1 - 4)K_2(\sqrt{r_1})]/2,$$
$$C_2 = r_1[\xi r_1 I_0(\sqrt{r_1}) + (\eta r_1 - 4)I_2(\sqrt{r_1})]/2, \tag{8}$$

where $0 \leq \xi \equiv t_\theta(r_1) < \eta \equiv b_\theta(r_1) < 1$. The critical radius r_1 separating the two regions and determined from $\epsilon_\theta(r_b) = 0$, must be such that the inequalitites in (6) and (7) are satisfied.

The determination of r_1 is best accomplished numerically. However, it can be shown that $C_1 > 0$, and if we let $r_{\max}$ be the solution to $C_1 = 0$ for r_1, then $r_1 < r_{\max} < r^*$ and $r_1 \to r_{\max}$ corresponds to $r_b \to \infty$. Furthermore, it may be shown that inequalities (7) are always satisfied, so that the two regime solution (5) and (7) is always kinematically admissible.

The generalized stresses are determined from the equilibrium equations (1), $T_x = T_\theta$, $B_x = B_\theta$ for $r < r_1$ and $B_\theta = 0$ for $r \geq r_1$ subject to continuity of B_x at r_1 and the statical condition $T_x(r_b) = B_x(r_b)$. If the resulting stresses satisfy $T_x \geq 0$ everywhere and $B_x \leq 0$ for $r \leq r_1$ and $B_x \geq 0$ for $r \geq r_1$, then they are minimal. In particular, if the loading consists of a concentrated load applied to the central boss, $w = w_0$, it is straightforward to show that these inequalities are indeed satisfied.

Clamped Outer Edge. Suppose now that the outer edge $r = r_b$ is clamped. Arguments identical to those for the preceding example again lead to the regime (A, d) for the inner region $r_a \leq r \leq r_1$, where r_1 satisfies inequality (6) and the strain rates are given by equation (5).

At the outer edge, the support conditions require $t_\theta(r_b) = b_\theta(r_b) = 0$. Evaluation of equations (2) at r_b shows that $t_x t_\theta \leq 0$ and $b_x b_\theta \leq 0$ near the outer edge. The regime near that edge, therefore, consists of the corners C or F and c or f: Anticipating that $N_x \geq 0$, $M_x \geq 0$ and $\epsilon_x = b_x + t_x \geq 0$, the regime (C, f) for the outer region $r_2 \leq r \leq r_b$ is obtained. Integration of equations (2) now furnishes

$$1 \geq t_\theta = (1/4r)(r - r_b)(r - r_b - 4) > 0, \quad t_x \equiv -1,$$
$$-1 \leq b_\theta = (1/4r)(r - r_b)(r - r_b + 4) < 0, \quad b_x \equiv 1. \tag{9}$$

Equations (9) will satisfy their appropriate inequalities if $r_2 \geq r_{\min}$ where

$$r_{\min} = \begin{cases} r_b + 4 - 2(4 + r_b)^{1/2} & \text{for} \quad r_b \leq 12 \\ r_b - 4 & \text{for} \quad r_b \geq 12 \end{cases}. \tag{10}$$

For $r_b \leq 12$, $t_\theta(r_{\min}) = 1$ and for $r_b \geq 12$, $b_\theta(r_{\min}) = 0$.

Since $t_\theta(r_1) + b_\theta(r_1) < 0$ and $t_\theta(r_2) + b_\theta(r_2) > 0$, it follows that $r_1 < r_2$ and at least one intermediate region $r_1 < r < r_2$ exists. Assuming

[2] For a definition of all nondimensionalized variables used in this Note, see Reference [1].

a three-regime solution, the condition $t_\theta(r_2) > 0$, $-1 < b_\theta(r_1) < 0$ and $N_x \geq 0$ lead to regime (A, f) for the middle region. Therefore the strain rates are still given by equations (7) and (8). The two critical radii r_1 and r_2 are determined from continuity of t_θ and b_θ at r_2. Thus

$$C_1 = -r_2[\rho r_2 K_0(\sqrt{r_2}) + (\gamma r_2 - 4)K_2(\sqrt{r_2})]/2,$$
$$C_2 = r_2[\rho r_2 I_0(\sqrt{r_2}) + (\gamma r_2 - 4)I_2(\sqrt{r_2})]/2, \quad (11)$$

where $\rho \equiv t_\theta(r_2)$ and $\gamma \equiv -b_\theta(r_2)$. The existence of r_1 and r_2 where $r_1 < r_{\max}$ and $r_2 \geq r_{\min}$ may easily be established numerically be solving equations (8) and (11) for given r_a and r_b.

Once again, it may be shown that the inequalities imposed by (7) on the strain rates are satisfied, so that the three regime solution (A, d), (A, f) and (C, f) is always kinematically admissible. If the stresses, obtained from equations (1) corresponding to each regime satisfy $T_x \geq 0$, $B_x \leq 0$ for $r < r_1$, $T_x \geq 0$, $B_x \geq 0$ for $r_1 < r < r_2$ and $T_x \leq 0$, $B_x \geq 0$ for $r \geq r_2$, then they are the minimal stresses. In particular, these inequalities will be satisifed for a concentrated load applied to the central boss.

Summary

Optimal designs for cones which are either hinged or clamped at the outer edge have been presented for a certain class of loads. The designs are completely determined by the sequence of minimal regimes. For the hinged shell these regimes were (A, d) and (A, f), and for the clamped shell they were found to be $(A, d)(A, f)$ and (C, f). If $r_b \gg r_a$, which is often the case, the region governed by the regime (A, f) will consist of almost the entire domain of the shell. The regime (A, d) is necessary merely to meet the fixed inner edge condition, and in the case of the clamped shell the regime (C, f) is needed near the outer edge for the same purpose.

References

1 Reiss, R., "Minimal Weight Design for Conical Shells," ASME JOURNAL OF APPLIED MECHANICS, Vol. 41, Sept. 1974, pp. 599–603.

2 Drucker, D. C., and Shield, R. T., "Design for Minimum Weight," *Proceedings of the 9th International Congress of Applied Mechanics*, Vol. 5, Brussels, 1956, pp. 212–222.

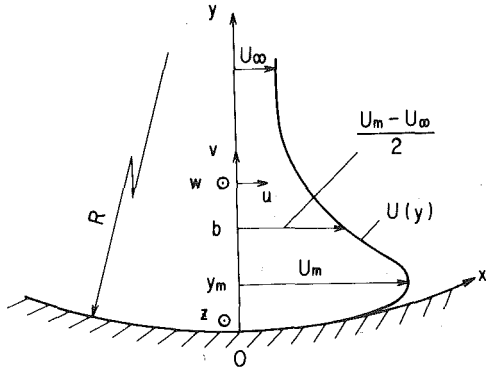

Fig. 1 Wall jet and coordinate system

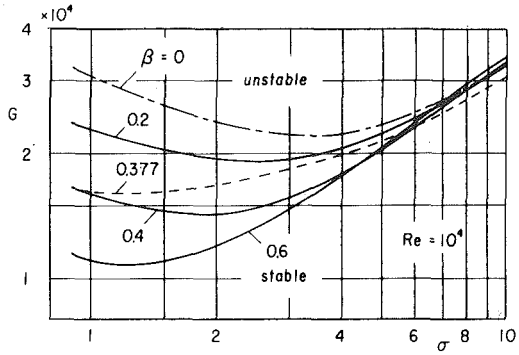

Fig. 2 Neutral stability curves for turbulent wall jet

Taylor-Görtler Instability of Turbulent Wall Jets Along Concave Surfaces

R. Kobayashi[1] and N. Fujisawa[2]

Turbulent wall jets have attracted considerable attention, because they are concerned in boundary-layer control and heating, cooling, drying or thermal insulation of solid surfaces. The purpose of this Note is to consider a critical condition for Taylor-Görtler instability of a turbulent wall jet along a concave wall, as a result of which longitudinal vortices are expected to occur as secondary flow in the wall jet. The appearance of the longitudinal vortices might influence momentum, heat, and mass transfer in turbulent wall jets. Tani [1] first found experimentally the longitudinal vortices appearing in turbulent boundary layers along concave walls, and Sandmayr [2] made theoretical consideration for the instability problem of the turbulent boundary layer, in which an eddy-viscosity concept was used for the Reynolds stress. For wall jets, Kahawita [3] and Kobayashi and Tomita [4] studied a laminar flow case. Kobayashi, et al. [4], also considered a turbulent wall jet in a still fluid. Wall jets are often applied in a moving stream, where a ratio (β) of the free-stream velocity to the maximum velocity in the wall jet varies downstream. We consider here the Taylor-Görtler instability of turbulent wall jets for various values of the ratio β.

Theory

An orthogonal curvilinear coordinate system (x, y, z) is taken as shown in Fig. 1. A free stream with a uniform velocity U_∞ and also a two-dimensional incompressible wall jet are directed along the axis x. The radius R of the curvature on the wall remains constant in the x-direction and is far larger than the thickness b of the wall jet. In turbulent wall jets, it is known that a location of zero Reynolds stress ($\tau_R = 0$) does not coincide with a position of maximum velocity. Although an eddy-viscosity concept breaks down at the position of maximum velocity, we use the eddy-viscosity ϵ for the turbulent wall jets, as the primary consideration, in order to relate the Reynolds stress to the basic flow field. We shall now suppose that the basic turbulent wall jet is slightly perturbed with the type of longitudinal vortices, which may be expressed as

$$u = U(y) + \hat{u}(y)e^{\gamma t}\cos \alpha z,$$
$$v = \hat{v}(y)e^{\gamma t}\cos \alpha z, \quad w = \hat{w}(y)e^{\gamma t}\sin \alpha z \quad (1)$$

with the wavenumber α and a measure γ of the growth rate of the disturbances. We obtain finally a set of perturbation equations governing the present linear instability problem in the neutral state ($\gamma = 0$) as follows:

$$M\overline{u}'' + M'\overline{u}' - \sigma^2 M\overline{u} = \overline{U'v}, \quad (2)$$

$$M\overline{v}^{(4)} + 2M'\overline{v}''' + (M'' - 2\sigma^2 M)\overline{v}'' - 2\sigma^2 M'\overline{v}' + \sigma^2(M'' + \sigma^2 M)\overline{v} = -2\sigma^2 G^2 \overline{U}\overline{u}, \quad (3)$$

$$\overline{v}' + \sigma\overline{w} = 0, \quad (4)$$

[1] Professor, Institute of High Speed Mechanics, Tohoku University, Sendai, Japan.

[2] Graduate student of Tohoku University.

Manuscript received by ASME Applied Mechanics Division, July, 1979.

a three-regime solution, the condition $t_\theta(r_2) > 0$, $-1 < b_\theta(r_1) < 0$ and $N_x \geq 0$ lead to regime (A, f) for the middle region. Therefore the strain rates are still given by equations (7) and (8). The two critical radii r_1 and r_2 are determined from continuity of t_θ and b_θ at r_2. Thus

$$C_1 = -r_2[\rho r_2 K_0(\sqrt{r_2}) + (\gamma r_2 - 4)K_2(\sqrt{r_2})]/2,$$
$$C_2 = r_2[\rho r_2 I_0(\sqrt{r_2}) + (\gamma r_2 - 4)I_2(\sqrt{r_2})]/2, \quad (11)$$

where $\rho \equiv t_\theta(r_2)$ and $\gamma \equiv -b_\theta(r_2)$. The existence of r_1 and r_2 where $r_1 < r_{\max}$ and $r_2 \geq r_{\min}$ may easily be established numerically be solving equations (8) and (11) for given r_a and r_b.

Once again, it may be shown that the inequalities imposed by (7) on the strain rates are satisfied, so that the three regime solution (A, d), (A, f) and (C, f) is always kinematically admissible. If the stresses, obtained from equations (1) corresponding to each regime satisfy $T_x \geq 0$, $B_x \leq 0$ for $r < r_1$, $T_x \geq 0$, $B_x \geq 0$ for $r_1 < r < r_2$ and $T_x \leq 0$, $B_x \geq 0$ for $r \geq r_2$, then they are the minimal stresses. In particular, these inequalities will be satisifed for a concentrated load applied to the central boss.

Summary

Optimal designs for cones which are either hinged or clamped at the outer edge have been presented for a certain class of loads. The designs are completely determined by the sequence of minimal regimes. For the hinged shell these regimes were (A, d) and (A, f), and for the clamped shell they were found to be $(A, d)(A, f)$ and (C, f). If $r_b \gg r_a$, which is often the case, the region governed by the regime (A, f) will consist of almost the entire domain of the shell. The regime (A, d) is necessary merely to meet the fixed inner edge condition, and in the case of the clamped shell the regime (C, f) is needed near the outer edge for the same purpose.

References

1 Reiss, R., "Minimal Weight Design for Conical Shells," ASME JOURNAL OF APPLIED MECHANICS, Vol. 41, Sept. 1974, pp. 599–603.

2 Drucker, D. C., and Shield, R. T., "Design for Minimum Weight," *Proceedings of the 9th International Congress of Applied Mechanics*, Vol. 5, Brussels, 1956, pp. 212–222.

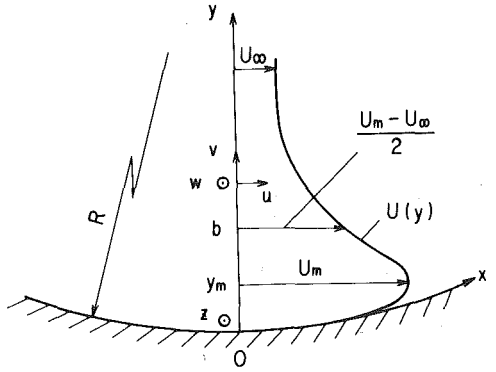

Fig. 1 Wall jet and coordinate system

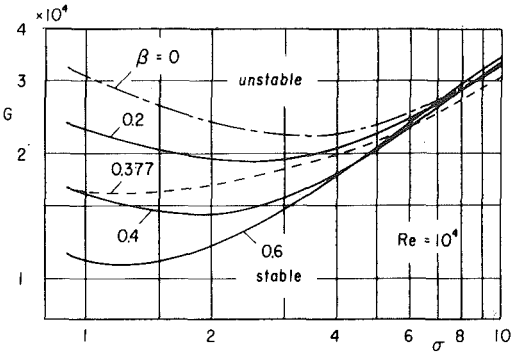

Fig. 2 Neutral stability curves for turbulent wall jet

Taylor-Görtler Instability of Turbulent Wall Jets Along Concave Surfaces

R. Kobayashi[1] and N. Fujisawa[2]

Turbulent wall jets have attracted considerable attention, because they are concerned in boundary-layer control and heating, cooling, drying or thermal insulation of solid surfaces. The purpose of this Note is to consider a critical condition for Taylor-Görtler instability of a turbulent wall jet along a concave wall, as a result of which longitudinal vortices are expected to occur as secondary flow in the wall jet. The appearance of the longitudinal vortices might influence momentum, heat, and mass transfer in turbulent wall jets. Tani [1] first found experimentally the longitudinal vortices appearing in turbulent boundary layers along concave walls, and Sandmayr [2] made theoretical consideration for the instability problem of the turbulent boundary layer, in which an eddy-viscosity concept was used for the Reynolds stress. For wall jets, Kahawita [3] and Kobayashi and Tomita [4] studied a laminar flow case. Kobayashi, et al. [4], also considered a turbulent wall jet in a still fluid. Wall jets are often applied in a moving stream, where a ratio (β) of the free-stream velocity to the maximum velocity in the wall jet varies downstream. We consider here the Taylor-Görtler instability of turbulent wall jets for various values of the ratio β.

Theory

An orthogonal curvilinear coordinate system (x, y, z) is taken as shown in Fig. 1. A free stream with a uniform velocity U_∞ and also a two-dimensional incompressible wall jet are directed along the axis x. The radius R of the curvature on the wall remains constant in the x-direction and is far larger than the thickness b of the wall jet. In turbulent wall jets, it is known that a location of zero Reynolds stress ($\tau_R = 0$) does not coincide with a position of maximum velocity. Although an eddy-viscosity concept breaks down at the position of maximum velocity, we use the eddy-viscosity ϵ for the turbulent wall jets, as the primary consideration, in order to relate the Reynolds stress to the basic flow field. We shall now suppose that the basic turbulent wall jet is slightly perturbed with the type of longitudinal vortices, which may be expressed as

$$u = U(y) + \hat{u}(y)e^{\gamma t}\cos \alpha z,$$
$$v = \hat{v}(y)e^{\gamma t}\cos \alpha z, \quad w = \hat{w}(y)e^{\gamma t}\sin \alpha z \quad (1)$$

with the wavenumber α and a measure γ of the growth rate of the disturbances. We obtain finally a set of perturbation equations governing the present linear instability problem in the neutral state ($\gamma = 0$) as follows:

$$M\overline{u}'' + M'\overline{u}' - \sigma^2 M\overline{u} = \overline{U'v}, \quad (2)$$

$$M\overline{v}^{(4)} + 2M'\overline{v}''' + (M'' - 2\sigma^2 M)\overline{v}'' - 2\sigma^2 M'\overline{v}' + \sigma^2(M'' + \sigma^2 M)\overline{v} = -2\sigma^2 G^2 \overline{U}\overline{u}, \quad (3)$$

$$\overline{v}' + \sigma\overline{w} = 0, \quad (4)$$

[1] Professor, Institute of High Speed Mechanics, Tohoku University, Sendai, Japan.

[2] Graduate student of Tohoku University.

Manuscript received by ASME Applied Mechanics Division, July, 1979.

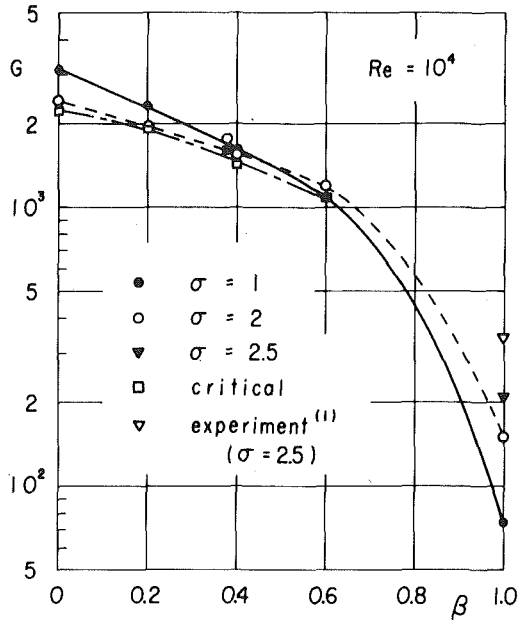

Fig. 3 Variations of G in neutral state with the velocity ratio β

where the primes denote differentiation with respect to η ($= y/y_m$), and $\overline{U} = U/U_m$, $\overline{u} = \hat{u}/U_m$, $\overline{v} = \hat{v}y_m/\nu$, $\overline{w} = \hat{w}y_m/\nu$, $\sigma = \alpha y_m$, $G = \mathrm{Re}\sqrt{y_m/R}$, $\mathrm{Re} = U_m y_m/\nu$, $M = (\mu + \rho\epsilon)/\mu$ (ρ: the density of the fluid, μ: its viscosity, ν: the kinematic viscosity). G is called the Görtler parameter, and Re is the Reynolds number.

The boundary conditions which arise from the requirements of no slip at the wall ($\eta = 0$) and of disappearance as $\eta \to \infty$ are $\overline{u} = \overline{v} = \overline{v}' = 0$ in view of continuity equation (4).

Results and Discussions

The present instability problem is now reduced to find the Görtler parameter G as an eigenvalue together with two components $\overline{u}(\eta)$ and $\overline{v}(\eta)$ of the perturbation velocities as eigenfunctions. $\overline{w}(\eta)$ is then obtained from equation (4). The set of the differential equations (2) and (3) was numerically solved by finite-difference technique and successive approximation procedure. Fig. 2 shows neutral stability curves in relation of the Görtler parameter G to the dimensionless wavenumber σ of the longitudinal vortices for several values of the velocity ratio $\beta = U_\infty/U_m$, where the stable range is below each neutral curve. Because detail data for distributions of the velocity $U(y)$ and the Reynolds stress in the turbulent wall jet along a concave wall are absent, we used in the present calculations the experimental results by Bradshaw and Gee [5] for a turbulent wall jet along a flat plate in a case of $\beta = 0$, by Irwin [6] for $\beta = 0.377$ and by Kruka and Eskinazi [7] for $\beta = 0.2$, 0.4, and 0.6. Fig. 2 indicates that, as the velocity ratio β increases, the stable range becomes smaller and the critical Görtler parameter (G_c) and the associated wavenumber (σ_c) are decreased. Fig. 2 is in a case of the Reynolds number $\mathrm{Re} = 10^4$. Calculations for different values of the Reynolds number ($\mathrm{Re} = 5 \times 10^3 \sim 2 \times 10^5$) show that the value of G in the neutral state increases with increasing Reynolds number as a function $G \sim \mathrm{Re}^n$ with $n = 1.0 \sim 1.1$ for $\beta = 0 \sim 0.6$.

Further calculations were carried out for $\beta = 1$, which corresponds to a turbulent boundary layer. Experimental values of the Reynolds stress by Klebanoff [8] were used in order to obtain a neutral stability curve. It was found that the parameter G in the neutral condition increases with Re, where n is $0.3 \sim 0.5$ in the same range of Re in the wall jets.

Fig. 3 shows the effect of the velocity ratio β to the parameter G in the neutral condition for $\sigma = 1$, 2, 2.5, and also at the critical condition. It is concluded from Fig. 3 that turbulent wall jets are more stable for occurrence of the longitudinal vortices than turbulent boundary layers, and that turbulent wall jets with less β are more stable. The fact comes from an increase of the eddy-viscosity ϵ in wall jets with less β.

References

1 Tani, I., "Production of Longitudinal Vortices in the Boundary Layer Along a Concave Wall," *Journal of Geophysical Research*, Vol. 67, No. 8, 1962, pp. 3075–3080.

2 Sandmayr, G., "Über das Auftreten von Längswirbeln in turbulenten Grenzschichten an konkaven Wänden," *Deutsche Luft-und Raumfahrt Forschungsbericht*, 66–41, June 1966, DVL-Bericht No. 504.

3 Kahawita, R. A., "Instability of Laminar Wall Jets Along Curved Surfaces," *AIAA Journal*, Vol. 13, No. 11, 1975, pp. 1517–1518.

4 Kobayashi, R., and Tomita, T., "Instability of Wall Jets Along Concave Walls," in Japanese, *Memoirs of Institute of High Speed Mechanics*, Tohoku University, Sendai, Japan, Vol. 40, No. 371, 1977, pp. 51–73.

5 Bradshaw, P., and Gee, M. T., "Turbulent Wall Jets With and Without an External Stream," A.R.C., R. & M., No. 3252, 1960.

6 Irwin, H. P. A. H., "Measurements in a Self-Preserving Plane Wall Jet in a Positive Pressure Gradient," *Journal of Fluid Mechanics*, Vol. 61, Part 1, 1973, pp. 33–63.

7 Kruka, V., and Eskinazi, S., "The Wall-Jet in a Moving Stream," *Journal of Fluid Mechanics*, Vol. 20, Part 4, 1964, pp. 555–579.

8 Klebanoff, P. S., "Characteristics of Turbulence in a Boundary Layer With Zero Pressure Gradient," NACA Report 1247, 1954.

A Remark on the Use of the Decomposition $\mathbf{F} = \mathbf{F}_e\mathbf{F}_p$ in Plasticity

J. Casey[1] and P. M. Naghdi[2]

General Background

The nonlinear theory of elastic-plastic materials developed by Green and Naghdi [1, 2] employs the total strain and plastic strain among its independent kinematical variables.[3] Another theory by Lee [3] utilizes an intermediate stress-free configuration, together with the associated multiplicative decomposition of the deformation gradient. As pointed out by Green and Naghdi [4], Lee's development is valid only for initially isotropic materials. Other authors, among them Mandel [5] and Lubliner [6], have more recently made use of the multiplicative decomposition and have claimed that the theory of Green and Naghdi is unduly restrictive in that (see, e.g., [6, p. 165]) it is applicable only to "certain special cases of isotropy." The main purpose of this Note is to show that if full invariance requirements are invoked, then the theories employing the multiplicative decomposition lose the generality attributed to them [5, 6] relative to the development in [1, 2]. In addition, although a complete list of references on the subject is not cited, some aspects of the present discussion will serve to clarify certain misunderstandings in the literature on plasticity involving the use of the multiplicative decomposition without satisfying full invariance requirements.

Let X be a particle of an elastic-plastic body $\mathcal{B}$ and denote by $\mathbf{x}$ and $\mathbf{x}$, respectively, the positions of X in a fixed reference configuration

[1] Department of Mechanical Engineering, University of California, Berkeley, Calif. 94720. Assoc. Mem. ASME.

[2] Department of Mechanical Engineering, University of California, Berkeley, Calif. 94720. Fellow ASME.

[3] The theory of elastic-plastic materials in [1, 2] includes thermal effects and is developed within the framework of a thermodynamical theory. Although we confine attention to the purely mechanical aspects of the subject, the basic theory referred to here can be interpreted in the context of the isothermal theory and corresponds to a second form of the theory discussed in Section 4 of [2].

Manuscript received by ASME Applied Mechanics Division, October, 1979; final revision, March, 1980.

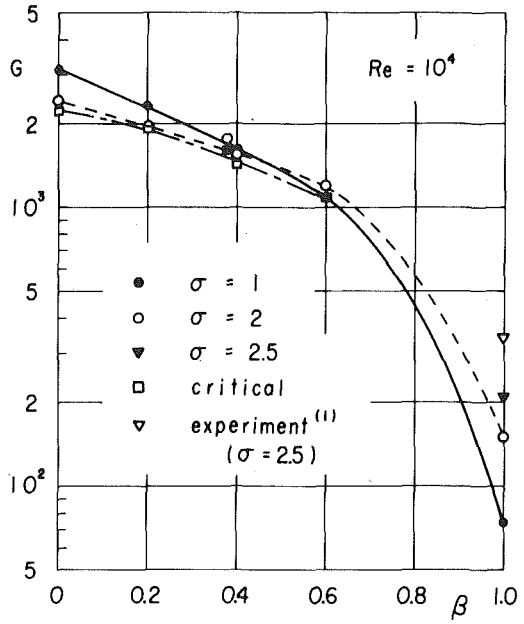

Fig. 3 Variations of G in neutral state with the velocity ratio β

where the primes denote differentiation with respect to η ($= y/y_m$), and $\overline{U} = U/U_m$, $\overline{u} = \hat{u}/U_m$, $\overline{v} = \hat{v}y_m/\nu$, $\overline{w} = \hat{w}y_m/\nu$, $\sigma = \alpha y_m$, $G = \mathrm{Re}\sqrt{y_m/R}$, $\mathrm{Re} = U_m y_m/\nu$, $M = (\mu + \rho\epsilon)/\mu$ (ρ: the density of the fluid, μ: its viscosity, ν: the kinematic viscosity). G is called the Görtler parameter, and Re is the Reynolds number.

The boundary conditions which arise from the requirements of no slip at the wall ($\eta = 0$) and of disappearance as $\eta \to \infty$ are $\overline{u} = \overline{v} = \overline{v}' = 0$ in view of continuity equation (4).

Results and Discussions

The present instability problem is now reduced to find the Görtler parameter G as an eigenvalue together with two components $\overline{u}(\eta)$ and $\overline{v}(\eta)$ of the perturbation velocities as eigenfunctions. $\overline{w}(\eta)$ is then obtained from equation (4). The set of the differential equations (2) and (3) was numerically solved by finite-difference technique and successive approximation procedure. Fig. 2 shows neutral stability curves in relation of the Görtler parameter G to the dimensionless wavenumber σ of the longitudinal vortices for several values of the velocity ratio $\beta = U_\infty/U_m$, where the stable range is below each neutral curve. Because detail data for distributions of the velocity $U(y)$ and the Reynolds stress in the turbulent wall jet along a concave wall are absent, we used in the present calculations the experimental results by Bradshaw and Gee [5] for a turbulent wall jet along a flat plate in a case of $\beta = 0$, by Irwin [6] for $\beta = 0.377$ and by Kruka and Eskinazi [7] for $\beta = 0.2$, 0.4, and 0.6. Fig. 2 indicates that, as the velocity ratio β increases, the stable range becomes smaller and the critical Görtler parameter (G_c) and the associated wavenumber (σ_c) are decreased. Fig. 2 is in a case of the Reynolds number $\mathrm{Re} = 10^4$. Calculations for different values of the Reynolds number ($\mathrm{Re} = 5 \times 10^3 \sim 2 \times 10^5$) show that the value of G in the neutral state increases with increasing Reynolds number as a function $G \sim \mathrm{Re}^n$ with $n = 1.0 \sim 1.1$ for $\beta = 0 \sim 0.6$.

Further calculations were carried out for $\beta = 1$, which corresponds to a turbulent boundary layer. Experimental values of the Reynolds stress by Klebanoff [8] were used in order to obtain a neutral stability curve. It was found that the parameter G in the neutral condition increases with Re, where n is $0.3 \sim 0.5$ in the same range of Re in the wall jets.

Fig. 3 shows the effect of the velocity ratio β to the parameter G in the neutral condition for $\sigma = 1$, 2, 2.5, and also at the critical condition. It is concluded from Fig. 3 that turbulent wall jets are more stable for occurrence of the longitudinal vortices than turbulent boundary layers, and that turbulent wall jets with less β are more stable. The fact comes from an increase of the eddy-viscosity ϵ in wall jets with less β.

References

1 Tani, I., "Production of Longitudinal Vortices in the Boundary Layer Along a Concave Wall," *Journal of Geophysical Research*, Vol. 67, No. 8, 1962, pp. 3075–3080.

2 Sandmayr, G., "Über das Auftreten von Längswirbeln in turbulenten Grenzschichten an konkaven Wänden," *Deutsche Luft-und Raumfahrt Forschungsbericht*, 66–41, June 1966, DVL-Bericht No. 504.

3 Kahawita, R. A., "Instability of Laminar Wall Jets Along Curved Surfaces," *AIAA Journal*, Vol. 13, No. 11, 1975, pp. 1517–1518.

4 Kobayashi, R., and Tomita, T., "Instability of Wall Jets Along Concave Walls," in Japanese, *Memoirs of Institute of High Speed Mechanics*, Tohoku University, Sendai, Japan, Vol. 40, No. 371, 1977, pp. 51–73.

5 Bradshaw, P., and Gee, M. T., "Turbulent Wall Jets With and Without an External Stream," A.R.C., R. & M., No. 3252, 1960.

6 Irwin, H. P. A. H., "Measurements in a Self-Preserving Plane Wall Jet in a Positive Pressure Gradient," *Journal of Fluid Mechanics*, Vol. 61, Part 1, 1973, pp. 33–63.

7 Kruka, V., and Eskinazi, S., "The Wall-Jet in a Moving Stream," *Journal of Fluid Mechanics*, Vol. 20, Part 4, 1964, pp. 555–579.

8 Klebanoff, P. S., "Characteristics of Turbulence in a Boundary Layer With Zero Pressure Gradient," NACA Report 1247, 1954.

A Remark on the Use of the Decomposition $\mathbf{F} = \mathbf{F}_e\mathbf{F}_p$ in Plasticity

J. Casey[1] and P. M. Naghdi[2]

General Background

The nonlinear theory of elastic-plastic materials developed by Green and Naghdi [1, 2] employs the total strain and plastic strain among its independent kinematical variables.[3] Another theory by Lee [3] utilizes an intermediate stress-free configuration, together with the associated multiplicative decomposition of the deformation gradient. As pointed out by Green and Naghdi [4], Lee's development is valid only for initially isotropic materials. Other authors, among them Mandel [5] and Lubliner [6], have more recently made use of the multiplicative decomposition and have claimed that the theory of Green and Naghdi is unduly restrictive in that (see, e.g., [6, p. 165]) it is applicable only to "certain special cases of isotropy." The main purpose of this Note is to show that if full invariance requirements are invoked, then the theories employing the multiplicative decomposition lose the generality attributed to them [5, 6] relative to the development in [1, 2]. In addition, although a complete list of references on the subject is not cited, some aspects of the present discussion will serve to clarify certain misunderstandings in the literature on plasticity involving the use of the multiplicative decomposition without satisfying full invariance requirements.

Let X be a particle of an elastic-plastic body $\mathcal{B}$ and denote by $\mathbf{x}$ and $\mathbf{x}$, respectively, the positions of X in a fixed reference configuration

[1] Department of Mechanical Engineering, University of California, Berkeley, Calif. 94720. Assoc. Mem. ASME.

[2] Department of Mechanical Engineering, University of California, Berkeley, Calif. 94720. Fellow ASME.

[3] The theory of elastic-plastic materials in [1, 2] includes thermal effects and is developed within the framework of a thermodynamical theory. Although we confine attention to the purely mechanical aspects of the subject, the basic theory referred to here can be interpreted in the context of the isothermal theory and corresponds to a second form of the theory discussed in Section 4 of [2].

Manuscript received by ASME Applied Mechanics Division, October, 1979; final revision, March, 1980.

κ_0 and the current configuration κ at time t. Let $\mathbf{F}$, which for convenience we express as a function of X and t, be the deformation gradient relative to the configuration κ_0 and recall that $\det \mathbf{F} > 0$, where det stands for determinant. The transpose and inverse operations will be denoted by superscripts T and -1, respectively, and $\mathbf{I}$ is the unit tensor.

Now it may be observed that if $\mathbf{H}$ is any tensor function of X and t with $\det \mathbf{H} > 0$, then $\mathbf{F} = (\mathbf{F}\mathbf{H}^{-1})\mathbf{H}$ with the property that $\det(\mathbf{F}\mathbf{H}^{-1}) > 0$. Hence, $\mathbf{F}$ can always be decomposed—with evident nonuniqueness—as a product in which both factors have positive determinants. Such a decomposition. namely,

$$\mathbf{F} = \mathbf{F}_e\mathbf{F}_p, \tag{1}$$

with $\det \mathbf{F}_e > 0$, $\det \mathbf{F}_p > 0$ is used in plasticity theory. However, the use of (1) in plasticity is supplemented with further restrictions which reduce the extent of nonuniqueness but result in possible nonexistence of the decomposition. To elaborate, let dX be an arbitrary material line element of $\mathcal{B}$ in the neighborhood of the particle X and let $d\mathbf{X}$ and $d\mathbf{x} = \mathbf{F}\,d\mathbf{X}$ be the corresponding line elements in the configurations κ_0 and κ, respectively. Put $d\mathbf{y} = \mathbf{F}_p\,d\mathbf{X}$. Then, $d\mathbf{x} = \mathbf{F}_e\,d\mathbf{y}$ by (1). Considering all material line elements dX at X in $\mathcal{B}$, we can form a local configuration from the elements $d\mathbf{y}$; the collection of such local configurations (for all X in $\mathcal{B}$) is usually referred to in the literature on plasticity as an intermediate stress-free configuration $\bar{\kappa}$; in the special case of homogeneous deformations for which $\mathbf{F}_e$ and $\mathbf{F}_p$ are independent of X, $\bar{\kappa}$ will be a global configuration of $\mathcal{B}$. We observe that as part of the definition of $\bar{\kappa}$, it must be required that

(a) For each $\mathbf{x}$, the portion of $\mathcal{B}$ that occupies an arbitrarily small neighborhood of $\mathbf{x}$ be reduced to a state of zero stress;[4] and

(b) The quantity

$$\mathbf{E}_p = \frac{1}{2}(\mathbf{F}_p{}^T\mathbf{F}_p - \mathbf{I}), \tag{2}$$

called plastic strain, has the same value[5] at the particle X in $\bar{\kappa}$ and κ. The deformation of $d\mathbf{X}$ into $d\mathbf{y}$ is then interpreted as plastic and that of $d\mathbf{y}$ into $d\mathbf{x}$ as elastic. Let $\mathbf{e}_i$ and $\mathbf{e}_A$ be fixed orthonormal bases associated with the configurations κ and κ_0, respectively. Then, the components F_{iA} of $\mathbf{F}$ referred to these bases satisfy the compatibility conditions $\partial F_{iA}/\partial X_B = \partial F_{iB}/\partial X_A$ with respect to reference position $\mathbf{X} = X_A\mathbf{e}_A$, while the tensors $\mathbf{F}_e$ and $\mathbf{F}_p$ in general do not satisfy any compatibility conditions; and, consequently, the configuration $\bar{\kappa}$ cannot be mapped smoothly into κ_0 or κ.

Issues Involved in the Use of (1)

Three main issues are involved in the use of the multiplicative decomposition (1). These are: (*i*) existence of a configuration such as $\bar{\kappa}$, (*ii*) uniqueness of $\bar{\kappa}$ or equivalently of the factors $\mathbf{F}_e$, $\mathbf{F}_p$, and (*iii*) the invariance requirements under superposed rigid body motions to be satisfied by $\mathbf{F}_e$, $\mathbf{F}_p$ and their consequent effects on the constitutive equations. We discuss these issues separately.

***(i)* Existence.** As was pointed out in [4], it is possible to reduce the stresses in a material element to zero without changing $\mathbf{E}_p$ if and only if the origin $\mathcal{O}$ in stress space lies in the region $\mathcal{S}$ bounded by the yield surface $\partial\mathcal{S}$. It is not always the case that $\mathcal{O}$ belongs to $\mathcal{S}$ and therefore if (1) is assumed, it will involve a restriction on possible constitutive equations and/or possible deformations. On the other hand, if such restrictions are not imposed, then the decomposition (1) will not always exist.

***(ii)* Uniqueness.** It follows from the requirement (b) that in any two intermediate stress-free configurations corresponding to the same current configuration κ, $\mathbf{E}_p$ has the same value at the particle X. Hence, in view of (1) and (2), $\mathbf{F}_p$ and $\mathbf{F}_e$ are not unique to the extent that they are determined only to within a proper orthogonal tensor function[6] $\mathbf{Z}$ of X, t so that $\mathbf{F}_e\mathbf{Z}^T$, $\mathbf{Z}\mathbf{F}_p$ also satisfy (1) and leave the left-hand side of (2) unchanged. It then follows that the configuration $\bar{\kappa}$ is locally determined at time t only to within a rigid displacement.[7]

***(iii)* Invariance Requirements.** First, we recall that in response to certain remarks made by Lee [3], Green and Naghdi [4] studied the possibility of accommodating the decomposition (1) within the framework of their general thermodynamical theory [1, 2] in which, in addition to temperature θ and work-hardening parameter κ, the kinematical variables were the total strain $\mathbf{E} = \frac{1}{2}(\mathbf{F}^T\mathbf{F} - \mathbf{I})$ and the plastic strain $\mathbf{E}_p$ introduced as a primitive variable. In [1, 2] $\mathbf{E}_p$ and κ were assumed to be unaltered under superposed rigid body motions. It was established in [4] that by assuming the decomposition (1) and making the identification between the *primitive* quantity $\mathbf{E}_p$ in [1, 2] and the *defined* quantity $\mathbf{E}_p$ in (2), that a theory utilizing the variables $\mathbf{F}_e$ and $\mathbf{F}_p$ could be derived from that of Green and Naghdi [1, 2].

With reference to the invariance requirements, we recall that physical considerations demand that certain fields and functions entering the theory be indifferent[8] to any transformation which takes the present configuration κ of a body rigidly into a configuration κ^+. Since $\bar{\kappa}$ is locally just another configuration, then by the same physical reasoning, it was assumed in [4] that these fields and functions are also indifferent to a transformation that independently replaces the intermediate configuration $\bar{\kappa}$ by a configuration $\bar{\kappa}^+$ related to $\bar{\kappa}$ through a superposed rigid body motion. Let $\kappa \to \kappa^+$ and $\bar{\kappa} \to \bar{\kappa}^+$ by independent superposed rigid body motions. Then, we have the transformations $\mathbf{F} \to \mathbf{F}^+$, $\mathbf{F}_e \to \mathbf{F}_e{}^+$ and $\mathbf{F}_p \to \mathbf{F}_p{}^+$ with

$$\mathbf{F}^+ = \mathbf{Q}(t)\mathbf{F} = \mathbf{F}_e{}^+\mathbf{F}_p{}^+, \quad \mathbf{F}_e{}^+ = \mathbf{Q}(t)\mathbf{F}_e\bar{\mathbf{Q}}^T(t), \quad \mathbf{F}_p{}^+ = \bar{\mathbf{Q}}(t)\mathbf{F}_p, \tag{3}$$

where $\mathbf{Q}(t)$ and $\bar{\mathbf{Q}}(t)$ are proper orthogonal tensor-valued functions of time only corresponding, respectively, to the arbitrary rigid body rotations in the motions through which $\kappa \to \kappa^+$ and $\bar{\kappa} \to \bar{\kappa}^+$. Clearly, $\mathbf{E}_p$ in (2) and $\mathbf{E}$ will remain unaltered under the foregoing transformations and the work-hardening parameter κ is assumed to also remain unaltered. Furthermore we assume that the stress tensor which appears in the constitutive discussion, namely, the symmetric Piola-Kirchhoff stress $\mathbf{S}$ for both configurations $\bar{\kappa}$ and κ, remains unaltered under the transformations $\kappa \to \kappa^+, \bar{\kappa} \to \bar{\kappa}^+$. It is then clear that $\bar{\kappa}$ satisfies requirements (a) and (b) if and only if $\bar{\kappa}^+$ does, i.e., $\bar{\kappa}^+$ is an intermediate stress-free configuration if and only if $\bar{\kappa}$ is. In particular, since we can now conclude that $\mathbf{S} = \mathbf{0}$ in $\bar{\kappa}^+$ if $\mathbf{S} = \mathbf{0}$ in $\bar{\kappa}$, it follows that requirement (a) does not further reduce the lack of uniqueness mentioned under (*ii*).

The invariance requirements (3) were observed by Green and Naghdi [4][9] and were later used by Naghdi and Trapp [9] in effecting an essential reduction in the form of the strain-energy response function. In contrast to the full invariance requirements, those adopted by many authors correspond to (3) but with $\bar{\mathbf{Q}}(t) = \mathbf{I}$. In some cases, for example [3], erroneous results were avoided because the analysis was restricted to isotropic materials. However, Mandel [5] introduces the idea of an[10] "isoclinic" stress-free intermediate configuration $\hat{\kappa}$, i.e., one that has a *fixed orientation* relative to a set of axes in space, and adopts invariance requirements corresponding to

[4] The reduction to a state of zero stress is in the context of the purely mechanical theory only. The corresponding reduction in the thermodynamical theory can be discussed similarly.

[5] This requirement, as already noted by Green and Naghdi [4], is implied by the usual statement that the total strain associated with the element $d\mathbf{y}$ is a "plastic strain" and is equal to the plastic strain associated with the element $d\mathbf{x}$.

[6] There is a dependency on X since the stress-free configuration is local.

[7] At this stage of our discussion, it cannot be said whether the requirement (a) can reduce this lack of uniqueness. We return to this later; see the end of the paragraph containing (3).

[8] We use the term indifferent for brevity to mean *unaltered* or *unaltered apart from orientation* as defined in [7]. The notations $\mathbf{F}^+$, $\mathbf{E}^+$, etc., here are in line with those in [7] and correspond to $\mathbf{F}^*$, $\mathbf{E}^*$, etc., in [4].

[9] Invariance requirements of the form (3) were also adopted independently by Sidoroff [8], although he appeals to the principle of material frame-indifference.

[10] Actually, Mandel [5, p. 728] employs the terminology "configurations isoclines."

(3) with $\bar{\mathbf{Q}}(t) = \mathbf{I}$. The notion of a fixed orientation used in [5] is itself not an invariant one. For Mandel's scheme to have any physical relevance, his results must be indifferent to the choice of fixed orientation. This leads one to demand that the full invariance requirements[11] (3) be satisfied. We discuss this further in the following, but note here that Mandel's scheme is adopted by Lubliner [6] who repeats the criticisms of [1, 4] stated in [5].

We have already indicated that the definition of a stress-free configuration (involving the requirements (a) and (b) noted earlier) determines $\bar{\kappa}$ only to within a rigid displacement at time t. In this connection, it is perhaps natural to ask if by introducing a further assumption one could choose a unique $\bar{\kappa}$ from among all possible intermediate stress-free configurations and thereby obtain a unique choice for $\mathbf{F}_p$. In examining this possibility, one is immediately led to conclude that unless a nonuniqueness of rotation $\bar{\mathbf{Q}}$ remains in $\bar{\kappa}$, the full invariance requirements (3) will not be satisfied. To elaborate, consider for example a possible additional assumption that $\mathbf{F}_e$ be symmetric positive-definite. Then, application of $(3)_2$ shows that $\mathbf{F}_e{}^+$ is not symmetric positive-definite unless $\bar{\mathbf{Q}}(t)$ is set equal to $\mathbf{Q}(t)$ in (3). But, such a stipulation on the invariance requirements (although it may be specified mathematically) is unduly restrictive on physical grounds. Similarly, an assumption that $\mathbf{F}_p$ be symmetric positive-definite is not an invariant idea since $\mathbf{F}_p{}^+$ will not be symmetric positive-definite. It should be kept in mind that the invariance requirements (3) embody the idea that at time t all intermediate stress-free configurations differing from one another by a rigid displacement are physically indistinguishable and there are no physical grounds for choosing one of them rather than another. However, while $\bar{\kappa}$ and hence $\mathbf{F}_p$ cannot be chosen uniquely, it is important to note that $\mathbf{E}_p$ can be chosen uniquely, for example through the definition (2).

Implication of Invariance Requirements Stated Under (*iii*)

In what follows we shall need to have available some results from [1, 2, 4]. Interpreting the isothermal case of the theory in [1, 2] as corresponding to the purely mechanical theory we obtain

$$\psi = \hat{\psi}(\mathbf{E}, \mathbf{E}_p, \kappa), \quad \mathbf{S} = \rho_0 \frac{\partial \hat{\psi}}{\partial \mathbf{E}}, \tag{4}$$

as properly invariant constitutive equations for the strain energy per unit mass and the symmetric Piola-Kirchhoff stress tensor $\mathbf{S}$, where ρ_0 is the mass density in the configuration κ_0. It is understood that the response function $\hat{\psi}$ in (4) is expressed as a symmetric function of $\mathbf{E}$. In addition, for fixed values of $\mathbf{E}_p$ and κ, the yield surface $\partial\mathcal{S}$ in stress space is given in invariant form by

$$\phi(\mathbf{S}, \mathbf{E}_p, \kappa) = 0. \tag{5}$$

In the theory of Green and Naghdi [1, 2], $\mathbf{E}_p$ is a primitive kinematical quantity and no kinematical relation between $\mathbf{E}$ and $\mathbf{E}_p$ is assumed. The limitations concerning existence discussed under (i) do not arise in this general framework; and, if only for this reason, it seems to be preferable in a general theory of plasticity to employ $\mathbf{E}$ and $\mathbf{E}_p$ rather than $\mathbf{F}_e$ and $\mathbf{F}_p$. Again for the same reason, it seems preferable when using $\mathbf{E}$ and $\mathbf{E}_p$ not to introduce stress-free configurations as part of the general theory.[12] As soon as the identification between the primitive $\mathbf{E}_p$ of [1, 2] and the defined quantity $\mathbf{E}_p$ in (2) is made, the theory of [1, 2] loses some of its generality and the discussion (i) of existence becomes relevant. In the remainder of this Note we assume that this identification has been made.

We now recall polar decompositions of the invertible tensors $\mathbf{F}$, $\mathbf{F}_e$, and $\mathbf{F}_p$ and define deformation tensors $\mathbf{C}$, $\mathbf{C}_e$, and $\mathbf{C}_p$ as follows:

$$\mathbf{F} = \mathbf{R}\mathbf{M}, \quad \mathbf{C} = \mathbf{F}^T\mathbf{F} = \mathbf{M}^2, \tag{6}$$

$$\mathbf{F}_e = \mathbf{R}_e\mathbf{M}_e, \quad \mathbf{C}_e = \mathbf{M}_e{}^2,$$

and

$$\mathbf{F}_p = \mathbf{R}_p\mathbf{M}_p, \quad \mathbf{C}_p = \mathbf{M}_p{}^2 = 2\mathbf{E}_p + \mathbf{I}, \tag{7}$$

where $\mathbf{R}$, $\mathbf{R}_e$, $\mathbf{R}_p$ are proper orthogonal tensors and $\mathbf{M}$, $\mathbf{M}_e$, $\mathbf{M}_p$ are symmetric positive-definite tensors. We note that in view of (1), (6), and (7), $\mathbf{C}$ may be expressed as

$$\mathbf{C} = \mathbf{M}_p\mathbf{R}_p{}^T\mathbf{C}_e\mathbf{R}_p\mathbf{M}_p. \tag{8}$$

When $\kappa \to \kappa^+, \bar{\kappa} \to \bar{\kappa}^+$, then $\mathbf{R} \to \mathbf{R}^+$, $\mathbf{M} \to \mathbf{M}^+$, etc., and it can be deduced from (3), (6), and (7) that

$$\mathbf{R}^+ = \mathbf{Q}(t)\mathbf{R}, \quad \mathbf{M}^+ = \mathbf{M}, \quad \mathbf{C}^+ = \mathbf{C}, \quad \mathbf{E}^+ = \mathbf{E},$$

$$\mathbf{R}_e{}^+ = \mathbf{Q}(t)\mathbf{R}_e\bar{\mathbf{Q}}^T(t), \quad \mathbf{M}_e{}^+ = \bar{\mathbf{Q}}(t)\mathbf{M}_e\bar{\mathbf{Q}}^T(t), \quad \mathbf{C}_e{}^+ = \bar{\mathbf{Q}}(t)\mathbf{C}_e\bar{\mathbf{Q}}^T(t),$$

$$\mathbf{R}_p{}^+ = \bar{\mathbf{Q}}(t)\mathbf{R}_p, \quad \mathbf{M}_p{}^+ = \mathbf{M}_p, \quad \mathbf{C}_p{}^+ = \mathbf{C}_p, \quad \mathbf{E}_p{}^+ = \mathbf{E}_p. \tag{9}$$

Once the decomposition (1) is admitted, the strain energy ψ may be expressed in the equivalent forms

$$\psi = \psi_1(\mathbf{F}_e, \mathbf{F}_p, \kappa) = \psi_2(\mathbf{F}, \mathbf{F}_p, \kappa). \tag{10}$$

Since ψ must remain unaltered under the transformations $\kappa \to \kappa^+, \bar{\kappa} \to \bar{\kappa}^+$, then considering first the function ψ_1 in $(10)_1$ we obtain

$$\psi = \psi^+ = \psi_1(\mathbf{F}_e{}^+, \mathbf{F}_p{}^+, \kappa^+) = \psi_1(\mathbf{Q}(t)\mathbf{F}_e\bar{\mathbf{Q}}^T(t), \bar{\mathbf{Q}}(t)\mathbf{F}_p, \kappa) \tag{11}$$

for arbitrary proper orthogonal $\mathbf{Q}(t)$, $\bar{\mathbf{Q}}(t)$, where $(3)_{2,3}$ have been used. Recalling $(6)_3$ and $(7)_1$ we choose $\bar{\mathbf{Q}}(t) = \mathbf{R}_p{}^T$ and $\mathbf{Q}(t) = \mathbf{R}_p{}^T\mathbf{R}_e{}^T$ in (11) so that

$$\psi = \psi_1(\mathbf{R}_p{}^T\mathbf{M}_e\mathbf{R}_p, \mathbf{M}_p, \kappa) \tag{12}$$

and we note the presence of $\mathbf{R}_p$ in the arguments of (12). We have shown that a necessary condition for the satisfaction of invariance requirements is that ψ_1 in $(10)_1$ depend on $\mathbf{F}_e$, $\mathbf{F}_p$, κ only through the arguments appearing in (12). It is readily seen, with the help of (9), that taking ψ_1 in the form (12) is also sufficient for the satisfaction of invariance requirements. Observing the relations $\mathbf{R}_p{}^T\mathbf{M}_e\mathbf{R}_p = (\mathbf{R}_p{}^T\mathbf{C}_e\mathbf{R}_p)^{1/2}$ and $\mathbf{M}_p = \mathbf{C}_p{}^{1/2}$, we can express ψ as a properly invariant function of $\mathbf{R}_p{}^T\mathbf{C}_e\mathbf{R}_p$, $\mathbf{C}_p$, κ. This was the form used in Section 4 of [4]. Considering now the function ψ_2 in $(10)_2$, it can be shown by a similar argument that a necessary and sufficient condition for the satisfaction of invariance requirements is that ψ_2 can depend on $\mathbf{F}$, $\mathbf{F}_p$, κ only in the forms

$$\psi = \psi_2(\mathbf{M}, \mathbf{M}_p, \kappa) = \psi_3(\mathbf{C}, \mathbf{C}_p, \kappa) = \hat{\psi}(\mathbf{E}, \mathbf{E}_p, \kappa), \tag{13}$$

the last of which is that employed in [1, 2, 4, 9]. Indeed, in view of (8), the reduced forms (12) and (13) are equivalent.

We now return to Mandel's development [5] and introduce the notations $\hat{\mathbf{F}}_p$, $\hat{\mathbf{R}}_p$, $\hat{\mathbf{M}}_p$ for the values of $\mathbf{F}_p$, $\mathbf{R}_p$, $\mathbf{M}_p$ associated with his "isoclinic" stress-free configuration $\hat{\kappa}$, as well as $\hat{\boldsymbol{\pi}} = \hat{\mathbf{F}}_p\mathbf{S}\hat{\mathbf{F}}_p{}^T/\det\hat{\mathbf{F}}_p$. A typical result in Mandel's development is an equation of the form[13]

$$\hat{\phi}(\hat{\boldsymbol{\pi}}) = 0 \tag{14}$$

for a yield surface in stress space. Applying the invariance requirements (3) and assuming $\hat{\phi}$ to be invariant, we obtain

[11] It is clear that any chosen isoclinic configuration $\hat{\kappa}$ at time t may be regarded as corresponding to $\bar{\mathbf{Q}}(t) = \mathbf{I}$. A different choice of orientation will then result in a different $\bar{\mathbf{Q}}(t)$. If this choice is to be arbitrary, then $\bar{\mathbf{Q}}(t)$ must be arbitrary also.

[12] In special cases, of course, it may be desirable for purposes of interpretation or experimental identification to make use of such stress-free configurations in order to identify $\mathbf{E}_p$ by the form (2). Another way of identifying plastic strain is through the use of an assumption which would require that $\mathbf{E}_p$ reduce to $\mathbf{E}$ when $\mathbf{S} = \mathbf{0}$ (see property 3 on p. 122 of [2]).

[13] The notation $\hat{\phi}$ in (14) corresponds to $\hat{f}$ in (8.4) of [5] and we have suppressed Mandel's variables $T, \hat{\boldsymbol{\alpha}}_j$ since they do not affect the present discussion. It is important to note that we would still employ the full invariance requirements (3) even if these variables were included. Our $\hat{\mathbf{F}}_p$, $\hat{\mathbf{R}}_p$, $\hat{\mathbf{M}}_p$, $\mathbf{S}$ correspond, respectively, to $\hat{\mathbf{P}}$, $\hat{\mathbf{Q}}$, $\mathbf{L}$, $\boldsymbol{\pi}_0$ of [5] and the work-hardening parameter κ is not explicitly exhibited in (14).

$$\hat{\phi}(\hat{\pi}) = \hat{\phi}(\hat{\pi}^+) = \hat{\phi}(\bar{\mathbf{Q}}(t)\hat{\mathbf{F}}_p\mathbf{S}\hat{\mathbf{F}}_p{}^T\bar{\mathbf{Q}}^T/\det\hat{\mathbf{F}}_p) \tag{15}$$

for arbitrary proper orthogonal $\bar{\mathbf{Q}}(t)$. With the help of (15), the polar decomposition $\hat{\mathbf{F}}_p = \hat{\mathbf{R}}_p\hat{\mathbf{M}}_p$, the fact that $\hat{\mathbf{M}}_p = \mathbf{M}_p$ by virtue of requirement (*b*) and choosing $\bar{\mathbf{Q}}(t) = \hat{\mathbf{R}}_p{}^T$, (14) reduces to

$$\hat{\phi}(\mathbf{M}_p\mathbf{S}\mathbf{M}_p/\det\mathbf{M}_p) = 0. \tag{16}$$

Thus $\hat{\phi}$ can depend on the argument $\hat{\pi}$ only through $\mathbf{S}$ and $\mathbf{M}_p$. Clearly, the left-hand side of (16) can be written as a different function $\phi(\mathbf{S}, \mathbf{E}_p)$. Hence, apart from the work-hardening parameter κ not included in (14), the form (16) of the yield surface is equivalent to (5) which is that used by Green and Naghdi [1, 2]. Parallel arguments apply to other relevant equations in [5] and it should now be clear that the criticism of [1, 4] by Mandel and others who have adopted his scheme is unjustified.

It should be emphasized that in deducing (12), (13), and (16) no assumptions were made concerning material symmetry and consequently these equations are valid for a material which is anisotropic in its reference configuration. Some authors, for example Mandel [5], regard equations such as (5) and (13) to be valid only for special materials which are "isotropic in the intermediate configuration." However, we have just seen that the invariance requirements (3) imply that constitutive equations such as $(10)_2$ always satisfy an equation of the form (13).

Finally a comment must be made about a paper by Silhavy [10]. In the context of a functional-type theory, he has attempted to prove that the appropriate transformation law for $\mathbf{F}_p$ is $\mathbf{F}_p \to \mathbf{F}_p$ (or $p \to p$ in the notation of [10]), i.e., $\bar{\mathbf{Q}}(t) = \mathbf{I}$ in (3). However, his main proposition (Proposition 4 in [10]) states that a certain *set* $\mathcal{P}_{qf}(\pi_0, \mathbf{N})$ is equal to a set $\mathcal{P}_f(\pi_0, \mathbf{N})$. As Silhavy himself points out, there may be more than one element in the set $\mathcal{P}_{qf}(\pi_0, \mathbf{N})$. Therefore, it cannot be deduced from Silhavy's Proposition 4 that $\mathbf{F}_p \to \mathbf{F}_p$ under superposed rigid body motions.[14]

Acknowledgment

The results reported here were obtained in the course of research supported by the U.S. Office of Naval Research under Contract N00014-75-C-0148, Project NR 064-436, with the University of California, Berkeley.

References

1 Green, A. E., and Naghdi, P. M., "A General Theory of an Elastic-Plastic Continuum," *Archive for Rational Mechanics and Analysis*, Vol. 18, 1965, pp. 251–281.

2 Green, A. E., and Naghdi, P. M., "A Thermodynamic Development of Elastic-Plastic Continua," *Proceedings of the IUTAM Symposium on Irreversible Aspects of Continuum Mechanics and Transfer of Physical Characteristics in Moving Fluids*, Springer-Verlag, 1966, pp. 117–131.

3 Lee, E. H., "Elastic-Plastic Deformation at Finite Strains," ASME JOURNAL OF APPLIED MECHANICS, Vol. 36, 1969, pp. 1–6.

4 Green, A. E , and Naghdi, P. M., "Some Remarks on Elastic-Plastic Deformation at Finite Strain," *International Journal of Engineering Science*, Vol. 9, 1971, pp. 1219–1229.

5 Mandel, J., "Equations Constitutives et Directeurs dans les Milieux Plastiques et Viscoplastiques," *International Journal of Solids and Structures*, Vol. 9, 1973, pp. 725–740.

6 Lubliner, J., "A Thermodynamic Yield Criterion in Viscoplasticity," *Acta Mechanica*, Vol. 30, 1978, pp. 165–174.

7 Green, A. E., and Naghdi, P. M., "A Note on Invariance Under Superposed Rigid Body Motions," *Journal of Elasticity*, Vol. 9, 1979, pp. 1–8.

8 Sidoroff, F., "Quelques Réflexions sur le Principe d'Indifférence Matérielle pour un Milieu ayant un État Relâché," *Compte Rendus de l'Académie des Sciences*, Paris, Vol. 271, Série A, 1970, pp. 1026–1029.

9 Naghdi, P. M., and Trapp, J. A., "On Finite Elastic-Plastic Deformation of Metals," ASME JOURNAL OF APPLIED MECHANICS, Vol. 41, 1974, pp. 254–260.

10 Silhavy, M., "On Transformation Laws for Plastic Deformations of Materials With Elastic Range," *Archive for Rational Mechanics and Analysis*, Vol. 63, 1977, pp. 169–182.

[14] For example, in plane geometry a rotation of the unit circle C through an angle of 45 deg, say, maps C into itself but it certainly cannot be argued that each point of C is mapped into itself.

Large Amplitude Vibration of Skew Orthotropic Plates

M. Sathyamoorthy[1]

Introduction

Large amplitude flexural vibrations of plates of various geometries have been reported by several investigators [1]. The studies carried out so far, in many cases, do not incorporate the effects of transverse shear and rotatory inertia in the analysis. Although several theories [1] have been proposed to account for these effects, numerical applications are not available. Wu and Vinson [2] have studied the effects of transverse shear deformation and rotatory inertia on the large amplitude vibration of rectangular orthotropic plates based on assumed expressions for transverse displacement w as well as the slope functions α and β. Furthermore, the formulation is based on the Berger approximation. Recently, the author [3] has studied the nonlinear vibration behavior of isotropic skew plates with the aid of a system of two equations in terms of the stress function, F, and the lateral displacement, w. The approach presented in reference [3] eliminates α and β from the governing equations. Therefore, it is not necessary to assume functional forms for these slopes in the solution. It has been shown in reference [4] that a system of governing equations whose solutions do not require the assumptions of α and β gives better numerical results.

In this Note, the nonlinear governing equations applicable for the large amplitude flexural vibrations of moderately thick orthotropic skew plates are given in terms of F and w following the procedure in [3]. These equations are then solved using the Galerkin method on the basis of an assumed lateral mode. The assumed mode shape is restricted to one term in order to keep the algebraic and numerical work involved within reasonable limits. Numerical results indicate that the transverse shear and rotatory inertia effects are important for moderately thick orthotropic skew plates.

Analysis

The governing dynamic equations for an orthotropic skew plate in oblique coordinate system (see Fig. 1 in [3]) which account for transverse shear deformation and rotatory inertia can be derived following the procedure in reference [3]. The final form of these equations in terms of the stress function F and transverse displacement w are

$$F_{,xxxx} + k_1F_{,yyyy} + k_2F_{,xxyy} + k_3F_{,xxxy} + k_4F_{,xyyy} = CE_\eta(w_{,xy}{}^2 - w_{,xx}w_{,yy}) \tag{1}$$

$$N(I_1) + R(w) = 0 \tag{2}$$

where

$$k_1 = C^4\{t_1{}^2(m^2 + t_1{}^2) + k^2\}, \quad k_2 = 6S^2 + m^2C^2, \quad k_3 = -4S$$

$$k_4 = -2S(2S^2 + m^2C^2), \quad k^2 = E_\eta/E_\xi, \quad q^2 = \nu_{\xi\eta}, \quad p^2 = G_{\xi\eta}\nu'/E_\xi$$

$$m^2 = (k^2 - q^4 - 2p^2q^2)/p^2, \quad t_1 = S/C, \quad S = \sin\theta, \quad C = \cos\theta$$

$$I_1 = I + 2D_{17}w_{,xy} - D_{18}w_{,yy} - D_{19}w_{,xx} = C\rho hw_{,tt}. \tag{3}$$

In equations (3), $E_\xi, E_\eta, \nu_{\xi\eta}, \nu_{\eta\xi}, G_{\xi\eta}, G_{\xi z}, G_{\eta z}$ are the elastic orthotropic constants of the material of the plate. x and y are the oblique coordinates, ξ, η are the rectangular Cartesian coordinates, and θ is the skew angle. The differential operators N and R in equation (2), and the quantity I in equations (3) are the same as those in [3]. The various coefficients which are required to fully define N and R are given in

[1] Assistant Professor, Department of Mechanical and Industrial Engineering, Clarkson College of Technology, Potsdam, N.Y. 13676.

Manuscript received by ASME Applied Mechanics Division, June, 1979; final revision, February, 1980.

$$\hat{\phi}(\hat{\pi}) = \hat{\phi}(\hat{\pi}^+) = \hat{\phi}(\bar{\mathbf{Q}}(t)\hat{\mathbf{F}}_p\mathbf{S}\hat{\mathbf{F}}_p{}^T\bar{\mathbf{Q}}^T/\det\hat{\mathbf{F}}_p) \tag{15}$$

for arbitrary proper orthogonal $\bar{\mathbf{Q}}(t)$. With the help of (15), the polar decomposition $\hat{\mathbf{F}}_p = \hat{\mathbf{R}}_p\hat{\mathbf{M}}_p$, the fact that $\hat{\mathbf{M}}_p = \mathbf{M}_p$ by virtue of requirement (*b*) and choosing $\bar{\mathbf{Q}}(t) = \hat{\mathbf{R}}_p{}^T$, (14) reduces to

$$\hat{\phi}(\mathbf{M}_p\mathbf{S}\mathbf{M}_p/\det\mathbf{M}_p) = 0. \tag{16}$$

Thus $\hat{\phi}$ can depend on the argument $\hat{\pi}$ only through $\mathbf{S}$ and $\mathbf{M}_p$. Clearly, the left-hand side of (16) can be written as a different function $\phi(\mathbf{S}, \mathbf{E}_p)$. Hence, apart from the work-hardening parameter κ not included in (14), the form (16) of the yield surface is equivalent to (5) which is that used by Green and Naghdi [1, 2]. Parallel arguments apply to other relevant equations in [5] and it should now be clear that the criticism of [1, 4] by Mandel and others who have adopted his scheme is unjustified.

It should be emphasized that in deducing (12), (13), and (16) no assumptions were made concerning material symmetry and consequently these equations are valid for a material which is anisotropic in its reference configuration. Some authors, for example Mandel [5], regard equations such as (5) and (13) to be valid only for special materials which are "isotropic in the intermediate configuration." However, we have just seen that the invariance requirements (3) imply that constitutive equations such as $(10)_2$ always satisfy an equation of the form (13).

Finally a comment must be made about a paper by Silhavy [10]. In the context of a functional-type theory, he has attempted to prove that the appropriate transformation law for $\mathbf{F}_p$ is $\mathbf{F}_p \to \mathbf{F}_p$ (or $p \to p$ in the notation of [10]), i.e., $\bar{\mathbf{Q}}(t) = \mathbf{I}$ in (3). However, his main proposition (Proposition 4 in [10]) states that a certain *set* $\mathcal{P}_{qf}(\pi_0, \mathbf{N})$ is equal to a set $\mathcal{P}_f(\pi_0, \mathbf{N})$. As Silhavy himself points out, there may be more than one element in the set $\mathcal{P}_{qf}(\pi_0, \mathbf{N})$. Therefore, it cannot be deduced from Silhavy's Proposition 4 that $\mathbf{F}_p \to \mathbf{F}_p$ under superposed rigid body motions.[14]

Acknowledgment

The results reported here were obtained in the course of research supported by the U.S. Office of Naval Research under Contract N00014-75-C-0148, Project NR 064-436, with the University of California, Berkeley.

References

1 Green, A. E., and Naghdi, P. M., "A General Theory of an Elastic-Plastic Continuum," *Archive for Rational Mechanics and Analysis*, Vol. 18, 1965, pp. 251–281.

2 Green, A. E., and Naghdi, P. M., "A Thermodynamic Development of Elastic-Plastic Continua," *Proceedings of the IUTAM Symposium on Irreversible Aspects of Continuum Mechanics and Transfer of Physical Characteristics in Moving Fluids*, Springer-Verlag, 1966, pp. 117–131.

3 Lee, E. H., "Elastic-Plastic Deformation at Finite Strains," ASME JOURNAL OF APPLIED MECHANICS, Vol. 36, 1969, pp. 1–6.

4 Green, A. E , and Naghdi, P. M., "Some Remarks on Elastic-Plastic Deformation at Finite Strain," *International Journal of Engineering Science*, Vol. 9, 1971, pp. 1219–1229.

5 Mandel, J., "Equations Constitutives et Directeurs dans les Milieux Plastiques et Viscoplastiques," *International Journal of Solids and Structures*, Vol. 9, 1973, pp. 725–740.

6 Lubliner, J., "A Thermodynamic Yield Criterion in Viscoplasticity," *Acta Mechanica*, Vol. 30, 1978, pp. 165–174.

7 Green, A. E., and Naghdi, P. M., "A Note on Invariance Under Superposed Rigid Body Motions," *Journal of Elasticity*, Vol. 9, 1979, pp. 1–8.

8 Sidoroff, F., "Quelques Réflexions sur le Principe d'Indifférence Matérielle pour un Milieu ayant un État Relâché," *Compte Rendus de l'Académie des Sciences*, Paris, Vol. 271, Série A, 1970, pp. 1026–1029.

9 Naghdi, P. M., and Trapp, J. A., "On Finite Elastic-Plastic Deformation of Metals," ASME JOURNAL OF APPLIED MECHANICS, Vol. 41, 1974, pp. 254–260.

10 Silhavy, M., "On Transformation Laws for Plastic Deformations of Materials With Elastic Range," *Archive for Rational Mechanics and Analysis*, Vol. 63, 1977, pp. 169–182.

[14] For example, in plane geometry a rotation of the unit circle C through an angle of 45 deg, say, maps C into itself but it certainly cannot be argued that each point of C is mapped into itself.

Large Amplitude Vibration of Skew Orthotropic Plates

M. Sathyamoorthy[1]

Introduction

Large amplitude flexural vibrations of plates of various geometries have been reported by several investigators [1]. The studies carried out so far, in many cases, do not incorporate the effects of transverse shear and rotatory inertia in the analysis. Although several theories [1] have been proposed to account for these effects, numerical applications are not available. Wu and Vinson [2] have studied the effects of transverse shear deformation and rotatory inertia on the large amplitude vibration of rectangular orthotropic plates based on assumed expressions for transverse displacement w as well as the slope functions α and β. Furthermore, the formulation is based on the Berger approximation. Recently, the author [3] has studied the nonlinear vibration behavior of isotropic skew plates with the aid of a system of two equations in terms of the stress function, F, and the lateral displacement, w. The approach presented in reference [3] eliminates α and β from the governing equations. Therefore, it is not necessary to assume functional forms for these slopes in the solution. It has been shown in reference [4] that a system of governing equations whose solutions do not require the assumptions of α and β gives better numerical results.

In this Note, the nonlinear governing equations applicable for the large amplitude flexural vibrations of moderately thick orthotropic skew plates are given in terms of F and w following the procedure in [3]. These equations are then solved using the Galerkin method on the basis of an assumed lateral mode. The assumed mode shape is restricted to one term in order to keep the algebraic and numerical work involved within reasonable limits. Numerical results indicate that the transverse shear and rotatory inertia effects are important for moderately thick orthotropic skew plates.

Analysis

The governing dynamic equations for an orthotropic skew plate in oblique coordinate system (see Fig. 1 in [3]) which account for transverse shear deformation and rotatory inertia can be derived following the procedure in reference [3]. The final form of these equations in terms of the stress function F and transverse displacement w are

$$F_{,xxxx} + k_1F_{,yyyy} + k_2F_{,xxyy} + k_3F_{,xxxy} + k_4F_{,xyyy} = CE_\eta(w_{,xy}{}^2 - w_{,xx}w_{,yy}) \tag{1}$$

$$N(I_1) + R(w) = 0 \tag{2}$$

where

$$k_1 = C^4\{t_1{}^2(m^2 + t_1{}^2) + k^2\}, \quad k_2 = 6S^2 + m^2C^2, \quad k_3 = -4S$$

$$k_4 = -2S(2S^2 + m^2C^2), \quad k^2 = E_\eta/E_\xi, \quad q^2 = \nu_{\xi\eta}, \quad p^2 = G_{\xi\eta}\nu'/E_\xi$$

$$m^2 = (k^2 - q^4 - 2p^2q^2)/p^2, \quad t_1 = S/C, \quad S = \sin\theta, \quad C = \cos\theta$$

$$I_1 = I + 2D_{17}w_{,xy} - D_{18}w_{,yy} - D_{19}w_{,xx} = C\rho hw_{,tt}. \tag{3}$$

In equations (3), $E_\xi, E_\eta, \nu_{\xi\eta}, \nu_{\eta\xi}, G_{\xi\eta}, G_{\xi z}, G_{\eta z}$ are the elastic orthotropic constants of the material of the plate. x and y are the oblique coordinates, ξ, η are the rectangular Cartesian coordinates, and θ is the skew angle. The differential operators N and R in equation (2), and the quantity I in equations (3) are the same as those in [3]. The various coefficients which are required to fully define N and R are given in

[1] Assistant Professor, Department of Mechanical and Industrial Engineering, Clarkson College of Technology, Potsdam, N.Y. 13676.

Manuscript received by ASME Applied Mechanics Division, June, 1979; final revision, February, 1980.

Table 1 Values of $(T/T_0)10^4$ for a rectangular plate

w_0/h \ $h/2a$	$r = 0.5$			$r = 1.0$		
	1/10	1/20	*	1/10	1/20	*
0	10182[a]	10044	10000	10337	10081	10000
	12935[b]	10776	10000	12847	10757	10000
0.5	9931	9822	9795	10075	9860	9793
	12077	10388	9761	12019	10374	9761
1.0	9323	9262	9245	9429	9286	9239
	10325	9470	9133	10286	9464	9134
1.5	8544	8519	8501	8605	8533	8491
	8614	8372	8309	8597	8378	8310

* = transverse shear and rotatory inertia effects excluded
[a] = isotropic
[b] = orthotropic

Table 2 Values of $(T/T_0)10^4$ for a 15° skew plate

w_0/h \ $h/2a$	$r = 0.5$			$r = 1.0$		
	1/10	1/20	*	1/10	1/20	*
0	10183[a]	10043	10000	10328	10078	10000
	13167[b]	10839	10000	13114	10832	10000
0.5	9977	9845	9822	10079	9883	9817
	12947	10751	9948	12884	10729	9940
1.0	9424	9358	9338	9532	9376	9322
	12395	10498	9796	12286	10455	9766
1.5	8714	8687	8666	8751	8672	8637
	11613	10130	9558	11489	10043	9494

* = transverse shear and rotatory inertia effects excluded
[a] = isotropic
[b] = orthotropic

Table 3 Values of $(T/T_0)10^4$ for a 30° skew plate

w_0/h \ $h/2a$	$r = 0.5$			$r = 1.0$		
	1/10	1/20	*	1/10	1/20	*
0	10188[a]	10042	10000	10313	10069	10000
	14013[b]	11070	10000	14246	11149	10000
0.5	10028	9910	9885	10141	9913	9870
	13943	11032	9988	14123	11094	9978
1.0	9659	9575	9561	9735	9558	9509
	13764	10972	9950	13872	10986	9911
1.5	9122	9089	9084	9127	9000	8983
	13495	10868	9889	13477	10825	9803

* = transverse shear and rotatory inertia effects excluded
[a] = isotropic
[b] = orthotropic

Appendix of reference [3]. However, the coefficients a_{ij}, $E_1 - E_3$ are to be changed as given later to take into account the orthotropy of the plate material.

$$a_{11} = E_1/C^3, \quad a_{22} = C\{E_2 + E_1t_1^4 + 2t_1^2(E_3 + 2G_{\xi\eta})\}$$

$$a_{44} = (G_{\xi\eta} + E_1t_1^2)/C$$

$$a_{55} = G_{\xi z}/C, \quad a_{66} = CG_{\eta z} + St_1G_{\xi z}, \quad a_{12} = (E_3 + E_1t_1^2)/C$$

$$a_{14} = -E_1t_1/C^2, \quad a_{24} = -t_1(2G_{\xi\eta} + E_1t_1^2 + E_3),$$

$$a_{56} = -t_1G_{\xi z} \quad (4)$$

where

$$E_1 = E_\xi/\nu', \quad E_2 = E_\eta/\nu', \quad E_3 = E_\xi\nu_{\eta\xi}/\nu' = E_\eta\nu_{\xi\eta}/\nu',$$

$$\nu' = 1 - \nu_{\xi\eta}\nu_{\eta\xi}$$

when the normal stress σ_z is assumed to be zero [3].

Equations (1) and (2) represent a system of two equations governing the large amplitude flexural vibrations of orthotropic skew plates. The effects of transverse shear deformation and rotatory inertia are included in these equations. By taking $k_1 - k_4$ and a_{ij} suitably, as indicated in Appendix of [3], these two equations can be readily reduced to the corresponding equations applicable for isotropic skew plates [3]. Equations (1) and (2) are nonlinear and coupled and hence exact solutions to these are very difficult to obtain.

Example

Approximate solutions are given here for the large amplitude free flexural vibrations of an orthotropic skew plate of dimensions $2a$ and $2b$. A single-mode expression for w is chosen to satisfy the boundary conditions along the clamped edges as well as the appropriate geometrical requirements [3] as

$$w = \frac{f(\tau)}{4} h \left(1 + \cos\frac{\pi x}{a}\right)\left(1 + \cos\frac{\pi y}{b}\right) \quad (5)$$

Substituting equation (5) in equation (1) and assuming that the edges of the plate are movable [3], a solution for F is determined. The expression for F as well as the coefficient $a_1 - a_{10}$ in F are the same as in [3] except that in this case the quantity E in the coefficient d is to be replaced by E_η. The expression for F thus obtained and the lateral displacement w in equation (5) are now substituted in equation (2) and is satisfied approximately by integrating the error function over the area of the plate. This procedure leads to a time-differential equation in F as follows:

$$b_1\frac{d^6f}{d\tau^6} + b_2\frac{d^4f_1}{d\tau^4} + b_3\frac{d^2f_2}{d\tau^2} + b_4f + b_5f^3 = 0 \quad (6)$$

where the nondimensional time $\tau = tq^{1/2}$, $q = E_\xi/(\rho a^2)$,

$$b_1 = c_4, \; b_2 = c_3, \; b_3 = c_2, \; b_4 = c_1, \; b_5 = c_5,$$

$$b_6 = c_8/(24c_3), \quad b_7 = c_6/(3c_2)$$

$$f_1 = b_2(f + b_6f^3), \quad f_2 = b_3(f + b_7f^3) \quad (7)$$

The coefficients $c_1 - c_8$ in equation (7) are defined in the Appendix of reference [3].

Equation (6) is the modal equation applicable for the large amplitude-free, flexural vibration of a clamped orthotropic skew plate with movable edges. Solutions to this nonlinear equation have been obtained using the numerical Runge-Kutta method. The ratio of the nonlinear period of vibration T, including the effects of the transverse shear deformation and rotatory inertia, to the corresponding linear period T_0 of a classical plate, not including these effects, has been computed for different nondimensional amplitudes (w_0/h), plate aspect ratios (r), skew angles (θ), and thickness-to-length ratios $(h/2a)$ of isotropic and orthotropic plates. For the sake of easy comparison results where these effects are not considered are also presented. These are shown in Tables 1, 2, and 3. The material constants of the orthotropic plate are taken to be $k^2 = 0.057$, $q^2 = 0.256$, $G_{\xi\eta}/E_\xi = G_{\xi z}/E_\xi = 0.02$, $G_{\eta z}/E_\xi = 0.011$ as in reference [2]. In the case of isotropic plates $k^2 = 1$, $q^2 = 0.3$, and $G/E = 0.385$.

Conclusions

The effects of transverse shear deformation and rotatory inertia on the large amplitude vibration of rectangular and skew plates are shown by an increase in the period ratio although the increase is less at moderately large amplitudes. The relationship between the period and amplitude in all the cases investigated here is seen to exhibit the hardening type of nonlinearity, i.e., period decreases with increasing amplitude. The effect of the particular type of orthotropy that is considered here is to produce a significant increase in the nonlinear period, the increase being more at high aspect ratios. It can be observed that orthotropic plates, whether rectangular or skew, are more sensitive to the influences of transverse shear deformation and rotatory inertia than isotropic plates. Also, the influences of these effects on the nonlinear dynamic behavior of orthotropic skew plates is seen to increase with the skew angle. The transverse shear and rotatory inertia effects play a very important role particularly for moderately thick orthotropic plates whereas for all practical purposes these effects have no influence on thin plates with thickness-to-length ratio less than 0.025.

References

1 Chia, C. Y., *Nonlinear Analysis of Plates*, Mc Graw-Hill, New York, 1980.

2 Wu, C. I., and Vinson, J. R., "On the Nonlinear Oscillations of Plates Composed of Composite Materials," *Journal of Composite Materials*, Vol. 3, 1969, pp. 548–561.

3 Sathyamoorthy, M., "Vibration of Skew Plates at Large Amplitudes Including Shear and Rotatory Inertia Effects," *International Journal of Solids and Structures*, Vol. 14, 1978, pp. 869–880.

4 Sathyamoorthy, M., "Effects of Large Amplitude, Shear, and Rotatory Inertia on Vibration of Rectangular Plates," *Journal of Sound and Vibration*, Vol. 63, 1979, pp. 161–167.

Solution of Poisson's Equation in a Semicircular Region With a Hole[1]

A. K. Naghdi[2]

Introduction

Solutions of Poisson's and Laplace's equations in a multiply connected circular region have been derived by a few authors in recent years. Among these authors are Redberger and Charles [1], Snyder and Goldstein [2], Gaydon and Nuttall [3], El-Saden [4], Rowley and Payne [5], and Ling [6] who investigated the problems of fully developed laminar flow, two-dimensional heat conduction and torsion of prismatic bars. However, the solutions of the aforementioned equations have not been completely investigated for the case of a semicircular region with a circular cutout. In this investigation, first, a closed-form solution for the Green's function satisfying a homogeneous outer boundary condition is derived. Next, this function is utilized to generate certain eigenfunctions of Laplace's equation. Finally, these eigenfunctions are combined with an appropriate closed-form particular integral of the governing equation to form the desired solution. Numerical results for the cases of two-dimensional heat conduction and viscous fluid flow are presented.

Analysis

Consider a semicircular region containing a circular cutout as shown in Fig. 1. Choose a set of dimensionless polar coordinates $\rho = r/R$, θ with the origin at point 0, and let ϕ be the angle measured from a radial line at the center of the circular hole. The solution of Poisson's equation

$$\frac{\partial^2\bar{\psi}}{\partial\rho^2}+\frac{1}{\rho}\frac{\partial\bar{\psi}}{\partial\rho}+\frac{1}{\rho^2}\frac{\partial^2\bar{\psi}}{\partial\theta^2}=\bar{s} \tag{1}$$

in which $\bar{s}$ = constant, satisfying the conditions

$$\begin{aligned}\bar{\psi}&=0 \quad \text{on the outer boundary}\\ \bar{\psi}&=h(\phi) \quad \text{on the inner boundary}\end{aligned} \tag{2}$$

is sought in the following form:

$$\bar{\psi}=\tilde{\psi}+A_0\bar{\psi}_0{}^*+A_1\bar{\psi}_1{}^*+\ldots+A_j\bar{\psi}_j{}^*+\ldots +B_1\bar{\psi}_1{}^0+B_2\bar{\psi}_2{}^0+\ldots+B_j\bar{\psi}_j{}^0+\ldots \tag{3}$$

in which $\tilde{\psi}$ is a particular solution of the governing equation, $\bar{\psi}_j{}^*$, $\bar{\psi}_j{}^0$ are certain eigenfunctions of Laplace's equation and A_j, B_j are certain unknown constants to be determined. Each individual function $\bar{\psi}_j{}^*$ or $\bar{\psi}_j{}^0$ as well as $\tilde{\psi}$ is required to satisfy the homogeneous outer boundary condition

$$\left.\begin{aligned}\bar{\psi}_j{}^*=\bar{\psi}_j{}^0=\tilde{\psi}=0, \quad \text{at} \quad &\rho=1,\\ &\theta=0,\\ &\theta=\pi.\end{aligned}\right\} \tag{4}$$

These functions are now derived.

Derivation of $\bar{\psi}_j{}^*$ and $\bar{\psi}_j{}^0$

In order to derive these eigenfunctions, the following technique is followed. First, the solution of Poisson's equation

$$\nabla^2\tilde{\psi}^*=\sum_{n=1}^{\infty}s_n{}^*\,\delta\,(\rho-\rho_0)\sin n\theta, \tag{5}$$

in which $s_n{}^*$ are constants and δ is the unit impulse function, is sought in the form

$$\tilde{\psi}^*=\sum_{n=1}^{\infty}f_n(\rho)\sin n\theta. \tag{6}$$

The substitution of relation (6) into equation (5) gives

$$\frac{d^2f_n\,(\rho)}{d\rho^2}+\frac{1}{\rho}\frac{df_n\,(\rho)}{d\rho}-\frac{n^2}{\rho^2}f_n\,(\rho)=s_n{}^*\,\delta\,(\rho-\rho_0). \tag{7}$$

The complementary solution f_{nc} of the differential equation (7) is obtained in the usual way, and its particular integral f_{np} is found with the known method of variation of parameters [7]. In the derivation of f_{np} it is considered that the function must be continuous at $\rho=\rho_0$. Thus, employing the condition $f_n(\rho)=0$ at $\rho=1$, the following results are obtained:

$$\left.\begin{aligned}\tilde{\psi}^*&=\sum_{n=1}^{\infty}\frac{s_n{}^*}{2n}\rho_0{}^{n+1}\,(\rho^n-\rho^{-n})\sin n\theta \qquad \text{for } \rho\geq\rho_0,\\ \tilde{\psi}^*&=\sum_{n=1}^{\infty}\frac{s_n{}^*}{2n}\,(\rho_0{}^{n+1}-\rho_0{}^{-n+1})\,\rho^n\sin n\theta \qquad \rho<\rho_0\end{aligned}\right\} \tag{8}$$

The Green's function is now obtained from (8) by substituting the appropriate Fourier coefficients for a concentrated source in place of $s_n{}^*$. The final results are as follows:

$$\left.\begin{aligned}\tilde{\psi}_c{}^*&=\frac{2P}{\pi R^2}\left\{\sum_{n=1}^{\infty}\frac{\rho_0{}^n}{n}\,(\rho^n-\bar{\rho}^n)\left[\cos n\,(\theta_0+\theta)-\cos n\,(\theta_0-\theta)\right]\right\}=\bar{\psi}_{\mathrm{I}}\,(\rho,\theta,\rho_0,\theta_0) \quad \text{for } \rho\geq\rho_0,\\ \tilde{\psi}_c{}^*&=\frac{2P}{\pi R^2}\left\{\sum_{n=1}^{\infty}\frac{\rho^n}{n}\,(\rho_0{}^n-\bar{\rho}_0{}^n)\left[\cos n\,(\theta_0+\theta)-\cos n\,(\theta_0-\theta)\right]\right\}=\bar{\psi}_{\mathrm{II}}\,(\rho,\theta,\rho_0,\theta_0) \quad \text{for} \quad \rho<\rho_0,\end{aligned}\right\} \tag{9}$$

in which P is the magnitude of the concentrated source. Note that in relations (9)

$$\bar{\psi}_{\mathrm{II}}\,(\rho,\theta,\rho_0,\theta_0)=\bar{\psi}_{\mathrm{I}}\,(\rho_0,\theta,\rho,\theta_0).$$

It has been shown previously [8–10] that series similar to those involved in (9) have closed-form sums:

$$\left.\begin{aligned}&\sum_{n=1}^{\infty}\frac{\bar{e}^{n\xi}}{n}\cos n\alpha=F_1(\xi,\alpha),\\ &F_1(\xi,\rho)=\frac{1}{2}\ln\frac{\cosh\xi-1}{\cosh\xi-\cos\alpha}-\ln(1-\bar{e}^{\xi}) \quad \xi>0,\\ &\sum_{n=1}^{\infty}\frac{\bar{e}^{n\xi}}{n}\sin n\alpha=F_2(\xi,\alpha),\\ &F_2(\xi,\alpha)=-\frac{\alpha}{2}+\arctan\left[\frac{(1+\cosh\xi)\tan\dfrac{\alpha}{2}}{\sinh\xi}\right]\\ &F_2(\xi,\alpha)=-F_2[\xi,(2\pi-\alpha)] \quad \xi>0,\ 2\pi>\alpha>\pi.\end{aligned}\right\} \tag{10}$$

[1]The author wishes to thank the Department of Computer Services of IUPUI for providing CDC 6600 computer time for this investigation.

[2]Professor of Aeronautical-Astronautical Engineering and Mathematical Sciences, Purdue School of Engineering and Technology at Indianapolis, Ind. 46205.

Manuscript received by ASME Applied Mechanics Division, November, 1979; final revision, March, 1980.

2 Wu, C. I., and Vinson, J. R., "On the Nonlinear Oscillations of Plates Composed of Composite Materials," *Journal of Composite Materials*, Vol. 3, 1969, pp. 548–561.

3 Sathyamoorthy, M., "Vibration of Skew Plates at Large Amplitudes Including Shear and Rotatory Inertia Effects," *International Journal of Solids and Structures*, Vol. 14, 1978, pp. 869–880.

4 Sathyamoorthy, M., "Effects of Large Amplitude, Shear, and Rotatory Inertia on Vibration of Rectangular Plates," *Journal of Sound and Vibration*, Vol. 63, 1979, pp. 161–167.

Solution of Poisson's Equation in a Semicircular Region With a Hole[1]

A. K. Naghdi[2]

Introduction

Solutions of Poisson's and Laplace's equations in a multiply connected circular region have been derived by a few authors in recent years. Among these authors are Redberger and Charles [1], Snyder and Goldstein [2], Gaydon and Nuttall [3], El-Saden [4], Rowley and Payne [5], and Ling [6] who investigated the problems of fully developed laminar flow, two-dimensional heat conduction and torsion of prismatic bars. However, the solutions of the aforementioned equations have not been completely investigated for the case of a semicircular region with a circular cutout. In this investigation, first, a closed-form solution for the Green's function satisfying a homogeneous outer boundary condition is derived. Next, this function is utilized to generate certain eigenfunctions of Laplace's equation. Finally, these eigenfunctions are combined with an appropriate closed-form particular integral of the governing equation to form the desired solution. Numerical results for the cases of two-dimensional heat conduction and viscous fluid flow are presented.

Analysis

Consider a semicircular region containing a circular cutout as shown in Fig. 1. Choose a set of dimensionless polar coordinates $\rho = r/R$, θ with the origin at point 0, and let ϕ be the angle measured from a radial line at the center of the circular hole. The solution of Poisson's equation

$$\frac{\partial^2\bar{\psi}}{\partial\rho^2}+\frac{1}{\rho}\frac{\partial\bar{\psi}}{\partial\rho}+\frac{1}{\rho^2}\frac{\partial^2\bar{\psi}}{\partial\theta^2}=\bar{s} \tag{1}$$

in which $\bar{s}$ = constant, satisfying the conditions

$$\begin{aligned}\bar{\psi}&=0 \quad \text{on the outer boundary}\\ \bar{\psi}&=h(\phi) \quad \text{on the inner boundary}\end{aligned} \tag{2}$$

is sought in the following form:

$$\bar{\psi}=\tilde{\psi}+A_0\bar{\psi}_0{}^*+A_1\bar{\psi}_1{}^*+\ldots+A_j\bar{\psi}_j{}^*+\ldots + B_1\bar{\psi}_1{}^0+B_2\bar{\psi}_2{}^0+\ldots+B_j\bar{\psi}_j{}^0+\ldots \tag{3}$$

in which $\tilde{\psi}$ is a particular solution of the governing equation, $\bar{\psi}_j{}^*$, $\bar{\psi}_j{}^0$ are certain eigenfunctions of Laplace's equation and A_j, B_j are certain unknown constants to be determined. Each individual function $\bar{\psi}_j{}^*$ or $\bar{\psi}_j{}^0$ as well as $\tilde{\psi}$ is required to satisfy the homogeneous outer boundary condition

$$\left.\begin{aligned}\bar{\psi}_j{}^*=\bar{\psi}_j{}^0=\tilde{\psi}=0, \quad \text{at} \quad &\rho=1,\\ &\theta=0,\\ &\theta=\pi.\end{aligned}\right\} \tag{4}$$

These functions are now derived.

Derivation of $\bar{\psi}_j{}^*$ and $\bar{\psi}_j{}^0$

In order to derive these eigenfunctions, the following technique is followed. First, the solution of Poisson's equation

$$\nabla^2\tilde{\psi}^*=\sum_{n=1}^{\infty}s_n{}^*\,\delta\,(\rho-\rho_0)\sin n\theta, \tag{5}$$

in which $s_n{}^*$ are constants and δ is the unit impulse function, is sought in the form

$$\tilde{\psi}^*=\sum_{n=1}^{\infty}f_n(\rho)\sin n\theta. \tag{6}$$

The substitution of relation (6) into equation (5) gives

$$\frac{d^2f_n\,(\rho)}{d\rho^2}+\frac{1}{\rho}\frac{df_n\,(\rho)}{d\rho}-\frac{n^2}{\rho^2}f_n\,(\rho)=s_n{}^*\,\delta\,(\rho-\rho_0). \tag{7}$$

The complementary solution f_{nc} of the differential equation (7) is obtained in the usual way, and its particular integral f_{np} is found with the known method of variation of parameters [7]. In the derivation of f_{np} it is considered that the function must be continuous at $\rho=\rho_0$. Thus, employing the condition $f_n(\rho)=0$ at $\rho=1$, the following results are obtained:

$$\left.\begin{aligned}\tilde{\psi}^*&=\sum_{n=1}^{\infty}\frac{s_n{}^*}{2n}\rho_0{}^{n+1}\,(\rho^n-\rho^{-n})\sin n\theta \quad &&\text{for } \rho\geq\rho_0,\\ \tilde{\psi}^*&=\sum_{n=1}^{\infty}\frac{s_n{}^*}{2n}\,(\rho_0{}^{n+1}-\rho_0{}^{-n+1})\,\rho^n\sin n\theta \quad &&\rho<\rho_0\end{aligned}\right\} \tag{8}$$

The Green's function is now obtained from (8) by substituting the appropriate Fourier coefficients for a concentrated source in place of $s_n{}^*$. The final results are as follows:

$$\left.\begin{aligned}\tilde{\psi}_c{}^*&=\frac{2P}{\pi R^2}\left\{\sum_{n=1}^{\infty}\frac{\rho_0{}^n}{n}\,(\rho^n-\bar{\rho}^n)\left[\cos n\,(\theta_0+\theta)-\cos n\,(\theta_0-\theta)\right]\right\}=\bar{\psi}_{\mathrm{I}}\,(\rho,\theta,\rho_0,\theta_0) \quad \text{for } \rho\geq\rho_0,\\ \tilde{\psi}_c{}^*&=\frac{2P}{\pi R^2}\left\{\sum_{n=1}^{\infty}\frac{\rho^n}{n}\,(\rho_0{}^n-\bar{\rho}_0{}^n)\left[\cos n\,(\theta_0+\theta)-\cos n\,(\theta_0-\theta)\right]\right\}=\bar{\psi}_{\mathrm{II}}\,(\rho,\theta,\rho_0,\theta_0) \quad \text{for} \quad \rho<\rho_0,\end{aligned}\right\} \tag{9}$$

in which P is the magnitude of the concentrated source. Note that in relations (9)

$$\bar{\psi}_{\mathrm{II}}\,(\rho,\theta,\rho_0,\theta_0)=\bar{\psi}_{\mathrm{I}}\,(\rho_0,\theta,\rho,\theta_0).$$

It has been shown previously [8–10] that series similar to those involved in (9) have closed-form sums:

$$\left.\begin{aligned}&\sum_{n=1}^{\infty}\frac{\bar{e}^{n\xi}}{n}\cos n\alpha=F_1(\xi,\alpha),\\ &F_1(\xi,\rho)=\frac{1}{2}\ln\frac{\cosh\xi-1}{\cosh\xi-\cos\alpha}-\ln(1-\bar{e}^{\xi}) \quad \xi>0,\\ &\sum_{n=1}^{\infty}\frac{\bar{e}^{n\xi}}{n}\sin n\alpha=F_2(\xi,\alpha),\\ &F_2(\xi,\alpha)=-\frac{\alpha}{2}+\arctan\left[\frac{(1+\cosh\xi)\tan\dfrac{\alpha}{2}}{\sinh\xi}\right]\\ &F_2(\xi,\alpha)=-F_2[\xi,(2\pi-\alpha)] \quad \xi>0,\ 2\pi>\alpha>\pi.\end{aligned}\right\} \tag{10}$$

[1]The author wishes to thank the Department of Computer Services of IUPUI for providing CDC 6600 computer time for this investigation.

[2]Professor of Aeronautical-Astronautical Engineering and Mathematical Sciences, Purdue School of Engineering and Technology at Indianapolis, Ind. 46205.

Manuscript received by ASME Applied Mechanics Division, November, 1979; final revision, March, 1980.

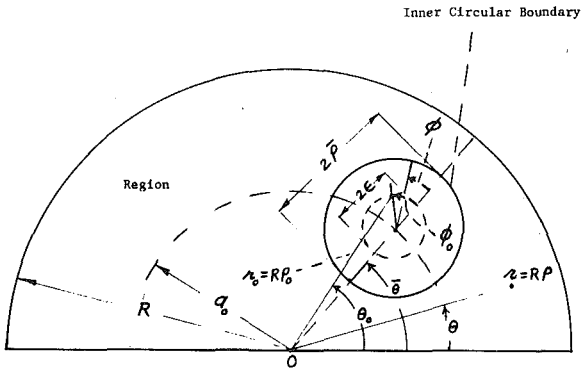

Fig. 1 Semicircular region with a circular cutout.

Since $\rho_0 < 1$ it is evident that $\bar{\psi}_I$ and $\bar{\psi}_{II}$ can be written in closed forms. For example one writes

$$\bar{\psi}_I(\rho, \theta, \rho_0, \theta_0) = F_1(-\ln \rho\,\rho_0, \alpha_1) - F_1(-\ln \rho\rho_0, \alpha_2) - F_1\left(-\ln \frac{\rho_0}{\rho}, \alpha_1\right) + F_1\left(-\ln \frac{\rho_0}{\rho}, \alpha_2\right),$$
$$\alpha_1 = \theta_0 + \theta, \quad \alpha_2 = \theta_0 - \theta, \quad \text{for} \quad \rho > \rho_0. \tag{11}$$

Excluding the point of application of the concentrated source, it is not too difficult to show that the Green's function $\tilde{\psi}_c$ is harmonic in both regions $\rho > \rho_0$ and $\rho < \rho_0$ and that is possesses continuous derivatives of any order as ρ approaches ρ_0.

Consider now a small circular path with radius ϵ at the center of the circular inner boundary (see Fig. 1). Multiplying $\tilde{\psi}_c^*$ by $\cos j\,\phi_0$, $\sin j\,\phi_0$ and integrating the results on this path, the linearly independent eigenfunctions $\bar{\psi}_j^*$ and $\bar{\psi}_j{}^0$ are derived in the form of integrals

$$\bar{\psi}_j = \int_0^{2\pi} \tilde{\psi}_c^*(\rho, \theta, \rho_0, \theta_0) \cos j\phi_0 \epsilon d\phi_0,$$
$$\bar{\psi}_j{}^0 = \int_0^{2\pi} \tilde{\psi}_c^*(\rho, \theta, \rho_o, \theta_0) \sin j\phi_0 \epsilon d\phi_0. \tag{12}$$

Determination of $\tilde{\psi}$

The right-hand side of equation (1) is expanded in Fourier series, and the ordinary technique of solving partial differential equations is applied to yield the following solution:

$$\tilde{\psi} = \bar{s}\left[-\sum_{n=1,3,5}^{\infty} \frac{4\rho^n}{\pi(2+n)(2-n)n} \sin n\theta + 4\rho^2 \sum_{n=1,3,5}^{\infty} \frac{1}{\pi(2+n)(2-n)n} \sin n\theta\right], \tag{13}$$

which satisfies a homogeneous outer boundary condition. Employing partial fraction technique, and utilizing relations (10), the first series in the right-hand side of (13) is written in closed form. The second series is also summed with a similar technique, however for the sake of brevity the intermediate steps are avoided. The final result is

$$\tilde{\psi} = -\frac{4\bar{s}}{\pi}\left\{\frac{1}{4}F_2(-\ln \rho, \theta) - \frac{1}{8\rho^2}[\rho \sin\theta + F_2(-\ln\rho, \theta)\cos 2\theta - F_1(-\ln\rho, \theta)\sin 2\theta] - \frac{\rho^2}{8}[-\rho\sin\theta + F_2(-\ln\rho, \theta)\cos 2\theta + F_1(-\ln\rho, \theta)\sin 2\theta]\right\} + \bar{s}\frac{\rho^2}{4}(1 - \cos 2\theta) \quad \rho < 1. \tag{14}$$

Applications in Steady-State Two-Dimensional Heat Conduction and Laminar Fluid Flow

For the case of two-dimensional steady-state heat conduction in an infinitely long semicircular cylinder with a circular cylindrical cavity and without a heat source the particular solution $\tilde{\psi}$ is set equal to zero. It is assumed that the nondimensional temperature $\overline{T}$ is zero on the outer boundary and has a constant value of 1 on the inner boundary. Since the homogeneous outer boundary condition is automatically satisfied by the eigenfunctions $\bar{\psi}_j^*$ and $\bar{\psi}_j{}^0$, it remains only to satisfy the inner boundary condition. To achieve this goal, $2i + 2$ terms in series (3) are selected and the condition $\overline{T} = 1$ at $m > 2i + 2$ points of the inner boundary is satisfied. This procedure gives a set of m by $2i + 2$ linear algebraic equations, which are normalized and solved approximately by the method of least square error [11]. The dimensionless temperature distribution for a symmetrical configuration is presented in Table 1. For the case of fully developed laminar viscous flow in a semicircular channel with a circular cylindrical inner core the particular solution $\tilde{\psi}$ is not zero as $(1/\mu)(\partial p/\partial z) = \text{const} \neq 0$. Here $\partial p/\partial z$ is the rate of change of pressure along the length of the channel, and μ is the absolute viscosity. The axial velocity in this case is zero at both inner and outer boundaries. The procedure of numerical solution is identical to that of the case of heat conduction. Denoting by W_0 the axial velocity at $\rho = 0.6$ and $\theta = 19\pi/32$ the values of dimensionless velocity $\overline{W} = W/W_0$ for a nonsymmetrical configuration are given in Table 2.

The solution obtained in this investigation are very accurate. For example, employing 32 equations with 24 unknowns the inner boundary condition is satisfied with relative error of the order 10^{-5}. It is interesting to note that the solution $\bar{\psi}$ given by relation (3) can also be employed for the cases in which the inner cutout is noncircular.

Table 1 The values of the nondimensional temperature $\overline{T}$ versus ρ and θ for the case in which $\overline{T} = 0$, $\overline{T} = 1$, respectively, on the outer and inner boundaries, and for $\bar{\alpha}_0 = \alpha_0/R = 0.3, \theta = \pi/2$, and $\bar{\rho} = 0.1$

$N = 32\theta/\pi$ θ in rad	$\rho = 0.2$	$\rho = 0.4$	$\rho = 0.6$	$\rho = 0.8$
4	0.206763	0.183056	0.111839	0.049988
8	0.446777	0.405957	0.237204	0.103775
12	0.754586	0.717176	0.369337	0.155086
14	0.918345	0.900144	0.418825	0.172355
16	0.999999	0.999996	0.437899	0.178692

Table 2 The values of the nondimensional velocity $\overline{W}$ for various ρ and θ for the case of $\bar{\alpha}_0 = \alpha_0/R = 0.5, \theta = 1$ rad, and $\bar{\rho} = 0.15$

$$\bar{s} = \frac{R^2\,\partial p/\partial z}{\mu W_0} = -48.742452$$

$N = 32\theta/\pi$ θ in rad	$\rho = 0.2$	$\rho = 0.4$	$\rho = 0.6$	$\rho = 0.8$
1	0.134031	0.250670	0.403591	0.432428
7	0.583469	0.161994	0.314148	0.469944
13	0.830446	0.091766	0.119459	0.132802
19	1.087369	1.270978	1.000000	0.465454
25	0.975399	1.498714	1.478780	0.933460

References

1 Redberger, P. J., and Charles, M. W., "Axial Laminar Flow in a Circular Pipe Containing a Fixed Eccentric Core," *Canadian Journal of Chemical Engineers* Vol. 40, No. 4, Aug. 1962, pp. 148–151.

2 Snyder, W. T., and Goldstein, G. A., "An Analysis of Fully Developed Laminar Flow in an Eccentric Annulus," *AIChE Journal*, Vol. 11, No. 3, May 1965, pp. 462–467.

3 Gaydon, F. A., and Nuttall, H., "Viscous Flow through Tubes of Multiply Connected Cross Sections, ASME JOURNAL OF APPLIED MECHANICS, Vol. 26, 1959, pp. 573–576.

4 El-Saden, M. R., "Heat Conduction in an Eccentrically Hollow, Infinitely Long Cylinder With Internal Heat Generation," ASME *Journal of Heat Transfer*, Vol. 83, Nov. 1961, pp. 510–512.

5 Rowley, J. C., and Payne, J. B., "Steady-State Temperature Solution

for a Heat Generating Circular Cylinder Cooled by a Ring of Holes," ASME *Journal of Heat Transfer*, Vol. 86, 1964, pp. 531–536.

6 Ling, C. B., "Torsion of a Circular Tube With Longitudinal Circular Holes," *Quarterly of Applied Mathematics*, Vol. 5, No. 2, July 1947, pp. 168–181.

7 Miller, F. H., *Partial Differential Equations*, 11th ed., Wiley, 1965.

8 Kantorovich, L. V., and Krylov, V. I., *Approximate Methods of Higher Analysis*, Interscience Publishers, Inc. New York—The Netherlands, 1964.

9 Naghdi, A. K., and Gersting, J. M., Jr., "The Effect of a Tranverse Shear Acting on the Edge of a Circular Cutout in a Simply Supported Circular Cylindrical Shell," *Ingenieur—Archive*, Vol. 42, No. 2, Jan. 1973, pp. 141–150.

10 Naghdi, A. K., "On the Convergence of Series Solutions for a Short Beam" ASME JOURNAL OF APPLIED MECHANICS Vol, 41, pp. 530–531 1974.

11. Hildebrand, F. B., *Introduction to Numerical Analysis*, McGraw-Hill, New York, 1956.

Homogenization and Smoothing: A Unified View of Two Derivations of Effective Property Theories and Extensions

L. Fishman[1] and J. J. McCoy[2]

The response of a continuum characterized by two widely differing length scales, parameterized by the dimensionless ratio ϵ, is considered in the context of the composite materials problem. The development of a bulk property theory appropriate in the $\epsilon \to 0$ limit is examined, both from the perspective of the deterministic homogenization literaure and the smoothing method associated with statistical continuum theory, and a unified framework is established. The extension of bulk property theories through the development of ordered expansions in powers of ϵ is discussed and specifically related to analogous treatments in linear-gas relaxation theory.

Introduction

The purpose of this Note is to emphasize a structural unity of two procedures, one termed a smoothing and one termed an homogenization, which have received attention for deriving macroscale equations for continua that exhibit heterogeneity on a microscale. The task of deriving such equations can be said to comprise the composite materials problem.

While intended to address the same problems, the two procedures have been historically associated with different modelings of the microscale heterogeneity and further, from a formal mathematical viewpoint, with different limiting processes. Smoothing [1] has been associated with a statistical description of the microscale variability, formally, in a weak fluctuation strength limit; homogenization, as presented in recent studies [2–7], has been associated with a periodic modeling, formally, in the limit of small-scale variations. Although the periodic modeling problems considered possess a fundamental underlying stochastic interpretation [8], the inherent structural unity encompassing both smoothing and homogenization is emphasized in a most transparent manner through the introduction into the microscale description in homogenization of the novel concept of a movable origin [5, 6]. Averaging over the location of the movable origin can then be used to identify and to separate micro and macroresponse measures in homogenization, in the same manner as ensemble averaging is used in smoothing; indeed, the averaging operation can be viewed in the context of an ensemble average.

The existence of a common framework does not preclude differences in the calculational details of the two procedures, as they are usually presented. Further, these calculational details lead quite naturally to a duality in the interpretations made at the macroscale level, a fact which we would emphasize.

It is to be noted that the large amount of research on these procedures notwithstanding, their specific applications to physical problems are often formal. Hence, the validity of such application is often somewhat uncertain. Particular examples in smoothing, for instance, include the assumed convergence properties of the effective index operator and the subsequent heuristic two-scale analysis of the macroscale equation [9]. Likewise, homogenization in the strict context of the composite materials problem, that is the direct derivation of macroscale response equations from the microscale equations, involves a formal perturbational ansatz, termed a two-scale smoothing by Keller [7], which can be related to a proper two-scale asymptotic treatment [7, 8]. Further, the replacement of a nonlocal, integral operator by a infinite-order differential operator, as is implicitly accomplished in homogenization, is known, from experience, to be fraught with danger. Questions of the mathematical rigor of homogenization, of smoothing, and of the replacement previously mentioned have been raised in a rather extensive and diverse literature. A discussion of these questions within the context of the composite materials problem is available [10].

Derivation of Macroscale Equations

The equations governing the state of stress in a heterogeneous linearly elastic solid are written

$$\partial_i \tau_{ij} = f_j, \tag{1a}$$

$$\tau_{ij} = C_{ijkl}(\mathbf{x}) e_{kl}, \quad \mathbf{x} \text{ in } D \tag{1b}$$

$$\delta_{ikm}\delta_{jln}\partial_l\partial_k e_{mn} = 0, \tag{1c}$$

along with boundary conditions, taken here to be traction conditions; i.e.,

$$n_j \tau_{ij} = t_i, \quad \mathbf{x} \text{ in } \partial D \tag{1d}$$

The response field variables are the symmetric stress τ_{ij}, and strain, e_{ij}, tensors; f_i is a body force term taken to vary on the macroscale; C_{ijkl} is the microscale varying elastic moduli tensor. The alternating tensor is denoted by δ_{ijk}. Further, the prescribed surface normal, n_i, and surface traction, t_i, are also taken to vary on the macroscale. Equation (1a) is a statement of momentum balance; equation (1b) is Hooke's law; and equation (1c) is a compatibility requirement that the strain tensor is derivable from a displacement vector according to

$$e_{ij} = \frac{1}{2}(\partial_j u_i + \partial_i u_j) \tag{1e}$$

The microscale heterogeneity is modeled in two ways:

1 $C_{ijkl}(\mathbf{x})$ is a statistically homogeneous, random field

2 $C_{ijkl}(\mathbf{x})$ is described by a periodic function of unit period, denoted by $C_{ijkl}(\boldsymbol{\xi})$ where $\boldsymbol{\xi} = (\mathbf{x} - \mathbf{b})/\epsilon$.

In the second modeling, $\mathbf{b}$ locates the origin of a material property grid and ϵ is a small dimensionless number that relates the length scale natural for describing the heterogeneity, the $\boldsymbol{\xi}$ scale, to that natural for describing the specimen geometry. This length scale ratio, appearing explicitly in the periodic modeling, is implicitly understood as a correlation range measure in the stochastic modeling [8]. We note that there is no need to explicitly introduce it in the stochastic modeling at this point.

We now introduce a projection operator, P, which effects an averaging. For the stochastic modeling the average is an ensemble average, over an random function space; for the periodic modeling the average is also an ensemble average, over the continuous parameter, $\mathbf{b}$, taken now to be a random variable that can range over the unit cell with

[1] The Catholic University of America, Washington, D.C. 20064.

[2] The Catholic University of America, Washington, D.C. 20064. Mem. ASME.

Manuscript received by ASME Applied Mechanics Division, March, 1980; final revision, April, 1980.

for a Heat Generating Circular Cylinder Cooled by a Ring of Holes," ASME *Journal of Heat Transfer*, Vol. 86, 1964, pp. 531–536.

6 Ling, C. B., "Torsion of a Circular Tube With Longitudinal Circular Holes," *Quarterly of Applied Mathematics*, Vol. 5, No. 2, July 1947, pp. 168–181.

7 Miller, F. H., *Partial Differential Equations*, 11th ed., Wiley, 1965.

8 Kantorovich, L. V., and Krylov, V. I., *Approximate Methods of Higher Analysis*, Interscience Publishers, Inc. New York—The Netherlands, 1964.

9 Naghdi, A. K., and Gersting, J. M., Jr., "The Effect of a Tranverse Shear Acting on the Edge of a Circular Cutout in a Simply Supported Circular Cylindrical Shell," *Ingenieur—Archive*, Vol. 42, No. 2, Jan. 1973, pp. 141–150.

10 Naghdi, A. K., "On the Convergence of Series Solutions for a Short Beam" ASME JOURNAL OF APPLIED MECHANICS Vol, 41, pp. 530–531 1974.

11. Hildebrand, F. B., *Introduction to Numerical Analysis*, McGraw-Hill, New York, 1956.

Homogenization and Smoothing: A Unified View of Two Derivations of Effective Property Theories and Extensions

L. Fishman[1] and J. J. McCoy[2]

The response of a continuum characterized by two widely differing length scales, parameterized by the dimensionless ratio ϵ, is considered in the context of the composite materials problem. The development of a bulk property theory appropriate in the $\epsilon \to 0$ limit is examined, both from the perspective of the deterministic homogenization literaure and the smoothing method associated with statistical continuum theory, and a unified framework is established. The extension of bulk property theories through the development of ordered expansions in powers of ϵ is discussed and specifically related to analogous treatments in linear-gas relaxation theory.

Introduction

The purpose of this Note is to emphasize a structural unity of two procedures, one termed a smoothing and one termed an homogenization, which have received attention for deriving macroscale equations for continua that exhibit heterogeneity on a microscale. The task of deriving such equations can be said to comprise the composite materials problem.

While intended to address the same problems, the two procedures have been historically associated with different modelings of the microscale heterogeneity and further, from a formal mathematical viewpoint, with different limiting processes. Smoothing [1] has been associated with a statistical description of the microscale variability, formally, in a weak fluctuation strength limit; homogenization, as presented in recent studies [2–7], has been associated with a periodic modeling, formally, in the limit of small-scale variations. Although the periodic modeling problems considered possess a fundamental underlying stochastic interpretation [8], the inherent structural unity encompassing both smoothing and homogenization is emphasized in a most transparent manner through the introduction into the microscale description in homogenization of the novel concept of a movable origin [5, 6]. Averaging over the location of the movable origin can then be used to identify and to separate micro and macroresponse measures in homogenization, in the same manner as ensemble averaging is used in smoothing; indeed, the averaging operation can be viewed in the context of an ensemble average.

The existence of a common framework does not preclude differences in the calculational details of the two procedures, as they are usually presented. Further, these calculational details lead quite naturally to a duality in the interpretations made at the macroscale level, a fact which we would emphasize.

It is to be noted that the large amount of research on these procedures notwithstanding, their specific applications to physical problems are often formal. Hence, the validity of such application is often somewhat uncertain. Particular examples in smoothing, for instance, include the assumed convergence properties of the effective index operator and the subsequent heuristic two-scale analysis of the macroscale equation [9]. Likewise, homogenization in the strict context of the composite materials problem, that is the direct derivation of macroscale response equations from the microscale equations, involves a formal perturbational ansatz, termed a two-scale smoothing by Keller [7], which can be related to a proper two-scale asymptotic treatment [7, 8]. Further, the replacement of a nonlocal, integral operator by a infinite-order differential operator, as is implicitly accomplished in homogenization, is known, from experience, to be fraught with danger. Questions of the mathematical rigor of homogenization, of smoothing, and of the replacement previously mentioned have been raised in a rather extensive and diverse literature. A discussion of these questions within the context of the composite materials problem is available [10].

Derivation of Macroscale Equations

The equations governing the state of stress in a heterogeneous linearly elastic solid are written

$$\partial_i \tau_{ij} = f_j, \tag{1a}$$

$$\tau_{ij} = C_{ijkl}(\mathbf{x}) e_{kl}, \quad \mathbf{x} \text{ in } D \tag{1b}$$

$$\delta_{ikm}\delta_{jln}\partial_l\partial_k e_{mn} = 0, \tag{1c}$$

along with boundary conditions, taken here to be traction conditions; i.e.,

$$n_j \tau_{ij} = t_i, \quad \mathbf{x} \text{ in } \partial D \tag{1d}$$

The response field variables are the symmetric stress τ_{ij}, and strain, e_{ij}, tensors; f_i is a body force term taken to vary on the macroscale; C_{ijkl} is the microscale varying elastic moduli tensor. The alternating tensor is denoted by δ_{ijk}. Further, the prescribed surface normal, n_i, and surface traction, t_i, are also taken to vary on the macroscale. Equation (1a) is a statement of momentum balance; equation (1b) is Hooke's law; and equation (1c) is a compatibility requirement that the strain tensor is derivable from a displacement vector according to

$$e_{ij} = \frac{1}{2}(\partial_j u_i + \partial_i u_j) \tag{1e}$$

The microscale heterogeneity is modeled in two ways:

1 $C_{ijkl}(\mathbf{x})$ is a statistically homogeneous, random field

2 $C_{ijkl}(\mathbf{x})$ is described by a periodic function of unit period, denoted by $C_{ijkl}(\boldsymbol{\xi})$ where $\boldsymbol{\xi} = (\mathbf{x} - \mathbf{b})/\epsilon$.

In the second modeling, $\mathbf{b}$ locates the origin of a material property grid and ϵ is a small dimensionless number that relates the length scale natural for describing the heterogeneity, the $\boldsymbol{\xi}$ scale, to that natural for describing the specimen geometry. This length scale ratio, appearing explicitly in the periodic modeling, is implicitly understood as a correlation range measure in the stochastic modeling [8]. We note that there is no need to explicitly introduce it in the stochastic modeling at this point.

We now introduce a projection operator, P, which effects an averaging. For the stochastic modeling the average is an ensemble average, over an random function space; for the periodic modeling the average is also an ensemble average, over the continuous parameter, $\mathbf{b}$, taken now to be a random variable that can range over the unit cell with

[1] The Catholic University of America, Washington, D.C. 20064.

[2] The Catholic University of America, Washington, D.C. 20064. Mem. ASME.

Manuscript received by ASME Applied Mechanics Division, March, 1980; final revision, April, 1980.

uniform distribution. Ultimately the projection operator is to be interpreted for both models in terms of a spatial average taken over the microscale. Thus a projected quantity is to vary only on the macroscale. With P, all the field variables can be resolved into a projected component, say $\langle C \rangle = PC$ and a fluctuating component, say $C' = (I - P)C$ according to the identity

$$C_{ijkl} = \langle C_{ijkl} \rangle + C'_{ijkl} \tag{2}$$

We note that $\langle C_{ijkl} \rangle$ is a constant, in the specific application, by viture of the statistical homogeneity of $C_{ijkl}(\mathbf{x})$.

Coupled boundary-value problems can be written on the separate components of the response fields by first projecting equation (1) and by subsequently subtracting the projected equation from the original. These problems are

$$\partial_i \langle \tau_{ij} \rangle = f_j, \tag{3a}$$

$$\langle \tau_{ij} \rangle = \langle C_{ijkl} \rangle \langle e_{kl} \rangle + \langle C'_{ijkl} e'_{kl} \rangle, \quad \mathbf{x} \text{ in } D \tag{3b}$$

$$\delta_{ikm} \delta_{jln} \partial_k \partial_l \langle e_{mn} \rangle = 0, \tag{3c}$$

and

$$n_i \langle \tau_{ij} \rangle = t_j, \quad \mathbf{x} \text{ in } \partial D \tag{3d}$$

together with

$$\partial_i \tau'_{ij} = 0, \tag{4a}$$

$$\tau'_{ij} = \langle C_{ijkl} \rangle e'_{kl} + (I - P) C'_{ijkl} e'_{kl} + C'_{ijkl} \langle e_{kl} \rangle, \quad \mathbf{x} \text{ in } D \tag{4b}$$

$$\delta_{ikm} \delta_{jln} \partial_k \partial_l e'_{mn} = 0, \tag{4c}$$

and

$$n_i \tau'_{ij} = 0, \quad \mathbf{x} \text{ in } \partial D \tag{4d}$$

Equations (4), which can be written as a single field equation on the fluctuating displacement field, $u'_i(\mathbf{x})$; i.e.,

$$\langle C_{ijkl} \rangle \partial_j \partial_k u'_l + (I - P) \partial_j (C'_{ijkl} \partial_k u'_l) = -\partial_j (C'_{ijkl} \langle e_{kl} \rangle) \tag{5}$$

along with the homogeneous boundary condition, equation (4d), are to be solved and the result substituted into equation (3b). This equation then provides an effective, nonlocal, constitutive relationship between the projected stress tensor, $\langle \tau_{ij} \rangle$, and the projected strain tensor, $\langle e_{ij} \rangle$. Notice that since the boundary condition, equation (4d), enters the problem that determines u'_i, the effective constitutive equation is, in the strictest sense, specimen-dependent.

Except for the insignificant difference in the interpretation to be given to the projection, the procedure as outlined is the same for the two modelings. A difference is now introduced, in the manner of effecting a solution of equation (5). The literature treating the stochastic modeling identifies a measure of the strength of the heterogeneity, $|C'_{ijkl}|/|\langle C_{ijkl} \rangle|$, and constructs a perturbation series solution of equation (5) in powers of this strength parameter. The result is termed a smoothing in that the formal method is the linear counterpart of the Bogoliubov-Krylov-Mitropolski method of averaging for nonlinear differential equations [11, 12]. The literature treating the periodic modeling exploits the two-length scale nature of the problem and constructs a series solution of equation (5) in powers of ϵ. The result of the second is termed an homogenization in that in the broadest sense homogenization derives from consideration of the question of replacing a heterogeneous material by an "equivalent" homogeneous one in the appropriate $\epsilon \to 0$ limit [2].

Since the detailed calculations of smoothing are available [13–16] for both the mechanics and similar problems, they will not be reproduced. The effective, nonlocal, constitutive equation is written

$$\langle \tau_{ij}(\mathbf{x}) \rangle = C^*_{ijkl} \langle e_{kl}(\mathbf{x}) \rangle + \int \mathscr{C}_{ijkl}(\mathbf{x}, \mathbf{x}') \langle e_{kl}(\mathbf{x}') \rangle d\mathbf{x}' \tag{6}$$

where C^*_{ijkl} has been chosen so as to incorporate all singular behavior of the two-point dyadic field, $\mathscr{C}_{ijkl}(\mathbf{x}, \mathbf{x}')$, which has been constructed such that

$$\int \mathscr{C}_{ijkl}(\mathbf{x}, \mathbf{x}') d\mathbf{x}' = 0 \tag{7}$$

It is to be noted that the derivation provides infinite series prescriptions, the terms of which are given by well-described quadratures of multipoint correlation functions of $C_{ijkl}(\mathbf{x})$. It is also to be noted that the validity of equation (6) is not limited by the magnitude of any length-scale ratio. The specimen dependence of the constitutive equation appears in the prescriptions for C^*_{ijkl} and $\mathscr{C}_{ijkl}(\mathbf{x}, \mathbf{x}')$. It has been argued [13, 14] that this dependence is limited to layers of boundary surfaces of a thickness that is measured on the microscale. Neglecting these layers, then, C^*_{ijkl} is a constant that is properly termed an effective, elastic moduli tensor; $\mathscr{C}_{ijkl}(\mathbf{x}, \mathbf{x}')$ is a function of difference coordinates alone; and, the integral is a convolution.

An iteration solution of equation (5) in terms of the length-scale ratio, ϵ, assumes, *a priori*, existence of two separable scales related by the small parameter ϵ in a manner reflecting the detailed nature of the microscopic process and the appropriate limit under consideration. That is, that the solution field $u'_i(\mathbf{x})$ can be written as $u'_i(\mathbf{x}, \mathbf{y})$, where $\mathbf{y}$ is to be treated as an independent variable in the analysis, and to be equated to $\mathbf{x}/\epsilon$ once the analysis is complete. The introduction of a single correlation range parameter in this manner, while appropriate for the assumed form of the periodic modeling, must be assumed to provide a consistent and sufficient description of the stochastic modeling as would be the case, for example, of the randomly modulated oscillator characterized by an Uhlenbeck-Ornstein process [1]. Explicitly introducing the two-scale concept into equation (5), the equation on $u'_i(\mathbf{x}, \mathbf{y})$ is written,

$$\begin{aligned} &\langle C_{ijkl} \rangle \partial_j{}^{(y)} \partial_k{}^{(y)} u'_l + (I - P) \partial_j{}^{(y)} (C'_{ijkl} \partial_k{}^{(y)} u'_l) + \epsilon [2 \langle C_{ijkl} \rangle \partial_k{}^{(y)} \\ &\quad + (I - P) C'_{ijkl} \partial_k{}^{(y)} + (I - P)(\partial_k{}^{(y)} C'_{ijkl})] \partial_j{}^{(x)} u'_l \\ &\quad + \epsilon^2 [\langle C_{ijkl} \rangle + (I - P) C'_{ijkl}] \partial_j{}^{(x)} \partial_k{}^{(x)} u'_l \\ &\quad = -\epsilon (\partial_j{}^{(y)} C'_{ijkl}) \langle e_{kl} \rangle - \epsilon^2 C'_{ijkl} \partial_j{}^{(x)} \langle e_{kl} \rangle \end{aligned} \tag{8}$$

where the superscripts x and y denote derivatives with respect to the macro and microcoordinates, respectively. We note, with reference to equation (8), that $\langle C_{ijkl} \rangle$ is a constant; $C'_{ijkl}(\mathbf{x})$ is a function of microcoordinates alone; and $\langle e_{ij}(\mathbf{x}) \rangle$ is assumed to be a function of macrocoordinates alone.

A solution of equation (8) is next constructed by the following ansatz. We formally express the fluctuating displacement field as

$$u'_j = \sum_{n=0}^{\infty} \epsilon^n u_j{}^{(n)}; \tag{9}$$

we substitute this in equation (8); and we equate terms in like powers of ϵ. The result is a sequence of equations

$$\begin{aligned} &L_{il}{}^{(y)} u_l{}^{(0)} = 0 \\ &L_{il}{}^{(y)} u_l{}^{(1)} = -(\partial_j{}^{(y)} C'_{ijkl}) \langle e_{kl} \rangle - M_{ijl}{}^{(y)} \partial_j{}^{(x)} u_l{}^{(0)} \\ &L_{il}{}^{(y)} u_l{}^{(2)} = -C'_{ijkl} \partial_j{}^{(x)} \langle e_{kl} \rangle \\ &\qquad \vdots \\ &\qquad\qquad - M_{ijl}{}^{(y)} \partial_j{}^{(x)} u_l{}^{(1)} - N_{ijkl}{}^{(y)} \partial_j{}^{(x)} \partial_k{}^{(x)} u_l{}^{(0)} \\ &\qquad\qquad \vdots \\ &L_{il}{}^{(y)} u_l{}^{(n)} = -M_{ijl}{}^{(y)} \partial_j{}^{(x)} u_l{}^{(n-1)} \\ &\qquad \vdots \\ &\qquad\qquad - N_{ijkl}{}^{(y)} \partial_j{}^{(x)} \partial_k{}^{(x)} u_l{}^{(n-2)}, \quad n > 2 \\ &\qquad\qquad \vdots \end{aligned} \tag{10}$$

where $L_{il}{}^{(y)}$, $M_{ijl}{}^{(y)}$, and $N_{ijkl}{}^{(y)}$ are differential operators defined over the microscale according to

$$\begin{aligned} &L_{il}{}^{(y)} \phi_l = \langle C_{ijkl} \rangle \partial_j{}^{(y)} \partial_k{}^{(y)} \phi_l + (I - P) \partial_j{}^{(y)} (C'_{ijkl} \partial_k{}^{(y)} \phi_l), \\ &M_{ijl}{}^{(y)} \phi_{jl} = [2 \langle C_{ijkl} \rangle \partial_k{}^{(y)} + (I - P) C'_{ijkl} \partial_k{}^{(y)} \\ &\qquad\qquad + (I - P)(\partial_k{}^{(y)} C'_{ijkl})] \phi_{jl}, \end{aligned} \tag{11}$$

and

$$N_{ijkl}{}^{(y)} \phi_{jkl} = [\langle C_{ijkl} \rangle + (I - P) C'_{ijkl}] \phi_{jkl} \tag{12}$$

Having previously argued that the averaging process in the $\epsilon \to 0$

limit represents the appropriate macroscale response function, the solutions of equation (10) are constructed as

$$\begin{aligned} u_i^{(0)}(\mathbf{x},\mathbf{y}) &= 0, \\ u_i^{(1)}(\mathbf{x},\mathbf{y}) &= X_{ijk}^{(1)}(\mathbf{y})\langle e_{jk}(\mathbf{x})\rangle, \\ u_i^{(2)}(\mathbf{x},\mathbf{y}) &= X_{ijkl}^{(2)}(\mathbf{y})\,\partial_j^{(x)}\langle e_{kl}(\mathbf{x})\rangle, \\ &\vdots \qquad\qquad \vdots \end{aligned} \tag{13}$$

etc., with auxiliary functions $\{X^{(n)}(\mathbf{y})\}$ defined through the equations,

$$\begin{aligned} L_{ij}^{(y)}X_{jkl}^{(1)} &= -(\partial_m^{(y)}C'_{imnp})\delta_{kn}\delta_{lm}, \\ L_{ij}^{(y)}X_{jklm}^{(2)} &= -(C'_{irst} + M_{irp}^{(y)}X_{pst}^{(1)})\delta_{kr}\delta_{ls}\delta_{mt}, \\ &\vdots \qquad\qquad \vdots \end{aligned} \tag{14}$$

etc., where δ_{ij} is the Kronecker delta. Determination of the auxiliary functions $\{X^{(n)}(\mathbf{y})\}$ requires the specification of boundary conditions. The homogeneous conditions expressed by equation (4*d*) are not appropriate in this regard since they apply to a boundary surface that is defined on the **x** scale; whereas the differential operators in equation (14) refer to the **y** scale. In homogenization with a periodic microscale, it is usual to require that the auxiliary functions $\{X^{(n)}(\mathbf{y})\}$ also be periodic; for a stochastic microstructure a more appropriate choice would be a prescribed asymptotic behavior for $|\mathbf{y}|$ large [7, 8].

Equations (9) and (13) formally provide the solution of equation (5); and the result is now to be substituted into equation (3*b*) to obtain the effective constitutive equation. In particular we require

$$\langle C'_{ijkl}e'_{kl}\rangle = \frac{1}{\epsilon}\langle C'_{ijkl}\partial_k^{(y)}u'_l\rangle + \langle C'_{ijkl}\partial_k^{(x)}u'_l\rangle \tag{15}$$

which upon substitution gives an infinite series in powers of ϵ. We write, for the effective constitutive equation,

$$\begin{aligned} \langle\tau_{ij}\rangle = [\langle C_{ijkl}\rangle + \langle C'_{ijmn}\partial_m^{(y)}X_{nkl}^{(1)}\rangle]\langle e_{kl}\rangle + \epsilon[\langle C'_{ijkl}X_{lmn}^{(1)}\rangle \\ + \langle C'_{ijlp}\partial_l^{(y)}X_{pkmn}^{(2)}\rangle]\partial_k^{(x)}\langle e_{mn}\rangle + \mathcal{O}(\epsilon^2) \end{aligned} \tag{16}$$

Discussion

Two comments with regard to equation (16) appear to be warranted at this point. One is that the procedure does not provide a prescription for the elastic moduli parameters in terms of quadratures. That is, one still is required to invert equation (14) in order to determine the coefficients of equation (16). Of course the problem expressed by equation (14) is, in a sense, canonical requiring that it be solved only once. Then, equation (16) is defined for all problems. The second comment is that the derivation procedure clearly does not account for the enforcement of the boundry condition given by equation (4*d*). Previous boundary-effect analysis [13] indicates, however, that such effects should be confined to a microscale layer, thus suggesting that the derived constitutive relation will serve in some sense as an outer-layer approximation to the correct bulk behavior.

We can compare the prescriptions for the effective constitutive relation as given by smoothing, equation (6), and by homogenization, equation (16). A formal relationship can be established by applying the Kramers-Moyal expansion [17, 18] to equation (6), thereby formally replacing the integral operator by an infinite-order partial differential operator parameterized in terms of the transfer moments of the kernel and subsequently ordering the expansion by expanding the transfer moments in terms of the presumably identifiable small parameter ϵ. What emerges is a dual interpretation of the relationship between the macroscale behavior and its microscale foundations in terms of (1) averages over a sequence of well-defined microscale problems, and (2) an infinite set of correlation functions reflecting the statistical description of the medium.

Finally, we can discuss the set of equations one must solve in order to obtain the projected response field in a particular application. Equations (3*a*), (3*c*), (3*d*), and (6) can be shown to define a well-posed boundary-value problem so long as the constitutive equation gives rise to a nonlocal strain energy measure that is positive-definite, which has also been demonstrated to be the case [15]. Replacing equation (6) with equation (16), followed by a truncation suggests a sequence of approximate theories, expressible by differential equations on the projected displacement field, $\langle u_i(\mathbf{x})\rangle$, of increasingly higher order. Several comments regarding this procedure are to be made. First, the construction procedure of Babŭska [2–4] demonstrates that the lowest-order approximation, a bulk property theory, does give solutions with an error of $\mathcal{O}(\epsilon)$. Second, retention of higher-order derivatives in equation (16), in order to obtain extensions of the bulk property theory, introduces a need to supplement the boundary conditions given by equation (3*d*). Finally, it is known from experience that replacing a nonlocal integral operator by an infinite-order differential operator to obtain a sequence of approximations commonly leads to unphysical results. Beran and McCoy [19] established, for example, that explicit expressions for the material parameters for the first-order correction to a bulk property theory, which can be identified with a strain gradient theory, violate the positive-definite requirement for the strain-energy density of that theory. Examples of similar difficulties abound in the literature of mathematically similar problems. In particular, we cite the literature relating to linear-gas relaxation theories [18].

As noted in the Introduction, the calculations presented in this Note and in much of the literature treating homogenization and smoothing are formal. Questions remain concerning, for example, the mathematical rigor of the procedures and the detailed underlying relationship between stochastic processes and their appropriate scalings and the assumption of a single-parameter correlation description.

A literature does exist, however, which attempts to address these questions; and a discussion of some of this literature in the context of the composite materials problem is available [10].

Acknowledgment

The work reported here was supported under grants by the National Science Foundation (ENG-76 11549 and ENG-78 20613). The authors would also like to acknowledge many discussions with Prof. R. Vaishnav.

References

1 For an extensive discussion with references and applications see ... Frisch, U., "Wave Propagation in Random Media," *Probabilistic Methods in Applied Mathematics—I,* Bharucha-Reid, A. T., ed., Academic Press, New York, 1968, pp. 76–198.

2 Babŭska, I., "Homogenization and Its Application: Mathematical and Computational Problems," *Numerical Solution of Partial Differential Equations—III,* Hubbard B., ed., Academic Press, New York, 1976, pp. 89–116.

3 Babŭska, I., "Solution of Interface Problems by Homogenization—I," *SIAM Journal of Mathematical Analysis,* Vol. 7, No. 5, 1976, pp. 603–634.

4 Babuška, I., "Solution of Interface Problems by Homogenization—II, *SIAM Journal of Mathematical Analysis,* Vol. 7, No. 5, 1976, pp. 635–645.

5 Burgers, J. M., "On Some Problems of Homogenization," *Quarterly of Applied Mathematics,* Vol. XXXV, No. 4, 1978, pp. 421–434.

6 Maewal, A., "Homogenization for Transient Heat Conduction," ASME JOURNAL OF APPLIED MECHANICS, Vol. 46, Dec. 1979, pp. 945–946.

7 Keller, J. B., "Effective Behavior of Heterogeneous Media," *Statistical Mechanics and Statistical Methods in Theory and Applications,* Landman, R., ed., Plenum, New York, 1977, pp. 631–644.

8 Papanicolaou, G. C., "Asymptotic Analysis of Stochastic Equations," *Studies in Probability Theory, M.A.A. Studies in Mathematics,* Vol. 18, Rosenblatt, M., ed., The Mathematical Association of America, 1978, pp. 111–179.

9 McCoy, J. J., "On the Calculation of Bulk Properties of Heterogeneous Materials," *Quarterly of Applied Mathematics,* Vol. XXXVII, No. 2, 1979, pp. 137–149.

10 Fishman, L., and McCoy, J. J., "A Unified View of Bulk Property Theories for Stochastic and Periodic Media," submitted for publication.

11 Bogoliubov, N. N., and Mitropolski, I., *Asymptotic Methods in the Theory of Nonlinear Oscillations,* Gordon and Breach, New York, 1961.

12 Krylov, N., and Bogoliubov, N. N., *Introduction to Nonlinear Mechanics,* Princeton University Press, Princeton, N. J., 1949.

13 Beran, M. J., and McCoy, J. J., "Mean Field Variations in a Statistical Sample of Heterogeneous Linearly Elastic Solids," *International Journal of Solids and Structures,* Vol. 6, 1970, pp. 1035–1054.

14 Beran, M. J., and McCoy, J. J., "Mean Field Variation in Random Media," *Quarterly of Applied Mathematics,* Vol. XXVIII, No. 2, 1970, pp. 245–258.

15 McCoy, J. J., "Statistical Average Response of a Bounded Linearly Elastic Solid," *Proceedings of the 1st International Conference on Structural Mechanics in Reactor Technology,* Berlin, 6M, 1971, pp. 539–553.

16 McCoy, J. J., "Macroscopic Response of Continua With Random Mi-

crostructures," *Mechanics Today*, Vol. 6, ed., Nemat-Nasser, S., Pergamon Press, in press.

17 Andersen, K., and Shuler, K. E., "On the Relaxation of the Hard-Sphere Rayleigh and Lorentz Gas," *Journal of Chem. Phys.*, Vol. 40, 1964, pp. 633–650.

18 Hoare, M. R., "The Linear Gas," *Adv. Chem. Phys.*, Vol. 20, 1971, pp. 135–214.

19 Beran, M. J., and McCoy, J. J., "The Use of Strain Gradient Theory for Analysis of Random Media," *International Journal of Solids and Structures*, Vol. 6, 1970, pp. 1267–1275.

Steady-State Solution of Navier's Equation in Cylindrical Curvilinear Coordinates

B. S. Berger[1] and B. Alabi[2]

Steady-state problems in plane elasticity for the half space have received considerable attention [1]. The radiation condition at infinity has been approximately satisfied by the introduction of a viscous boundary, a semianalytic energy transmitting boundary, [1, 3] and a method based on the properties of the transmission of D'Alembert forces, [4]. In the following the solution of Navier's equation given in [5] for the static and transient cases is modified for the steady-state case. The radiation condition at infinity is satisfied through a change of the dependent variable.

A complete solution of the reduced elastodynamic equations is given in terms of the Lamé potentials by

$$\nabla^2\phi + \beta_1{}^2\phi + (F/c_1{}^2) = 0 \tag{1}$$

$$\nabla^2\overline{\nabla} + \beta_2{}^2\overline{\psi} + (\hat{F}/c_2{}^2) = 0 \tag{2}$$

where $\beta_1 = \omega/c_1$, $\beta_2 = \omega/c_2$, $c_1 = \sqrt{(\lambda + 2\mu/\rho}$, $c_2 = \sqrt{\mu/\rho}$, $\overline{U} = \overline{\nabla}\phi + \overline{\nabla}\cdot\overline{\psi}$, $\overline{F} = \overline{\nabla}F + \overline{\nabla}\cdot\hat{F}$, $\overline{\nabla}\cdot\hat{F} = 0$ and $\overline{\psi}$ satisfies the gauge condition, $\overline{\nabla}\cdot\overline{\psi} = 0$. The displacement, $\overline{U}_0$, body force, $\overline{F}_0$, and stress tensor, $\overline{T}_0$, are expressed, respectively, as products of functions, $\overline{U}$, $\overline{F}$, and $\overline{T}$, of the spatial coordinates and ω with exp $(-i\omega t)$; see [6]. Denote the coordinates of a point in a rectangular Cartesian coordinate system by X_i, $i = 1,3$. Define the orthogonal cylindrical curvilinear coordinate system x_i, $i = 1,3$ by $x_1 = x_1(X_1, X_2)$, $x_2 = x_2(X_1, X_2)$ and $x_3 = X_3$. Then $g_{11} = g_{11}(x_1, x_2)$, $g_{22} = g_{22}(x_1, x_2)$, $g_{33} = 1$ and $g_{ij} = 0$ for $i \neq j$, where g_{ij} are the components of the metric tensor associated with the coordinate system, x_i. Assume that the scalar ϕ and the component of $\overline{\psi}$ with respect to the x_3-axis, ψ_3, are even functions while ψ_1 and ψ_2 are odd functions of x_3. The axial variable, x_3, may be suppressed in (1), (2) through separation of variables, differencing for bodies of finite extent in x_3 or application of the Fourier transform for the infinite case; see [5]. For notational economy ϕ, ψ_1, ψ_2, ψ_3 will subsequently denote both tensor components of ϕ and $\overline{\psi}$ as well as their Fourier transforms with respect to x_3. Taking the Fourier transform of (1) and (2) and expanding gives

$$(1/\sqrt{g_{11}g_{22}})\,((\sqrt{g_{22}/g_{11}}\,\phi_{,1})_{,1} + (\sqrt{g_{11}/g_{22}}\,\phi_{,2})_{,2}) + (\beta_1{}^2 - \alpha^2)\phi + (F/c_1{}^2) = 0 \tag{3}$$

$$B_{,1} + i\alpha\psi_{3,1} - (\sqrt{g_{11}/g_{22}}\,(1/\sqrt{g})_{,2})\,(\psi_{2,1} - \psi_{1,2}) + (1/g_{22})\,(\psi_{1,22} - \psi_{2,12}) + (\beta_2{}^2 - \alpha^2)\psi_1 + (\hat{F}_1/c_2{}^2) = 0 \tag{4}$$

$$B_{,2} + i\alpha\psi_{3,2} + (\sqrt{g_{22}/g_{11}}\,(1/\sqrt{g})_{,1})\,(\psi_{2,1} - \psi_{1,2}) + (1/g_{11})\,(\psi_{2,11} - \psi_{1,12}) + (\beta_2{}^2 - \alpha^2)\psi_2 + (\hat{F}_2/c_2{}^2) = 0 \tag{5}$$

$$-i\alpha\sqrt{g}\,B + \sqrt{g_{11}/g_{22}}\,(\psi_{3,22} + i\alpha\psi_{2,2}) + (\sqrt{g_{11}/g_{22}})_{,2}\,(\psi_{3,2} + i\alpha\psi_2) + \sqrt{g_{22}/g_{11}}\,(\psi_{3,11} + i\alpha\psi_{1,1}) + (\sqrt{g_{22}/g_{11}})_{,1}\,(\psi_{3,1} + i\alpha\psi_1) + \sqrt{g}\,\beta_2{}^2\psi_3 + (\sqrt{g}\,\hat{F}_3/c_2{}^2) = 0 \tag{6}$$

where

$$B = (1/\sqrt{g_{11}g_{22}})\,((\sqrt{g_{22}/g_{11}}\,\psi_1)_{,1} + (\sqrt{g_{11}/g_{22}}\,\psi_2)_{,2}) - i\alpha\psi_3$$

and $(\,)_{,i}$ denotes the partial derivative with respect to x_i. The guage condition becomes

$$(\sqrt{g_{22}/g_{11}}\,\psi_1)_{,1} + (\sqrt{g_{11}/g_{22}}\,\psi_2)_{,2} - i\alpha\sqrt{g_{11}g_{22}}\,\psi_3 = 0 \tag{7}$$

while the components of the displacement vector are given by

$$u_1 = \phi_{,1} + \sqrt{g_{11}/g_{22}}\,(\psi_{3,2} + i\alpha\psi_2),$$

$$u_2 = \phi_{,2} - \sqrt{g_{22}/g_{11}}\,(\psi_{3,1} + i\alpha\psi_1),$$

$$u_3 = -i\alpha\phi + (1/\sqrt{g_{11}g_{22}})\,(\psi_{2,1} - \psi_{1,2}).$$

In two dimensions, orthogonal coordinates with specific coordinate lines may be found through a variety of means, including numerical conformal mapping, see [5]. Define the X_i rectangular Cartesian coordinates such that X_3 is along the axis of a cylinder while X_1 and X_2 are in a plane perpendicular to X_3. In the case of the grooved semi-infinite plane X_1 and X_3 are in the plane of the surface, $X_2 = 0$, X_3 is parallel to the axis of the groove and X_2 points into the interior of the half space. A conformal mapping of the grooved half plane into the rectangle $0 < x_1 \leq 1$, $-\pi/2 \leq x_2 \leq \pi/2$ is given by

$$Z = \sum_{n=1}^{N} a_n z^{(2n-3)} \tag{8}$$

where $Z = X_1 + iX_2$, $z = x_1 \exp(ix_2)$, the boundary at infinity is mapped onto the line $x_1 = 0$, $-\pi/2 \leq x_2 \leq \pi/2$ and the cross section of the groove is assumed to be symmetric with respect to the X_2-axis. Effective numerical methods for the computation of the coefficients a_n are given in [5]. Equation (8) may be used to compute the components of the metric, g_{ij}, appearing in (3)–(7), [5]. Through conformal mapping or other means, [7], coordinate transformations may be found such that the transformed reduced equations may be solved over the finite rectangle, $0 < x_1 \leq 1$, $-\pi/2 \leq x_2 \leq \pi/2$.

To insure only outgoing waves, the difference solution for the semi-infinite elastic medium must satisfy the Sommerfeld radiation condition at infinity. [6]. Thus the radiation condition must be satisfied on $x_1 = 0$ in the x_1, x_2 coordinates. To assure an outgoing wave consider the change of dependent variables

$$\phi = f \exp(\alpha_1/x_1) \tag{9}$$

$$\psi_i = h_i \exp(\alpha_2/x_1) \tag{10}$$

where $\alpha_1 = ia_1\omega/c_1$, $\alpha_2 = ia_1\omega/c_2$, $f(x_1, x_2, \alpha)$, and $h_i(x_1, x_2, \alpha) = 0$ for $x_1 = 0$ and a_1 is the coefficient of z in the first term of (8). It is seen that (9) and (10) approach the form required for outward going waves as $x_1 \to$ o. It should be noted that the change of variable, (9) and (10), is not necessary for finite elastic bodies. Substituting (9) into (3) gives

$$G7\,f_{11} + Q7\,f_{,1} + Q8\,f + Q2\,f_{,2} + G8\,f_{,22} + (F/c_1{}^2)\exp(-\alpha_1/x_1) = 0 \tag{11}$$

where $G7 = 1/g_{11}$, $G8 = 1/g_{22}$, $Q7 = Q1 - 2{\cdot}G7{\cdot}\alpha_1/x_1{}^2$, $Q8 = G7(2{\cdot}\alpha_1/x_1{}^3 + \alpha_1{}^2/x_1{}^4) - Q1{\cdot}\alpha_1/x_1{}^2 + \beta_1{}^2 - \alpha^2$, $Q1 = (G7{\cdot}G8{\cdot}g_{22,1} - G9{\cdot}g_{11,1})/2$, and $Q2 = (G7{\cdot}G8{\cdot}g_{11,2} - G10{\cdot}g_{22,2})/2$. Substituting (10) into (4) gives equations, omitted for brevity, which determine h_i, $i = 1,3$. Equation (11) and the equations for h_i were expressed in finite-difference from and solved over a rectangle in the x_1, x_2 coordinates. Stress and displacement boundary conditions are developed in [5].

In order to establish the computational utility of the foregoing, numerical studies were made for comparison with analytic solutions. The values of material constants used in all calculations are as follows:

[1] Professor, Department of Mechanical Engineering, University of Maryland, College Park, Md., 20742.

[2] Graduate Student, Department of Mechanical Engineering, Imperial College of Science and Technology, London, England.

Manuscript received by ASME Applied Mechanics Division, October, 1978; final revision, March, 1980.

crostructures," *Mechanics Today*, Vol. 6, ed., Nemat-Nasser, S., Pergamon Press, in press.

17 Andersen, K., and Shuler, K. E., "On the Relaxation of the Hard-Sphere Rayleigh and Lorentz Gas," *Journal of Chem. Phys.*, Vol. 40, 1964, pp. 633–650.

18 Hoare, M. R., "The Linear Gas," *Adv. Chem. Phys.*, Vol. 20, 1971, pp. 135–214.

19 Beran, M. J., and McCoy, J. J., "The Use of Strain Gradient Theory for Analysis of Random Media," *International Journal of Solids and Structures*, Vol. 6, 1970, pp. 1267–1275.

Steady-State Solution of Navier's Equation in Cylindrical Curvilinear Coordinates

B. S. Berger[1] and B. Alabi[2]

Steady-state problems in plane elasticity for the half space have received considerable attention [1]. The radiation condition at infinity has been approximately satisfied by the introduction of a viscous boundary, a semianalytic energy transmitting boundary, [1, 3] and a method based on the properties of the transmission of D'Alembert forces, [4]. In the following the solution of Navier's equation given in [5] for the static and transient cases is modified for the steady-state case. The radiation condition at infinity is satisfied through a change of the dependent variable.

A complete solution of the reduced elastodynamic equations is given in terms of the Lamé potentials by

$$\nabla^2\phi + \beta_1{}^2\phi + (F/c_1{}^2) = 0 \tag{1}$$

$$\nabla^2\overline{\nabla} + \beta_2{}^2\overline{\psi} + (\hat{F}/c_2{}^2) = 0 \tag{2}$$

where $\beta_1 = \omega/c_1$, $\beta_2 = \omega/c_2$, $c_1 = \sqrt{(\lambda + 2\mu/\rho}$, $c_2 = \sqrt{\mu/\rho}$, $\overline{U} = \overline{\nabla}\phi + \overline{\nabla}\cdot\overline{\psi}$, $\overline{F} = \overline{\nabla}F + \overline{\nabla}\cdot\hat{F}$, $\overline{\nabla}\cdot\hat{F} = 0$ and $\overline{\psi}$ satisfies the gauge condition, $\overline{\nabla}\cdot\overline{\psi} = 0$. The displacement, $\overline{U}_0$, body force, $\overline{F}_0$, and stress tensor, $\overline{T}_0$, are expressed, respectively, as products of functions, $\overline{U}$, $\overline{F}$, and $\overline{T}$, of the spatial coordinates and ω with exp $(-i\omega t)$; see [6]. Denote the coordinates of a point in a rectangular Cartesian coordinate system by X_i, $i = 1,3$. Define the orthogonal cylindrical curvilinear coordinate system x_i, $i = 1,3$ by $x_1 = x_1(X_1, X_2)$, $x_2 = x_2(X_1, X_2)$ and $x_3 = X_3$. Then $g_{11} = g_{11}(x_1, x_2)$, $g_{22} = g_{22}(x_1, x_2)$, $g_{33} = 1$ and $g_{ij} = 0$ for $i \neq j$, where g_{ij} are the components of the metric tensor associated with the coordinate system, x_i. Assume that the scalar ϕ and the component of $\overline{\psi}$ with respect to the x_3-axis, ψ_3, are even functions while ψ_1 and ψ_2 are odd functions of x_3. The axial variable, x_3, may be suppressed in (1), (2) through separation of variables, differencing for bodies of finite extent in x_3 or application of the Fourier transform for the infinite case; see [5]. For notational economy ϕ, ψ_1, ψ_2, ψ_3 will subsequently denote both tensor components of ϕ and $\overline{\psi}$ as well as their Fourier transforms with respect to x_3. Taking the Fourier transform of (1) and (2) and expanding gives

$$(1/\sqrt{g_{11}g_{22}})\,((\sqrt{g_{22}/g_{11}}\,\phi_{,1})_{,1} + (\sqrt{g_{11}/g_{22}}\,\phi_{,2})_{,2}) + (\beta_1{}^2 - \alpha^2)\phi + (F/c_1{}^2) = 0 \tag{3}$$

$$B_{,1} + i\alpha\psi_{3,1} - (\sqrt{g_{11}/g_{22}}\,(1/\sqrt{g})_{,2})\,(\psi_{2,1} - \psi_{1,2}) + (1/g_{22})\,(\psi_{1,22} - \psi_{2,12}) + (\beta_2{}^2 - \alpha^2)\psi_1 + (\hat{F}_1/c_2{}^2) = 0 \tag{4}$$

$$B_{,2} + i\alpha\psi_{3,2} + (\sqrt{g_{22}/g_{11}}\,(1/\sqrt{g})_{,1})\,(\psi_{2,1} - \psi_{1,2}) + (1/g_{11})\,(\psi_{2,11} - \psi_{1,12}) + (\beta_2{}^2 - \alpha^2)\psi_2 + (\hat{F}_2/c_2{}^2) = 0 \tag{5}$$

$$-i\alpha\sqrt{g}\,B + \sqrt{g_{11}/g_{22}}\,(\psi_{3,22} + i\alpha\psi_{2,2}) + (\sqrt{g_{11}/g_{22}})_{,2}\,(\psi_{3,2} + i\alpha\psi_2) + \sqrt{g_{22}/g_{11}}\,(\psi_{3,11} + i\alpha\psi_{1,1}) + (\sqrt{g_{22}/g_{11}})_{,1}\,(\psi_{3,1} + i\alpha\psi_1) + \sqrt{g}\,\beta_2{}^2\psi_3 + (\sqrt{g}\,\hat{F}_3/c_2{}^2) = 0 \tag{6}$$

where

$$B = (1/\sqrt{g_{11}g_{22}})\,((\sqrt{g_{22}/g_{11}}\,\psi_1)_{,1} + (\sqrt{g_{11}/g_{22}}\,\psi_2)_{,2}) - i\alpha\psi_3$$

and $(\,)_{,i}$ denotes the partial derivative with respect to x_i. The guage condition becomes

$$(\sqrt{g_{22}/g_{11}}\,\psi_1)_{,1} + (\sqrt{g_{11}/g_{22}}\,\psi_2)_{,2} - i\alpha\sqrt{g_{11}g_{22}}\,\psi_3 = 0 \tag{7}$$

while the components of the displacement vector are given by

$$u_1 = \phi_{,1} + \sqrt{g_{11}/g_{22}}\,(\psi_{3,2} + i\alpha\psi_2),$$

$$u_2 = \phi_{,2} - \sqrt{g_{22}/g_{11}}\,(\psi_{3,1} + i\alpha\psi_1),$$

$$u_3 = -i\alpha\phi + (1/\sqrt{g_{11}g_{22}})\,(\psi_{2,1} - \psi_{1,2}).$$

In two dimensions, orthogonal coordinates with specific coordinate lines may be found through a variety of means, including numerical conformal mapping, see [5]. Define the X_i rectangular Cartesian coordinates such that X_3 is along the axis of a cylinder while X_1 and X_2 are in a plane perpendicular to X_3. In the case of the grooved semi-infinite plane X_1 and X_3 are in the plane of the surface, $X_2 = 0$, X_3 is parallel to the axis of the groove and X_2 points into the interior of the half space. A conformal mapping of the grooved half plane into the rectangle $0 < x_1 \leq 1$, $-\pi/2 \leq x_2 \leq \pi/2$ is given by

$$Z = \sum_{n=1}^{N} a_n z^{(2n-3)} \tag{8}$$

where $Z = X_1 + iX_2$, $z = x_1 \exp(ix_2)$, the boundary at infinity is mapped onto the line $x_1 = 0$, $-\pi/2 \leq x_2 \leq \pi/2$ and the cross section of the groove is assumed to be symmetric with respect to the X_2-axis. Effective numerical methods for the computation of the coefficients a_n are given in [5]. Equation (8) may be used to compute the components of the metric, g_{ij}, appearing in (3)–(7), [5]. Through conformal mapping or other means, [7], coordinate transformations may be found such that the transformed reduced equations may be solved over the finite rectangle, $0 < x_1 \leq 1$, $-\pi/2 \leq x_2 \leq \pi/2$.

To insure only outgoing waves, the difference solution for the semi-infinite elastic medium must satisfy the Sommerfeld radiation condition at infinity. [6]. Thus the radiation condition must be satisfied on $x_1 = 0$ in the x_1, x_2 coordinates. To assure an outgoing wave consider the change of dependent variables

$$\phi = f \exp(\alpha_1/x_1) \tag{9}$$

$$\psi_i = h_i \exp(\alpha_2/x_1) \tag{10}$$

where $\alpha_1 = ia_1\omega/c_1$, $\alpha_2 = ia_1\omega/c_2$, $f(x_1, x_2, \alpha)$, and $h_i(x_1, x_2, \alpha) = 0$ for $x_1 = 0$ and a_1 is the coefficient of z in the first term of (8). It is seen that (9) and (10) approach the form required for outward going waves as $x_1 \to$ o. It should be noted that the change of variable, (9) and (10), is not necessary for finite elastic bodies. Substituting (9) into (3) gives

$$G7\,f_{11} + Q7\,f_{,1} + Q8\,f + Q2\,f_{,2} + G8\,f_{,22} + (F/c_1{}^2)\exp(-\alpha_1/x_1) = 0 \tag{11}$$

where $G7 = 1/g_{11}$, $G8 = 1/g_{22}$, $Q7 = Q1 - 2{\cdot}G7{\cdot}\alpha_1/x_1{}^2$, $Q8 = G7(2{\cdot}\alpha_1/x_1{}^3 + \alpha_1{}^2/x_1{}^4) - Q1{\cdot}\alpha_1/x_1{}^2 + \beta_1{}^2 - \alpha^2$, $Q1 = (G7{\cdot}G8{\cdot}g_{22,1} - G9{\cdot}g_{11,1})/2$, and $Q2 = (G7{\cdot}G8{\cdot}g_{11,2} - G10{\cdot}g_{22,2})/2$. Substituting (10) into (4) gives equations, omitted for brevity, which determine h_i, $i = 1,3$. Equation (11) and the equations for h_i were expressed in finite-difference from and solved over a rectangle in the x_1, x_2 coordinates. Stress and displacement boundary conditions are developed in [5].

In order to establish the computational utility of the foregoing, numerical studies were made for comparison with analytic solutions. The values of material constants used in all calculations are as follows:

[1] Professor, Department of Mechanical Engineering, University of Maryland, College Park, Md., 20742.

[2] Graduate Student, Department of Mechanical Engineering, Imperial College of Science and Technology, London, England.

Manuscript received by ASME Applied Mechanics Division, October, 1978; final revision, March, 1980.

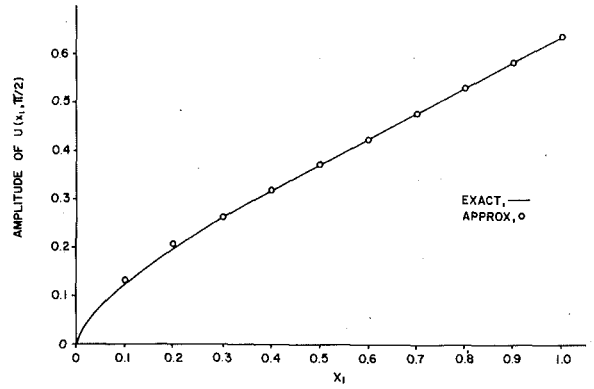

Fig. 1

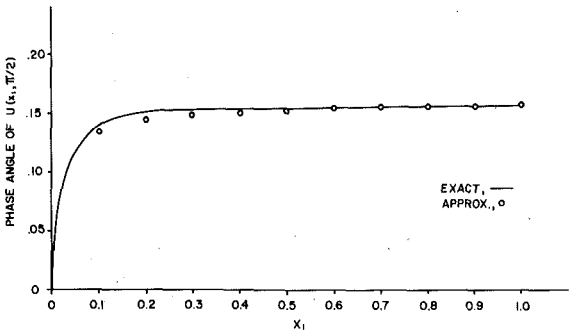

Fig. 2

$\nu = 0.3$, $E = 207.\cdot10^9$, $G = 79.615\cdot10^9$, $\rho = 7850$ for steel in mks units.

Consider an ungrooved plane, $X_2 = 0$. For this geometry the coefficients in (8) are $a_1 = 1/2$, $a_2 = 1/2$, and $a_n = 0$ for $n > 0$.
Let

$$\phi = A_1 H_0^{(1)}(\beta_1\sqrt{X_1^2 + (X_2 + a)^2}),$$
$$\bar{\psi} = 0, \quad F = 0, \quad \hat{F} = 0.$$

Then (1) and (2) are satisfied and the displacements on the boundary, $X_2 = 0$, and throughout the half space may be found from $\overline{U} = \overline{\nabla}\phi$. The amplitude of the displacement and the phase angle, for the exact solution and the numerical approximation are shown in Figs. 1 and 2, respectively, for $x_2 = \pi/2$. In the computation $\Delta 1 = 0.1$, $\Delta 2 = \pi/10$, $\omega = 500$, $\alpha = 1$, $A_1 = 1$ and the boundary displacements utilized in the computation were found from ϕ and $\bar{\psi}$ defined previously. Numerical solutions for the infinite medium containing a circular hole and the semi-infinite plane containing a semicircular groove have been found to be in agreement with exact solutions.

Conclusions

The method given here effectively extends the coordinate transformation techniques of [5] to the steady-state solution without recourse to artifically imposed boundaries. Numerical solutions are in good agreement with known analytic solutions.

Acknowledgments

The encouragement of Prof. Peter Grootanhius and the assistance of the staff of the Department of Mechanical Engineering, Imperial College, London, are greatly appreciated. Computations were performed at the Imperial College, London, and the University of Maryland, College Park, Md.

References

1 Lysmer, T., and Wass, G., "Shear Waves In Plane Infinite Structures," *Journal of Engineering Mechanics Division,* ASCE, Vol. 98, Feb. 1972, pp. 85–105.

2 Lysmer, T., and Kuhlemeyer, R. G., "Finite Dynamic Model For Infinite Media," *Journal of Engineering Mechanics Division,* ASCE, Vol. 95, Aug. 1969, pp. 859–877.

3 Kansel, E., Roesset, J. M., and Waas, G., "Dynamic Analysis of Footings On Layered Media," *Journal of Engineering Mechanics Division,* ASCE, Vol. 101, Oct. 1975, pp. 679–693.

4 Ang., A. H. S. and Newmark, N. M., "Development of a Transmitting Boundary for Numerical Wave Motion Calculations," Report To The Defense Atomic Support Agency, Washington, D. C., Apr. 1971.

5 Berger, B. S., and Alabi, B., "Solution of Navier's Equation In Cylindrical Curvilinear Coordinates," ASME JOURNAL OF APPLIED MECHANICS, Vol. 45, No. 4, Dec. 1978, pp. 812–816.

6 Eringen, A. C., and Suhubi, E. S., *Elastodynamics,* Vol. II, Academic Press, New York, 1975.

7 Berger, B. S., and Curtis, D. M., "Finite Difference Boundary Deformation Techniques in the Analysis of Elastic Bodies of Revolution," PhD Thesis, Department of Mechanical Engineering, University of Maryland, College Park, Md., Mar. 1980.

On the Computation of the Confluent Hypergeometric Function at Densely Spaced Points

P-T. D. Spanos[1]

An algorithm is described for computing the values of the confluent hypergeometric function at several points spaced densely along an interval of real numbers. Numerical data obtained by using this algorithm and pertaining to a commonly made approximation for the first-passage problem of the response amplitude of a lightly damped and randomly excited linear oscillator are presented.

Introduction

In engineering and scientific applications, it is often necessary to compute the values of the confluent hypergeometric function $M(a, b, z)$ [1] for given values of the independent variable z, and the parameters a and b. The function $M(a, b, z)$ is defined as the nontrivial solution of the ordinary differential equation

$$z\frac{d^2M}{dz^2} + (b - z)\frac{dM}{dz} - aM = 0 \tag{1}$$

which is finite at $z = 0$. This solution can be represented by the following series [1, 2]:

$$M(a, b, z) = 1 + \frac{A_1}{B_1}\frac{z}{1!} + \frac{A_2}{B_2}\frac{z^2}{2!} \ldots + \frac{A_n}{B_n}\frac{z^n}{n!} + \ldots, \tag{2}$$

where

$$A_n = a(a + 1) \ldots (a + n - 1), \quad A_0 = 1,$$
$$B_n = b(b + 1) \ldots (b + n - 1), \quad B_0 = 1. \tag{3}$$

Equation (2) can be used, without concern about efficiency, to compute the value of $M(a, b, z)$ at a single or a few points z. However, this approach may require excessive computational time if for a particular problem it is desired to compute the values of $M(a, b, z)$ at a large number of points z. This will be the case, for example, if it is required to plot the values of $M(a, b, z)$ versus z, or to compute numerically integrals, the integrands of which involve $M(a, b, z)$. Numerical computations of this nature would require the values of

[1] Assistant Professor of Engineering Mechanics, The University of Texas at Austin, Austin, Texas, 78712. Assoc. Mem. ASME.

Manuscript received by ASME Applied Mechanics, September, 1979; final revision, March, 1980.

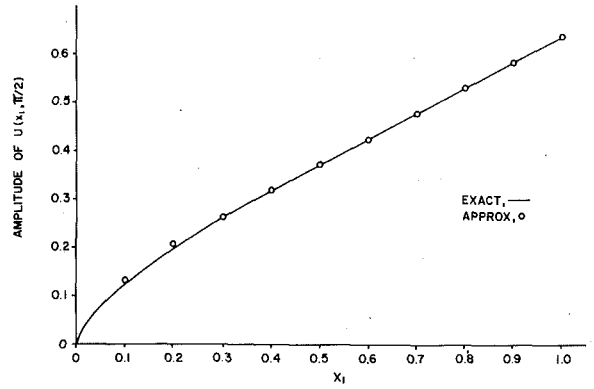

Fig. 1

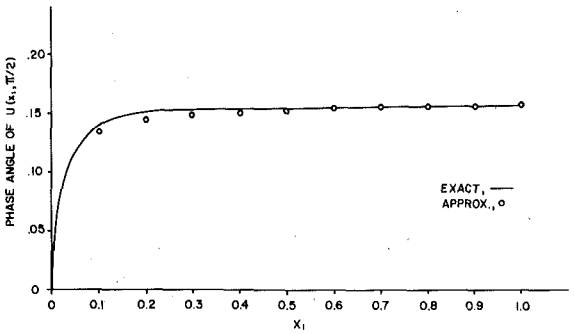

Fig. 2

$\nu = 0.3$, $E = 207.\cdot 10^9$, $G = 79.615\cdot 10^9$, $\rho = 7850$ for steel in mks units.

Consider an ungrooved plane, $X_2 = 0$. For this geometry the coefficients in (8) are $a_1 = 1/2$, $a_2 = 1/2$, and $a_n = 0$ for $n > 0$.
Let

$$\phi = A_1 H_0^{(1)}(\beta_1 \sqrt{X_1^2 + (X_2 + a)^2}),$$
$$\bar{\psi} = 0, \quad F = 0, \quad \hat{F} = 0.$$

Then (1) and (2) are satisfied and the displacements on the boundary, $X_2 = 0$, and throughout the half space may be found from $\overline{U} = \overline{\nabla}\phi$. The amplitude of the displacement and the phase angle, for the exact solution and the numerical approximation are shown in Figs. 1 and 2, respectively, for $x_2 = \pi/2$. In the computation $\Delta 1 = 0.1$, $\Delta 2 = \pi/10$, $\omega = 500$, $\alpha = 1$, $A_1 = 1$ and the boundary displacements utilized in the computation were found from ϕ and $\bar{\psi}$ defined previously. Numerical solutions for the infinite medium containing a circular hole and the semi-infinite plane containing a semicircular groove have been found to be in agreement with exact solutions.

Conclusions

The method given here effectively extends the coordinate transformation techniques of [5] to the steady-state solution without recourse to artifically imposed boundaries. Numerical solutions are in good agreement with known analytic solutions.

Acknowledgments

The encouragement of Prof. Peter Grootanhius and the assistance of the staff of the Department of Mechanical Engineering, Imperial College, London, are greatly appreciated. Computations were performed at the Imperial College, London, and the University of Maryland, College Park, Md.

References

1 Lysmer, T., and Wass, G., "Shear Waves In Plane Infinite Structures," *Journal of Engineering Mechanics Division,* ASCE, Vol. 98, Feb. 1972, pp. 85–105.

2 Lysmer, T., and Kuhlemeyer, R. G., "Finite Dynamic Model For Infinite Media," *Journal of Engineering Mechanics Division,* ASCE, Vol. 95, Aug. 1969, pp. 859–877.

3 Kansel, E., Roesset, J. M., and Waas, G., "Dynamic Analysis of Footings On Layered Media," *Journal of Engineering Mechanics Division,* ASCE, Vol. 101, Oct. 1975, pp. 679–693.

4 Ang., A. H. S. and Newmark, N. M., "Development of a Transmitting Boundary for Numerical Wave Motion Calculations," Report To The Defense Atomic Support Agency, Washington, D. C., Apr. 1971.

5 Berger, B. S., and Alabi, B., "Solution of Navier's Equation In Cylindrical Curvilinear Coordinates," ASME JOURNAL OF APPLIED MECHANICS, Vol. 45, No. 4, Dec. 1978, pp. 812–816.

6 Eringen, A. C., and Suhubi, E. S., *Elastodynamics,* Vol. II, Academic Press, New York, 1975.

7 Berger, B. S., and Curtis, D. M., "Finite Difference Boundary Deformation Techniques in the Analysis of Elastic Bodies of Revolution," PhD Thesis, Department of Mechanical Engineering, University of Maryland, College Park, Md., Mar. 1980.

On the Computation of the Confluent Hypergeometric Function at Densely Spaced Points

P-T. D. Spanos[1]

An algorithm is described for computing the values of the confluent hypergeometric function at several points spaced densely along an interval of real numbers. Numerical data obtained by using this algorithm and pertaining to a commonly made approximation for the first-passage problem of the response amplitude of a lightly damped and randomly excited linear oscillator are presented.

Introduction

In engineering and scientific applications, it is often necessary to compute the values of the confluent hypergeometric function $M(a, b, z)$ [1] for given values of the independent variable z, and the parameters a and b. The function $M(a, b, z)$ is defined as the nontrivial solution of the ordinary differential equation

$$z\frac{d^2M}{dz^2} + (b - z)\frac{dM}{dz} - aM = 0 \tag{1}$$

which is finite at $z = 0$. This solution can be represented by the following series [1, 2]:

$$M(a, b, z) = 1 + \frac{A_1}{B_1}\frac{z}{1!} + \frac{A_2}{B_2}\frac{z^2}{2!} \ldots + \frac{A_n}{B_n}\frac{z^n}{n!} + \ldots, \tag{2}$$

where

$$A_n = a(a + 1) \ldots (a + n - 1), \quad A_0 = 1,$$
$$B_n = b(b + 1) \ldots (b + n - 1), \quad B_0 = 1. \tag{3}$$

Equation (2) can be used, without concern about efficiency, to compute the value of $M(a, b, z)$ at a single or a few points z. However, this approach may require excessive computational time if for a particular problem it is desired to compute the values of $M(a, b, z)$ at a large number of points z. This will be the case, for example, if it is required to plot the values of $M(a, b, z)$ versus z, or to compute numerically integrals, the integrands of which involve $M(a, b, z)$. Numerical computations of this nature would require the values of

[1] Assistant Professor of Engineering Mechanics, The University of Texas at Austin, Austin, Texas, 78712. Assoc. Mem. ASME.

Manuscript received by ASME Applied Mechanics, September, 1979; final revision, March, 1980.

$M(a, b, z)$ at a set of densely spaced points. For this purpose it is logical to attempt to develop a numerical scheme which leads from the value of $M(a, b, z)$ to the value of $M(a, b, z + \Delta z)$, where Δz is a small increment. This idea is the basis of an alternative computational algorithm for $M(a, b, z)$ presented in this Note. Numerical data obtained by applying this algorithm for $b = 1$ are presented. The data pertain to a first-passage problem formulated in connection with a Markovian approximation of the amplitude of the response of a lightly damped linear structure to a white random excitation.

Formulation

The objective of relating the value of $M(a, b, z)$ to $M(a, b, z + \Delta z)$ leads to a Taylor expansion of $M(a, b, z + \Delta z)$ in the neighborhood of z. The specific expansion can be expressed as

$$M(a, b, z + \Delta z) = M(a, b, z) + \sum_{i=1}^{n} \frac{1}{i!} \frac{d^i M}{dz^i} (\Delta z)^i + R, \tag{4}$$

where the derivatives d^iM/dz^i are evaluated at z, R is the remainder of the Taylor expansion, and n is an integer representing the highest order of the derivatives used in the expansion. The derivatives appearing in equation (4) can be expressed as

$$\frac{d^i M(a, b, z)}{dz^i} = \frac{A_i}{B_i} M(a + i, b + i, z), \tag{5}$$

where

$$azM(a + 1, b + 1, z) = b(1 - b + z)M(a, b, z) + b(b - 1)M(a - 1, b - 1, z) \tag{6}$$

Substituting equation (5) into equation (4) yields

$$M(a, b, z + \Delta z) = M(a, b, z) + \sum_{i=1}^{N} \frac{1}{i!} \frac{A_i}{B_i} M(a + i, b + i, \Delta z)(\Delta z)^i + R. \tag{7}$$

Clearly, the value of R will be negligible for $\Delta z < 1$ and $n = N$, an appropriately large number. In this case, the value of $M(a, b, z + \Delta z)$ can be computed in terms of the values of $M(a - 1, b - 1, z)$, $M(a, b, z), \ldots, M(a + N, b + N, z)$.

Mechanization

Assume that it is desired to compute the values of $M(\bar{a}, \bar{b}, z)$ at equally spaced points $z = 0, \Delta z, 2\Delta z, \ldots$ along the real axis. For this purpose, first the equation

$$M(a, b, 0) = 1 \tag{8}$$

is used to determine the values of $M(a, b, 0)$ for $(a, b) = \{(\bar{a} - 1, \bar{b} - 1); (\bar{a}, \bar{b}); \ldots; (\bar{a} + N, \bar{b} + N)\}$. Then, the equation

$$M(a, b, z + \Delta z) \approx \hat{M}(a, b, z + \Delta z) \equiv M(a, b, z) + \sum_{i=1}^{N} \frac{1}{i!} \frac{A_i}{B_i} M(a + i, b + i, z)(\Delta z)^i \tag{9}$$

is used for $z = 0$, and $(a, b) = \{(\bar{a} - 1, \bar{b} - 1); (\bar{a}, \bar{b})\}$ to compute the values of $M(\bar{a} - 1, \bar{b} - 1, z + \Delta z)$ and $M(\bar{a}, \bar{b}, z + \Delta z)$. Upon determining the values of $M(\bar{a}, \bar{b}, \Delta z)$ and $M(\bar{a} - 1, \bar{b} - 1, \Delta z)$, the values of $M(\bar{a} + 1, \bar{b} + 1, \Delta z)$, $M(\bar{a} + 2, \bar{b} + 2, \Delta z), \ldots$ and $M(\bar{a} + N, \bar{b} + N, \Delta z)$ are computed by using equation (6) for $(a, b) = \{(\bar{a}, \bar{b}); (\bar{a} + 1, \bar{b} + 1); \ldots (\bar{a} + N - 1, \bar{b} + N - 1)\}$. This numerical scheme is repeated to compute the value of $M(\bar{a}, \bar{b}, 2\Delta z)$ by setting $z = \Delta z$ into equation (9). Obviously, the values of $M(\bar{a}, \bar{b}, 3\Delta z)$, $M(\bar{a}, \bar{b}, 4\Delta z)$ and so forth can be computed by substituting corresponding values of z into equation (9) and repeating the same numerical scheme.

Note for Special Values of $\bar{a}$ and $\bar{b}$

It is noted that for $b = -m(m = 0, 1, 2, \ldots,)$, the function $M(a, b, z)$ is indeterminate unless $a = -n(0, 1, \ldots,)$, where $m = n, n + 1, n + 2, \ldots,$. Seemingly this fact would imply that equation (6) for $b = 0$ or $b = 1$ cannot be applied for all values of a. However, a careful examination of equation (6) reveals that it is only necessary to assure that

$$\lim_{b \to 0} b\, M(a, b, z) = \text{finite} \tag{10}$$

for this equation to be meaningful. Equation (10) can be readily verified by considering equation (2). It must be noted, as well, that for $a = -n(n = 0, 1, \ldots,)$ and for values of $b \neq -m(m = n + 1, n + 2, \ldots,)$ the function $M(a, b, z)$ terminates and becomes a polynomial of z. In this case, already existing efficient algorithms for the computation of polynomials can be used for the computation of $M(a, b, z)$.

Accuracy

Clearly, the accuracy of the presented numerical scheme depends on the step Δz and the number N of terms used in equation (9). Its computational advantages, in comparison with the traditional method which uses equation (2), are based on the fact that if equation (2) is truncated at $n = L$ and equation (4) is truncated at $n = N$, the values of the remainders will be $O(z^L)$ and $O(\Delta z^N)$, respectively. Therefore, for large values of z, for example $z = 100\Delta z$, the same accuracy for $M(\bar{a}, \bar{b}, z)$ would be yielded by equation (2) and equation (9) for $N \ll L$.

An Application

Consider the equation of motion of a lightly damped linear structure excited by a broad-band process $w(t)$ of spectral density $S(\omega)$

$$\ddot{x} + 2\zeta\omega_0\dot{x} + \omega_0^2 x = w(t); \quad \zeta \ll 1. \tag{11}$$

Assume that the problem has been normalized so that the expression $\pi S(\omega_0)/2\zeta\omega_0^3$ for the stationary variance of the response is equal to unity. Furthermore, consider the probability $P_B(\tau)$ of the response envelope

$$a^2(t) = x^2(t) + \dot{x}^2(t)/\omega_0^2; \quad a(0) = A \tag{12}$$

not exceeding the barrier $B > 0$ during the interval $(0, \tau]$. Then, $P_B(\tau)$ can be approximated by the expression [4, 5]

$$P_B(A, \tau) = \sum_{i=1}^{\infty} C_{i,B} e^{-2\zeta\omega_0\lambda_{i,B}\tau} M(-\lambda_{i,B}, 1, \tfrac{1}{2}A^2). \tag{13}$$

The symbol $\lambda_{i,B}$ represents the eigenvalues of a boundary-value problem formulated by application of the separation of variables technique on the backward Kolmogorov equation associated with an approximation of $a(t)$ by a Markov process [3–5]. The symbol $C_{i,B}$ represents constant coefficients given by the equation

$$C_{i,B} = \int_0^{1/2B^2} M(-\lambda_{i,B}, 1, s)e^{-s}ds \Big/ \int_0^{1/2B^2} M^2(-\lambda_{i,B}, 1, s)e^{-s}ds. \tag{14}$$

Repeated citations have been made in the literature, for example, in reference [4], of the fact that no convenient tables of M are available for numerical computation based on equation (13). It is noted that for an initially quiescent structure, $A = 0$, equation (13) becomes

$$P_B(0, \tau) = \sum_{i=1}^{\infty} C_{i,B} e^{-2\zeta\omega_0\lambda_{i,B}\tau}. \tag{15}$$

Thus, for a quiescent structure, it is only necessary to compute $C_{i,B}$ for the determination of $P_B(0, \tau)$. This fact has motivated the computation of $C_{i,B}$ by applying the presented algorithm for $\bar{b} = 1$. Three values of the barrier have been considered $\{B = 1, 2, 3\}$. The corresponding values of $\lambda_{i,B}$, $i = 1, \ldots, 9$ given in Table 1 have been taken from reference [4]. The computed values of $C_{i,B}$ are shown in Table 2. These values have been obtained by using $\Delta z = 0.05$ and $N = 6$ in the present algorithm, and they have been validated by using the series representation of $M(a, b, z)$, equation (2), with $n = 30$. Also shown in Table 2 is the sum S_9

Table 1 Eigenvalues $\lambda_{i,B}$; $i = 1, \ldots, 9$; barrier $B = \{1, 2, 3\}$

i \ B	1.0	2.0	3.0
1	2.418811	0.329478	0.040987
2	14.774574	3.465318	1.548872
3	36.984065	9.023553	4.030491
4	69.061214	17.044586	7.597266
5	111.007448	27.531894	12.258870
6	162.823090	40.486194	18.016587
7	224.508247	55.907712	24.870726
8	296.062962	73.796536	32.821393
9	377.487360	94.152710	41.868630

Table 2 Coefficients $C_{i,B}$; $i = 1, \ldots, 9$; barrier $B = \{1, 2, 3\}$

i \ B	1.0	2.0	3.0
1	1.48815	1.24559	1.06187
2	−0.85412	−0.42215	−0.10970
3	0.67095	0.32214	0.08837
4	−0.57185	−0.27241	−0.07626
5	0.50706	0.24076	0.06800
6	−0.46037	−0.21822	−0.06191
7	0.42463	0.20109	0.05721
8	−0.39613	−0.18747	−0.05349
9	0.37270	0.17631	0.05030
Sum	1.18102	1.08564	1.02439

$$S_9 = \sum_{i=1}^{9} C_{i,B}. \tag{16}$$

Clearly, the theoretical value S_∞ is

$$S_\infty \equiv \sum_{i=1}^{\infty} C_{i,B} = \lim_{\tau \to 0} \sum_{i=1}^{\infty} C_{i,B}\, e^{-2\omega_0 \lambda_{i,B} \tau} = \lim_{\tau \to 0} P_B(\tau) = 1. \tag{17}$$

Examining Table 2, it is seen that the truncation of S_∞ to S_9 generates a considerable error for $P_B(0, \tau)$ as $\tau \to 0$. For example, for $B = 1$ the error is close to 20 percent. The value of S_9 has been used in reference [4] to plot $P_B(0, \tau)$ versus τ for $B = \{1, 2, 3\}$. Interestingly, the truncation error neither has been reported nor has it been shown in reference [4].

Summary

An algorithm has been presented for the computation of the confluent hypergeometric function $M(a, b, z)$ at a set of densely spaced real points. The basis of the algorithm is the Taylor representation at $M(a, b, z + \Delta z)$ in terms of $M(a, b, z)$, and utilization of a recursive formula for the derivatives of the confluent hypergeometric function. Numerical data obtained by application of this algorithm for a special class of confluent hypergeometric functions are presented. The data pertain to the first-passage problem of a commonly used Markovian approximation for the amplitude of the response of a lightly damped linear structure to white random excitation.

References

1 Abramowitz, M., and Stegun, J., *Handbook of Mathematical Functions With Formulas, Graphs, and Mathematical Tables,* Dover, 1965, Chapter 13.

2 Slater, L. J., "On the Evaluation of the Confluent Hypergeometric Function," *Proceedings of the Cambridge Philosophical Society,* Vol. 49, 1953, pp. 612–622.

3 Ariaratnam, S. T., and Pi, H. N., "On the First-Passage Time for Envelope Crossing for a Linear Oscillator," *International Journal of Control,* Vol. 18, 1973, pp. 89–96.

4 Lennox, W. C., and Fraser, D. A., "On the First-Passage Distribution for the Envelope of a Nonstationary Narrow-Band Stochastic Process," ASME JOURNAL OF APPLIED MECHANICS, Vol. 41, 1974, pp. 793–797.

5 Spanos, P-T. D., "Numerical Aspects of the First-Passage Equation for the Response Amplitude of a Vibrating Linear Structure," Texas Institute for Computational Mechanics, Report TICOM-7916, 1979, pp. 1–29.

Journal of Applied Mechanics

Discussion

Computation of Rigid-Body Rotation in Three-Dimensional Space From Body-Fixed Linear Acceleration Measurements[1]

L. E. Goodman[2] and A. R. Robinson.[3] The subject paper by Mital and King represents a valuable contribution to the practical problem of determining rotation histories from dynamical measurements. The main algorithm, the experimental validation of the computation and the discussion of error minimization are all interesting and useful. In describing the basis of the computation procedure, however, the authors are guilty of a slight verbal infelicity that may mislead readers unfamiliar with the literature of the subject. The statements in question occur in the first paragraph of the section entitled "Computation of Rotation From Accelerometer Data." The following discussion is offered in an effort to clarify matters.

The computational method presented in the subject paper is based on what the authors term the "Goodman-Robinson" theorem (authors' reference [8]). The correct bibliographic reference to this theorem is given below [8].[4] Briefly, the theorem concerns a rigid body constrained to turn about a fixed point, 0, which is also the origin of a set of body-fixed axes, x, y, z (not necessarily orthogonal). Consider a fixed sphere of unit radius centered on 0. As the body moves, the intersection with the sphere of any one of the body-fixed axes, say x, describes a curve on the sphere. From any starting point at $t = 0$ the body will, at time t, have reached a new position that could have been reached by a single rotation Φ. The Goodman-Robinson theorem asserts that the component of Φ about the x-axis, ϕ_x, is given by the expression (equation (4) in [8]):

$$\phi_x = \int_0^t \omega_x \, dt + A_x \pm 2m\pi$$

Here ω_x (t) is the x-component of the angular velocity; A_x is the area on the unit sphere bounded by the curve traced by the intersection of the x-axis with the sphere plus a closure arc corresponding to the negative of Φ; and m is an integer or zero. Similar expressions hold for ϕ_y and ϕ_z. The theorem is exact. No "correction term" has been omitted. In fact, no additional term is possible.

In technological applications of the Goodman-Robinson theorem it is often desirable to express A_x in terms of other geometric parameters that are of interest. After it is proven in [8], the theorem is first illustrated by a simple example in which the area A_x is computed exactly. Then the theorem is applied to solve what Dr. Bortz in the authors' reference [6] terms "the famous coning problem." In this application the area A_x is small compared with 4π. In this circumstance it is permissible to replace A_x by the corresponding area on the tangent plane—what cartographers would call the central or gnomonic projection of A_x. In the technological problem to which Dr. Bortz applies the Goodman-Robinson theorem, on the other hand, A_x is not necessarily small and he, quite correctly, employs an exact expression for A_x. So also in the authors' paper under discussion. This expression for A_x entails adding a term to the area of the central projection and it is this addition that the authors appear to have in mind when they write of a correction term. This term, however, has nothing to do with the theorem itself. That theorem is completely and correctly stated and proved in [8].

Authors' Closure

The authors appreciate the comments made by Professors Goodman and Robinson relative to the usefulness of the method proposed in the paper. We agree that the Goodman-Robinson theorem does contain a correction term Ax and that the word "omit" in our paper was a poor choice. What we meant to say was that we needed an exact expression which was not available in reference [8]. It should be noted that Bortz [6] derived the expression for the orientation vector independently of the Goodman-Robinson theorem and that his expression was more suitable and accurate for the computation of rigid-body rotation from linear accelerometer measurements. We apologize for the error in reference [8] which was rectified by the discussants.

Stability of a Rotor Partially Filled With a Viscous Incompressible Fluid[1]

F. G. Kollmann.[2] This discusser would like to congratulate the authors on their very valuable contribution to this interesting field and also would like to draw their attention to the following:

1 The first comprehensive analytical solution for the inviscid case

[1] By N. K. Mital and A. I. King and published in the December, 1979, issue of the ASME JOURNAL OF APPLIED MECHANICS, Vol. 46, No. 4, pp. 925–930.

[2] University of Minnesota, Department of Civil and Mineral Engineering, Minneapolis, Minn. 55455.

[3] University of Illinois, Department of Civil Engineering, Urbana, Ill. 61801.

[4] [8] Goodman, L.E., and Robinson, A.R., "Effect of Finite Rotations on Gyroscopic Sensing Devices," ASME JOURNAL OF APPLIED MECHANICS, Vol. 25, 1958, pp. 210–213.

[1] By S. L. Hendricks and J. B. Morton, and published in the December, 1979, issue of the ASME JOURNAL OF APPLIED MECHANICS, Vol. 46, pp. 913–918.

[2] Professor, Technische Universität Braunschweig, Institut für Maschinenelemente und Fördertechnik, Langer Kamp 19B, 3300 Braunschweig, Germany.

was given by Kuipers [1] where he compared his theoretically predicted stability charts [2] with the discusser's experimental results and excellent agreement was found.

2 The authors' remark, that the discusser attempted no analysis is a little bit misleading. The discusser used a lumped mass model for the trapped liquid and could predict the independence of the critical spin frequency from the mass of the contained fluid but by the discusser's model, he was not able to analyze the interaction of the motions of the rotor and the fluid waves.

3 The discusser is interested to learn, whether the authors have performed experimental investigations to confirm their theoretical predictions.

References

1 Kuipers, M., "On the Stability of a Flexible Mounted Rotating Cylinder Partially Filled With Liquid," *Applied Scientific Research,* Section A, Vol. 13, 1964, pp. 121–137.

2 Kuipers, M., "Die Instabilität eines federnd gelagerten und teilweise mit Flüssigkeit gefüllten umlaufenden Hohlzylinders," *Forschung im Ingenieur-Wesen,* Vol. 32, No. 6, 1966, pp. 194–195.

Authors' Closure

The author is indebted to Dr. Kollmann for bringing the two references to his and the reader's attention. The article by Kuipers supports the author's assertion that both external rotor damping and damping due to the viscosity of the entrapped fluid must be considered in order to have a consistent theory.

The author apologizes for any misconceptions that may have arisen concerning Dr. Kollmann's article.

The authors have not performed any comprehensive experiments to date. A few unreported experiments have been conducted using a rotor which was clamped at one end and free at the other. The experiments confirmed the dramatic rise in the upper stability boundary when rotor damping was increased (Fig. 6). Since the experimental rotor allowed the cup to tilt (creating gyroscopic stiffening effects in the rotor and exciting axial dependence in the fluid waves), a direct comparison with the current theory was not attempted. A more comprehensive theory incorporating axial dependence in the fluid motion has now been completed and will be reported in another paper. In the meantime the author would encourage Dr. Kollmann or anyone else to undertake a comprehensive experimental investigation.

Dynamic Response of a Cylindrical Shell in a Potential Fluid[1]

R. L. Citerley.[2] The authors have touched upon several problem areas that can be encountered in the analysis of fluid-structure systems. Three points in particular should be addressed.

1 In solving a transient response problem for an incompressible fluid, the authors attributed the observed numerical instability to the addition of the fluid, arguing that the Houbolt difference operator is unconditionally stable. The proof of stability for this operator has been given only for symmetric systems [1]. Using a finite-difference formulation of the Sander's shell equations, with displacements and moment resultants as fundamental variables, results in system equations which are nonsymmetric. Thus a formal proof of unconditional stability is lacking for the problem under consideration. The same basic shell equations, coupled with a compressible fluid, produced a similar instability phenomenon in a recent study [2]. The instability was removed by using a spatial Euler difference operator rather than central difference at the fluid-shell interface. It can be shown that the eigenvalues, γ, of the system $[K]\{d\} = \gamma[M]\{d\}$ will provide the insight with respect to numerical stability. Using an incompressible fluid, either the "stiffness" matrix, K, or the "mass" matrix, M, can be modified to account for the fluid. These matrices are generally full and nonsymmetric for the particular geometries encountered in the nuclear energy field [3]. Further, the eigenvalues may even be complex, but will appear as conjugate pairs. Using a diagonal mass matrix to represent the fluid for all harmonic responses, although attractive for its economy, is only correct for rigid body motions and must be applied only to the mass terms corresponding to the normal displacement.

2 When representing a fully coupled fluid-structure system with an incompressible fluid, responses are instantaneously felt throughout the domain, and are solely determined by the accelerations of the wetted interface and imposed pressures. Therefore, when performing an eigenvalue analysis, the fundamental variables are those of the shell. With a compressible fluid, the pressures at points within the fluid must be added as fundamental variables in the vector $\{d\}$, in the foregoing. Again, an eigenvalue analysis can be performed, but the physical interpretation of results becomes a little more involved. In either case, for containment shells some eigenvalues will have the same, or nearly the same values as predicted for the empty shell, but the corresponding eigenvectors will be considerably different. Whether or not these modes should still be classified as shell modes is simply a matter of semantics. As the fluid height approaches the shell height, the magnitude of the eigenvalues associated with shell responses will dramatically change under the incompressible assumption. Little reduction in the "shell natural frequency" is observed by the introduction of compressibility, but additional "acoustic modes" will now be present. The eigenvalues corresponding to these acoustic modes can greatly differ from the rigid wall modes. Of course, the acoustic modes are, by definition, affected by compressibility. For a narrow annular fluid configuration with a 12.91 m fluid height, several acoustic modes would exist within the frequency range of interest (<500 Hz); whereas, for a 0.7 m fluid height, the first acoustic mode is at 525 Hz.

Generally, when a fluid-structure system is excited by an imposed pressure or volume source within the fluid, and one is concerned with fluid responses (i.e., the acoustic modes), the dynamic characteristics of the fluid take on a greater importance than do the structure modes. Conversely, when the structure is excited by an externally applied surface or body force, and one is concerned about containment responses only, the dynamic characteristics of the structure begin to take precedence. If one can perform an eigenvalue analysis for a reasonable frequency bandwidth, then periodic, random or transient analyses become straightforward tasks. Wave propagation problems are more readily solved by direct time integration since they are equivalent to a modal response involving a very large number of contributing modes.

3 Experimental verification of a numerical procedure for fluid-structure analysis is not a trivial task. As noted by the authors, specific boundary conditions may be difficult to achieve. Numerical procedures are available for combining structural modes of a dry structure with either incompressible or compressible fluids [4]. In this way, measured data of nonideal boundary conditions of the dry structure can be directly coupled with a fluid. However, it has been this writer's experience that minute volumes of air, either entrapped in pockets or in the form of bubbles at the fluid-structure interface, have a far greater effect on acoustic modes than does structural compliance [5]. Only after careful treatment of the water, such as raising the fluid temperature to near boiling and the addition of wetting agents, can consistent results over a wide frequency band be obtained. Further,

[1] By G. E. Cummings, and H. Brandt, and published in the December, 1979, issue of the ASME JOURNAL OF APPLIED MECHANICS, Vol. 46, pp. 772–778.

[2] Anamet Laboratories, Inc., P.O. Box 831, San Carlos, Calif. 94070.

the local sonic speed or celerity of the fluid is only very weakly sensitive to pressure over the range cited.

References

1 Johnson, D. E., "A Proof of the Stability of the Houbolt Method," *AIAA Journal*, Vol. 4 No. 8, Aug. 1966, pp. 1450 and 1451.

2 Citerley, R. L., Gibson, W., and Dilbeck, C. S., "Nonlinear Dynamic Analysis of the Primary Containment Vessels, Fukushima 6 and Tokai 2," Anamet Report No. 275.270-B, June 1975.

3 Ball, R. E., and Citerley, R. L., "Fluid Mass Matrices for Thin Shell-of-Revolution Tanks," ASME *Dynamics of Fluid-Structure Systems in the Energy Industry*, PVP-39, June 1979.

4 MacNeal, R. H., Citerley, R. L., and Chargin, M., "A New Method for Analyzing Fluid-Structure Interaction Using MSC/NASTRAN," presented at the 5th International Conference on Structural Mechanics in Reactor Technology (SMiRT), Berlin, Germany, August 13–17, 1979.

5 Citerley, R. L., Kienholz, D. A., and Gibson, W. C., "Assessment of Structural Effects in Acoustic Transient Experiments," paper to be presented at the ASME 1980 Pressure Vessels and Piping Conference, San Francisco, August 12–15, 1980.

The Nonlinear Behavior of Elastic Slender Straight Beams Undergoing Small Strains and Moderate Rotations[1]

Dewey H. Hodges.[2] The subject paper deals with mathematical modeling of the nonlinear behavior of beams. A set of equations is derived and used to investigate the static behavior of a slender cantilever beam loaded transversely at the free end. Since the loading is not necessarily along the principal axes, the principal bending deflections and torsion are coupled elastically. In a strictly linear theory there would be no torsion; thus the presence of torsion is, itself, a manifestation of nonlinear behavior. The agreement obtained with experimental data achieved in the subject paper is excellent and confirms that one may apply the geometric nonlinear theory of elasticity to beams with confidence provided an adequate degree of nonlinearity is retained in the mathematical model to account for large deflections.

The same problem was treated by Dowell, et al., in [1]. The analytical results of [1] and those of the subject paper agree quite well as long as w, the bending deflection in the plane of greatest flexural flexibility, remains relatively small compared to the beam length. In fact, analytical results of [1] depart from those of the subject paper only when w ceases to be a small fraction of the beam length. An examination of the w equation (33b) in the subject paper reveals that in addition to linear and second-degree terms, several terms of third degree in the deflections appear. These terms are retained in the authors' original derivation of these equations [2] for the special case when I_{22}/I_{33} is large compared to unity. Although not stated in the subject paper, these third-degree terms constitute the *only* difference between the equations of [1] and the subject paper. Thus the improved agreement reported in the subject paper must be due to the presence of these third-degree terms and not to the reasons indicated in the paper. The two main reasons given for the improved agreement shown in the subject paper are now examined.

The first reason is mentioned on Page 162, Column 1, where the authors attribute the accuracy of their results to "a more careful and consistent" derivation than in [1]. The original derivation of the authors' equations [2] concludes with a set of nonlinear equations of second degree in bending and torsion deflections. These equations are intended for applications to rotating blades and are based on the assumption that bending and torsion rigidities are of the same order of magnitude. For the special case where I_{22}/I_{33} and EI_{22}/GJ are large compared to unity, the authors endeavored to retain third-degree terms whenever they are multiplied by a large coefficient in the equations. It is not clear that appropriate measures were taken, however, to ensure that *all* third-degree terms multiplying the large coefficients were retained. In fact, only terms through second degree were retained in the bending curvature expressions, and it was never demonstrated that third-degree terms from these expressions would not appear in the final equations. Moreover, the final equations in the subject paper, because of the particular third-degree terms retained, do not have a self-adjoint structural operator. While it is acknowledged that the authors deserve credit for adding appropriate higher-degree terms to the equations to improve the correlation with experimental data, this, in itself, does not necessarily imply a higher degree of care or consistency.

The second reason given by the authors appears in the Concluding Remarks section: "The superior agreement obtained with the present equations is due to differences between the final equations of equilibrium used here and those given in [3]. These differences have been discussed with considerable detail in [2]." (Reference numbers refer to those of this discussion). The first sentence, by itself, appears to be referring to the third-degree terms retained in equation (33b) because the ratio I_{22}/I_{33} is large compared to unity for the particular beam considered. This is not the intended meaning according to the second sentence, however, because differences related to these third degree terms are *not* discussed in [2]. The differences between the equations of [2, 3] that are discussed in [2] relate to the second-degree equations only and have been recently clarified in [4, 5]. The final second-degree nonlinear equations of [2, 3], while differing slightly for pretwisted beams [4], are actually equivalent for the present case of a nonrotating beam without pretwist [5]. Therefore, the improved agreement reported in the subject paper does not prove that the equations for rotating blade applications derived in [2] are more "reliable" nor that they "can be used with confidence" any more than those of [3]. The results simply prove that the equations of the subject paper are more accurate than those of [1] when applied to problems in which the bending deflection w may exceed a small fraction of the blade length and the ratio I_{22}/I_{33} is large compared to unity. These cases are not treated in [1] in which the squares of bending slopes were assumed to be negligible with respect to unity and the equations were taken directly from [3] where I_{22} and I_{33} were assumed to be the same order of magnitude [3, pp. 8, 9].

References

1 Dowell, E. H., Traybar, J., and Hodges, D. H., "An Experimental Theoretical Correlation Study of Nonlinear Bending and Torsion Deformations of a Cantilever Beam," *Journal of Sound and Vibration*, Vol. 50, No. 4, 1977, pp. 533–544.

2 Rosen, A., and Friedmann, P., "Nonlinear Equations of Equilibrium for Elastic Helicopter or Wind Turbine Blades Undergoing Moderate Deformation," University of California, Los Angeles, School of Engineering and Applied Science Report UCLA-ENG-7718 (revised edition) June 1977; also available NASA CR-159478, Dec. 1978.

3 Hodges, D. H., and Dowell, E. H., "Nonlinear Equations of Motion for the Elastic Bending and Torsion of Twisted Nonuniform Rotor Blades," NASA TN D-7818, Dec. 1974.

4 Hodges, D. H., "Torsion of Pretwisted Beams Due to Axial Loading," ASME JOURNAL OF APPLIED MECHANICS, Vol. 47, June 1980, pp. 393–397.

5 Hodges, D. H., Ormiston, R. A., and Peters, D. A., "On the Nonlinear Deformation Geometry of Euler-Bernoulli Beams," NASA TP-1566, 1980.

K. R. V. Kaza[3] **and R. G. Kvaternik.**[4] The paper derives nonlinear equilibrium equations for a beam and studies its nonlinear behavior

[1] By A. Rosen and P. Friedmann, and published in the March, 1979, issue of the ASME JOURNAL OF APPLIED MECHANICS, Vol. 46, pp. 161–168.

[2] Research Scientist, Rotorcraft Dynamics Division, Aeromechanics Laboratory, U.S. Army Research and Technology Laboratories, Ames Research Center, Moffett Field, Calif. 94035.

[3] Adjunct Associate Professor, Mechanical Engineering Department, The University of Toledo, Toledo, Ohio.

[4] Aerospace Engineer, Structures and Dynamics Division, NASA Langley Research Center, Hampton, Va.

the local sonic speed or celerity of the fluid is only very weakly sensitive to pressure over the range cited.

References

1 Johnson, D. E., "A Proof of the Stability of the Houbolt Method," *AIAA Journal*, Vol. 4 No. 8, Aug. 1966, pp. 1450 and 1451.

2 Citerley, R. L., Gibson, W., and Dilbeck, C. S., "Nonlinear Dynamic Analysis of the Primary Containment Vessels, Fukushima 6 and Tokai 2," Anamet Report No. 275.270-B, June 1975.

3 Ball, R. E., and Citerley, R. L., "Fluid Mass Matrices for Thin Shell-of-Revolution Tanks," ASME *Dynamics of Fluid-Structure Systems in the Energy Industry*, PVP-39, June 1979.

4 MacNeal, R. H., Citerley, R. L., and Chargin, M., "A New Method for Analyzing Fluid-Structure Interaction Using MSC/NASTRAN," presented at the 5th International Conference on Structural Mechanics in Reactor Technology (SMiRT), Berlin, Germany, August 13–17, 1979.

5 Citerley, R. L., Kienholz, D. A., and Gibson, W. C., "Assessment of Structural Effects in Acoustic Transient Experiments," paper to be presented at the ASME 1980 Pressure Vessels and Piping Conference, San Francisco, August 12–15, 1980.

The Nonlinear Behavior of Elastic Slender Straight Beams Undergoing Small Strains and Moderate Rotations[1]

Dewey H. Hodges.[2] The subject paper deals with mathematical modeling of the nonlinear behavior of beams. A set of equations is derived and used to investigate the static behavior of a slender cantilever beam loaded transversely at the free end. Since the loading is not necessarily along the principal axes, the principal bending deflections and torsion are coupled elastically. In a strictly linear theory there would be no torsion; thus the presence of torsion is, itself, a manifestation of nonlinear behavior. The agreement obtained with experimental data achieved in the subject paper is excellent and confirms that one may apply the geometric nonlinear theory of elasticity to beams with confidence provided an adequate degree of nonlinearity is retained in the mathematical model to account for large deflections.

The same problem was treated by Dowell, et al., in [1]. The analytical results of [1] and those of the subject paper agree quite well as long as w, the bending deflection in the plane of greatest flexural flexibility, remains relatively small compared to the beam length. In fact, analytical results of [1] depart from those of the subject paper only when w ceases to be a small fraction of the beam length. An examination of the w equation (33b) in the subject paper reveals that in addition to linear and second-degree terms, several terms of third degree in the deflections appear. These terms are retained in the authors' original derivation of these equations [2] for the special case when I_{22}/I_{33} is large compared to unity. Although not stated in the subject paper, these third-degree terms constitute the *only* difference between the equations of [1] and the subject paper. Thus the improved agreement reported in the subject paper must be due to the presence of these third-degree terms and not to the reasons indicated in the paper. The two main reasons given for the improved agreement shown in the subject paper are now examined.

The first reason is mentioned on Page 162, Column 1, where the authors attribute the accuracy of their results to "a more careful and consistent" derivation than in [1]. The original derivation of the authors' equations [2] concludes with a set of nonlinear equations of second degree in bending and torsion deflections. These equations are intended for applications to rotating blades and are based on the assumption that bending and torsion rigidities are of the same order of magnitude. For the special case where I_{22}/I_{33} and EI_{22}/GJ are large compared to unity, the authors endeavored to retain third-degree terms whenever they are multiplied by a large coefficient in the equations. It is not clear that appropriate measures were taken, however, to ensure that *all* third-degree terms multiplying the large coefficients were retained. In fact, only terms through second degree were retained in the bending curvature expressions, and it was never demonstrated that third-degree terms from these expressions would not appear in the final equations. Moreover, the final equations in the subject paper, because of the particular third-degree terms retained, do not have a self-adjoint structural operator. While it is acknowledged that the authors deserve credit for adding appropriate higher-degree terms to the equations to improve the correlation with experimental data, this, in itself, does not necessarily imply a higher degree of care or consistency.

The second reason given by the authors appears in the Concluding Remarks section: "The superior agreement obtained with the present equations is due to differences between the final equations of equilibrium used here and those given in [3]. These differences have been discussed with considerable detail in [2]." (Reference numbers refer to those of this discussion). The first sentence, by itself, appears to be referring to the third-degree terms retained in equation (33b) because the ratio I_{22}/I_{33} is large compared to unity for the particular beam considered. This is not the intended meaning according to the second sentence, however, because differences related to these third degree terms are *not* discussed in [2]. The differences between the equations of [2, 3] that are discussed in [2] relate to the second-degree equations only and have been recently clarified in [4, 5]. The final second-degree nonlinear equations of [2, 3], while differing slightly for pretwisted beams [4], are actually equivalent for the present case of a nonrotating beam without pretwist [5]. Therefore, the improved agreement reported in the subject paper does not prove that the equations for rotating blade applications derived in [2] are more "reliable" nor that they "can be used with confidence" any more than those of [3]. The results simply prove that the equations of the subject paper are more accurate than those of [1] when applied to problems in which the bending deflection w may exceed a small fraction of the blade length and the ratio I_{22}/I_{33} is large compared to unity. These cases are not treated in [1] in which the squares of bending slopes were assumed to be negligible with respect to unity and the equations were taken directly from [3] where I_{22} and I_{33} were assumed to be the same order of magnitude [3, pp. 8, 9].

References

1 Dowell, E. H., Traybar, J., and Hodges, D. H., "An Experimental Theoretical Correlation Study of Nonlinear Bending and Torsion Deformations of a Cantilever Beam," *Journal of Sound and Vibration*, Vol. 50, No. 4, 1977, pp. 533–544.

2 Rosen, A., and Friedmann, P., "Nonlinear Equations of Equilibrium for Elastic Helicopter or Wind Turbine Blades Undergoing Moderate Deformation," University of California, Los Angeles, School of Engineering and Applied Science Report UCLA-ENG-7718 (revised edition) June 1977; also available NASA CR-159478, Dec. 1978.

3 Hodges, D. H., and Dowell, E. H., "Nonlinear Equations of Motion for the Elastic Bending and Torsion of Twisted Nonuniform Rotor Blades," NASA TN D-7818, Dec. 1974.

4 Hodges, D. H., "Torsion of Pretwisted Beams Due to Axial Loading," ASME JOURNAL OF APPLIED MECHANICS, Vol. 47, June 1980, pp. 393–397.

5 Hodges, D. H., Ormiston, R. A., and Peters, D. A., "On the Nonlinear Deformation Geometry of Euler-Bernoulli Beams," NASA TP-1566, 1980.

K. R. V. Kaza[3] **and R. G. Kvaternik.**[4] The paper derives nonlinear equilibrium equations for a beam and studies its nonlinear behavior

[1] By A. Rosen and P. Friedmann, and published in the March, 1979, issue of the ASME JOURNAL OF APPLIED MECHANICS, Vol. 46, pp. 161–168.

[2] Research Scientist, Rotorcraft Dynamics Division, Aeromechanics Laboratory, U.S. Army Research and Technology Laboratories, Ames Research Center, Moffett Field, Calif. 94035.

[3] Adjunct Associate Professor, Mechanical Engineering Department, The University of Toledo, Toledo, Ohio.

[4] Aerospace Engineer, Structures and Dynamics Division, NASA Langley Research Center, Hampton, Va.

under static loading. The development is set forth as a basis for deriving general nonlinear aeroelastic equations of motion for helicopter and wind-turbine rotor blades. This Discussion clarifies the recent background of the derivation of nonlinear equations of motion of rotor blades, and points out some apparent errors and inconsistencies in the derivations in the subject paper as well as in [1–2], where the details of the derivation are given.

The literature already contains several treatments of nonlinear aeroelastic rotor equations, including development of beam equations as a special case. A starting point for deriving nonlinear equations has been the linear equations derived in [3] for a rotating twisted blade. Several investigators extended [3] to include the nonlinear effects of finite displacements (see, e.g., [4–9]). There are some controversies about the basic ingredients needed to derive the nonlinear equations. These basic ingredients are:

1 Nonlinear expressions for the bending curvatures and twist.

2 A nonlinear expression for the rotational transformation matrix between the coordinates of the deformed and undeformed blade.

3 Nonlinear strain-displacement relations.

In [6–9], the authors of this Discussion addressed several fundamental aspects of the derivation of the second-degree nonlinear aeroelastic equations for rotor blades in forward flight in an attempt to place the derivation on a firm foundation, and set forth certain principles and guidelines to be followed both in establishing the basic ingredients and in deriving the nonlinear equations. The subject paper and [1–2], in emphasizing the same principles and guidelines, add little to the contributions of [6–9].

With regard to the errors, the x-component of the virtual rotation is given as $n_x = \delta\phi$ in [1–2].[4] This is incorrect. The correct expression is

$$n_x = \delta\phi + w_{,x}\delta v_{,x} \tag{1}$$

The expression for the variation of the twist, $\delta\tau$, given in equation D-36c of (2) is thus also incorrect. The correct expression is

$$\delta\tau = \delta\phi_{,x} + w_{,x}\delta v_{,x} + v_{,xx}\delta w_{,x} \tag{2}$$

These errors lead to missing and erroneous terms in the final equations obtained from the principle of virtual work.

The expressions for the virtual rotation components n_y and n_z and for the variation of the bending curvatures $\delta\kappa_y$ and $\delta\kappa_z$ are inconsistent with the basic assumptions of small strains and "moderate" rotations, whereby $u_{,x}$, $v^2{}_{,x}$, $w^2{}_{,x}$, and ϕ^2 are neglected compared to unity. The consistent expressions for n_y and n_z are

$$n_y = -\delta w_{,x} + \phi\delta v_{,x} \tag{3}$$

$$n_z = \delta v_{,x} + \phi\delta w_{,x} \tag{4}$$

Similarly, one can show that the consistent expressions for the variation of the bending curvatures are

$$\delta\kappa_y = \delta v_{,xx} + \phi\delta w_{,xx} + w_{,xx}\delta\phi \tag{5}$$

$$\delta\kappa_z = \delta w_{,xx} - \phi\delta v_{,xx} - v_{,xx}\delta\phi \tag{6}$$

which are not in agreement with the expressions given in [2]. These inconsistencies lead to inconsistent third-degree terms in the final equations.

Oddly, a parallel Newtonian development in the papers yields identical final equations even though no error is made corresponding to the missing term $w_{,x}\delta v_{,x}$ in the expression for n_x. This occurred because the assumptions of small strains and moderate rotations were inconsistently applied in the development of the Newtonian equations.

More fundamentally, the assumption of moderate rotations is an inappropriate foundation for a rigorous derivation of the nonlinear aeroelastic equations of motion of helicopter and wind-turbine blades. The implications of discarding $v^2{}_{,x}$, $w^2{}_{,x}$, and ϕ^2 compared to unity in the rotational transformation matrix were examined in [6–8]. Two consequences are:

1 If ϕ^2 is neglected compared to unity for a rotating blade, a well-known linear inertia term is lost in the torsion equation. Many other investigators have included this term but have introduced it nonrigorously as an applied load.

2 If the terms $v^2{}_{,x}$ and $w^2{}_{,x}$ are neglected compared to unity, some second-degree nonlinear aerodynamic terms are lost which are of the same order as other terms which are retained. Also, some spurious second-degree terms appear in the shear strains if the strains are obtained by using this transformation matrix (although correct shear strain expressions follow directly from the correct curvature expressions).

Finally, three tension-torsion coupling terms given in [3] are missing from the torsion equation, namely, $(Tk_A^2\phi_{,x})_{,x}$, $(Tk_A^2\theta_{G,x})_{,x}$, and $((EB_1\theta_{G,x}^2\phi_{,x})_{,x}$. In [1], the authors of the subject paper took issue with [3], stating that these three terms were incorrect. Subsequently, they conceded ([2] and subject paper) that the first term does exist but discarded it as negligible for closed and solid cross sections. They have apparently held to the position that the other two terms are incorrect. But a wide body of literature (see, e.g., [10–13]) clearly establishes the validity of all three terms for small strains.

References

1 Rosen, A., and Friedmann, P., "Nonlinear Equations of Equilibrium for Elastic Helicopter or Wind Turbine Blades Undergoing Moderate Deformation," University of California at Los Angeles, School of Engineering and Applied Science Report, UCLA-ENG-7718, Jan. 1977.

2 Rosen, A., and Friedmann, P., "Nonlinear Equations of Equilibrium for Elastic Helicopter or Wind Turbine Blades Undergoing Moderate Deformation," University of California at Los Angeles, School of Engineering and Applied Science Report, UCLA-ENG-7718 (revised edition), June 1977; also available NASA CR-159478, Dec. 1978.

3 Houbolt, J. C., and Brooks, G. W., "Differential Equations of Motion for Combined Flapwise Bending, Chordwise Bending, and Torsion of Twisted Nonuniform Rotor Blades," NACA Report 1346, 1958.

4 Friedmann, P., "Influence of Structural Damping, Preconing, Offsets and Large Deflections on the Flap-Lag-Torsional Stability of a Cantilevered Rotor Blade," Paper No. 75-780, AIAA/ASME/SAE 16th Structures, Structural Dynamics and Materials Conference, Denver, Colo., May 1975.

5 Hodges, D. H., and Ormiston, R. A., "Stability of Elastic Bending and Torsion of Uniform Cantilever Rotor Blades in Hover With Variable Structural Coupling," NASA TN D-8192, Apr. 1976.

6 Kaza, K. R. V., and Kvaternik, R. G., "A Critical Examination of the Flap-Lag Dynamics of Helicopter Rotor Blades in Hover and Forward Flight," Paper No. 1034, American Helicopter Society 32nd Annual National Forum, Washington, D.C., May 1976.

7 Kvaternik, R. G., and Kaza, K. R. V., "Nonlinear Curvature Expressions for Combined Flapwise Bending, Edgewise Bending, Torsion and Extension of Twisted Rotor Blades," NASA TM X-73997, Dec. 1976.

8 Kaza, K. R. V., and Kvaternik, R. G., "Nonlinear Aeroelastic Equations for Combined Flapwise Bending, Chordwise Bending, Torsion, and Extension of Twisted Nonuniform Rotor Blades in Forward Flight," NASA TM-74059, Aug. 1977.

9 Kaza, K. R. V., and Kvaternik, R. G., "Nonlinear Flap-Lag-Axial Equations of a Rotating Beam," *AIAA Journal*, June 1977, pp. 871–874.

10 Biot, M. A., "Increase of Torsional Stiffness of a Prismatic Bar Due to Tension," *Journal of Applied Physics*, Vol. 10, Dec. 1939, pp. 860–864.

11 Den Hartog, J. P., *Advanced Strength of Materials*, McGraw-Hill, New York, 1952.

12 Goodier, J. N., Torsion, Chapter 36, *Handbook of Engineering Mechanics*, ed., Flügge, W., 1962.

13 Zickel, J., "Pretwisted Beams and Columns," ASME JOURNAL OF APPLIED MECHANICS, Vol. 33, June 1966, pp. 165–175.

Authors' Closure

Closure to the Comments of Dewey A. Hodges. The authors would like to thank Dr. Hodges for complimenting them on the excellent agreement between the theoretical results obtained in the

[5] The Nomenclature of the subject paper and [1–2] is used.

subject paper and the experimental results obtained in reference [1]. However, they would also like to identify a few inaccurate statements and errors which unfortunately are present in Dr. Hodges comment.

In his comment Dr. Hodges makes frequent use of concepts such as "linear terms," "second-order terms," and "third-order terms." An attempt to use such concepts in an accurate and consistent theory is *a priori* doomed to fail as it happened to Dr. Hodges when he attempted to compare the results of his calculations to his own experimental results [1]. The theory derived in reference [2] is based on the assumption of "small strains and moderate rotations."

According to this theory both elastic strains and terms involving products of elastic rotations (or slopes) are negligible when compared to unity. At the same time these quantities *are not negligible compared to unity when they are multiplied by quantities much larger than one.* The theory developed by Hodges, et al., failed to reproduce the test results because it violated this rule. Therefore in the concluding remarks of reference [1] dealing with the discrepancies between theory and experimental results, Hodges, et al., suggest that these differences are ". . . consistent with the basic assumption of the Hodges-Dowell theory in which squares of bending slopes are neglected compared to one." This remark is incorrect. The discrepancy between theory and experiment was due to the authors' failure to apply the rule governing the neglect of strains and terms involving products of the elastic rotations, compared to unity, in a consistent manner.

Since the theory described in the paper which is the subject matter of this discussion *also* utilizes the approach whereby, "squares of bending slopes are neglected compared to one" and nevertheless achieves excellent agreement with the experimental results, it is clear that the superior agreement is due to the consistency of the theory. This statement is clarified further below. In references [1, 3] the source of the inconsistency was due to the artificial classification of terms as linear terms, second-order terms, and third-order terms. Furthermore, use of this classification as a basis for neglecting terms, instead of neglecting terms by applying the rule of "small strains and moderate rotations," was the source of the inaccuracies introduced in the theory derived in reference [3]. In reference [2] the systematic application of this rule was followed and various sets of equilibrium equations were obtained.

As pointed out by Hodges reference [2] contains various sets of equilibrium equations which correspond to various stiffness ratios of the rod. Each of these sets of equilibrium equations is consistent within the framework of the assumption of "small strains and moderate rotations." The experiments described in [1] which were the basis of the comparison between theory and experiment in the subject paper were performed on rods for which (EI_{22}/GJ) and (I_{22}/I_{33}) were much larger than one. Therefore in order to compare with the experimental results the equilibrium equations corresponding to this situation have to be used. This situation could not be simulated by the equations in reference [3] because "third-order terms" were neglected in violation of the "small strains and moderate rotations rule."

Regarding the comment on "the nonself adjoint structural operator" it is not clear why Dr. Hodges expects to encounter such an operator in such a *nonlinear* problem [2].

In his comment Hodges states that "An examination of the w equation (33b) in the subject paper reveals that in addition to linear and second-degree terms, several terms of third degree in deflections appear. . . . Although not stated in the subject paper, these third-degree terms constitute the *only* difference between the equations of [1] and the subject paper. Thus the improved agreement reported in the subject paper must be due to the presence of those third degree terms and not to the reasons indicated in the paper."

This statement is difficult to understand in view of the fact that a comparison of equations (33a–c) of the subject paper and equations (1) of [1], which takes only a few minutes, clearly shows additional differences for the equation for v and ϕ. As a matter of fact Hodges makes a serious oversight by attributing the good agreement between theory and test to these terms in equations (33b). Even if these terms are neglected the agreement between theory and experiment would still be very good. As a matter of fact the terms which have escaped Hodges attention and which appear in equation (33c) for ϕ, such as the term containing $\phi w''^2_{xx}$ are the important reason for obtaining good agreement between theory and test.

Hodges comment, in his last paragraph is even more difficult to comprehend. If according to *his* statement the theory which he has derived is applicable to cases where "I_{22} and I_{33} are assumed to be of the same order of magnitude" why did he perform the experiments on beams where these conditions were violated, i.e., $I_{22}/I_{33} = 16$? Is it reasonable to compare experimental results with a theory *a priori* known to be *in violation of the conditions of the experiment,* and what could be the potential value of such a comparison?

Finally, it should be noted, that the versions of the equations of equilibrium derived in both references [2, 3] which have been used in rotodynamics applications, are very similar, and therefore they have produced almost identical results.

References

1 Dowell, E. H., Traybar, J., and Hodges, D. H., "An Experimental Theoretical Correlation Study of Nonlinear Bending and Torsion Deformations of a Cantilever Beam," *Journal of Sound Vibration,* Vol. 50, No. 4, 1977, pp. 533–544.

2 Rosen, A., and Friedmann, P., "Nonlinear Equations of Equilibrium for Elastic Helicopter or Wind Turbine Blades Undergoing Moderate Deformation," UCLA-ENG-7718(revised edition), June 1977, also available as NASA-CR-159478, Dec. 1978.

3 Hodges, D. H., and Dowell, E. H., "Nonlinear Equations of Motion for the Elastic Bending and Torsion of Twisted Nonuniform Rotor Blades," NASA TN D-7818, Dec. 1974.

Closure to the Discussion by Kaza and Kvaternik. The discussion by Drs. Kaza and Kvaternik is quite strange mainly because, as will be shown below, it really has very little to do with the subject paper itself. Each of their comments are rebutted below.

1 In equations (1)–(6) of their comment, Kaza and Kvaternik, present what they believe to be the "correct" expressions which in their view replace the "incorrect" expressions in reference [1]. First of all it should be noted that the subject paper, which is based on reference [1] does not use at all the chapter dealing with, derivation of the equations of equilibrium by the use of the principle of virtual work, which is the chapter of reference [1] in which Kaza and Kvaternik have identified what they believe to be "errors." Therefore, in essence it is completely immaterial whether that particular chapter of reference [1] is correct or not because the subject paper does not utilize it. However as far as Kaza and Kvaternik's comment goes, it should be pointed out that the derivations presented in reference [1], were carried out in detail using vector algebra. Therefore one would expect the incorrect expressions and the errors to be identified in a specific manner instead of presenting six equations which are true, simply because they say so! Similar arguments were employed in the middle ages to prove that the earth is flat.

2 Since Kaza and Kvaternik have decided that derivation of the equations based on the principle of virtual work is incorrect they encounter a severe problem in attempting to explain how reference [1] shows complete agreement between the equations of equilibrium obtained by using the principle of virtual work and those obtained by using the Newtonian approach which was presented in the subject paper. So they state "The assumptions of small strains and moderate rotations were inconsistently applied in the development of the Newtonian equations," again this statement is made without any proof or explanation, and rests on the same nonexistent logical foundation as their previous statement.

3 Kaza and Kvaternik continue their discussion by stating "More fundamentally, the assumption of moderate rotations is an inappropriate foundation for a rigorous derivation of the nonlinear aeroelastic equations of motion of helicopter and wind turbine blades," they base this opinion on the need to retain some inertia terms together with some second-order aerodynamic terms. Again consistent with their somewhat confused state of mind these terms are never explicitely identified. At this point the authors would like to note that the subject

paper *deals exclusively with the structural aspects* of a beam undergoing moderate deflections, and therefore their comments have no relevance to the subject under discussion, since aerodynamic and inertia terms are not involved in the derivation of a structural theory.

4 Next Kaza and Kvaternik make a number of comments pertaining to pretwist. First, it should be emphasized that the subject paper deals with a beam which had *no pretwist*, therefore again their discussion is somewhat irrelevant. However, we would like to refer them to a number of recent studies [2–4] and hope that these references will clarify this item.

Within the framework of their discussion Kaza and Kvaternik state, "The subject paper and [1], in emphasizing the same principles and guidelines, adds little to the contributions present in the reports and papers by Kaza and Kvaternik." While Kaza and Kvaternik are entitled to this, somewhat modest opinion, the consistency of their derivation are contested in reference [5]. Unfortunately, Kaza and Kvaternik have never used their equations to solve a structural problem for which experimental results are available. In view of the *excellent agreement between theory and experiment exhibited in the subject paper,* which is never mentioned by Kaza and Kvaternik in their discussion, it appears that they prefer to make unfounded claims, instead of applying the scientific method to a typical test case.

References

1 Rosen A., and Friedmann, P., "Nonlinear Equations of Equilibrum for Elastic Helicopter or Wind Turbine Blades Undergoing Moderate Deformation," UCLA-ENG-7718 (revised edition), June 1977; also available as NASA CR-159478, Dec. 1978.

2 Rosen, A., "The Effect of Initial Twist on the Torsional Rigidity of Beams—Another Point of View," TAE Report No. 360, Apr. 1978.

3 Rosen, A., "The Effect of Initial Twist on the Torsion Rigidity of Beams—Another Point of View," ASME JOURNAL OF APPLIED MECHANICS, Vol. 47, June 1980, pp. 389–392.

4 Hodges, D. H., "Torsion of Pretwisted Beams Due to Axial Loading," ASME JOURNAL OF APPLIED MECHANICS, Vol. 47, June 1980, pp. 393–397.

5 Hodges, D. H., Ormiston, R. A., and Peters, D. A., "On the Nonlinear Deformation Geometry of Euler-Bernoulli Beams," NASA TP 1566, 1980.

Journal of Applied Mechanics

Book Reviews

Nonlinear Oscillations. By Ali Hasan Nayfeh and Dean T. Mook. Wiley-Interscience. 1979. Pages 704. Price $35.

REVIEWED BY P. HOLMES[1]

I shall survey the contents of this book before making some general comments. I close with a few specific comments on the organization, clarity, and viewpoint of the book, and on some of the topics omitted.

Chapter 1 constitutes an extended abstract of the entire work. The next four chapters cover conservative, nonconservative, externally, and parametrically excited single-degree-of-freedom oscillators. The authors then go on to treat n-degree-of-freedom systems, continuous systems, and traveling waves. Each chapter ends with a set of exercises, many of which represent nontrivial pieces of research, and the 70-page bibilography contains over 1500 references. The book therefore provides a comprehensive sampler of the nonlinear vibration problems which occur in engineering.

This text lies firmly within the classical engineering tradition of nonlinear oscillations; the first half of the book is essentially a new version of such texts as those by Minorsky, Hayashi, or Stoker. However, this serves as an introduction to the authors' main aim of covering recent work on multidegree of freedom and continuous systems, which they do in Chapters 5–8. Topics such as the forced oscillations of n-degree-of-freedom systems with quadratic and cubic nonlinearities and of finite strings, beams, and plates are covered, as well as longitudinal and transverse traveling waves in bars. In connection with traveling waves, a nice presentation of the method of characteristics is given and shock fitting is discussed. The authors' recent work on modal saturation in coupled quadratic systems is also covered.

The analytical methods described include phase plane analysis, and the Poincaré-Lindstedt and multiple time-scale perturbation methods. The averaging technique is mentioned several times but dismissed somewhat cursorily. In the section on parametric oscillations, Hill's infinite determinant and the method of strained parameters are discussed. Numerical integration is not covered, but is appealed too frequently for comparison and "checking" perturbation solutions.

It is perhaps easiest to characterize the book by noting that the topics omitted include bifurcation theory and all the recent (past 1960) developments in the qualitative theory of many dimensional dynamical systems due to Arnold, Moser, Smale, et al. In fact early developments in the theory of two-dimensional (free oscillator) systems were already well covered in the "Theory of Oscillators" by Andronov, Vitt, and Khaiken (1966) (now unfortunately out of print) and in the two books by Andronov, Leontovich, Gordon and Maier (1971, 1973). These omissions are therefore not to be criticized, but do serve neatly to delineate the authors' viewpoint (although references to Arnold's and Moser's work on Hamiltonian systems *are* included and even recent work on inverse scattering and exact solutions of integrable infinite dimensional systems, such as the Korteweg-deVries equation, is mentioned).

Each chapter begins with a brief literature survey and the text contains many physical examples; these and the frequent references to the figures enhance its clarity. The introductory chapter, since it abstracts from later material, is occasionally confusing and the figures are not always fully explained, but this is a small price to pay for an extended guide to the whole book. I have a few other minor complaints: The passing reference to catastrophe theory (pp. 170–171) is merely confusing, since it does not even supply a useful reference to the application to Duffing's equation. The list of references, which pretends to completeness, is patchy—for instance much of the significant recent work on galloping oscillations is omitted. But in spite of these and other minor carps, the book is generally very good and can be recommended to all engineers and applied mathematicians wishing for a comprehensive treatment of nonlinear vibrations from the viewpoint of perturbation theory.

I wish to close with some more general comments on nonlinear oscillations, and in particular to point out some important features of nonlinear oscillations which are *not* amenable to straightforward analysis by perturbation methods. Following the work of Poincaré and Birkhoff, neither of whom are referenced in this book, Smale showed in the early 60's that the two-dimensional (Poincaré) map associated with a forced oscillator might be expected to contain infinite sets of recurrent periodic and *nonperiodic* motions. Cartwright, Littlewood, and Levinson [1] had already found such motions in the forced van der Pol equation, but Smale provided the first coherent geometrical description [2]. Recently Levi [3] has extended this in detailed studies of forced van der Pol type relaxation oscillations, and the forced Duffing equation:

$$\ddot{x} - x + x^3 = \epsilon(f \cos wt - \delta\dot{x}), \quad \epsilon \ll 1,$$

has also been studied [4]. In both cases, and in the weakly nonlinear Duffing equation:

$$\ddot{x} + \omega_0{}^2 x = \epsilon(-\alpha x^3 + \gamma \cos \Omega t), \quad \Omega \approx \omega_0, \epsilon \ll 1,$$

it can be shown that infinitely many bounded nonperiodic orbits and periodic orbits of arbitrarily high period exist. These orbits are densely intertwined in such a way that the system can exhibit extremely sensitive dependence on initial conditions and can also exhibit sustained, nonperiodic or *chaotic* oscillations. Ueda and Hayashi had produced dramatic analog computer maps of such motions as early as 1973 [5].

These chaotic motions are unobtainable directly by perturbation or averaging analyses, although their presence can be inferred by careful use of those techniques. Any future text on nonlinear oscillations which hopes to provide a comprehensive coverage should not ignore such deterministic chaos.

References

1 Levinson, N., "A Second-Order Differential Equation With Singular Solutions," *Ann Math*, Vol. 50 (1), 1949, pp. 127–153.

2 Smale, S., "Differentiable Dynamical Systems," *Bull. Amer. Math. Soc.*, Vol. 73, 1967, pp. 747–817.

3 Levi, M., *Qualitative Analysis of the Periodically Forced Relaxation Oscillations*, PhD thesis, New York University, 1978.

[1] Department of Theoretical and Applied Mechanics, Cornell University, Ithaca, N.Y. 14853.

4 Holmes, P. J., "A Nonlinear Oscillator With a Strange Attractor," *Philosophical Transactions of the Royal Society*, London, Series A, Vol. 292, No. 1394, 1979, pp. 419–448.

5 Ueda, Y., Hayashi, C., and Akamatsu, N., "Computer Simulation of Nonlinear Ordinary Differential Equations and Nonperiodic Oscillations," *Elec. and Comm. in Japan*, Series A, Vol. 56, No. 4, 1973, pp. 27–34.

Vibrations of Elastic Structural Members. By Edward B. Magrab. Sijthoff and Noordhoff, Alphen aan den Rijn, The Netherlands. 1979. Pages 400. Price $60.

REVIEWED BY A. LEISSA[2]

The book is of broader scope than the title implies, for considerable attention is also devoted to general, dynamic response, as well as vibratory response, and to wave propagation. The work is divided into chapters as follows:

I	Some Mathematical Preliminaries; 45 pages.
II	Vibrations of Strings; 27 pages.
III	Vibration of Membranes; 20 pages.
IV	Flexural Vibrations of Beams—Part I: Bernoulli-Euler Theory; 78 pages.
V	Flexural Vibrations of Beams—Part II: Timoshenko Theory; 44 pages.
VI	Vibrations of Plates—Part I: Thin Plate Theory; 58 pages.
VII	Vibrations of Plates—Part II. Mindlin—Timoshenko Theory; 36 pages.
VIII	Vibrations of Shells: General Theory for Shells of Revolution; 17 pages.
IX	Vibrations of Cylindrical Shells; 29 pages.
X	Vibrations of Spherical Shells; 19 pages.

The first chapter presents an excellent discussion of orthogonal functions, a summary of their orthogonality properties and how they may be determined and utilized, as well as other mathematical topics frequently referred to later in the book. Subsequent chapters are typically each further divided into sections dealing with (and in this order): derivation of the governing differential equation and boundary conditions (from Hamilton's principle); interpretation of the boundary conditions; boundary conditions and generation of normal modes; wave propagation and dispersion; free vibrations for certain classical problems; and forced and aperiodic motion.

Although no homework problems are given, the reviewer would definitely recommend the book for a first, graduate level course in dynamics of continuous, elastic systems, as well as to the reader desiring otherwise to broaden the scope of his/her understanding of the subject. The work is carefully done, and adequate reference to the voluminous literature of the field is given.

Numerical Methods in Fluid Dynamics. Edited by H. J. Wirz and J. J. Smolderen. McGraw-Hill Book Co., Hightstown, N. J. 1979. Pages xiii-399. Price $35.

REVIEWED BY E. M. MURMAN[3]

This book is a publication of six lectures presented at the von Karman Institute. Each lecture was given by a noted authority in the field and represents an up-to-date description of the topic. The editing and printing of the book is of high quality.

Three of the chapters are on various aspects of transonic flow computations. A chapter by Jameson presents an excellent article on the computation of steady transonic flow problems. Starting from the small disturbance equation, the numerical methods are developed for the exact potential equation. Results for two and three-dimensional flows are presented. The chapter by Ballhaus summarizes recent progress in the computation of transonic flow for three-dimensional shapes using the small disturbance theory and for unsteady transonic flow. Several design applications using numerical optimization are also presented. The chapter by Schmidt focuses on various approaches for computing wing body problems of interest to the aerodynamic designer.

A chapter by Kraus discusses panel methods and illustrates the degree of complexity in the geometrical problems which can now be computed. A section is included on nonlinear vortex wake methods.

Two chapters deal with computing viscous flows. At one end of the spectrum, incompressible laminar flows occurring in physiological problems are discussed by Mueller. The complicated geometries which must be treated are of primary concern in this work. Mueller notes that for this speed regime, numerical computations are perhaps easier than experiments. The other chapter by Belotserkovskii summarizes several areas of high speed viscous flow.

In summary the book appears to be a valuable addition to the archival literature in this area.

High Velocity Deformation of Solids. Edited by K. Kawata and J. Shioiri. Springer-Verlag, Berlin, Heidelberg, New York. 1978. Pages xviii-452. Price $42.90.

REVIEWED BY T. NICHOLAS[4]

The high velocity deformation of solids has been the subject of periodic national and international conferences and symposia over the past several decades. The most recent symposium in this specialized technical area was held in Tokyo, Japan, in Aug. 1977. The papers presented at this IUTAM sponsored symposium are presented in a single volume and cover the subjects of theory and experiment, micro, and macromechanisms, and applications to a variety of materials. The emphasis, throughout, is on material behavior rather than on structural response. Works from a number of different countries are represented and provide a global view of the state-of-the-art in this subject area. As such, the subject book is one of the premiere references in the field of impact mechanics. For the U.S.A. audience, it is one of the rare opportunities to learn of the extent and nature of work being carried out in the host country, Japan, as well as Great Britain, France, USSR, Poland, and other countries. These works are normally not readily available to the English speaking audience.

The book consists of 39 papers ranging in size from 4 one page summaries to a comprehensive treatment of ricochet of spherical ended projectiles by Johnson and Daneshi. Drucker presents a clever approximate solution to spall and cratering problems that are otherwise mathematically intractable. There is a detailed study of friction and inertia in the Hopkinson bar by Klepaczko and Malinowski. Hayashi and Tanimoto present some interesting dynamic biaxial data on aluminum. And Lindholm discusses deformation maps at high dislocation velocity. In total, 24 of the papers represent invited presentations by experts from around the world. Space limitations preclude extensive detail in most papers and necessitate very small figures in some instances. However, this collection of papers is extremely comprehensive in scope and represents the works of the top people both here and abroad as a scan of the table of contents will quickly

---

[2] Professor of Engineering Mechanics, Ohio State University, Columbus, Ohio 43210.

[3] Vice President, General Manager, Flow Research Company, 21414 68th Avenue South, Kent, Wash. 98031.

[4] U.S. Air Force, Air Force Materials Laboratory, Wright Patterson AFB, Ohio 45433.

4 Holmes, P. J., "A Nonlinear Oscillator With a Strange Attractor," *Philosophical Transactions of the Royal Society*, London, Series A, Vol. 292, No. 1394, 1979, pp. 419–448.

5 Ueda, Y., Hayashi, C., and Akamatsu, N., "Computer Simulation of Nonlinear Ordinary Differential Equations and Nonperiodic Oscillations," *Elec. and Comm. in Japan*, Series A, Vol. 56, No. 4, 1973, pp. 27–34.

Vibrations of Elastic Structural Members. By Edward B. Magrab. Sijthoff and Noordhoff, Alphen aan den Rijn, The Netherlands. 1979. Pages 400. Price $60.

REVIEWED BY A. LEISSA[2]

The book is of broader scope than the title implies, for considerable attention is also devoted to general, dynamic response, as well as vibratory response, and to wave propagation. The work is divided into chapters as follows:

I	Some Mathematical Preliminaries; 45 pages.
II	Vibrations of Strings; 27 pages.
III	Vibration of Membranes; 20 pages.
IV	Flexural Vibrations of Beams—Part I: Bernoulli-Euler Theory; 78 pages.
V	Flexural Vibrations of Beams—Part II: Timoshenko Theory; 44 pages.
VI	Vibrations of Plates—Part I: Thin Plate Theory; 58 pages.
VII	Vibrations of Plates—Part II. Mindlin—Timoshenko Theory; 36 pages.
VIII	Vibrations of Shells: General Theory for Shells of Revolution; 17 pages.
IX	Vibrations of Cylindrical Shells; 29 pages.
X	Vibrations of Spherical Shells; 19 pages.

The first chapter presents an excellent discussion of orthogonal functions, a summary of their orthogonality properties and how they may be determined and utilized, as well as other mathematical topics frequently referred to later in the book. Subsequent chapters are typically each further divided into sections dealing with (and in this order): derivation of the governing differential equation and boundary conditions (from Hamilton's principle); interpretation of the boundary conditions; boundary conditions and generation of normal modes; wave propagation and dispersion; free vibrations for certain classical problems; and forced and aperiodic motion.

Although no homework problems are given, the reviewer would definitely recommend the book for a first, graduate level course in dynamics of continuous, elastic systems, as well as to the reader desiring otherwise to broaden the scope of his/her understanding of the subject. The work is carefully done, and adequate reference to the voluminous literature of the field is given.

Numerical Methods in Fluid Dynamics. Edited by H. J. Wirz and J. J. Smolderen. McGraw-Hill Book Co., Hightstown, N. J. 1979. Pages xiii-399. Price $35.

REVIEWED BY E. M. MURMAN[3]

This book is a publication of six lectures presented at the von Karman Institute. Each lecture was given by a noted authority in the field and represents an up-to-date description of the topic. The editing and printing of the book is of high quality.

Three of the chapters are on various aspects of transonic flow computations. A chapter by Jameson presents an excellent article on the computation of steady transonic flow problems. Starting from the small disturbance equation, the numerical methods are developed for the exact potential equation. Results for two and three-dimensional flows are presented. The chapter by Ballhaus summarizes recent progress in the computation of transonic flow for three-dimensional shapes using the small disturbance theory and for unsteady transonic flow. Several design applications using numerical optimization are also presented. The chapter by Schmidt focuses on various approaches for computing wing body problems of interest to the aerodynamic designer.

A chapter by Kraus discusses panel methods and illustrates the degree of complexity in the geometrical problems which can now be computed. A section is included on nonlinear vortex wake methods.

Two chapters deal with computing viscous flows. At one end of the spectrum, incompressible laminar flows occurring in physiological problems are discussed by Mueller. The complicated geometries which must be treated are of primary concern in this work. Mueller notes that for this speed regime, numerical computations are perhaps easier than experiments. The other chapter by Belotserkovskii summarizes several areas of high speed viscous flow.

In summary the book appears to be a valuable addition to the archival literature in this area.

High Velocity Deformation of Solids. Edited by K. Kawata and J. Shioiri. Springer-Verlag, Berlin, Heidelberg, New York. 1978. Pages xviii-452. Price $42.90.

REVIEWED BY T. NICHOLAS[4]

The high velocity deformation of solids has been the subject of periodic national and international conferences and symposia over the past several decades. The most recent symposium in this specialized technical area was held in Tokyo, Japan, in Aug. 1977. The papers presented at this IUTAM sponsored symposium are presented in a single volume and cover the subjects of theory and experiment, micro, and macromechanisms, and applications to a variety of materials. The emphasis, throughout, is on material behavior rather than on structural response. Works from a number of different countries are represented and provide a global view of the state-of-the-art in this subject area. As such, the subject book is one of the premiere references in the field of impact mechanics. For the U.S.A. audience, it is one of the rare opportunities to learn of the extent and nature of work being carried out in the host country, Japan, as well as Great Britain, France, USSR, Poland, and other countries. These works are normally not readily available to the English speaking audience.

The book consists of 39 papers ranging in size from 4 one page summaries to a comprehensive treatment of ricochet of spherical ended projectiles by Johnson and Daneshi. Drucker presents a clever approximate solution to spall and cratering problems that are otherwise mathematically intractable. There is a detailed study of friction and inertia in the Hopkinson bar by Klepaczko and Malinowski. Hayashi and Tanimoto present some interesting dynamic biaxial data on aluminum. And Lindholm discusses deformation maps at high dislocation velocity. In total, 24 of the papers represent invited presentations by experts from around the world. Space limitations preclude extensive detail in most papers and necessitate very small figures in some instances. However, this collection of papers is extremely comprehensive in scope and represents the works of the top people both here and abroad as a scan of the table of contents will quickly

---

[2] Professor of Engineering Mechanics, Ohio State University, Columbus, Ohio 43210.

[3] Vice President, General Manager, Flow Research Company, 21414 68th Avenue South, Kent, Wash. 98031.

[4] U.S. Air Force, Air Force Materials Laboratory, Wright Patterson AFB, Ohio 45433.

ERRATUM

Erratum on "Amplitude-Frequency Characteristics of Large-Amplitude Vibrations of Sandwich Plates," B. M. Karmakar, published in the March, 1979, issue of the ASME JOURNAL OF APPLIED MECHANICS, Vol. 46, pp. 230–231.

The first line in the Introduction of the foregoing Note should read:

Yu [1] has treated nonlinear vibrations of sandwich plates and the equations derived by him include the transverse shear effect.

The next to the last line in the section, "Results and Discussion," should read:

The present study shows that Berger's approximate method can be applied to dynamic cases of sandwich plates.